In Vivo Cryotechnique in Biomedical Research and Application for Bioimaging of Living Animal Organs

Shinichi Ohno
Nobuhiko Ohno
Nobuo Terada
Editors

Springer

In Vivo Cryotechnique in Biomedical Research and Application for Bioimaging of Living Animal Organs

Shinichi Ohno • Nobuhiko Ohno
Nobuo Terada
Editors

In Vivo Cryotechnique in Biomedical Research and Application for Bioimaging of Living Animal Organs

Springer

Editors
Shinichi Ohno
Department of Anatomy and Molecular Histology
Interdisciplinary Graduate School of Medicine and Engineering
University of Yamanashi
Yamanashi, Japan

Nobuhiko Ohno
Department of Anatomy and Molecular Histology
Interdisciplinary Graduate School of Medicine and Engineering
University of Yamanashi
Yamanashi, Japan

Nobuo Terada
Division of Health Sciences
Shinshu University Graduate School of Medicine
Nagano, Japan

Department of Anatomy and Molecular Histology
Interdisciplinary Graduate School of Medicine and Engineering
University of Yamanashi
Yamanashi, Japan

ISBN 978-4-431-55722-7 ISBN 978-4-431-55723-4 (eBook)
DOI 10.1007/978-4-431-55723-4

Library of Congress Control Number: 2015952637

Springer Tokyo Heidelberg New York Dordrecht London

Printed on acid-free paper

Springer Japan KK is part of Springer Science+Business Media (www.springer.com)

Preface

We medical and biological scientists want to know the real in vivo morphology and also the immunolocalizations of all molecular components in functioning cells and tissues of living animal organs; we need the "living animal morphology," not the dead (nor conventionally prepared with fixatives) animal one. Recently, the live imaging of cells and tissues of animals with fluorescence-labeled proteins by gene manipulation has become increasingly popular in biological fields. For those reasons, we should now examine the histological or immunohistochemical tissue sections of living animal organs which must be exactly compatible with their live imaging, usually clarified by recently developed digital imaging techniques.

In our opinion, the already developed immunohistochemical or morphological research performed by in vivo cryotechnique (IVCT) depends exclusively on functioning cells and tissues of living animal organs, so it is now necessary to publish a new, innovative book, reviewing especially the real morphofunctional findings in vivo of cells and tissues of living animal organs. However, until now there has been no such book about living animal morphology on permanent tissue section preparations corresponding to the digital live imaging of fluorescence-labeled soluble or structural molecules.

In the past few decades, we have developed an original IVCT to capture the dynamically changing morphology and immunolocalizations of signal molecules and receptors of cells and tissues in addition to detecting soluble probes of living animal organs, reported in more than 60 biomedical papers in the last 20 years. Therefore, the publication of such an innovative review focusing on our research field is both significant and timely.

We hope that this volume will provide many readers with a good opportunity to learn about IVCT, including cryobiopsy, for their future studies. Finally, we are grateful to all the authors who have contributed to this publication.

Yamanashi, Japan — Shinichi Ohno
Yamanashi, Japan — Nobuhiko Ohno
Nagano, Japan — Nobuo Terada

Contents

Part I
Overview

Introduction

1

Shinichi Ohno

Abstract

Morphological studies with light or electron microscopy and scanning probe microscopy have been major approaches to understand physiological and pathological features of living animal organs. Although other rapid progresses of research techniques in molecular or genetic biology have been realized to establish new molecular or biological fields, morphological techniques are still necessary for more precise understanding of living animal organs. For routine morphological analyses, both chemical fixation and alcohol dehydration have been commonly used to keep cells and tissues, but they always bring about many morphological artifacts, including tissue shrinkage and extraction of components. To the contrary, both quick-freezing and high-pressure freezing methods of resected fresh tissues have been also contributed to reduction of such morphological artifacts, but they have to be resected from living animal organs with blood supply. The in vivo cryotechnique (IVCT) has been found to be extremely useful to arrest transient physiological processes of cells and tissues and also to maintain their intra- and extracellular components in situ. The IVCT has already allowed us to perform novel morphological investigations of cells and tissues in living animal organs and will further contribute to new medical and biological fields with "living animal morphology."

Keywords

Microscopy • Conventional fixation • Quick-freezing • In vivo cryotechnique • Soluble components

The morphological study with light or electron microscopy in addition to scanning probe microscopy has been one of the major approaches to understand physiological and pathological features of living animal organs in medical and biological fields. Especially, the conventional electron microscopy, developed in the last half of the twentieth century, greatly facilitated the enormous progress of ultrastructural analyses of cells and tissues, which has been now indispensable in morphological field with many applications. Although other rapid progresses of research techniques in molecular or genetic biology have been realized to establish new molecular or biological fields in the past few decades, various morphological techniques are still necessary for more precise understanding of cells and tissues in living animal organs. In such approach cases, their obtained structures should always reflect some functional aspects of the living animal organs.

For the routine morphological analyses, both chemical fixation and alcohol dehydration have been commonly used as easy preparation procedures to keep cells and tissues, but they always bring about many morphological artifacts, including tissue shrinkage and extraction of components, of dynamically changing organs in vivo (Fig. 1.1a, b) [1–3]. To

S. Ohno (✉)
Department of Anatomy and Molecular Histology,
Interdisciplinary Graduate School of Medicine and Engineering,
University of Yamanashi, 1110 Shimokato, Chuo City,
Yamanashi 409-3898, Japan
e-mail: sohno@yamanashi.ac.jp

S. Ohno et al. (eds.), *In Vivo Cryotechnique in Biomedical Research and Application for Bioimaging of Living Animal Organs*, DOI 10.1007/978-4-431-55723-4_1

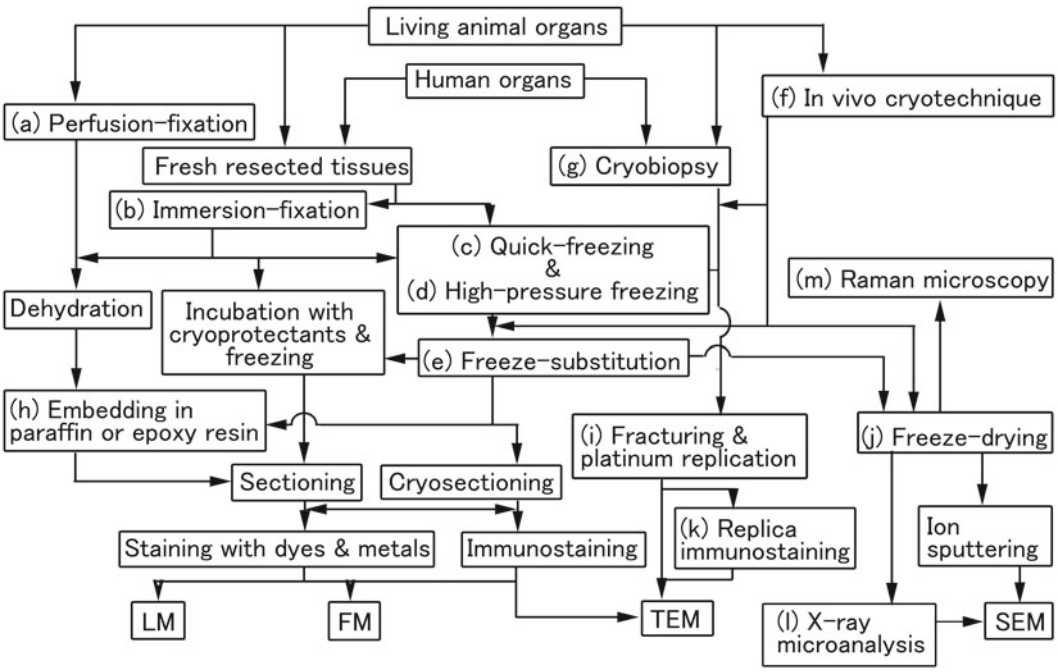

Fig. 1.1 A flowchart of various preparation steps for light microscopy (*LM*), fluorescence microscopy (*FM*), transmission electron microscopy (*TEM*), and scanning electron microscopy (*SEM*). The perfusion- (**a**) or immersion- (**b**) fixation and dehydration steps, the quick-freezing (**c**) and high-pressure freezing (**d**) methods, and the "in vivo cryotechnique" (**f**) are described with connection with their following preparation steps. Note that all preparation steps, following the quick-freezing and high-pressure freezing methods, are also available after the "in vivo cryotechnique" (**f**). To apply the "in vivo cryotechnique" to human organs, a new cryotechnique of biopsy, termed as "cryobiopsy" (**g**), would be necessary, as described in the new cryobiopsy chapter

the contrary, both conventional quick-freezing and high-pressure freezing methods of resected fresh organ tissues, by which they are quickly frozen for physical fixation, can be also contributed to reduction of such morphological artifacts (Fig. 1.1c, d) [4, 5], but they have to be resected from living animal organs with blood supply for the freezing. Therefore, those animal specimens are inevitably exposed to stresses of ischemia and anoxia, exhibiting only dead morphological states of animal organ tissues without normal blood circulation. For the past years, the original "in vivo cryotechnique" was also developed to demonstrate new dynamically changing morphology and immunolocalizations of functional proteins in cells and tissues at light or electron microscopic levels (Fig. 1.1f) and clarify morphofunctional significance of cells and tissues in living animal organs [6–8], as described in the next paragraph.

As everyone knows, the final goal of morphological and immunohistochemical studies in our biological or medical fields is that all findings examined in animal experiments should reflect the physiologically functional background. Therefore, the preservation of all original components in targeted cells and tissues of animals is necessary for describing the functional morphology of living animal organs. It has been generally accepted that morphological findings of various animal organs were easily modified by stopping their blood supply, because of ischemia or anoxia. There had been a need to develop a new preparation technique for freezing the living animal organs in vivo and then obtaining their acceptable morphology and also immunolocalizations of original soluble components in functioning cells and tissues. We have already developed the "in vivo cryotechnique" (IVCT) not only for their morphology, but also for immunohistochemistry of many soluble components in various living animal organs [6–9]. All physiological processes of them were immediately immobilized in the vitreous ice by IVCT, and every component in the cells and tissues was maintained in situ at the time of freezing. Thus, the ischemic or anoxic artificial effects on them could be minimized by the newly developed IVCT. Our specially designed liquid cryogen system with or without a cryoknife has totally solved the morphological and immunohistochemical problems which are inevitable by the conventional preparation methods at a light or electron microscopic level [6, 8]. The IVCT has been found to be extremely useful to arrest transient physiological processes of cells and tissues and also to maintain their intra- and extracellular components in situ, such as rapidly changing signal molecules, membrane channels, and receptors, as described before [8, 9].

As described above, the IVCT has already allowed us to perform novel morphological investigations of cells and tissues in living animal organs and will further contribute to new medical and biological fields with "living animal mor-

phology" during the present twenty-first century. Therefore, the purpose of the present review book is to describe the basic mechanism of cryotechniques and significant cryotechnical meanings of IVCT and additionally review new morphological and immunohistochemical findings in addition to fluorescence-labeled probes in the biological and medical fields. Then, some previous reviews or original papers are also cited in the references, considering the significance of IVCT in this book.

References

1. Furukawa T, Ohno S, Oguchi H, Hora K, Tokunaga S, Furuta S (1991) Morphometric study of glomerular slit diaphragms fixed by rapid-freezing and freeze-substitution. Kidney Int 40:621–624
2. Yoshimura A, Ohno S, Nakano K, Oniki H, Inui K, Ideura T, Koshikawa S (1991) Three-dimensional ultrastructure of anionic sites of the glomerular basement membrane by a quick-freezing and deep-etching method using a cationic tracer. Histochemistry 96:107–113
3. Ohno S, Hora K, Furukawa T, Oguchi H (1992) Ultrastructural study of the glomerular slit diaphragm in fresh unfixed kidneys by a quick-freezing method. Virchows Arch B Cell Pathol 61:351–358
4. Yu Y, Leng CG, Kato Y, Ohno S (1997) Ultrastructural study of glomerular capillary loops at different perfusion pressures as revealed by quick-freezing, freeze-substitution and conventional fixation methods. Nephron 76:452–459
5. Yu Y, Leng CG, Kato Y, Terada N, Fujii Y, Ohno S (1998) Ultrastructural study of anionic sites in glomerular basement membranes at different perfusion pressures by quick-freezing and deep-etching method. Nephron 78:88–95
6. Ohno S, Terada N, Fujii Y, Ueda H, Takayama I (1996) Dynamic structure of glomerular capillary loop as revealed by an in vivo cryotechnique. Virchows Arch 427:519–527
7. Ohno S, Baba T, Terada N, Fujii Y, Ueda H (1996) Cell biology of kidney glomerulus. Int Rev Cytol 166:181–230
8. Ohno N, Terada N, Fujii Y, Baba T, Ohno S (2004) "In vivo cryotechnique" for paradigm shift to "living morphology" of animal organs. Biomed Rev 15:1–19
9. Terada N, Ohno N, Li Z, Fujii Y, Baba T, Ohno S (2006) Application of in vivo cryotechnique to the examination of cells and tissues in living animal organs. Histol Histopathol 21:265–272

Biomedical Significance and Development of "IVCT"

2

Shinichi Ohno

Abstract

Preparation procedures after resection of animal tissues are commonly a series of chemical fixation, alcohol dehydration, paraffin or epoxy resin embedding, thick or thin sectioning, and dye or metal staining steps. During such preparation steps, various kinds of inevitable artifacts always modify their original morphology. Some problems are both molecular movement and structural changes of cells and tissues during the fixation time. Another problem is that dynamic morphological images in vivo are difficult to be captured by the conventional chemical fixation. Then, a strong effort of morphologists has been made to avoid such technical artifacts during the conventional preparation steps. The quick-freezing (QF) method was introduced for biological specimens at the middle of the twentieth century. For the final morphological purpose, various preparation procedures can be chosen after the quick-freezing. One of them is freeze-substitution (FS) fixation, in which the frozen specimens are usually incubated in cooled organic solvents containing chemical fixatives at about −80 °C. However, the freeze-substituted specimens are known to be affected to some extent by the organic solvents. Another deep-etching (DE) replication method has been developed, in which replica membranes of freeze-fractured and deeply etched tissues are obtained by rotary-shadowing with platinum metal at lower temperatures below −100 °C under high vacuum conditions. However, some pieces of tissues have to be always resected and taken out from living animal organs. Thus, the dynamically changing morphology of living animal organs is hardly investigated by the conventional QF method. To overcome these technical problems, it is necessary to avoid the tissue resection step of living animal organs and directly freeze them in vivo under normal blood circulation. The IVCT was an original technique to directly cryofix living animal organs without separating their tissues from blood circulation. The most significant point of IVCT is that normal blood circulation into living animal organs is strictly preserved at the exact moment of freezing.

Keywords

Tissue shrinkage • Quick-freezing • Freeze-substitution • Deep-etching

S. Ohno (✉)
Department of Anatomy and Molecular Histology,
Interdisciplinary Graduate School of Medicine and Engineering,
University of Yamanashi, 1110 Shimokato, Chuo City,
Yamanashi 409-3898, Japan
e-mail: sohno@yamanashi.ac.jp

S. Ohno et al. (eds.), *In Vivo Cryotechnique in Biomedical Research and Application for Bioimaging of Living Animal Organs*, DOI 10.1007/978-4-431-55723-4_2

2.1 Inevitable Problems with Conventional Preparation Techniques

In most morphological studies of living animal organs, several preparation procedures after the resection of their tissues are commonly a series of chemical fixation, alcohol dehydration, paraffin or epoxy resin embedding, thick or thin sectioning, and dye or metal staining steps, followed by final observation with a light or electron microscope (Fig. 1.1a, b). During such preparation steps, various kinds of inevitable technical artifacts always modify their original morphology, especially owing to the conventional fixation and dehydration steps [1–6]. The first routine fixation is usually performed with common chemical fixatives, such as paraformaldehyde, glutaraldehyde, and osmium tetroxide for light or electron microscopy. However, some technical problems have already been pointed out about the first chemical fixation step [4]. One of the problems is both molecular movement and structural changes of cells and tissues easily happening during the fixation time. For example, small or large soluble components, such as proteins, lipids, and carbohydrates, are easily translocated in the cells and tissues before the cross-linking effect of chemical fixatives. Another problem is that dynamic morphological images in vivo of cells and tissues, such as muscle contraction and bloodflow, are difficult to be captured by the conventional chemical fixation [4], because some of time intervals are always necessary to complete the molecular cross-linking with the chemical fixatives.

There are also other technical problems during the following preparation steps, such as alcohol dehydration and routinely embedding in paraffin wax or epoxy resin at high temperatures. It has been well known that the common alcohol dehydration easily causes shrinkage of resected tissue blocks. In the case of final embedding in epoxy resin for electron microscopy, the common polymerization step usually needs heating up at 35°, 45°, and 60 °C for 12 h each, which might cause additional heat effects on dehydrated biological specimens. Even during the routine observation in an electron microscope, ultrathin sections stained with uranium and lead metals have to be put into highly vacuumed chambers and undergo the heating damage at more than 100 °C induced by accelerating electron beams. Although the conventional preparation techniques had such several artificial problems about preservation of cells and tissues, many ultrastructural studies have already yielded important morphofunctional findings during the last twentieth century and also extremely contributed to academic achievement in biological and medical fields. To the contrary, a strong effort of morphologists has been made to avoid such technical artifacts during the conventional preparation steps for electron or light microscopy. For that purpose, the quick-freezingmethod was introduced for biological specimens at the middle of the twentieth century and dramatically improved during the late twentieth century, resulting in development of high-pressure freezing especially at an electron microscopic level.

2.2 Quick-Freezing (QF) Method for Resected Fresh Tissues

The QF method is one of the physical cryofixation techniques, by which resected biological specimens from animal organs are not chemically fixed, but quickly embedded in vitrified ice crystals as soon as possible (Fig. 1.1c). The term "vitrification" usually means the ice formation without any visible ice crystals at an electron microscopic level, which could often destroy ultrastructures of cells and tissues at lower speeds of freezing. In the case of resected fresh animal tissues without cryoprotectants, their well-freezing condition has to be obtained either at very high cooling rate (usually more than 10^5°C/s) or under very high pressures (a few thousand times higher than atmospheric pressure). For the last few decades, various kinds of QF methods have been developed for that purpose. By the "slamming QF" method, resected fresh animal tissues are usually slammed onto copper blocks cooled down in liquid helium (−269 °C) or liquid nitrogen (−196 °C). Another "plunging QF" method is to plunge them into liquid cryogens, such as propane alone or isopentane–propane mixture (−193 °C) cooled in liquid nitrogen. The two QF methods fortunately prevent formation of detectable ice crystals in tissue areas less than 10 μm deep from the contacted tissue surface onto cooled copper metals or cryogens. To the contrary, another later developed high-pressure freezing is a little different method from the QF methods (Fig. 1.1d), because it is always performed under very high pressures to achieve the vitrification in relatively broad tissue areas.

For the final morphological purpose, various preparation procedures can be chosen after the quick-freezing (Fig. 1.1c) and also high-pressure freezing methods (Fig. 1.1d). One of them is freeze-substitution (FS) fixation (Fig. 1.1e), in which the frozen specimens are usually incubated in cooled organic solvents containing chemical fixatives, such as osmium tetroxide, glutaraldehyde, and paraformaldehyde, at about −80 °C [7–9]. After the FS fixation, they are commonly embedded in epoxy resin, paraffin wax, or other hydrophilic materials for the next polymerization and sectioning steps (Fig. 1.1h). However, the freeze-substituted specimens are known to be affected to some extent by the organic solvents and such chemical fixatives during the substitution time. To solve such an FS problem, another deep-etching (DE) replication method has been already developed, in which replica membranes of freeze-fractured and deeply etched tissues are obtained by rotary-shadowing with platinum metal and

carbon at lower temperatures below −100 °C under high vacuum conditions (Fig. 1.1i). Therefore, the QF-DE method is now considered to prevent the ultrastructural artifacts as induced by the organic solvents of the FS method.

As described above, one merit of the QF method is better preservation of intra- or extracellular materials with fewer morphological artifacts [2, 3, 10, 11], which was often used for obtaining new ultrastructural findings for the past few decades. However, no matter what kinds of cryotechniques are used for the physical cryofixation, some pieces of tissues have to be always resected and taken out from living animal organs for the next freezing step. It is often pointed out that their morphology should be inevitably changed during the preparation steps, because of ischemia and anoxia. Thus, the dynamically changing morphology of living animal organs, depending on various blood pressures, is hardly investigated by the conventional QF or high-pressure freezing method [12, 13]. Furthermore, immunohistochemical analyses of changing receptors, membrane channels or signal molecules, would be more difficult to perform in the specimens prepared by the conventional cryotechniques. To overcome these technical problems, it is necessary to avoid the tissue resection step of living animal organs and directly freeze them in vivo under normal blood circulation. Although a few pioneering studies with cryotechniques were introduced for solving the technical problems of ischemia and anoxia, it was still difficult to establish a new cryotechnique until the developing time of IVCT, which could constantly yield satisfactory morphology in vivo of living animal organs.

2.3 Development of In Vivo Cryotechnique (IVCT)

The newly developed IVCT at the years of 1994–1996 was an original technique to directly cryofix living animal organs without separating their tissues from blood circulation (Fig. 1.1f) [12]. Briefly, after exposing the living animal organs under anesthesia, it is quickly performed by cutting them with a cryoknife precooled in liquid nitrogen (−196 °C) and simultaneously pouring the isopentane–propane cryogen (−193 °C) over them, being followed with liquid nitrogen, under a newly developed "in vivo cryoapparatus" (Fig. 2.1)

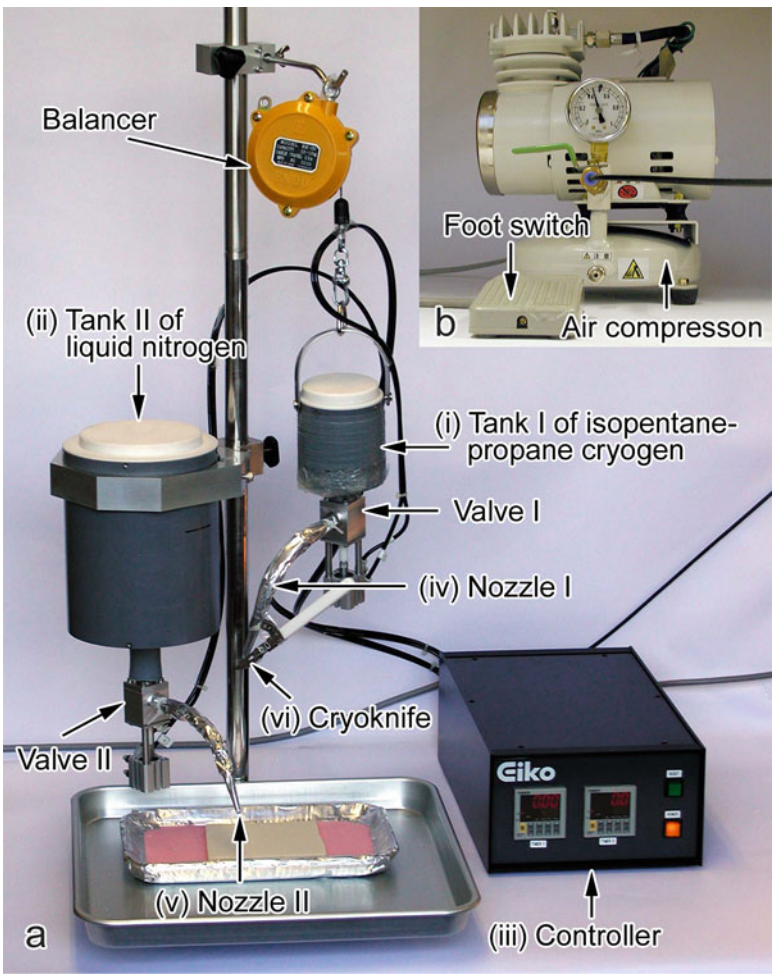

Fig. 2.1 Photographs of the newly developed "in vivo cryoapparatus." (**a**) The main part of the apparatus set up on a table. (**b**) Another system operating the valves controlling IP cryogen or liquid nitrogen release is placed under the table. As a target organ is cut with the cryoknife (*vi*), the isopentane–propane (*IP*) cryogen in tank 1 is immediately poured through nozzle 1 onto it. Then liquid nitrogen (−196 °C) is poured through nozzle 2 from tank 2 (*ii*). The opening time of valves 1 and 2 started by pushing the foot switch (**b**) is automatically regulated by the controller (**a**, *iii*) with the support of the air compressor (**b**)

[13]. By combination of the cryoknife with the liquid cryogen, good vitrification of frozen tissues in vivo can be obtained within several micrometers deep from the cryocut tissue surface at an electron microscopic level [12]. Additionally, at a light microscopic level, the good tissue areas without detectable ice crystals are deeper than a few hundreds of micrometers from the cryocut tissue surface because the common spatial resolution of the light microscope is much lower to detect tiny ice crystals of cells and tissues caused by slow freezing speeds [5, 6]. The most significant point of IVCT is that normal blood circulation into living animal organs is strictly preserved at the exact moment of freezing. So it becomes possible to immediately cryofix all cells and tissues of living animal organs with fewer technical artifacts always caused by either ischemia or anoxia. Therefore, we can now examine extra- and intracellular structures and molecular distributions in the dynamic "living" states of animals, which were hardly detected by other conventional cryotechniques.

References

1. Furukawa T, Ohno S, Oguchi H, Hora K, Tokunaga S, Furuta S (1991) Morphometric study of glomerular slit diaphragms fixed by rapid-freezing and freeze-substitution. Kidney Int 40:621–624
2. Yoshimura A, Ohno S, Nakano K, Oniki H, Inui K, Ideura T, Koshikawa S (1991) Three-dimensional ultrastructure of anionic sites of the glomerular basement membrane by a quick-freezing and deep-etching method using a cationic tracer. Histochemistry 96:107–113
3. Ohno S, Hora K, Furukawa T, Oguchi H (1992) Ultrastructural study of the glomerular slit diaphragm in fresh unfixed kidneys by a quick-freezing method. Virchows Arch B Cell Pathol 61:351–358
4. Terada N, Ohno S (2004) Immunohistochemical application of cryotechniques to native morphology of cells and tissues. Acta Histochem Cytochem 37:339–345
5. Zea-Aragon A, Terada N, Ohno N, Fujii Y, Baba T, Ohno S (2004) Effects of anoxia on serum immunoglobulin and albumin leakage through blood–brain barrier in mouse cerebellum as revealed by cryotechniques. J Neurosci Methods 138:89–95
6. Ohno N, Terada N, Murata S, Katoh R, Ohno S (2005) Application of cryotechniques with freeze-substitution for the immunohistochemical demonstration of intranuclear pCREB and chromosome territory. J Histochem Cytochem 53:55–62
7. van Harreveld A, Trubatch J (1975) Synaptic changes in frog brain after stimulation with potassium chloride. J Neurocytol 4:33–46
8. Jehl B, Bauer R, Dorge A, Rick R (1981) The use of propane/isopentane mixtures for rapid freezing of biological specimens. J Microsc 123:307–309
9. Cole R, Matuszek G, See C, Rieder CL (1990) A simple pneumatic device for plunge-freezing cells grown on electron microscopy grids. J Electron Microsc Tech 16:167–173
10. Yu Y, Leng CG, Kato Y, Ohno S (1997) Ultrastructural study of glomerular capillary loops at different perfusion pressures as revealed by quick-freezing, freeze-substitution and conventional fixation methods. Nephron 76:452–459
11. Yu Y, Leng CG, Kato Y, Terada N, Fujii Y, Ohno S (1998) Ultrastructural study of anionic sites in glomerular basement membranes at different perfusion pressures by quick-freezing and deep-etching method. Nephron 78:88–95
12. Ohno S, Terada N, Fujii Y, Ueda H, Takayama I (1996) Dynamic structure of glomerular capillary loop as revealed by an in vivo cryotechnique. Virchows Arch 427:519–527
13. Ohno N, Terada N, Fujii Y, Baba T, Ohno S (2004) "In vivo cryotechnique" for paradigm shift to "living morphology" of animal organs. Biomed Rev 15:1–19

How to Perform "IVCT"

3

Shinichi Ohno

Abstract

The isopentane-propane (IP) cryogen (−193 °C) was manually poured over exposed animal organs by the original in vivo cryotechnique (IVCT), which were simultaneously cryocut with a precooled cryoknife in liquid nitrogen (−196 °C) with a group of three persons. The in vivo frozen animal organs were cracked off from the animal body in the liquid nitrogen and then plunged into the liquid nitrogen. To perform the IVCT more easily, the "in vivo cryoapparatus" has been commercially available all over the world. The IVCT was originally performed with a handmade "in vivo cryoapparatus." The operation manual about the new "in vivo cryoapparatus" is briefly described in this chapter. When the IVCT is used only for light microscopic observation, it can be more simply performed without any special cryoapparatus. So the simple "in vivo" freezing method is performed only by pouring the IP cryogen (−193 °C) directly onto living animal organs. This simple cryoprocedure usually allows us to make an easy performance of IVCT at a light microscopic level. In the prepared such specimens, good morphological preservation is within less than a few hundred micrometers away from the frozen tissue surface at a light microscopic level. The procedures to prepare the mixed isopentane-propane cryogen were described in this chapter.

Keywords

Isopentane-propane cryogen • In vivo cryoapparatus • Cryoknife

3.1 Introduction

The IVCT has been performed with the already developed "in vivo cryoapparatus" around the year 2000, which will be described in the next paragraph. As the original IVCT in 1994–1996, the isopentane-propane (IP) cryogen (−193 °C) was manually poured over exposed animal organs, which were simultaneously cryocut with a precooled cryoknife in liquid nitrogen (−196 °C) with a group of three persons [1]. After pouring the IP cryogen for several seconds, additionally followed by liquid nitrogen, the in vivo frozen animal organs were cracked off from the animal body in the liquid nitrogen and then plunged into the liquid nitrogen for preservation. Thereafter, some frozen target tissue pieces were taken out with a dental electric drill in the liquid nitrogen. However, a series of the preparation procedures were sometimes difficult for an operator alone to manually perform all the procedures by oneself and constantly obtain well-frozen tissue specimens. To perform the IVCT more easily, the "in vivo cryoapparatus" (EIKO Corporation, Hitachinaka, Ibaraki, Japan) has been commercially available all over the world [2, 3]. The operation manual about the "in vivo cryoapparatus" was described in detail in another paper [2]. After performing IVCT and then removing the frozen

S. Ohno (✉)
Department of Anatomy and Molecular Histology,
Interdisciplinary Graduate School of Medicine and Engineering,
University of Yamanashi, 1110 Shimokato, Chuo City,
Yamanashi 409-3898, Japan
e-mail: sohno@yamanashi.ac.jp

S. Ohno et al. (eds.), *In Vivo Cryotechnique in Biomedical Research and Application for Bioimaging of Living Animal Organs*, DOI 10.1007/978-4-431-55723-4_3

tissues from animal organs, various following preparation steps are usually chosen for each morphological analysis (Fig. 1.1e, i, j, m).

3.2 Practical Procedures of In Vivo Cryoapparatus

The IVCT was originally performed with a handmade "in vivo cryoapparatus" within a group of three persons, which was described before [1]. The operation manual about the new "in vivo cryoapparatus" is briefly described in the next paragraph (Fig. 2.1). Step 1: Pour some amounts of liquid nitrogen into two reservoirs (Fig. 2.1a(i), (ii)) to be cooled down. After the cooling of the reservoirs starts, they should be continuously cooled with liquid nitrogen. If they are temporarily warmed up, some water produced by melting of attached frost covers all parts of the valves. When the reservoirs are cooled down again below zero degree, the valves are completely frozen and immobilized. Step 2: Set timers of the controller (Fig. 2.1a(iii)) and press the foot switch (Fig. 2.1b) to check if the liquid nitrogen in the reservoirs correctly comes through the nozzles (Fig. 2.1a(iv), (v)). This trial is important to prevent machinery accidents. Step 3: Pour the isopentane-propane cryogen into the reservoir (Fig. 2.1a(i)). The cryogen is prepared beforehand by bubbling propane gas in liquid isopentane precooled in liquid nitrogen and always agitated with a magnet stirrer. The ratio of isopentane to propane should be 1:2–1:3 to achieve the maximal cooling ability at about −193 °C [4]. Step 4: Expose a target organ of living animals under anesthesia. Step 5: Set timers of the controller (Fig. 2.1a(iii)), and precool the cryoknife (Fig. 2.1a(vi)) in liquid nitrogen pooled in another container. A piece of sponge is sometimes attached to the cryoknife, to absorb some amounts of liquid nitrogen and keep the cryoknife cooled during transferring over the exposed organ. Step 6: Bring the cooled cryoknife (Fig. 2.1a(vi)) onto the exposed target organ and press the foot switch (Fig. 2.1b). Immediately after pressing, cryocut the animal organ manually with the cryoknife, and then pour the IP cryogen through the nozzle (Fig. 2.1a(iv)), which was already initiated by pressing the foot switch and automatically regulated by the controller. In several seconds after pouring the IP cryogen, liquid nitrogen is also automatically poured onto the frozen organ through another nozzle (Fig. 2.1a(v)). Step 7: Put the frozen organ as a whole in liquid nitrogen and preserve it until removal. Step 8: Get target tissue parts from the frozen organ in the liquid nitrogen by a dental electric drill. After performing IVCT and then removing the frozen tissues, various following preparation steps are chosen for each morphological analysis (Fig. 1.1e, i, j, m).

3.3 IVCT for Light Microscopy

When the IVCT is used only for light microscopic observation, it can be more simply performed without any special cryoapparatus (Fig. 3.1) [5]. In such a case, the strictly freezing level without any visible ice crystal formation is not always necessary for morphological examination, because of lower spatial resolution by light microscopy. So the simple "in vivo" freezing method is performed only by pouring the IP cryogen (-193 °C) directly onto living animal organs (Fig. 3.1) [5]. The pouring time for several seconds should be long enough to obtain well-frozen cells and tissues, because the cooling speed of the cryogen is much faster than liquid nitrogen alone. This simple cryoprocedure usually allows us to make an easy performance of IVCT at a light microscopic level. In the prepared such specimens, good morphological preservation is within less than a few hundred micrometers away from the frozen tissue surface at a light microscopic level. To analyze deeper areas of the frozen tissues, living animal organs must be cut with a cryoknife precooled down in liquid nitrogen [1], as described above, instead of simply pouring the liquid IP cryogen.

3.4 How to Prepare the Mixed Isopentane-Propane Cryogen

Step 1: Hang a 50-ml glass beaker containing a magnetic stirring bar in a Styrofoam box (Fig. 3.2a). Step 2: Place the box on a magnetic stirrer and check that the stirring bar rotates in the beaker (Fig. 3.2b). Step 3: Remove the beaker from the box and fill the box with an appropriate amount of

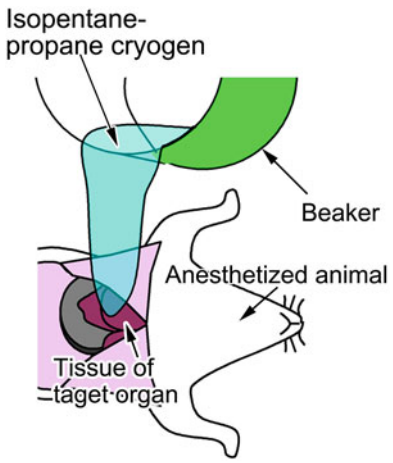

Fig. 3.1 Simple manual IVCT for light microscopy by pouring the isopentane-propane (*IP*) cryogen over targeted organs of anesthetized animals

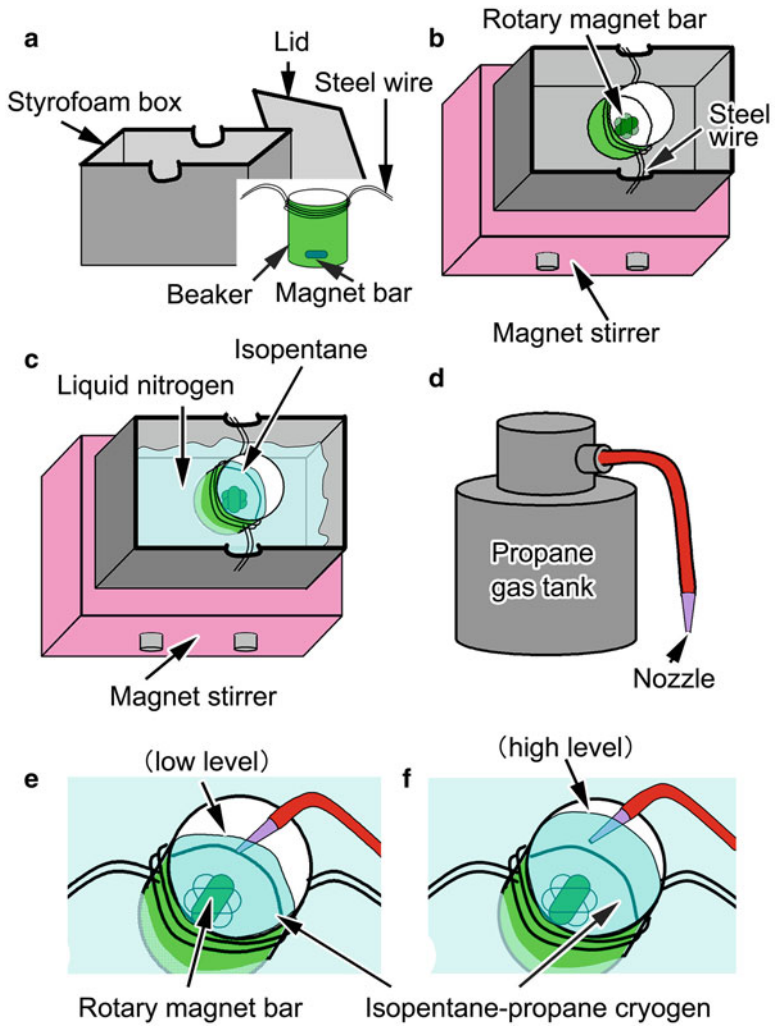

Fig. 3.2 Schematic drawings which show how to prepare the isopentane-propane (*IP*) cryogen in a homemade plunge-freeze apparatus. (**a**) A Styrofoam box with slits to hold the ends of the steel wire wrapped around a 50-ml beaker with the box lid. The beaker contains a magnetic stirring bar. (**b**) The beaker wrapped with the steel wire is hung in the Styrofoam box, which is on a magnetic stirrer, so that the stirring bar can smoothly rotate in the beaker. (**c**) Liquid nitrogen (−196 °C) is poured into the box with the beaker containing about 15 ml of liquid isopentane, which is continuously stirred with the stirring bar. When the bottom side of the beaker becomes submerged in the liquid nitrogen, the liquid nitrogen immediately begins to bubble. The magnetic bar should be continuously stirring the liquid isopentane alone. (**d**) Propane gas is blown out of a nozzle (*arrow*) to be quickly liquefied. (**e**) The propane gas is continuously jetted out of the nozzle into the cooled isopentane where it quickly liquefies, and the mixed IP cryogen level gradually elevates. (**f**) The amount of liquid IP cryogen is reaching to about 45 ml and the release of propane gas from the nozzle is finally stopped

liquid nitrogen so that it will be submerged in liquid nitrogen when the beaker is placed back in the box (Fig. 3.2c). Step 4: Pour 15 ml of liquid isopentane into the beaker at room temperature. Hang the beaker in the box containing the liquid nitrogen and stir the isopentane. The initial extensive bubbling of the liquid nitrogen will decrease as the isopentane cools (Fig. 3.2c). Step 5: When the peripheral part of the isopentane cools almost to the temperature of the liquid nitrogen (−196 °C) and begins to solidify, immediately place the tip of the nozzle from the propane gas tank in the cooled isopentane (Fig. 3.2d) and vigorously blow the propane gas into the cooled isopentane to liquefy the propane gas. Step 6: When the level of isopentane-propane cryogen in the beaker gradually increases, reaching a volume of about 45 ml (Fig. 3.2e, f), a ratio of isopentane to propane with 1:2–1:3, immediately stop the propane gas flow. Step 7: Cover the Styrofoam box to minimize exposure of the prepared isopentane-propane cryogen to humid air.

References

1. Ohno S, Terada N, Fujii Y, Ueda H, Takayama I (1996) Dynamic structure of glomerular capillary loop as revealed by an in vivo cryotechnique. Virchows Arch 427:519–527
2. Ohno N, Terada N, Fujii Y, Baba T, Ohno S (2004) "In vivo cryotechnique" for paradigm shift to "living morphology" of animal organs. Biomed Rev 15:1–19
3. Zea-Aragon A, Terada N, Ohno N, Fujii Y, Baba T, Ohno S (2004) Effects of anoxia on serum immunoglobulin and albumin leakage through blood–brain barrier in mouse cerebellum as revealed by cryotechniques. J Neurosci Methods 138:89–95
4. Jehl B, Bauer R, Dorge A, Rick R (1981) The use of propane/isopentane mixtures for rapid freezing of biological specimens. J Microsc 123:307–309
5. Terada N, Ohno N, Saitoh S, Ohno S (2007) Immunohistochemical detection of hypoxia in mouse liver tissues treated with pimonidazole using "in vivo cryotechnique". Histochem Cell Biol 128:253–261

Technical Merits with "IVCT"

4

Shinichi Ohno

Abstract

The main purpose of in vivo cryotechnique (IVCT) is to make all biological components of cells and tissues of functioning organs promptly frozen in living animals. However, the necessary freezing times are always different at each depth from the frozen tissue surface, because thermal conductance of cooling within cells and tissues is due to the continuous movement of thermal energy. Therefore, only surface tissue layers within certain depths, such as about 10 or 200 μm, are frozen enough to prevent formation of visible ice crystals at electron or light microscopic levels, respectively. With the metal contact freezing method, they are slightly compressed on the cooled copper metal due to crash impact, even though some spacers and cushions are always inserted between specimens and the cooled metal block. To the contrary, with liquid cryogen, such as the isopentane-propane mixture precooled in liquid nitrogen, the frozen tissues can retain their original morphological states without mechanical compression damages. To examine deeper tissue areas from the frozen tissue surface, we always need to cryocut any functioning organs of living animals under anesthesia. When a cryoknife precooled in liquid nitrogen passes through the living animal organ, the exposed tissue surface in direct contact with the cryoknife is first frozen in the same way as the metal contact method. Practically, at an electron microscopic level, well-frozen tissue areas appear to occupy a very narrow band, less than 10 μm deep from the contact tissue surface.

Keywords

Thermal conductance • Ice crystal • Liquid cryogen • Metal contact freezing

4.1 Tissue Depth of Well-Frozen Areas

The main purpose of IVCT is to make all biological components of cells and tissues of functioning organs promptly frozen in living animals [1, 2]. However, the necessary freezing times are always different at each depth from the frozen tissue surface, because thermal conductance of cooling within cells and tissues is due to the continuous movement of thermal energy. Therefore, only surface tissue layers within certain depths, such as about 10 or 200 μm, are frozen enough to prevent formation of visible ice crystals at electron or light microscopic levels, respectively [1, 2]. The layered areas at the same depth from frozen tissue surface are supposed to be quickly frozen nearly at the same time. Therefore, by routinely cutting the epoxy resin or paraffin blocks almost horizontally to the frozen tissue surface on an ultramicrotome or a microtome, we can get similarly well-frozen tissue morphology over wide areas of living animal organs.

S. Ohno (✉)
Department of Anatomy and Molecular Histology,
Interdisciplinary Graduate School of Medicine
and Engineering, University of Yamanashi,
1110 Shimokato, Chuo City, Yamanashi 409-3898, Japan
e-mail: sohno@yamanashi.ac.jp

S. Ohno et al. (eds.), *In Vivo Cryotechnique in Biomedical Research and Application for Bioimaging of Living Animal Organs*, DOI 10.1007/978-4-431-55723-4_4

4.2 Plunging or Slamming Cryotechniques

To obtain the wide surface areas of well-frozen tissues by the common quick-freezing methods, considerable amounts of liquid nitrogen are usually necessary for plunging resected fresh tissues in the cryogen, or otherwise slamming them onto copper metal blocks precooled in liquid nitrogen. With the metal contact freezing method, they are slightly compressed on the cooled copper metal due to crash impact [3], even though some spacers and cushions are always inserted between specimens and the cooled metal block. To the contrary, with liquid cryogen, such as the IP mixture precooled in liquid nitrogen [1, 4, 5], the frozen tissues can retain their original morphological states without mechanical compression damages. This concept for usage of liquid cryogen was already reconfirmed in the experimental system by jetting human blood samples into the liquid cryogen, referred to as "in vitro cryotechnique for erythrocytes," to examine dynamically changing erythrocyte shapes at different blood flowing speeds [6, 7].

4.3 Thermal Conductance

To examine deeper tissue areas from the frozen tissue surface, we always need to cryocut any functioning organs of living animals under anesthesia [1]. When a cryoknife precooled in liquid nitrogen passes through the living animal organ, the exposed tissue surface in direct contact with the cryoknife is first frozen in the same way as the metal contact method [1]. The mechanical damage of cryocut tissues is rarely detected, if target organs could be quickly passed through with the cryoknife. Then, the widely cryocut tissues are additionally frozen by another liquid cryogen of the IP mixture which is simultaneously poured over them. In this process, physical speeds of the moving cryoknife and freezing intensity of the cryogen are critical for necessary time to achieve the in vivo freezing of living animal organs. Practically, at an electron microscopic level, well-frozen tissue areas appear to occupy a very narrow band, less than 10 μm deep from the contact tissue surface [1]. Although thermal conductivity gradually changes in living animal organ tissues, depending on concentrations of biological materials, some well-frozen tissue areas are seen next to the damaged ones with larger ice crystals even at the same distance from the frozen tissue surface, probably because of different concentrations of soluble components in various areas of cells and tissues.

References

1. Ohno S, Terada N, Fujii Y, Ueda H, Takayama I (1996) Dynamic structure of glomerular capillary loop as revealed by an in vivo cryotechnique. Virchows Arch 427:519–527
2. Ohno S, Baba T, Terada N, Fujii Y, Ueda H (1996) Cell biology of kidney glomerulus. Int Rev Cytol 166:181–230
3. van Harreveld A, Trubatch J (1975) Synaptic changes in frog brain after stimulation with potassium chloride. J Neurocytol 4:33–46
4. Jehl B, Bauer R, Dorge A, Rick R (1981) The use of propane/isopentane mixtures for rapid freezing of biological specimens. J Microsc 123:307–309
5. Cole R, Matuszek G, See C, Rieder CL (1990) A simple pneumatic device for plunge-freezing cells grown on electron microscopy grids. J Electron Microsc Tech 16:167–173
6. Terada N, Fujii Y, Kato Y, Ueda H, Baba T, Ohno S (1998) Scanning electron microscopic study of erythrocyte shapes artificially jetted through tubes at different pressures by 'in vitro cryotechnique for erythrocytes'. J Electron Microsc 47:489–493
7. Terada N, Ohno S (1998) Dynamic morphology of erythrocytes revealed by cryofixation technique. Acta Anat Nippon 73:587–593

Part II
Application of 'IVCT' to Various Mouse Organs

Histochemical Analyses of Living Mouse Liver Under Different Hemodynamic Conditions

5

Nobuhiko Ohno, Nobuo Terada, and Shinichi Ohno

Abstract

Morphology and molecular distribution in animal liver tissues were examined using "in vivo cryotechnique" (IVCT) and compared with findings obtained with other conventional tissue preparation methods. Open sinusoids with flowing erythrocytes were clearly observed under normal blood circulation, and blood congestion and sinusoidal collapse were apparent in liver under ischemic or heart-arrest conditions. Sinusoidal collapse was also apparent with conventional tissue preparation methods, including immersion-fixation and quick-freezing (QF) methods of resected tissues, while perfusion-fixation artificially dilated the sinusoidal cavities. The IVCT and QF method well maintained immunoreactivity of soluble serum proteins including albumin and immunoglobulins as well as glycogen in hepatocytes detected by periodic acid-Schiff (PAS) staining. Rapid molecular translocation of serum proteins into hepatocytes was immunohistochemically observed after tissue resection with the QF method. IVCT was useful to examine dynamic morphology under different hemodynamic states and also immunodistribution of soluble components in living mouse livers under physiological and pathological states with higher time resolution.

Keywords

Liver morphology • In vivo cryotechnique • Immunohistochemistry • Periodic acid-Schiff staining • Serum proteins

5.1 Introduction

The liver receives a large volume of blood supply and is a dynamic organ changing its blood circulation and metabolic states [1, 2]. Previous studies pointed out that the liver morphology is altered depending on different physiological and pathological states [3–6]. Dynamic morphological alterations of sinusoids and sinusoidal lining cells are indicated by new methods such as intravital microscopy with fluorescence imaging [7–10]. For morphological and immunohistochemical analyses of liver tissues under different hemodynamic conditions, "in vivo cryotechnique" (IVCT) was used to examine the dynamically changing morphology of living mouse livers under different hemodynamic conditions [11]. The findings obtained by IVCT were also compared with those obtained by conventional chemical-fixation and quick-freezing methods.

N. Ohno, M.D., Ph.D. (✉) • S. Ohno
Department of Anatomy and Molecular Histology, Interdisciplinary Graduate School of Medicine and Engineering, University of Yamanashi, 1110 Shimokato, Chuo City, Yamanashi 409-3898, Japan
e-mail: nohno@yamanashi.ac.jp

N. Terada
Division of Health Sciences, Shinshu University Graduate School of Medicine, 3-1-1 Asahi, Matsumoto City, Nagano 390-8621, Japan

Department of Anatomy and Molecular Histology, Interdisciplinary Graduate School of Medicine and Engineering, University of Yamanashi, 1110 Shimokato, Chuo City, Yamanashi 409-3898, Japan

S. Ohno et al. (eds.), *In Vivo Cryotechnique in Biomedical Research and Application for Bioimaging of Living Animal Organs*, DOI 10.1007/978-4-431-55723-4_5

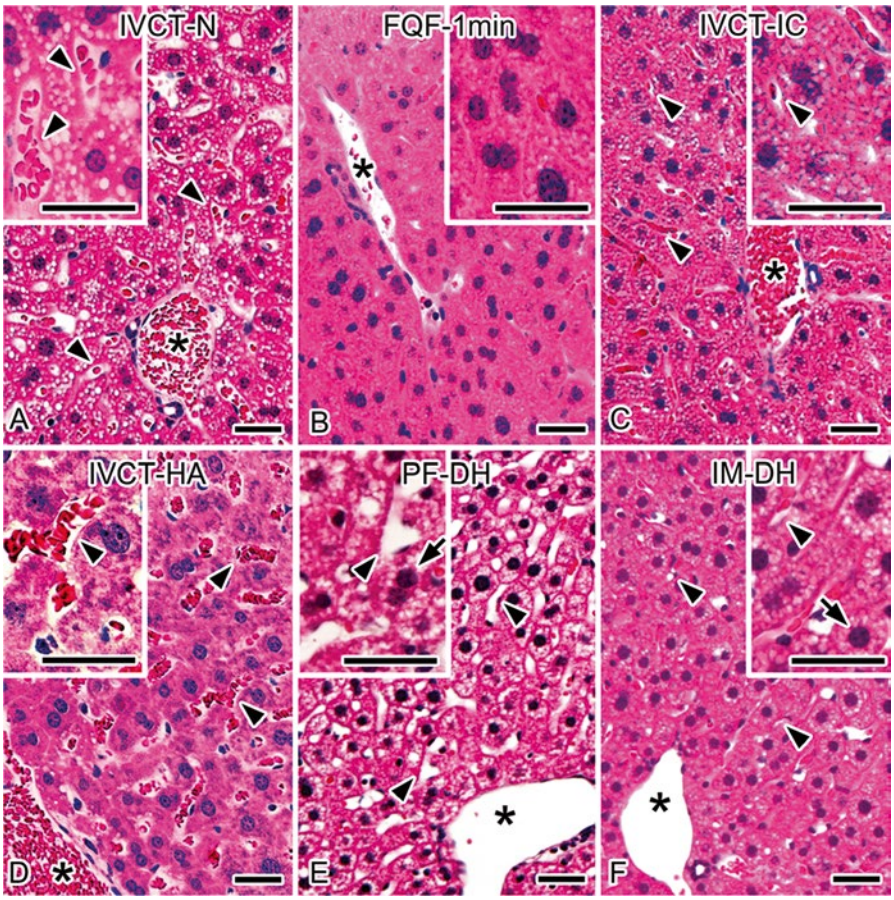

Fig. 5.1 Sections prepared by various preparation methods and stained with hematoxylin-eosin show that widely open sinusoids are clearly detected with "in vivo cryotechnique" under normal blood circulation (IVCT-N; **a**, *arrowheads*) but collapsed with IVCT under ischemic conditions (IVCT-IC; **c**, *arrowheads*). Such sinusoidal collapse is more prominently seen with quick freezing of resected fresh specimens (FQF-1 min; **b**). Sinusoids with congested erythrocytes are dilated with IVCT after heart arrest (IVCT-HA; **d**, *arrowheads*). With perfusion-fixation followed by alcohol dehydration (PF-DH), sinusoids are opened without erythrocytes due to perfusion pressure (**e**, *arrowheads*). Sinusoids are mostly collapsed with immersion fixation followed by alcohol dehydration (IM-DH; **f**, *arrowheads*). Some nuclei of hepatocytes appear smaller with PF-DH and IM-DH (**e**, **f**; *arrows*). *Asterisks*: interlobular veins. *Bars*: 30 μm (The figure was reproduced from Ohno et al. [11])

5.2 Morphological Features of Living Mouse Liver

Compared with conventional immersion fixation followed by alcohol dehydration (IM-DH), conventional perfusion-fixation followed by alcohol dehydration (PF-DH) could show morphology of the liver with intra-sinusoidal pressure [12, 13]. However, it was impractical to reproduce normal blood circulation of the liver, which is supplied from a couple of different blood circulation system with variable blood pressures [1, 14]. Therefore, the artificial perfusion pressures in PF-DH usually affected the native liver morphology, which is also modified by the subsequent tissue preparation steps [15–20].

On the other hand, IVCT can reveal dynamic morphological alterations of liver under different hemodynamic conditions [11]. Sinusoidal cavities were open with many flowing erythrocytes in specimens prepared with IVCT (Fig. 5.1). In contrast, the sinusoidal cavities were almost completely collapsed when liver tissues were cryofixed following tissue resection (FQF) (Fig. 5.1). The sinusoidal collapse was also prominent when IVCT was used under ischemic conditions after ligation of portal veins and hepatic arteries [11]. With IVCT under the heart-arrest condition, sinusoids were rather dilated with congested erythrocytes (Fig. 5.1). On the other hand, erythrocytes were not present in wide sinusoids with PF-DH, whereas the sinusoids were collapsed with IM-DH (Fig. 5.1). In addition, PF-DH and IM-DH make hepatocellular nuclei appearing smaller, presumably due to shrinkage of nuclei during dehydration [11]. Dynamic morphology of living mouse liver was also revealed by morphometric analyses with IVCT and immunostaining for immunoglobulin G1 (IgG1) in sinusoids and Igκ in bile canaliculi [11]. The morphometric analyses supported that (1) the width of sinusoids was significantly reduced in specimens prepared with IVCT under ischemic conditions and FQF but was significantly increased in those prepared with IVCT under heart-arrest condition and (2) with FQF, the width of bile canaliculi was significantly reduced. The nuclear diameter was similar with IVCT or FQF but was significantly

reduced with PF-DH. Shrinkage of liver tissues is one of the major artifacts caused in the conventional tissue preparation methods, which consequently decrease nuclear diameter of hepatocytes [3, 21–23]. Therefore, application of IVCT to histochemical and morphological studies of liver tissues in living mice can reveal their dynamic changes under different hemodynamic conditions compared with conventional chemical-fixation or cryofixation methods.

IVCT also maintained the ultrastructures of living animal livers under normal blood circulation in tissue areas within several micrometers from the tissue surface [11]. Widely open sinusoids surrounded by fenestrated endothelial cells were clearly observed, and Disse's spaces were widely opened in some areas [11]. Processes of endothelial cells often extended into sinusoidal cavities, and bile canaliculi with microvilli and tight junctions were also open in living liver tissues. In contrast, sinusoids and Disse's spaces were almost entirely collapsed by IM-DH.

Tissue resection, essential in the conventional QF method, may cause artifacts due to ischemia or anoxia on the mouse hepatic morphology. Tissue resection might cause cellular swelling due to rapid entry of extracellular components into the cytoplasm of ischemic cells [24, 25]. The severer collapse of sinusoids and decreased sizes of bile canaliculi observed with FQF may be attributable to these artificial swellings caused by tissue resection. "Intravital microscopy" is a powerful approach to solve such technical problems [5, 7] and enables time-lapse observation of sinusoids and certain cells in vivo [8–10]. On the other hand, the dynamically changing morphology of cells and tissues can be examined on tissue sections with IVCT without artifacts induced by tissue resection, perfusion-fixation, and alcohol dehydration [26–28]. IVCT in combination with other techniques, including physiological monitoring or intravital microscopy, could be useful for immunohistochemical and ultrastructural studies of living liver tissues.

5.3 Distribution of Serum Proteins and Glycogen

Distribution of serum proteins in mouse liver was also clearly detected with IVCT [11]. Under normal blood circulation, immunostaining for IgG1, Igκ, or albumin was observed along sinusoidal edges (Fig. 5.2). Igκ immunostaining also represents IgA and was found in bile canaliculi

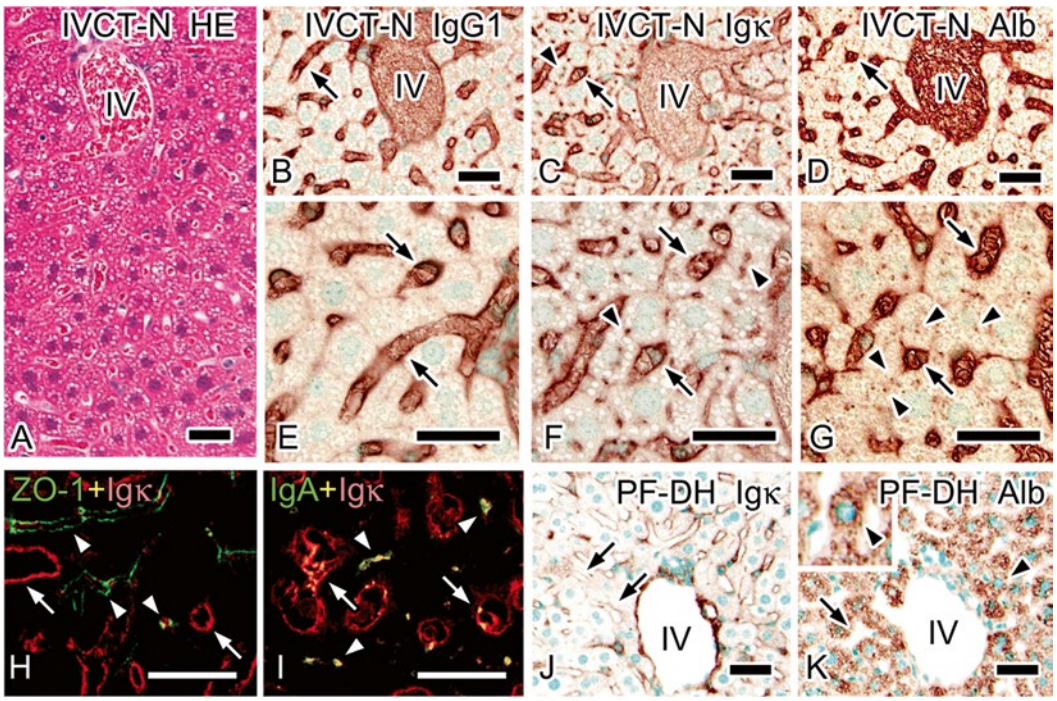

Fig. 5.2 Light micrographs of specimens prepared with "in vivo cryotechnique" under normal circulation (IVCT-N; **a**–**i**) or perfusion-fixation followed by alcohol dehydration (PF-DH; **j**, **k**). Serial sections are stained with hematoxylin-eosin (HE; **a**) or immunostained for immunoglobulin G1 heavy chain (IgG1; **b**, **e**), immunoglobulin kappa light chain (Igκ; **c**, **f**, **j**), or albumin (**d**, **g**, **k**). All serum proteins are clearly immunolocalized in sinusoids with IVCT-N (**b**–**g**, *arrows*), while immunostaining for Igκ and albumin is also detected among hepatic plates (**f**, **g**; *arrowheads*). Double immunofluorescence labeling for Igκ (**h**, **i**; *red*) and zonula occludens-1 (ZO-1; **h**; *green*) or immunoglobulin A (IgA; **i**; *green*) in cryosections prepared by IVCT-N shows that immunostaining for Igκ is detected between parallel ZO-1 immunostaining for tight junctions between hepatic plates (**h**; *arrowheads*) and is also seen together with that of IgA (**i**; *arrowheads*). Igκ or IgA is also immunolocalized in sinusoids (**h**, **i**; *arrows*). Immunoreactivity of Igκ or albumin is dramatically diminished in sinusoids with PF-DH (**j**, **k**; *arrows*), but some albumin in hepatocytes becomes condensed (**k**; *arrowheads*). *IV* interlobular veins. *Bars*: 30 μm (The figure was reproduced from Ohno et al. [11])

located in hepatic plates visualized by tight junctions immunopositive for ZO-1. Albumin immunoreactivity appeared as small dots and was observed in hepatocytes, presumably detected in Golgi areas. In tissue specimens prepared with PF-DH, immunostaining for serum proteins including Igκ and albumin was less clearly observed (Fig. 5.2).

Soluble glycogen in hepatocytes was also well maintained with IVCT [11]. Abundant glycogen as visualized by strong periodic acid-Schiff (PAS) staining was detected in hepatocytes located around centrilobular sinusoids and periportal zones with IVCT under normal blood circulation. In contrast, by FQF, the PAS staining was partially decreased in the peripheral cytoplasm of hepatocytes around centrilobular sinusoids. By PF-DH, such loss of PAS staining was more clearly observed in periportal zones, and PAS staining intensity in the cytoplasm was decreased in some hepatocytes located in the centrilobular areas. Decrease of PAS staining was worst in the liver specimens prepared by IM-DH.

Soluble molecules can be moved or lost in conventional tissue preparation methods such as PF-DH or IM-DH [29–32]. However, IVCT and QF do not use aqueous fixatives during specimen preparation and thus well-preserve soluble components in the specimens [29, 31–33]. Signal molecules influencing hepatic microvasculature have been studied under pathological conditions [5–7, 34]. The nutritional state, such as the glycogen storage of hepatocytes, could be important for injury caused by ischemia-reperfusion stress during liver transplantation [35]. Therefore, the localization of soluble molecules would be effectively examined in living animal livers using IVCT.

5.4 Disrupted Cell Membrane Integrity

Because of the excellent preservation of soluble molecules in situ by the quick freezing followed by freeze-substitution, these methods also revealed that immunoreactivity of serum proteins is detected in some hepatocyte cytoplasm after tissue resection (Fig. 5.3) [11]. Interestingly, immunostaining for IgG1 and Igκ in the serial sections demonstrated that these serum proteins were colocalized in the same hepatocyte. The IgG1- and Igκ-immunopositive hepatocytes were also immunopositive for albumin, while some hepatocytes were immunopositive only for albumin (Fig. 5.3). Such diffuse immunostaining for the serum proteins was not detected with IVCT [11]. Since the molecular size of IgG is larger than that of albumin, the immunoreactivity of serum proteins in hepatocytes indicated size-dependent translocation of soluble serum proteins due to rapid permeability alterations of cell membranes caused by tissue resection. Actually, the disruption of the cell membranes is a hallmark of necrosis [36]. Soluble serum proteins as well as extrinsic dye would be easily translocated into hepatocytes upon necrosis which is characterized by size-dependent changes of cell membrane permeability following anoxia/ischemia. IVCT could be useful to analyze the integrity of hepatocyte cell membranes under physiological and pathological conditions in living animal liver.

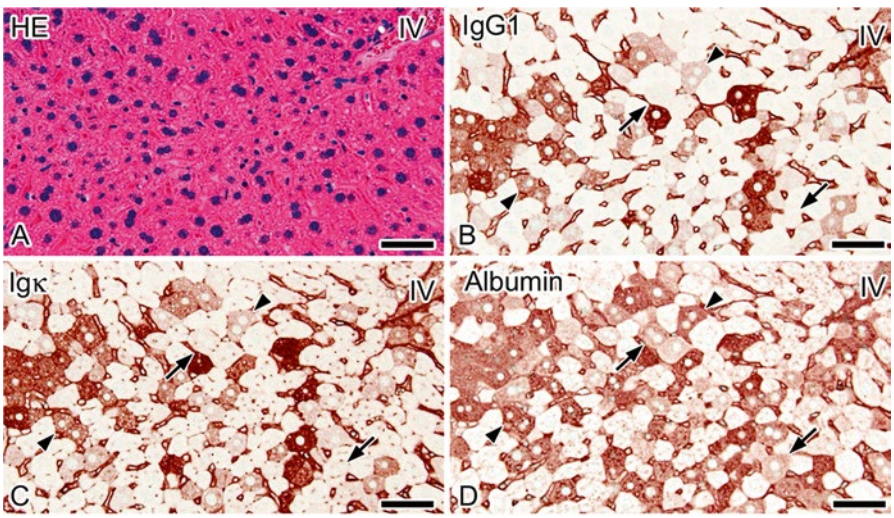

Fig. 5.3 Serial sections prepared by quick freezing of fresh tissues 5 min after resection (FQF-5 min) and stained with hematoxylin-eosin (HE; **a**) or immunostained for immunoglobulin G1 heavy chain (IgG1; **b**), immunoglobulin kappa light chain (Igκ; **c**), or albumin (**d**) show that cytoplasm of some hepatocytes, indistinguishable with HE staining (**a**), is immunostained for IgG1, Igκ, and albumin (**b–d**; *arrows*, *arrowheads*). Immunodistribution of IgG1 and Igκ appears similar (**b**, **c**), whereas some albumin-immunopositive hepatocytes are not immunostained for IgG1 or Igκ (**b–d**; *arrows*). *IV* interlobular vein. *Bars*: 50 μm (The figure was reproduced from Ohno et al. [11])

5.5 Concluding Remarks

IVCT better retains soluble molecules in the liver, such as glycogen and serum proteins, which can be easily translocated during conventional chemical-fixation methods. IVCT is also a powerful approach to analyze the permeability of hepatocyte cell membranes which is easily affected under noxious stimuli. The dynamic and functional "living morphology" of mouse livers is observed under different physiological or pathological conditions with IVCT.

References

1. Ekataksin W, Kaneda K (1999) Liver microvascular architecture: an insight into the pathophysiology of portal hypertension. Semin Liver Dis 19(4):359–382
2. Greenway CV, Stark RD (1971) Hepatic vascular bed. Physiol Rev 51(1):23–65
3. Braet F, Wisse E (2002) Structural and functional aspects of liver sinusoidal endothelial cell fenestrae: a review. Comp Hepatol 1(1):1
4. McCuskey RS (2000) Morphological mechanisms for regulating blood flow through hepatic sinusoids. Liver 20(1):3–7
5. McCuskey RS, Reilly FD (1993) Hepatic microvasculature: dynamic structure and its regulation. Semin Liver Dis 13(1):1–12
6. Ueno T, Bioulac-Sage P, Balabaud C, Rosenbaum J (2004) Innervation of the sinusoidal wall: regulation of the sinusoidal diameter. Anat Rec 280(1):868–873
7. Clemens MG, Zhang JX (1999) Regulation of sinusoidal perfusion: in vivo methodology and control by endothelins. Semin Liver Dis 19(4):383–396
8. McCuskey RS, Bethea NW, Wong J, McCuskey MK, Abril ER, Wang X et al (2005) Ethanol binging exacerbates sinusoidal endothelial and parenchymal injury elicited by acetaminophen. J Hepatol 42(3):371–377
9. Okumura S, Takei Y, Kawano S, Nagano K, Masuda E, Goto M et al (1994) Vasoactive effect of endothelin-1 on rat liver in vivo. Hepatology 19(1):155–161
10. Pannen BH, Al-Adili F, Bauer M, Clemens MG, Geiger KK (1998) Role of endothelins and nitric oxide in hepatic reperfusion injury in the rat. Hepatology 27(3):755–764
11. Ohno N, Terada N, Ohno S (2006) Histochemical analyses of living mouse liver under different hemodynamic conditions by "in vivo cryotechnique". Histochem Cell Biol 126(3):389–398
12. Fahimi HD (1967) Perfusion and immersion fixation of rat liver with glutaraldehyde. Lab Invest 16(5):736–750
13. Wisse E (1970) An electron microscopic study of the fenestrated endothelial lining of rat liver sinusoids. J Ultrastruct Res 31(1):125–150
14. Saxena R, Theise ND, Crawford JM (1999) Microanatomy of the human liver-exploring the hidden interfaces. Hepatology 30(6):1339–1346
15. Chan FL, Inoue S (1994) Lamina lucida of basement membrane: an artefact. Microsc Res Tech 28(1):48–59
16. Fraser R, Bowler LM, Day WA, Dobbs B, Johnson HD, Lee D (1980) High perfusion pressure damages the sieving ability of sinusoidal endothelium in rat livers. Br J Exp Pathol 61(2):222–228
17. Furukawa T, Ohno S, Oguchi H, Hora K, Tokunaga S, Furuta S (1991) Morphometric study of glomerular slit diaphragms fixed by rapid-freezing and freeze-substitution. Kidney Int 40(4):621–624
18. Hippe-Sanwald S (1993) Impact of freeze substitution on biological electron microscopy. Microsc Res Tech 24(5):400–422
19. Kellenberger E, Johansen R, Maeder M, Bohrmann B, Stauffer E, Villiger W (1992) Artefacts and morphological changes during chemical fixation. J Microsc 168(Pt 2):181–201
20. Yu Y, Leng CG, Kato Y, Ohno S (1997) Ultrastructural study of glomerular capillary loops at different perfusion pressures as revealed by quick-freezing, freeze-substitution and conventional fixation methods. Nephron 76(4):452–459
21. Bignold LP (2002) Hypothesis for the influence of fixatives on the chromatin patterns of interphase nuclei, based on shrinkage and retraction of nuclear and perinuclear structures. Br J Biomed Sci 59(2):105–113
22. Ohno S, Terada N, Fujii Y, Ueda H, Takayama I (1996) Dynamic structure of glomerular capillary loop as revealed by an in vivo cryotechnique. Virchows Arch 427(5):519–527
23. Wisse E, De Zanger RB, Charels K, Van Der Smissen P, McCuskey RS (1985) The liver sieve: considerations concerning the structure and function of endothelial fenestrae, the sinusoidal wall and the space of Disse. Hepatology 5(4):683–692
24. Van Harreveld A, Biber MP (1962) Conductivity changes in some organs after circulatory arrest. Am J Physiol 203:609–614
25. von Zglinicki T, Rimmler M, Purz HJ (1986) Fast cryofixation technique for X-ray microanalysis. J Microsc 141(Pt 1):79–90
26. Ohno N, Terada N, Fujii Y, Baba T, Ohno S (2004) "In vivo cryotechnique" for paradigm shift to "living morphology" of animal organs. Biomed Rev 15:1–19
27. Ohno N, Terada N, Murata S, Katoh R, Ohno S (2005) Application of cryotechniques with freeze-substitution for the immunohistochemical demonstration of intranuclear pCREB and chromosome territory. J Histochem Cytochem 53(1):55–62
28. Terada N, Ohno N, Li Z, Fujii Y, Baba T, Ohno S (2006) Application of in vivo cryotechnique to the examination of cells and tissues in living animal organs. Histol Histopathol 21(3):265–272
29. Li Z, Terada N, Ohno N, Ohno S (2005) Immunohistochemical analyses on albumin and immunoglobulin in acute hypertensive mouse kidneys by "in vivo cryotechnique". Histol Histopathol 20(3):807–816
30. Schaart G, Hesselink RP, Keizer HA, van Kranenburg G, Drost MR, Hesselink MK (2004) A modified PAS stain combined with immunofluorescence for quantitative analyses of glycogen in muscle sections. Histochem Cell Biol 122(2):161–169
31. von Schack ML, Fakan S (1994) Retention of glycogen in cryosubstituted mouse liver. Histochemistry 102(6):451–455
32. Zea-Aragon Z, Terada N, Ohno N, Fujii Y, Baba T, Ohno S (2004) Effects of anoxia on serum immunoglobulin and albumin leakage through blood-brain barrier in mouse cerebellum as revealed by cryotechniques. J Neurosci Methods 138(1–2):89–95
33. Terada N, Ohno N, Li Z, Fujii Y, Baba T, Ohno S (2005) Detection of injected fluorescence-conjugated IgG in living mouse organs using "in vivo cryotechnique" with freeze-substitution. Microsc Res Tech 66(4):173–178
34. Rockey DC (2003) Vascular mediators in the injured liver. Hepatology 37(1):4–12
35. Quintana AB, Guibert EE, Rodriguez JV (2005) Effect of cold preservation/reperfusion on glycogen content of liver. Concise Rev Ann Hepatol 4(1):25–31
36. Rosser BG, Gores GJ (1995) Liver cell necrosis: cellular mechanisms and clinical implications. Gastroenterology 108(1):252–275

Three-Dimensional Reconstruction of Liver Tissues with Confocal Laser Scanning Microscopy

6

Yurika Saitoh, Nobuo Terada, Nobuhiko Ohno, and Shinichi Ohno

Abstract

Soluble proteins and glycogen particles are well preserved in paraffin-embedded sections prepared by in vivo cryotechnique (IVCT) followed by freeze-substitution (FS) fixation. We performed confocal laser scanning microscopic analyses on the distributions of glycogen with periodic acid–Schiff (PAS) staining and serum proteins with immunostaining for mouse liver tissues. Livers showed a red fluorescence signal of PAS staining in hepatocytes and immunofluorescence of immunoglobulin kappa (Igκ) light chain in blood vessels and bile canaliculi. By three-dimensional (3D) reconstruction of serial optical sections, interconnecting hepatic sinusoids and bile canaliculi were detected with Igκ immunostaining between trabecular hepatocytes that were PAS stained. In addition, 100-μm-thick PAS or eosin-stained slices provided 3D-structural images more than 30 μm in thickness away from tissue surfaces, showing blood vessels with flowing erythrocytes and networks of bile ducts and canaliculi. IVCT with histochemical analyses enabled us to visualize native hepatocytic glycogen and 3D structures, such as vascular networks, reflecting their living states by confocal laser scanning microscopy.

Keywords

Three-dimensional reconstruction • PAS staining • Eosin staining • Confocal laser scanning microscopy

6.1 Introduction

Recently, some in vivo vital imaging methods, such as blood circulation monitoring and confocal endomicroscopy, are often used for observation of animal living states, but their images are of lower magnification and it is difficult to show three-dimensional (3D) images with high spatial resolution, as compared with common histological ones [1, 2]. However, common histological images also have a big problem which is difficult to obtain reflecting living states. Using conventional preparation procedures to obtain common histological images, diffusion or extraction artifacts of soluble components are inevitably caused by the preparation steps of tissue resection or perfusion fixation [3]. Therefore, we have developed "in vivo cryotechnique (IVCT)" or "cryobiopsy" combined with freeze-substitution (FS) fixation to retain

Y. Saitoh (✉) • N. Ohno • S. Ohno
Department of Anatomy and Molecular Histology, Interdisciplinary Graduate School of Medicine and Engineering, University of Yamanashi, 1110 Shimokato, Chuo City, Yamanashi 409-3898, Japan
e-mail: yurikas@yamanashi.ac.jp

N. Terada
Division of Health Sciences, Shinshu University Graduate School of Medicine, 3-1-1 Asahi, Matsumoto City, Nagano 390-8621, Japan

Department of Anatomy and Molecular Histology, Interdisciplinary Graduate School of Medicine and Engineering, University of Yamanashi, 1110 Shimokato, Chuo City, Yamanashi 409-3898, Japan

S. Ohno et al. (eds.), *In Vivo Cryotechnique in Biomedical Research and Application for Bioimaging of Living Animal Organs*, DOI 10.1007/978-4-431-55723-4_6

distributions of soluble proteins, amino acids, and glycogen in living mouse organs [4–8]. In this section, we demonstrate detailed 3D images reflecting living states to show the ability of IVCT combined with confocal laser scanning microscopy.

6.2 3D Reconstruction Images of PAS Staining and Immunostaining for Ig

IVCT-FS followed by paraffin embedding is easily able to maintain and detect soluble proteins and glycogen particles. The glycogen particles are routinely detected by PAS staining and PAS-reaction products emit yellow-red fluorescence signals [9, 10]. The paraffin-embedded specimens were cut into slices of 4–15 μm in thickness and mounted on glass slides. Some tissue slices were routinely deparaffinized and then used for PAS staining and immunostaining for Igκ. They were finally observed with a confocal laser scanning microscope (CLSM, FV-1000; Olympus, Tokyo, Japan) and computerized to automatically make 10–50 serial optical sections at intervals of around 0.5 μm. CLSM has the merit of reconstructing 3D images from recorded digital data of serial optical sections. The 3D reconstruction was performed using FV10-ASW software (Olympus). By reconstruction from 29 serial optical sections of 6-h-fasting liver tissues, we obtained 3D images of PAS staining and Igκ immunostaining data (Fig. 6.1). Most hepatocytes showed PAS-stained aggregates with a red color in the cytoplasm (Fig. 6.1a). With green fluorescent signals for Igκ, hepatic sinusoids (black arrows in Fig. 6.1a–e), bile canaliculi (white arrows in Fig. 6.1a–e), and hepatocytic nuclei (blue fluorescent signals in Fig. 6.1a–e) were detected among the red glycogen aggregates (Fig. 6.1a–e). Moreover, by optically cutting the X/Z planes of the digital images, blood vessels (black arrows in Fig. 6.1c) and bile canaliculi (white arrows in Fig. 6.1c) were more clearly detected within about 12 μm in thickness, as revealed by the Igκ immunostaining (Fig. 6.1c). At a higher magnified view of the 3D reconstruction image (Fig. 6.1d), bile canaliculi were found to be connecting with each other to form networks (white arrows in Fig. 6.1d), but some canaliculi hid behind the glycogen aggregates of hepatocytes in comparison with the z-stacked two-dimensional image of the same area (black arrowheads in Fig. 6.1d, e).

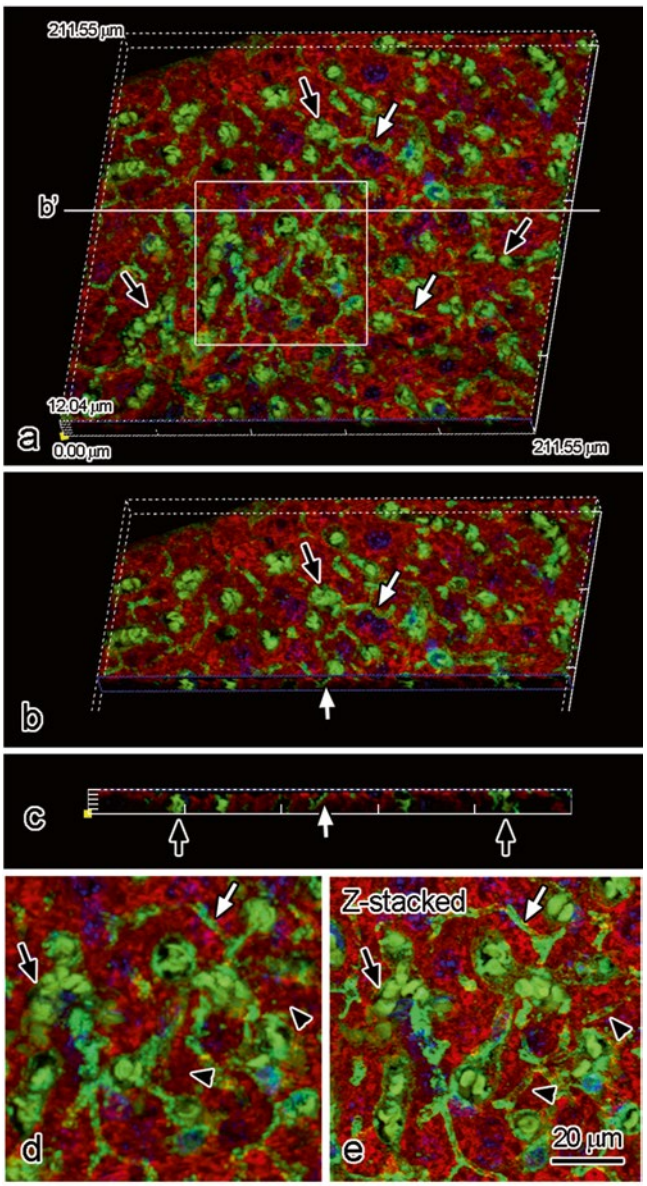

Fig. 6.1 Three-dimensional reconstruction of triple-fluorescence images obtained by confocal laser scanning microscopy with PAS staining (*red*), immunostaining for immunoglobulin kappa light chain (*green*), and TO-PR-O3 (*blue*) in fasting mouse livers. X/Z plane (*white line* **b** in **a**) was digitally cut for 3D-reconstructed image (**b**), and their X/Z plane view is shown in (**c**). (**d**): Higher magnified view of the *boxed area* in (**a**). (**e**): Two-dimensional (Z-stacked of 29 serial optical sections) view of the *boxed area* in (**a**). *Black arrows*: hepatic sinusoids, *white arrows*: bile canaliculi. *Bar*: 20 μm

6.3 3D Reconstruction Images of PAS Staining in 100 μm Paraffin Slices

It has known that the antibodies for immunostaining are able to penetrate into tissue sections around 10 μm because of their molecular sizes. To the contrary, dyes used for usual PAS staining and hematoxylin–eosin (HE) staining easily penetrate into deep areas of tissues. Therefore, we further tried to perform 3D reconstruction of 100 μm paraffin slices stained with PAS under the CLSM (Fig. 6.2). To obtain thicker paraffin slices, paraffin-embedded specimens were cut at 100 μm thickness using a cryostat machine at around −10 °C and mounted on MAS-coated glass slides. Such a low temperature enabled us to make thicker paraffin slices than usual. The 100-μm-thick slices could be treated by

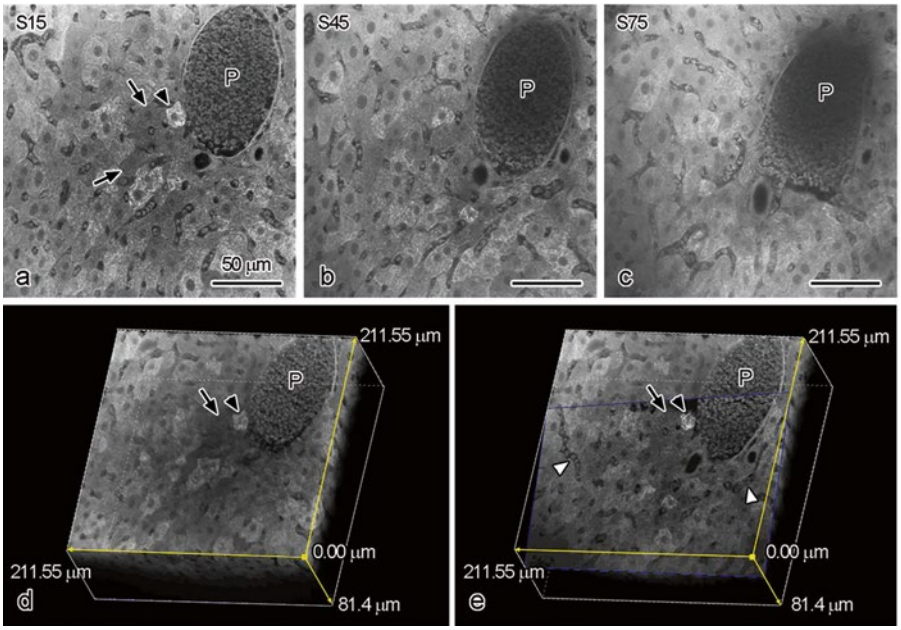

Fig. 6.2 Serial optical sections of the fasted mouse livers (**a**–**c**) and three-dimensional reconstruction of a 100 μm slice stained with PAS obtained by confocal laser scanning microscopy (CLSM) (**d**, **e**). With CLSM, serial 186 optical sections are obtained: the 15th (**a**: 6.16 μm in depth), 45th (**b**: 19.36 μm in depth), and 75th (**c**: 32.56 μm in depth) optical sections are shown as typical examples. (**c**): The X/Z planes were shown the three-dimensionally reconstructed images. (**e**): Optically cutting oblique digital plane. *Bars*: 50 μm

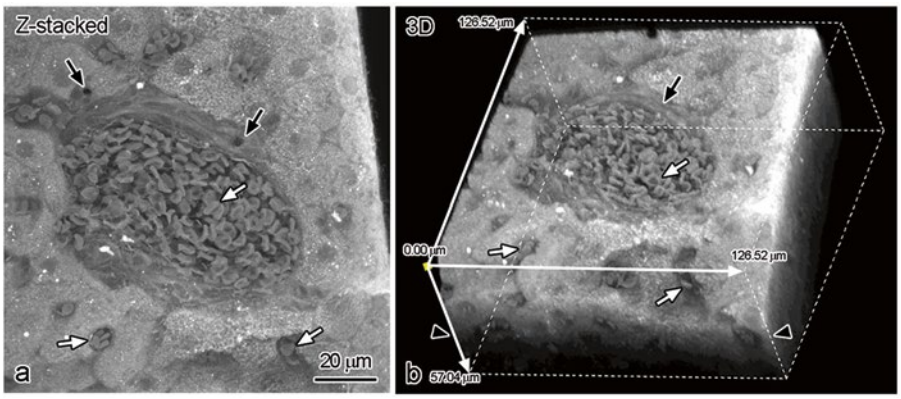

Fig. 6.3 Three-dimensional reconstruction of eosin-stained tissue images in a 100-μm section of normal mouse liver obtained by CLSM. By CLSM, 125 serial optical sections are obtained. (**a**) An accumulated digital image of the 125 optical sections with Z-series. (**b**) 3D-reconstructed images of the 125 optical sections. *Black arrows*: interlobular bile ducts, *white arrows*: biconcave disk shapes of erythrocytes, *black arrowheads*: about 30 μm in depth

usual deparaffinization and dehydration. The 3D reconstruction was performed on 186 serial optical sections of fasting mouse liver tissues at intervals of 0.896 μm. Because each optical section overlaps the adjacent sections with half of its thickness, the total thickness was 81.4 μm (Fig. 6.2d, e). In mouse livers under the fasting condition, we identified a strongly PAS-positive hepatocyte near the portal vein (arrowheads in Fig. 6.2a, d, e) and some PAS-negative ones (arrows in Fig. 6.2a, d, e). In contrast, the intensity of erythrocyte autofluorescence was much weaker than that of PAS staining (P in Fig. 6.2), and the portal veins were hardly detected at areas of more than 20 μm in depth (P in Fig. 6.2b). Some PAS-stained hepatocytes were still detectable at areas of more than 30 μm in depth (Fig. 6.2c). By optically cutting X/Y/Z planes (Fig. 6.2e), interconnecting sinusoidal networks (white arrowheads in Fig. 6.2e) were detected in the 3D-reconstructed digital images.

6.4 3D Reconstruction Images of Eosin Staining in 100-μm Paraffin Slices

Eosin dye commonly used for HE staining has been already known to emit yellow-red fluorescence signals [11, 12]. Under the CLSM, it is detectable by fluorescence wavelengths at 645–745 nm and excitation wavelength at 633 nm. The eosin dye stains cytoplasm, which enables us to obtain better construction of bile ducts and erythrocytes. 3D reconstruction was performed on 125 serial optical sections at intervals of 0.932 μm. Because each digital sectional image overlaps the adjacent sections with half of its thickness, the total thickness was 57.04 μm. By digital accumulation of Z-series optical sections (Fig. 6.3a), interlobular bile ducts were clearly detected (arrows in Fig. 6.3a). In a portal vein and sinusoids, erythrocytes were found to be shaped like biconcave disks (white arrows in Fig. 6.3a, b). The CLSM

enabled us to demonstrate functional liver structures in vivo with eosin staining alone within 25 μm in depth from the cut tissue surface (arrowheads in Fig. 6.3b) by X/Z planes in the reconstructed images. Thus, it became possible to visualize 3D structure images of IVCT-prepared tissues of living mouse livers with CLSM.

6.5 Conclusion

We have reported 3D-reconstructive images of paraffin-embedded liver tissues reflecting their living states. Paraffin-embedded specimens are commonly applicable to various staining procedures for pathological examinations. Recently, according to advanced confocal endomicroscopic techniques, intravital 3D images could be available in clinical medicine. However, such images are insufficient for the critical diagnosis and unable to take advantage of existing pathological preparation techniques. The freeze-substituted specimens prepared by our cryotechniques are useful to obtain 3D-constructive images reflecting intravital cells and tissues and their histochemically stained sections. Therefore, the IVCT could also confirm the intravital imaging associated with pathological information. This text is mainly quoted from Reference [13].

References

1. De Palma GD (2009) Confocal laser endomicroscopy in the "in vivo" histological diagnosis of the gastrointestinal tract. World J Gastroenterol 15:5770–5775
2. Kopácová M, Bures J, Osterreicher J, Kvetina J, Pejchal J, Tachecí I, Kunes M, Spelda S, Rejchrt S (2009) Confocal laser endomicroscopy in experimental pigs. Methods of ex vivo imaging. Cas Lek Cesk 148:249–253
3. Brandzaeg P (1982) Tissue preparation methods for immunohistochemistry. In: Bullock GR, Petrusz P (eds) Techniques in Immunocytochemistry, 1st edn. Academic, London, pp 1–75
4. Fujii Y, Ohno N, Li Z, Terada N, Baba T, Ohno S (2006) Morphological and histochemical analyses of living mouse livers by new 'cryobiopsy' technique. J Electron Microsc 55:113–122
5. Ohno N, Terada N, Bai Y, Saitoh S, Nakazawa T, Nakamura N, Naito I, Fujii Y, Katoh R, Ohno S (2008) Application of cryobiopsy to morphological and immunohistochemical analyses of xenografted human lung cancer tissues and functional blood vessels. Cancer 113:1068–1079
6. Saitoh Y, Terada N, Saitoh S, Ohno N, Fujii Y, Ohno S (2010) Histochemical approach of cryobiopsy for glycogen distribution in living mouse livers under fasting and local circulation loss conditions. Histochem Cell Biol 133:229–239
7. Terada N, Ohno N, Saitoh S, Saitoh Y, Ohno S (2009) Immunoreactivity of glutamate in mouse retina inner segment of photoreceptors with in vivo cryotechnique. J Histochem Cytochem 57:883–888
8. Zea-Aragón Z, Terada N, Ohno N, Fujii Y, Baba T, Ohno S (2004) Effects of anoxia on serum immunoglobulin and albumin leakage through blood-brain barrier in mouse cerebellum as revealed by cryotechniques. J Neurosci Methods 138:89–95
9. Li Z, Ohno N, Terada N, Zhou D, Yoshimura A, Ohno S (2006) Application of periodic acid-Schiff fluorescence emission for immunohistochemistry of living mouse renal glomeruli by an "in vivo cryotechnique". Arch Histol Cytol 69:147–161
10. Schaart G, Hesselink RP, Keizer HA, van Kranenburg G, Drost MR, Hesselink MK (2004) A modified PAS stain combined with immunofluorescence for quantitative analyses of glycogen in muscle sections. Histochem Cell Biol 122:161–169
11. Goldstein DJ (1969) The fluorescence of elastic fibres stained with eosin and excited by visible light. Histochem J 1:187–198
12. Lev R, Stoward PJ (1969) On the use of eosin as a fluorescent dye to demonstrate mucous cells and other structures in tissue sections. Histochemie 20:363–377
13. Saitoh Y, Terada N, Saitoh S, Ohno N, Fujii Y, Ohno S (2010) Three-dimensional reconstruction of living mouse liver tissues using cryotechniques with confocal laser scanning microscopy. J Electron Microsc (Tokyo) 59:513–525

7 Application of "In Vivo Cryotechnique" to Immunohistochemical Detection of Hypoxia in Mouse Liver Tissues Treated with Pimonidazole

Nobuo Terada, Yurika Saitoh, Nobuhiko Ohno, and Shinichi Ohno

Abstract

Pimonidazole irreversibly binds to hypoxic cells with low oxygen tension in living animal organs. In this chapter, we present distribution of hypoxic cells in mouse liver tissues with "in vivo cryotechnique" (IVCT) by immunostaining for protein adducts of reductively activated pimonidazole (PARaPi). Pimonidazole was intraperitoneally injected into living mice, and then after various times of hypoxia, their livers were immobilized by IVCT. The frozen liver tissues were freeze-substituted and immunostained for PARaPi. In liver tissues with 30 s of hypoxia, some hepatocytes in the pericentral zones were strongly immunostained. Thus, IVCT revealed hypoxic cells with improved time resolution in tissue sections.

Keywords

Hypoxic cells • Pimonidazole • In vivo cryotechnique • Freeze substitution

7.1 Usefulness of Pimonidazole as a Hypoxic Marker and In Vivo Cryotechnique (IVCT)

To evaluate time-dependent changes of cells and tissues, IVCT has the merit of instantly freezing biological and also chemical materials in vivo [1, 2]. The subsequent freeze substitution (FS) is thought to substantially preserve their morphology and localization with fixatives at low temperatures by substituting hyaline ice crystals with organic solvents, such as acetone and alcohol, in which biological components are almost immobile during such a preparation step. In our previous studies, soluble proteins in blood vessels were demonstrated to be well preserved at their original sites under different hemodynamic conditions [2–4].

Pimonidazole binds to thiol-containing proteins specifically in hypoxic cells [5]. Protein adducts of reductively activated pimonidazole (PARaPi) have been used as immunogens for the production of antibodies (Fig. 7.1a), which were used for immunohistochemical detection of hypoxia of cells with partial oxygen tensions below 10 mmHg under various pathological conditions [6–13]. Because commonly used chemical fixation needs uncertain interval for completion of the cross-linking reaction of tissue components, it was difficult to focus on initial timing of PARaPi production in any hypoxic animal tissues. In the present chapter, we demonstrate the time-dependent states of intracellular hypoxia in mouse liver tissues. Precise methods and results have been reported in the previous paper [14].

N. Terada, M.D., Ph.D. (✉)
Division of Health Sciences, Shinshu University Graduate School of Medicine, 3-1-1 Asahi, Matsumoto City, Nagano 390-8621, Japan

Department of Anatomy and Molecular Histology, Interdisciplinary Graduate School of Medicine and Engineering, University of Yamanashi, 1110 Shimokato, Chuo City, Yamanashi 409-3898, Japan
e-mail: nobuot@shinshu-u.ac.jp

Y. Saitoh • N. Ohno • S. Ohno
Department of Anatomy and Molecular Histology, Interdisciplinary Graduate School of Medicine and Engineering, University of Yamanashi, 1110 Shimokato, Chuo City, Yamanashi 409-3898, Japan

S. Ohno et al. (eds.), *In Vivo Cryotechnique in Biomedical Research and Application for Bioimaging of Living Animal Organs*, DOI 10.1007/978-4-431-55723-4_7

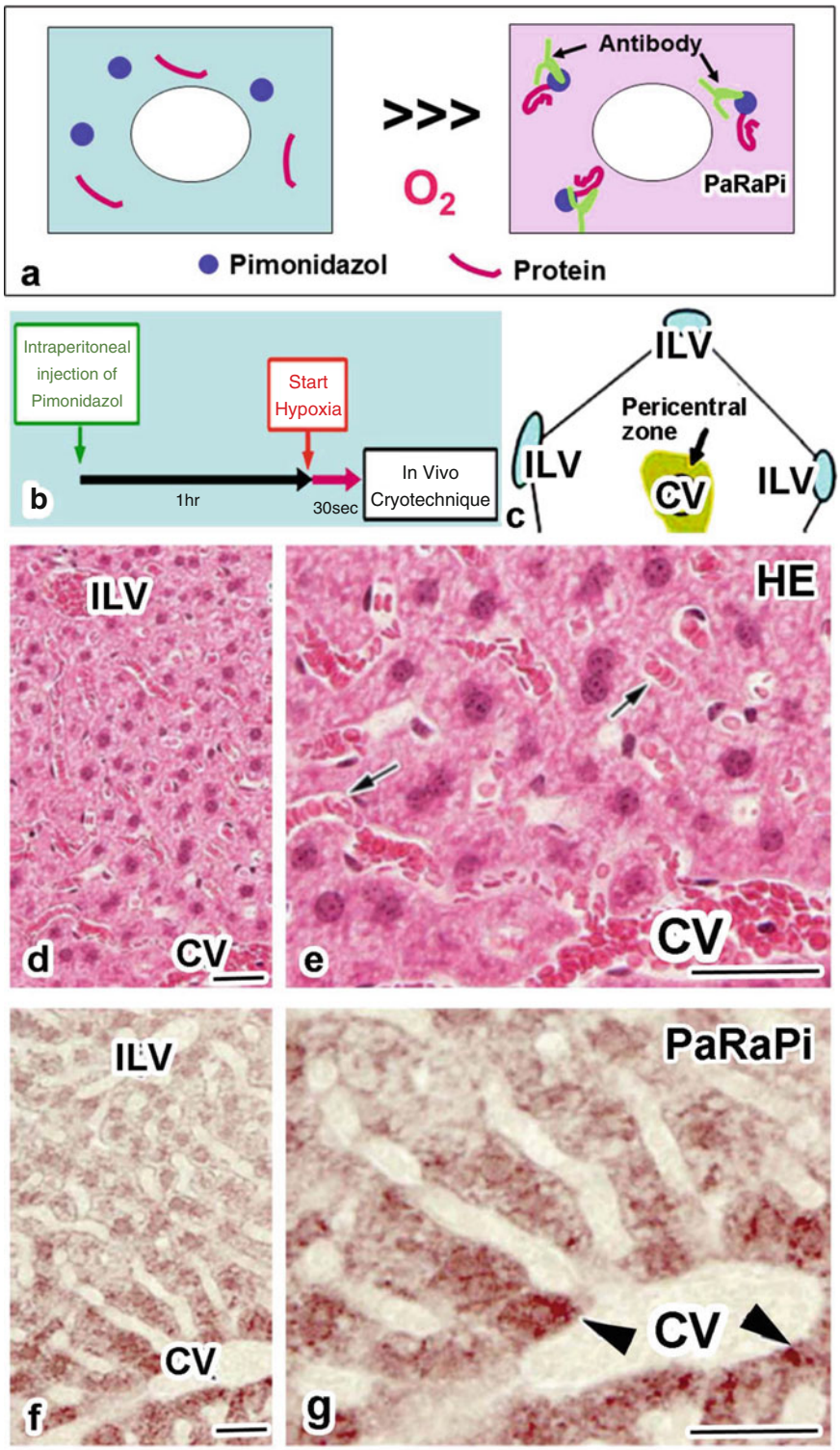

Fig. 7.1 (**a**) Pimonidazole binds to general proteins under ischemia due to adduction, and the antibody reacts to the protein adducts of reductively activated pimonidazole (PARaPi). (**b**) Experimental protocol shown in this chapter; one hour after the intraperitoneal injection of pimonidazole, in vivo cryotechnique (IVCT) was performed at 30 s of hypoxia. (**c**) Schematic representation of the hepatic lobule after 30 s of hypoxia, which is immunostained for PARaPi in pericentral zone. (**d**–**g**) HE staining images (**d**, **e**) and immunostaining images for PARaPi (**f**, **g**) in mouse liver tissues after 30 s of hypoxia. The PARaPi immunostaining is obtained around central veins (CV; *arrowheads* in **g**), but it is very weak around interlobular veins (ILV). Precise data have been reported in the previous paper (Terada et al. [14]). *Bars*: **d**–**g**, 50 μm

7.2 How to Detect PARaPi Immunohistochemically in IVCT Tissues?

We demonstrate brief protocol of immunohistochemical approach for the IVCT tissue samples. Pimonidazole was intraperitoneally injected into mice. One hour after the injection of pimonidazole, the mice were anesthetized with pentobarbital. Their respiration stopped by inhalation of nitrogen gas in plastic bags, and at various interval times after their respiration completely stopped, their livers were surgically exposed, and an isopentane–propane mixture precooled in liquid nitrogen was directly poured on them, as described in the procedure for IVCT [1, 4].

The frozen liver tissues were freeze-substituted in acetone containing paraformaldehyde and embedded in paraffin. For immunostaining of PARaPi, deparaffinized sections were immunostained with commercially available FITC-conjugated anti-PARaPi monoclonal antibody followed by horseradish peroxidase (HRP)-conjugated anti-FITC monoclonal antibody. The immunoreaction products were visualized using the peroxidase enzyme reaction with metal-enhanced 3,3′-diaminobenzidine (DAB). This immunoperoxidase staining enables us to obtain better sensitivity.

7.3 Immunostaining for PARaPi in Normal and Hypoxic Liver Tissues

In normal liver tissues with IVCT, cells immunopositive for PARaPi were rarely observed, indicating oxygen tension in liver tissues was well retained under normal blood circulation.

At 30 s of hypoxia (Fig. 7.1b), erythrocytes formed typical rouleaux in sinusoids (Fig. 7.1d, e), and the PARaPi was strongly immunostained than in the normal liver, especially in some hepatocytes of the pericentral zone (Fig. 7.1f, g). The further from the central vein, the less immunoreactivity of PARaPi was detected, indicating that a change of the hypoxic state was detectable within 30 s by IVCT, as schematically demonstrated in Fig. 7.1c.

After 1 min of hypoxia, most hepatocytes in all hepatic zones were immunopositive for PARaPi, indicating that they were in a hypoxic state. The relative intensity of PARaPi immunoreactivity was stronger in hepatocytes of the pericentral zone than in those of other zones, and hepatocytes showed various degrees of immunoreactivity against PARaPi even in the periportal zone. To evaluate whether such changes of cell membrane permeability occurred in such hypoxic cells, serial sections were possible to be immunostained for mouse serum IgG1. IgG1 was immunostained in blood vessels and intercellular spaces, but not inside the hepatocytes, indicating that the changes of PARaPi immunostaining were not due to diffusion of cytoplasmic proteins into extracellular spaces.

7.4 Application of IVCT Followed by FS for Immunoblotting Analyses

In addition, immunoblotting analyses can be done on FS samples. By immunoblotting, the intensity of immunoreactivity for PARaPi was observed after hypoxia for 3 min, whereas it was much weaker with the normal liver tissues in vivo. Thus, it was possible to examine the same tissue samples by immunohistochemistry and immunoblotting analyses.

7.5 Concluding Remarks

When IVCT is used, we need no attention for a state of perfusion fixation caused by blood coagulation after stopping circulation. Therefore, IVCT would be a useful way to evaluate the distribution pattern of hypoxic cells in mouse liver tissues.

References

1. Ohno S, Terada N, Fujii Y, Ueda H, Takayama I (1996) Dynamic structure of glomerular capillary loop as revealed by an in vivo cryotechnique. Virchow's Arch 427:519–527
2. Terada N, Ohno N, Ohguro H, Li Z, Ohno S (2006) Immunohistochemical detection of phosphorylated rhodopsin in light-exposed retina of living mouse with in vivo cryotechnique. J Histochem Cytochem 54:479–486
3. Li Z, Ohno N, Terada N, Ohno S (2006) Immunolocalization of serum proteins in living mouse glomeruli under various hemodynamic conditions by "in vivo cryotechnique". Histochem Cell Biol 126:399–406
4. Ohno N, Terada N, Ohno S (2006) Histochemical analyses of living mouse liver under different hemodynamic conditions by "in vivo cryotechnique". Histochem Cell Biol 126:389–398
5. Gross MW, Karbach U, Groebe K, Franko AJ, Mueller-Klieser W (1995) Calibration of misonidazole labeling by simultaneous measurement of oxygen tension and labeling density in multicellular spheroids. Int J Cancer 61:567–573
6. Raleigh JA, Franko AJ, Koch CJ, Born JL (1985) Binding of misonidazole to hypoxic cells in monolayer and spheroid culture. Br J Cancer 51:229–235
7. Kennedy AS, Raleigh JA, Perez GM, Calkins DP, Thrall DE, Novotny DB, Varia MA (1997) Proliferation and hypoxia in human squamous cell carcinoma of the cervix: first report of combined immunohistochemical assays. Int J Radiat Oncol Biol Phys 37:897–905
8. Hoeckel M, Vaupel P (2001) Biological consequences of tumor hypoxia. Semin Oncol 28:36–41

9. Samoszuk MK, Walter H, Mechetner E (2004) Improved immunohistochemical method for detecting hypoxia gradients in mouse tissues and tumors. J Histochem Cytochem 52:837–839
10. Yaromina A, Zips D, Thames HD, Eicheler W, Krause M, Rosner A, Haase M, Petersen C, Raleigh JA, Quennet V, Walenta S, Mueller-Klieser W, Baumann M (2006) Pimonidazole labelling and response to fractionated irradiation of five human squamous cell carcinoma (hSCC) lines in nude mice: the need for a multivariate approach in biomarker studies. Radiother Oncol 81:122–129
11. Semenza GL (2002) HIF-1 and tumor progression: pathophysiology and therapeutics. Trends Mol Med 8:62–67
12. Pugh CW, RatcliVe PJ (2003) Regulation of angiogenesis by hypoxia: role of HIF system. Nat Med 9:677–684
13. Danylkova NO, Pomeranz HD, Alcala SR, McLoon LK (2006) Histological and morphometric evaluation of transient retinal and optic nerve ischemia in rat. Brain Res 1096:20–29
14. Terada N, Ohno N, Saitoh S, Ohno S (2007) Immunohistochemical detection of hypoxia in mouse liver tissues treated with Pimonidazole using “in vivo cryotechnique”. Histochem Cell Biol 128:253–261

Immunohistochemical Detection of Soluble Immunoglobulins in Small Intestines

8

Satoshi Shimo, Sei Saitoh, Yurika Saitoh, Nobuhiko Ohno, and Shinichi Ohno

Abstract

We performed immunohistochemical or ultrastructural analyses of living mouse small intestines prepared by "in vivo cryotechnique" (IVCT). Living morphological states of small intestinal tissues, including flowing erythrocytes and opening blood vessels, were observed on paraffin-embedded sections prepared with IVCT. IgA was immunolocalized in many plasma cells of the lamina propria mucosa, intestinal matrices, and also in epithelial cells of the intestinal villi and crypts. Both IgG1 and IgM immunoreactivities were mainly detected in blood vessels, whereas only IgG1 was also immunolocalized in interstitial matrices of mucous membranes. Confocal laser scanning micrographs of double-fluorescence immunostaining for IgA immunoreactivity are detected in the cytoplasm of epithelial cells as well as plasma cells in the lamina propria mucosa. On the other hand, by electron microscopy, intracellular ultrastructures of epithelial cells were well preserved in tissue areas 5–10 μm away from the cryogen-contact surface tissues. Apical microvilli of epithelial cells contained dynamically waving actin filaments. Furthermore, highly electron-dense organelles, such as mitochondria, in addition to endoplasmic reticulum and ribosomes, were well preserved under the widely organized terminal web. Additionally, Epon-embedded thick sections were treated with sodium ethoxide, followed by antigen retrieval, and immunostained for various proteins, such as IgA, Igκ, IgG1, IgM, J-chain, and albumin. IgA immunoreactivity was detected as a tiny dot-like pattern in the cytoplasm of some epithelial cells and plasma cells localized in the lamina propria. The J-chain and Igκ immunoreactivities were also detected in the same local areas as those of IgA. Thus, IVCT was useful for the preservation of soluble serum proteins and ultrastructural analyses of dynamically changing epithelial cells of living mouse small intestines.

Keywords

Small intestine • In vivo cryotechnique • Immunohistochemistry • Immunoglobulin A • Ultrastructure

S. Shimo
Department of Occupational Therapy, Health Science University, 7187 Kodachi, Fujikawaguchiko, Yamanashi 401-0380, Japan

S. Saitoh • Y. Saitoh • N. Ohno • S. Ohno, M.D., Ph.D. (✉)
Department of Anatomy and Molecular Histology, Interdisciplinary Graduate School of Medicine and Engineering, University of Yamanashi, 1110 Shimokato, Chuo City, Yamanashi 409-3898, Japan
e-mail: sohno@yamanashi.ac.jp

8.1 Introduction

The animal intestinal mucosa is well known to maintain highly developed immunological systems with circulating immunoglobulins (Igs), which contribute to some defensive barriers against foreign antigens, such as pathogenic viruses, bacteria, and other toxic materials [1–3]. Recently, in vivo imaging using intravital microscopy and fluorescence-

S. Ohno et al. (eds.), *In Vivo Cryotechnique in Biomedical Research and Application for Bioimaging of Living Animal Organs*, DOI 10.1007/978-4-431-55723-4_8

imaging techniques has revealed dynamically changing mucosal immunity in gastrointestinal tracts of living animals [4, 5]. Therefore, preservation of soluble immunoglobulins in situ for immunohistochemistry is essential to examine the mucosal immunity in living animal intestines without morphological artifacts during the specimen preparation steps, such as tissue shrinkage, antigen masking, and diffusion of soluble proteins, during the conventional preparation steps [6–8]. The "in vivo cryotechnique" (IVCT) can directly cryofix living mouse small intestines under normal blood circulation and soluble serum proteins of tissues for preservation of their antigenicity.

8.2 Immunolocalizations of Various Igs in Paraffin Thick Sections

To examine immunodistributions of various classes of Igs in the living mouse small intestines, the common peroxidase-DAB immunostainings for IgA, Igκ, IgG1, and IgM were performed on serial paraffin sections in the tissue specimens prepared with IVCT-FS (Freeze-substitution). Their well-frozen tissue areas were always checked with HE staining (Fig. 8.1a, b), showing flowing erythrocytes in open blood vessels (arrowhead in Fig. 8.1b). Many IgA-immunopositive plasma cells were observed in the lamina propria mucosa of the intestinal villi (arrowheads in Fig. 8.1c), and the IgA immunoreactivity was also detected in the cytoplasm of epithelial cells. The Igκ-immunopositive plasma cells were also observed in the same areas of the lamina propria mucosa (arrowheads in Fig. 8.1d). IgA, Ig-G1, and IgM were differently immunolocalized between blood vessels and interstitial matrices of intestinal mucous membranes, indicating the existence of some molecular barriers between the interstitial matrices and blood vessels. It is of concern that such IgA immunodistribution may be time-dependently changing in living mouse intestines under normal and pathological conditions. On the other hand, with conventional perfusion-fixation followed by dehydration, Ig immunoreactivity decreases and diffuses cytoplasmic immunostaining for Igs [9–11]. Such a discrepancy between our immunohistochemical data by IVCT and previous reports may be due to the conventional preparation procedures, resulting in various levels of immunoreactivity and translocation of soluble Igs.

Furthermore, to examine what class of Ig was produced in identical plasma cells and immunolocalized in epithelial cells of the intestinal mucosa, double-fluorescence immunostaining for IgA and IgG1 was performed for tissue samples, as prepared with IVCT-FS which were examined with confocal laser scanning microscopy (Fig. 8.1g–i). The IgA immunoreactivity was clearly detected in almost all plasma cells in the lamina propria mucosa, as well as in the cytoplasm of some epithelial cells (Fig. 8.1g, i). In addition, small granular immunoreaction products were more clearly observed in the apical cytoplasm of the epithelial cells at some optical section levels under the confocal laser scanning microscope (asterisks in Fig. 8.1g). However, the IgG1 immunoreactivity was mainly detected in blood vessels of intestinal villi and a few plasma cells at these intestinal areas (Fig. 8.1h, i). IVCT is reasonable to prevent translocation of soluble proteins that easily occurs during the conventional chemical fixation of aqueous solutions [12, 13] because it can immediately capture all dynamic biological movements within milliseconds at the time of freezing, as already shown by our time-dependent studies of signal molecules with IVCT [14, 15]. In addition, artificial antigen masking of various target molecules, which was sometimes problematic on immunohistochemistry [16–18], was also improved with IVCT followed by FS, as reported before [19]. The well-frozen tissue areas with few visible ice crystals were within 300–400 μm from the frozen tissue surface at the light microscopic level. At the electron microscopic level, however, meshwork-like structures damaged by the tiny ice crystal formation were usually observed in the deep frozen tissues of living animal organs, and these ice crystal sizes always depended on the distance from the frozen tissue surface [20]. These fine meshwork-like structures probably aid more effective penetration of antibodies during immunohistochemical steps, resulting in formation of antigen-antibody complexes [19].

8.3 Electron Micrographs of Epithelial Cells in Intestinal Tissues Prepared by IVCT

At the electron microscopic level, the uppermost part of the cytoplasm or the cuticular border of epithelial cells consists of numerous microvilli, containing filaments that extend into the deep cytoplasm and intermingle with the terminal web, as shown in Fig. 8.2. No cytoplasmic organelles of the terminal web region were seen, but the actin microfilament bundles were organized along their entire length, as well as microfilament networks in the terminal web [21, 22]. On the other hand, many cytoplasmic organelles including numerous mitochondria, endoplasmic reticulum, and ribosome were localized under the terminal web region, as shown in Fig. 8.2c, d. Morphological alteration was probably due to rapidly changing solute permeability of cell membranes during perfusion-fixation with artificial perfusion pressure [23–25]. Such relatively high pressure in the interstitium during perfusion-fixation may also cause other dilations in intercellular spaces between epithelial cells, such as lateral interdigitation and alterations in the total cell sizes. Therefore, careful attention must be paid to preserve the native ultrastructure of cells and tissues and not lose them during the tissue

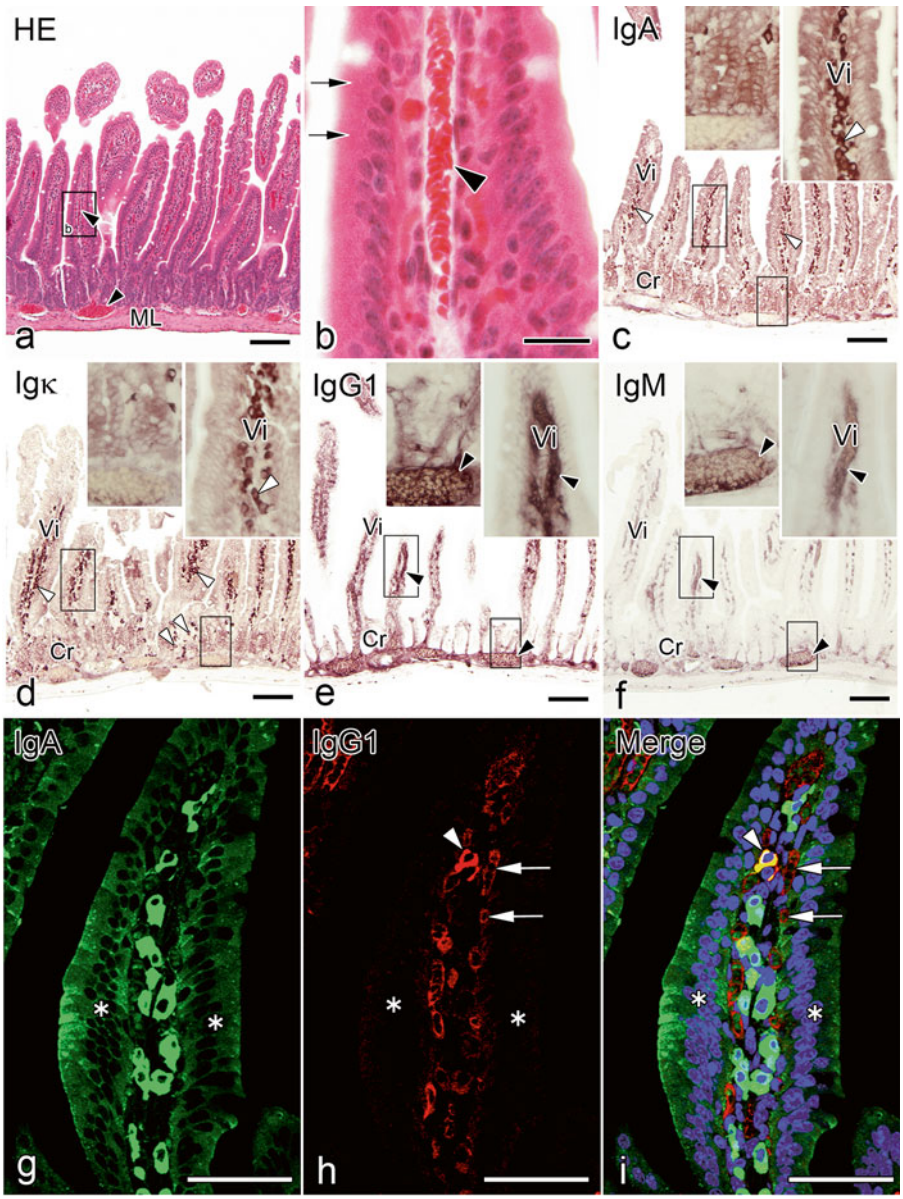

Fig. 8.1 Light micrographs of HE staining (HE; **a**, **b**), immunostaining for IgA (**c**), Igκ (**d**), IgG1 (**e**), and IgM (**f**), confocal laser scanning micrographs of double-fluorescence immunostaining for IgA (**g**), IgG1 (**h**), and merge (**i**) in paraffin sections of the mouse small intestines prepared with IVCT. (**a**) and (**b**) Flowing erythrocytes are well preserved in open blood vessels (*arrowheads* in **a**, **b**). (**b**) Higher magnified view of the rectangular part in (**a**). The epithelial morphology is well preserved with few ice crystals at the light microscopic level (*arrows* in **b**). (**c**) Many IgA-immunopositive plasma cells are mainly observed in intestinal villi (*white arrowheads*). Epithelial cells are also IgA-immunopositive along intestinal crypts (*small inset*) and villi (*large inset*). (**d**) Igκ-immunopositive plasma cells (*white arrowheads*) are abundant in the villi and crypt areas. (**e**) IgG1 immunoreactivity is detected in interstitial matrices of intestinal villi and crypts, as well as inside blood vessels (*arrowheads*), whereas it is hardly detected in the cytoplasm of epithelial cells. (**f**) IgM immunoreactivity is detected only in blood vessels (*arrowheads*). (**g**–**i**) IgA immunoreactivity (*green* in **a**, **c**) is detected in the cytoplasm of epithelial cells (*asterisks*), as well as plasma cells in the lamina propria mucosa. However, IgG1 immunoreactivity (*red* in **h**, **i**) is detected in some plasma cells (*arrowheads*) and blood vessels (*arrows*). (**i**) From a color-merged image of (**g**) and (**h**), IgA- and IgG1-double immunopositive plasma cells are identified in the intestinal mucosa (*arrowheads*; *yellow*). *Cr* crypt, *ML* muscle layer, *Vi* villi. *Bars*: (**a**–**f**) 100 μm, (**g**–**i**) 50 μm (From Shimo S et al., J Immunol Methods 361(1–2):64–74, 2010)

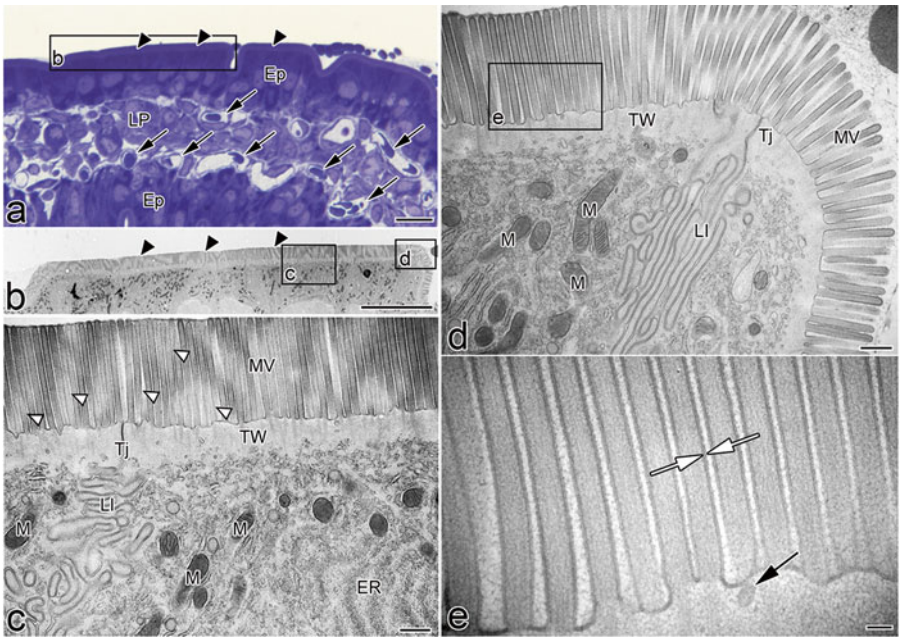

Fig. 8.2 Electron micrographs of the apical cytoplasm of living mouse intestinal epithelial cells prepared by IVCT. (**a**) Epon thick section stained with toluidine blue. The cuticular border and open blood capillaries are seen (*arrowheads* and *arrows*). (**b**) At lower magnification, microvilli show a conspicuous surface structure. This layer is the band that shows low-intensity staining with toluidine blue. In regions under the microvilli, the electron-lucent band appears to be separated from the deeper cytoplasm. (**c**) The microvilli of epithelial cells are frequently seen to have different electron density from the slicing plane because they are waving back and forth (*white arrowheads*). Furthermore, many cytoplasmic organelles are abundantly localized under the terminal web, such as electron-dense mitochondria, obliquely cut endoplasmic reticulum, and ribosome. (**e**) At a higher magnification in (**d**), the separating inner or outer leaflets of the apposed cell membranes are visible along the microvilli (*white arrows*). *Ep* epithelial cell, *ER* endoplasmic reticulum, *LI* lateral interdigitation, *LP* lamina propria, *M* mitochondria, *MV* microvilli, *TJ* tight junction, *TW* terminal web. *Bars*: (**a**, **b**) 10 μm, (**c**, **d**) 500 nm, (**e**) 100 nm (From Shimo S et al., Microscopy 64(3):189–203, 2015)

preparation steps, which may be compatible with functional analyses by in situ imaging to visualize the intestinal mucosal immunity [26–28].

8.4 Immunolocalizations of IgA, J-Chain, and Igκ in Epon Thick Sections

Immunolocalizations of soluble IgA, J-chain, and Igκ were compared with each other in the small intestinal tissues of living mice, which were prepared by IVCT. By IVCT, IgA-immunopositive plasma cells were detected from the middle to the basal areas of the lamina propria, and also small granular immunoreaction products were clearly detected in the apical cytoplasm of epithelial cells in intestinal villi, as shown in Fig. 8.3a, b. J-chain- and Igκ-immunopositive plasma cells were also observed in the same areas of the lamina propria. However, the correspondence of Epon-embedded thick sections to electron microscopic images has been difficult to achieve because of much less localization of IgA in some apical areas of epithelial cells. Immunostaining for IgA, small granular immunoreaction products were detected in the epithelial cells, corresponding to vesicular structures, which were revealed in an ultrathin section by electron microscopy, as shown in Fig. 8.2, by using the in vivo cryoapparatus (Eiko Engineering, Hitachinaka, Ibaraki, Japan) in combination with the cryoknife with cryogen [29].

8.5 Concluding Remarks

Paraffin-embedded sections prepared with IVCT better remain soluble serum immunoglobulins in the small intestine, such as IgA, which can be easily translocated during conventional chemical-fixation methods. Furthermore, the immunostaining of conventional Epon-embedded thick sections prepared by IVCT-FS and the antigen retrieval treatment clearly revealed the immunoreactivities of soluble serum proteins in functional cells and tissues of living mouse small intestines, which would be compared with the captured dynamic ultrastructures in ultrathin Epon sections by IVCT.

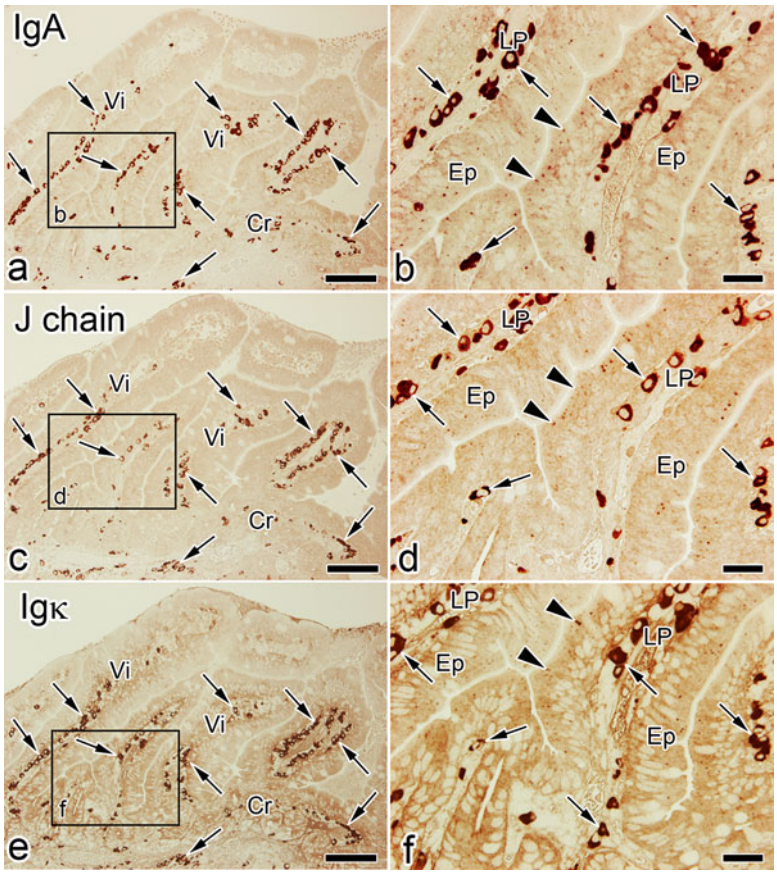

Fig. 8.3 Light micrographs of immunostaining for IgA (**a**, **b**), J-chain (**c**, **d**) and Igκ (**e**, **f**) in serial Epon thick sections of living mouse small intestines prepared by IVCT. (**a**, **b**) Many IgA-immunopositive plasma cells are mainly localized in the lamina propria of intestinal villi from their middle to basal areas (*arrows* in **b**). Both J-chain- (**c**, **d**) and Igκ- (**e**, **f**) immunopositive plasma cells (*arrows*) are also abundant in the villus areas. They are seen as numerous small granular immunoreaction products in the apical cytoplasm of some epithelial cells (*arrowheads* **d**, **f**), similar to those of IgA (*arrowheads* **b**). However, the villus tip areas are rarely detected for IgA in the cytoplasm of epithelial cells or plasma cells. *Cr* crypt, *Ep* epithelial cell, *LP* lamina propria, *Vi* villus. *Bars*: (**a**, **c**, **e**) 50 μm, (**b**, **d**, **f**) 20 μm (From Shimo S et al., Microscopy 64(3):189–203, 2015)

References

1. Wines BD, Hogarth PM (2006) IgA receptors in health and disease. Tissue Antigens 68(2):103–114
2. Tezuka H, Abe Y, Iwata M, Takeuchi H, Ishikawa H, Matsushita M, Shiohara T, Akira S, Ohteki T (2007) Regulation of IgA production by naturally occurring TNF/iNOS-producing dendritic cells. Nature 448(7156):929–933
3. Friedman HI, Cardell RR Jr (1972) Effects of puromycin on the structure of rat intestinal epithelial cells during fat absorption. J Cell Biol 52(1):15–40
4. Hosoe N, Miura S, Watanabe C, Tsuzuki Y, Hokari R, Oyama T, Fujiyama Y, Nagata H, Ishii H (2004) Demonstration of functional role of TECK/CCL25 in T lymphocyte-endothelium interaction in inflamed and uninflamed intestinal mucosa. Am J Physiol Gastrointest Liver Physiol 286(3):G458–G466
5. Zinselmeyer BH, Dempster J, Gurney AM, Wokosin D, Miller M, Ho H, Millington OR, Smith KM, Rush CM, Parker I, Cahalan M, Brewer JM, Garside P (2005) In situ characterization of CD4+ T cell behavior in mucosal and systemic lymphoid tissues during the induction of oral priming and tolerance. J Exp Med 201(11):1815–1823
6. Ohno N, Terada N, Bai Y, Saitoh S, Nakazawa T, Nakamura N, Naito I, Fujii Y, Katoh R, Ohno S (2008) Application of cryobiopsy to morphological and immunohistochemical analyses of xenografted human lung cancer tissues and functional blood vessels. Cancer 113(5):1068–1079
7. Saitoh S, Terada N, Ohno N, Ohno S (2008) Distribution of immunoglobulin-producing cells in immunized mouse spleens revealed with “in vivo cryotechnique”. J Immunol Methods 331(1–2):114–126
8. Ohno S, Terada N, Ohno N, Saitoh S, Saitoh Y, Fujii Y (2010) Significance of ‘in vivo cryotechnique’ for morphofunctional analyses of living animal organs. J Electron Microsc 59(5):395–408
9. Erlandsen SL, Rodning CB, Montero C, Parsons JA, Lewis EA, Wilson ID (1976) Immunocytochemical identification and localization of immunoglobulin A within Paneth cells of the rat small intestine. J Histochem Cytochem 24(10):1085–1092
10. Satoh Y, Ishikawa K, Tanaka H, Ono K (1986) Immunohistochemical observations of immunoglobulin A in the Paneth cells of germ-free and formerly-germ-free rats. Histochemistry 85(3):197–201
11. Shimo S, Saitoh S, Terada N, Ohno N, Saitoh Y, Ohno S (2010) Immunohistochemical detection of soluble immunoglobulins in living mouse small intestines using an in vivo cryotechnique. J Immunol Methods 361(1–2):64–74

12. Kent SP (1984) Intracellular diffusion of myoglobin. A manifestation of early cell injury in myocardial ischemia in dogs. Arch Pathol Lab Med 108(10):827–830
13. Zea-Aragón Z, Terada N, Ohno N, Fujii Y, Baba T, Ohno S (2004) Effects of anoxia on serum immunoglobulin and albumin leakage through blood-brain barrier in mouse cerebellum as revealed by cryotechniques. J Neurosci Methods 138(1–2):89–95
14. Terada N, Ohno N, Ohguro H, Li Z, Ohno S (2006) Immunohistochemical detection of phosphorylated rhodopsin in light-exposed retina of living mouse with in vivo cryotechnique. J Histochem Cytochem 54(4):479–486
15. Saitoh S, Terada N, Ohno N, Saitoh Y, Soleimani M, Ohno S (2009) Immunolocalization of phospho-Arg-directed protein kinase-substrate in hypoxic kidneys using in vivo cryotechnique. Med Mol Morphol 42(1):24–31
16. Brandtzaeg P (1981) Prolonged incubation time in immunohistochemistry: effects on fluorescence staining of immunoglobulins and epithelial components in ethanol- and formaldehyde-fixed paraffin-embedded tissues. J Histochem Cytochem 29(11):1302–1315
17. Shi SR, Key ME, Kalra KL (1991) Antigen retrieval in formalin-fixed, paraffin-embedded tissues: an enhancement method for immunohistochemical staining based on microwave oven heating of tissue sections. J Histochem Cytochem 39(6):741–748
18. O'Leary TJ, Mason JT (2004) A molecular mechanism of formalin fixation and antigen retrieval. Am J Clin Pathol 122(1):154–155
19. Ohno N, Terada N, Murata S, Katoh R, Ohno S (2005) Application of cryotechniques with freeze-substitution for the immunohistochemical demonstration of intranuclear pCREB and chromosome territory. J Histochem Cytochem 53(1):55–62
20. Ohno S, Terada N, Fujii Y, Ueda H, Takayama I (1996) Dynamic structure of glomerular capillary loop as revealed by an in vivo cryotechnique. Virchows Arch 427(5):519–527
21. Hirokawa N, Heuser JE (1981) Quick-freeze, deep-etch visualization of the cytoskeleton beneath surface differentiations of intestinal epithelial cells. J Cell Biol 91(2 Pt 1):399–409
22. Drenckhahn D, Gröschel-Stewart U (1980) Localization of myosin, actin, and tropomyosin in rat intestinal epithelium: immunohistochemical studies at the light and electron microscope levels. J Cell Biol 86(2):475–482
23. Ashworth CT, Luibel FJ, Stewart SC (1963) The fine structural localization of adenosine triphosphatase in the small intestine, kidney, and liver of the rat. J Cell Biol 17:1–18
24. Friend DS (1965) The fine structure of Brunner's glands in the mouse. J Cell Biol 25(3):563–576
25. Nagura H, Nakane PK, Brown WR (1980) Secretory component in immunoglobulin deficiency: an immunoelectron microscopic study of intestinal epithelium. Scand J Immunol 12(4):359–363
26. Glenney JR Jr, Glenney P (1983) Spectrin, fodrin, and TW260/240: a family of related proteins lining the plasma membrane. Cell Motil 3(5–6):671–682
27. Hirokawa N, Tilney LG, Fujiwara K, Heuser JE (1982) Organization of actin, myosin, and intermediate filaments in the brush border of intestinal epithelial cells. J Cell Biol 94(2):425–443
28. Shimo S, Saitoh S, Saitoh Y, Ohno N, Ohno S (2015) Morphological and immunohistochemical analyses of soluble proteins in mucous membranes of living mouse intestines by cryotechniques. Microscopy 64(3):189–203
29. Ohno N, Terada N, Saitoh S, Ohno S (2007) Extracellular space in mouse cerebellar cortex revealed by in vivo cryotechnique. J Comp Neurol 505(3):292–301

Detection of MAPK Signal Transduction Proteins in an Ischemia/Reperfusion Model of Small Intestines

9

Jiaorong Chen, Nobuo Terada, Yurika Saitoh, Zheng Huang, Nobuhiko Ohno, and Shinichi Ohno

Abstract

Intestinal ischemia and ischemia/reperfusion rapidly progress to tissue destruction and reconstruction of functional organs. To date, precise immunolocalizations and the timing of appearance of cell-signaling components under such conditions have not been well visualized in conventional tissue sections. For immunohistochemistry, we have proposed that soluble molecules including cell-signaling proteins are well retained by our in vivo cryotechnique (IVCT). Mitogen-activated protein kinase (MAPK) signal transduction pathways have been reported to be activated under various types of cell damage, and cyclic AMP response element-binding protein (CREB) was directly phosphorylated with various cellular stimuli. In this study, both the expression and the immunolocalization of ERK1/2, a member of the MAPK family, were examined in mouse intestinal tissues by IVCT. Under normal conditions, although ERK1/2 was widely immunolocalized in the cytoplasm of epithelial cells, phosphorylated (p) ERK1/2 was slightly detected in a small amount of epithelial cells in crypt and top parts of the villi. In 20 min ischemia, more pERK1/2 immunolocalization was detected in epithelial cells of the crypt part. In 60 min ischemia, however, its immunoreactivity was remarkably increased in wide areas of epithelial cells. In these 20 min and 60 min ischemia groups, another phosphorylated CREB was also immunostained in the nuclei of the same epithelial cell areas of pERK1/2. By ischemia 20 min reperfusion 60 min experiments, pERK1/2 immunointensity was reduced in the crypt areas. In 60 min ischemia with 60 min reperfusion, however, it was still strongly immunolocalized in epithelial cells of the crypts. Thus, rapidly changing ERK1/2 phosphorylation was visualized in the intestinal epithelial stem cells of mouse small intestine.

J. Chen
Department of Anatomy, Interdisciplinary Graduate School of Medicine and Engineering, University of Yamanashi, 1110 Shimokato, Chuo City, Yamanashi 409-3898, Japan

Department of Anatomy and Histochemistry & Embryology, Hubei University of Chinese Medicine, Wuhan, People's Republic of China

N. Terada
Division of Health Sciences, Shinshu University Graduate School of Medicine, 3-1-1 Asahi, Matsumoto City, Nagano 390-8621, Japan

Department of Anatomy and Molecular Histology, Interdisciplinary Graduate School of Medicine and Engineering, University of Yamanashi, 1110 Shimokato, Chuo City, Yamanashi 409-3898, Japan

Y. Saitoh • N. Ohno • S. Ohno, M.D., Ph.D. (✉)
Department of Anatomy, Interdisciplinary Graduate School of Medicine and Engineering, University of Yamanashi, 1110 Shimokato, Chuo City, Yamanashi 409-3898, Japan
e-mail: sohno@yamanashi.ac.jp

Z. Huang
Department of Anatomy, Interdisciplinary Graduate School of Medicine and Engineering, University of Yamanashi, 1110 Shimokato, Chuo City, Yamanashi 409-3898, Japan

Department of Pathology, The Central Hospital of Wuhan, Wuhan, People's Republic of China

S. Ohno et al. (eds.), *In Vivo Cryotechnique in Biomedical Research and Application for Bioimaging of Living Animal Organs*, DOI 10.1007/978-4-431-55723-4_9

Keywords
In vivo cryotechnique • ERK1/2 • CREB • Phosphorylation • Intestine • Ischemia/reperfusion

9.1 Introduction

Intestinal ischemia/reperfusion is an important clinical topic because it can often cause various subsequent multi-organ failure syndromes. It has already been proven that intestinal ischemia/reperfusion leads to severe damage of intestinal mucous epithelial barriers [4]. Such injury could also induce apoptosis of interstitial cells of Cajal, smooth muscle cells, and enteric neurons, which usually contributes to gastrointestinal motility disorders [8, 13]. Therefore, we have been interested in the actual immunolocalization and timing of expression of signaling molecules related to intestinal ischemia/reperfusion.

The mitogen-activated protein kinase (MAPK) signal transduction pathways are common conserved mechanisms of eukaryotic cell regulation. Many mammals have been reported to have several MAPK family proteins: extracellular signal-regulated kinases (ERK1/2, p44/p42), c-jun NH_2-terminal kinases 1/2 (JNK1/2, p54/p46), p38 MAPK, and ERK5. Recently, a molecular mechanism involving phosphorylation of the ERK signal pathway has been reported under myocardial ischemia/reperfusion, which plays a role in the antiapoptotic and cardioprotective effects of nitric oxide [7]. However, the ERK1/2 effect on neurons after ischemia is controversial. One report concluded that ERK1/2 caused neuronal damage [1], while another concluded that ERK1/2 supported neuronal survival [5].

We have already demonstrated that our in vivo cryotechnique (IVCT) is a powerful tool to examine not only pure morphological findings [2] but also the immunolocalization of signal transduction molecules in cells and tissues reflecting their living states. IVCT followed by freeze-substitution fixation (FS) ensured the preservation of many biological molecules at their original sites and also molecular structures of the signal molecules [10, 11]. In the present study, to evaluate the involvement of ERK1/2 signal transduction after intestinal ischemia/reperfusion injury, we examined the phosphorylation of ERK1/2 and CREB at different time intervals of ischemia/reperfusion by IVCT-FS.

9.2 Histology and Immunolocalization of ERK1/2 and pERK1/2 in Normal Mouse Small Intestine by Various Preparative Methods

By IVCT-FS, functional histological features of small intestinal tissues were shown upon HE staining, such as flowing erythrocytes in blood vessels (Fig. 9.1a, d). By ERK1/2 immunostaining, positive findings were widely detected in the cytoplasm of epithelial cells (Fig. 9.1b, e). On the other hand, pERK1/2 was detected mainly in epithelial cells at crypt areas and top parts of villi (Fig. 9.1c, f). By QF-FS, similar morphological images of epithelial cells were shown upon HE staining, although the blood vessels had collapsed (Fig. 9.1g, j). The ERK1/2 immunolocalization was similar to that with IVCT-FS (Fig. 9.1h, k), while pERK1/2 was more strongly immunostained in epithelial cells at crypt areas (Fig. 9.1i), which may have been due to hypoxia in the resected intestinal tissues.

By IM-DH, congested erythrocytes and shrinkage of cells and tissues were observed upon HE staining (Fig. 9.1m, p). ERK1/2 immunoreaction was detected in both cytoplasm and nuclei of cells in all mucous layers (Fig. 9.1n, q). However, pERK1/2 was detected only in epithelial cells at the top parts of villi, but not in the crypt areas (Fig. 9.1o, r). By PF-DH, erythrocytes were washed out during perfusion fixation; the cytoplasm of epithelial cells was strongly stained with eosin, and the total cell volumes and their nuclei had shrunk (Fig. 9.1s, v). ERK1/2 immunoreaction was detected mainly in the nuclei of epithelial cells of all layers (Fig. 9.1t, w), but pERK1/2 was hardly detected in those areas (Fig. 9.1u, x). Thus, different immunolocalizations of ERK1/2 and pERK1/2 were demonstrated by the different preparative methods. In particular, pERK was hardly detected with IM-DH or PF-DH. We assumed that IVCT-FS more clearly revealed morphological images and immunolocalization of pERKs, mostly reflecting their living states, with less effect of ischemia or technical diffusion artifacts.

9.3 ERK1/2 and pERK1/2 in 20 min Ischemia Group with IVCT-FS and IM-DH

Using morphological images with HE staining (Fig. 9.2a), many erythrocytes were shown to be congested in blood vessels, and some epithelial cells at the top parts of villi were swollen due to ischemia (Fig. 9.2a, d, g, j). The immunolocalization of ERK1/2 was seen in the cytoplasm of epithelial cells (Fig. 9.2b, e, h, k), which was almost the same as that of the sham operation group. pERK1/2 immunostaining was clearly detected in the cytoplasm and nuclei of epithelial cells in the crypt (arrowheads in Fig. 9.2f, l), but not in epithelial cells at the top parts of villi (Fig. 9.2i). Such immunopositive staining of both ERK1/2 and pERK1/2 was confirmed by performing IVCT from the luminal sides (the inset in Fig. 9.2b and the left inset in Fig. 9.2c), by detecting the immunostaining of ERK1/2 in the cytoplasm of epithelial cells and pERK1/2 in the epithelial cells at the crypt areas. Immunostaining patterns of ERK1/2 and pERK1/2 were

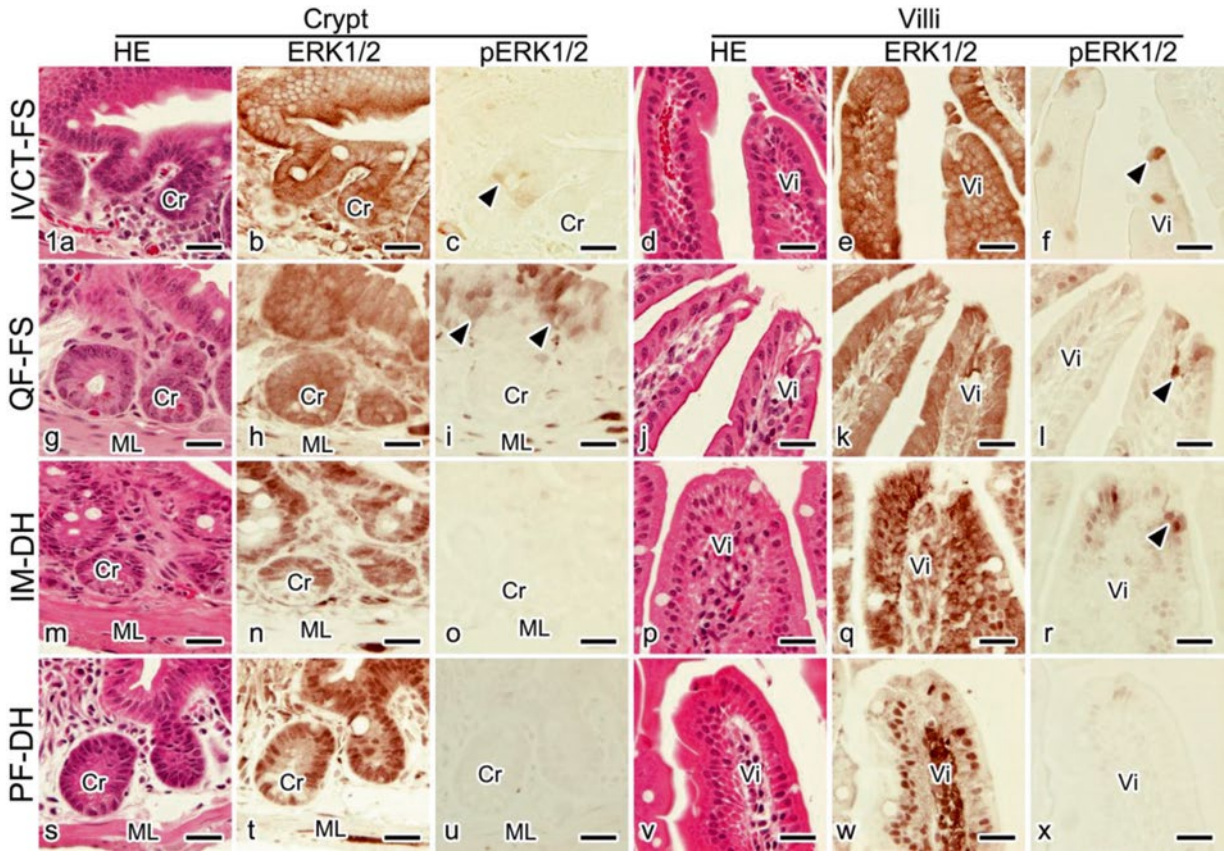

Fig. 9.1 Light microscopic images of HE staining (**a**, **d**, **g**, **j**, **m**, **p**, **s**, **v**) and immunostaining of ERK1/2 (**b**, **e**, **h**, **k**, **n**, **q**, **t**, **w**) and phosphorylated ERK1/2 (**c**, **f**, **i**, **l**, **o**, **r**, **u**, **x**) on serial paraffin sections in mouse small intestine with different preparative methods, such as IVCT-FS (**a**–**f**), QF-FS (**g**–**l**), IM-DH (**m**–**r**), and PF-DH (**s**–**x**), in crypts (**a**–**c**, **g**–**i**, **m**–**o**, **s**–**u**) and villi (**d**–**f**, **j**–**l**, **p**–**r**, **v**–**x**). *Arrowheads* (**c**, **f**, **i**, **l**, **r**) show the immunopositive staining of pERK1/2 in the crypts and villi. *ML* muscular layer, *Cr* crypt, and *Vi* villi. *Bars*, 20 μm

slightly different with another IM-DH preparation under the 20 min ischemia conditions (insets in Fig. 9.2d–i). Intestinal tissues were mostly shrunken due to alcohol dehydration during the conventional tissue preparation (insets in Fig. 9.2d, g). ERK1/2 was immunolocalized in both cytoplasm and nuclei of cells in all layers (insets in Fig. 9.2e, h). The immunolocalization of pERK1/2 was weakly detected in the nuclei of epithelial cells at crypt areas, compared with the immunostaining of pERK1/2 with IVCT after 20 min ischemia, not at the top areas of villi (insets in Fig. 9.2f, i). These findings indicate that the ERK1/2 signal transduction was usually activated in the intestinal epithelial stem cells under ischemia for 20 min.

9.4 ERK1/2 and pERK1/2 in 20 min Ischemia with 60 min Reperfusion Group Prepared by IVCT-FS

Using morphological images with HE staining (Fig. 9.3a, d, g, j), erythrocytes of various shapes were observed in the blood vessels of mucous membranes, probably reflecting their blood reperfusion at the time of freezing, and epithelial cells at the top parts of villi were also examined after 60 min reperfusion at higher magnification (Fig. 9.3d, g, j). After a series of 20 min ischemia with 60 min reperfusion, the microvascular blood flow could be first visualized with QD injection via the heart. As shown on the serial sections, it was easy to judge the morphology in all layers of intestinal tissues with HE staining (insets in Fig. 9.3a). Some QD-positive blood vessels (arrows in insets of Fig. 9.3b) and other QD-negative blood vessels (double arrowheads in insets of Fig. 9.3b) were easily distinguishable in such specimens. The no-reflow phenomenon sometimes reflects the failure of blood flow after reperfusion into ischemic areas, as already reported [3], and causes some cell and tissue damage [6]. This no-reflow phenomenon was easily visualized by the combination of IVCT with QD injection under such ischemia/reperfusion injury. The immunolocalization of ERK1/2 was seen in the cytoplasm of epithelial cells (Fig. 9.3b, e, h, k), which was similar to that of the sham operation group. In contrast, pERK1/2 immunostaining was detected only in some epithelial cells in crypt areas (arrowheads in Fig. 9.3f), as well as those at the top parts of villi (Fig. 9.3i). In some crypt areas, pERK1/2 was immunonegative in epithelial cells (Fig. 9.3l). These findings indicate that the activation of ERK1/2 signal transduction was recovered in some parts of

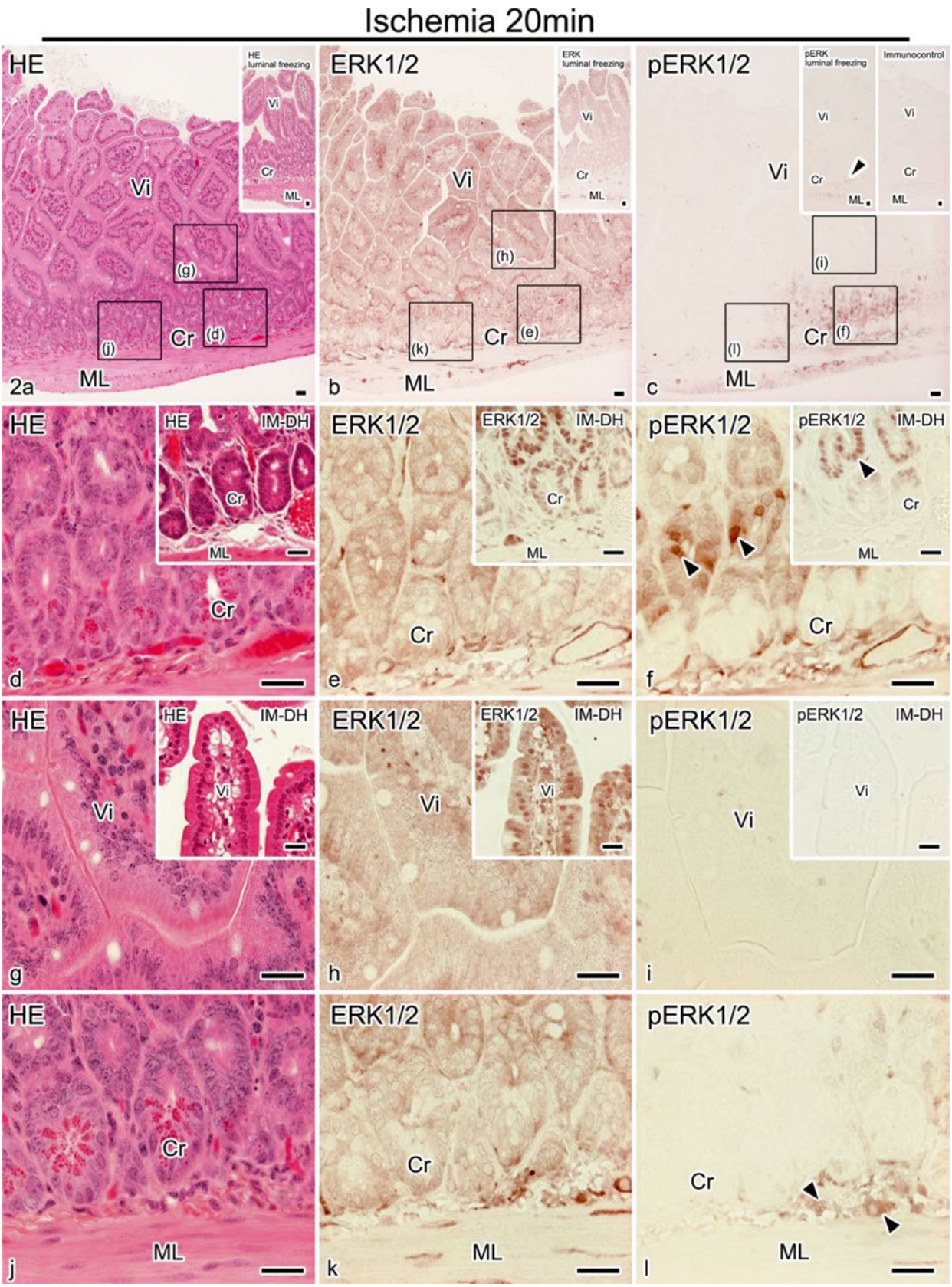

Fig. 9.2 Light microscopic images of HE staining (**a**, **d**, **g**, **j**) and immunostaining of ERK1/2 (**b**, **e**, **h**, **k**) and pERK1/2 (**c**, **f**, **i**, **l**) on serial paraffin sections in living mouse small intestines with IVCT and IM-DH under the 20 min ischemic conditions. *Inset* in (**a**): HE staining by preparing samples with freezing from luminal sides. *Inset* in (**b**): immunostaining of ERK1/2 by preparing samples with freezing from the luminal sides. *Left inset* in (**c**): immunostaining of pERK1/2 by preparing samples with freezing from the luminal sides. *Right inset* in (**c**): immunocontrol with a secondary antibody alone. *Inset* in (**d**–**i**): HE staining and immunostaining of ERK1/2 and pERK1/2 on serial paraffin sections in mouse small intestines with IM-DH. (**d**–**l**): highly magnified image of *rectangles* shown in the *top panel*. *Arrowheads* in (**f**, **l**) show the immunopositive staining of pERK1/2 in epithelial cells of crypts. *ML* muscular layer, *Cr* crypt, and *Vi* villi. *Bars*, 20 μm

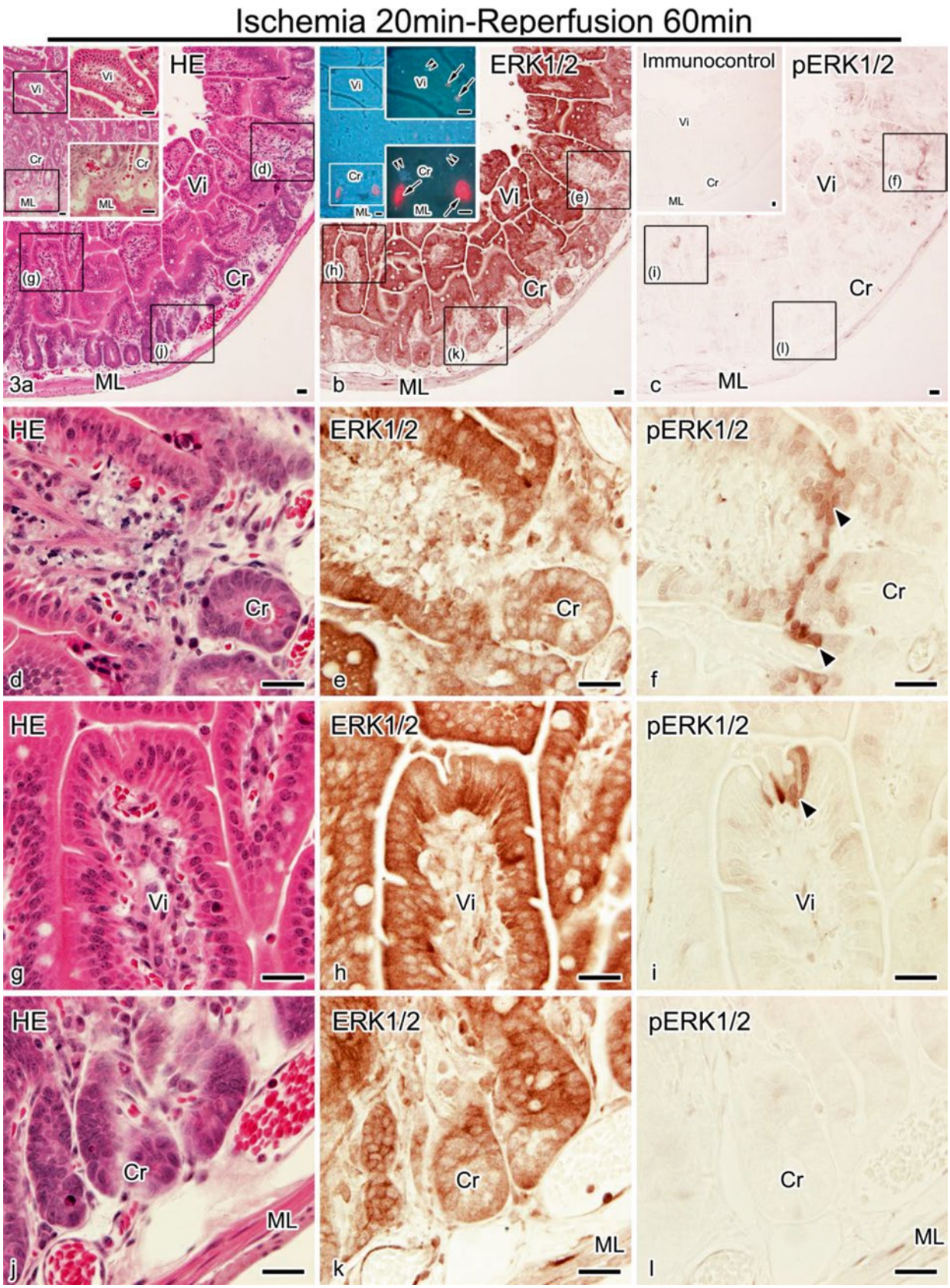

Fig. 9.3 Light microscopic images of HE staining (**a**, **d**, **g**, **j**), immunostaining of ERK1/2 (**b**, **e**, **h**, **k**) and pERK1/2 (**c**, **f**, **i**, **l**), and QD fluorescence images on serial paraffin sections in living mouse small intestines with IVCT under 20 min ischemia with 60 min reperfusion. *Inset* in (**a**): HE staining on the sections of QD injection sample. *Inset* in (**b**): fluorescence image of QD under ultraviolet light. *Inset* in (**c**): immunocontrol with a secondary antibody alone. (**d**–**l**): highly magnified images of *rectangles* shown in the *top panel*. *Arrows* (*inset* in **b**) show QD-positive blood vessels. *Double arrowheads* (*inset* in **b**) show QD-negative blood vessels. *Arrowheads* (**f**, **i**) show the immunopositive staining of pERK1/2 in epithelial cells at crypt areas and top parts of villi. *ML* muscular layer, *Cr* crypt, and *Vi* Villi. *Bars*, 20 μm

the intestinal epithelial stem cells during 60 min reperfusion after 20 min ischemia damage.

9.5 Concluding Remarks

In the present study, an ischemia/reperfusion model of mouse small intestine was produced, and native morphological images of the frozen specimens were obtained by our original IVCT [9]. Therefore, functional features of circulating erythrocytes could be morphologically captured on intestinal tissue sections by IVCT-FS, as previously reported in several animal organs [10, 12, 14, 15]. The IVCT could also precisely reveal rapid changes of signaling molecules, in combination with dynamic morphological alterations. Thus, we assume that IVCT, which avoids the conventional technical problems, is very useful to perform accurate examination of the alteration of rapidly changing signal transduction molecules in living mouse intestines after ischemia/reperfusion. Some of the present data were already published in our paper, Histochem Cell Biol (2013) 140: 491–505, and cited with their permissions.

References

1. Campos-Gonzalez R, Kindy MS (1992) Tyrosine phosphorylation of microtubule-associated protein kinase after transient ischemia in the gerbil brain. J Neurochem 59:1955–1958
2. Chen J, Terada N, Ohno N, Saitoh S, Saitoh Y, Ohno S (2011) Immunolocalization of membrane skeletal protein, 4.1G, in enteric glial cells in the mouse large intestine. Neurosci Lett 488:193–198
3. Eeckhout E, Kern MJ (2001) The coronary no-reflow phenomenon: a review of mechanisms and therapies. Eur Heart J 22:729–739
4. Fink MP, Delude RL (2005) Epithelial barrier dysfunction: a unifying theme to explain the pathogenesis of multiple organ dysfunction at the cellular level. Crit Care Clin 21:177–196
5. Hu BR, Wieloch T (1994) Tyrosine phosphorylation and activation of mitogen-activated protein kinase in the rat brain following transient cerebral ischemia. J Neurochem 62:1357–1367
6. Kishi T, Yamada A, Okamatsu S, Sunagawa K (2007) Percutaneous coronary arterial thrombectomy for acute myocardial infarction reduces no-reflow phenomenon and protects against left ventricular remodeling related to the proximal left anterior descending and right coronary artery. Int Heart J 48:287–302
7. Li DY, Tao L, Liu H, Christopher TA, Lopez BL, Ma XL (2006) Role of ERK1/2 in the anti-apoptotic and cardioprotective effects of nitric oxide after myocardial ischemia and reperfusion. Apoptosis 11:923–930
8. Mei F, Guo S, He YT, Zhu J, Zhou DS, Niu JQ, Wang HZ, Tian YP (2009) Apoptosis of interstitial cells of Cajal, smooth muscle cells, and enteric neurons induced by intestinal ischemia and reperfusion injury in adult guinea pigs. Virchows Arch 454:401–409
9. Ohno S, Terada N, Fujii Y, Ueda H, Takayama I (1996) Dynamic structure of glomerular capillary loop as revealed by an in vivo cryotechnique. Virchows Arch 427:519–527
10. Ohno S, Terada N, Ohno N, Saitoh S, Saitoh Y, Fujii Y (2010) Significance of in 'vivo cryotechnique' for morphofunctional analyses of living animal organs. J Electron Microsc 59:395–408
11. Saitoh S, Terada N, Ohno N, Saitoh Y, Soleimani M, Ohno S (2009) Immunolocalization of phosphor-Arg-directed protein kinase-substrate in hypoxic kidneys using in vivo cryotechnique. Med Mol Morphol 42:24–31
12. Saitoh Y, Terada N, Saitoh S, Ohno N, Jin T, Ohno S (2012) Histochemical analyses and quantum dot imaging of microvascular blood flow with pulmonary edema in living mouse lungs by "in vivo cryotechnique". Histochem Cell Biol 137:137–151
13. Silva MA, de Meirelles LR, Bustorff-Silva JM (2007) Changes in intestinal motility and in the myenteric plexus in a rat model of intestinal ischemia-reperfusion. J Pediatr Surg 42:1062–1065
14. Takayama I, Terada N, Baba T, Ueda H, Fujii Y, Kato Y, Ohno S (2000) Dynamic ultrastructure of mouse pulmonary alveoli revealed by an in vivo cryotechnique in combination with freeze-substitution. J Anat 197:199–205
15. Terada N, Kato Y, Fujii Y, Ueda H, Baba T, Ohno S (1998) Scanning electron microscopic study of flowing erythrocytes in hepatic sinusoids as revealed by "in vivo cryotechnique". J Electron Microsc 47:67–72

Histological Study and LYVE-1 Immunolocalization of Mesenteric Lymph Nodes

10

Yuqin Bai, Bao Wu, Nobuo Terada, Nobuhiko Ohno, Yurika Saitoh, and Shinichi Ohno

Abstract

The "in vivo cryotechnique" (IVCT) is a powerful tool to directly freeze living animal organs in order to maintain biological components in frozen tissues, reflecting their native states. In this study, mesenteric lymph nodes of living mice were directly frozen with IVCT, and we did morphological studies and immunohistochemical analyses on a hyaluronic acid receptor, LYVE-1. In lymph nodes, widely open lymphatic sinuses were observed, and many lymphocytes adhered to inner endothelial cells along subcapsular sinuses. The LYVE-1 was clearly immunolocalized at inner endothelial cells of subcapsular sinuses, as well as those of medullary sinuses. Conventional pre-embedding electron microscopy also showed LYVE-1 immunolocalization along both the apical and basal sides of cell membranes of inner endothelial cells. By triple immunostaining for LYVE-1, smooth muscle actin, and type IV collagen, the LYVE-1 was immunolocalized only in the inner endothelial cells, but not in outer ones which were surrounded by collagen matrix and smooth muscle cells. Thus, the functional morphology of lymph nodes in vivo was demonstrated and LYVE-1 immunolocalization in inner endothelial cells of subcapsular sinuses suggests hyaluronic acid incorporation into lymph node parenchyma.

Keywords

Immunohistochemistry • In vivo cryotechnique • LYVE-1 • Mesenteric lymph node

Y. Bai, M.D., Ph.D. (✉)
Department of Anatomy and Molecular Histology, Interdisciplinary Graduate School of Medicine and Engineering, University of Yamanashi, 1110 Shimokato, Chuo City, Yamanashi 409-3898, Japan

Department of Pathology, Medical College of Chifeng University, Ying Bin Road, Chifeng 024000, Inner Mongolua, People's Republic of China
e-mail: baiyuqincn2000@aliyun.com

N. Terada
Division of Health Sciences, Shinshu University Graduate School of Medicine, 3-1-1 Asahi, Matsumoto City, Nagano 390-8621, Japan

Department of Anatomy and Molecular Histology, Interdisciplinary Graduate School of Medicine and Engineering, University of Yamanashi, 1110 Shimokato, Chuo City, Yamanashi 409-3898, Japan

B. Wu • N. Ohno • Y. Saitoh • S. Ohno
Department of Anatomy and Molecular Histology, Interdisciplinary Graduate School of Medicine and Engineering, University of Yamanashi, 1110 Shimokato, Chuo City, Yamanashi 409-3898, Japan

10.1 Introduction

Lymph nodes are peripheral lymphatic organs connecting afferent lymphatic vessels to efferent ones via subcapsular, intermediate, and medullary sinuses. Some markers specific for lymphatic vessels are lymphatic vessel endothelial hyaluronan receptor-1 (LYVE-1) [1, 2], vascular endothelial growth factor receptor-3 (VEGFR-3) [3], prox1 [4], and podoplanin [5]. LYVE-1 is a 322-amino acid transmembranous glycoprotein homologous to an inflammatory leukocyte-homing receptor, CD44, and both of them are receptors for hyaluronic acid [6, 7]. In lymphatic sinuses of rat lymph nodes, LYVE-1 was reported to be localized in endothelial and reticular cells of medullary sinuses [2]. Recently, it was also reported that a type of macrophage expressed LYVE-1 in some lymphatic vessels [8]. Therefore, it is of interest to examine the LYVE-1 immunolocalization

S. Ohno et al. (eds.), *In Vivo Cryotechnique in Biomedical Research and Application for Bioimaging of Living Animal Organs*, DOI 10.1007/978-4-431-55723-4_10

in lymph nodes because they have specific lymph sinuses surrounded by endothelial cells which connect to the lymphatic vessels.

To clarify the morphological states of functioning animal organs, we have already proposed that the "in vivo cryotechnique" (IVCT) is a powerful tool by which living animal organs are directly frozen in vivo [9]. IVCT can prevent morphological artifacts of cells and tissues caused by tissue-resection and immersion- or perfusion-fixation [10]. It is also possible to examine immunolocalization of soluble proteins, as well as small amino acids, with high immunoreactivity, reflecting their original localization [11]. We performed morphofunctional analyses of mouse mesenteric lymph nodes under normal blood circulation prepared with IVCT and examined immunolocalization in situ of LYVE-1, type IV collagen, and smooth muscle actin in the lymph nodes.

10.2 Histological Findings of Living Mouse Lymph Node Tissue

Histological features of living mouse mesenteric lymph nodes were obtained with IVCT, such as widely open lymphatic sinuses and original locations of flowing lymphocytes, as shown in Fig. 10.1. Subcapsular sinuses of lymph nodes have been thought to play some important roles for filtering lymph fluid to transport and process invading antigens into their parenchyma, as well as both adhesion and migration of immune cells and also metastatic cancer cells [8, 12]. Thus, as the wide lumen of lymphatic sinuses and flowing lymphocytes were maintained by using IVCT, it may reflect the natural subcapsular sinuses of functional lymph nodes. Round fenestrations of endothelial cells were demonstrated at the parenchymal sides of the subcapsular sinus walls [13], indicating that the inner endothelial cells are used as a route for antigens and/or free cells to pass from the lymphatic sinuses to the parenchyma of lymph nodes. As IVCT has been used to avoid various technical artifacts, such as shrinkage and distortion always caused by conventional preparation methods [10, 14], other dynamic experiments with fluorescent-marker injection are also under consideration [15].

10.3 LYVE-1 Immunolocalization in Mouse Lymph Node Tissue

The LYVE-1 was immunolocalized in the inner endothelial cells and reticular cells of subcapsular sinuses, but not in outer ones or in afferent lymphatic vessels, as shown in Fig. 10.2. Immunoelectron microscopy also showed LYVE-1 in both luminal and basal cell membrane surfaces of inner endothelial cells, but immunoreactivity of LYVE-1 was strongly observed in the luminal sides than that of inner sides, as shown in Fig. 10.2j, k. The immunolocalization of LYVE-1 was first identified as a lymph-specific receptor for hyaluronic acid (HA) [1]. In addition, rather than facilitating

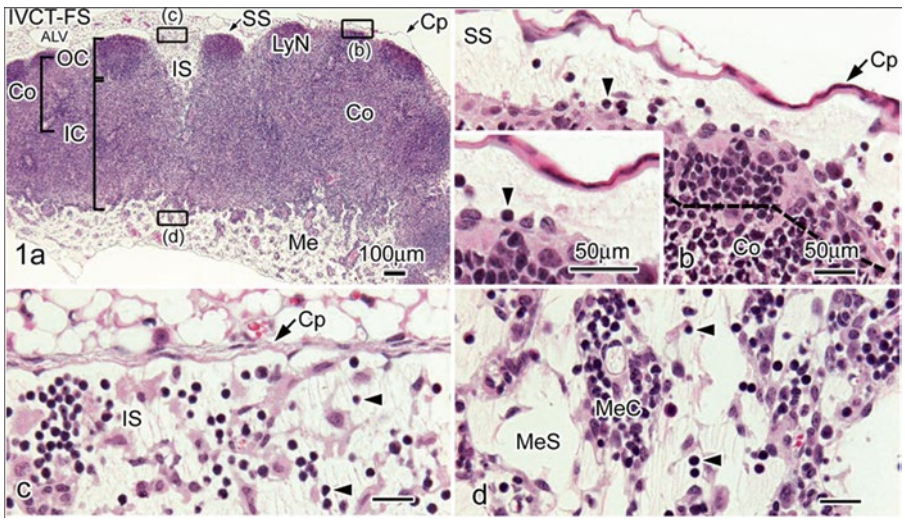

Fig. 10.1 Light micrographs of hematoxylin-eosin (HE) staining for paraffin sections of mesenteric lymph nodes prepared by IVCT followed by FS fixation. (**a**) Lower magnified view of a lymph node showing wide areas from the cortex (Co) to medulla (Me). In the cortex, outer (OC) and inner (IC) cortices are observed. *Cp* capsule, *ALV* afferent lymphatic vessel, *IS* intermediate sinus, *LyN* lymphatic nodule, and *SS* subcapsular sinus. The deep areas of *dotted lines* in this lymph node are showing tissue damage caused by ice crystal formation (**b**). The panels (*b*), (*c*), and (*d*) are higher magnified views of three parts shown as *rectangles* in (**a**). (**b**) Space of subcapsular sinus (SS) is opening, and the outside is surrounded by a capsule (Cp). Small lymphocytes with dense chromatin in nuclei are localized along inner endothelial cells of SS (*arrowheads* in **b**). (**c**) An intermediate sinus (IS) is connecting from SS. (**d**) Medullary cords (MeC) and open medullary sinuses (MeS) are clearly observed in the medulla of lymph nodes in vivo. Lymphocytes are observed in intermediate and medullary sinuses (*arrowheads* in **c**, **d**). *Bars* = 100 μm (**a**), 50 μm (**b**–**d**)

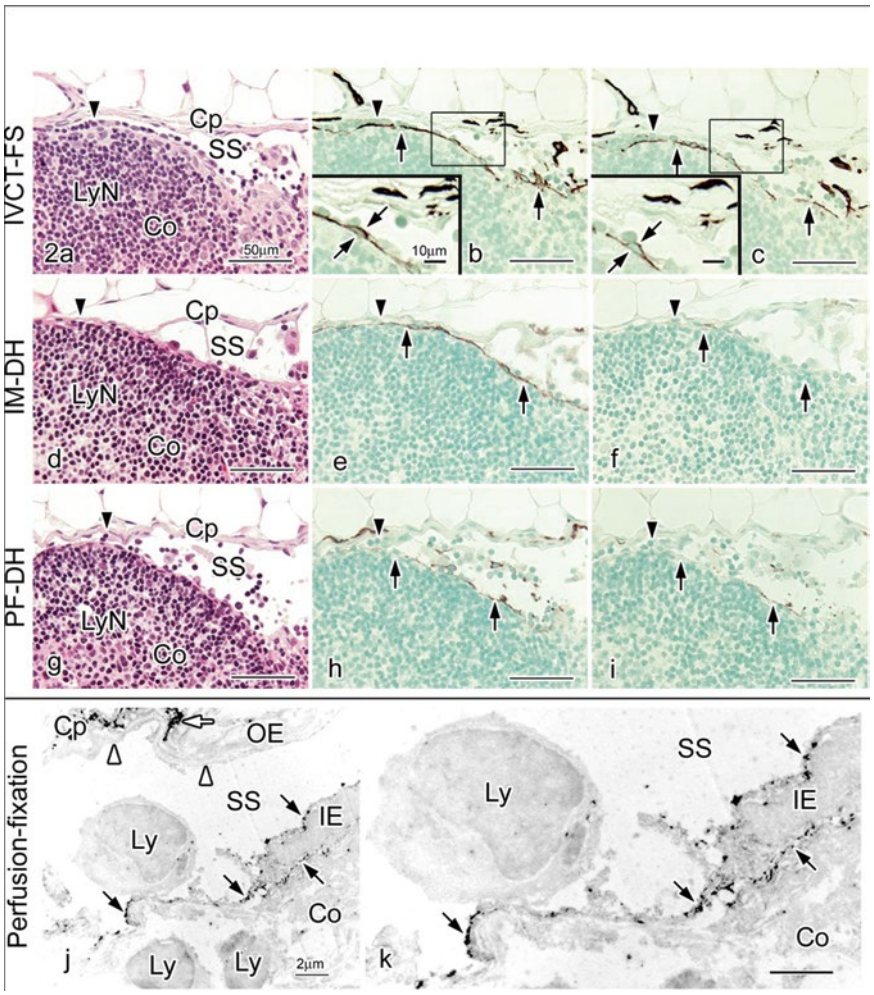

Fig. 10.2 Hematoxylin-eosin (HE) staining (**a**, **d**, **g**) and LYVE-1 immunostaining with different concentrations of primary anti-LYVE-1 antibody (1:300 in **b**, **e**, **h** and 1:7500 in **c**, **f**, **i**) in serial paraffin sections prepared by IVCT-FS (**a**–**c**), immersion fixation followed by alcohol dehydration (IM-DH; **d**–**f**) or perfusion fixation followed by alcohol dehydration (PF-DH; **g**–**i**). *Insets* in (**b**) and (**c**) are highly magnified views of inner endothelial cells shown by the *squares*. With IVCT-FS, a row of lymphocytes along subcapsular sinus (SS) is observed in this area (*arrowhead* in **a**), compared to IM-DH or PF-DH (*arrowheads* in **d**, **g**). The LYVE-1 immunoreactivity is more clearly detected at a 1:7500 primary antibody dilution in samples with IVCT-FS (**c**), but it is decreased in samples with IM-DH (**f**) or PF-DH (**i**). (**j** and **k**) Pre-embedding immunoelectron microscopy for LYVE-1 in a mesenteric lymph node. The LYVE-1 is immunolocalized at both luminal and basal cell membrane surfaces of inner endothelial cells (IE, *black arrows*) along subcapsular sinus (SS), but not in outer endothelial cells (OE, *white arrowheads*). The LYVE-1 is also immunolocalized in some cells in the interstitium of capsules (Cp) surrounding SS (*white arrow*). *Co,* cortex; *Cp,* capsule; *LyN,* lymphatic nodule; *Ly,* lymphocyte; **k**, higher magnification of IE. *Bars* = 50 μm (**a**–**i**), 10 μm (*insets* of **b**, **c**), 2 μm (**j**, **k**)

degradation of HA, it was thought to be involved in HA transportation across lymphatic endothelial cells, specifically movement of accumulated HA from lymphatic sinuses to the lymph node parenchyma [7]. The possible roles of the lymphatic endothelial cells in HA homeostasis are also modified with HA binding by sialylation and self-association [16]. In addition, it was already shown that injected fluorophore-conjugated HA was taken through the endothelial cells of subcapsular sinuses [17]. The flow of lymphatic fluid was examined by injection of fluorophore-conjugated gelatin into the peritoneal cavity [18], showing its movement through endothelial cells to medullary labyrinths. But in the previous studies, by using injection of soluble substances with different molecular weights, the lymphatic parenchyma was impenetrable to those molecules with about 70 kD [19]. The IVCT could be used to keep the morphology in situ of lymph nodes, and dynamic experiments with fluorescence-labeled tracers will be possible to clarify it.

Our findings that the LYVE-1 was present at both luminal and basal surfaces of inner endothelial cells and that the immunolocalization of LYVE-1 is more strongly observed in the apical sides of inner endothelial cells, also interesting to note that many small lymphocytes were attached to inner endothelial cells in subcapsular sinuses, as shown in

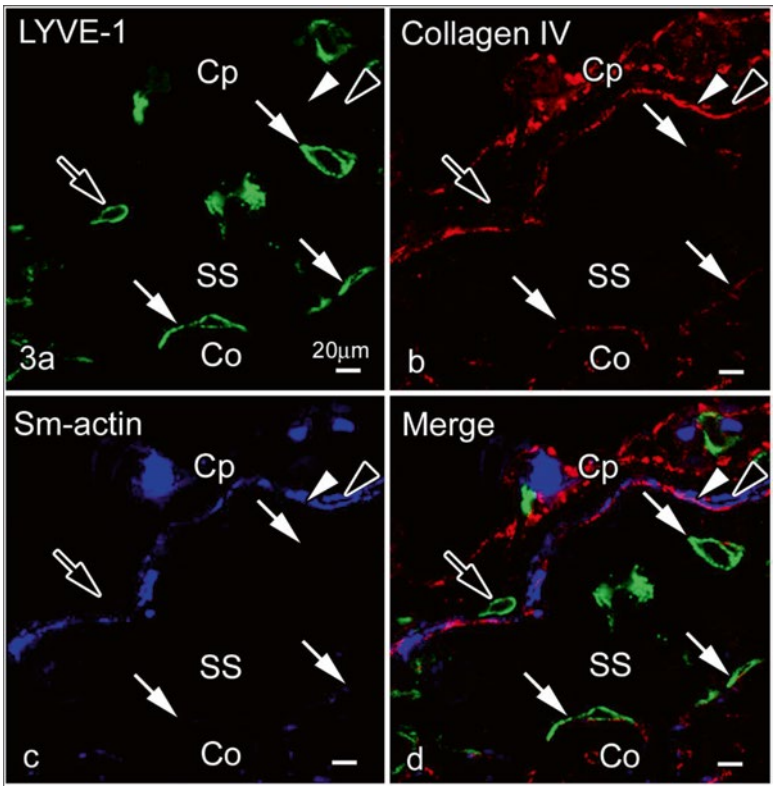

Fig. 10.3 Immunofluorescence labeling of LYVE-1 in cryosections of a mesenteric lymph node prepared by IVCT-FS. Triple-immunofluorescence staining for LYVE-1 (*green* in **a**, **d**), type IV collagen α2 chain (Collagen IV; *red* in **b**, **d**), and smooth muscle actin (Sm-actin; *blue* in **c**, **d**). Intensity of type IV collagen (*white arrowheads* in **b**, **d**) and Sm-actin (*black arrowheads* in **c**, **d**) immunoreactivities is relatively strong along outer sides of SS. LYVE-1-immunopositive cells are observed in the capsular stroma (*black arrows* in **a**–**d**). The LYVE-1 is immunolocalized in inner endothelial cells along SS and reticular cells (*white arrows* in **a**–**d**), where type IV collagen or Sm-actin is faintly immunostained. *Bar,s* = 20 μm (**a**–**d**)

Fig. 10.2a–c, are well compatible with this functional concept. LYVE-1 immunolocalization is different between inner and outer endothelial cells of subcapsular sinuses, probably reflecting the different functions for the transportation of HA and also the adhesion or migration of CD44-positive lymphocytes [6, 16]. Such different features between inner and outer endothelial cells were already reported by another histochemical approach for hydrolytic enzymes [20].

10.4 Relation of Type IV Collagen or Smooth Muscle Actin and LYVE-1 Immunopositive Endothelial Cells in Subcapsular Sinuses

LYVE-1 was not expressed in outer endothelial cells contacting with type IV collagen and/or smooth muscle cells, as shown in Fig. 10.3. This finding is also consistent with a study of developing lymph vessels, in which mature lymphatic vessels surrounded by smooth muscle cells usually reduced the LYVE-1 expression [21]. As it was already reported to be expressed in some types of macrophages [22] and other cells [23], identification of such cell types in the capsules will be another topic for future studies.

10.5 Concluding Remarks

Functioning tissue structures of mesenteric lymph nodes of living mice, probably reflecting their living states, were clearly described by the IVCT-FS method, and their LYVE-1 immunolocalization in the subcapsular sinus was also visualized in the inner endothelial cells, not in the outer ones. The present figures were already published in our paper, Acta Histochem Cytochem (2011) 44:81–90, and cited with their permissions.

References

1. Banerji S, Ni J, Wang SX, Clasper S, Su J, Tammi R, Jones M, Jackson DG (1999) LYVE-1, a new homologue of the CD44 glycoprotein, is a lymph-specific receptor for hyaluronan. J Cell Biol 144(4):789–801

2. Ohtani O, Ohtani Y (2008) Structure and function of rat lymph nodes. Arch Histol Cytol 71(2):69–76
3. Kaipainen A, Korhonen J, Mustonen T, van Hinsbergh VW, Fang GH, Dumont D, Breitman M, Alitalo K (1995) Expression of the fms-like tyrosine kinase 4 gene becomes restricted to lymphatic endothelium during development. Proc Natl Acad Sci U S A 92(8):3566–3570
4. Petrova TV, Mäkinen T, Mäkelä TP, Saarela J, Virtanen I, Ferrell RE, Finegold DN, Kerjaschki D, Ylä-Herttuala S, Alitalo K (2002) Lymphatic endothelial reprogramming of vascular endothelial cells by the Prox-1 homeobox transcription factor. EMBO J 21(17):4593–4599
5. Breiteneder-Geleff S, Soleiman A, Kowalski H, Horvat R, Amann G, Kriehuber E, Diem K, Weninger W, Tschachler E, Alitalo A, Kerjaschki D (1999) Angiosarcomas express mixed endothelial phenotypes of blood and lymphatic capillaries. Podoplanin as a specific marker for lymphatic endothelium. Am J Pathol 154(2):385–394
6. Jackson DG, Prevo R, Clasper S, Banerji S (2001) LYVE-1, the lymphatic system and tumor lymphangiogenesis. Trends Immunol 22(6):317–321
7. Prevo R, Banerji S, Ferguson DJ, Clasper S, Jackson DG (2001) Mouse LYVE-1 is an endocytic receptor for hyaluronan in lymphatic endothelium. J Biol Chem 276(22):19420–19430
8. Phan TG, Grigorova I, Okada T, Cyster JG (2007) Subcapsular encounter and complement-dependent transport of immune complexes by lymph node B cells. Nat Immunol 8(9):992–1000
9. Saitoh S, Terada N, Ohno N, Ohno S (2008) Distribution of immunoglobulin-producing cells in immunized mouse spleens revealed with "in vivo cryotechnique". J Immunol Methods 331(1–2):114–126
10. Bai Y, Ohno N, Terada N, Saitoh S, Nakazawa T, Nakamura N, Katoh R, Ohno S (2009) Immunolocalization of serum proteins in xenografted mouse model of human tumor cells by various cryotechniques. Histol Histopathol 24(6):717–728
11. Ohno N, Terada N, Ohno S (2006) Histochemical analyses of living mouse liver under different hemodynamic conditions by "in vivo cryotechque". Histochem Cell Biol 126(3):389–398
12. Qian CN, Berghuis B, Tsarfaty G, Bruch M, Kort EJ, Ditlev J, Tsarfaty I, Hudson E, Jackson DG, Petillo D, Chen J, Resau JH, Teh BT (2006) Preparing the "soil": the primary tumor induces vasculature reorganization in the sentinel lymph node before the arrival of metastatic cancer cells. Cancer Res 66(21):10365–10376
13. Szakal AK, Holmes KL, Tew JG (1983) Transport of immune complexes from the subcapsular sinus to lymph node follicles on the surface of nonphagocytic cells, including cells with dendritic morphology. J Immunol 131(4):1714–1727
14. Chan FL, Inoue S (1994) Lamina lucida of basement membrane: an artefact. Microsc Res Tech 28(1):48–59
15. Terada N, Ohno N, Li Z, Fujii Y, Baba T, Ohno S (2005) Detection of injected fluorescence-conjugated IgG in living mouse organs using "in vivo cryotechnique" with freeze-substitution. Microsc Res Tech 66(4):173–178
16. Jackson DG (2009) Immunological functions of hyaluronan and its receptors in the lymphatics. Immunol Rev 230(1):216–231
17. Sharma R, Wang W, Rasmussen JC, Joshi A, Houston JP, Adams KE, Cameron A, Ke S, Kwon S, Mawad ME, Sevick-Muraca EM (2007) Quantitative imaging of lymph function. Am J Physiol Heart Circ Physiol 292(6):109–118
18. Ohtani O, Ohtani Y, Carati CJ, Gannon BJ (2003) Fluid and cellular pathways of rat lymph nodes in relation to lymphatic labyrinths and Aquaporin-1 expression. Arch Histol Cytol 66(3):261–272
19. Gretz JE, Norbury CC, Anderson AO, Proudfoot AE, Shaw S (2000) Lymph-borne chemokines and other low molecular weight molecules reach high endothelial venules via specialized conduits while a functional barrier limits access to the lymphocyte microenvironments in lymph node cortex. J Exp Med 192(10): 1425–1440
20. Crocker J, Williams M (1984) An enzyme histochemical study of the sinuses of reactive lymph nodes. J Pathol 142(1):31–38
21. Tammela T, Saaristo A, Holopainen T, Lyytikkä J, Kotronen A, Pitkonen M, Abo-Ramadan U, Ylä-Herttuala S, Petrova TV, Alitalo K (2007) Therapeutic differentiation and maturation of lymphatic vessels after lymph node dissection and transplantation. Nat Med 13(12):1458–1466
22. Cho CH, Koh YJ, Han J, Sung HK, Jong LH, Morisada T, Schwendener RA, Brekken RA, Kang G, Oike Y, Choi TS, Suda T, Yoo OJ, Koh GY (2007) Angiogenic role of LYVE-1-positive macrophages in adipose tissue. Circ Res 100(4):e47–57
23. Jiang S, Bailey AS, Goldman DC, Swain JR, Wong MH, Streeter PR, Fleming WH (2008) Hematopoietic stem cells contribute to lymphatic endothelium. PLoS One 3(11), e3812

Distribution of Immunoglobulin-Producing Cells in Immunized Mouse Spleens

11

Sei Saitoh, Nobuo Terada, Nobuhiko Ohno, and Shinichi Ohno

Abstract

To identify immunoglobulin (Ig)-producing cells with immunohistochemistry, conventional methods of preparation using chemical fixatives have problems such as the artificial diffusion of components and antigen masking. The "diffusion artifact" is caused by the translocation of soluble proteins like Ig from the serum to cytoplasm or vice versa. We have examined the immunolocalization of serum proteins, such as Ig kappa light chain (Igκ), IgG1 heavy chain (IgG1), and albumin, in immunized mouse spleens after a peritoneal injection of human hemoglobin. Better preservation of morphology and immunoreactivity was obtained with the "in vivo cryotechnique" (IVCT) followed by freeze-substitution than with conventional preparative methods. Although Ig-producing cells were not clearly detected in red pulp of 2-day-immunized spleens with the conventional methods, Igκ-immunopositive cells with rich cytoplasm were detected in the red pulp with IVCT, especially in the subcapsular and peritrabecular areas, where IgG1-immunopositive cells were rarely observed. In 7-day-immunized spleens prepared with IVCT, Igκ- or IgG1-immunopositive cells were mostly located in peritrabeculae. The development of Ig-producing cells was clarified in the specimens prepared with IVCT, which proved to be useful for analyzing the native morphology and distribution of Ig-producing cells.

Keywords

Antigen masking • Diffusion artifact • Immunohistochemistry • Immunoglobulin-producing cell • Living mouse spleen

11.1 Introduction

The chemical fixation and alcohol dehydration processes commonly used to prepare tissue sections yield structural artifacts such as shrinkage and distortion [1, 2]. Conventional immunohistochemical techniques for immunoglobulin (Ig) in plasma cells and Ig-producing cells of animal organs have several problems, such as molecular "diffusion artifacts" [3–5] and antigen masking, with chemical fixation and alcohol dehydration. In the present study, we have produced immunized mouse spleens and examined whether molecular "diffusion artifacts" as well as structural changes of cells and tissues can be avoided with "in vivo cryotechnique" (IVCT) followed by freeze-substitutionfixation (FS).

S. Saitoh, M.D., Ph.D. (✉) • N. Ohno • S. Ohno
Department of Anatomy and Molecular Histology, Interdisciplinary Graduate School of Medicine and Engineering, University of Yamanashi, 1110, Shimokato, Chuo City, Yamanashi 409-3898, Japan
e-mail: ssaitoh@yamanashi.ac.jp

N. Terada
Division of Health Sciences, Shinshu University Graduate School of Medicine, 3-1-1 Asahi, Matsumoto City, Nagano 390-8621, Japan

Department of Anatomy and Molecular Histology, Interdisciplinary Graduate School of Medicine and Engineering, University of Yamanashi, 1110 Shimokato, Chuo City, Yamanashi 409-3898, Japan

S. Ohno et al. (eds.), *In Vivo Cryotechnique in Biomedical Research and Application for Bioimaging of Living Animal Organs*, DOI 10.1007/978-4-431-55723-4_11

11.2 Morphological Features of Living Mouse Spleen

Light microscopic images with HE staining showed a natural histology of the spleens in normal living mice (Fig. 11.1). The tissue structure of the frozen and freeze-substituted spleens could be divided into the classical white pulp and red pulp (Fig. 11.1a). By preparing paraffin sections in parallel to the frozen spleen surface, well-preserved white pulp was broadly obtained in the living mouse spleens with bloodcirculation, judging from the few ice crystals formed (Fig. 11.1b, inset). In the white pulp, the population density of splenic cells clearly differed between the periarterial lymphoid sheath (PALS) and germinal center (Fig. 11.1a, b). Large nuclei of some splenic cells at the germinal center were weakly stained with hematoxylin (Fig. 11.1b), but other smaller nuclei were strongly stained in the white pulp, as compared to those in the marginal zones (Fig. 11.1c). The red pulp area consists of splenic sinuses containing many flowing erythrocytes, which were surrounded by splenic cords (Fig. 11.1d, e). Next, we will make the evaluation of thenuclear shrinkage of splenic cells caused by various fixations.

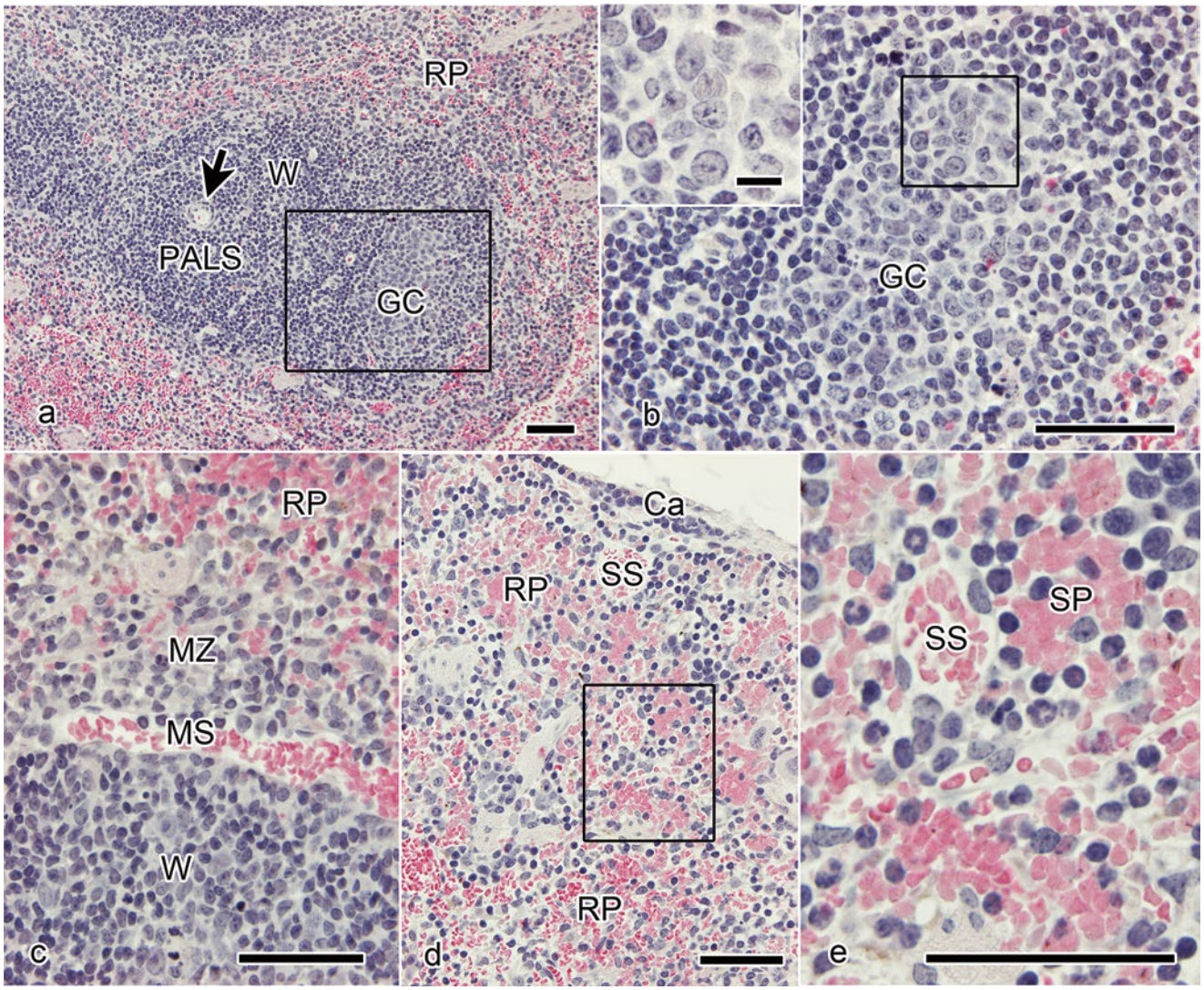

Fig. 11.1 Light micrographs of hematoxylin–eosin (HE)-stained sections of normal mouse spleen, prepared with the in vivo cryotechnique (IVCT) followed by freeze-substitution (FS). (**a**) Low-magnified view of the white pulp (W) and red pulp (RP). A central artery (*arrow*), periarterial lymphoid sheath (PALS), and germinal center (GC) are shown in the white pulp. (**b**) A highly magnified image of the *rectangular box* in (**a**). Weakly hematoxylin-stained nuclei of splenic cells are shown in the germinal center (GC), which are further magnified in the *inset*. (**c**) A marginal sinus (MS) containing many erythrocytes is occasionally seen between the white pulp (W) and the marginal zone (MZ). (**d**) In the red pulp, many erythrocytes are densely accumulated. (**e**) Highly magnified image of the *rectangular box* in (**d**). Many flowing erythrocytes are clearly observed in the splenic sinus (SS) and splenic pulp (SP). Ca: splenic capsule. *Bars*; 50 μm (**a–e**) and 10 μm (*inset* in **b**)

11.3 Evaluation of Nuclear Shrinkage of the Splenic Cells Caused by IVCT-FS and Conventional Fixation Methods

To examine the artificial shrinkage of nuclei during the chemical fixation and dehydration steps, the 2-day-immunized mouse spleens prepared by the cryotechniques were compared with those prepared by conventional chemical fixation and alcohol dehydration. To judge the changes in nuclear size, lengths of the major or minor axis of nuclei were measured as parameters for statistical analyses. ($V=4/3\pi a^2 b$; $a=1/2$ of the minor axis, $b=1/2$ of the major axis, $\pi=3.14$) [6]. The nuclear volume of specimens prepared with IVCT, PF–QF, FT–QF, PF–DH, and IM–DH was 59.35 ± 3.37, 46.33 ± 2.78, 55.56 ± 4.26, 29.77 ± 1.52, and 42.46 ± 3.63 μm^3 (mean ± standard error (SE)), respectively, showing that both PF–DH and IM–DH induced significant shrinkage of nuclei, as compared with IVCT. These findings indicate that chemical fixation and alcohol dehydration are both responsible for the shrinkage of nuclei in immunized splenic cells during tissue preparation.

11.4 Evaluation of Antigen Masking and Diffusion Artifact of Ig-Producing Plasma Cells Prevented by IVCT-FS

The antigen retrieval effect was assumed to be caused by breaks of the cross-linked molecules [7]. The cryofixation usually produces tiny ice crystals in the cells and tissues during the freezing step, and the formed mesh structures are well preserved during the freeze-substitution step without tissue shrinkage, enabling easy penetration of antibodies throughout the tissues. In the present study, the IVCT methods followed by FS improved it without any antigen retrieval treatment, as shown in Fig. 11.2a–c. However, Igκ-immunoreactivity of some cells in the immunized splenic tissues was not clearly detected with the conventional PF–DH, as shown in Fig. 11.2d–f. Thus, the combination of cryofixation and FS probably decreased the extent of antigen masking, in addition to reducing the diffusion of soluble components.

Two patterns of Igκ immunolocalization were detected in the spleens prepared by three different cryotechniques, followed with HRP-immunostaining: (1) extracellular matrix and (2) cytoplasm of some cells. To clearly categorize these patterns, double immunofluorescence staining of Igκ and extracellular albumin was performed on the same paraffin sections prepared with IVCT, which were observed under a confocal laser scanning microscope (Fig. 11.2g–j). No "diffusion artifacts" of immunostaining, such as the penetration of albumin into the cytoplasm of some cells, was detected, showing that the colocalization of Igκ and albumin was observed only in the extracellular matrix, not in the cytoplasm of Ig-producing cells (Fig. 11.2i–j). Thus, cryopreparation with IVCT did not affect the immunolocalization patterns of soluble serum proteins in vivo. Such molecular diffusion in animal tissues is inevitable during the chemical fixation and alcohol dehydration processes, as was already reported in the case of large malignant cells like Reed–Sternberg cells of Hodgkin's lymphoma [3–5]. Therefore, inadequate fixation with IM–DH sometimes caused more severe diffusion of soluble serum components. The high-pressure stress during perfusion–fixation also changed the permeability of cell membranes of living hepatocytes, resulting in the artificial diffusion of serum components [8]. Considering these problems, IVCT is the best way to avoid this "diffusion artifact."

11.5 Distribution of Ig-Producing Cells in Normal or Immunized Mouse Spleens

In the normal mouse spleen (day 0), a small number of cells immunostained for Igκ and IgG1 were aggregated or scattered in the peritrabeculae of red pulp (Fig. 11.3a–c). In the 2-day-immunized mouse spleen (Fig. 11.3d–f), the white pulp structure became more irregularly arranged, and marginal zones were well developed, as revealed on HE-stained sections (Fig. 11.3d). Many Igκ-immunopositive cells were located in the peritrabeculae and the red pulp under the splenic capsules (Fig. 11.3e), where fewer IgG1-immunopositive cells were observed (Fig. 11.3f). In the 7-day-immunized mouse spleen (Fig. 11.3g–i), tissue structures of both white pulp and marginal zones became much more irregularly arranged on the HE-stained sections (Fig. 11.3g), as compared to those in the 2-day-immunized mouse spleen (Fig. 11.3d), showing that splenic cells usually present in the white pulp were dispersed into the red pulp (Fig. 11.3g). At this time, the number of large splenic cells with basophilic cytoplasm was increased in the peritrabeculae (Fig. 11.3g). Many Igκ-immunopositive cells were located in the peritrabeculae and the red pulp (Fig. 11.3h). Moreover, many more IgG1-immunopositive cells were detected in the peritrabeculae (Fig. 11.3i), as compared with the 2-day-immunized mouse spleen (Fig. 11.3f).

11.6 Concluding Remarks

Our finding was that Igκ-immunopositive and IgG1-immunonegative cells, reflecting early developing B lymphocytes, were mainly located in the red pulp along splenic capsules and trabeculae. Previous studies indicated that PALS was an important locus to promote development of Ig-producing cells, but did not show the functional significance of capsules and trabeculae in the red pulp. This discrepancy might be due to the easy loss of Ig-immunoreactivity in such immature B lymphocytes, as shown in Fig. 11.2a–f, indicating that the red pulp is a major functional zone for the

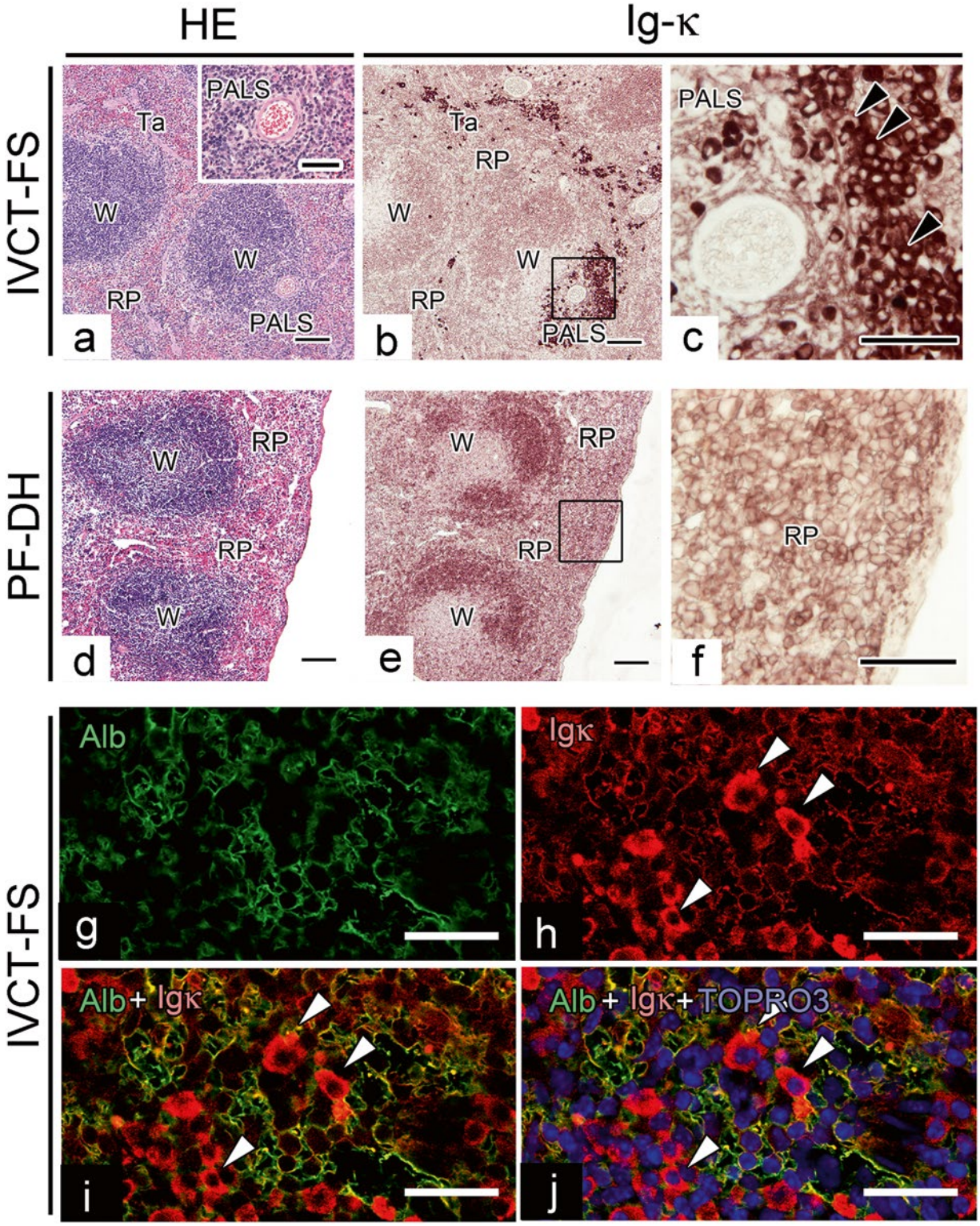

Fig. 11.2 Light micrographs of 2-day-immunized mouse spleen tissues, prepared with three cryofixation methods. (**a**)–(**c**); IVCT. (**d**)–(**f**); PF–DF. The same tissue areas are shown in serial sections stained with HE (**a**, **d**) and also immunostained for immunoglobulin κ light chain (Igκ) (**b**, **e**), respectively. The images of *rectangular boxes* in (**b**) and (**e**) are highly magnified in (**c**) and (**f**), respectively. The Igκ in the specimens prepared with IVCT (**b**, **c**) is mainly detected in the cytoplasm of Ig-producing cells (*arrowheads*). Notably, it is clearly located in periarterial lymphoid sheath (PALS) (*inset* of **a**, **c**) in the living mouse spleen with bloodcirculation, prepared with IVCT (**a**, **b**, **c**). The Igκ in the specimens prepared with PF–DH (**c**) is weakly detected in the shrunken cytoplasm of smaller splenic cells in the red pulp (RP), as compared with those shown in IVCT (**b**) *Bars*; 100 μm (**a**, **b**, **d**, **e**), 50 μm (**c**, **f** *inset* of **a**). Confocal laser scanning micrographs of double fluorescence immunolabeling for albumin (**g**, Alb; *green*) and the immunoglobulin κ light chain (**h**, Igκ; *red*) in 2-day-immunized mouse spleens, as prepared with IVCT followed by FS. TO-PRO-3 (**j**, TP3; *blue*) was also used for labeling nuclei. (**g**) Albumin is detected in the extracellular matrix, but not in the cytoplasm of cells with blood circulation. (**h**) Igκ is mainly detected in the cytoplasm of possible Ig-producing cells (*arrowheads*) and also in the extracellular matrix. (**i**) Merged double, fluorescence image (Alb+Igκ; *yellow*) shows the colocalization of albumin and Igκ in the extracellular matrix, but not in the cytoplasm of the Ig-producing cells. (**j**) Merged triple fluorescence image (Alb+Igκ+TP3) shows no colocalization of albumin, Igκ, and TO-PRO-3 in nuclei. *Bars*: 30 μm

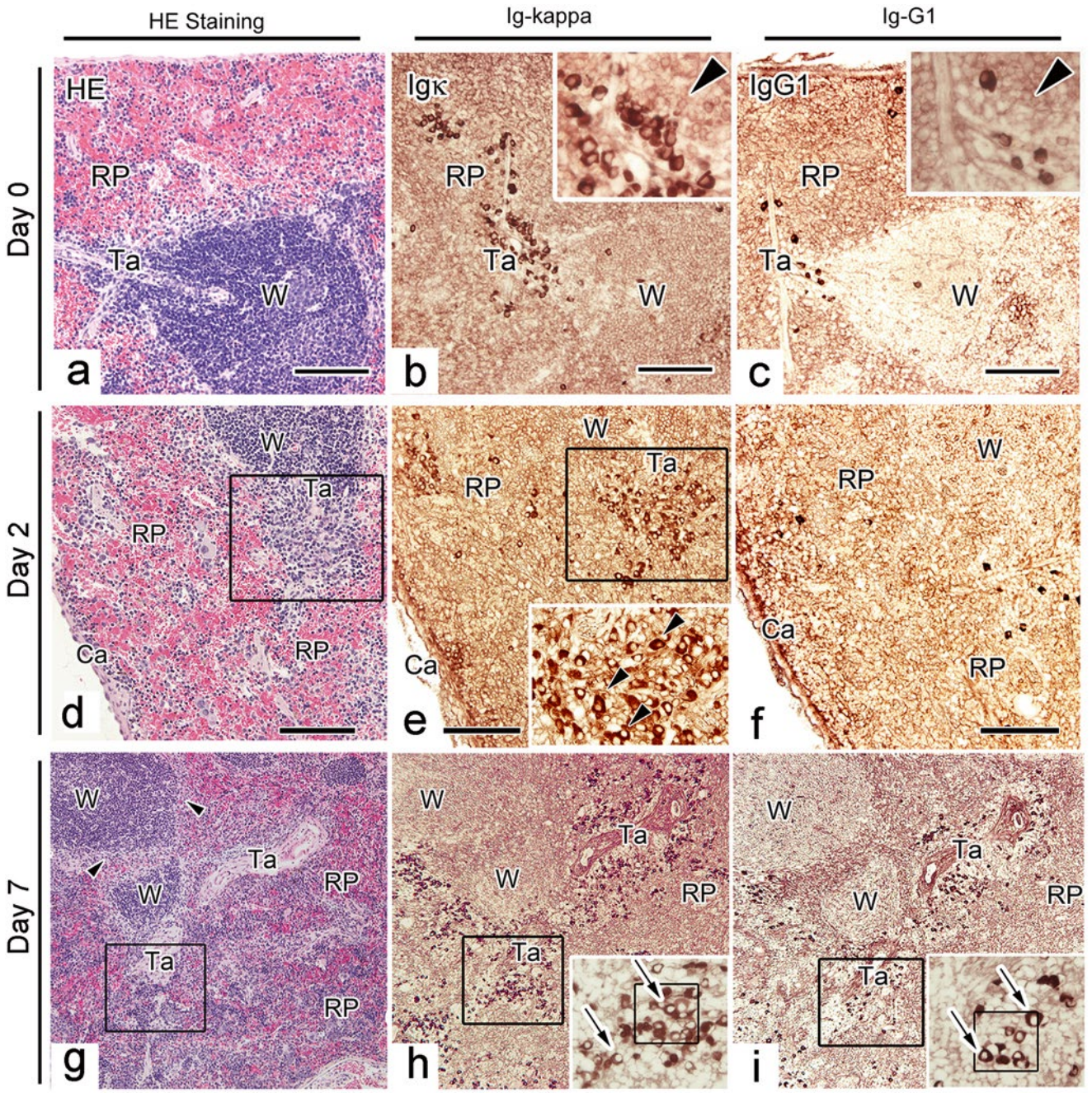

Fig. 11.3 Light micrographs of immunized mouse spleens prepared by IVCT followed by FS. The same tissue areas are shown on serial sections stained with HE (**a**, **d**, **g**) and immunostained for Igκ (**b**, **e**, **h**) and the immunoglobulin G1 heavy chain (**c**, **f**, **i**). Both Igκ and IgG1 are detected in the cytoplasm of Ig-producing cells in the peritrabeculae (Ta), and also in sinusoids (*insets* of **b** and **c**; *arrowheads*) in non-immunized condition (day 0). (**d**) Many basophilic cells (*arrowheads*) are located in the peritrabeculae (Ta). (**e**) Igκ-immunopositive cells (*arrowheads*) are abundant in the peritrabeculae (Ta) and under the capsule (Ca). (**f**) IgG1-immunopositive cells are much less abundant in the same area. (**a**) Tissue structures of both white pulp (W) and the marginal zone (*arrowheads*) become more irregular, as compared to those of the 2-day-immunized mouse spleens (day 2) (**g**) Some large splenic cells with hematoxylin-stained cytoplasm are located in the peritrabeculae corresponding to *rectangular box*. (**h**) Many Igκ-immunopositive cells (*inset*, *arrows*) are grouped in the peritrabeculae (Ta) near bloodvessels. (**i**) Many IgG1-immunopositive cells (*inset*, *arrows*) are also located in the peritrabeculae (Ta) and red pulp (RP) with blood circulation in the 7-day-immunized mouse spleens (day 7). *Bars*; 100 μm, *RP* red pulp, *W* white pulp

production of splenic B lymphocytes in the immunized mouse spleen. Direct immunolabeling of B lymphocytes has been recently detected in germinal centers of mouse lymph nodes by two-photon laser scanning microscopy [9]. The in vivo immunodetection of Ig-producing cells with fewer technical artifacts, as prepared by IVCT, is essential to examine immunologically functional areas of living spleens, in combination with the "in vivo imaging" technique [10].

References

1. Leu FJ, Chen CF, Sun AM (1993) A new method of tissue processing that causes no shrinkage or distortion. Lab Invest 69(1):121–130
2. Chan FL, Inoue S (1994) Lamina lucida of basement membrane: an artefact. Microsc Res Tech 28(1):48–59
3. Mason DY, Bell JI, Christensson B, Biberfeld P (1980) An immunohistological study of human lymphoma. Clin Exp Immunol 40(2):235–248
4. Mason DY, Biberfeld P (1980) Technical aspects of lymphoma immunohistology. J Histochem Cytochem 28(8):731–745
5. Poppema S, Elema JD, Halie MR (1978) The significance of intracytoplasmic proteins in Reed–Sternberg cells. Cancer 42(2):1793–1803
6. Koulish S, Kleinfeld RG (1964) The role of the nucleolus. I. Tritiated cytidine activity in liver parenchymal cells of thioacetamide-treated rats. J Cell Biol 23:39–51
7. Gown A, Wever ND, Battifora H (1993) Microwave-based antigenic unmasking: a revolutionary new technique for routine immunohistochemistry. Appl Immunohistochem 1:256–266
8. Terada N, Ohno N, Saitoh S, Ohno S (2007) Immunohistochemical detection of hypoxia in mouse liver tissues treated with pimonidazole using "in vivo cryotechnique". Histochem Cell Biol 128(3):253–261
9. Schwickert TA, Lindquist RL, Shakhar G, Livshits G, Skokos D, Kosco-Vilbois MH, Dustin ML, Nussenzweig MC (2007) In vivo imaging of germinal centres reveals a dynamic open structure. Nature 446(7131):83–87
10. Saitoh S, Terada N, Ohno N, Ohno S (2008) Distribution of immunoglobulin-producing cells in immunized mouse spleens revealed with "in vivo cryotechnique". J Immunol Methods 331(1–2): 114–126

12 Alteration of Erythrocyte Shapes in Various Organs of Living Mice or Under Blood Flow Conditions

Shinichi Ohno, Nobuo Terada, and Yasuhisa Fujii

Abstract

Dynamic changes in the shape of erythrocytes circulating in large blood vessels and hepatic sinusoids of living mice were examined by IVCT. The abdominal aorta, inferior vena cava, or liver organs were cryo-cut with a precooled knife in liquid nitrogen (−196 °C), and the liquid isopentane-propane cryogen (−193 °C) was simultaneously poured over them for additionally freezing. They were routinely freeze-substituted in acetone containing 2 % osmium tetroxide. Some specimens were embedded in Quetol 812, and ultrathin sections were cut and examined by transmission electron microscopy. Serial ultrathin sections were used to reconstruct 3-dimensional images of native erythrocytes. Others were transferred into t-butyl alcohol and freeze-dried for scanning electron microscopy. The shapes of circulating erythrocytes appeared to be varied in the abdominal aorta or hepatic sinusoids. To the contrary, erythrocytes in the inferior vena cava were approximately biconcave discoid in shape. In hepatic sinusoids, flowing erythrocytes formed variously changing shapes, and they were easily changed into discoid shapes under the heart-arrest condition. Moreover, electrolyte contents were also changed between two conditions, as revealed by X-ray microanalysis, showing low potassium and high sodium within the erythrocytes after the heart arrest. Our IVCT was useful for clarifying the in vivo morphology of erythrocytes circulating in blood vessels.

Keywords

In vivo cryotechnique • Flowing erythrocytes • Blood vessel • X-ray microanalysis • Anoxia

12.1 Introduction

Mammalian erythrocytes usually maintain their biconcave discoid shapes in vitro, but they are always changing their forms under complicated dynamic conditions in blood vessels [1]. The deformability of flowing erythrocytes of living animals is an important factor in such a situation. However, the morphological appearance of erythrocytes was unknown in various blood vessels of living animal organs, because of some limitations in the conventional preparation techniques for light or electron microscopy. It was also difficult to directly observe flowing behaviors of erythrocytes in large blood vessels with their thick blood vessel walls and hepatic sinusoids in solid clumped liver organs. Therefore, the con-

S. Ohno, M.D., Ph.D. (✉) • Y. Fujii
Department of Anatomy and Molecular Histology, Interdisciplinary Graduate School of Medicine and Engineering, University of Yamanashi, 1110 Shimokato, Chuo City, Yamanashi 409-3898, Japan
e-mail: sohno@yamanashi.ac.jp

N. Terada
Division of Health Sciences, Shinshu University Graduate School of Medicine, 3-1-1 Asahi, Matsumoto City, Nagano 390-8621, Japan

Department of Anatomy and Molecular Histology, Interdisciplinary Graduate School of Medicine and Engineering, University of Yamanashi, 1110 Shimokato, Chuo City, Yamanashi 409-3898, Japan

S. Ohno et al. (eds.), *In Vivo Cryotechnique in Biomedical Research and Application for Bioimaging of Living Animal Organs*, DOI 10.1007/978-4-431-55723-4_12

ventional morphological studies with the immersion or perfusion fixation method have not revealed the true functional morphology of circulating erythrocytes under various blood flow conditions. In the present study, we have used the IVCT to examine the behavior of flowing erythrocytes in living mouse organs, such as large blood vessels, in addition to hepatic sinusoids. So, the abdominal aorta, inferior vena cava, and liver organs of anesthetized mice were prepared by IVCT, as described before [2, 3]. The frozen organs were submitted to the routine freeze-substitution fixation method for scanning or transmission electron microscopy.

12.2 Flowing Erythrocytes in Abdominal Aorta and Inferior Vena Cava

Three-dimensional shapes of flowing erythrocytes in vivo appeared to be various at a high-speed flow in the abdominal aorta, and some ellipsoidal or curved erythrocytes were always observed, as captured by the IVCT (Fig. 12.1a, b). To the contrary, most erythrocytes flowing at a low speed in the inferior vena cava usually formed almost biconcave discoid shapes (Fig. 12.1c, d). For the past years, all of the erythrocytes in stored blood for human transfusion have been known to have the typical biconcave discoid shapes. However, in large blood vessels in vivo, physiological rheology should be also considered, in relation to their bulk flow [4]. The arterial flow was reported to be usually laminar, especially in the abdominal aorta [5]. A high shear rate in a large artery was determined by a rapid flow velocity, ~100 cm/s [6]. It thus provided a possibility for erythrocyte deformation as a result of external force stresses. In the present study, many erythrocyte shapes were seen to be varied in the aorta, some being stretched along the direction of blood flow. Conversely, a low shear rate in venous blood flow of the inferior vena cava, probably at a velocity of 30 cm/s [6], resulted in erythrocyte shapes approximately with the biconcave discoid.

In response to the fluid shear forces, erythrocytes were easily changed from the resting biconcave discoid shape into an ellipsoid form and aligned with their long axes parallel to the fluid stream. Such temporary erythrocyte deformability in large blood vessels was clearly examined by the present IVCT. It is tempting to conclude that the erythrocyte deformability completely differs between the abdominal aorta and the inferior vena cava, because hematocrit, plasma viscosity, and erythrocyte aggregation are significantly higher in venous blood than in arterial blood [7]. Therefore, the erythrocyte deformability in the blood vessels should be adapted to the blood flow conditions and in relation to their functions in oxygen delivery. It has been apparent that the shape and elasticity of flowing erythrocytes in human diseases are important for explaining the etiology of certain pathological conditions [8, 9]. Some hemolytic anemias, for example, are closely related to increased mechanical fragility of erythrocyte membranes [10], which would be confirmed in vivo by the IVCT.

12.3 Dynamically Changing of Flowing Erythrocyte Shapes in Hepatic Sinusoids of Living Mice

We have also applied the IVCT to examining the flowing erythrocyte shapes in hepatic sinusoids of living mouse livers (Fig. 12.1e), as reported before [3]. Their morphological features were different from those flowing in the abdominal aorta and inferior vena cava, as described above. Some wide spaces between flowing erythrocytes with various shapes were usually observed in the hepatic sinusoids with open spaces of Disse (Fig. 12.1e, asterisk). After the artificial heart arrest, however, they were changed to be congested in the sinusoidal lumen (Fig. 12.1f). Such erythrocyte shapes were completely different from those in the sinusoids of living mouse livers, and most of them appeared to be typical biconcave discoid shapes. Moreover, hepatic sinusoids and spaces of Disse between hepatocytes and endothelial cells were completely collapsed (Fig. 12.1f, asterisk).

The flowing erythrocytes kept various shapes in hepatic sinusoids, not typical biconcave discoid shapes, probably responding to hemodynamic stresses. In the isotonic physiological solution, erythrocyte shapes are generally known to be regular and uniform to form the biconcave discoid shapes. Some distance between the erythrocyte surface and the endothelium has the physiological significance of erythrocyte-capillary relationship, resulting in reduction of the diffusion distance and increased shear stresses. Moreover, the erythrocyte deformation to allow its passage through networks of narrow blood capillaries also increases the contact surface of the endothelium and erythrocytes themselves and effectively broadens their surface area for gas diffusion. With the erythrocyte deformation, the whole surface structure of erythrocytes, including membrane-skeletal proteins under the erythrocyte lipid membranes, must be responsible for constantly flowing through the narrow blood vessels [11, 12].

12.4 Element Detection of Flowing or Congesting Erythrocytes in Hepatic Sinusoids by X-Ray Microanalysis

The IVCT was already developed for examining the erythrocyte shapes flowing in large blood vessels and hepatic sinusoids of living mice, as described above [2, 3]. However, there has been no report about electrolyte concentrations of erythrocytes in vivo under blood flowing conditions. Recently, the variable pressure SEM has been often used to

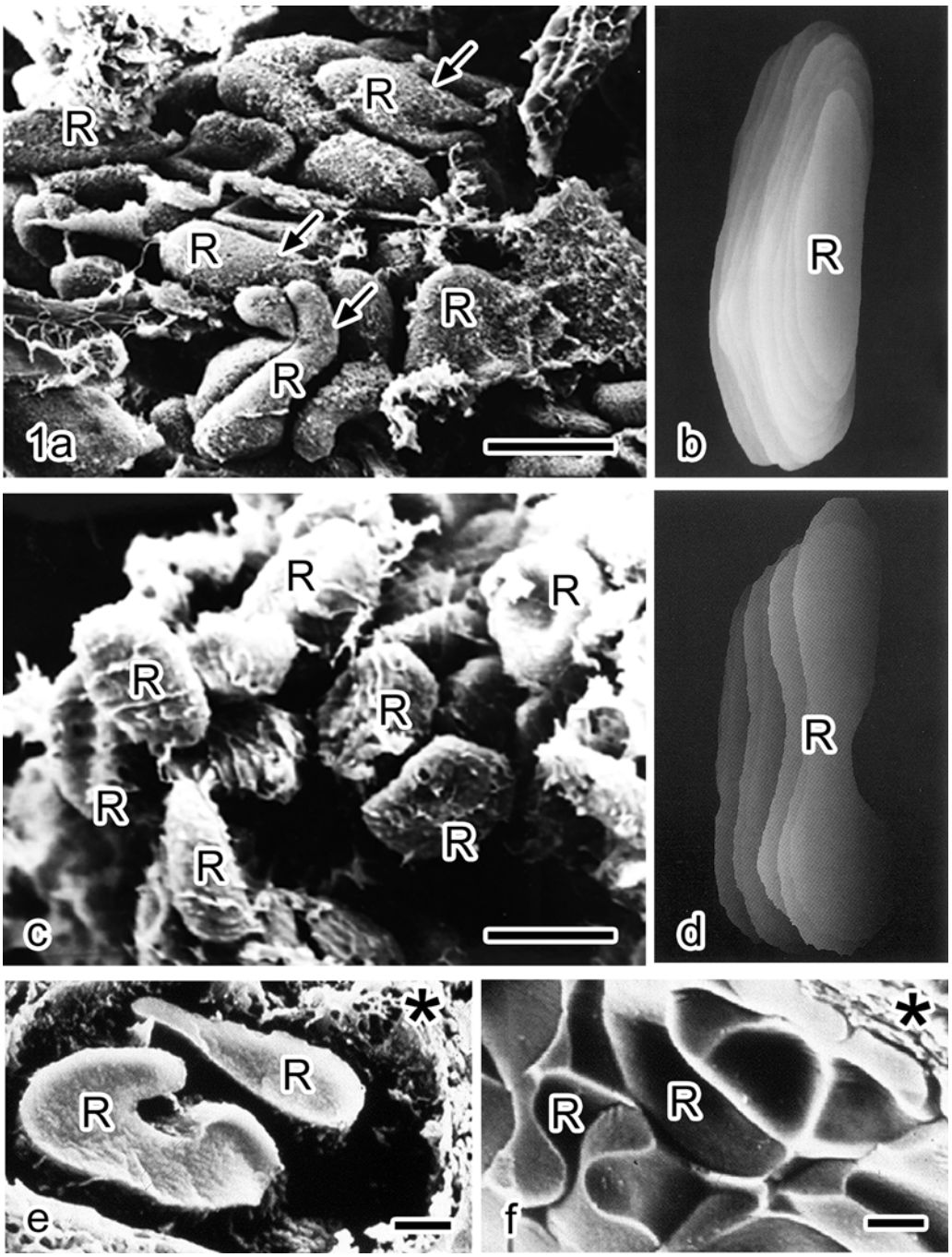

Fig. 12.1 Scanning electron micrographs of flowing erythrocytes in abdominal aorta (**a**) and inferior vena cava (**c**) of living mice, in addition to both images reconstructed by serial ultrathin sections (**b**, **d**) under the normal blood flow condition, as prepared by IVCT. *Bars*: 5 μm. (**a**) and (**b**) Flowing erythrocytes in the abdominal aorta appear to be various in shape (R), and some of them are stretched into ellipsoidal shapes (*arrows*). (**c**) and (**d**) Flowing erythrocytes in the inferior vena cava are mostly resembling the typical biconcave discoid shapes (R). (**e**) and (**f**) Scanning electron micrographs of erythrocytes in hepatic sinusoids of mice under normal blood flow (**e**) or heart-arrest (**f**) condition, as prepared by IVCT. *Bars*: 1 μm. (**e**) In a freeze-fractured sinusoid, flowing erythrocytes are seen to be variously shaped (R). *Asterisks*, open space of Disse. (**f**) Under the heart-arrest condition, erythrocytes are aggregated in the collapsed sinusoid to form the typical biconcave discoid shapes (R). *Asterisks*, collapsed space of Disse

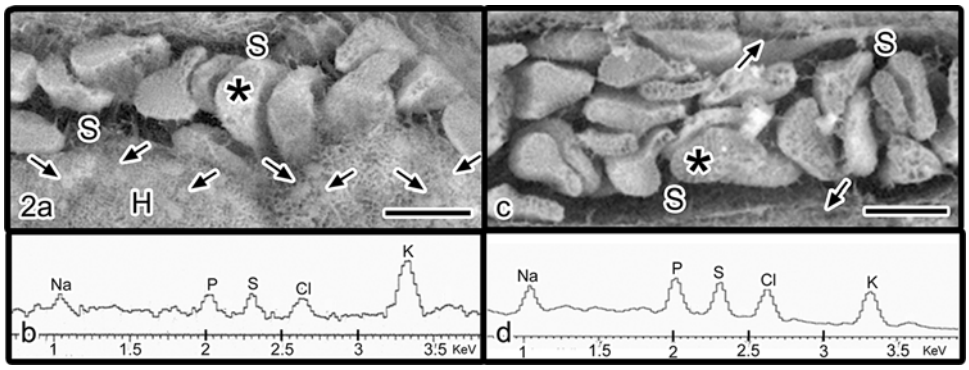

Fig. 12.2 (**a**) Scanning electron micrographs of freeze-fractured hepatic sinusoids of living mice under normal blood flow condition, which were examined by the variable pressure SEM. Images of liver tissues without any metal coating were obtained with backscattered electron beams. Flowing erythrocytes with various shapes are observed in the hepatic sinusoids (S). Freeze-fractured hepatocytes (H) are also observed and some cell organelles can be detected in their cytoplasm (*arrows*). *Bars*: 5 μm. (b) X-ray microanalysis data of flowing erythrocytes (**a**, *asterisk*) under the normal blood flow condition. The potassium peak (K) is the highest, and the left sodium peak (Na) is the lowest. (**c**) In hepatic sinusoids (S) of the heart-arrested mouse, erythrocytes are aggregated to each other, but the space of Disse is still observed (*arrows*). (**d**) X-ray microanalysis data of erythrocytes (*asterisk*) in the heart-arrested mouse liver. The potassium peak (K) is clearly decreased in comparison with that of the normal blood flow, but the sodium peak (Na) is relatively increased

observe hydrated and uncoated biological specimens. In the present study by using the IVCT combined with the common freeze-drying method, we have examined the uncoated erythrocyte morphology and electrolyte elements of sinusoidal erythrocytes under the normal blood flow or heart-arrest condition by the variable pressure SEM equipped with X-ray microanalysis system.

The mice were anesthetized with sodium pentobarbital, and their liver organs were routinely prepared by the IVCT, as described before [3]. The frozen liver tissue surface was routinely freeze-fractured with another cryoknife in the liquid nitrogen, as reported before [3]. The specimens were then freeze-dried at −95 °C in a freeze-etching apparatus (10^{-5} Pa) for 24 h, as reported before [13, 14]. The freeze-dried specimens were gradually warmed up to room temperature. They were attached onto carbon plates by using graphite-containing resin, and some were coated with carbon alone. They were finally analyzed by Hitachi S-4300 SEM or S-3000 N variable pressure SEM equipped with X-ray microanalysis system (accelerating voltage; 10 kV, vacuum condition; 30 Pa, illumination current; 50 μA, analytical time; 950 s), or conventional S-4500 SEM (Hitachi High-Technologies Corporation, Tokyo, Japan) at an accelerating voltage of 10 kV. The analyzed elements were Na (sodium), P (phosphorus), S (sulfur), Cl (chloride), and K (potassium).

Figure 12.2a shows the freeze-fractured liver tissues of living mice under normal blood flow condition, as observed by the variable pressure SEM. Three-dimensional natural images of hepatocytes in living mice and various shapes of flowing erythrocytes in hepatic sinusoids were easily detected without any metal coating. Small oval-shaped cell organelles were faintly seen in the cytoplasm of hepatocytes (Fig. 12.2a, arrows). The X-ray microanalysis data of flowing erythrocytes were obtained under the normal blood flow condition (Fig. 12.2b). The highest potassium peak was seen at the right side, and the lower sodium peak was observed at the left side. To the contrary, Fig. 12.2c shows another freeze-fractured liver tissue of mice under the heart-arrest condition. Some erythrocytes with biconcave discoid shapes were congested in the sinusoidal spaces because of stopping blood flow. The spaces of Disse were slightly detected (Fig. 12.2c, arrows). The X-ray microanalysis data of erythrocytes were similarly obtained under the heart-arrest condition (Fig. 12.2d). The potassium peak was relatively decreased, but the sodium peak was slightly increased, probably because of anoxia condition. Other phosphorus, sulfur, and chloride elements were relatively at the similar peak level under both conditions (Fig. 12.2b, d).

Elemental changes of flowing erythrocytes in hepatic sinusoids of mouse liver tissues have been clarified under the different hemodynamic conditions by the variable pressure SEM with X-ray microanalysis. The IVCT in combination with the variable pressure SEM would be a powerful tool for analyzing the biological samples with less technical artifacts of diffusion or extraction about atomic elements of cells and tissues in living animal organs. Some microenvironmental conditions against flowing erythrocytes in hepatic sinusoids of living mice may cause dynamically functional changes of ion transport systems of erythrocyte membranes, which are also related to their morphological changes, as revealed in the present study.

References

1. Maeda N (1996) Erythrocyte rheology in microcirculation. Jpn J Physiol 46:1–14
2. Xue M, Kato Y, Terada N, Fujii Y, Baba T, Ohno S (1998) Morphological study by an 'in vivo cryotechnique' of the shape of erythrocytes circulating in large blood vessels. J Anat 193:73–79
3. Terada N, Kato Y, Fujii Y, Ueda H, Baba T, Ohno S (1998) Scanning electron microscopic study of flowing erythrocytes in hepatic sinusoids as revealed by 'in vivo cryotechnique'. J Electron Microsc 47:67–72
4. Stuart J, Nash GB (1990) Red cell deformability and haematological disorders. Blood Rev 4:141–147
5. Robinson K (1978) Abdominal aorta. In: James DG (ed) Circulation of the blood. Pitman Medical, Tunbridge Wells, pp 173–175
6. Klug PP, Lessin LS, Radice P (1974) Rheological aspects of sickle cell disease. Arch Int Med 133:577–590
7. Mokken FC, Waart FJ, Henny CP, Goedhart PT, Gelb AW (1996) Differences in peripheral arterial and venous hemorheologic parameters. Ann Hematol 73:135–137
8. Athanassiou G, Symeonidis A, Kourakli A, Missirlis YF, Zoumbos NC (1992) Deformability of the erythrocyte membrane in patients with myelodysplastic syndromes. Acta Haematol 87:169–172
9. Cynober T, Mohandas N, Tchernia G (1996) Red cell abnormalities in hereditary spherocytosis: relevance to diagnosis and understanding of the variable expression of clinical severity. J Lab Clin Med 128:259–269
10. Rybicki AC, Qiu JJ, Musto S, Rosen NL, Nagel RL, Schwartz RS (1993) Human erythrocyte protein 4.2 deficiency associated with hemolytic anemia and a homozygous 40 glutamic acid-lysine substitution in the cytoplasmic domain of band 3. Blood 81:2155–2165
11. Shiga T, Maeda N, Kon K (1990) Erythrocyte rheology. Crit Rev Oncol Hematol 10:9–48
12. Terada N, Fujii Y, Ueda H, Ohno S (1997) Immunocytochemical study of human erythrocyte membrane skeletons under stretching conditions by quick-freezing and deep-etching method. J Anat 190:397–404
13. Ohno S, Hora K, Furukawa T, Oguchi H (1992) Ultrastructural study of the glomerular slit diaphragm in fresh unfixed kidneys by a quick-freezing method. Virchows Arch B Cell Pathol 61:351–358
14. Yoshimura A, Ohno S, Nakano K, Oniki H, Inui K, Ideura T, Koshikawa S (1991) Three-dimensional ultrastructure of anionic sites of the glomerular basement membrane by a quick-freezing and deep-etching method using a cationic tracer. Histochemistry 96:107–113

Dynamic Ultrastructure of Smooth Muscle Cells in Dystrophin-Deficient mdx or Normal scn Mice

13

Shinichi Ohno

Abstract

Duodenal smooth muscle cells of normal scn mice and dystrophin-deficient mdx mice were prepared by the in vivo cryotechnique (IVCT). The IVCT revealed more realistic ultrastructures of functional smooth muscle cells in both scn and mdx mice. In the scn mice, they were surrounded by compact extracellular matrix and had large gap junctions and closed caveolae with electron-dense contents. In the dystrophic mdx mice, however, the extracellular matrix was often torn off from the surface of the smooth muscle cells. The dystrophic mdx mouse had smooth muscle cells equipped with small gap junctions and uneven dense plaques in comparison with the normal scn mouse. They were surrounded with some incomplete basal lamina. The dystrophic smooth muscle cells also represented the atypical arrangement of caveolae, which were fusing together with neighboring caveolae. Such ultrastructural changes were mainly seen in the regions of caveolae, suggesting that a primary cause of the smooth muscle injury might be induced by the lack of normal arrangements of functional cell membranes.

Keywords

Smooth muscle cell • Dystrophin-deficient mouse • In vivo cryotechnique • Basement membrane • Caveolae

13.1 Introduction

Dystrophin, the product of the Duchenne muscular dystrophy (DMD) gene, is present in all muscle types in normal individuals [1]. Its absence or the presence of incomplete version of the protein is responsible for the appearance of human DMD. The dystrophic mdx mice also lack dystrophin due to an X-linked mutation as well as the human DMD [2]. In striated muscles, the DMD patients present extensive and progressive skeletal muscle necrosis and the development of a life-threatened dilated cardiomyopathy [1]. Normal dystrophin expression in smooth muscle cells is similar to that observed in the striated muscle, and it disappears in DMD patients [3–5]. Dystrophin binds the filamentous actin cytoskeletons and is normally expressed in a complex of transmembrane proteins that interact with external components of the basal lamina [6, 7]. This complex forms a structural bridge between the external basal lamina and the internal cytoskeletons, and the absence of dystrophin produces a defect in the membrane structural support that renders the skeletal muscle susceptible to ruptures of cell membranes during the course of contractile activity [1]. In fact, it was reported that normal myotubes were about fourfold stiffer than myotubes cultured from mdx mice [8].

In the smooth muscle, the basal lamina serves a mechanical role in the transmission of force. It could be also regarded as constituting intramuscular microtendons, and the complex is an important region for the force transduction [9]. On the

S. Ohno, M.D., Ph.D. (✉)
Department of Anatomy and Molecular Histology,
Interdisciplinary Graduate School of Medicine and Engineering,
University of Yamanashi, 1110 Shimokato,
Chuo City, Yamanashi 409-3898, Japan
e-mail: sohno@yamanashi.ac.jp

S. Ohno et al. (eds.), *In Vivo Cryotechnique in Biomedical Research and Application for Bioimaging of Living Animal Organs*, DOI 10.1007/978-4-431-55723-4_13

other hand, cell membranes of the smooth muscle cell display two alternating structural domains at the electron microscopic level: (1) densely staining plaques that correspond to the adherens junctions and (2) intervening uncoated regions which are rich in membrane invaginations of caveolae [10]. This simple bipartite domain organization of cell membranes in the smooth muscle contrasts with the more complex organization of those in the skeletal muscle. A number of molecules including caveolin, Ca^{2+}-ATPase, and IP3 receptor-like protein have been reported to be localized at caveolae [11], which suggests their role in diverse cytoplasmic processes such as signal transduction. The dystrophin is also specifically localized in the caveolae-rich domains of cell membranes in the smooth muscle, together with caveolin [10, 11]. The aim of this chapter is to describe pathological changes of the smooth muscle cells of mdx mice, prepared by IVCT [12], at an ultrastructural level.

13.2 Different Ultrastructures of Contracting Smooth Muscle Cells Between mdx and scn Mice

Intestinal organs of normal scn mice or dystrophin-deficient mdx mice under pentobarbital anesthesia were surgically exposed in their abdomen and put on a thin plastic plate. The IVCT was similarly performed, as described previously [12]. Some of the frozen specimens were routinely freeze-substituted in acetone containing 2 % osmium tetroxide and embedded in epoxy resin. Ultrathin sections were cut, stained with uranium acetate and lead citrate, and observed with TEM. In the specimens of normal living mice, smooth muscle cells in outer muscle layers of intestines were located close to each other, and their spontaneous contraction could be often observed in some areas of the cytoplasm (Fig. 13.1a, b). To the contrary, irregularly shaped caveolae and fusion of several caveolae could be more often seen in the mdx mice than those in the normal mice (Fig. 13.1c). Additionally, intercellular spaces between smooth muscle cells were enlarged (Fig. 13.1c), and extracellular matrices were partially disrupted under the muscle contracting condition in the specimens obtained from the dystrophin-deficient mdx mice (Fig. 13.1d).

13.3 Significant Meaning of Smooth Muscle Cells in the mdx Mice

In the present study, ultrastructural changes of the smooth muscle cells of mdx mice were clearly revealed by IVCT. It was suggested that dystrophin deficiency induced impairment of normal cell morphology, not only in the striated muscles but also in the smooth muscle cells. In dystrophic mammals, histopathological changes have been less examined in smooth muscle cells in comparison with the striated muscles [4, 5]. In the present study, smooth muscle cells with an appearance of typical necrosis or apoptosis could not be identified among thousands of examined muscle cells of the mdx mice. The reason why almost smooth muscle cells survive without normal dystrophin expression is still unknown, but there are some possibilities as follows. The elevation of the free cytosolic Ca^{2+} concentration, a potential trigger to induce cell necrosis, was revealed in the mdx skeletal muscle [13]. To the contrary, as measured with the fluorescent Ca^{2+} indicator fura-2, cytosolic Ca^{2+} concentration is not elevated in resting smooth muscle cells of mdx mice [14]. The maintenance of intracellular Ca^{2+} metabolism may contribute to keep homeostasis of the smooth muscle cells of the mdx mice [15].

13.4 Morphological Merits of IVCT for Functioning Smooth Muscles

In the present study, we have used our IVCT, which makes it possible to observe the morphology of dynamic cells in anesthetized animals [12]. We have already noticed that ultrastructures obtained from the specimens prepared by the conventional preparation methods contained lots of inevitable technical artifacts. In the other words, "normal" ultrastructures obtained by the standard electron microscopy are not "natural" ones. Indeed, even in the smooth muscle cells of the normal scn mice, the conventional ultrastructural features, such as opening electron-lucent caveolae, short gap junctions, and so-called basal lamina, are definitely different from those obtained by the IVCT. The IVCT produced a very compact extracellular matrix between closely spaced smooth muscle cells in the scn mice. In contrast, dramatic

Fig. 13.1 Electron micrographs of intestinal smooth muscle cells in normal scn mice (**a**, **b**) and dystrophin-deficient mdx mice (**c**, **d**). They were prepared by the "in vivo cryotechnique" (IVCT), followed by freeze-substitution and embedding in epoxy resin. (**a**) and (**b**) The intercellular matrix between contracting smooth muscle cells (SM1, SM2) is tightly attached to each other in the normal scn mice (*large arrows*). *Inset*, non-contracting smooth muscle cells. *Small arrows*, caveolae. *M* mitochondria. (**c**) The intercellular spaces between smooth muscle cells are widely dilated in the dystrophin-deficient mdx mice (*large arrows*), as compared with those of the normal scn mice. SM1, SM2, and SM3, smooth muscle cells. Additionally, irregularly shaped or fusing caveolae are also seen in smooth muscle cells of the mdx mice (*small arrows*). (**d**) They are more widely dilated in the contracting smooth muscle cells of the mdx mice (large arrows). *M* mitochondria. *Small arrows*, caveolae. *Bars*: 0.5 μm

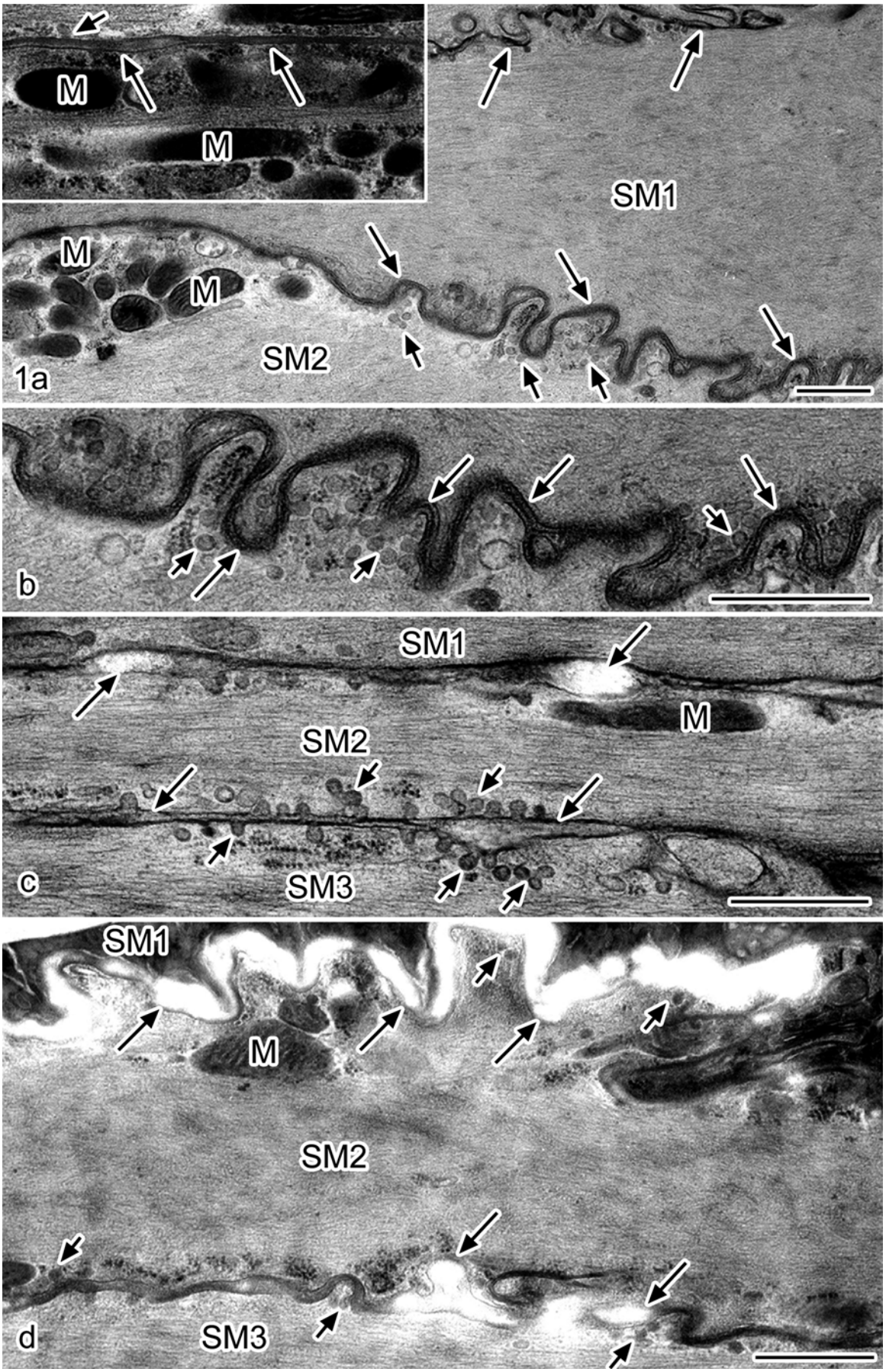

Fig. 13.1 (continued)

changes of basement membranes in the mdx mice were also clearly revealed by the IVCT. The extracellular matrix or basal lamina has been suggested as intramuscular microtendons that provide mechanical support during contractions of the smooth muscle layer. Although the extracellular matrix in the normal scn mice was revealed by the IVCT, showing a tighter and more compact arrangement between adjacent smooth muscle cells, the intramembrane protein dystrophin has a role to connect extracellular matrix to the cell membrane of smooth muscle cells. The extracellular matrix was easily torn off from the smooth muscle cells in the mdx mice, because of impaired molecular functions of dystrophin to maintain compact structures of smooth muscle layers. Such impairment should affect the force transmission within the extracellular matrix as "microtendons" and may decrease the substantial force of the contraction of the smooth muscle layers [9].

13.5 Concluding Remarks

Thus, the IVCT has revealed morphological features of spontaneously contracting smooth muscle cells in the normal living mouse intestine and clarified their clear difference of extracellular matrix and caveolae from those in the dystrophin-deficient mdx mice.

References

1. Carlson CG (1998) The dystrophinopathies: an alternative to the structural hypothesis. Neurobiol Dis 5:3–15
2. Sicinski P, Allan YG, Ryder-Cook AS, Barnard EA, Darlison MG, Barnard PJ (1989) The molecular basis of muscular dystrophy in the mdx mouse: a point mutation. Science 244:1578–1580
3. Harricane MC, Augier N, Leger J, Anoal M, Cavadore C, Mornet D (1991) Ultrastructural localization of dystrophin in chicken smooth muscle. Cell Biol Intern Rep 15:687–697
4. Marbini A, Gemignani F, Bellanova MF, Guidetti D, Ferrari A (1996) Immunohistochemical localization of utrophin and other cytoskeletal proteins in skin smooth muscle in neuromuscular diseases. J Neurol Sci 143:156–160
5. Marbini A, Marcello N, Bellanova MF, Guidetti D, Ferrari A, Gemignani F (1995) Dystrophin expression in skin biopsy immunohistochemical localisation of striated muscle type dystrophin. J Neurol Sci 129:29–33
6. Byers TJ, Kunkel LM, Watkins SC (1991) The subcellular distribution of dystrophin in mouse skeletal, cardiac, and smooth muscle. J Cell Biol 115:411–421
7. Brown RH Jr (1997) Dystrophin-associated proteins and the muscular dystrophies. Annu Rev Med 48:457–466
8. Pasternak C, Wong S, Elson EL (1995) Mechanical function of dystrophin in muscle cells. J Cell Biol 128:355–361
9. Gabella G (1981) Structure of smooth muscle. In: Buelbring E, Brading AF, Jones AW, Tomita T (eds) An assessment of current knowledge. University of Texas Press, Austin, pp 1–46
10. North AJ, Galazkiewicz B, Byers TJ, Glenney JR Jr, Small JV (1993) Complementary distributions of vinculin and dystrophin define two distinct sarcolemma domains in smooth muscle. J Cell Biol 120:1159–1167
11. Okamoto T, Schlegel A, Scherer PE, Lisanti MP (1998) Caveolins, a family of scaffolding proteins for organizing "preassembled signaling complexes" at the plasma membrane. J Biol Chem 273:5419–5422
12. Ohno S, Terada N, Fujii Y, Ueda H, Takayama I (1996) Dynamic structure of glomerular capillary loop as revealed by an in vivo cryotechnique. Virchows Arch 427:519–527
13. McCarter GC, Denetclaw WFJ, Reddy P, Steinhardt RA (1997) Lipofection of a cDNA plasmid containing the dystrophin gene lowers intracellular free calcium and calcium leak channel activity in mdx myotubes. Gene Ther 4:483–487
14. Boland B, Himpens B, Casteels R, Gillis JM (1993) Lack of dystrophin but normal calcium homeostasis in smooth muscle from dystrophic mdx mice. J Muscle Res Cell Motil 14:133–139
15. Khurana TS, Prendergast RA, Alameddine HS, Tomé FM, Fardeau M, Arahata K, Sugita H, Kunkel LM (1995) Absence of extraocular muscle pathology in Duchenne's muscular dystrophy: role for calcium homeostasis in extraocular muscle sparing. J Exp Med 182:467–475

Dynamic Bioimaging of Serum Proteins in Beating Mouse Hearts

14

Liye Shi, Nobuo Terada, Yurika Saitoh, Nobuhiko Ohno, and Shinichi Ohno

Abstract

In vivo cryotechnique (IVCT) was performed for diastolic heart tissue under the condition of monitoring with electrocardiogram (ECG). Other mouse hearts were prepared with conventional perfusion-fixation (PF-DH) or immersion-fixation followed by dehydration (IM-DH) and quick-freezing of resected heart tissues (FQF). Immunolocalizations of albumin, immunoglobulin G1 (IgG1), intravenously injected bovine serum albumin (BSA), and connexin 43 were examined after different intervals of BSA injection. In the case of IVCT, the exact stop time of beating mouse hearts was recorded by ECG. Both albumin and BSA were well preserved in intercalated disks and T tubules of cardiomyocytes in addition to blood vessels and interstitial matrices. IgG1 was immunolocalized in interstitial matrices of heart tissues in addition to their blood vessels. IVCT has proved to be more useful for the morphofunctional examination of dynamically changing heart tissue than conventional preparation methods.

Keywords

In vivo cryotechnique • Serum protein • Microenvironment • Mouse heart tissue

14.1 Introduction

In the present study, we have morphologically and immunohistochemically examined living mouse heart tissues monitored by electrocardiogram, as prepared with IVCT, and mainly focused on the immunolocalization of various serum proteins that contribute to the homeostasis of the microenvironment around the cardiomyocytes. In addition, we have described the time-dependent double immunolocalizations of intrinsic or extrinsic serum proteins at different time intervals after the bovine serum albumin (BSA) injection.

14.2 Experimental Design and Tissue Preparation

Male C57BL/6J mice, aged 6–8 weeks, were prepared by IVCT method (Fig. 14.1d) [7]. Other conventional preparation methods were also used (Fig. 14.1a–c), including IM-DH or PF-DH [10] and FQF [5, 6]. Mice prepared with

L. Shi
Department of Anatomy and Molecular Histology, Interdisciplinary Graduate School of Medicine and Engineering, University of Yamanashi, 1110 Shimokato, Chuo City, Yamanashi, 409-3898, Japan

Department of Cardiovascular Medicine, The First Hospital of China Medical University, Shenyang, China

N. Terada
Division of Health Sciences, Shinshu University Graduate School of Medicine, 3-1-1 Asahi, Matsumoto City, Nagano 390-8621, Japan

Department of Anatomy and Molecular Histology, Interdisciplinary Graduate School of Medicine and Engineering, University of Yamanashi, 1110 Shimokato, Chuo City, Yamanashi 409-3898, Japan

Y. Saitoh • N. Ohno • S. Ohno, M.D., Ph.D. (✉)
Department of Anatomy and Molecular Histology, Interdisciplinary Graduate School of Medicine and Engineering, University of Yamanashi, 1110 Shimokato, Chuo City, Yamanashi, 409-3898, Japan
e-mail: sohno@yamanashi.ac.jp

S. Ohno et al. (eds.), *In Vivo Cryotechnique in Biomedical Research and Application for Bioimaging of Living Animal Organs*, DOI 10.1007/978-4-431-55723-4_14

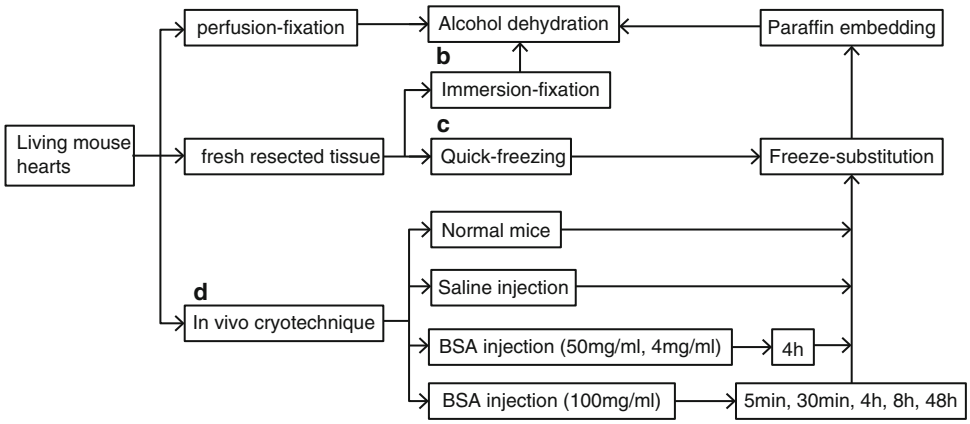

Fig. 14.1 A flow chart of different experimental procedures, including perfusion-fixation (**a**), immersion-fixation (**b**), quick-freezing (**c**), and in vivo cryotechnique (**d**) for living mouse hearts

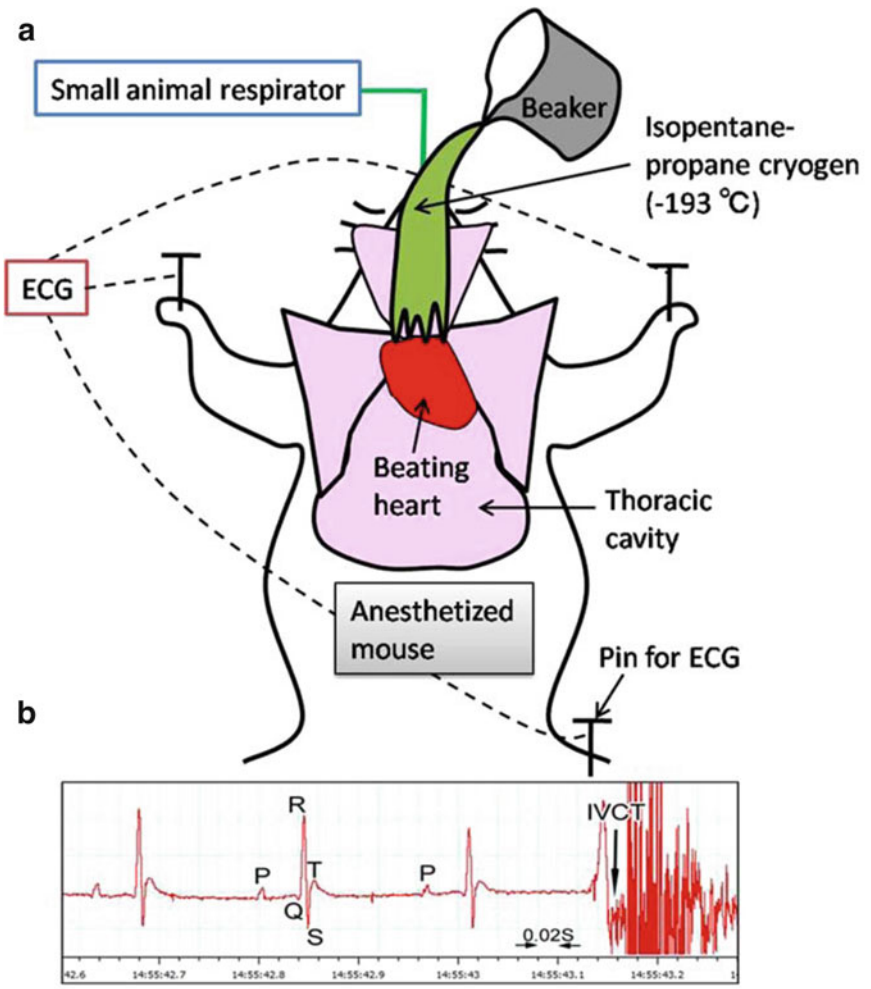

Fig. 14.2 A schematic drawing shows how to perform "in vivo cryotechnique" (IVCT) for living mouse heart with monitoring electrocardiogram (ECG) (**a**). Beating heart of an anesthetized mouse on a small animal respirator is exposed after opening the thoracic cavity, which is cryofixed by pouring isopentane-propane cryogen (−193 °C) precooled in liquid nitrogen (**b**). An example of ECG shows typical *P*, *Q*, *R*, *S*, and *T* points, and the exact time of stopping with IVCT is indicated by an *arrow*

IVCT were divided into several experimental groups and a control group. In the experimental groups, 50 μl of 100 mg/ml BSA with low endotoxin in sterile saline was injected via tail veins into the anesthetized mice. After BSA injection, IVCT was performed at different time intervals of 5 min, 30 min, 4 h, 8 h, and 48 h (Fig. 14.1d). For another experiment, 50 μl of 4 mg/ml or 100 mg/ml BSA was similarly injected into mice and IVCT was also performed at 4-h time intervals before cryofixation [1, 8]. In the control group, mice were prepared without BSA injection or only with an injection of 50 μl of physiological saline. All these mice were automatically monitored using an electrocardiogram (ECG) apparatus (Fig. 14.2) when IVCT was performed.

14.3 Immunohistochemistry of Serum Proteins

Paraffin sections of about 3 μm thick were routinely deparaffinized and stained with hematoxylin-eosin (HE). The other deparaffinized sections were stained with immunoperoxidase-DAB methods for each antibody. The primary antibodies were goat or rabbit anti-mouse albumin, goat anti-mouse immunoglobulin G1 (IgG1), sheep anti-BSA, and rabbit anticonnexin 43 antibodies. The secondary antibodies were biotinylated anti-goat IgG, biotinylated anti-rabbit IgG, and biotinylated donkey anti-sheep IgG antibodies [3]. For immunofluorescence staining of the albumin, IgG1, and connexin 43, the secondary antibodies were Alexa Fluor 488-conjugated donkey anti-goat IgG and Alexa Fluor 594-conjugated donkey anti-rabbit IgG antibodies, which were incubated together with TOPRO-3. For the immunofluorescence staining of BSA, the tissue sections were visualized using Alexa Fluor 546-conjugated streptavidin after incubation with primary sheep anti-BSA antibody and biotinylated donkey anti-sheep IgG antibody.

All the immunostained sections were embedded in glycerol or VECTASHIELD, and their light micrographs were taken using either a light microscope or a confocal laser scanning microscope.

14.4 Semiquantitative Analyses of Immunoreaction Intensity

For the semiquantitative analyses of IgG1 immunoreactivity as reported previously [12], 20 micrographs of heart tissue immunostained for IgG1 were randomly selected from the 4-h BSA injection group and the normal group or four different preparation method groups. The immunoreactivity in their blood vessels, interstitial matrices, and cardiomyocytes was classified into five categories, which were negative (–), unclear (±), immunopositive (+), moderately immunopositive (2+), and strongly immunopositive (3+), by three investigators under a light microscope. Such semiquantitative data of IgG1 immunoreactivity were statistically analyzed by the nonparametric Kruskal-Wallis H-test using SPSS 11.5 software for Windows. A score of $P<0.05$ was considered to constitute a significant difference between the control and different experimental groups.

14.5 Morphological Analyses of Heart Specimens

As shown in Fig. 14.3a with IVCT, the blood vessels are clearly open and contain flowing erythrocytes. However, with FQF (Fig. 14.3b), erythrocytes are aggregated in the blood vessels of the resected heart tissue owing to loss of blood pressure. With PF-DH, no erythrocytes are seen in the widely opened blood vessels (Fig. 14.3c), although, with IM-DH, erythrocytes are seen in the collapsed blood vessels (Fig. 14.3d).

In specimens prepared with IVCT, immunoreactivity of albumin was detected not only in the blood vessels but also on the lateral side among the cardiomyocytes representing the interstitial matrices. It was also detected in the intercalated disks and T tubules of cardiomyocytes (Fig. 14.3e). The immunolocalization of albumin observed with FQF was similar to that with IVCT (Fig. 14.3f), showing that it was detected in the intercalated disks and T tubules of cardiomyocytes in addition to the blood vessels and interstitial matrices. In contrast, in specimens prepared with PF-DH (Fig. 14.3g), the immunoreactivity of albumin became obscure in all parts. Some albumin was washed out from the blood vessels or the interstitium and some got into the cytoplasm of some cardiomyocytes, showing diffusion artifacts because of perfusion pressure (Fig. 14.3g, curved arrow). In specimens prepared with IM-DH (Fig. 14.3h), less albumin was seen in the intercalated disks and T tubules of cardiomyocytes. Semiquantitative analyses of serum albumin immunoreactivity among the four different preparation methods were carried out for the immunostained heart tissue of normal mice (Table 14.1).

14.6 Immunolocalization of Serum Proteins in Living Mouse Heart Tissue

With IVCT, the exact stopping time of a beating heart was accurately recorded by ECG (Fig. 14.4a), reflecting the living heart morphology at the time of freezing. In the present study, albumin passed across the vascular endothelium into the interstitium (Fig. 14.4c), and IgG1 also passed across the vascular endothelium and immunolocalized in the interstitium in addition to the blood vessels (Fig. 14.4d). Furthermore, serum albumin also got into the intercalated disks and T tubules of cardiomyocytes (Fig. 14.4c). In addition, connexin 43 was clearly immunolocalized at gap junctions distributed in the intercalated disks (Fig. 14.4e).

Double immunofluorescence staining for albumin and IgG1 revealed that albumin was immunolocalized in the intercalated disks and T tubules (Fig. 14.5a–d) and that both albumin and IgG1 were also immunolocalized in both the blood vessels and interstitium. Double immunofluorescence staining for albumin and connexin 43 (Fig. 14.5e–h) revealed that the albumin was detected close to connexin 43, without overlapping with it, which represents the intercalated disk at the longitudinal terminal of the cardiomyocytes [11]. Double immunofluorescence staining for connexin 43 and IgG1 revealed that IgG1 was not immunolocalized in the intercalated disk (Fig. 14.5i–l). They were more clearly shown at higher magnification (Fig. 14.5d, h, l).

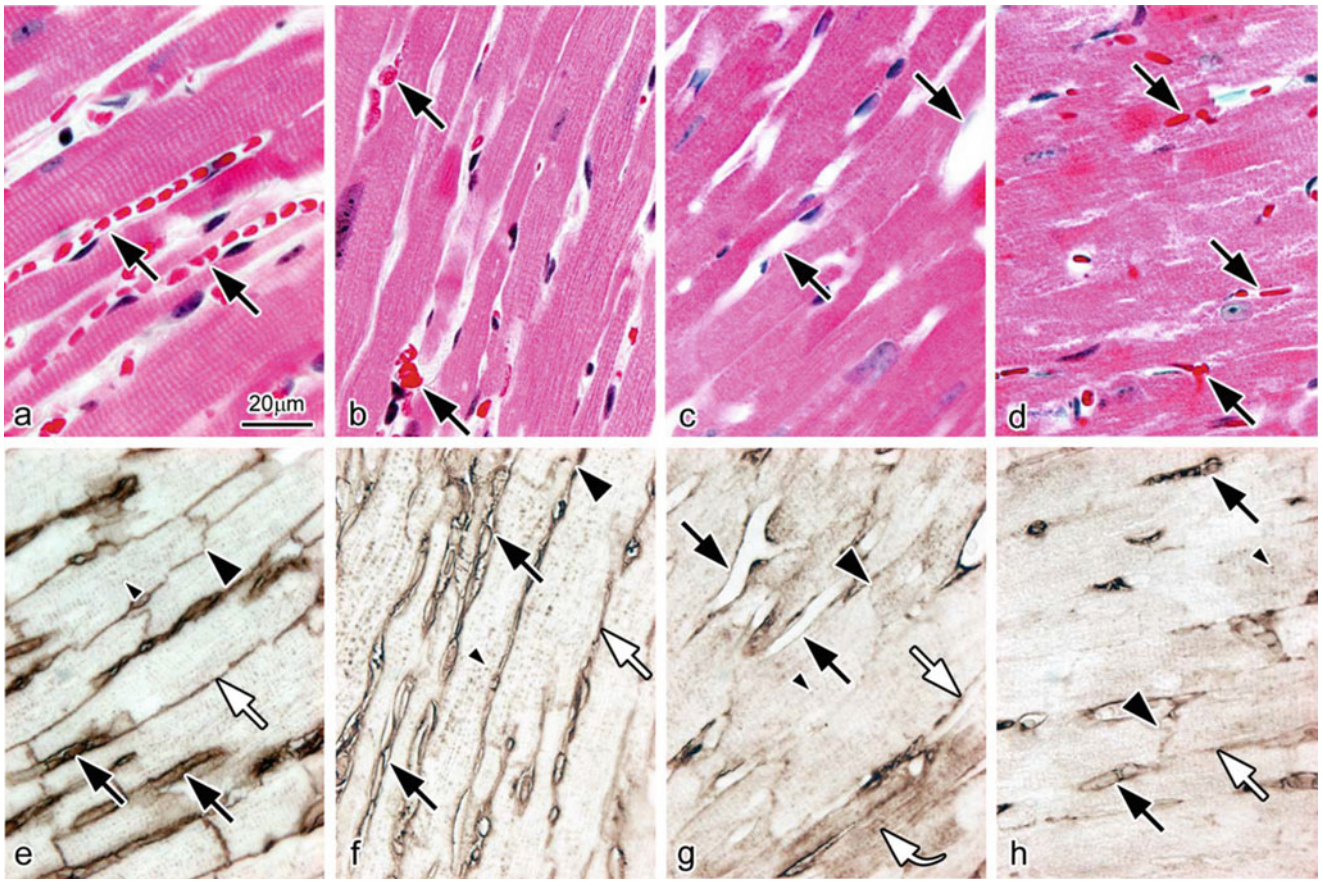

Fig. 14.3 Light micrographs of hematoxylin-eosin staining (HE; **a**–**d**) and immunostaining for serum albumin (Albumin; **e**–**h**) on serial sections prepared by IVCT (**a**, **e**), FQF (**b**, **f**), and PF-DH (**c**, **g**) or IM-DH (**d**, **h**). *Bar* = 20 μm

Table 14.1 Semiquantitative comparison among immunoreactivities of serum albumin in mouse heart tissues with different preparation methods

	IVCT	FQF	PF-DH	IM-DH
Blood vessel	2+	+	±	+
Interstitium	2+	+	−~+	±
Intercalated disk	2+	+	−~+	−~+
T tubule	+	+	−~+	−~+
Cytoplasm of cardiomyocyte	−	−	−~+	±

Negative, (−); unclear, (±); immunopositive, (+); moderately immunopositive, (2+)

14.7 Time-Dependent Immunolocalizations of Albumin and IgG1 After BSA Injection

With the saline injection, BSA immunoreactivity was not detected in living mouse heart tissue (Fig. 14.6d). At 5 min after BSA injection, BSA was immunolocalized only in the blood vessels (Fig. 14.6h). At 30 min, it was immunolocalized both in the blood vessels and interstitium and in intercalated disks and T tubules of cardiomyocytes (Fig. 14.6l), in a pattern similar to that of albumin (Fig. 14.6j). At 48 h, it disappeared from the intercalated disks, T tubules, and also the interstitium and was only immunolocalized in the blood vessels (Fig. 14.6x). IgG1 was also slightly immunolocalized in the intercalated disks at 4 h after the BSA injection (Fig. 14.6o) and recovered to its normal immunolocalization of mouse heart tissue at 8 h (Fig. 14.6s). Semiquantitative comparison among relative immunoreactivities of albumin, BSA, and IgG1 in different areas of the heart tissue was performed for normal mice and the mice with different BSA injections (Table 14.2). Semiquantitative analyses of IgG1 immunoreactivity in different areas of the heart tissue were also performed in normal mice and the 4 h BSA injection mice (Table 14.3). The recorded ECGs were first compared

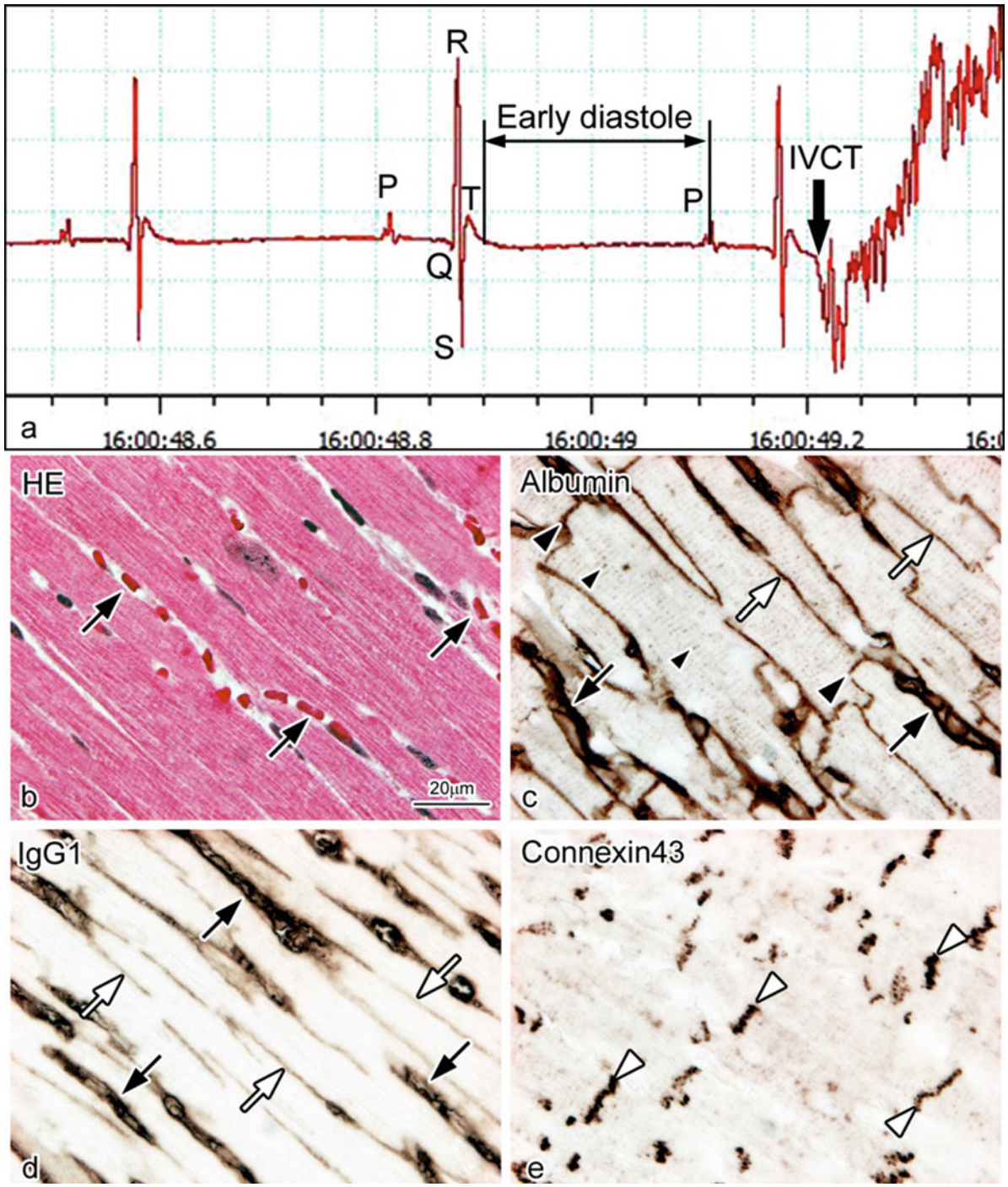

Fig. 14.4 Light micrographs of serial sections of mouse heart tissues prepared by IVCT. They were stained with hematoxylin-eosin (HE; **b**) or immunostained for albumin (**c**), immunoglobulin G1 (IgG1; **d**), and connexin 43 (**e**). By electrocardiogram (**a**), the exact stopping time of a diastolic heart is accurately recorded, reflecting its living morphology (**b**). *Bar*=20 μm

between the experimental and control groups to check whether there were any changes of electrical impulses after the BSA injection. As shown in Fig. 14.6y–aa, there were no significant differences between BSA injection samples.

The BSA was immunolocalized only in blood vessels at 5 min after BSA injection (Fig. 14.7a, c). At 30 min, it was immunolocalized in the blood vessels, interstitium, and both the intercalated disks and T tubules of cardiomyocytes (Fig. 14.7d, f), in the same pattern as that of mouse serum albumin. At higher magnification (Fig. 14.7f: inset), the BSA was closely immunolocalized in the intercalated disks with connexin 43. At 48 h, it was immunolocalized only in the

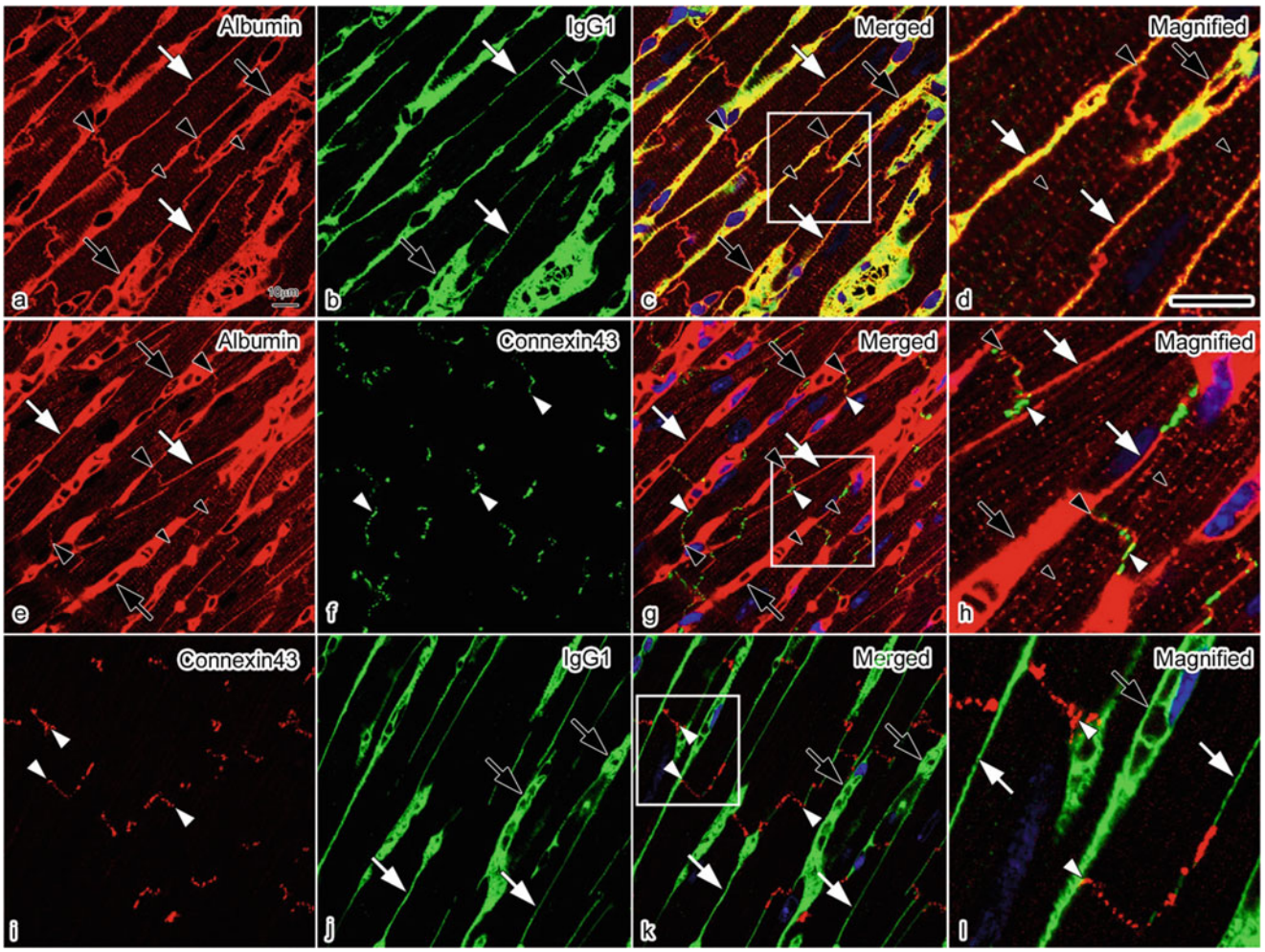

Fig. 14.5 Confocal laser scanning micrographs of double immunofluorescence staining for albumin (*red*) and IgG1 (*green*) (**a**–**d**), albumin (*red*) and connexin 43 (*green*) (**e**–**h**), and connexin 43 (*red*) and IgG1 (*green*) (**i**–**l**) in living mouse heart tissues with IVCT. *Bars* = 10 μm

blood vessels and disappeared from the interstitium, intercalated disks, and T tubules (Fig. 14.7g, i).

14.8 Discussion

As the dynamic microenvironment around the cardiomyocytes is closely associated with the transduction of electrical signals and mechanical contraction or relaxation coupling between them at intercalated disks [4], the histopathological characteristics of such a microenvironment are more significant for indicating the physiological and pathological states of the beating heart than was previously thought. The present immunohistochemical findings with ECG monitoring suggest that the new IVCT could prevent the common artificial changes in cells and tissues due to ischemia and anoxia and could contribute to morphofunctional and immunohistochemical examinations of a living mouse heart, as shown in Fig. 14.3.

The intercalated disks between individual cardiomyocytes are a main site of their interconnection and possess considerable functional significance in terms of the mechanism of contraction or relaxation of the total myocardium [2]. Although many studies have been reported to describe the characterization of the intercalated disks, little convincing data have been provided as to whether soluble components in vivo can freely pass through the intercalated disks of living animal hearts and create the extracellular microenvironment around the functioning cardiomyocytes. The present study with IVCT is the first to immunohistochemically demonstrate the localization of endogenous serum proteins with different molecular sizes at the intercalated disks of the beating hearts in situ and also to indicate more clearly the effect of BSA injection on serum components in the extracellular microenvironment. In the present study, it was shown that mouse serum albumin of about 69 kDa molecular weight was translocated across the vascular endothelium into interstitial matrices of living mouse heart tissue in addition to its

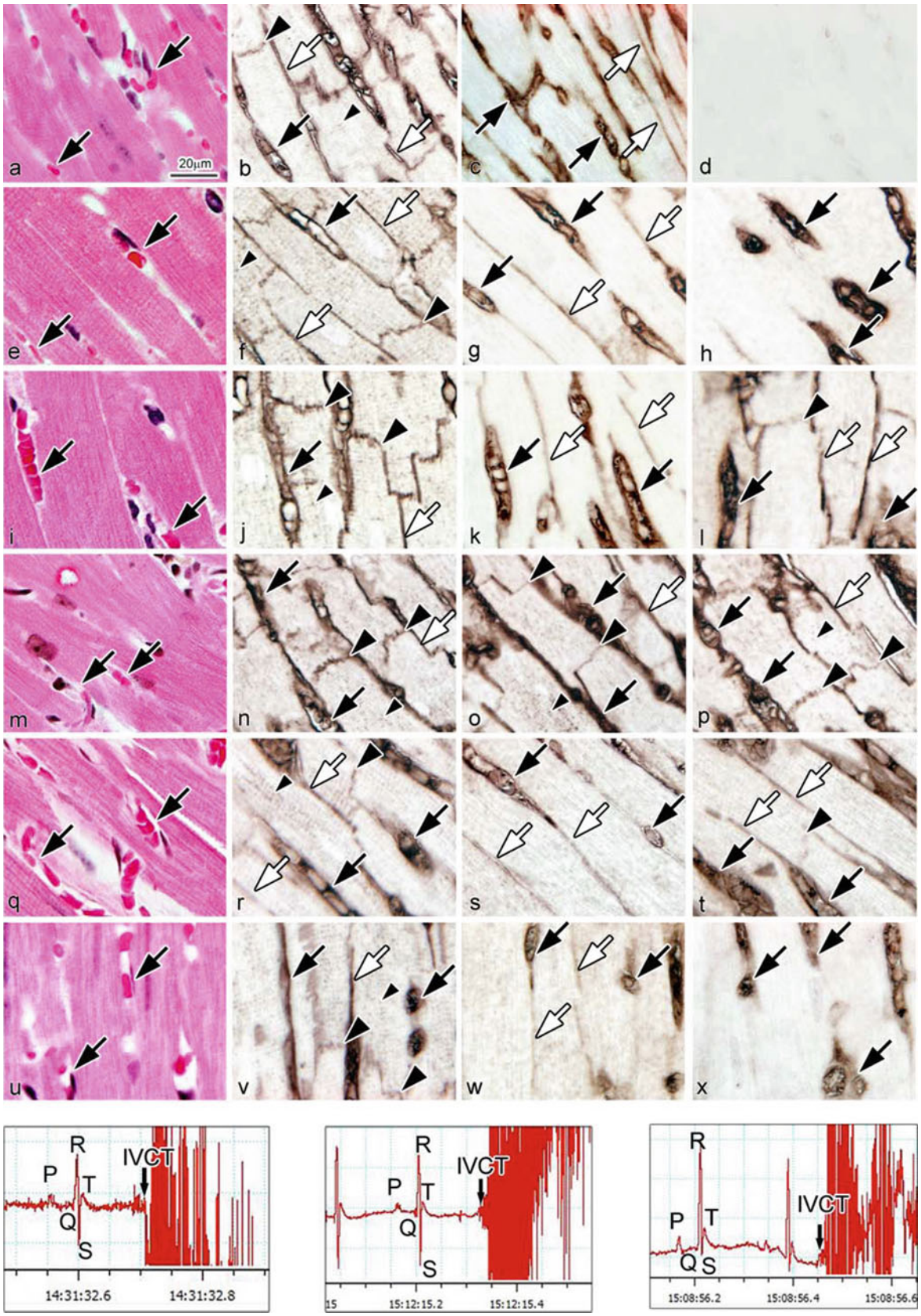

Fig. 14.6 Light micrographs of HE-stained heart sections with IVCT after saline injection (**a**) or at various times after the BSA injection (**e**, **i**, **m**, **q**, **u**). Serial sections are immunostained for albumin (**b**, **f**, **j**, **n**, **r**, **v**), IgG1 (**c**, **g**, **k**, **o**, **s**, **w**), and BSA (**d**, **h**, **l**, **p**, **t**, **x**). (**y**)–(aa) *Arrows* in ECG show the exact times of freezing hearts with IVCT at 5 min (**y**), 4 h (**z**), and 48 h (aa) after the BSA injection, showing early diastolic phases. *Bar* = 20 μm

Table 14.2 Semiquantitative comparison among immunoreactivities of albumin (Alb), BSA, and IgG1 in living mouse hearts with IVCT under normal and saline injection or at various time intervals after BSA (100 mg/ml) injection

	Normal or saline injection			BSA injection														
				5 min			30 min			4 h			8 h			48 h		
	Alb	BSA	IgG1	Alb	BSA	IgG1	Alb	BSA	IgG1	Alb	BSA	IgG1	Alb	BSA	IgG1	Alb	BSA	IgG1
Blood vessel	3+	−	2+	3+	3+	2+	3+	3+	2+	3+	3+	2+	3+	3+	2+	3+	2+	2+
Interstitium	2+	−	+	2+	−	+	2+	2+	+	2+	2+	+	2+	2+	+	2+	−	+
Intercalated disk	+	−	−	+	−	−	+	±	−	+	±	±	+	±	−	+	−	−
T tubule	+	−	−	+	−	−	+	±	−	+	±	±	+	±	−	+	−	−

Negative, (−); unclear, (±); immunopositive, (+); moderately immunopositive, (2+); strongly immunopositive, (3+)

Table 14.3 Semiquantitative comparison of relative IgG1 immunoreactivity in different areas of living mouse heart tissues

	−	±	+	2+
Blood vessels				
Normal	0	0	0	20
BSA injection 4 h	0	0	0	20
Interstitium				
Normal	0	5	15	0
BSA injection 4 h	0	2	18	0
Intercalated disk				
Normal	20	0	0	0
BSA injection 4 h	0	12	8	0

Negative, (−); unclear, (±); immunopositive, (+); moderately immunopositive, (2+)
*$P < 0.05$

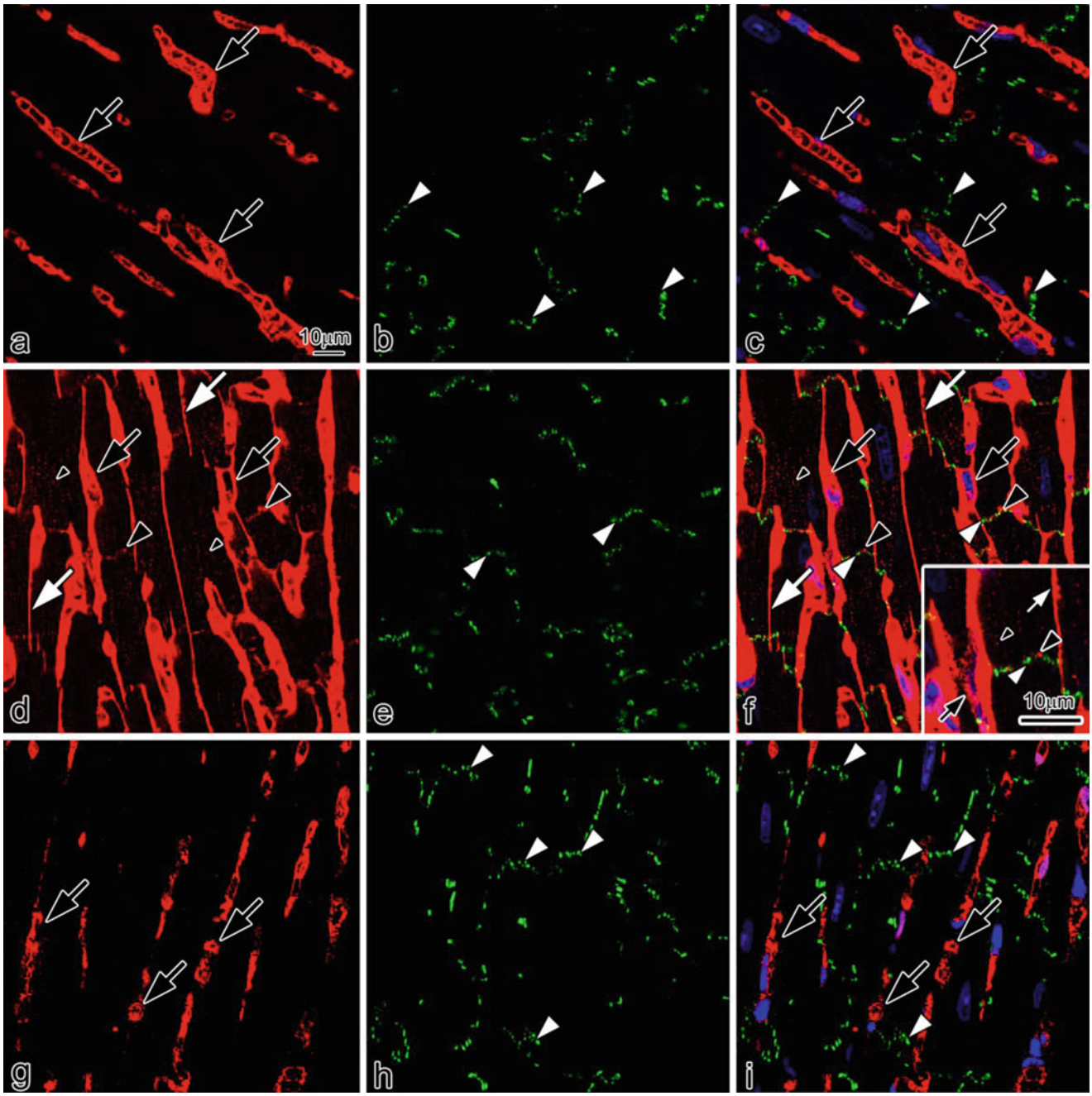

Fig. 14.7 Confocal laser scanning micrographs of double immunofluorescence staining for BSA (**a**, **d**, **g**; *red color*) and connexin 43 (**b**, **e**, **h**; *green color*) on the sections of mouse heart tissues prepared by IVCT at 5 min (**a**–**c**), 30 min (**d**–**f**), and 48 h (**g**–**i**) after the BSA injection. *Bars* = 10 μm

localization within the blood vessel. It was also immunolocalized at the intercalated disks of cardiomyocytes and their T tubules under normal blood circulation. Then, we confirmed that the exogenous BSA also crossed the vascular endothelium into the interstitium of living mouse hearts and entered the intercalated disks and T tubules of cardiomyocytes 30 min after BSA injection. The distribution in vivo of its own serum albumin in the interstitium, intercalated disks, and T tubules of living mice heart tissues indicated that the mouse albumin might be one of the components that support the extracellular microenvironment around each cardiomyocyte of the functioning heart.

IgG1 of about 150 kDa molecular weight was also translocated across the vascular endothelium into the interstitium of living mouse heart tissue. Although one previous morphological study clarified the nitrated albumin transport across the continuous vascular endothelium [9], the present study with IVCT showed the immunolocalization of such intermediate-sized serum proteins, IgG1, in the living mouse heart interstitium [10]. In addition, compared with serum albumin, the larger IgG1 could not enter either the intercalated disks or the T tubules of cardiomyocytes under normal blood circulation conditions. These immunohistochemical differences of serum proteins after BSA injection indicated that the molecular sizes might also be responsible for the intercalated disk and T tubule selectivity in beating heart tissues. In the present study, the time-dependent immunolocalization of exogenous BSA was revealed in the interstitial matrix and cardiomyocytes by IVCT. The abnormal immunolocalization of serum IgG1 at the intercalated disks and T tubules was displayed 4 h after BSA injection with a concentration of 100 mg/ml, although there was no abnormal immunolocalization of serum IgG1 when the concentration of injected BSA was decreased to 4 mg/ml. Although the mechanism of such abnormal IgG1 localization has yet to be clarified, the time intervals after the BSA injection and its concentrations were both critical factors for the translocation of serum proteins in vivo through the blood capillaries of the living mouse heart.

In conclusion, the present immunohistochemical study with ECG monitoring demonstrated that the distribution of soluble serum proteins was precisely revealed by the IVCT without the preparation artifacts usually caused by the conventional chemical fixation and dehydration. With IVCT, serum albumin in vivo was found to be one of the components that contributed to the extracellular microenvironment around cardiomyocytes, and the different immunolocalizations of serum proteins indicated molecular selectivity at the intercalated disks. When the cardiac microcirculation in vivo, including the regulatory mechanisms of functional coupling between cardiomyocytes and the propagation of electrical impulses at the intercalated disks, can be intensely studied because of its clinical significance in heart disease, IVCT will provide a useful approach for immunohistochemical and morphofunctional studies of cardiac microcirculation and microenvironment under various heart conditions in living animals.

Acknowledgments The authors disclosed the citation of repeated contents already published in Acta Histochem. Cytochem. 44(2):61–72, 2011 and also the use of Figs. 6.1.1–7 from the same article with their permissions.

References

1. Bai Y, Ohno N, Terada N, Saitoh S, Nakazawa T, Nakamura N, Katoh R, Ohno S (2009) Immunolocalization of serum proteins in xenografted mouse model of human tumor cells by various cryotechniques. Histol Histopathol 24:717–728
2. Hoyt RH, Cohen ML, Saffitz JE (1989) Distribution and three-dimensional structure of intercellular junctions in canine myocardium. Circ Res 64:563–574
3. Li Z, Ohno N, Terada N, Ohno S (2006) Immunolocalization of serum proteins in living mouse glomeruli under various hemodynamic conditions by 'in vivo cryotechnique'. Histochem Cell Biol 126:399–406
4. Noorman M, van der Heyden MA, Cox MG, Hauer RN, de Bakker JM, van Rijen HV (2009) Cardiac cell-cell junctions in health and disease: electrical versus mechanical coupling. J Mol Cell Cardiol 47:23–31
5. Ohno N, Terada N, Ohno S (2004) Advanced application of the in vivo cryotechnique to immunohistochemistry for animal organs. Acta Histochem Cytochem 37:357–364
6. Ohno N, Terada N, Murata S, Katoh R, Ohno S (2005) Application of cryotechniques with freeze-substitution for the immunohistochemical demonstration of intranuclear pCREB and chromosome territory. J Histochem Cytochem 53:55–62
7. Ohno N, Terada N, Ohno S (2006) Histochemical analyses of living mouse liver under different hemodynamic conditions by 'in vivo cryotechnique'. Histochem Cell Biol 126:389–398
8. Ohno N, Terada N, Bai Y, Saitoh S, Nakazawa T, Nakamura N, Naito I, Fujii Y, Katoh R, Ohno S (2008) Application of cryobiopsy to morphological and immunohistochemical analyses of xenografted human lung cancer tissues and functional blood vessels. Cancer 113:1068–1079
9. Predescu D, Predescu S, Malik AB (2002) Transport of nitrated albumin across continuous vascular endothelium. Proc Natl Acad Sci U S A 99:13932–13937
10. Rippe B, Rosengren BI, Carlsson O, Venturoli D (2002) Transendothelial transport: the vesicle controversy. J Vasc Res 39:375–390
11. Smith JH, Green CR, Peters NS, Rothery S, Severs NJ (1991) Altered patterns of gap junction distribution in ischemic heart disease: an immunohistochemical study of human myocardium using laser scanning confocal microscopy. Am J Pathol 139:801–821
12. Zhou H, Ohno N, Terada N, Saitoh S, Naito I, Ohno S (2008) Permselectivity of blood follicle barriers in mouse ovaries of the mifepristone-induced polycystic ovary model revealed by in vivo cryotechnique. Reproduction 136:599–610

Histochemical Analyses and Quantum Dot Imaging of Microvascular Blood Flow with Pulmonary Edema

15

Yurika Saitoh, Nobuo Terada, Nobuhiko Ohno, and Shinichi Ohno

Abstract

Light microscopic imaging of blood vessels and distribution of serum proteins are essential to analyze hemodynamics in living animal lungs under normal respiration or respiratory diseases. In this section, we visualized dynamically changing morphology of paraffin specimens of mouse lungs. By hematoxylin-eosin staining, morphological features, such as shapes of alveolar septum and sizes of alveolar lumen, reflected their respiratory conditions in vivo, and alveolar capillaries were filled with variously shaped erythrocytes. To capture accurate time courses of blood flow in peripheral pulmonary alveoli, glutathione-coated quantum dots (QDs) were injected into right ventricles. QDs were localized in most arterioles and some alveolar capillaries at 1 s and later in venules at 2 s, reflecting a typical blood flow direction in vivo. For pathological visualization, IVCT was also applied to lungs of acute pulmonary hypertension mouse model. Erythrocytes were crammed in blood vessels, and some serum components leaked into alveolar lumens, as confirmed by mouse albumin immunostaining. Some separated collagen fibers and connecting elastic fibers were still detected in edematous tunica adventitia near terminal bronchioles.

Keywords

Quantum dot • Alveolar capillary • Pulmonary edema

15.1 Introduction

It is well known that animal lungs have abundant blood vessels, in which the whole venous blood flows from right ventricles of beating hearts and is immediately oxygenated in networks of alveolar capillaries. This dynamic blood flow and these structures under various respiratory conditions have been recently examined by new imaging techniques. Previously, it was reported that a rapid freezing was useful to obtain dynamic images of cat lung tissues [1, 2]. In the present study, we further examined detailed images of the microcirculation and microenvironment in mouse lung tissues with immunohistochemistry and injection of quantum dots (QDs). QDs have recently been used to detect intracellular trafficking, microvascular morphology, and diagnostic tumor targeting because of their strong and constant fluorescent signals [3–8]. Then, water-soluble glutathione (GSH)-coated QDs, which emitted a 650 nm wavelength fluorescent signal under ultraviolet (UV) light, were continuously injected into the right ventricles of their hearts (10 μl/s) for 1 or 2 s, and IVCT was performed for lungs at 1 or 2 s after the injection [9–11]. Dynamically changing images of microvascular

Y. Saitoh (✉) • N. Ohno • S. Ohno
Department of Anatomy and Molecular Histology, Interdisciplinary Graduate School of Medicine and Engineering, University of Yamanashi, 1110 Shimokato, Chuo City, Yamanashi 409-3898, Japan
e-mail: yurikas@yamanashi.ac.jp

N. Terada
Division of Health Sciences, Shinshu University Graduate School of Medicine, 3-1-1 Asahi, Matsumoto City, Nagano 390-8621, Japan

Department of Anatomy and Molecular Histology, Interdisciplinary Graduate School of Medicine and Engineering, University of Yamanashi, 1110 Shimokato, Chuo City, Yamanashi 409-3898, Japan

S. Ohno et al. (eds.), *In Vivo Cryotechnique in Biomedical Research and Application for Bioimaging of Living Animal Organs*, DOI 10.1007/978-4-431-55723-4_15

blood flow and distribution of serum proteins will be useful to examine microenvironments not only for physiological lung functions but also for pathological lungs. In particular, pulmonary edema is well known to be induced by functional failure of the left side of the hearts, which causes secondary pulmonary hypertension, resulting in leakage of serum components to alveolar lumen from anastomosing capillaries [12]. Therefore, we have further examined histological features and immunohistochemical localization of the leaked serum components and some connective tissue fibers in mouse lungs of the acute pulmonary hypertension model.

15.2 Morphological Features of Lung Tissues Under Artificial Respiration

To control respiration of mice, mouse trachea was surgically exposed and connected to a small animal ventilator. Exact optimal timing of images of respiratory conditions was achieved on the scale of seconds, as demonstrated with macroscopic images of living mouse lungs under expiration (Fig. 15.1a), showing contracted lung lobes, and under inspiration (Fig. 15.1c), showing inflated lobes. Cranial lobes of the right lungs were selected because of easy access to capture well-frozen lung tissues, and clear morphological findings were obtained with HE staining of expiratory (Fig. 15.1b) and inspiratory (Fig. 15.1d) lung specimens. In the lungs under expiration, slightly collapsed alveoli or alveolar sacs near the visceral pleura were observed in larger numbers, and their sizes became smaller than those in the inflated lungs under inspiration (Fig. 15.1b, d). Alveolar capillaries were clearly seen in alveolar septum, which were filled with variously shaped erythrocytes, mostly reflecting blood flow direction at the time of freezing (double black arrowheads in Fig. 15.1b, d). Although the capillary networks were expanding in parallel to the alveolar lumens under inspiration (Fig. 15.1d), they were folded to form thicker alveolar septum under expiration (Fig. 15.1b). Thus, optimal respiratory conditions were well retained with the IVCT.

15.3 Visualization of Blood Supply on Paraffin Sections

To visualize blood flow on paraffin sections, IVCT was immediately performed at 1 s (Fig. 15.2) after starting the continuous injection of QDs. Morphological findings with HE staining at 1 s show well-preserved lung tissue areas with little ice-crystal formation at a light microscopic level (Fig. 15.2a), and serial sections were also used for the QD analyses (Fig. 15.2b). To confirm microscopic structures without any staining in a fluorescence microscope, autofluorescence images with UV excitation were very useful for normal lung tissues, as shown in blue in Fig. 15.2b. At the

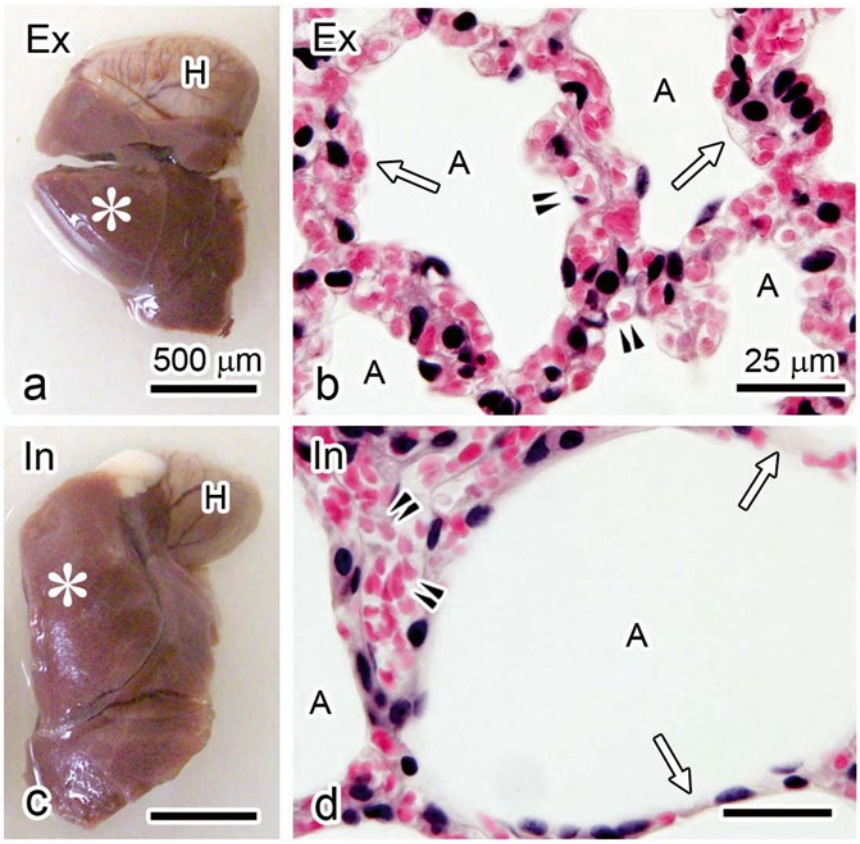

Fig. 15.1 Morphological features of mouse lungs. (**a**, **c**) Macroscopic images of normal mouse lungs under experimental expiration (Ex) and inspiration (In). (**b**, **d**) Light microscopic images with HE staining of the right cranial lobes. *White arrows*, alveolar septum. *Double black arrowheads*, alveolar capillaries filled with variously shaped erythrocytes. *Asterisk*, a cranial lobe of the right lung. *H*, heart; *Bars*, 500 μm in (**a**, **c**), 25 μm in (**b**, **d**)

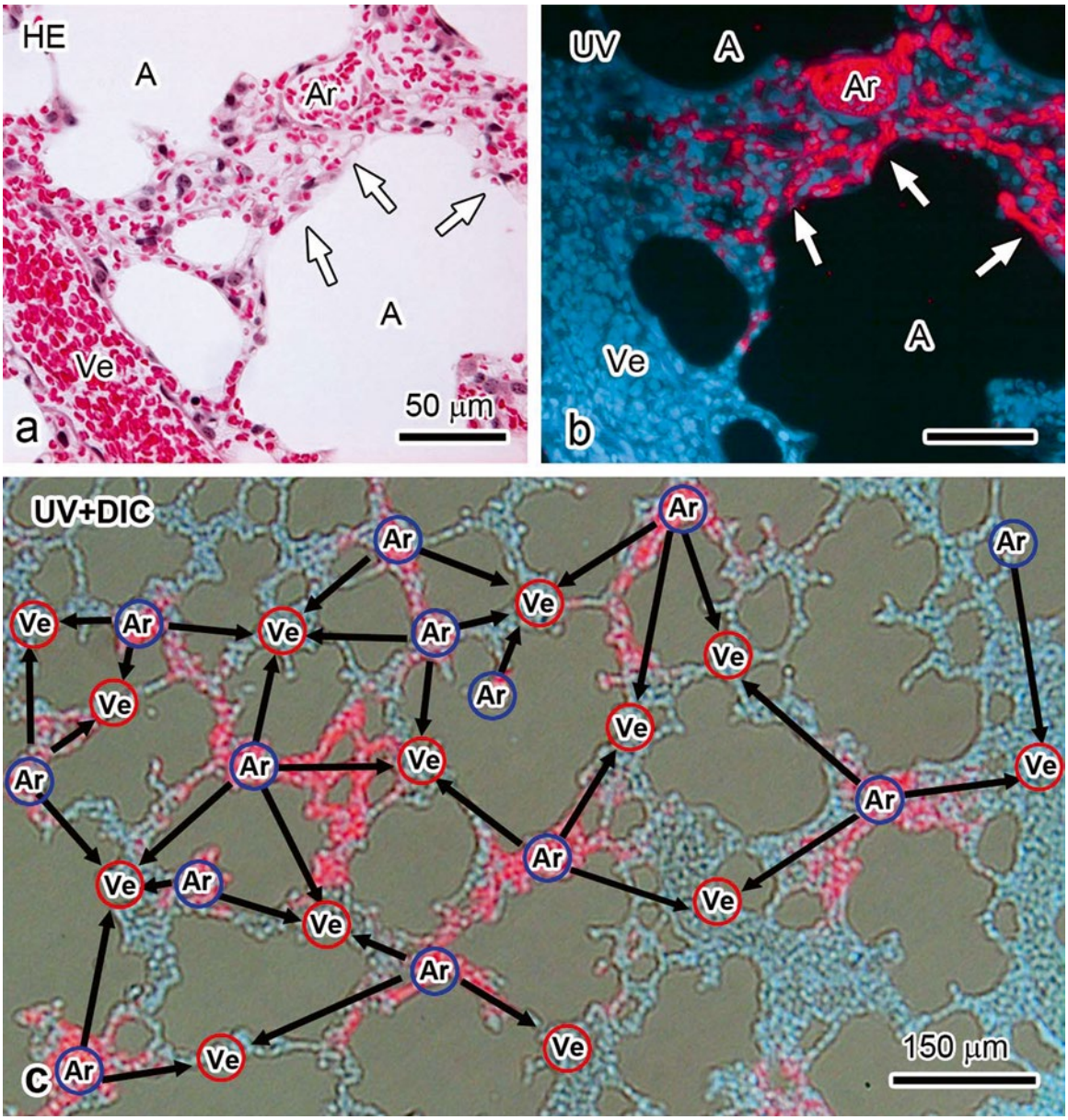

Fig. 15.2 Light micrographs of mouse lung tissues at 1 s after the QD injection, which are imaged by HE staining (HE; **a**), fluorescence with ultraviolet light (UV; **b**), and blood vessel arrangement, are depicted on the images that are merged with differential interference contrast image (UV + DIC; **c**). *White arrows*, alveolar capillaries filled with red fluorescent signals by QDs. *Blue circle* with *Ar*, arterioles. *Red circle* with *Ve*, venules. *Black arrows*, blood flows traced from an arteriole to some venules via alveolar capillaries. *A*, air space. *Bars*, 150 μm in (**c**) and 50 μm in (**a**, **b**)

same time, another red fluorescent signal of QDs was clearly detected in some blood vessels under the same UV excitation condition. Two types of large blood vessels were discriminated with the QD red signal. Some large blood vessels filled with the red signal of QDs were alternately situated among other large blood vessels without QDs (Fig. 15.2b, c). The blood vessels with the red signal demonstrated lung arterioles in bronchiolar connective tissues because some QDs were considered to initially flow into arterioles from the right ventricle (Ar in Fig. 15.2b, c). In addition, other QDs were localized in parts of alveolar capillaries connected to arterioles (white arrows in Fig. 15.2a, b), indicating that these QD images show an instant cessation of blood flow from arterioles to venules via alveolar capillaries. Figure 15.2c traces all locations of arterioles and venules in a lung tissue section. Thus, blood flow directions and distributions of blood vessels, such as arterioles and venules, were widely traced. In three-dimensional network structures of alveolar capillaries using these specimens, alveolar capillaries intricately connected with each other, naturally flowing erythrocytes, and segmented leukocytes were detected inside blood vessels, as shown in our original article [13].

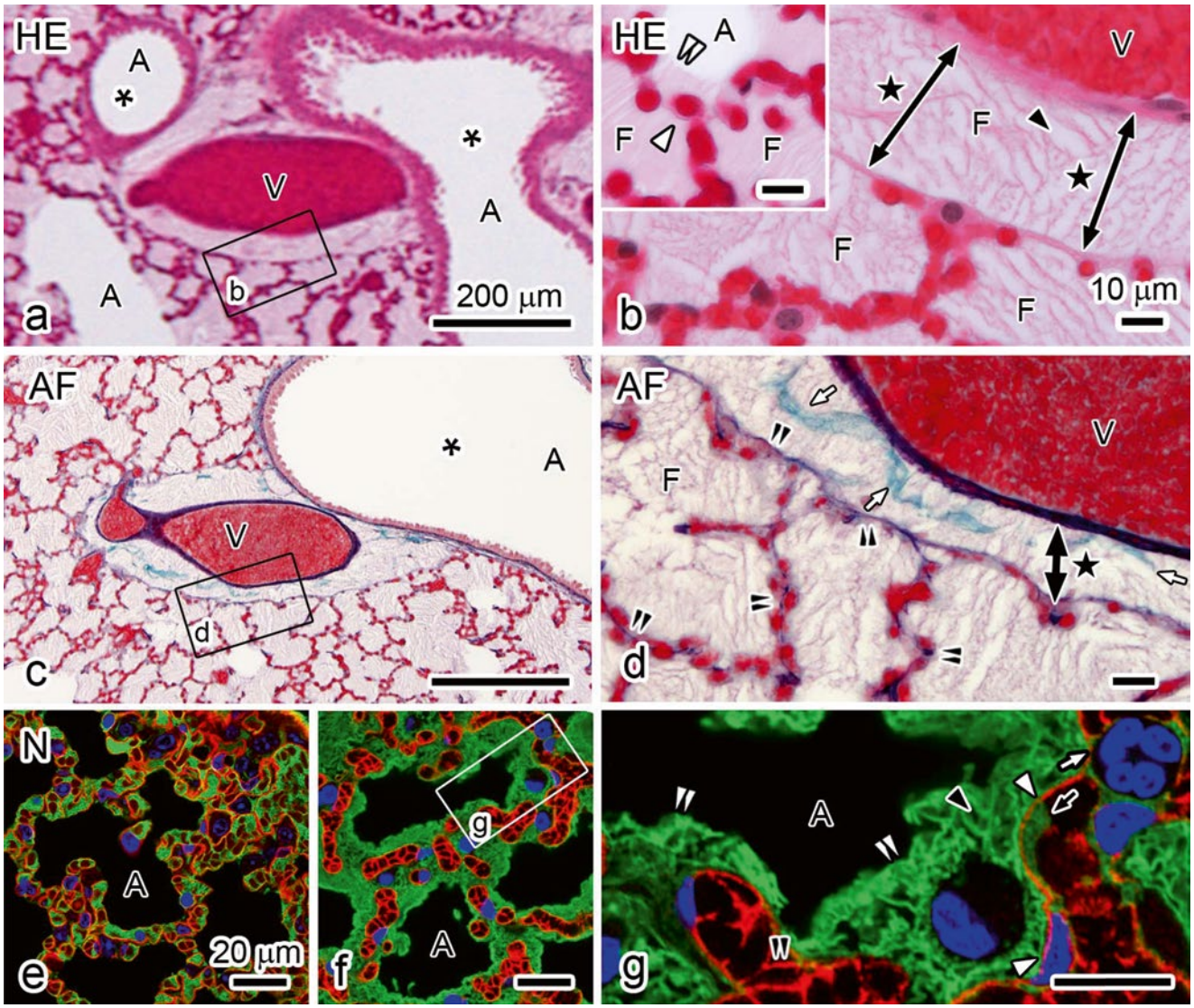

Fig. 15.3 Morphological findings of mouse lungs of HE (**a**, **b**), aldehyde fuchsin (AF; **c**, **d**), and double-immunofluorescence staining in acute pulmonary hypertension mice (**f**, **g**). (**e**) Image of double-immunofluorescence staining in mouse lungs under normal blood circulation (N). (**a**, **c**) Low magnified view of areas around terminal bronchioles (*asterisks*). (**b**, **d**) Highly magnified views of the *boxed areas* in (**a**, **c**). (**c**–**g**) Double-immunofluorescence staining for aquaporin-1 (AQP-1; *red*) and albumin (Alb; *green*) with nuclear DAPI staining (*blue*). *White arrowheads*, endothelial cells. *Double white arrowheads*, edge of leaked fluid (F). *Black arrow*, well-frozen plasma inside alveolar capillary. *Black arrowhead*, ice crystal. *White arrow*, leukocyte. *A*, air spaces. *Bars*, 200 μm in (**a**, **c**), 20 μm in (**e**, **f**), and 10 μm in (**b**, **d**, **g**)

15.4 Visualization of Pulmonary Edema on Paraffin Sections

Morphological imaging of pulmonary edema was evaluated using IVCT for mouse lungs of the acute pulmonary hypertension model (Fig. 15.3). At 7 min after clipping an ascending aorta, varicosis due to blood congestion was visible at the lung surface by the naked eye, and respiratory movement of the lung was gradually decreased. By HE staining of the pulmonary hypertension lung tissues (Fig. 15.3a, b), erythrocytes were seen to be packed in all blood vessels. Some luminal spaces, enclosed by alveolar septum including blood capillaries, were filled with slightly eosinophilic substances, which were supposedly serous exudate leaking from alveolar capillaries into alveolar spaces (Fig. 15.3a, b). Both eosin-positive and eosin-negative areas were seen in terminal bronchioles (asterisk in Fig. 15.3a), alveolar ducts, or alveolar spaces of some areas (Fig. 15.3a, inset in b), and their border was clearly detected (double white arrowheads in inset in Fig. 15.3b). Because the freezing condition of lung tissues became worse in a distant area far from the frozen tissue surface than that in the area near visceral pleura, some ice crystals were found, especially in eosin-positive substances (black

arrowhead in Fig. 15.3b), which probably reflected the leaked fluid from blood vessels. In comparison with the leaked fluid (F in Fig. 15.3b), tiny ice crystals were seen in good freezing area (inset in Fig. 15.3b). In connective tissues near terminal bronchioles, the exudate was seen to separate tunica adventitia from large blood vessels (double-headed arrows with black stars in Fig. 15.3b, d). Some collagen fibers were detected as green color with AF staining, which were discretely separated by exudate near terminal bronchioles (white arrows in Fig. 15.3d). To the contrary, elastic fibers were stained as purple color with AF staining in alveolar septum, which were still continuing at light microscopic level (double arrowheads in Fig. 15.3d), indicating elasticity of alveolar septum under pulmonary edema condition. To confirm whether the slightly eosinophilic substances with HE staining in the alveolar lumen (Fig. 15.3a, b) were serous exudate leaked out through blood vessels, two different types of lungs under normal circulation (Fig. 15.3e) or acute pulmonary hypertension (Fig. 15.3f, g) condition were compared by immunostaining for aquaporin-1 (AQP-1) and albumin. AQP-1 was already reported to be expressed and localized along cell membranes of endothelial cells in pulmonary blood vessels and erythrocytes [14–16]. In normal mouse lung tissues (Fig. 15.3e), bright contours of blood vessels were detected owing to strong immunostaining of AQP-1 along endothelial cells (red in Fig. 15.3e). In contrast, albumin immunostaining was mainly detected in blood vessels and slightly at interstitium of alveolar septum under normal blood circulation conditions (green in Fig. 15.3e). By the AQP-1 immunostaining, flowing erythrocyte membranes were slightly immunostained to contour their shapes (Fig. 15.3e), in addition to the endothelial cells. In mouse lung tissues with acute pulmonary hypertension (Fig. 15.3f, g), AQP-1 was also immunolocalized along cell membranes of endothelial cells and erythrocytes packed in alveolar capillaries (red in Fig. 15.3g). In contrast, immunostaining of albumin was clearly detected in the interstitial matrix outside the alveolar capillaries (green in Fig. 15.3g), but it was hardly detected in the alveolar capillaries because of much less space among tightly packed erythrocytes. Thus, because the leaked substances in alveolar lumens and interstitial matrices outside blood vessels consisted of much albumin, the slightly eosinophilic substances by HE staining, as shown in Fig. 15.3a, b, were determined to be mostly serous exudate derived from blood vessels under the experimental pulmonary edema.

15.5 Conclusion

We have achieved histochemical imaging of living mouse lungs under normal blood circulation or pulmonary hypertension conditions, reflecting their in vivo states. We think that these imaging techniques with IVCT will provide morphofunctional information about blood flow conditions and the location of serum proteins under respiration in the same tissue section, which would be compatible with other new techniques, such as intravital imaging, micro-CT, MRI, and PET of living animals. This text is mainly quoted from Reference [13].

References

1. Staub NC, Storey WF (1962) Relation between morphological and physiological events in lung studied by rapid freezing. J Appl Physiol 17:381–390
2. Staub NC (1963) The interdependence of pulmonary structure and function. Anesthesiology 24:831–854
3. Ballou B, Lagerholm BC, Ernst LA, Bruchez MP, Waggoner AS (2004) Noninvasive imaging of quantum dots in mice. Bioconjug Chem 15:79–86
4. Dickie R, Bachoo RM, Rupnick MA, Dallabrida SM, Deloid GM, Lai J, Depinho RA, Rogers RA (2006) Three-dimensional visualization of microvessel architecture of whole-mount tissue by confocal microscopy. Microvasc Res 72:20–26
5. Ferrara DE, Weiss D, Carnell PH, Vito RP, Vega D, Gao X, Nie S, Taylor WR (2006) Quantitative 3D fluorescence technique for the analysis of en face preparations of arterial walls using quantum dot nanocrystals and two-photon excitation laser scanning microscopy. Am J Physiol Regul Integr Comp Physiol 290:R114–123
6. Jamieson T, Bakhshi R, Petrova D, Pocock R, Imani M, Seifalian AM (2007) Biological applications of quantum dots. Biomaterials 28:4717–4732
7. Larson DR, Zipfel WR, Williams RM, Clark SW, Bruchez MP, Wise FW, Webb WW (2003) Water-soluble quantum dots for multiphoton fluorescence imaging in vivo. Science 300:1434–1436
8. Michalet X, Pinaud FF, Bentolila LA, Tsay JM, Doose S, Li JJ, Sundaresan G, Wu AM, Gambhir SS, Weiss S (2005) Quantum dots for live cells, in vivo imaging, and diagnostics. Science 307:538–544
9. Jin T, Fujii F, Komai Y, Seki J, Seiyama A, Yoshioka Y (2008) Preparation and characterization of highly fluorescent, glutathione-coated near infrared quantum dots for in vivo fluorescence imaging. Int J Mol Sci 9:2044–2061
10. Terada N, Saitoh Y, Saitoh S, Ohno N, Jin T, Ohno S (2010) Visualization of microvascular blood flow in mouse kidney and spleen by quantum dot injection with "in vivo cryotechnique". Microvasc Res 80:491–498
11. Tiwari A, Snure M (2008) Synthesis and characterization of ZnO nano-plant-like electrodes. J Nanosci Nanotechnol 8:3981–3987
12. Rimoldi SF, Yuzefpolskaya M, Allemann Y, Messerli F (2009) Flash pulmonary edema. Prog Cardiovasc Dis 52:249–259
13. Saitoh Y, Terada N, Saitoh S, Ohno N, Jin T, Ohno S (2012) Histochemical analyses and quantum dot imaging of microvascular blood flow with pulmonary edema in living mouse lungs by "in vivo cryotechnique". Histochem Cell Biol 137:137–151
14. King LS, Nielsen S, Agre P (1996) Aquaporin-1 water channel protein in lung: ontogeny, steroid-induced expression, and distribution in rat. J Clin Invest 97:2183–2191
15. Matsuzaki T, Hata H, Ozawa H, Takata K (2009) Immunohistochemical localization of the aquaporins AQP1, AQP3, AQP4, and AQP5 in the mouse respiratory system. Acta Histochem Cytochem 42:159–169
16. Verkman AS (2007) Role of aquaporins in lung liquid physiology. Respir Physiol Neurobiol 159:324–330

Dynamic Ultrastructure of Pulmonary Alveoli of Living Mice Under Respiratory Conditions

16

Shinichi Ohno, Nobuo Terada, and Yasuhisa Fujii

Abstract

A morphological approach to cell dynamics is usually difficult, since routine preparative techniques for electron microscopy always induce artefacts due to cessation of blood supply into organs. The in vivo cryotechnique followed by the freeze-substitution method reduces such technical problems. It was applied for examining the pulmonary alveoli of BALB/c mice in vivo. The following ultrastructural features were revealed. (1) A surfactant layer provided a continuous covering to the alveolar epithelium. (2) Typical lamellar structures in large alveolar epithelial cells were rarely detected. (3) Circulating erythrocytes with various shapes were observed in branching blood capillaries. (4) The close association between erythrocytes and the endothelium was seen at the peripheral alveolar septum. Such ultrastructural arrangements may be appropriate for the physiological functions of the pulmonary alveoli, such as exchanges of gases or materials in vivo.

Keywords

Functional alveolus • Surfactant layer • Atypical erythrocyte shape • Erythrocyte attachment • In vivo cryotechnique

16.1 Introduction

Although some ultrastructural features of animal lungs were described in the previous reports [1–3], they could provide not enough information about physiological functions of the lungs of living animals. This is because the conventional electron microscopy couldn't reveal pulmonary ultrastructures of the living animals during functional respiration. Such fixation procedures usually take several minutes, so it is hard to detect rapidly changing cellular events at the order of milliseconds. Conventional morphological studies had such defects for the examination of dynamic changes in organs in vivo. The ultrastructure of the lung has been examined [2, 3], as described above, but the authors were unable to investigate the appearances during respiration. Moreover, intercellular events during gas/material exchanges have not been examined in such studies, and conventional electron microscopy has provided little information about functional anatomy of the lung [1]. Therefore, the "in vivo cryotechnique" was applied to morphological analyses of mouse lungs inflated by mechanical ventilation [4]. In this study, we examined the in vivo ultrastructure of the pulmonary epithelium and endothelium and circulating erythrocytes in living mouse lungs during respiration.

S. Ohno, M.D., Ph.D. (✉) • Y. Fujii
Department of Anatomy and Molecular Histology, Interdisciplinary Graduate School of Medicine and Engineering, University of Yamanashi, 1110 Shimokato, Chuo City, Yamanashi 409-3898, Japan
e-mail: sohno@yamanashi.ac.jp

N. Terada
Division of Health Sciences, Shinshu University Graduate School of Medicine, 3-1-1 Asahi, Matsumoto City, Nagano 390-8621, Japan

Department of Anatomy and Molecular Histology, Interdisciplinary Graduate School of Medicine and Engineering, University of Yamanashi, 1110 Shimokato, Chuo City, Yamanashi 409-3898, Japan

S. Ohno et al. (eds.), *In Vivo Cryotechnique in Biomedical Research and Application for Bioimaging of Living Animal Organs*, DOI 10.1007/978-4-431-55723-4_16

16.2 Preparation Procedures of Living Mouse Lungs

Male BALB/c mice, weighing 20–30 g, were anaesthetised with sodium pentobarbital. A 23-gauge cannula was inserted into the trachea and sutured in place. The mouse was allowed to breathe spontaneously. The abdominal cavity and diaphragm were then opened, and mechanical ventilation with air was immediately initiated. At the moment of pulmonary distension, the whole lung organ was quickly frozen with the liquid isopentane-propane mixture (−193 °C) cooled with liquid nitrogen. The whole mouse body was transferred into liquid nitrogen, and the well-frozen parts of the lung were trimmed off with clippers in the liquid nitrogen [5]. The specimens were then processed for freeze substitution, as described below. They were first transferred into absolute acetone containing 2 % osmium tetroxide at −80 °C and kept for 24 h. They were also put into a deep freezer at −20 °C for 2 h and then into a refrigerator at 4 °C for 2 h. They were briefly washed in pure acetone at room temperature and embedded in Quetol 812. After routine polymerisation, ultrathin sections were prepared, contrasted with uranyl acetate and lead citrate and observed in a Hitachi H-600 electron microscope.

16.3 New Findings of Ultrastructures in Dynamically Changing Lungs

In thick sections stained with toluidine blue, as observed with a light microscope (Fig. 16.1a), dynamic structures of pleura and subpleural regions of the mouse lung, including inflated alveoli, interstitial or alveolar epithelial cells and flowing erythrocytes in blood vessels, were well preserved without any remarkable ice crystal damage. Moreover, close association between pulmonary alveoli and blood capillaries with flowing erythrocytes could be detected in ultrathin sections, as observed with an electron microscope (Fig. 16.1b–d). The flowing erythrocytes exhibited various shapes different from the typical biconcave discoid (Fig. 16.1c), as seen in other organs [6, 7]. Some of them were partially attached to endothelial cells (Fig. 16.1d), indicating that such erythrocyte-endothelium attachment might be effective for physiological functions of gas exchange [4]. The “in vivo cryotechnique” would be more useful for morphofunctional analyses of dynamically changing cells and tissues, which were hardly examined by the conventional preparation methods.

16.4 Flowing Erythrocyte Shapes in Pulmonary Alveoli

In the present study, we have examined the behaviour of erythrocytes in the blood capillaries within the alveolar septum. We showed the ultrastructure of circulating erythrocytes and clarified their appearance. They were not typical biconcave discoid, but displayed various shapes. Our previous studies also reconfirmed the similar observation on circulating erythrocytes in other organs [6, 8]. A close association between erythrocytes and endothelial cells was often seen in the peripheral regions of the alveoli. It may reflect intercellular communications during gas/material exchanges through a very narrow basement membrane [9, 10].

16.5 Concluding Remarks

In conclusion, our in vivo cryotechnique was useful for demonstrating the functional ultrastructure of living alveolar or pleural cells, which could not be investigated by the conventional electron microscopy. Most of the conventionally revealed ultrastructural appearances should be re-examined by the “in vivo cryotechnique” in order to clarify the more natural and functional arrangements.

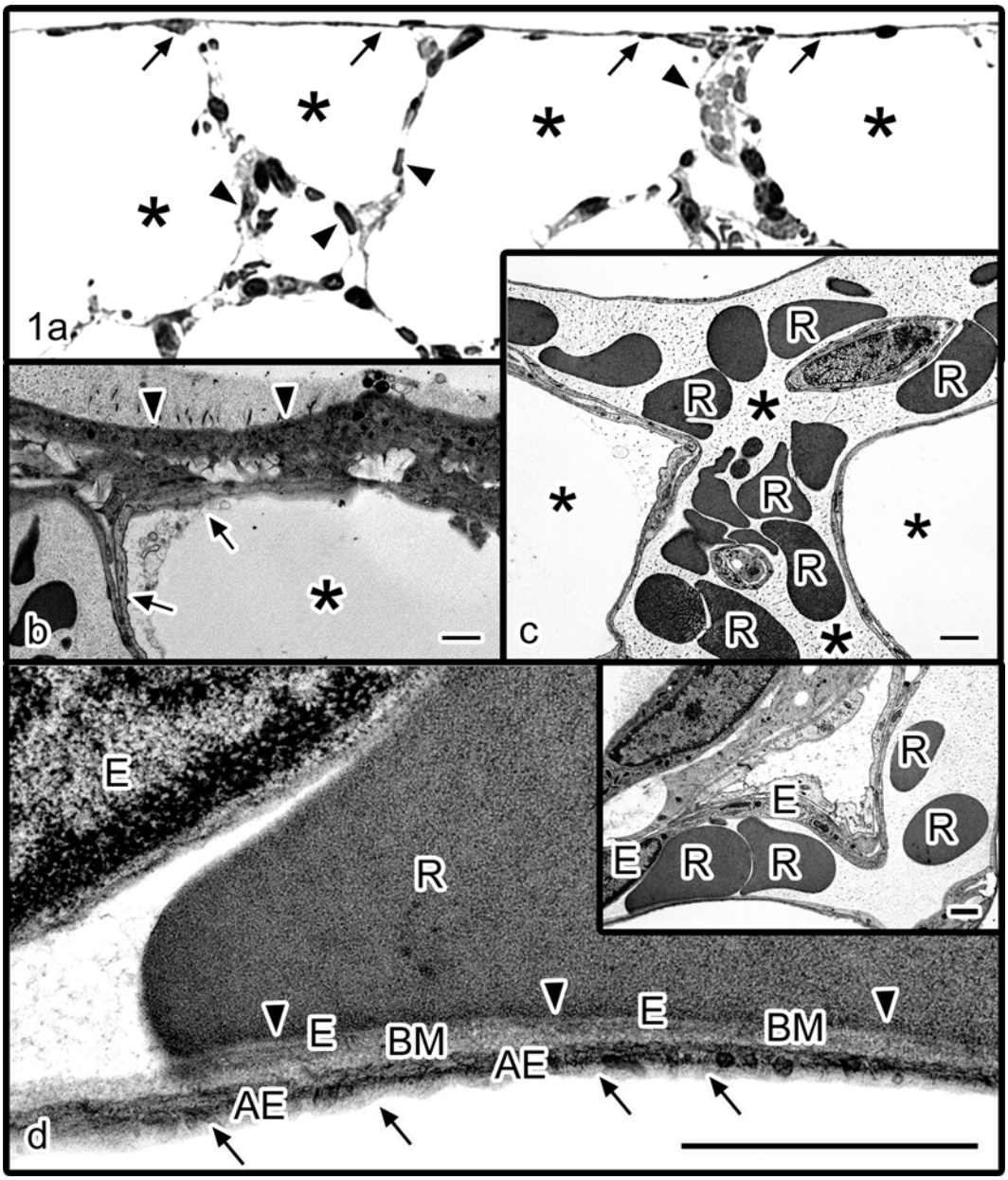

Fig. 16.1 Light (**a**) and electron (**b**–**d**) micrographs of pleural and pulmonary structures of inflating lungs of living mice, as prepared by the "in vivo cryotechnique". In the light micrograph (**a**), ballooning pulmonary alveoli (*asterisks*), structures of pleura (*arrows*) and flowing erythrocytes (*arrowheads*) in septal blood capillaries are well preserved in functioning lungs of living mice. (**b**) An electron micrograph is showing the mesothelial cell (*arrowheads*) and alveolar septum (*arrows*). *Asterisk*, pulmonary alveolus. (**c**) In another alveolar septum, pulmonary alveoli (*small asterisks*) and blood capillaries (*large asterisks*) are closely associated with each other. R, erythrocytes. (**d**) In the septal blood capillaries, flowing erythrocytes (R) exhibit their various shapes instead of typical biconcave discoid shapes (*inset*), and some erythrocytes are firmly attached to endothelial cells (*arrowheads*). The surfactant layer (*arrows*) is rarely preserved on the alveolar type I epithelial cell (*AE*). *BM* basement membrane, *E* endothelium. *Bars*, 1 μm

References

1. Bastacky J, Lee CY, Goerke J, Koushafar H, Yager D, Kenaga L, Speed TP, Chen Y, Clements JA (1995) Alveolar lining layer is thin and continuous: low-temperature scanning electron microscopy of rat lung. J Appl Physiol 79:1615–1628
2. Ham AW, Cormack DH (1978) Histology, 8th edn. JB Lippincott, Philadelphia
3. Weiss L, Greep RO (1977) Histology, 4th edn. McGraw-Hill, New York
4. Takayama I, Terada N, Baba T, Ueda H, Fujii Y, Kato Y, Ohno S (2000) Dynamic ultrastructure of mouse pulmonary alveoli revealed by an in vivo cryotechnique in combination with freeze-substitution. J Anat 197:199–205

5. Ohno S, Terada N, Fujii Y, Ueda H, Takayama I (1996) Dynamic ultrastructure of glomerular capillary loop as revealed by an in vivo cryotechnique. Virchows Arch 427:519–527
6. Terada N, Kato Y, Fujii Y, Ueda H, Baba T, Ohno S (1998) Scanning electron microscopic study of flowing erythrocytes in hepatic sinusoids as revealed by 'in vivo cryotechnique'. J Electron Microsc 47:67–72
7. Xue M, Baba T, Terada N, Kato Y, Fujii Y, Ohno S (2001) Morphological study of erythrocyte shapes in red pulp of mouse spleens revealed by an in vivo cryotechnique. Histol Histopathol 16:123–129
8. Xue M, Terada N, Fujii Y, Baba T, Ohno S (1998) Morphological study by an 'in vivo cryotechnique' of the shape of erythrocytes circulating in large blood vessels. J Anat 193:73–79
9. Groniowski J, Biczysko W (1964) Regulation of transport across pulmonary alveolar epithelial cell monolayers. Nature 204:745–747
10. Voccaro CA, Brody JS (1981) Structural features of alveolar wall basement membrane in the adult rat lung. J Cell Biol 91:427–437

Immunohistochemical Analysis of Various Serum Proteins in Living Mouse Thymus

17

Yuqin Bai, Bao Wu, Nobuo Terada, Yurika Saitoh, Nobuhiko Ohno, Sei Saitoh, and Shinichi Ohno

Abstract

It has been difficult to clarify the precise localizations of soluble serum proteins in thymic tissues of living animals with conventional immersion or perfusion fixation followed by alcohol dehydration owing to ischemia and anoxia. In this study, "in vivo cryotechnique" (IVCT) followed by freeze-substitution fixation was performed to examine the thymic structures of living mice and immunolocalizations of intrinsic or extrinsic serum proteins, which were albumin, immunoglobulin G1 (IgG1), IgA, and IgM, as well as intravenously injected bovine serum albumin (BSA). Mouse albumin was more clearly immunolocalized in blood vessels and interstitial matrices of the thymic cortex than in tissues prepared by the conventional methods. The immunoreactivities of albumin and IgG1 were stronger than those of IgA and IgM in the interstitium of subcapsular cortex. The injected BSA was time-dependently immunolocalized in blood vessels and the interstitium of corticomedullary areas at 3.5 h after its injection and then gradually diffused into the interstitium of the whole cortex at 6 and 12 h. Thus, IVCT revealed definite immunolocalizations of serum albumin and IgG1 in the interstitium of thymus of living mice, indicating different accessibility of serum proteins from the corticomedullary areas, not from the subcapsular cortex of living animals, depending on various molecular sizes and concentrations.

Keywords

Mouse thymus • In vivo cryotechnique • Serum proteins • Immunolocalization • Blood–thymus barrier

17.1 Introduction

The animal thymus is a primary lymphoid organ, where bone marrow-derived T-cell precursors undergo a complex process of maturation, eventually resulting in migration of mature thymocytes to T-cell-dependent areas of peripheral lymphoid organs [1]. However, it has been controversial that

Y. Bai, M.D., Ph.D. (✉)
Department of Anatomy and Molecular Histology, Interdisciplinary Graduate School of Medicine and Engineering, University of Yamanashi, 1110 Shimokato, Chuo City, Yamanashi 409-3898, Japan

Department of Pathology, Medical College of Chifeng University, Ying Bin Road, Chifeng, Inner Mongolua 024000, People's Republic of China
e-mail: baiyuqincn2000@aliyun.com

B. Wu • Y. Saitoh • N. Ohno • S. Saitoh • S. Ohno
Department of Anatomy and Molecular Histology, Interdisciplinary Graduate School of Medicine and Engineering, University of Yamanashi, 1110 Shimokato, Chuo City, Yamanashi 409-3898, Japan

N. Terada
Division of Health Sciences, Shinshu University Graduate School of Medicine, 3-1-1 Asahi, Matsumoto City, Nagano 390-8621, Japan

Department of Anatomy and Molecular Histology, Interdisciplinary Graduate School of Medicine and Engineering, University of Yamanashi, 1110 Shimokato, Chuo City, Yamanashi 409-3898, Japan

S. Ohno et al. (eds.), *In Vivo Cryotechnique in Biomedical Research and Application for Bioimaging of Living Animal Organs*, DOI 10.1007/978-4-431-55723-4_17

such selection of thymocytes depends on the entrance of soluble extrinsic molecules as antigens from blood vessels into the thymus. The flow system of soluble molecules from blood vessels into the interstitial matrices of the thymus has already been examined by artificial injection of an extrinsic component, such as horseradish peroxidase (HRP), into blood vessels [2]. As HRP distribution was clearly shown to be restricted around blood vessels of corticomedullary areas, but not in the interstitium of thymic cortex, the concept of a "blood–thymus barrier" was then proposed, which is generally connected to the function of thymocytes. However, some researchers also doubted the validity of the concept of the blood–thymus barrier because of the existence of some injected labeled serum albumin or bovine serum albumin (BSA) in the thymic cortex [3, 4] and also considered there was little morphological evidence of completely sealed structures of blood vessel walls [5, 6]. These morphological findings and serum protein immunolocalizations were always obtained in tissue specimens prepared with conventional chemical fixation and alcohol dehydration (DH), which easily cause technical artifacts as a result of the slow chemical reaction of the fixatives [7–9]. Thus, the immunolocalization in vivo of soluble serum proteins in the whole interstitium of thymic cortex has remained unclear.

By IVCT, target organs of any living animal can be directly frozen without artificial tissue resection or perfusion fixation, which enables dynamic molecular changes of cells and tissues to be characterized without the technical artifacts that are usually caused by conventional tissue preparation methods [10–12]. In particular, the IVCT-prepared specimens very efficiently retain soluble extra- and intracellular molecules in situ, in combination with subsequent freeze-substitution (FS) fixation. Therefore, immunolocalizations of functional molecules and dynamic structural changes in vivo can be demonstrated in paraffin-embedded tissue sections [13–17]. We tried to clarify accurate immunolocalizations of various serum proteins in living mouse thymus to reevaluate the concept of the blood–thymus barrier.

17.2 Distribution of Intrinsic Serum Proteins in Living Mouse Thymus

The IVCT enabled us to reveal the native histology of the functioning thymus of living mice under normal blood circulation (Fig. 17.1a, b), with homeostatic immunolocalizations of intrinsic serum proteins passing through blood circulation into the interstitium of the thymic cortex, probably reflecting their living state (Fig. 17.1), which could not be demonstrated by the conventional preparation methods. Different immunolocalizations of serum proteins in the thymic interstitium were clearly detected in living mouse tissues prepared by IVCT without common diffusion artifacts of soluble serum proteins, which were shown to be problematic for the conventional preparation methods [9, 15]. The distribution of serum proteins throughout the interstitial matrices depends on their molecular weight, including horseradish peroxidase, as reported previously [2]. Both albumin (MW, 69 kDa) and IgG1 (MW, 150 kDa) are relatively small molecules compared with dimeric IgA (MW, 385 kDa) and pentameric IgM (MW, 970 kDa) [12, 18]. The immunolocalization of mouse albumin in the interstitium of the whole cortex indicates that some serum components that have a molecular weight similar to that of albumin probably enter the interstitial matrices of cortex from blood vessels in the corticomedullary areas. However, it has not been clear until now that leakage of various serum proteins through blood vessels depends on not only molecular size or charge but also on molecular concentration in the blood vessels.

17.3 Distribution of Extrinsic BSA in Living Mouse Thymus

By IVCT, it has become clear that the injected BSA diffused out from blood vessels of the corticomedullary areas but not from blood capillaries in the subcapsular areas of cortex. As shown in Fig. 17.2b, it did not leak out through the blood capillaries until 2 h after BSA injection. However, it leaked out earlier through the blood capillaries of connective tissues at 1 h with the same BSA concentration, as previously reported [19]. In addition, immunoreactive intensities of intravenously injected BSA in the interstitium were variously detected, depending on time intervals after the injection and also BSA concentration (Figs. 17.2 and 17.3). Therefore, these findings are compatible with the existence of functional barriers along blood capillaries of the subcapsular cortex, although molecular permeability through blood vessels in the corticomedullary areas is higher than that in the thymic cortex, as already reported [20]. As shown with albumin and BSA immunolocalizations in the thymic cortex of living mice prepared with IVCT, it is concluded that soluble serum proteins have difficulty in directly entering the thymic cortex because of the blood–thymus barrier, but they are diffused throughout the whole cortex from the corticomedullary areas.

17.4 Concluding Remarks

The morphology of normal living mouse thymus and distribution of intrinsic or extrinsic serum proteins could be clearly detected by IVCT. The molecular size or charge and molecular concentration are related to permselectivity of blood–thymus barrier for different serum proteins, and also the histological layers responsible for the barrier functions of blood–thymus barrier would be important during T-cell differentiation in vivo. The present figures were already published in our paper, Med Mol Morphol (2012) 45:129–139, and cited with their permissions.

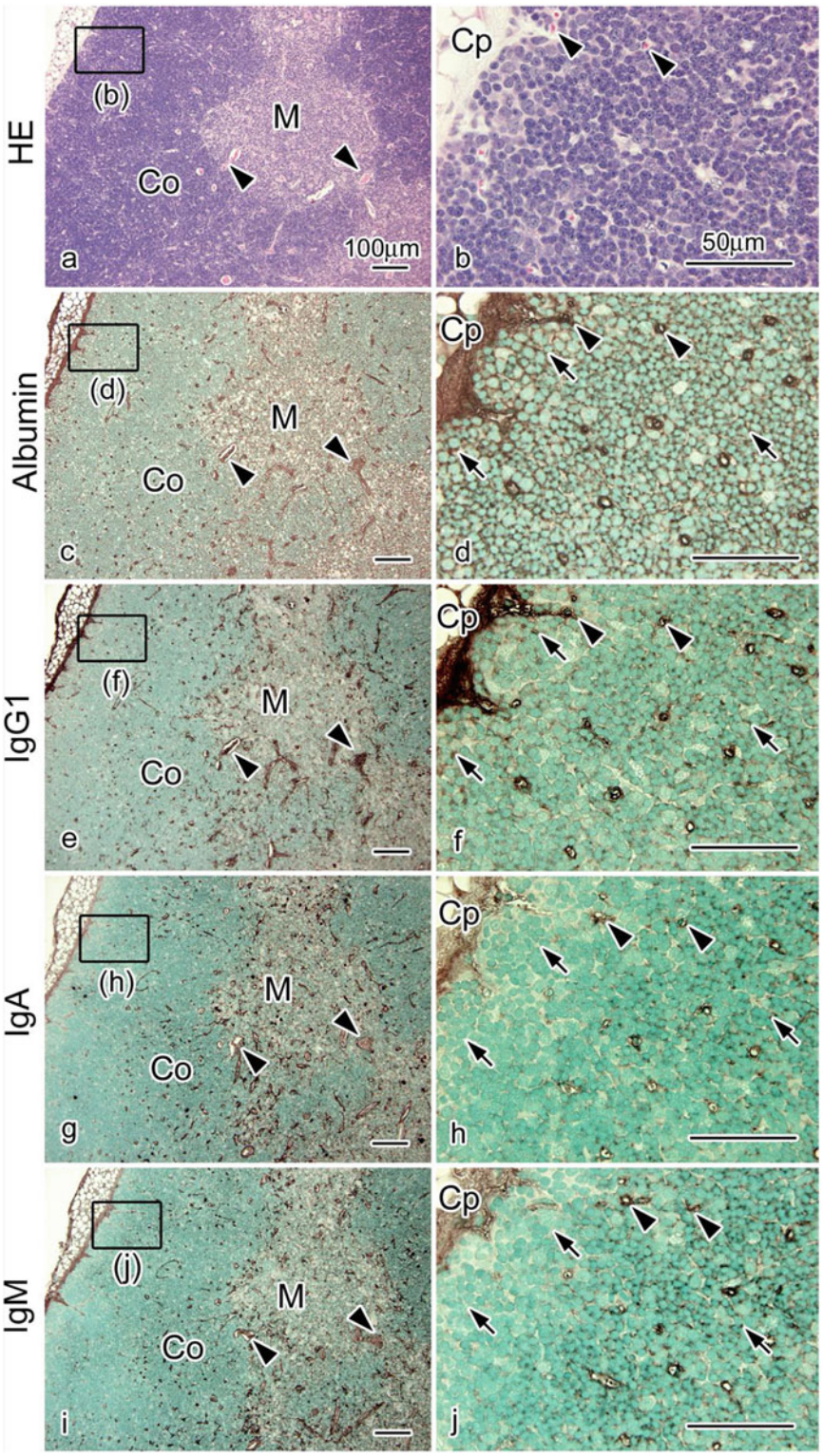

Fig. 17.1 Light micrographs of serial paraffin sections of living mouse thymic tissues prepared by IVCT, which are stained with H&E (**a**, **b**) or immunostained for albumin (**c**, **d**), IgG1 (**e**, **f**), IgA (**g**, **h**), and IgM (**i**, **j**). Each micrograph (**b**, **d**, **f**, **h**, **j**) is a highly magnified view of area enclosed in squares in **a**, **c**, **e**, **g**, and **i**, respectively. *Co* cortex, *M* medulla, *Cp* capsule. All the proteins—albumin, IgG1, IgA, and IgM—are immunolocalized in blood vessels at low magnification (*arrowheads* in **a**, **c**, **e**, **g**, **i**). At a higher magnification, both albumin and IgG1 are evenly immunolocalized in the interstitium of whole cortex (*arrows* in **d**, **f**). *Inset* in **d** shows immunocontrol without the primary antibody at the same magnification. However, both IgA and IgM immunostaining are detected less in the subcapsular cortex (*arrows* in **h**, **j**). *Bars* **a**, **c**, **e**, **g**, **i** 100 μm; **b**, **d**, **f**, **h**, **j** 50 μm

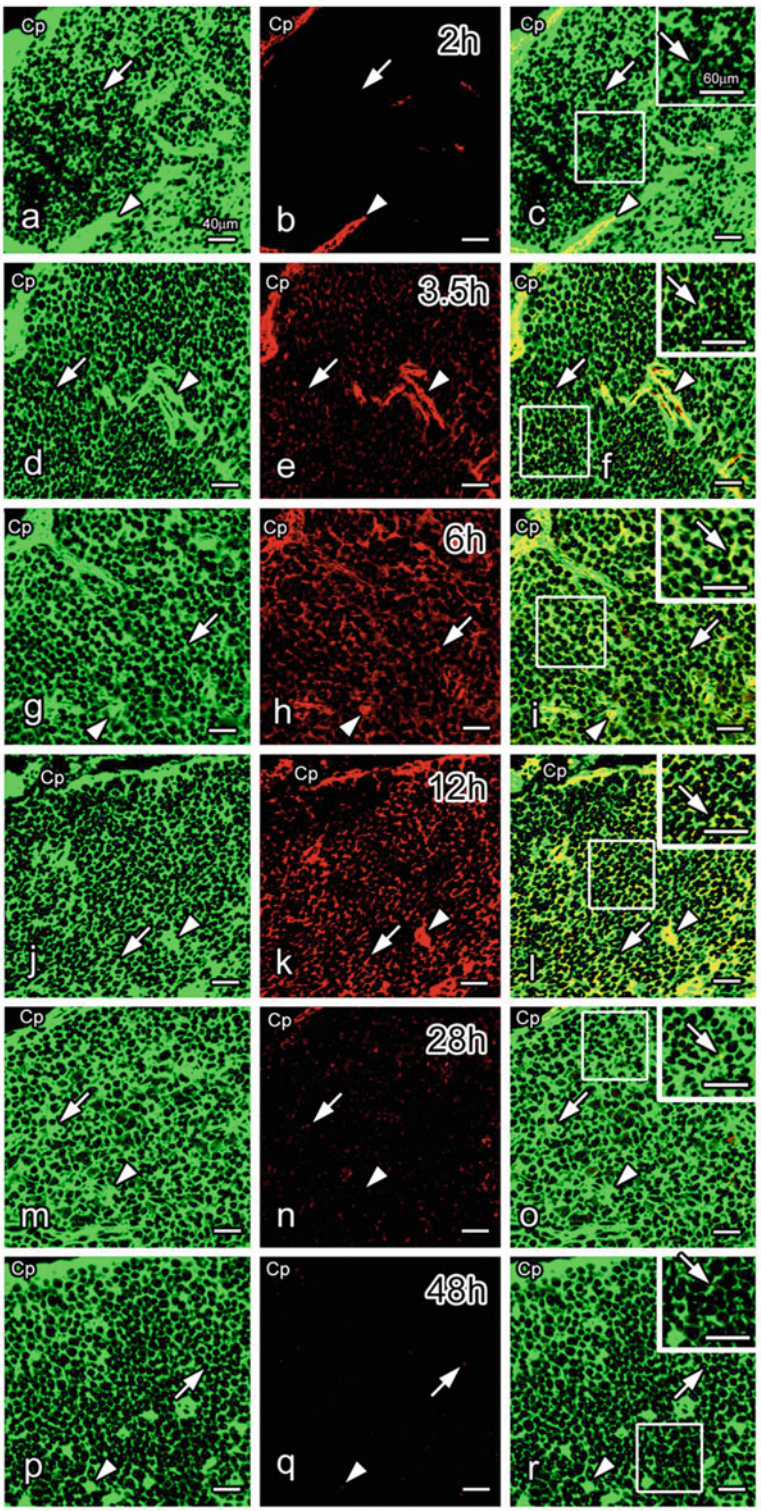

Fig. 17.2 Double immunofluorescence staining of thymic cortical tissues prepared with IVCT for albumin (*green* in **a**, **d**, **g**, **j**, **m**, **p**) and intravenously injected bovine serum albumin (BSA; *red* in **b**, **e**, **h**, **k**, **n**, **q**) at 2 (**a**–**c**), 3.5 (**d**–**f**), 6 (**g**–**i**), 12 (**j**–**l**), 28 (**m**–**o**), or 48 (**p**–**r**) h after BSA injection. Albumin (**a**, **d**, **g**, **j**, **m**, **p**) is immunolocalized in blood vessels (*arrowheads*) and the interstitium of the whole cortex (*arrows*). At 2 h, BSA immunoreactivity is detected only in blood vessels (*arrowheads* in **b**, **c**). However, it is weakly detected in the interstitium at 3.5 h (*arrows* in **e**, **f**) in addition to the blood vessels (*arrowheads* in **e**, **f**). At 6 and 12 h, it is more widely seen in the interstitium (*arrows* in **h**, **i**, **k**, **l**), although it is detected less in the blood vessels (*arrowheads* in **n**, **o**, **q**, **r**) and the interstitium (*arrows* in **n**, **o**, **q**, **r**) at 28 and 48 h. *Cp* capsule. Bars 40 μm, *insets* 60 μm

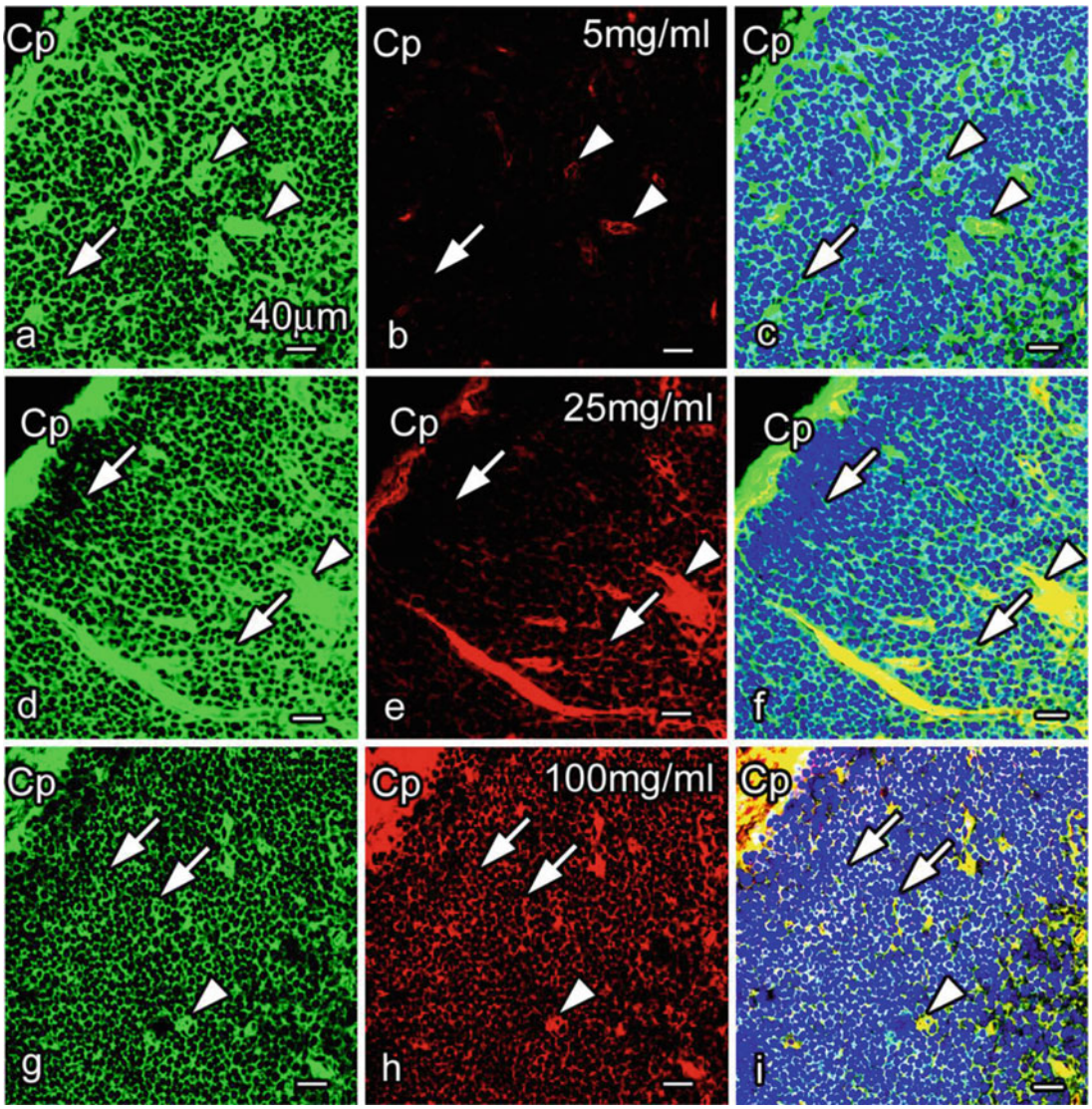

Fig. 17.3 Double immunofluorescence staining for albumin (*green* in **a**, **d**, **g**) and intravenously injected bovine serum albumin (BSA; *red* in **b, e**, **h**) of various concentrations [5 (**a**–**c**), 25 (**d**–**f**), or 100 mg/ml (**g**–**i**)] in IVCT-prepared thymic tissues at 6 h after the BSA injection. Albumin is immunolocalized in blood vessels (*arrowheads* in **a, d**, **g**) and the interstitium of cortex (*arrows* in **a, d**, **g**). BSA immunostaining is mainly detected in blood vessels (*arrowheads* in **b**) and weakly in the interstitium with 5 mg/ml BSA (*arrows* in **b**). With 25 or 100 mg/ml BSA, it is strongly detected in the interstitium of the cortex and corticomedullary areas (*arrows* in **e, f, h**, **i**), in addition to blood vessels (*arrowheads* in **d**–**i**). *Cp* capsule. Bars 40 μm

References

1. Lind EF, Prockop SE, Porritt HE, Petrie HT (2001) Mapping precursor movement through the postnatal thymus reveals specific microenvironments supporting defined stages of early lymphoid development. J Exp Med 194(2):127–134
2. Raviola E, Karnovsky MJ (1972) Evidence for a blood–thymus barrier using electron-opaque tracers. J Exp Med 136(3):466–498
3. Sainte-Marie G (1963) Antigen penetration into the thymus. J Immunol 91:840–845
4. Kouvalainen K, Gitlin D (1967) Passage of antigens across the vascular barrier of the thymus. Nature (London) 214(5088):592–593
5. Ito T, Hoshino T (1966) Light and electron microscopic observations on the vascular pattern of the thymus of the mouse. Arch Histol Jpn 27(1):351–361
6. Henry L, Durrant TE, Anderson G (1992) Pericapillary collagen in the human thymus: implications for the concept of the 'blood–thymus' barrier. J Anat 181(Pt1):39–46
7. Hopwood D (1969) Fixatives and fixation: a review. Histochem J 1(4):323–360
8. Mason DY, Biberfeld P (1980) Technical aspects of lymphoma immunohistology. J Histochem Cytochem 28(8):731–745
9. Hopwood D (1985) Cell and tissue fixation, 1972–1982. Histochem J 17(4):389–442

10. Ohno S, Terada N, Fujii Y, Ueda H, Takayama I (1996) Dynamic structure of glomerular capillary loop as revealed by an in vivo cryotechnique. Virchows Arch 427(5):519–527
11. Ohno N, Terada N, Bai Y, Saitoh S, Nakazawa T, Nakamura N, Naito I, Katoh R, Ohno S (2008) Application of cryobiopsy to morphological and immunohistochemical analyses of xenografted human lung cancer tissues and functional blood vessels. Cancer 113(5):1068–1079
12. Bai Y, Ohno N, Terada N, Saitoh S, Nakazawa T, Nakamura N, Katoh R, Ohno S (2009) Immunolocalization of serum proteins in xenografted mouse model of human tumor cells by various cryotechniques. Histol Histopathol 24(6):717–728
13. Terada N, Ohno N, Li Z, Fujii Y, Baba T, Ohno S (2006) Application of in vivo cryotechnique to the examination of cells and tissues in living animal organs. Histol Histopathol 21(3):265–272
14. Ohno N, Terada N, Ohno S (2006) Histochemical analyses of living mouse liver under different hemodynamic conditions by "in vivo cryotechnique". Histochem Cell Biol 126(3):389–398
15. Saitoh S, Terada N, Ohno N, Ohno S (2008) Distribution of immunoglobulin-producing cells in immunized mouse spleens revealed with "in vivo cryotechnique". J Immunol Methods 331(1–2):114–126
16. Shimo S, Saitoh S, Terada N, Ohno N, Saitoh Y, Ohno S (2010) Immunohistochemical detection of soluble immunoglobulins in living mouse small intestines using an in vivo cryotechnique. J Immunol Methods 361(1–2):64–74
17. Zhou H, Ohno N, Terada N, Saitoh S, Fujii Y, Ohno S (2007) Involvement of follicular basement membrane and vascular endothelium in blood-follicle barrier formation of mice revealed by 'in vivo cryotechnique'. Reproduction 134(2):307–317
18. Henry L, Anderson G (1990) Immunoglobulins in Hassall's corpuscles of the human thymus. J Anat 168:185–197
19. Bai Y, Ohno N, Terada N, Saitoh S, Nakazawa T, Nakamura N, Katoh R, Ohno S (2011) Differential distribution of blood-derived proteins in xenografted human adenocarcinoma tissues by in vivo cryotechnique and cryobiopsy. Med Mol Morphol 44(2):93–102
20. Abe K, Ito T (1974) Vascular permeability in the thymus of the mouse. Arch Histol Jpn 36(4):251–264

18 Immunohistochemistry and Enzyme Histochemistry of HRP for Demonstration of Blood Vessel Permeability in Mouse Thymic Tissues

Bao Wu, Nobuhiko Ohno, Yurika Saitoh, Yuqin Bai, Zheng Huang, Nobuo Terada, and Shinichi Ohno

Abstract

The "in vivo cryotechnique" (IVCT) is useful to capture dynamic blood flow conditions. We injected various concentrations of horseradish peroxidase (HRP) into anesthetized mice via left ventricles to examine architectures of thymic blood vessels and their permeability at different time intervals. At 30 s after HRP injection, enzyme reaction products were weakly detected in interstitium around some thick blood vessels of corticomedullary boundary areas, but within capillaries of cortical areas. At 1 and 3 min, they were more widely detected in interstitium around all thick blood vessels of the boundary areas. At 10 min, they were diffusely detected throughout interstitium of cortical areas and more densely seen in medullary areas. At 15 min, however, they were uniformly detected throughout interstitium outside the blood vessels. At 30 min, phagocytosis of HRP by macrophages was scattered throughout the interstitium, which was accompanied by the decrease of HRP reaction intensity in interstitial matrices. Thus, time-dependent HRP distributions in living mice indicate that molecular permeability and diffusion depend on different areas of thymic tissues.

Keywords

Mouse thymus • In vivo cryotechnique • HRP • Immunolocalization • Enzyme histochemistry

18.1 Introduction

The living animal thymus is one of the lymphoid organs where lymphocyte precursors undergo complex processes of cellular maturation, resulting in translocation of mature thymocytes to peripheral lymphoid organs [1–3]. Previously, the flow system of molecules into the thymic interstitial matrices was examined by artificial injection of horseradish peroxidase (HRP) into the blood vessels [4]. As the injected HRP was found to be mainly localized in the interstitium of the corticomedullary boundary and medulla, the concept of the "blood-thymus barrier" was proposed, which had been postulated in the previous decade [5]. Other researchers, however, doubted the validity of its concept because of the existence of some injected bovine serum albumin (BSA) in the thymic cortex [6] and also

B. Wu • N. Ohno • Y. Saitoh • Y. Bai • Z. Huang • S. Ohno, M.D., Ph.D. (✉)
Department of Anatomy and Molecular Histology, Interdisciplinary Graduate School of Medicine and Engineering, University of Yamanashi, 1110 Shimokato, Chuo City, Yamanashi 409-3898, Japan
e-mail: sohno@yamanashi.ac.jp

N. Terada
Division of Health Sciences, Shinshu University Graduate School of Medicine, 3-1-1 Asahi, Matsumoto City, Nagano 390-8621, Japan

Department of Anatomy and Molecular Histology, Interdisciplinary Graduate School of Medicine and Engineering, University of Yamanashi, 1110 Shimokato, Chuo City, Yamanashi 409-3898, Japan

S. Ohno et al. (eds.), *In Vivo Cryotechnique in Biomedical Research and Application for Bioimaging of Living Animal Organs*, DOI 10.1007/978-4-431-55723-4_18

because of the little ultrastructural evidence of completely sealing features of blood vessel walls [7, 8]. Our "in vivo cryotechnique" (IVCT) was performed for the living mouse thymus to reveal the immunolocalization of intrinsic mouse serumproteins or extrinsic BSA injected via tail veins [9]. We also tried to identify the immunolocalization of extrinsic HRP in living mouse thymic tissues, which were directly injected via left ventricles, at short time intervals of second or minute orders by the IVCT-FS.

18.2 Morphological Findings of Living Mouse Thymic Tissues

By hematoxylin-eosin (HE) staining, two common zones were seen in the thymic tissues, namely, both the peripheral cortex and central medulla (Fig. 18.1). Extracellular spaces of the thymic interstitium with open blood vessels were well maintained in the specimens prepared by the IVCT method (Fig. 18.1b–f) because the interstitial tissues shrank much less during the preparation steps in comparison with the conventional preparation methods, as described previously [9]. A normal cortex/medulla ratio of thymic tissues would be close to 2:1 in a typical adult rodent, as already reported [10]. Interlobular arteries usually reached the medullary parenchyma at the end of septa and immediately branched into smaller arteries or arterioles (Fig. 18.1b). Most blood vessels in the cortex were blood capillaries, and thicker arterioles with diameters of 15–30 μm were found in the corticomedullary boundary areas (Fig. 18.1e, f). Those arterioles ran outward into blood capillary branches in the deep cortex (Fig. 18.1). Smaller capillaries lay beneath the capsule (Fig. 18.1c). Large and medium lymphocytes, which were actively proliferating, were most numerous in the cortex (Fig. 18.1b, f). In contrast, the thymic medulla showed much paler HE staining intensity with large reticulum cells, because of the much lower cellularity of thymocytes (Fig. 18.1d).

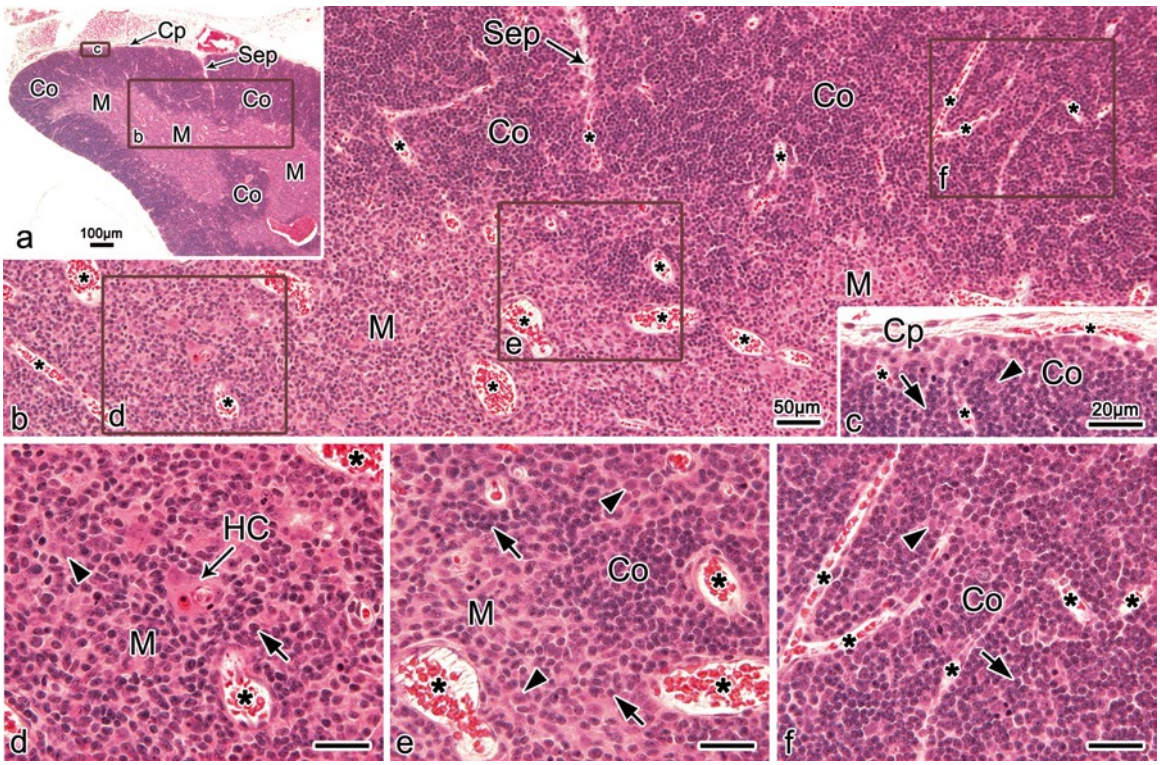

Fig. 18.1 Light micrographs of hematoxylin-eosin staining of paraffin sections of living mouse thymic tissues prepared by IVCT (**a**–**f**). (**a**) A low-magnification view of the thymic tissues shows widely panoramic tissue areas, extending from the superficial cortex (*Co*) under the capsule (*Cp*) to the deep medulla (*M*). (**b**–**f**) Each micrograph is a highly magnified view of the area enclosed with each *rectangle* in **a** and **b**. (**b**) Many small thymocytes, large epithelial reticulum cells, and open blood vessels (*asterisks*) with flowing erythrocytes are detected in the areas of the cortex (*Co*) and medulla (*M*). (**c**) Cortical blood capillaries with erythrocytes (*asterisks*) are seen in the subcapsular region in addition to capsular blood capillaries (*asterisks*). (**d**) The medulla (*M*) is composed of fewer thymocytes (*arrows*) and epithelial reticulum cells (*arrowheads*), and a Hassall's corpuscle (*HC*) is also seen. (**e**) Corticomedullary boundary areas contain thick blood vessels (*asterisks*), extending into both cortical (*Co*) and medullary (*M*) areas. Their opening lumen is the well-delineated endothelial cells and the basal lamina. (**f**) Note flowing erythrocytes in anastomosing blood capillaries of cortical tissues prepared with IVCT (*asterisks*). *Arrows* thymocytes, *Arrowheads* epithelial reticulum cells. Bars (**a**) 100 μm, (**b**, **d**–**f**) 50 μm, (**c**) 20 μm

18.3 Enzyme Histochemistry of Injected HRP in Cryosections of Thymic Tissues

Enzyme-reactive intensities of HRP with methyl green (MG) staining were detected at various time intervals in cryosections of mouse thymic tissues, which were injected with HRP (100 mg/ml) via left ventricles (Fig. 18.2). The DAB reactivity of HRP with high sensitivity was not found in the interstitium of the cortex without HRP injection (Fig. 18.2e, inset). However, flowing erythrocytes in the blood-vessels were usually positive for the DAB reaction in cryosections. Enzyme reaction products of injected HRP protein were serially localized not only in the blood vessels but also in the interstitial matrices of the thymic cortex of living mice (Fig. 18.2a–d). At 30 s after the HRP injection, enzyme reaction products were slightly detected in the interstitium around some thick blood vessels (Fig. 18.2a). Fine cortical vessels have diameters of 4–8 μm in largest dimension, as already shown in Fig. 18.1f. At 1 and 3 min, such enzyme reaction products were more widely found in the similar

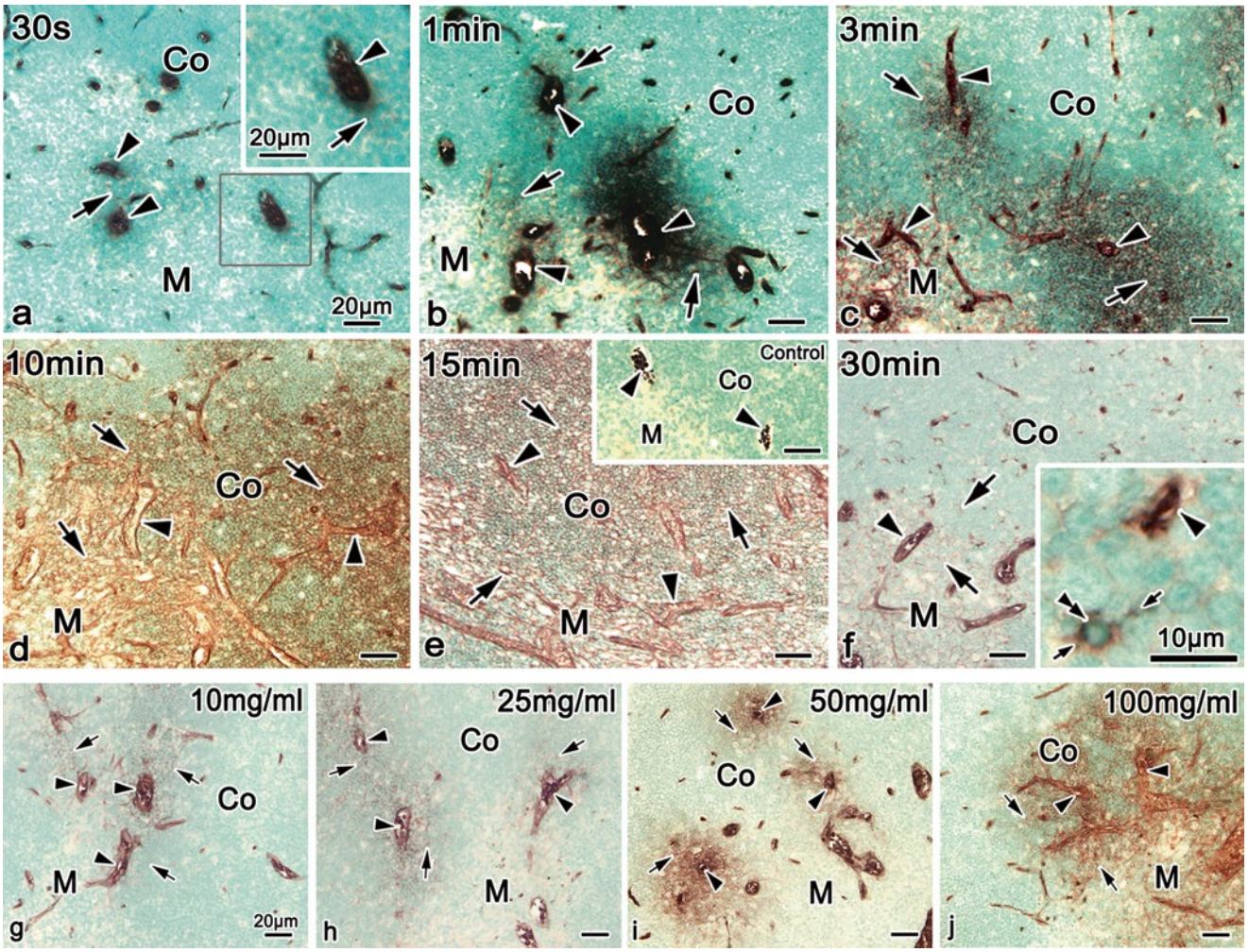

Fig. 18.2 Enzyme-histochemical images of DAB reaction of HRP in cryosections of mouse thymic tissues, which were injected with HRP (100 mg/ml) via left ventricles and prepared after various time intervals by IVCT. (**a**) At 30 s, HRP reaction products are slightly detected in the interstitium around some thick blood vessels in corticomedullary boundary areas (*arrows*) and also within other blood vessels (*arrowheads*). (**b**, **c**) At 1 and 3 min, they are more widely detected in the interstitium around thick blood vessels in corticomedullary boundary areas (*arrows*) and within some thick blood vessels in both cortical and medullary areas (*arrowheads*). (**d**) At 10 min, they are diffusely detected in all the interstitium of cortical and medullary areas (*arrows*). (**e**) At 15 min, they are uniformly distributed throughout all the interstitium of thymic tissues (*arrows*) in addition to perivascular spaces of blood vessels (*arrowheads*). Immunocontrol (*inset*). (**f**) At 30 min, HRP phagocytosis by macrophages (*double arrowheads*) is seen to be scattered, which is accompanied by the decrease of DAB reaction intensity in all interstitial matrices. The images (**g–j**), which were injected with various concentrations of HRP (10, 25, 50, and 100 mg/ml) via left ventricles and prepared at 3 min after HRP injection by IVCT. (**g–j**) HRP enzyme reactivities are variously detected in the interstitium (*arrows*) around some blood vessels in corticomedullary boundary areas and other thick blood vessels of the medulla, depending on the HRP concentration, but they are also found within blood vessels (*arrowheads*) in addition to tiny blood capillaries. *Arrowhead* blood vessel, *Small arrow* process, *Co* cortex, *M* medulla. Bars 20 μm, *insets* 10 μm

interstitium around thick blood vessels in the corticomedullary boundary areas (Fig. 18.2b, c). They appeared to be limited at variable distances in the interstitium from the permeable blood vessels. At 10 min, they were more diffusely detected in the interstitium of cortical areas and also detected in the interstitium of medullary areas (Fig. 18.2d). At 15 min, they were finally found to be distributed throughout all the interstitium of thymic tissues including both the cortex and medulla (Fig. 18.2e). In addition, at 30 min, HRP phagocytosis by many macrophages was seen throughout all the interstitium of the thymic tissues (Fig. 18.2f), which was accompanied by the rapid decrease of DAB reaction products in the interstitium of the cortex (Fig. 18.2f).

It was previously unknown that the leakage of HRP protein through the blood vessels depends on not only molecular sizes or charges but also on molecular concentrations in the blood vessels. At 3 min after their injection via left ventricles with lower concentrations of HRP, such as 10 and 25 mg/ml (Fig. 18.2g, h), a slight gradient of transudation into the interstitium through thick blood vessels was seen in the thymus of living mice, depending on the HRP concentration. The HRP enzyme reactivity was similarly detected in the interstitium around thick blood vessels in corticomedullary boundary areas and within some blood capillaries in the cortex (Fig. 18.2g, h). However, HRP enzyme reaction products were more heavily detected in the interstitium of inner cortical and medullary areas at higher concentrations of HRP, such as 50 and 100 mg/ml (Fig. 18.2i, j). A series of HRP injections with different concentrations revealed that the distribution of exogenous HRP was also dependent on the concentration of injected HRP. Therefore, no HRP was detected in the interstitium around blood capillaries in outer cortical areas at any concentration of injected HRP.

18.4 Immunolocalizations of HRP in Paraffin Sections and HRP Phagocytosis by Macrophages

To reexamine the thymic tissues at a higher resolution, both HE staining and HRP immunostaining were performed in serial paraffin sections of living mouse thymic tissues after short time intervals in the order of seconds to minutes and were injected with a lower concentration of HRP (25 mg/ml) via the left ventricle. At 30 s and 1 min (Fig. 18.3a–d), HRP immunoreactivity was detected only within the blood vessels. At 3 and 10 min, however, it was weakly detected in the interstitium around the blood vessels in corticomedullary boundary areas and within some blood capillaries in cortical areas (Fig. 18.3e–h). A striking feature was that immunostaining changes involved the inner cortex and especially the corticomedullary boundary of thymic tissues (Fig. 18.3f, h). Perivascular spaces of thick blood vessels were also immunopositive for HRP (Fig. 18.3f, h, insets). At 15 min, HRP immunoreactivity was more widely seen in the interstitium of the thymic cortex (Fig. 18.3i, j, arrows), but less than in the blood vessels (Fig. 18.3i, j, arrowheads). At 30 min, it was a little more heavily detected in the interstitium of the medulla (Fig. 18.3l, m) as compared with the cortex. The permeability of HRP across the blood capillary walls was hardly seen in the outer cortical areas, as shown in Fig. 18.3f, h. In addition, HRP phagocytosis by macrophages was clearly seen at 30 min after the HRP injection (Fig. 18.3m, double arrowheads), which was similar to that revealed by enzyme histochemistry of HRP (Fig. 18.2f).

The cryosections of mouse thymic cortical areas, which were injected with HRP (100 mg/ml) via left ventricles and prepared at 30 min by IVCT, were examined to show double-immunofluorescence staining for HRP (Fig. 18.3n, p) and Iba1, a macrophage marker (Fig. 18.3o, p), together with DAPI staining (Fig. 18.3p). The red fluorescence signals of Iba1 were mainly detected in the cytoplasm of macrophages, and the HRP immunostaining was also seen in macrophages (Fig. 18.3p, double arrowheads). The HRP immunofluorescence was still detected in the blood vessels 30 min after HRP injection (Fig. 18.3n, p, arrowheads), in addition to some local interstitial areas (Fig. 18.3n, p, arrows).

18.5 Discussion

The main feature of IVCT presented in this study was to obtain tissue specimens of living animal organs, which can strictly capture their dynamic circulation states including cells and tissues, as already discussed in detail [11]. The present study showed small molecular HRP with dose- and time-dependent leakage through different thymic blood vessels, because of the high time resolution of IVCT for dynamic

Fig. 18.3 (continued) interstitium (*arrows*) around blood vessels in corticomedullary boundary areas and within thick blood vessels (*arrowhead*). (**i**, **j**) At 15 min, it is more widely seen in the interstitium (*arrows*), as compared with blood vessels (*arrowheads*). (**k**) Immunocontrol. (**l**, **m**) In addition, HRP phagocytosis by macrophages (*double arrowheads*) is seen at 30 min after HRP injection. The immunofluorescence micrographs (**n**–**p**) of cryosections of thymic cortical areas at 30 min after HRP (100 mg/ml) injection via left ventricles of living mice, prepared by IVCT. Double-immunofluorescence staining for HRP (**n**, **p**, *green*) and ionized calcium-binding adapter molecule 1 (Iba1) (**o**, **p**, *red*) with nuclear DAPI staining (*blue*) show their colocalization in almost all macrophages. Iba1 immunofluorescence shows the macrophages of thymic tissues (**o**, **p**, *double arrowheads*), which contain HRP in their cytoplasm (**n**, **p**, *double arrowheads*). HRP immunostaining is still detected within the blood vessels (**n**, **p**, *arrowheads*) and some areas of the cortical interstitium among compact thymocytes (**n**, **p**, *arrows*). *Arrowheads* blood vessels, *Small arrows* processes, *Co* cortex, Bars 10 μm, *Cp* capsule, *Co* cortex, *M* medulla. Bars 10, 50 μm; *insets* 10, 20 μm

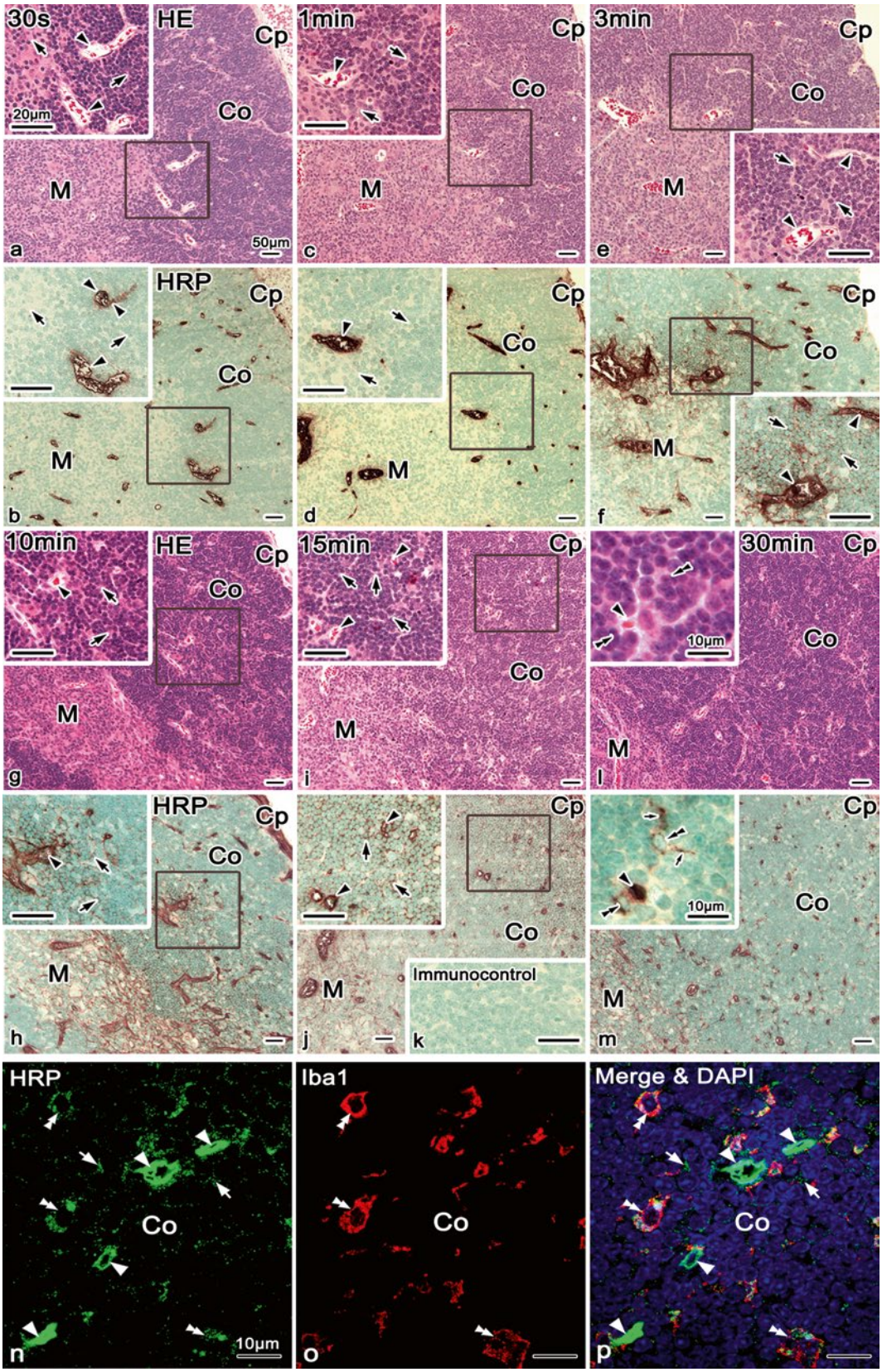

Fig. 18.3 Light microscopic images of hematoxylin-eosin (*HE*) staining (**a**, **c**, **e**, **g**, **i**, **l**) and HRP immunostaining (**b**, **d**, **f**, **h**, **j**, **m**) in serial paraffin sections of mouse thymic tissues, which were injected with a lower concentration of HRP (25 mg/ml) via left ventricles and prepared after various time intervals by IVCT. (**a**–**d**) At 30 s and 1 min, HRP immunoreactivity is detected only within blood vessels (*arrowheads*), not in the interstitium around them. (**e**, **f**) However, at 3 min, it is weakly detected in the interstitium (*arrows*) around blood vessels in corticomedullary boundary areas and within some thick blood vessels (*arrowheads*). (**g**, **h**) At 10 min, HRP immunoreactivity is also detected in the

functional structures [12]. Although the IVCT is a cryofixation method, which is not designed for time-lapse imaging, the present study also indicates that it is useful to examine the dynamically changing flux of extrinsic soluble HRP proteins in the thymic tissues. The IVCT was also found to be used for both enzyme-histochemical or immunohistochemical studies of soluble HRP circulation and would be helpful for other enzyme-histochemical analyses due to the remaining high sensitivity of cryofixed enzyme reactions.

It is well known that the animal thymus has a special vascular complex, conventionally termed the blood-thymus barrier [4, 9, 13–16], as an initial exposure site of lymphocytes to circulating antigens. The blood-thymus barrier has been assumed to be a reliable structure in the anatomical and functional sense, but foreign antigens can probably permeate its barrier under certain conditions. It has been also reported to consist of capillary endothelial cells, basal lamina of endothelium, perivascular spaces, basal lamina of epithelial reticulum cells, and finally epithelial reticulum cells themselves. A previous experiment using ultrastructural tracers of different molecular weights demonstrated that immunological lymphoid cells in the thymic cortex were usually protected from circulating antigenic molecules in contrast with those of the medulla [4]. The interstitial tissues with augmented permeability of antigen proteins under some conditions in vivo would increase the accessibility of thymocytes to blood-derived molecules. However, based on the experiment with BSA of various concentrations, as performed previously using the living mouse thymic tissues [9], we found that the injected BSA was time-dependently distributed throughout the thymic interstitium in hours to days, leaking from thick blood vessels at the corticomedullary boundary, but not from blood capillaries in outer cortical areas. In the present study, we have also revealed the similar localization of the HRP protein in the thymic interstitium of living mice in a few minutes, indicating the easy leakage of small molecular HRP into corticomedullary boundary areas. Therefore, these findings also supported the partial existence of a functional blood-thymus barrier, especially along blood capillaries of the outer cortex, although the molecular permeability of thick blood vessels, including some arterioles, in corticomedullary boundary areas was higher than that in the outer cortex, as already discussed [14, 16, 17]. The time- and concentration-dependent localization of antigenic HRP proteins might be helpful for other immunohistochemical analyses of native thymic structure tissues with various interstitial fluid pressures and also the determination of the immunological system in vivo.

In addition, other reports have already demonstrated that transudation into thymic interstitial matrices depended on the molecular weight of the administered substances [4, 6, 13, 15, 17–20]. The distribution of injected HRP of low molecular weight presented in this study seems to be additionally related to the vascular structures in the thymic cortex, because larger intrinsic IgA and IgM immunostaining intensities were less detected in the outer cortex in comparison with both extrinsic BSA and mouse original albumin, as already discussed [9]. Therefore, it is concluded that an incomplete blood-thymus barrier in the corticomedullary boundary areas usually contributes to such different morphofunctional data of thymic tissues of living mice, which was directly revealed by IVCT-FS, probably reflecting their living state.

In the thymus, as shown in Fig. 18.3n, p, macrophages around the blood vessels actively phagocytized the permeated HRP. Such phagocytotic functions of macrophages within 30 min might change the average molecular concentrations of HRP in the thymic interstitium, depending on the time course of flowing HRP molecules. Moreover, the phagocytosis of HRP into macrophages could induce their expression of specific antigens, probably resulting in the common positive or negative immunoreaction pathway in other thymic cells. Therefore, in a future study, the IVCT will be additionally used to clarify T-cell differentiation at various sites of thymic tissues, probably depending on the dynamic diffusion of various serum components in their microenvironment. A further experiment at an electron microscopic level will be also necessary to directly examine the HRP penetration of blood vessels and phagocytotic macrophages of living mice, which could be prepared by IVCT. Some re-arranged figures were already published in our paper, Acta Histochem Cytochem (2014) 47:273–288, and cited with their permissions.

References

1. Ladi E, Yin X, Chtanova T, Robey EA (2006) Thymic microenvironments for T cell differentiation and selection. Nat Immunol 7:338–343
2. Lind EF, Prockop SE, Porritt HE, Petrie HT (2001) Mapping precursor movement through the postnatal thymus reveals specific microenvironments supporting defined stages of early lymphoid development. J Exp Med 194:127–134
3. Pearse G (2006) Normal structure, function and histology of the thymus. Toxicol Pathol 34:504–514
4. Raviola E, Karnovsky MJ (1972) Evidence for a blood–thymus barrier using electron-opaque tracers. J Exp Med 136:466–498
5. Marshall AH, White RG (1961) The immunological reactivity of the thymus. Br J Exp Pathol 42:379–385
6. Sainte-Marie G (1963) Antigen penetration into the thymus. J Immunol 91:840–845
7. Henry L, Durrant TE, Anderson G (1992) Pericapillary collagen in the human thymus: implications for the concept of the 'blood-thymus' barrier. J Anat 181:39–46
8. Ito T, Hoshino T (1966) Light and electron microscopic observations on the vascular pattern of the thymus of the mouse. Arch Histol Jpn 27:351–361

9. Bai Y, Wu B, Terada N, Saitoh Y, Ohno N, Saitoh S, Ohno S (2012) Immunohistochemical analysis of various serum proteins in living mouse thymus with "in vivo cryotechnique". Med Mol Morphol 45:129–139
10. Elmore SA (2006) Enhanced histopathology of the thymus. Toxicol Pathol 34:656–665
11. Ohno S, Terada N, Ohno N, Saitoh S, Saitoh Y, Fujii Y (2010) Significance of 'in vivo cryotechnique' for morphofunctional analyses of living animal organs. J Electron Microsc 59:395–408
12. Terada N, Saitoh Y, Saitoh S, Ohno N, Jin T, Ohno S (2010) Visualization of microvascular blood flow in mouse kidney and spleen by quantum dot injection with "in vivo cryotechnique". Microvasc Res 80:491–498
13. Green I, Bloch K (1963) Uptake of particulate matter within the thymus of adult and new-born mice. Nature 200:1099–1101
14. Kendall MD (1991) Functional anatomy of the thymic microenvironment. J Anat 177:1–29
15. Kyewski BA, Fathman CG, Rouse RV (1986) Intrathymic presentation of circulating non-MHC antigens by medullary dendritic cells: an antigen-dependent microenvironment for T cell differentiation. J Exp Med 163:231–246
16. Roberts RL, Sandra A (1994) Transport of transferrin across the blood-thymus barrier in young rats. Tissue Cell 26:757–766
17. Drumea-Mirancea M, Wessels JT, Müller CA, Essl M, Eble JA, Tolosa E, Koch M, Reinhardt DP, Sixt M, Sorokin L, Stierhof Y, Schwarz H, Klein G (2006) Characterization of a conduit system containing laminin-5 in the human thymus: a potential transport system for small molecules. J Cell Sci 119:1396–1405
18. Kato S (1997) Thymic microvascular system. Microsc Res Tech 38:287–299
19. Kyewski BA, Fathman C, Kaplan H (1984) Intrathymic presentation of circulating non-major histocompatibility complex antigens. Nature 308:196–199
20. Müller SM, Stolt CC, Terszowski G, Blum C, Amagai T, Kessaris N, Iannarelli P, Richardson WD, Wegner M, Rodewald H (2008) Neural crest origin of perivascular mesenchyme in the adult thymus. J Immunol 180:5344–5351

Immunolocalization of Serum Proteins in Living Mouse Glomeruli Under Various Hemodynamic Conditions

19

Zilong Li, Nobuhiko Ohno, Nobuo Terada, and Shinichi Ohno

Abstract

The mechanisms of serum protein passage through glomerular capillary loops are unknown to us yet. We have visualized topographical changes of the serum proteins by "in vivo cryotechnique" in combination with immunohistochemistry. Albumin and immunoglobulin G, Ig kappa light chain, and IgG1 heavy chain were mainly immunolocalized in GCL, but not colocalized with zonula occludens-1 (ZO-1) under normotensive condition. Albumin and kappa light chain were immunolocalized in Bowman's space under heart-arrest condition and in quick-frozen fresh tissues. However, they were more clearly immunolocalized along basement membranes and in Bowman's space under acute hypertensive condition, indicating their increased passage through GCL. IgG was also more clearly localized in mesangial areas (MA) under acute hypertension, compared with that under the normotensive or heart-arrest condition. This study is the first direct visualization for glomerular passage of serum proteins under abnormal hemodynamic conditions by the "in vivo cryotechnique," which is a useful protocol for morphofunctional examination of living mouse GCL and immunohistochemical analyses of dynamically changing proteins.

Keywords

Serum proteins • In vivo cryotechnique • Acute hypertension • Immunohistochemistry

Z. Li, M.D. (✉)
Department of Nephrology, First Hospital of China Medical University, No.155 North Nanjing Street, Heping District, Shenyang, Liaoning 110001, China

Department of Anatomy, Interdisciplinary Graduate School of Medicine and Engineering, University of Yamanashi, 1110 Shimokato, Tamaho, Yamanashi 409-3898, Japan
e-mail: lzl1017@yahoo.com

N. Ohno • S. Ohno
Department of Anatomy and Molecular Histology, Interdisciplinary Graduate School of Medicine and Engineering, University of Yamanashi, 1110 Shimokato, Chuo City, Yamanashi, 409-3898, Japan

N. Terada
Division of Health Sciences, Shinshu University Graduate School of Medicine, 3-1-1 Asahi, Matsumoto City, Nagano 390-8621, Japan

Department of Anatomy and Molecular Histology, Interdisciplinary Graduate School of Medicine and Engineering, University of Yamanashi, 1110 Shimokato, Chuo City, Yamanashi 409-3898, Japan

19.1 Introduction

Hemodynamic factors exerted an important influence on the native morphology of glomerular capillary loops (GCL) in living mouse kidneys [1, 2]. In addition, they have been supposed to lead to the leakage of serum proteins in animal kidneys under pathological states and are also related to progression in human renal diseases [3, 4]. In such abnormal states, hyperfiltrated serum proteins in Bowman's space are usually processed for increased reabsorption in renal proximal tubules of living mouse kidneys [5], resulting in interstitial inflammation and fibrosis [6–10]. This may explain the histopathological progression of chronic renal diseases.

The glomerular filtration barriers play a role in charge- and/or size-selective barriers against serum proteins [11, 12]. Under normal blood circulation, the main GBM filtration can barrier serum albumin and immunoglobulin G (IgG) [13].

S. Ohno et al. (eds.), *In Vivo Cryotechnique in Biomedical Research and Application for Bioimaging of Living Animal Organs*, DOI 10.1007/978-4-431-55723-4_19

After acute hypertension induced by angiotensin II, albumin and IgG translocate in the GBM, urinary space, and mesangial matrix areas of rat kidneys [3]. However, the conventional preparation methods caused hemodynamic perturbation of GCL and translocation of serum proteins. Therefore, the renal glomerular selectivity of serum proteins has never been visualized because of such technical limitations of the specimen preparation.

As reported that morphological studies with the routine immersion or perfusion fixation were not able to clarify native structures of functioning kidneys in vivo [14, 15], the common fixatives, such as glutaraldehyde and paraformaldehyde, will cross-link in animal cells and tissues. In addition, they usually need considerable time to finish cross-linking, and some of them are usually washed out from the fixed specimens. Our ultimate goal of morphological studies is that all features of cells and tissues to be examined should reflect the physiological meaning under animal investigation. Therefore, the in situ preservation of cells and tissues in living animal organs is necessary for the histological studies to define their functioning structures in vivo. The "in vivo cryotechnique" can realize it by the combination of a precooled cryoknife with isopentane-propane cryogen [2, 16, 17]; all biological processes in the living animal organs were instantly stopped and embedded in the ice microenvironment using the "in vivo cryotechnique." Then the "in vivo cryotechnique" can be also followed by various preparation steps for morphological analyses [18]. The freeze-substituted specimens are then embedded in the paraffin wax, leaving some antigenic sites exposed in the frozen cells and tissues due to the formation of tiny ice crystals [19]. So we visualize the topographical distributions of soluble serum proteins in living mouse renal glomeruli using "in vivo cryotechnique," because their leakage from the glomerular capillary loops and also following reabsorption in the proximal convoluted tubules were assumed to be strictly time-dependent processes under an acute hypertensive condition.

19.2 Alteration of Serum Protein Distribution in Glomeruli Under Various Hemodynamic Conditions

In the present study, we have shown that the "in vivo cryotechnique" followed by the freeze substitution could visualize not only the morphology of living mouse kidneys under various hemodynamic conditions (Fig. 19.1) but also the immunolocalization of serum proteins in their glomeruli, as summarized (Fig. 19.2). The serum albumin and IgG were usually kept within GCL under the normal hemodynamic condition, except for the IgG in some MA, and neither albumin nor IgG was immunolocalized in Bowman's space of the living mouse glomeruli. However, under the acute hypertensive condition, the immunolocalization of IgG1 heavy chain was more clearly detected in MA than that under the normal hemodynamic condition [5].

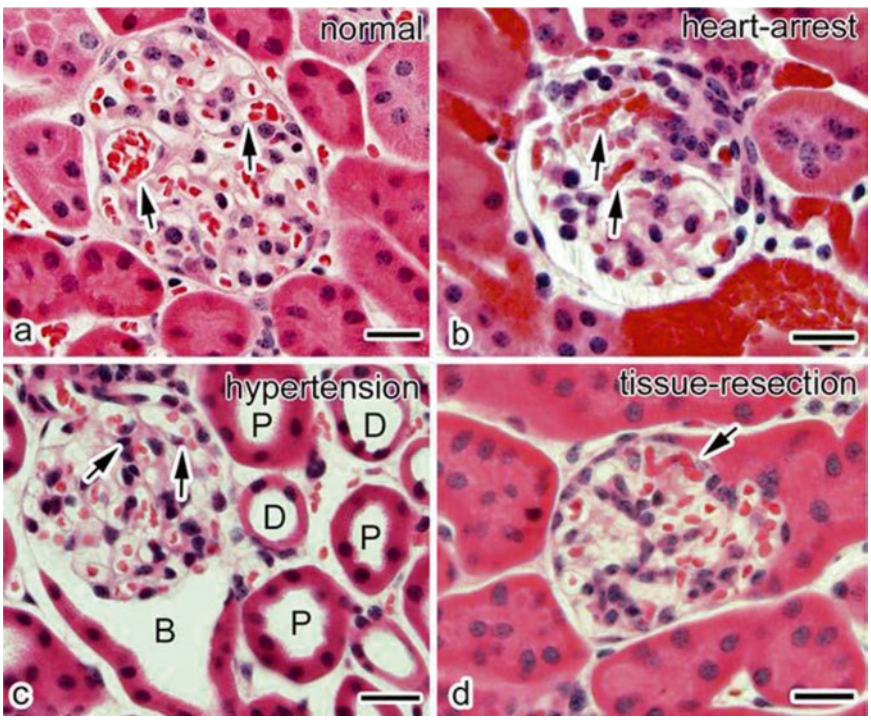

Fig. 19.1 Light micrographs of mouse renal cortical tissues prepared under various hemodynamic conditions; "in vivo cryotechnique" under normotensive (**a**, normal), heart-arrest (**b**, heart-arrest), and acute hypertensive (**c**, hypertension) conditions and tissue resection followed by quick-freezing (**d**, tissue resection). The glomerular capillary loops are kept open under the normotensive condition (**a**, *arrows*), but almost collapsed under the heart-arrest condition (**b**, *arrows*). They are widely open under the acute hypertensive condition (**c**, *arrows*), as compared with those under the normotensive condition. However, they are most severely collapsed in the specimens prepared by tissue resection followed by the quick-freezing (**d**, *arrow*). The luminal spaces of proximal (**c**, *P*) and distal (**c**, *D*) tubules and Bowman's spaces (**c**, *B*) under the acute hypertension condition are more clearly opened, as compared with those under the other hemodynamic conditions (**a**, **b**, **d**). *Scale bars* 20 μm

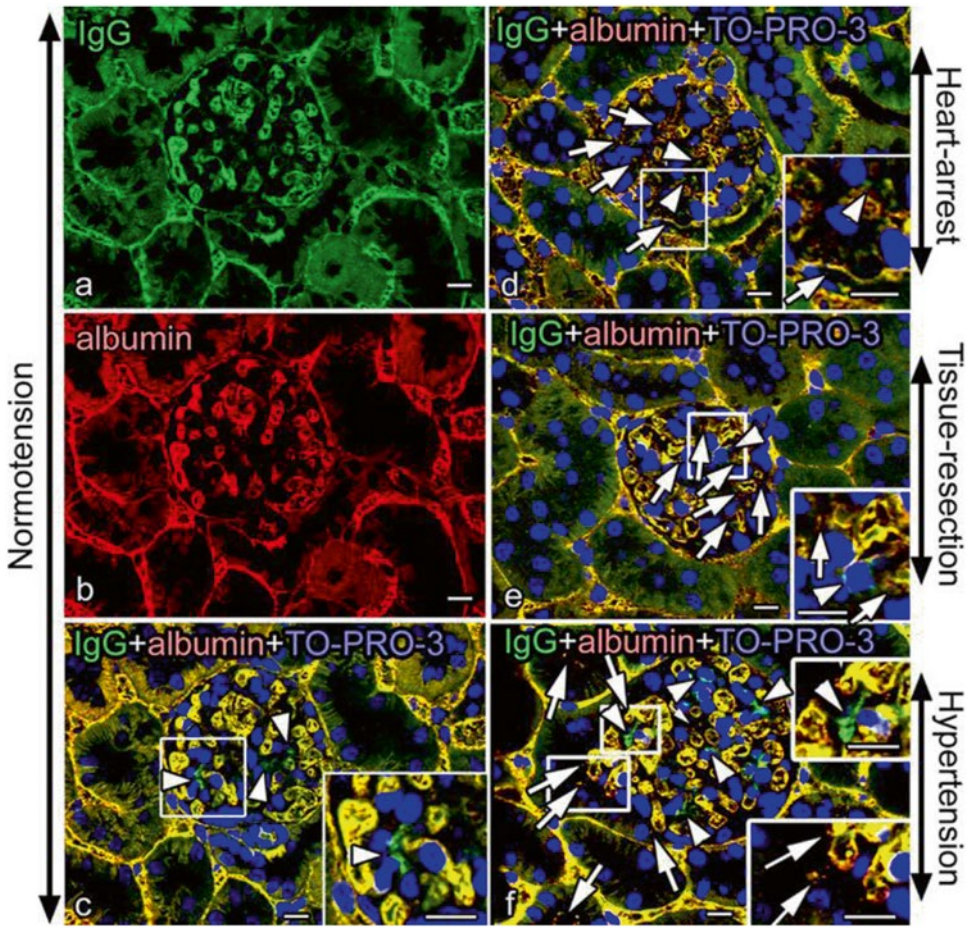

Fig. 19.2 Confocal laser scanning micrographs, showing immunolocalizations of IgG with the whole molecular weight (**a**, *IgG, green color*) and albumin (**b**, *red color*) in the renal glomeruli, obtained by the double immunofluorescence staining. Under the normotensive condition (**a**–**c**, normotension), both IgG and albumin immunolocalizations are detected within the glomerular capillary loops, and only IgG is also immunolocalized in the mesangial areas (*MA*) (**c**, *arrowheads*). Under the heart-arrest condition (**d**, heart-arrest) and tissue resection followed by the quick-freezing method (**e**, tissue resection), the immunoreaction products of both IgG and albumin are also found in Bowman's space (**d** and **e**, *arrows*), and only IgG is slightly immunolocalized in MA (**d** and **e**, *arrowheads*). Under the acute hypertensive condition (**f**, hypertension), large clumped immunoreaction products of IgG are more clearly seen in MA (**f**, *arrowheads*). The rapid translocation of both albumin and IgG is detected in some Bowman's spaces, and their reabsorption is also detected in the proximal convoluted tubules (**f**, *arrows*). *Scale bars* 10 μm

19.3 Mechanism of Immunolocalization of Serum Proteins in Glomeruli

The leakage of albumin and kappa light chain into Bowman's space was increased under the acute hypertensive condition, as also suggested by their reabsorption into the proximal tubules [5]. Moreover, their immunolocalization changes in the glomeruli were also due to the increased pressures in GCL, easily causing their passage through GBM. Some IgGs with the whole molecular weight were reported to be extensively trapped in the GBM under pathological conditions, such as membranoproliferative glomerulonephritis, membranous nephropathy, and lupus nephritis [20, 21]. In such cases, they may be hardly leaked out into Bowman's spaces, because of large molecular sizes, conformational changes, and immune complex formation. The leakage of both albumin and IgG from GCL into Bowman's spaces could be detected under the heart-arrest condition. In addition, their immunolocalization in the conventional specimens prepared by quick-freezing of the resected kidney tissues was almost similar to that observed under the heart-arrest condition.

19.4 Concluding Remarks

The "in vivo cryotechnique" followed by the freeze-substitution method would be a reliable tool to keep soluble serum proteins in situ and provide transient images of functioning glomeruli in the living mice. In addition, it also allowed us to examine the

precise immunodistribution of serum proteins leaked out of the glomeruli and their reabsorption into the renal proximal tubules under the various hemodynamic conditions. The present figures were already published in our paper, Histochem Cell Biol (2006) 26:399–406, and cited with their permissions.

References

1. Ohno S, Baba T, Terada N, Fujii Y, Ueda H (1996) Cell biology of kidney glomerulus. Int Rev Cytol 166:181–230
2. Ohno S, Terada N, Fujii Y, Ueda H, Takayama I (1996) Dynamic structure of glomerular capillary loop as revealed by an in vivo cryotechnique. Virchows Arch 427:519–527
3. Olivetti G, Kithier K, Giacomelli F, Wiener J (1981) Glomerular permeability to endogenous proteins in the rat: effects of acute hypertension. Lab Invest 44:127–137
4. Remuzzi G, Bertani T (1998) Pathophysiology of progressive nephropathies. N Engl J Med 339:1448–1456
5. Li Z, Terada N, Ohno N, Ohno S (2005) Immunohistochemical analyses on albumin and immunoglobulin in acute hypertensive mouse kidneys by "in vivo cryotechnique". Histol Histopathol 20:807–816
6. Gansevoort RT, Navis GJ, Wapstra FH, de Jong PE, de Zeeuw D (1997) Proteinuria and progression of renal disease: therapeutic implications. Curr Opin Nephrol Hypertens 6:133–140
7. Jerums G, Panagiotopoulos S, Tsalamandris C, Allen TJ, Gilbert RE, Comper WD (1997) Why is proteinuria such an important risk factor for progression in clinical trials? Kidney Int Suppl 63:S87–S92
8. Remuzzi G (1995) Abnormal protein traffic through the glomerular barrier induces proximal tubular cell dysfunction and causes renal injury. Curr Opin Nephrol Hypertens 4:339–342
9. Schreiner GF (1995) Renal toxicity of albumin and other lipoproteins. Curr Opin Nephrol Hypertens 4:369–373
10. Thomas ME, Brunskill NJ, Harris KP, Bailey E, Pringle JH, Furness PN, Walls J (1999) Proteinuria induces tubular cell turnover: a potential mechanism for tubular atrophy. Kidney Int 55:890–898
11. Reiser J, Kriz W, Kretzler M, Mundel P (2000) The glomerular slit diaphragm is a modified adherens junction. J Am Soc Nephrol 11:1–8
12. Rico M, Mukherjee A, Konieczkowski M, Bruggeman LA, Miller RT, Khan S, Schelling JR, Sedor JR (2005) WT1-interacting protein and ZO-1 translocate into podocyte nuclei after puromycin aminonucleoside treatment. Am J Physiol Renal Physiol 289:F431–F441
13. Fujigaki Y, Nagase M, Kobayasi S, Hidaka S, Shimomura M, Hishida A (1993) Intra-GBM site of the functional filtration barrier for endogenous proteins in rats. Kidney Int 43:567–574
14. Yu Y, Leng CG, Kato Y, Terada N, Fujii Y, Ohno S (1998) Ultrastructural study of anionic sites in glomerular basement membranes at different perfusion pressures by quick-freezing and deep-etching method. Nephron 78:88–95
15. Yu Y, Leng CG, Terada N, Ohno S (1998) Scanning electron microscopic study of the renal glomerulus by an in vivo cryotechnique combined with freeze-substitution. J Anat 192:595–603
16. Ohno N, Terada N, Fujii Y, Baba T, Ohno S (2004) "In vivo cryotechnique" for paradigm shift to "living morphology" of animal organs. Biomed Rev 15:1–19
17. Terada N, Ohno N, Li Z, Fujii Y, Baba T, Ohno S (2006) Application of in vivo cryotechnique to the examination of cells and tissues in living animal organs. Histol Histopathol 21(3):265–272
18. Ohno N, Terada N, Ohno S (2004) Advanced application of the in vivo cryotechnique to immunohistochemistry for animal organs. Acta Histochem Cytochem 37:357–364
19. Ohno N, Terada N, Murata S, Katoh R, Ohno S (2005) Application of cryotechniques with freeze-substitution for the immunohistochemical demonstration of intranuclear pCREB and chromosome territory. J Histochem Cytochem 53:55–62
20. Bijl M, Dijstelbloem HM, Oost WW, Bootsma H, Derksen RH, Aten J, Limburg PC, Kallenberg CG (2002) IgG subclass distribution of autoantibodies differs between renal and extra-renal relapses in patients with systemic lupus erythematosus. Rheumatology 41:62–67
21. Imai H, Hamai K, Komatsuda A, Ohtani H, Miura AB (1997) IgG subclasses in patients with membranoproliferative glomerulonephritis, membranous nephropathy, and lupus nephritis. Kidney Int 51:270–276

Immunohistochemical Analyses on Albumin and IgG in Acute Hypertensive Mouse Kidneys

20

Zilong Li, Nobuo Terada, Nobuhiko Ohno, and Shinichi Ohno

Abstract

The purpose of this study is to visualize topographical changes of serum proteins, albumin and IgG, passing through the mouse glomerular capillary loops and their reabsorption in renal proximal tubules by immunohistochemistry in combination with our "in vivo cryotechnique." Under the acute hypertensive condition, the albumin and kappa or lambda light chains, but not IgG1 heavy chain, were strongly immunolocalized in the apical cytoplasm of almost all proximal tubules. This study is the first in vivo visualization for glomerular passage of serum proteins and their transtubular absorption.

Keywords

In vivo cryotechnique • Acute hypertension • Mouse kidney • Immunohistochemistry • Serum proteins

20.1 Introduction

It has been already known that hemodynamic factors, such as blood pressure and flow, exert an important influence on native morphology of glomerular capillary loops in living mouse kidneys [1–3]. In such cases, hyperfiltrated serum proteins are usually processed for increased reabsorption in renal proximal tubules [4]. In the present study, dynamic distributions of soluble serum proteins in mouse kidneys were immunohistochemically examined by the "in vivo cryotechnique" from the viewpoint of different hemodynamics, because their leakage across the glomerular capillary loops and following reabsorption in proximal convoluted tubules were assumed to be strictly time-dependent processes under the acute hypertensive condition.

20.2 "In Vivo Cryotechnique" for Living Mouse Kidneys

Twelve adult C57BL/6 mice, weighting 20–30 g, were anesthetized with sodium pentobarbital. Then the abdominal cavity of four mice was open, and left kidneys were detected under normal blood circulation, as a control group. As the

Z. Li, M.D., Ph.D. (✉)
Department of Anatomy, Interdisciplinary Graduate School of Medicine and Engineering, University of Yamanashi, Tamaho, Japan

Department of Nephrology, First Hospital of China Medical University, No.155 North Nanjing Street, Heping District, Shenyang, Liaoning 110001, China
e-mail: lzl1017@yahoo.com

N. Terada
Division of Health Sciences, Shinshu University Graduate School of Medicine, 3-1-1 Asahi, Matsumoto City, Nagano 390-8621, Japan

Department of Anatomy and Molecular Histology, Interdisciplinary Graduate School of Medicine and Engineering, University of Yamanashi, 1110 Shimokato, Chuo City, Yamanashi 409-3898, Japan

N. Ohno • S. Ohno
Department of Anatomy and Molecular Histology, Interdisciplinary Graduate School of Medicine and Engineering, University of Yamanashi, 1110 Shimokato, Chuo City, Yamanashi 409-3898, Japan
e-mail: nobuot@shinshu-u.ac.jp; nohno@yamanashi.ac.jp
sohno@yamanashi.ac.jp

S. Ohno et al. (eds.), *In Vivo Cryotechnique in Biomedical Research and Application for Bioimaging of Living Animal Organs*, DOI 10.1007/978-4-431-55723-4_20

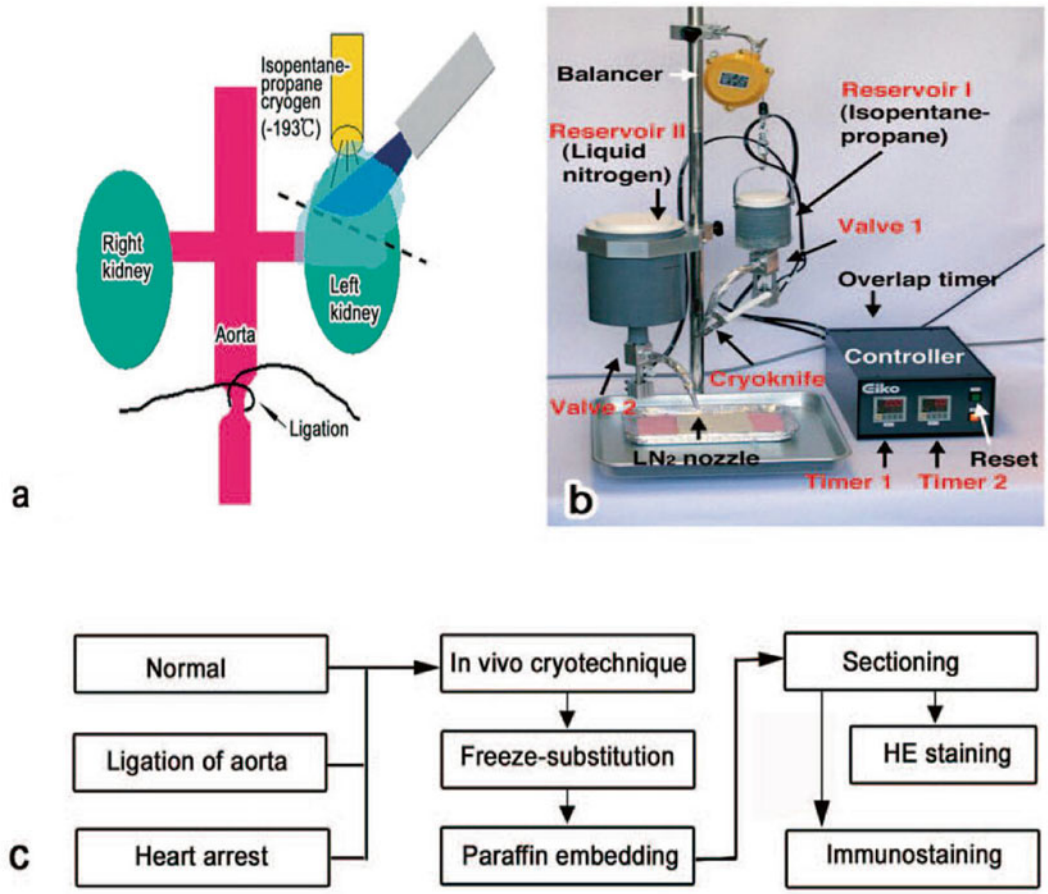

Fig. 20.1 (**a**) A schematic drawing of "in vivo cryotechnique" for mouse kidneys under acute hypertensive condition. The abdominal aorta is ligated by thin thread just below both renal arteries. A left kidney is directly frozen in vivo with a cryoknife, and the isopentane-propane cryogen (−193 °C) precooled in liquid nitrogen is simultaneously poured over the cryocut kidney under the "in vivo cryoapparatus," as shown in (**b**). (**c**) After the "in vivo cryotechnique," the frozen specimen is processed for immunohistochemistry, as following in the *flowchart*

first experimental group of four mice to examine the glomerular leakage and subsequent reabsorption of serum proteins in renal tubules, a mouse model with acute renal hypertension was prepared by ligation of the abdominal aorta just below branching renal arteries for 10 min [1, 5, 6] (Fig. 20.1). To examine the immunolocalization of serum proteins in kidneys under a heart-arrest condition as the second experimental group of four mice, the blood flow into kidneys was stopped due to heart arrest with overdoses of the injected anesthetic.

Then the "in vivo cryotechnique" was performed under such various blood flow conditions as described in the previous paragraph. Briefly, a cryoknife edge precooled in liquid nitrogen (−196 °C) was positioned over the left kidney (Fig. 20.1a). The mouse kidney was cut with the cryoknife edge, and liquid isopentane-propane cryogen (−193 °C) was simultaneously poured over it with an assistance of the "in vivo cryoapparatus" (VI-11; Eiko Engineer Co. Ibaraki, Japan) (Fig. 20.1b), which had been already invented for the purpose of "in vivo cryotechnique" [7]. The frozen kidneys were carefully trimmed out with a dental drill in liquid nitrogen and then processed for the following freeze-substitution step (Fig. 20.1c), as reported before [1–3].

20.3 Immunolocalization of Albumin and IgG in Renal Proximal Tubules

To examine the glomerular leakage and reabsorption of serum proteins in renal proximal tubules, the immunohistochemistry for albumin and IgG was performed on paraffin sections prepared by the "in vivo cryotechnique" (Fig. 20.2). Under the acute hypertensive condition, however, in addition to the similar immunolocalization under the normotension, both albumin (Fig. 20.2b, c) and IgG (Fig. 20.2e, f) were clearly immunolocalized along cell membranes containing apical brush borders and also in the apical cytoplasm of most proximal tubules (Fig. 20.2c, f).

20.4 Immunolocalization of IgG Light or Heavy Chains in Proximal Tubules

To examine whether IgGs with the full molecular length were leaked out through glomerular capillary loops under the acute hypertensive condition, another immunostaining analysis for

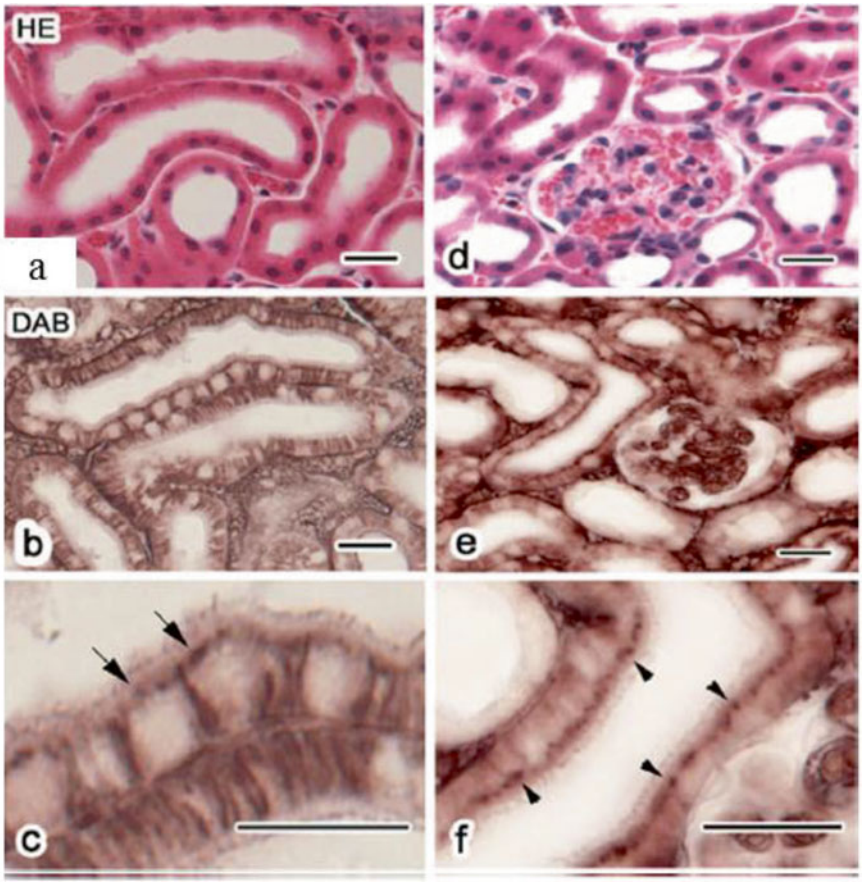

Fig. 20.2 Immunohistochemical localization of albumin (**a**-**c**) and IgG (**d**-**f**) in mouse kidneys under the acute hypertensive condition, as revealed by the "in vivo cryotechnique" (**a** and **d**, *HE* staining; **b** and **e**, peroxidase-*DAB*; **c** and **f**, higher magnified image). Under the acute hypertension, the immunolocalization of both albumin and IgG is clearly observed along the basolateral cell membranes and also in the apical cytoplasm of almost all proximal tubules (**b**, **c**, **e**, **f**). *Scale bar* 20 μm

the IgG light or heavy chain was performed, respectively, on serial paraffin sections (Fig. 20.3). In the cortex of mouse kidneys under such acute hypertension, both kappa (Fig. 20.3b) and lambda (date not shown) light chains' immunolabeling was clearly detected along the apical cell membranes of almost all proximal tubules, in the similar way to those revealed with the antibody against the full-length IgG described in the previous section. To the contrary, the antibody against the IgG1 heavy chain was not immunoreacted in such proximal tubular areas, but in the blood vessels and the interstitium (Fig. 20.3c).

20.5 Concluding Remarks

Under such an acute hypertensive condition, a high glomerular blood capillary pressure mechanically changed the passage barriers of molecular sieves in the glomerular basement membrane, as already observed at an electron microscopic level by the "in vivo cryotechnique" [1–3]. This high pressure of glomerular blood capillaries impaired the size-selective barrier function of the slit diaphragm and glomerular basement membrane, so that serum protein contents in the glomerular filtrate were probably increased, which in turn caused the active reabsorption of such filtered serum proteins, such as albumin and light chains of IgG, in proximal tubular epithelial cells, as shown in Fig. 20.2c, f [8–10].

We have also demonstrated the different immunolocalization between kappa or lambda light chains and heavy chains of IgG in the proximal tubules of living mouse kidneys under the hypertensive condition, as shown in Fig. 20.3. The kappa and lambda light chains were clearly immunolocalized in the apical cytoplasm of almost all proximal tubules, but no heavy chain of IgG immunostaining was observed in such areas (Fig. 20.3c). These findings indicate that low molecular weight proteins, such as light chains of IgG and serum albumin, easily leak in vivo through the glomerular basement membrane and also slit diaphragms and then are reabsorbed in the proximal tubules under the acute hypertensive condition [11, 12]. Some IgGs were reported to be extensively trapped in the glomerular basement membranes under some pathological conditions, such as membranoproliferative glomerulonephritis, membranous nephropathy, and lupus nephritis [13, 14]. In such cases, they may be difficult to be leaked out into Bowman's spaces, because of their large molecular chain structure and immune complexes.

In conclusion, the present "in vivo cryotechnique" followed by the freeze-substitution method can provide dynamically changing images of living animal renal tissues and also allows us to examine the in vivo distribution of filtered serum proteins and their reabsorption in the renal tubules. The present figures were already published in our paper, Histol Histopathol (2005) 20:807–816, and cited with their permissions.

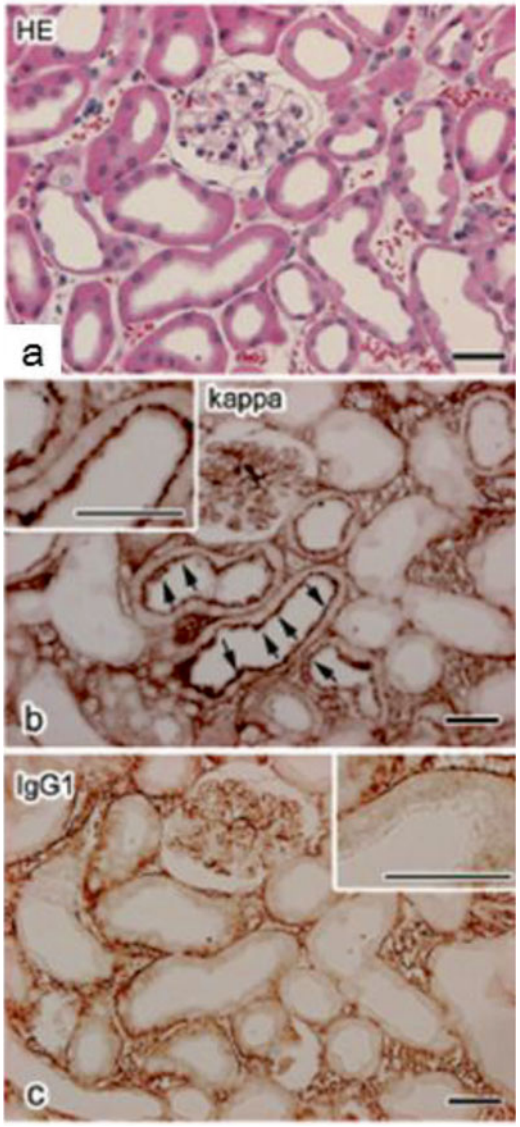

Fig. 20.3 Light micrographs of mouse renal cortices on serial sections by HE staining (**a**) and immunolabeled by two kinds of antibodies against kappa light chain (**b**) and IgG1 heavy chain (**c**) under the acute hypertensive condition. Strong immunolabeling of the kappa light chain is observed in the apical cytoplasm of almost all proximal tubules (**b**). To the contrary, the IgG1 heavy chain is not seen to be localized in the apical cytoplasm of the proximal tubules (**c**), but in the glomerular blood capillaries and blood vessels in the interstitium between the renal tubules. *Scale bar* 20 μm

References

1. Ohno S, Terada N, Fujii Y, Ueda H, Takayama I (1996) Dynamic structure of glomerular capillary loop as revealed by an in vivo cryotechnique. Virchows Arch 427:519–527
2. Ohno S, Baba T, Terada N, Fujii Y, Ueda H (1996) Cell biology of kidney glomerulus. Int Rev Cytol 166:181–230
3. Ohno S, Kato Y, Xiang T, Terada N, Takayama I, Fujii Y, Baba T (2001) Ultrastructural study of mouse renal glomeruli under various hemodynamic conditions by an "in vivo cryotechnique". Ital J Anat Embryol 106:431–438
4. Exaire E, Pollak VE, Pesce AJ, Ooi BS (1972) Albumin and globulin in the nephron of the normal rat and following the injection of aminonucleoside. Nephron 9:42–54
5. Roman RJ, Cowley AW Jr (1985) Characterization of a new model for the study of pressure-natriuresis in the rat. Am J Physiol 248:190–198
6. Zhang Y, Magyar CE, Norian JM, Holstein-Rathlou NH, Mircheff AK, McDonough AA (1998) Reversible effects of acute hypertension on proximal tubule sodium transporters. Am J Physiol Cell Physiol 274:1090–1100
7. Zea-Aragon Z, Terada N, Ohno N, Fujii Y, Baba T, Ohno S (2004) Effects of anoxia on serum immunoglobulin and albumin leakage through blood–brain barrier in mouse cerebellum as revealed by cryotechniques. J Neurosci Methods 138:89–95
8. Birn H, Fyfe JC, Jacobsen C, Mounier F, Verroust PJ, Orskov H, Willnow TE, Moestrup SK, Christensen EI (2000) Cubilin is an albumin binding protein important for renal tubular albumin reabsorption. J Clin Invest 105:1353–1361
9. Remuzzi G, Bertani T (1998) Pathophysiology of progressive nephropathies. N Engl J Med 339:1448–1456
10. Brunskill NJ (2000) Albumin and proximal tubular cells—beyond endocytosis. Nephrol Dial Transplant 15:1732–1734
11. Batuman V, Dreisbach AW, Cyran J (1990) Light-chain binding sites on renal brush-border membranes. Am J Physiol Renal Physiol 258:1259–1265
12. Batuman V, Guan S (1997) Receptor-mediated endocytosis of immunoglobulin light chains by renal proximal tubule cells. Am J Physiol Renal Physiol 272:521–530
13. Bijl M, Dijstelbloem HM, Oost WW, Bootsma H, Derksen RHWM, Aten J, Limburg PC, Kallenberg CGM (2002) IgG subclass distribution of autoantibodies differs between renal and extra-renal relapses in patients with systemic lupus erythematosus. Rheumatology 41:62–67
14. Imai H, Hamai K, Komatsuda A, Ohtani H, Miura AB (1997) IgG subclasses in patients with membranoproliferative glomerulonephritis, membranous nephropathy, and lupus nephritis. Kidney Int 51:270–276

Application of Novel "In Vivo Cryotechnique" in Living Animal Kidneys

21

Zilong Li, Xiaoyue Zhai, Nobuhiko Ohno, Nobuo Terada, and Shinichi Ohno

Abstract

To compare the influence of the different fixation procedures on the distribution of endogenous proteins of albumin and IgG in mouse glomeruli and identify the advantage of tissue fixation method in living mouse renal glomeruli by "in vivo cryotechnique" (IVCT), four different fixation methods were performed in mouse kidney tissues, such as (i) conventional immersion or (ii) quick-freezing following resected kidney tissues, (iii) quick-freezing following perfusion-fixation, and (iv) "in vivo cryotechnique" for living mouse kidneys. Kidney glomeruli were noticeably contracted after conventional immersion-fixation or quick-freezing following resection compared to glomeruli from tissues preserved by the IVCT. With the IVCT, both albumin and IgG were colocalized exclusively along or within the glomerular capillary loops; however, immunoreactivity of these proteins in the other three methods was clearly detected in Bowman's space and apical cytoplasm of the proximal tubules. With the IVCT, immunoreactivity of collagen type IV was very weak at the glomerular basement membrane (GBM) until microwave treatment, which increased its immunoreactivity. Using conventional fixation method, aquaporin-1 (AQP-1) is abundant in the apical and basolateral membranes of renal proximal tubules and descending thin limbs, but the proteins were prominent immunolocalization on the apical areas by "in vivo cryotechnique." The "in vivo cryotechnique" should be a reliable tool to maintain soluble serum proteins and AQP-1 in situ and capture transient images of functioning kidney in living mice.

Keywords

In vivo cryotechnique • Fixation procedures • Mouse kidney tissues

Z. Li, M.D., Ph.D. (✉)
Department of Nephrology, First Hospital of China Medical University, No.155 North Nanjing Street, Heping District, Shenyang, Liaoning 110001, China
e-mail: lzl1017@yahoo.com

X. Zhai
Department of Nephrology, China Medical University, Shenyang, People's Republic of China

N. Ohno • S. Ohno
Department of Anatomy and Molecular Histology, Interdisciplinary Graduate School of Medicine and Engineering, University of Yamanashi, 1110 Shimokato, Chuo City, Yamanashi 409-3898, Japan
e-mail: nobuot@shinshu-u.ac.jp; nohno@yamanashi.ac.jp
sohno@yamanashi.ac.jp

21.1 Introduction

Immersion-fixation and perfusion-fixation are well known to be tissue fixation techniques that have been applied widely in clinical and experimental research. However, these fixation procedures usually cause transient ischemia and hypoxia and

N. Terada
Division of Health Sciences, Shinshu University Graduate School of Medicine, 3-1-1 Asahi, Matsumoto City, Nagano 390-8621, Japan

Department of Anatomy and Molecular Histology, Interdisciplinary Graduate School of Medicine and Engineering, University of Yamanashi, 1110 Shimokato, Chuo City, Yamanashi 409-3898, Japan

S. Ohno et al. (eds.), *In Vivo Cryotechnique in Biomedical Research and Application for Bioimaging of Living Animal Organs*, DOI 10.1007/978-4-431-55723-4_21

translocation of components in cells and tissues, which can lead to changes in the tissues' construction and function [1, 2]. Furthermore, renal glomerular selectivity for permeable serum solutes and translocation of filtered serum proteins have never been directly visualized on paraffin sections by light microscopy (LM) due to the technical limitations in preparing specimens for immunohistochemistry using routine fixation methods. The common fixatives in buffer solution, such as glutaraldehyde and paraformaldehyde, need considerable time to completely cross-link and preserve the soluble substances during routine perfusion-fixation or immersion-fixation. Many of these soluble substances are washed from the specimens, and the translocation of soluble serum proteins occurs during the fixation period. In addition, the specimens from freeze-substitution technique are routinely embedded in paraffin wax, presumably leaving many antigenic sites exposed due to formation of tiny ice crystals in the frozen cells and tissues [3, 4]. To adequately define the functional structures of tissues and cells in vivo, the in situ preservation of cells and tissues in living animal organs is necessary. We previously developed the "in vivo cryotechnique"(IVCT) [5–7], which is designed to transiently arrest dynamic structures in living animal organs by the combination of a cryoknife precooled in liquid nitrogen (−196 °C) and liquid isopentane-propane cryogen (−193 °C). With this technique, all biological processes in living animal organs instantly stop and are embedded in the ice microenvironment while maintaining all their functional components in situ [2, 6].

In the present, the periodic acid-Schiff (PAS) staining was clearly detected in the specimens prepared by the "in vivo cryotechnique." Therefore, we have used the conventional PAS staining with its fluorescence emission as a marker for GBM. We compared the fluorescence emission of PAS staining with immunofluorescence of serum proteins, on the same section to analyze their distribution in the living mouse kidneys. On the other hand, the localization of AQP-1 in proximal tubules has never been directly visualized on paraffin sections by "in vivo cryotechnique."

21.2 PAS Staining and Immunolocalization of Albumin and IgG in Glomeruli

To visualize topographical migrations of serum proteins such as albumin or IgG passing through GBM filtration barriers under various fixation conditions, we used the PAS fluorescence emission as a marker for the GBM in combination with immunostaining for several serum proteins on the same sections. Under normotensive condition, immunoreaction products of both albumin and IgG were exclusively colocalized along or within the GCL, and only IgG immunolocalization was also seen in some mesangial areas. Neither albumin nor IgG was immunolocalized in Bowman's space. On the contrary, under quick-freezing after tissue resection and conventional immersion-fixation conditions, immunoreaction products of both albumin and IgG were found to be localized in Bowman's space. Under quick-freezing following perfusion-fixation condition, however, both of albumin and IgG were partially washed out and immunostaining was weakly detected in glomerular blood capillary loops than that under other conditions due to the perfusion-fixation. In addition, the immunostaining of both albumin and IgG was more clearly seen on apical cell membranes of proximal convoluted tubules and some Bowman's spaces at the artificial state washing out all of the circulating proteins (Fig. 21.1).

Under the normotensive condition by "in vivo cryotechnique," the immunofluorescence for albumin and IgG was exclusively detected in GCL with little colocalization with the PAS fluorescence emission, and IgG was also at MA. To the contrary, under the quick-freezing of resected kidney tissues or with immersion-fixation condition, both of the albumin and IgG immunoreactivity were also detected in Bowman's space. These findings suggest that some amounts of albumin or IgG, which are almost kept within GCL under the normotensive condition, easily pass through the GBM and translocate into Bowman's space under the quick-freezing of resected kidney tissues or immersion-fixation condition (Fig. 21.2).

21.3 Metal-Enhanced 3,3′-Diaminobenzidine (DAB) Staining of Collagen Type IV and Aquaporin-1(AQP-1) in Living Mouse Glomeruli and Proximal Tubules

The common HE staining was performed to examine native morphology in the living mouse kidneys, as obtained by the "in vivo cryotechnique." Well-preserved areas of renal cortices under normotensive conditions could be obtained within 300–400 μm from the frozen surface tissues without visible ice crystals at a light microscopic level, and the GCLs are kept open. Although collagen type IV is reported to be clearly immunolocalized in the GBM and MAs after a conventional fixation method, when we employed the "in vivo cryotechnique," we found marked immunolocalization of collagen type IV in the MAs, but only weakly immunolocalized on the GBM. To visualize the expression of water channel AQP-1 in living mouse proximal tubules, the immunostaining for AQP-1 was performed, respectively, on paraffin section with "in vivo cryotechnique" and perfusion-fixation methods. Using perfusion-fixation method, the immunoreaction product of AQP-1 was observed clearly along the basolateral membrane of proximal tubule, and its distribution was disorganized and irregular on the brush border and apical cell membrane along the proximal tubule due to the artificial state (Fig. 21.3).

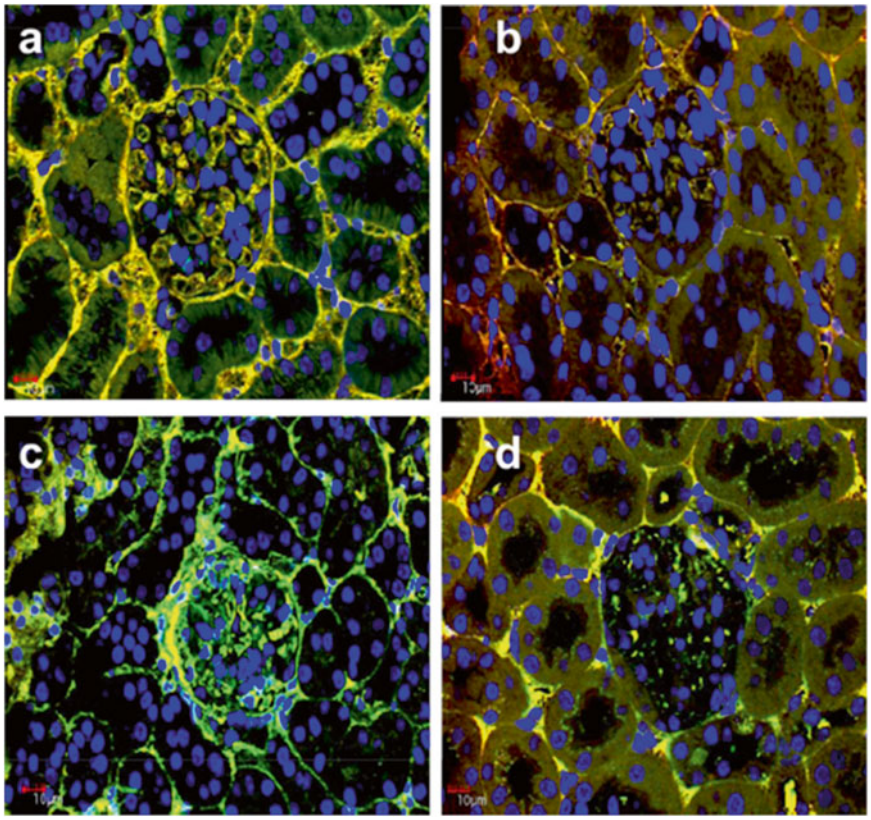

Fig. 21.1 Confocal laser scanning micrographs showing the distribution of endogenous albumin (*red color*) and IgG (*green color*) in living mouse glomeruli under four different fixation methods. (**a**) Both albumin and IgG were exclusively colocalized along or within the glomerular capillary loops (*GCLs*) with the "in vivo cryotechnique" (*IVCT*), (**b**) under quick-freezing following resection (*QF*), and (**c**) conventional immersion-fixation (*IF*); (**d**) we found both albumin and IgG in Bowman's space. Under quick-freezing following perfusion-fixation (*PF*), we detected a weak indication of both albumin and IgG in the GCLs, but more clearly detected these proteins in Bowman's space and on apical cell membranes of proximal convoluted tubules. *Scale bars* 10 mm

21.4 Concluding Remarks

The fluorescence emission of PAS staining allowed us to examine the precise immunolocalization of serum proteins at the GBM under various hemodynamic conditions of living mouse kidneys in combination with the "in vivo cryotechnique" followed by freeze substitution. In addition, the "in vivo cryotechnique" would be a reliable tool to observe soluble serum proteins and water channel AQP-1 in situ and capture transient images of functioning glomeruli in the living mice [1, 2, 5, 7–9]. The present figures were already published in our paper, Microsc Res Tech (2013) 76:113–120, and cited with their permissions.

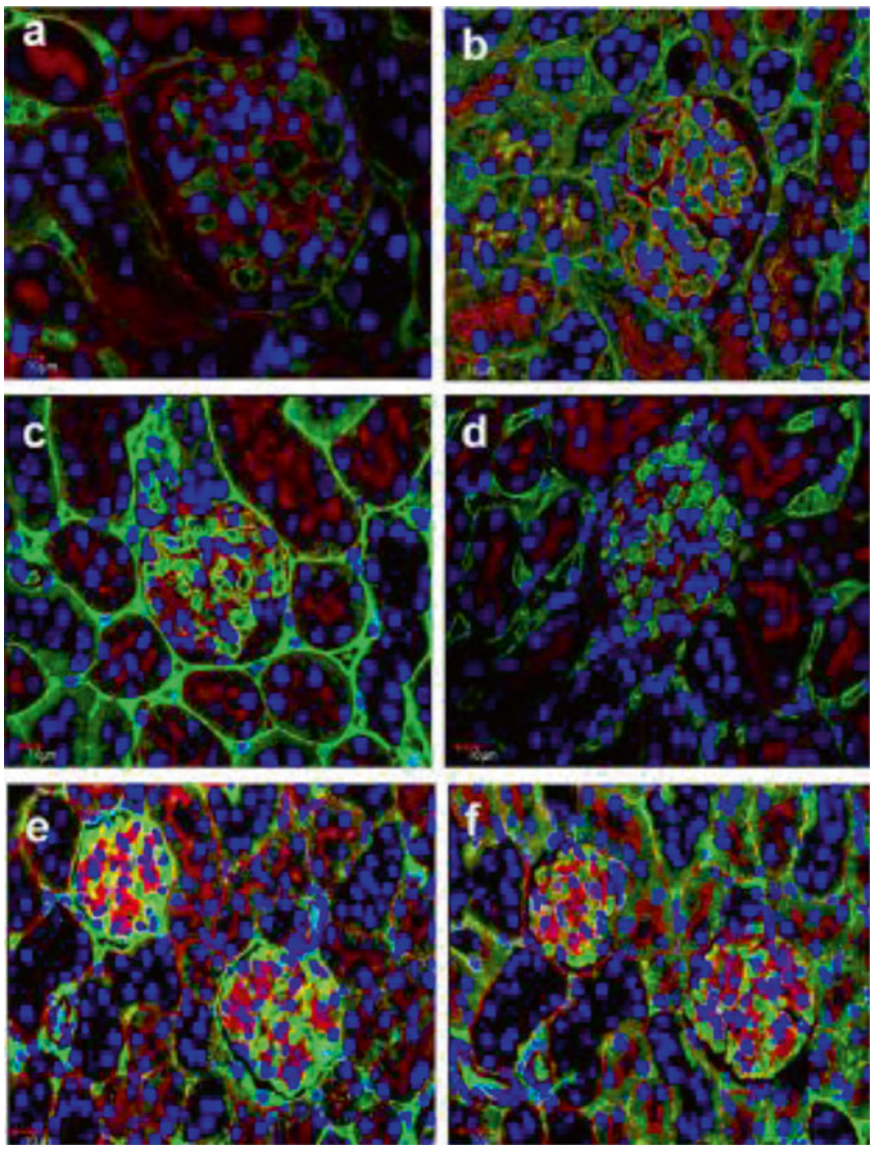

Fig. 21.2 Confocal laser scanning micrographs showing albumin or IgG (*green color*) passing through GBM filtration barriers under various fixation conditions using the PAS fluorescence emission (*red color*) as a marker for the GBM. With the IVCT (**a**, **b**), the immunofluorescence for albumin and IgG was exclusively detected in GCLs with little colocalization with the PAS fluorescence emission, and IgG was also in mesangial areas (**b**). After QF (**c**, **d**) or IF (**e**, **f**), both albumin and IgG immunoreactivities were detected in Bowman's space on the opposite side of the GCLs and bordered by the PAS-positive GBM. The overlapping images of albumin or IgG immunoreactivity with PAS fluorescence emission, represented by a *yellow color*, was more widely apparent with IF (**e**, **f**) than with QF (**c**, **d**). Scale bars 10 mm

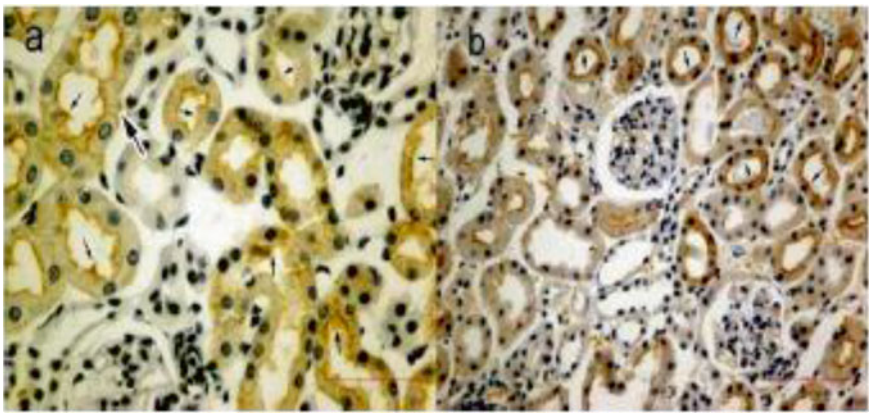

Fig. 21.3 Light micrographs showing immunolocalization of aquaporin-1 (AQP-1) in living mouse proximal tubules on paraffin section. Under PF, AQP-1 had a disorganized and irregular distribution on the brush border and apical cell membrane along the proximal tubules and was also clearly found along the basolateral membrane of the proximal tubules, which is an artificial state (**a**). With the IVCT, AQP-1 was labeled intensely and regularly on the brush border and apical cell membrane along the proximal tubules, but only weakly labeled along the basolateral membrane. There was also little immunostaining detected in the initial part of the proximal tubules (**b**)

References

1. Li Z, Ohno N, Terada N, Ohno S (2006) Immunolocalization of serum proteins in living mouse glomeruli under various hemodynamic conditions by "in vivo cryotechnique". Histochem Cell Biol 126(3):399–406
2. Ohno S, Terada N, Ohno N, Saitoh S, Saitoh Y, Fujii Y (2010) Significance of "in vivo cryotechnique" for morphofunctional analyses of living animal organs. J Electron Microsc (Tokyo) 59(5):395–408
3. Bridgman PC, Dailey ME (1989) The organization of myosin and actin in rapid frozen nerve growth cones. J Cell Biol 108(1):95–109
4. Ohno N, Terada N, Murata S, Katoh R, Ohno S (2005) Application of cryotechniques with freeze-substitution for the immunohistochemical demonstration of intranuclear pCREB and chromosome territory. J Histochem Cytochem 53(1):55–62
5. Ohno S, Terada N, Fujii Y, Ueda H, Takayama I (1996) Dynamic structure of glomerular capillary loop as revealed by an in vivo cryotechnique. Virchows Arch 427(5):519–527
6. Terada N, Ohno N, Li Z, Fujii Y, Baba T, Ohno S (2005) Detection of injected fluorescence-conjugated IgG in living mouse organs using "in vivo cryotechnique" with freeze-substitution. Microsc Res Tech 66(4):173–178
7. Terada N, Ohno N, Li Z, Fujii Y, Baba T, Ohno S (2006) Application of in vivo cryotechnique to the examination of cells and tissues in living animal organs. Histol Histopathol 21(3):265–272
8. Zhai XY, Fenton RA, Andreasen A, Thomsen JS, Christensen EI (2007) Aquaporin-1 is not expressed in descending thin limbs of short-loop nephrons. J Am Soc Nephrol 18(11):2937–2944
9. Mobasheri A, Marples D (2004) Expression of the AQP-1 water channel in normal human tissues: a semiquantitative study using tissue microarray technology. Am J Physiol Cell Physiol 286(3):C529–C537

Application of Periodic Acid-Schiff Fluorescence Emission for Immunohistochemistry of Living Mouse Renal Glomeruli

22

Zilong Li, Nobuo Terada, and Shinichi Ohno

Abstract

Glomerular basement membrane (GBM) plays a critical role in preventing serum protein leakage into Bowman's space. By using "in vivo cryotechnique (IVCT)," the periodic acid-Schiff (PAS) fluorescence emission was well-represented GBM instead of immunostaining of collagen type IV, which was difficult to observe without the microwave treatment in specimens. Serum protein distribution in living mouse glomeruli was better visualized with IVCT compared with other conventional methods. Under normal condition, immunoreaction products of albumin and immunoglobulin G heavy and light chains (IgG (H+L)) were localized within glomerular capillary loops (GCL) but not colocalized with the PAS fluorescence emission of the GBM. Under heart-arrest condition and with quick-freezing of resected tissues, albumin, IgG (H+L), immunoglobulin kappa light chain, and IgG1 heavy chain (IgG1) were immunolocalized within GCL and mesangial areas, but only albumin and kappa light chain were additionally immunolocalized in Bowman's space, indicating their passage through GBM. Under acute hypertensive condition, both albumin and kappa light chain, but not IgG1, were clearly immunolocalized along GBM and in Bowman's space, indicating their increased passage through GBM. The overlapped areas of PAS fluorescence emission and albumin or kappa light chain were appeared to be larger with quick-freezing and under the heart-arrest or acute hypertensive condition than under normal circulation, whereas those of PAS emission and IgG1 were not different among those conditions. These results suggest that PAS fluorescence emission combined with IVCT allowed us to investigate the serum proteins passing through GBM induced by hemodynamic changes.

Keywords

Glomerular basement membrane • Serum proteins • Hemodynamic changes • In vivo cryotechnique • PAS fluorescence emission

Z. Li, M.D., Ph.D. (✉)
Department of Nephrology, The First Hospital of China Medical University, No.155 North Nanjing Street, Heping District, Shenyang, Liaoning 110001, China

Department of Anatomy, Interdisciplinary Graduate School of Medicine and Engineering, University of Yamanashi, Chuo City, Yamanashi 409-3898, Japan
e-mail: lzl1017@yahoo.com

N. Terada
Division of Health Sciences, Shinshu University Graduate School of Medicine, 3-1-1 Asahi, Matsumoto City, Nagano 390-8621, Japan

Department of Anatomy and Molecular Histology, Interdisciplinary Graduate School of Medicine and Engineering, University of Yamanashi, 1110 Shimokato, Chuo City, Yamanashi 409-3898, Japan

S. Ohno
Department of Anatomy, Interdisciplinary Graduate School of Medicine and Engineering, University of Yamanashi, Chuo City, Yamanashi 409-3898, Japan
e-mail: nobuot@shinshu-u.ac.jp; sohno@yamanashi.ac.jp

S. Ohno et al. (eds.), *In Vivo Cryotechnique in Biomedical Research and Application for Bioimaging of Living Animal Organs*, DOI 10.1007/978-4-431-55723-4_22

22.1 Introduction

The hemodynamic changes in animal kidneys are well known to cause abnormal leakage of serum proteins through glomerular filtration barriers, leading to proteinuria, which is closely related to progression of renal diseases in experimental animal studies and clinical human cases [1, 2]. The charge- and size-selective glomerular filtration barriers against serum proteins were composed of highly fenestrated endothelium, glomerular basement membranes (GBM), and podocytes [3, 4]. Although there are some evidences [1, 5] suggesting key roles of GBM for the filtration barriers of serum proteins, one of the technical problems to reveal the immunolocalization of serum proteins would be due to their preparation procedures of the in situ drip-fixation with aqueous aldehyde fixatives [6].

The "in vivo cryotechnique" (IVCT) has been already developed for the past decade [7–9], which is designed to capture transiently dynamic morphology of living animal organs. Using IVCT followed by freeze substitution, the diffusion of soluble components would be mostly restricted [10], and many antigenic sites would be exposed in the frozen cells and tissues [11]. However, in living mouse kidney specimens prepared by IVCT, collagen type IV, laminin 5, fibronectin, and perlecan, the widely used markers for GBM [12–15], were not clearly immunostained. To elucidate the distribution alternation of serum proteins in living mouse kidney under various hemodynamic conditions, the fluorescence emission of periodic acid-Schiff (PAS) staining was utilized for representing GBM, and serum protein immunolocalizations were examined in living mouse kidneys by IVCT.

22.2 Application of PAS Fluorescence Emission for Glomerular Basement Membrane

The PAS staining of nephrons is specific for glomerular or tubular basement membranes, mesangial areas (MA), and proximal tubular brush borders in living mouse kidneys [16]. By using the common PAS staining (Fig. 22.1a) followed with immunostaining for zonula occludens-1 (ZO-1) (Fig. 22.1c), a specific marker of foot processes in glomeruli [17–20], the PAS fluorescence emission can be shown to be

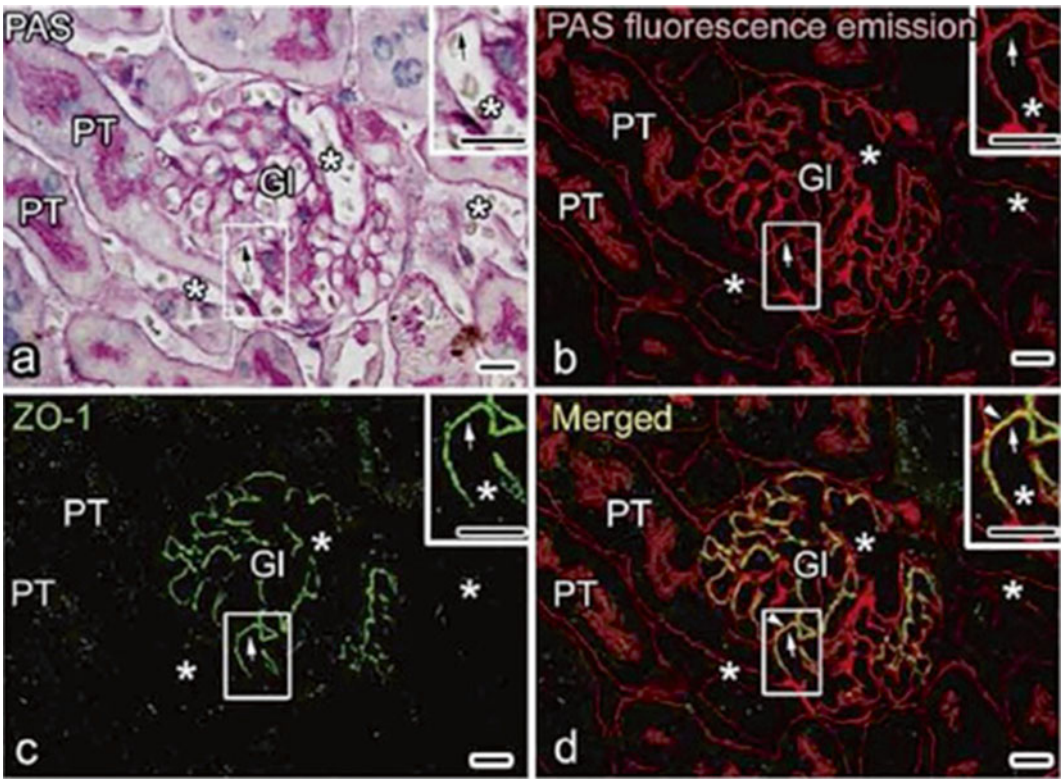

Fig. 22.1 Representative light micrograph (**a**) and confocal laser scanning micrographs (**b–d**) showing periodic acid-Schiff staining (*PAS*; **a**), its fluorescence emission (*PAS fluorescence emission*; **b**), and immunofluorescence staining for zonula occludens-1 (*ZO-1*; **c**) on the same section prepared by "in vivo cryotechnique" under the normotensive condition. The layer at glomerular basement membrane positive for PAS fluorescence emission mostly surrounds the glomerular capillary loops and closely localizes near the foot process layers visualized by the ZO-1 immunostaining (**d**, *arrows* and *arrowheads*). *Gl* glomeruli, *PT* proximal tubules, *asterisks* blood capillaries. *Scale bars* 10 μm

localized at the GBM and MA in the glomerulus (Fig. 22.1b). The fluorescence-merged image clearly showed that the immunofluorescence for ZO-1 mostly outlines the PAS fluorescence emission of the GBM (Fig. 22.1d), indicating fluorescence emission of PAS was effectively represented GBM. The immunostaining for GBM with specific antibodies against collage type IV was hardly successful in the specimens prepared with the IVCT (unpublished data), although the immunoreactivity of collagen type IV was increased at GBM after the microwave treatment on paraffin sections prepared with IVCT. The differences in "immunoreactivity" would be due to that small reagents in the PAS staining processes could be easily bound to the target molecular sites of the compact GBM with serum proteins, whereas larger molecules of antibodies were difficult to reach them using IVCT followed by freeze substitution.

22.3 Alternation of Serum Protein Distribution in Glomeruli Under Various Hemodynamic Conditions

As PAS fluorescence emission has been well identified to represent GBM, the distribution of serum proteins in living mouse glomeruli could be estimated by comparing the immunolocalization of serum proteins and GBM using PAS fluorescence emission combined with IVCT. Serial sections of kidneys under different hemodynamic conditions were prepared with IVCT and immunostained to detect the distribution of albumin, immunoglobulin G heavy and light chains (IgG (H+L)), as well as the kappa light chain and IgG1 heavy chains (IgG1) (Fig. 22.2).

Under normal hemodynamic condition, both serum albumin and IgG were almost kept within GCL (Fig. 22.2a, e), and their immunoreactivity was more widely overlapped with the PAS fluorescence emission under the acute hypertensive condition (Fig. 22.2d, h). Although the main filtration barrier was reported to be GBM itself by electron microscopy [5, 21], other reports also demonstrated that slit diaphragms of foot processes formed the ultimate filtration barrier for macromolecular permeability [22, 23]. Considering these previous reports, our findings suggest that more serum proteins reached the outer layer of GBM under the acute hypertensive condition and the slit diaphragms would play a significant role especially in such pathological or physiological states. The translocation of serum proteins may be due to the acutely increased pressures in the GCL, and if the blood pressures were temporarily so high, lots of serum proteins would leak out into Bowman's space.

Under abnormal conditions, the leakage of albumin (Fig. 22.2b–d) and kappa light chain (Fig. 22.2j–l), but not IgG1 (Fig. 22.2n–p), was clearly detected in Bowman's space. Serum proteins with low molecular weights, such as albumin and kappa light chains, could easily translocate to the urinary space and reabsorbed in the convoluted proximal tubules [24–27]. On the other hand, larger or cationic molecules, such as IgGs, were trapped in the GBM and hardly leaked out into Bowman's spaces under some physiological or pathological conditions, such as membranoproliferative glomerulonephritis, membranous nephropathy, and lupus nephritis [28–30]. The differences of protein immunolocalization are undoubtedly due to the size and charge selectivity of the GBM [31].

In the present experiment, the overlapping of PAS fluorescence emission with the IgG (H+L) immunoreactivity close to Bowman's space appeared to be prominent at some parts on one side of the GCL under the acute hypertensive condition (Fig. 22.2h). As such heterogeneity of leaking areas was also observed using extrinsic tracers [21], the leakage degree of serum proteins would exhibit their heterogeneous immunolocalizations not only among glomeruli but also among GCL under the acute hypertensive condition.

The leakage of both albumin and IgG (H+L) through GBM into Bowman's spaces was detected under the heart-arrest condition (Fig. 22.2b, f) or with the quick-freezing of the resected kidney tissues (Fig. 22.2c, g), which might be caused by low blood pressures and ischemia, resulting in serious alteration of GCL structures and molecular organization [5, 32]. Moreover, the ischemia or hypoxia, including the hypotensive condition, was reported to induce changes of the glomerular structures and also damages of intercellular junctions in renal vasculatures, resulting in the increased vascular permeability and local interstitial edema of kidneys [7, 33–35].

22.4 Concluding Remarks

In conclusion, the fluorescence emission of PAS staining allowed us to examine the precise immunolocalization of serum proteins at the GBM under various hemodynamic conditions of living mouse kidneys in combination with the IVCT followed by freeze substitution. In addition, the IVCT would be a reliable tool to observe soluble serum proteins in situ and capture transient images of functioning glomeruli in the living mice. Further detailed analyses, e.g., by using immunoelectron microscopy in conjunction with the "in vivo cryotechnique," would enable us to characterize the changes of soluble serum proteins around GBM, which may be new findings of clinical importance. The present figures were already published in our paper, Arch Histol Cytol (2006) 69:147–161, and cited with their permissions.

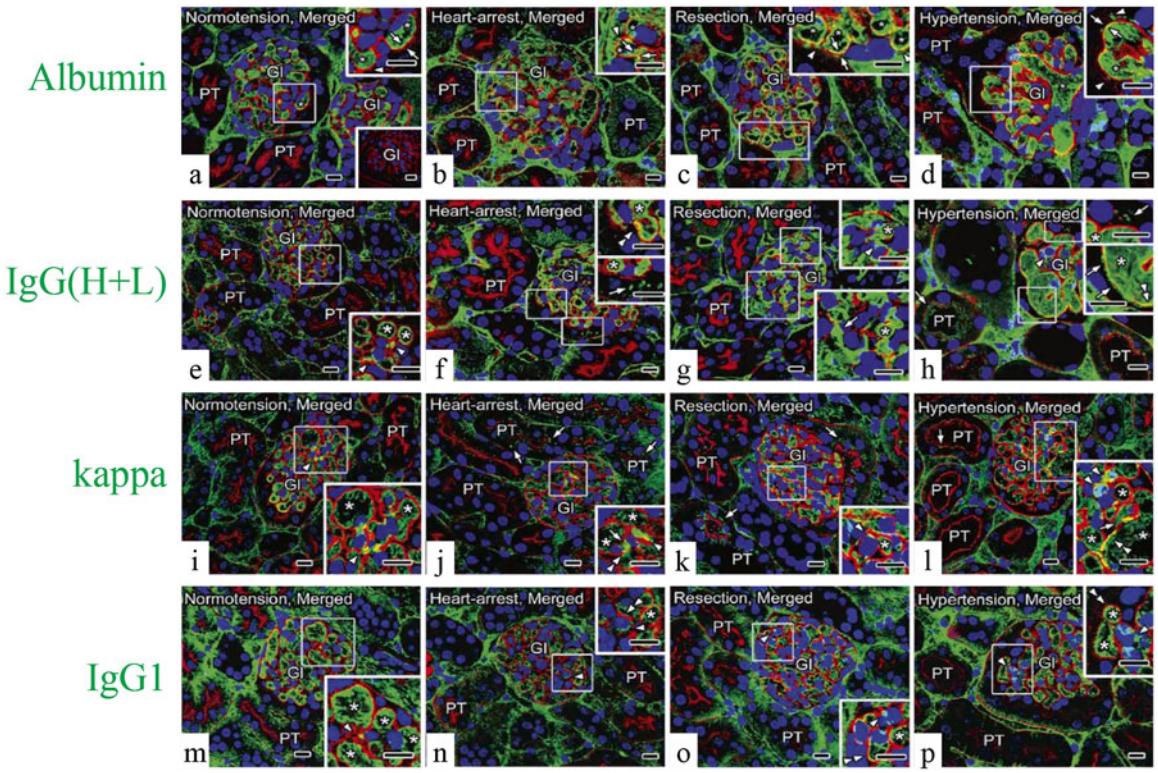

Fig. 22.2 Representative confocal laser scanning micrographs showing the alternation of serum protein (*green color*) distribution in living mouse kidney under various hemodynamic conditions using PAS fluorescence emission (*red color*). Nuclei are labeled with TO-PRO-3 (*blue color*). Under the normotensive condition (normotension), the immunolocalization of albumin (**a**) is primarily restricted within glomerular capillary loops (*GCL*; *arrowhead*) and slightly overlapped with the PAS fluorescence emission at glomerular basement membrane (*GBM*; *arrows*); immunolocalizations of immunoglobulin G high and light chains (IgG (H+L), **e**), the kappa light chain (kappa, **i**), and IgG1 heavy chain (IgG1, **m**) are detected within GCL and at some mesangial areas (*MA*; *arrowheads*). Under the heart-arrest condition (heart arrest) and in the kidney tissues quickly frozen after tissue resection (resection), the GCL are collapsed, and the leaked albumin is additionally immunolocalized in Bowman's space (**b** and **c**, *arrowheads*); immunoreaction products of IgG (H+L) are also localized in Bowman's space (**f** and **g**, *arrows*); kappa are clearly localized in Bowman's space and also proximal convoluted tubules (**j** and **k**, *arrows*); IgG1 are localized at MA (**n** and **o**, *arrowheads*), but neither in Bowman's space nor in proximal convoluted tubules. Under the acute hypertensive condition (hypertension), albumin is more clearly immunolocalized in Bowman's space (**d**, *arrowheads*); IgG (H+L) immunostaining is clearly detected in Bowman's space and also in proximal convoluted tubules (**h**, *arrows*); kappa is immunolocalized in Bowman's space (**l**, *right upper inset*, *arrows*), the MA (*arrowhead*), and the apical cytoplasm of some proximal tubules (*arrows*); IgG1 is detected exclusively within the GCL and at some MA (**p**, *arrowheads*), but not in Bowman's space. In addition, under the heart-arrest or acute hypertensive conditions and in the kidney tissues quickly frozen after tissue resection, the glomerular areas, where the immunoreactivity of albumin (**b**–**d**), IgG (H+L) (**f**–**h**), kappa (**j**–**l**), and PAS overlapped each other (*arrows*), respectively, appear to become wider than those under the normotensive condition (**a**, **e**, **i**, *arrows*), whereas the overlapping of IgG1 and PAS appears to be unchanged (**m**–**p**, *double arrowheads*). *Gl* glomeruli, *PT* proximal tubules, *asterisks* blood capillaries. *Scale bars* 10 μm

References

1. Olivetti G, Kithier K, Giacomelli F, Wiener J (1981) Glomerular permeability to endogenous proteins in the rat: effects of acute hypertension. Lab Invest 44:127–137
2. Remuzzi G, Bertani T (1998) Pathophysiology of progressive nephropathies. N Engl J Med 339:1448–1456
3. Reiser J, Kriz W, Kretzler M, Mundel P (2000) The glomerular slit diaphragm is a modified adherens junction. J Am Soc Nephrol 11:1–8
4. Rico M, Mukherjee A, Konieczkowski M, Bruggeman LA, Miller RT, Khan S, Schelling JR, Sedor JR (2005) WT1-interacting protein and ZO-1 translocate into podocyte nuclei after puromycin aminonucleoside treatment. Am J Physiol Renal Physiol 289:F431–F441
5. Fujigaki Y, Nagase M, Kobayasi S, Hidaka S, Shimomura M, Hishida A (1993) Intra-GBM site of the functional filtration barrier for endogenous proteins in rats. Kidney Int 43:567–574
6. Ryan GB, Karnovsky MJ (1976) Distribution of endogenous albumin in the rat glomerulus: role of hemodynamic factors in glomerular barrier function. Kidney Int 9:36–45
7. Ohno S, Terada N, Fujii Y, Ueda H, Takayama I (1996) Dynamic structure of glomerular capillary loop as revealed by an in vivo cryotechnique. Virchows Arch 427:519–527
8. Ohno N, Terada N, Fujii Y, Baba T, Ohno S (2004) "In vivo cryotechnique" for paradigm shift to "living morphology" of animal organs. Biomed Rev 15:1–19
9. Terada N, Ohno N, Li Z, Fujii Y, Baba T, Ohno S (2006) Application of in vivo cryotechnique to the examination of cells and tissues in living animal organs. Histol Histopathol 21:265–272

10. Bridgman PC, Dailey ME (1989) The organization of myosin and actin in rapid frozen nerve growth cones. J Cell Biol 108:95–109
11. Ohno N, Terada N, Murata S, Katoh R, Ohno S (2005) Application of cryotechniques with freeze-substitution for the immunohistochemical demonstration of intranuclear pCREB and chromosome territory. J Histochem Cytochem 53:55–62
12. Sorokin LM, Pausch F, Durbeej M, Ekblom P (1997) Differential expression of five laminin alpha (1-5) chains in developing and adult mouse kidney. Dev Dyn 210:446–462
13. Conde-Knape K (2001) Heparan sulfate proteoglycans in experimental models of diabetes: a role for perlecan in diabetes complications. Diabetes Metab Res Rev 17:412–421
14. van Vliet AI, van Alderwegen IE, Baelde HJ, de Heer E, Bruijn JA (2002) Fibronectin accumulation in glomerulosclerotic lesions: self-assembly sites and the heparin II binding domain. Kidney Int 61:481–489
15. Chow FY, Nikolic-Paterson DJ, Atkins RC, Tesch GH (2004) Macrophages in streptozotocin-induced diabetic nephropathy: potential role in renal fibrosis. Nephrol Dial Transplant 19:2987–2996
16. Nagato Y, Mitsui T, Kushida T, Kushida H (1985) Localization of periodate-Schiff reactive glycosaminoglycans in semi-thin sections embedded in GMA-Quetol 523-MMA–application of a method for correlative light and electron microscopy of identical sites. Tokai J Exp Clin Med 10:37–46
17. Schnabel E, Anderson JM, Farquhar MG (1990) The tight junction protein ZO-1 is concentrated along slit diaphragms of the glomerular epithelium. J Cell Biol 111:1255–1263
18. Angeles G, Owens SA, Ewers FW (2004) Fluorescence shell: a novel view of sclereid morphology with the Confocal Laser Scanning Microscope. Microsc Res Tech 63:282–288
19. Evans CM, Williams OW, Tuvim MJ, Nigam R, Mixides GP, Blackburn MR, DeMayo FJ, Burns AR, Smith C, Reynolds SD, Stripp BR, Dickey BF (2004) Mucin is produced by clara cells in the proximal airways of antigen-challenged mice. Am J Respir Cell Mol Biol 31:382–394
20. Schaart G, Hesselink RP, Keizer HA, van Kranenburg G, Drost MR, Hesselink MK (2004) A modified PAS stain combined with immunofluorescence for quantitative analyses of glycogen in muscle sections. Histochem Cell Biol 122:161–169
21. Farquhar MG, Wissig SL, Palade GE (1961) Glomerular permeability. I. Ferritin transfer across the normal glomerular capillary wall. J Exp Med 113:47–66
22. Graham RC Jr, Karnovsky MJ (1966) Glomerular permeability. Ultrastructural cytochemical studies using peroxidases as protein tracers. J Exp Med 124:1123–1134
23. Mundel P, Shankland SJ (2002) Podocyte biology and response to injury. J Am Soc Nephrol 13:3005–3015
24. Batuman V, Dreisbach AW, Cyran J (1990) Light-chain binding sites on renal brush-border membranes. Am J Physiol 258:F1259–F1265
25. Batuman V, Guan S (1997) Receptor-mediated endocytosis of immunoglobulin light chains by renal proximal tubule cells. Am J Physiol 272:F521–F530
26. Birn H, Fyfe JC, Jacobsen C, Mounier F, Verroust PJ, Orskov H, Willnow TE, Moestrup SK, Christensen EI (2000) Cubilin is an albumin binding protein important for renal tubular albumin reabsorption. J Clin Invest 105:1353–1361
27. Brunskill NJ (2000) Albumin and proximal tubular cells–beyond endocytosis. Nephrol Dial Transplant 15:1732–1734
28. Andrews PM, Bates SB (1985) Dose-dependent movement of cationic molecules across the glomerular wall. Anat Rec 212:223–231
29. Imai H, Hamai K, Komatsuda A, Ohtani H, Miura AB (1997) IgG subclasses in patients with membranoproliferative glomerulonephritis, membranous nephropathy, and lupus nephritis. Kidney Int 51:270–276
30. Bijl M, Dijstelbloem HM, Oost WW, Bootsma H, Derksen RH, Aten J, Limburg PC, Kallenberg CG (2002) IgG subclass distribution of autoantibodies differs between renal and extra-renal relapses in patients with systemic lupus erythematosus. Rheumatology (Oxford) 41:62–67
31. Kanwar YS (1984) Biophysiology of glomerular filtration and proteinuria. Lab Invest 51:7–21
32. Zea-Aragon Z, Terada N, Ohno N, Fujii Y, Baba T, Ohno S (2004) Effects of anoxia on serum immunoglobulin and albumin leakage through blood-brain barrier in mouse cerebellum as revealed by cryotechniques. J Neurosci Methods 138:89–95
33. Griffith LD, Bulger RE, Trump BF (1967) The ultrastructure of the functioning kidney. Lab Invest 16:220–246
34. Pagtalunan ME, Olson JL, Tilney NL, Meyer TW (1999) Late consequences of acute ischemic injury to a solitary kidney. J Am Soc Nephrol 10:366–373
35. Sutton TA, Mang HE, Campos SB, Sandoval RM, Yoder MC, Molitoris BA (2003) Injury of the renal microvascular endothelium alters barrier function after ischemia. Am J Physiol Renal Physiol 285:F191–F198

Immunohistochemical Analyses on Serum Proteins in Nephrons of Protein-Overload Mice

23

Nobuhiko Ohno, Daoyuan Zhou, Nobuo Terada, and Shinichi Ohno

Abstract

In living mouse kidneys, distributions of soluble proteins are usually difficult to analyze using conventional tissue preparation methods. However, "in vivo cryotechnique" (IVCT) followed by freeze-substitution is useful to examine immunolocalizations of the serum proteins in kidneys of bovine serum albumin (BSA)-overloaded mice. Following 2 days of daily intraperitoneal injection of BSA, proteinuria was evident, and BSA along with endogenous mouse albumin could be immunohistochemically detected in Bowman's space as well as urinary tubules of adult mouse kidneys with IVCT. Immunostaining for BSA and mouse albumin was detected in Bowman's space and proximal tubules of all nephrons, although IgG1 was not detected in about 45 % of nephrons. Immunolocalization of BSA and IgG1 observed with IVCT was different from those observed with the conventional preparation methods, which lack normal blood circulation of kidneys prior to fixation. The immunolocalization of BSA and mouse serum proteins observed with IVCT suggests that glomerular filtration barriers in living mice are functionally impaired in a manner dependent on each nephron at the early stages of the BSA-overload mouse model.

Keywords

Immunohistochemistry • In vivo cryotechnique • Bovine serum albumin • Protein-overload mouse • Proteinuria

23.1 Introduction

The proteinuria is a common feature of chronic renal diseases in clinical medicine. Normally, a fraction of intermediate molecular weight (IMW) proteins, whose molecular weight ranges from 40 kD to 100 kD, can pass through the glomerular barrier to get into Bowman's space [1, 2]. The IMW proteins including albumin and lower molecular weight (LMW) proteins whose molecular weight is less than 40 kD are reab-

N. Ohno, M.D., Ph.D. (✉) • S. Ohno
Department of Anatomy and Molecular Histology, Interdisciplinary Graduate School of Medicine and Engineering, University of Yamanashi, 1110 Shimokato, Chuo City, Yamanashi 409-3898, Japan
e-mail: nohno@yamanashi.ac.jp

D. Zhou
Department of Anatomy and Molecular Histology, Interdisciplinary Graduate School of Medicine and Engineering, University of Yamanashi, 1110 Shimokato, Chuo City, Yamanashi 409-3898, Japan

Department of Nephrology, Guangzhou Red Cross Hospital, Guangzhou, People Republic of China

Department of Medicine, Division of Nephrology, Showa University Fujigaoka Hospital, Yokohama, Japan

N. Terada
Division of Health Sciences, Shinshu University Graduate School of Medicine, 3-1-1 Asahi, Matsumoto City, Nagano 390-8621, Japan

Department of Anatomy and Molecular Histology, Interdisciplinary Graduate School of Medicine and Engineering, University of Yamanashi, 1110 Shimokato, Chuo City, Yamanashi 409-3898, Japan

S. Ohno et al. (eds.), *In Vivo Cryotechnique in Biomedical Research and Application for Bioimaging of Living Animal Organs*, DOI 10.1007/978-4-431-55723-4_23

sorbed almost completely in the proximal tubules [3]. In chronic kidney diseases, increased permeability of glomerular filtration barrier resulted in increased leakage of IMW proteins through the barrier, although leakage of higher molecular weight (HMW) proteins, including immunoglobulin G (IgG), is not obvious initially. When disruption of glomerular filtration barriers worsens, the HMW proteins leak out to appear in the proximal tubules and are subsequently excreted in the urine [4]. The "in vivo cryotechnique" (IVCT) followed by freeze-substitution can directly cryofix living animal organs and stabilize soluble proteins of cells and tissues for preservation of their antigenicity [5–8]; the in situ immunolocalizations of extrinsic BSA or endogenous mouse serum proteins were examined with IVCT in the BSA-overload mouse model [9]. The results were also compared with findings obtained with conventional tissue preparation methods [9].

23.2 BSA Immunolocalization in Nephrons of Living Mice

Animals show proteinuria after overloading bovine serum albumin (BSA) for a few days (Fig. 23.1) [9]. Immune complex deposition is absent from glomeruli, but the severe proteinuria has been related to morphological alterations of glomerular epithelium [10–13]. Reabsorption of serum proteins such as IgG and albumin was found in the tubular epithelium of BSA-overload rats [11, 13]. IVCT was performed by placing the living mouse kidney on rubber plate and cutting the kidneys with a cryoknife precooled in liquid nitrogen when the isopentane-propane cryogen was poured over the exposed kidneys (Fig. 23.1). IVCT revealed that many flowing erythrocytes could be seen inside the open glomerular capillary loops and blood vessels in interstitium of living mouse kidneys [9]. The exogenous BSA was clearly immunolocalized in those blood vessels and also the basal infolding in the proximal convoluted tubules. BSA immunostaining was weakly detected in Bowman's space [9], indicating that BSA passed through the glomerular basement membranes.

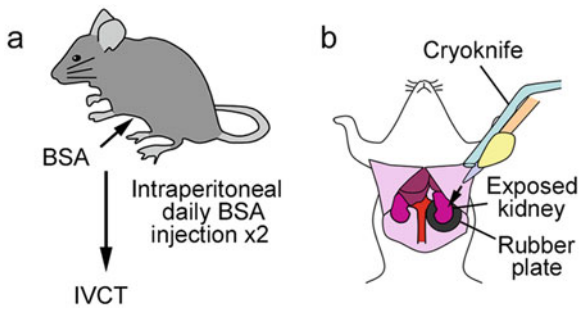

Fig. 23.1 Schematic drawing of experimental design and "in vivo cryotechnique" (IVCT) used in the study [9]. Following two consecutive daily intraperitoneal injection of bovine serum albumin (BSA), kidney specimens of those mice were prepared with IVCT (**a**). Control specimens were obtained following intraperitoneal injection of half saline instead of BSA. To obtain kidney specimens with IVCT, left kidneys were gently exposed under anesthesia, and they were simultaneously cut with cryoknife and contacted isopentane-propane cryogen (−196 °C) using "in vivo cryoapparatus" (**b**). Rubber plates were placed under the kidney to prevent translocation upon cutting

IVCT yields fewer morphological artifacts through direct cryofixation of the living animal kidneys in vivo. During the subsequent freeze-substitution step at about −80 °C, organic solvents with fixatives minimize diffusion of the serum proteins soluble to aqueous solution. Less compact cross-linking of structural components of cryotechniques preserves the antigenicity of molecules inside the tissue sections [14]. These advantages of IVCT presumably resulted in the clear immunolocalization of soluble serum proteins including BSA.

23.3 Immunolocalization of Various Serum Proteins

Immunostaining for IgG1 heavy chain (IgG1), kappa light chain (Kappa), and mouse albumin along with BSA on serial sections prepared with IVCT revealed distributions of serum proteins with different molecular weights in the identical nephrons of the BSA-overload mice [9]. Immunolocalization of Kappa showed free kappa light chains and all types of immunoglobulins containing kappa light chains, while immunolocalization of IgG1 indicated the localization of intact IgG1 molecules. BSA, mouse albumin, and Kappa but not IgG1 were immunohistochemically detected in Bowman's glomerular space and the apical cytoplasm of epithelium in proximal convoluted tubules in nine nephrons out of 21 (Fig. 23.2) [9]. In the other nephrons, all of Kappa, IgG1, BSA, and mouse albumin could be detected in the Bowman's spaces and proximal convoluted tubules (Fig. 23.2). Although both albumin and Kappa could be detected in almost all nephrons of the BSA-injected mice, immunoreactivity of albumin and Kappa was observed in seven glomeruli/five urinary tubules and in five glomeruli/six urinary tubules out of 20 nephrons of control mice, respectively [9]. IgG1 was not detected in any glomeruli or urinary tubules of nephrons from the control mice [9].

The immunolocalization of various molecular weight proteins which was different among nephrons in kidneys of the BSA-overload mouse might be attributable to defects in size and charge barrier of glomeruli [15]. Damage to the filtration barrier may first impair their charge-barrier functions and result in marked increase of albumin passage. The impaired charge barrier would first appear only in the limited number of nephrons, causing the functional heterogeneity of nephrons. Although the anionic sites of the glomerular basement membranes were histochemically unaltered [10, 13], glomerular anions were lost in the similar rat model produced by BSA overload [16]. Severer damage on the barrier structures results in impairment of the size-barrier function, and HMW

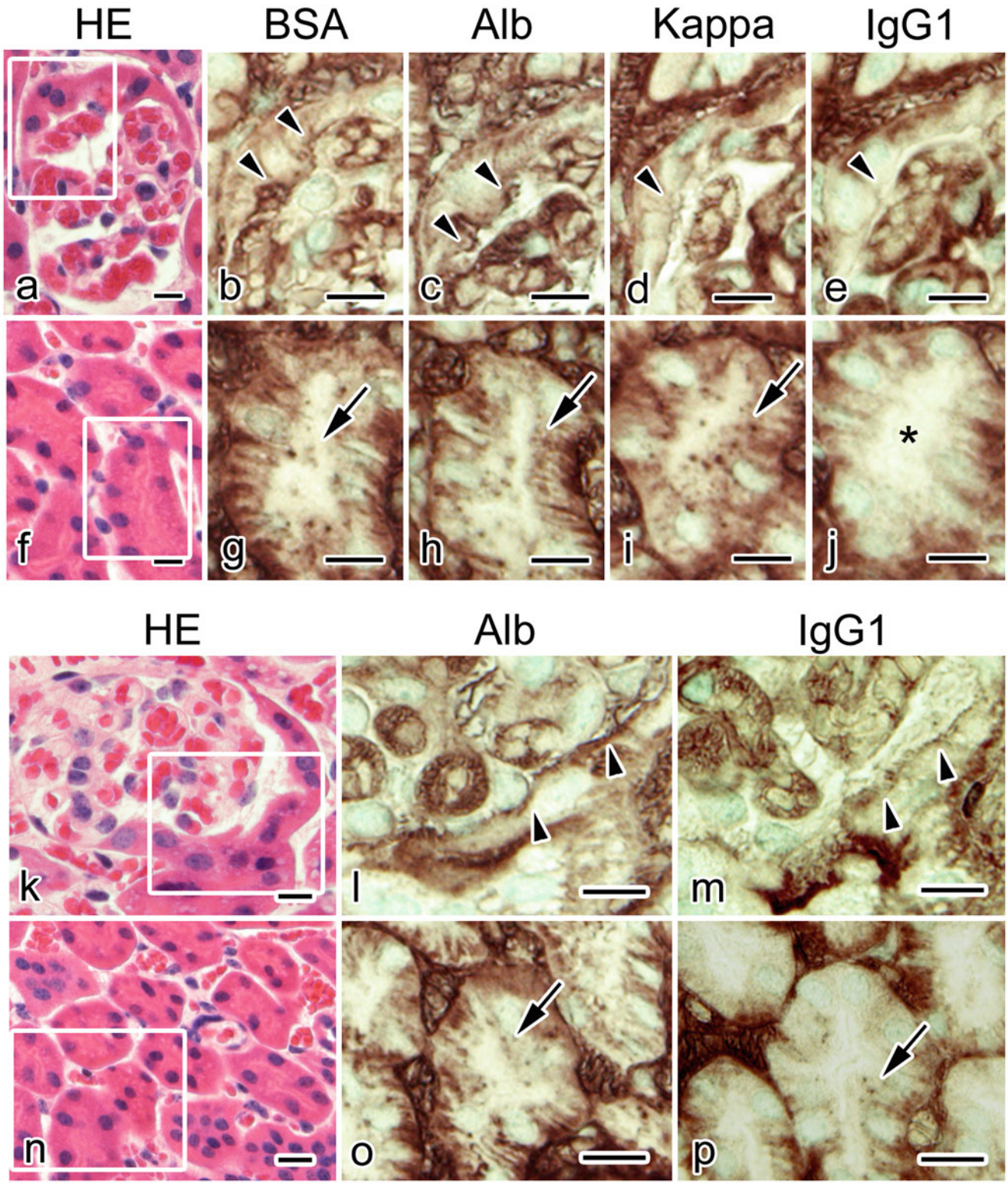

Fig. 23.2 Serial sections obtained from the BSA-overloaded mouse kidneys with "in vivo cryotechnique" and stained with hematoxylin-eosin (HE; **a**, **f**, **k**, **n**) or immunostained for bovine serum albumin (BSA; **b**, **g**), mouse albumin (Alb; **c**, **h**, **l**, **o**), mouse immunoglobulin kappa light chain (Kappa; **d**, **i**), and mouse immunoglobulin G1 heavy chain (IgG1; **e**, **j**, **m**, **p**) show that immunoreaction products of BSA, Alb, and Kappa, but not IgG1 (**e**, *arrowhead*; **j**, *asterisk*), are localized in Bowman's space (**b**, **c**, **d**, *arrowheads*) and proximal convoluted tubules (**g**, **h**, **i**, *arrows*) in some nephrons. In other nephrons, immunoreaction products of IgG1 are observed in the Bowman's space (**m**, *arrowheads*) and proximal convoluted tubules (**p**, *arrow*), together with those of Alb (**l**, *arrowheads*; **o**, *arrow*). Serial sections of the areas marked with rectangles in (**a**), (**f**), (**k**), and (**n**) are immunostained and magnified in (**b**)–(**e**), (**g**)–(**j**), (**l**)–(**m**), and (**o**)–(**p**), respectively. Scale bars: 10 μm. (The figure was adapted from Zhou et al. [9].)

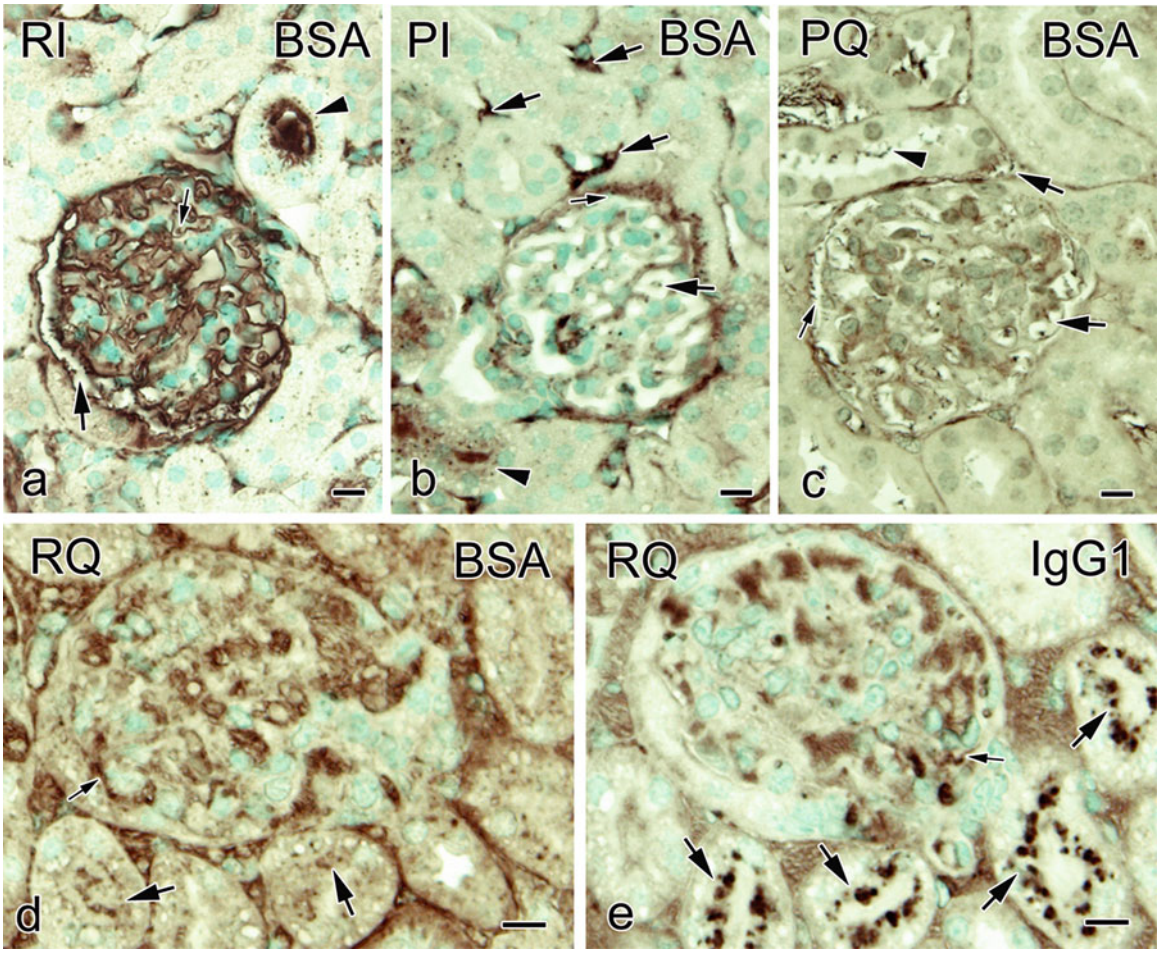

Fig. 23.3 Immunostaining for bovine serum albumin (BSA) in the BSA-overloaded mouse kidney prepared with tissue resection followed by immersion-fixation (RI; **a**), perfusion-fixation followed by immersion-fixation (PI; **b**), and perfusion-fixation followed by quick-freezing (PQ; **c**) shows that immunolocalization of BSA in the glomerular capillaries (**a**, *small arrow*; **b**, **c**, *large arrows*), Bowman's spaces (**a**, *large arrow*; **b**, **c**, *small arrows*), and urinary tubules (**a**–**c**, *arrowheads*) is significantly changed depending on the tissue preparation methods. Immunostaining for BSA (**d**) and mouse immunoglobulin G1 heavy chain (IgG1; **e**) in the BSA-overloaded mouse kidney prepared with tissue resection followed by quick-freezing (RQ) shows the passage of BSA into Bowman's space (**d**, *small arrow*) and urinary tubules (**d**, *large arrows*) and dotted immunoreaction products of IgG1 in Bowman's space (**e**, *small arrow*) and urinary tubules (**e**, *large arrows*). Scale bars: 10 μm (The figure was adapted from Zhou et al. [9])

proteins, including IgG, pass through the barrier. Previous studies showed impaired size selectivity in the rat BSA-overload model by measurement of the clearances of neutral dextrans [15]. The impairment of glomerular size barrier was already present in some nephrons of living mice even after 2 days of the daily BSA injection. Since serum proteins with different molecular weights immunolocalized differently in nephrons, damages on many nephrons may be spatially and temporally variable in the BSA-overloaded mice.

23.4 Comparisons with the Conventional Preparation Methods

The immunostaining for BSA was weakly remained inside the collapsed glomerular capillary loops, and more BSA immunoreactivity was observed in Bowman's space with the conventional immersion-fixation followed by dehydration method (Fig. 23.3) [9]. The dot-like BSA immunostaining was also observed within some of the tubular lumens, but the immunoreactivity of BSA was little in the basal striation parts of urinary tubules (Fig. 23.3). With perfusion-fixation, open lumens of glomerular capillary loops were observed, and weak BSA immunostaining was found in proximal convoluted tubules, Bowman's space, and the glomerular or interstitial blood capillaries. With perfusion-fixation followed by immersion-fixation, the immunostaining patterns resembled tissue samples prepared by perfusion-fixation followed by quick-freezing (Fig. 23.3). With the tissue resection followed by quick-freezing, on the other hand, the immunostaining for BSA at basal striation portions in the urinary tubules was detected, and large immunoreaction products of IgG1 were also observed within Bowman's space and in the apical cytoplasm of epithelial cells in uri-

nary tubules (Fig. 23.3). The findings clearly showed that the distribution of serum proteins was different among the preparation methods. The morphology as well as distribution of different molecules in kidneys can be affected by both ischemia and anoxia caused following common resection of tissue specimens. Heart arrest or tissue resection may cause translocation of the serum proteins into urinary space [17]. Furthermore, because of the artificial pressures which would wash out the serum proteins, perfusion-fixation significantly affects the immunolocalization of serum proteins [18–20].

23.5 Concluding Remarks

Application of IVCT to the mouse BSA-overload model clearly revealed immunolocalization of intrinsic and extrinsic serum proteins in glomeruli, Bowman's space, and urinary tubules. IVCT is a powerful approach to study nephron-specific pathology with proteinuria in animal disease models.

References

1. Chang RL, Deen WM, Robertson CR, Brenner BM (1975) Permselectivity of the glomerular capillary wall: III. Restricted transport of polyanions. Kidney Int 8(4):212–218
2. Chang RL, Ueki IF, Troy JL, Deen WM, Robertson CR, Brenner BM (1975) Permselectivity of the glomerular capillary wall to macromolecules. II. Experimental studies in rats using neutral dextran. Biophys J 15(9):887–906
3. Tojo A, Endou H (1992) Intrarenal handling of proteins in rats using fractional micropuncture technique. Am J Physiol 263(4 Pt 2):F601–F606
4. D'Amico G, Bazzi C (2003) Pathophysiology of proteinuria. Kidney Int 63(3):809–825
5. Liao X, Terada N, Ohno N, Li Z, Fujii Y, Baba T et al (2006) Immunohistochemical study of serum albumin in normal and cadmium-treated mouse testis organs by "in vivo cryotechnique". Histol Histopathol 21(1):35–40
6. Ohno N, Terada N, Murata S, Katoh R, Ohno S (2005) Application of cryotechniques with freeze-substitution for the immunohistochemical demonstration of intranuclear pCREB and chromosome territory. J Histochem Cytochem 53(1):55–62
7. Terada N, Ohno N, Li Z, Fujii Y, Baba T, Ohno S (2006) Application of in vivo cryotechnique to the examination of cells and tissues in living animal organs. Histol Histopathol 21(3):265–272
8. Terada N, Ohno N, Ohguro H, Li Z, Ohno S (2006) Immunohistochemical detection of phosphorylated rhodopsin in light-exposed retina of living mouse with in vivo cryotechnique. J Histochem Cytochem 54(4):479–486
9. Zhou D, Ohno N, Terada N, Li Z, Morita H, Inui K et al (2007) Immunohistochemical analyses on serum proteins in nephrons of protein-overload mice by "in vivo cryotechnique". Histol Histopathol 22(2):137–145
10. Davies DJ, Messina A, Thumwood CM, Ryan GB (1985) Glomerular podocytic injury in protein overload proteinuria. Pathology (Phila) 17(3):412–419
11. Eddy AA (1989) Interstitial nephritis induced by protein-overload proteinuria. Am J Pathol 135(4):719–733
12. Simpson LO, Shand BI (1983) Morphological changes in the kidneys of mice with proteinuria induced by albumin-overload. Br J Exp Pathol 64(4):396–402
13. Weening JJ, Van Guldener C, Daha MR, Klar N, van der Wal A, Prins FA (1987) The pathophysiology of protein-overload proteinuria. Am J Pathol 129(1):64–73
14. Terada N, Ohno N, Li Z, Fujii Y, Baba T, Ohno S (2005) Detection of injected fluorescence-conjugated IgG in living mouse organs using "in vivo cryotechnique" with freeze-substitution. Microsc Res Tech 66(4):173–178
15. Lemley KV (1993) Glomerular size selectivity during protein overload in the rat. Am J Physiol 264(6 Pt 2):F1046–F1051
16. Bliss DJ, Brewer DB (1985) Glomerular lysozyme binding in protein-overload proteinuria. Virchows Arch B Cell Pathol Incl Mol Pathol 48(4):351–359
17. Li Z, Ohno N, Terada N, Ohno S (2006) Immunolocalization of serum proteins in living mouse glomeruli under various hemodynamic conditions by "in vivo cryotechnique". Histochem Cell Biol 126(3):399–406
18. Hippe-Sanwald S (1993) Impact of freeze substitution on biological electron microscopy. Microsc Res Tech 24(5):400–422
19. Li Z, Terada N, Ohno N, Ohno S (2005) Immunohistochemical analyses on albumin and immunoglobulin in acute hypertensive mouse kidneys by "in vivo cryotechnique". Histol Histopathol 20(3):807–816
20. Shiurba R (2001) Freeze-substitution: origins and applications. Int Rev Cytol 206:45–96

24 Immunohistochemical Analyses of Serum Proteins in Puromycin Aminonucleoside Nephropathy of Living Rat Kidneys

Eri Kawashima, Yurika Saitoh, Nobuo Terada, Nobuhiko Ohno, Kiyoko Inui, Ashio Yoshimura, and Shinichi Ohno

Abstract

In vivo cryotechnique (IVCT) has been useful to examine native immunolocalizations of soluble proteins in animal kidneys, reflecting their living states. By using them, we have examined some immunolocalized proteins in nephrons of rat kidneys under experimental nephropathy induced by puromycin aminonucleoside (PAN) administration. At day 3 or day 9 after intraperitoneal PAN injection, IVCT was routinely performed for kidneys of anesthetized rats and followed by freeze-substitution fixation. Serial tissue sections were first stained with hematoxylin-eosin (HE) and then immunostained for serum albumin and IgG1. The excretion of urinary proteins began to increase at day 3. Plasma protein analyses indicated the typical nephrosis. At day 3, although little morphological changes were detected by HE staining, both albumin and IgG1 were immunolocalized along cytoplasm of podocytes and in apical parts of epithelial cells of proximal convoluted tubules. At day 9, intravascular congestion of erythrocytes was observed in almost all of the glomerular basement membranes (GBMs). Their relative immunoreactivities of albumin and IgG1 were weaker within blood vessels including GBMs. IVCT revealed dynamically changing processes of protein excretion and reabsorption in various segments of nephrons.

Keywords

In vivo cryotechnique • Nephron • Puromycin aminonucleoside

E. Kawashima, M.D. (✉)
Department of Anatomy and Molecular Histology, Interdisciplinary Graduate School of Medicine and Engineering, University of Yamanashi, Chuo City, Yamanashi 409-3898, Japan

Department of Medicine, Division of Nephrology, Showa University Fujigaoka Hospital, 1-30 Fujigaoka, Aoba-ku, Yokohama, Kanagawa 227-8501, Japan
e-mail: eri.kawashima@gmail.com

Y. Saitoh • N. Ohno • S. Ohno
Department of Anatomy and Molecular Histology, Interdisciplinary Graduate School of Medicine and Engineering, University of Yamanashi, 1110 Shimokato, Chuo City, Yamanashi 409-3898, Japan

N. Terada
Division of Health Sciences, Shinshu University Graduate School of Medicine, 3-1-1 Asahi, Matsumoto City, Nagano 390-8621, Japan

Department of Anatomy and Molecular Histology, Interdisciplinary Graduate School of Medicine and Engineering, University of Yamanashi, 1110 Shimokato, Chuo City, Yamanashi 409-3898, Japan

K. Inui • A. Yoshimura
Department of Medicine, Division of Nephrology, Showa University Fujigaoka Hospital, 1-30 Fujigaoka, Aoba-ku, Yokohama, Kanagawa 227-8501, Japan

S. Ohno et al. (eds.), *In Vivo Cryotechnique in Biomedical Research and Application for Bioimaging of Living Animal Organs*, DOI 10.1007/978-4-431-55723-4_24

24.1 Introduction

The PAN nephropathy model is well known to induce massive proteinuria by only one injection of PAN [1, 2]. Such pathological findings were already reported to resemble those in the human minimal change nephrotic syndrome (MCNS) [3]. It is also suggested that the PAN administration specifically damages glomerular podocytes, but it hardly influences other tubulointerstitial regions. Therefore, this PAN nephropathy model has been always accepted to be useful to analyze pathological conditions of the nephrotic syndrome and to evaluate medicines to decrease proteinuria for its clinical treatment. At a light microscopic level, little morphological changes were detected in nephrons of this PAN nephropathy model, which are clinically similar to human MCNS. At an electron microscopic level, however, typical effacements of foot processes of podocytes in glomerular basement membranes (GBMs) are characteristic findings, which are hardly clarified at lower resolution of light microscopy.

In normal rat kidneys, filtration of serum albumin and IgG through GBMs has been reported to be relatively restricted, because of molecular size barrier [4] and charge barrier [5] in the glomerular basement membrane. In human MCNS, molecular contents of proteinuria are highly selective, because albumin, but not IgG, is always detected in the urine. However, it has been difficult to evaluate direct immunolocalizations of the soluble serum IgG in kidney tissues by the conventional fixation methods, due to antigen masking and/or diffusion artifacts of such soluble proteins. In contrast, our IVCT and following freeze-substitution (FS) fixation have been reported to reveal precise immunolocalizations of serum proteins, such as albumin and IgG in living mouse kidneys [6–9], because soluble serum components were well retained, and tiny ice-crystal formation was helpful to increase the penetration of antibodies into tissue sections for the protein immunolocalization. Therefore, in this study, we have tried to demonstrate dynamically changing distributions of serum proteins in vivo under various hemodynamic states in experimental rat nephrons with PAN nephropathy by IVCT (Fig. 24.1).

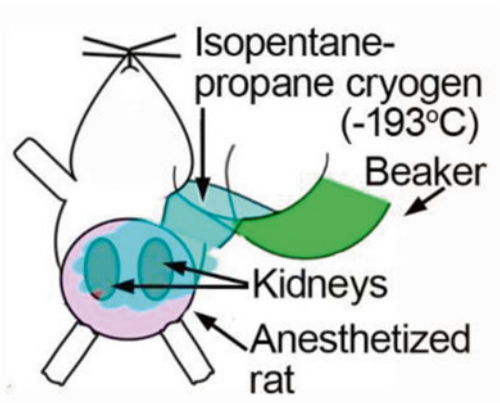

Fig. 24.1 Schematic representation of the way how to perform IVCT. Liquid isopentane-propane cryogen (−193 °C) was directly poured over the kidneys of anesthetized rats, which were then removed with a dental electric drill in liquid nitrogen. Such frozen kidneys by IVCT were processed to the freeze-substitution (*FS*) fixation

24.2 Proteinuria and Serum Examination

Daily amounts of urinary protein were shown in Fig. 24.2, depending on the days after the PAN injection and also administered PAN concentrations. The excreted protein amount was not increased in the control group (Fig. 24.2a). In the experimental group of 15 mg PAN injection, the amount of urinary protein was increased at day 3 and exceeded 300 mg/day at day 9 (Fig. 24.2a). In the lower 5 or 10 mg PAN-injection group (Fig. 24.2b), the protein amount in the urine was also slightly increased at day 3. Table 24.1 shows a list of biochemical analyses of serum albumin and creatinine. Significant hypoalbuminemia and renal dysfunctions were detected in the 15 mg PAN-injection group at day 9. In the 5 or 10 mg PAN-injection group, hypoalbuminemia was also detected at day 3.

24.3 Immunolocalizations of Serum Proteins Under Normal Condition

With HE staining, light micrographic images of normal rat kidneys were clearly observed without ischemia nor anoxia (Fig. 24.3a, b). Various shapes of erythrocytes reflecting their flowing condition in glomerular basement membranes (GBMs) were well retained in the HE-stained tissue sections (Fig. 24.3b; arrows). By immunostaining for albumin, its immunolocalization of the normal kidneys was mainly detected in GBMs and blood vessels in the interstitium between proximal or distal convoluted tubules (Fig. 24.3c, d). At higher magnification of a glomerulus (Fig. 24.3d, e), it was rarely detected in the outside of GBMs. In addition, the albumin immunolocalization was also detected at intercellular digitation or basal striations (Fig. 24.3f) and the apical cytoplasm of epithelial cells in some proximal tubules (PTs) at higher magnification of PTs (Fig. 24.3f). Immunolocalizations of IgG1 in normal rats were detected in GBMs and blood vessels of the interstitium (Fig. 24.3g, h). At higher magnification of a glomerulus (Fig. 24.3h, i), it was rarely detected in the outside of GBMs in the similar pattern of albumin. At higher magnification of PTs (Fig. 24.3j), it was rarely immunolocalized at basal striations unlike albumin. By the double-fluorescence staining with PAS and for albumin observed with confocal laser scanning microscopy, the albumin immunolocalizations were detected in the inside of GBMs (Fig. 24.3k–n) and in the apical cytoplasm of epithelial cells of PTs (Fig. 24.3o–r; arrows).

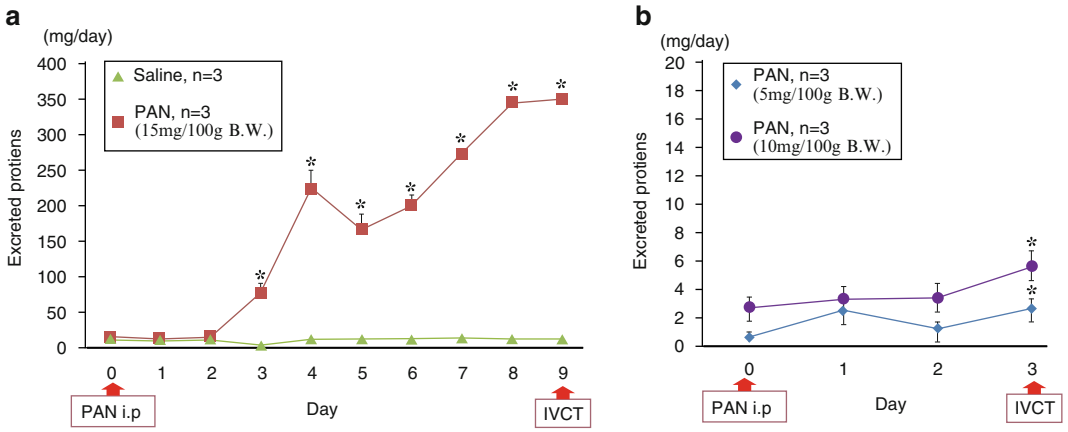

Fig. 24.2 Time-dependently changing graphs show daily amounts of urinary protein in the control group (**a**; *triangles*) and in the 15 mg PAN-injection group (**a**; *squares*) or in the 5 or 10 mg PAN-injection group (**b**; *rhombuses* and *circles*). Mean ± SE, $n = 3$ in each group, $^*p < 0.05$ vs. control (day 0)

Table 24.1 Biochemical serum examination

	PAN (mg)	Albumin (g/dl)	Creatinine (mg/dl)
Control	0	4.33 ± 0.25	0.30 ± 0.015
Day 3	5	3.73 ± 0.12	0.24 ± 0.064
	10	3.60 ± 0.17	0.25 ± 0.045
Day 9	15	1.53 ± 0.057	0.69 ± 0.015

Mean ± SD, $n = 3$ in each group

24.4 Histological Findings and Immunolocalizations of Serum Proteins in 3 Days After PAN Injection

At day 3 (Fig. 24.4), little histological changes were detected by HE staining at a light microscopic level (Fig. 24.4a, b), as compared to those of the normal rats. On the other hand, albumin was immunolocalized in GBMs and blood vessels in the interstitium between proximal or distal convoluted tubules (Fig. 24.4c), which were almost similar to those of normal kidneys. At day 3, when an increase of the urinary protein excretion was confirmed by the urine test (Fig. 24.2), albumin was clearly immunolocalized in the outside of GBMs (Fig. 24.4d; arrows). At higher magnification of a glomerulus (Fig. 24.4e; arrows), it appeared to be detected in podocytes, probably indicating their absorption of albumin. The similar albumin absorption into podocytes was detected in all nephrons (data not shown). At higher magnification of PTs (Fig. 24.4f), granular immunoreaction products were detected at the apical cytoplasm of proximal tubular epithelial cells, indicating abundant reabsorption of excreted albumin (Fig. 24.4f; arrowheads). A number of proximal tubules with such reabsorption were significantly increased, as compared to those in control rats. At day 3, IgG1 was also immunolocalized in the outside of GBMs (Fig. 24.4h; arrows). At higher magnification of a glomerulus, granular appearances of the immunoreaction products in podocytes were larger and clearer than those of the albumin (Fig. 24.4i; arrows). At higher magnification of PTs (Fig. 24.4j, arrowheads), granular immunoreaction products in the apical cytoplasm of epithelial cells were clearly detected. By double-fluorescence staining with PAS and albumin, albumin immunolocalizations were detected along GBMs (Fig. 24.4k–n), in podocytes at outer side of GBM (Fig. 24.4k–n; arrows), and at apical cytoplasm of proximal epithelial cells in PTs (Fig. 24.4o–r; arrowheads).

24.5 Histological Findings and Immunolocalizations of Serum Proteins in 9 Days After PAN Injection

At day 9 (Fig. 24.5), eosinophilic casts appeared in some lumens of renal tubules shown by HE staining (Fig. 24.5a; arrows). At higher magnification, many erythrocytes were congested in GBMs (Fig. 24.5b; arrows). Moreover, sizes of glomeruli and Bowman's capsules got expanded at day 9, as compared with those of normal kidneys at day 3. In some glomeruli, there was adhesion of capillary loops to Bowman's capsules and no cresent (Fig. 24.5b; arrowheads). By albumin immunostaining, the immunoreaction intensity was relatively weaker in GBMs, including other blood vessels, and in the interstitium (Fig. 24.5c), except for immunodeposit

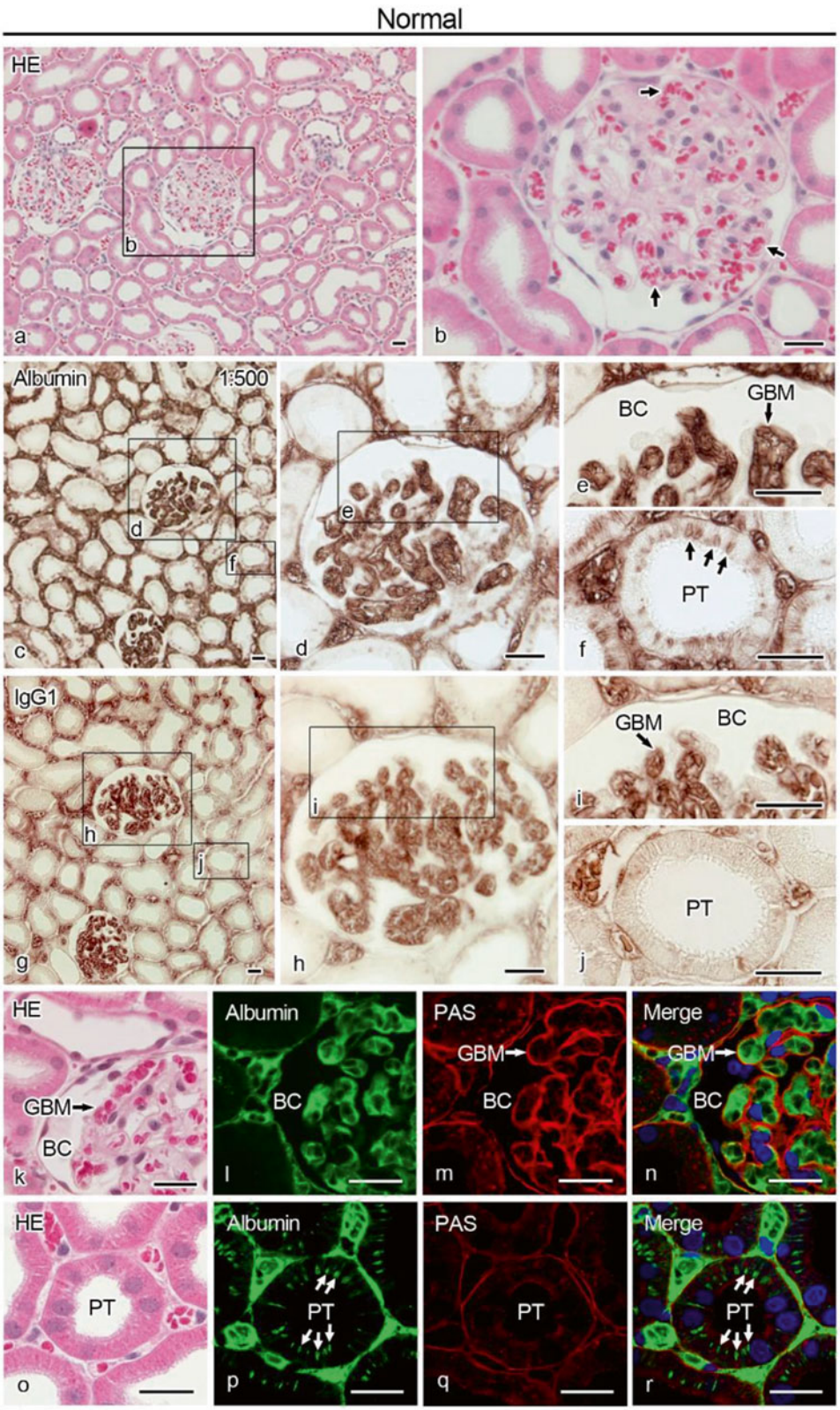

Fig. 24.3 HE staining and immunostaining of serum proteins in normal rat kidney tissues prepared with IVCT. By HE staining (**a**, **b**), flowing erythrocytes are well retained in blood vessels (**b**; *arrows*). By albumin immunostaining with a dilution of 1:500 (**c**–**f**), it is mostly detected in blood vessels in addition to intertubular matrices. At higher magnifications (**e**, **f**), it is clearly immunolocalized within glomerular basement membranes (*GBMs*) (**e**) and along some basal striations of proximal tubules (*PTs*), including blood vessels (**f**, *arrows*). IgG1 is also immunolocalized in blood vessel (**g**–**j**). At higher magnifications (**i**, **j**), it is clearly immunolocalized within GBMs (**i**), as similar to albumin (**e**), but hardly detected at basal striations of PTs (**j**). (**k**–**r**) HE-stained images (**k**, **o**) and confocal laser scanning microscopic images of PAS staining (**m**, **n**, **q**, **r**) and immunostaining of albumin (**l**, **n**, **p**, **r**). Albumin (**k**–**n**, *green color*) is immunolocalized in GBMs encircled with glomerular basement membranes (*GBMs*, *red color*), as shown by the PAS staining. It is also detected at some basal striations and lateral sides of PTs (**o**–**r**; *arrows*). Bars, 20 μm

casts in the lumen of renal tubules (Fig. 24.5c, f; arrows). At higher magnification, albumin immunoreactivity was decreased in the outside of GBMs (Fig. 24.5d, e), and its reabsorption into proximal tubular epithelial cells (Fig. 24.5f) was also decreased. In the similar way to albumin, intensity of the other IgG1 immunoreaction was much weaker in GBMs and blood vessels of the interstitium, whereas IgG1 was immunolocalized in casts of some renal tubules (Fig. 24.5g, j; arrows). At higher

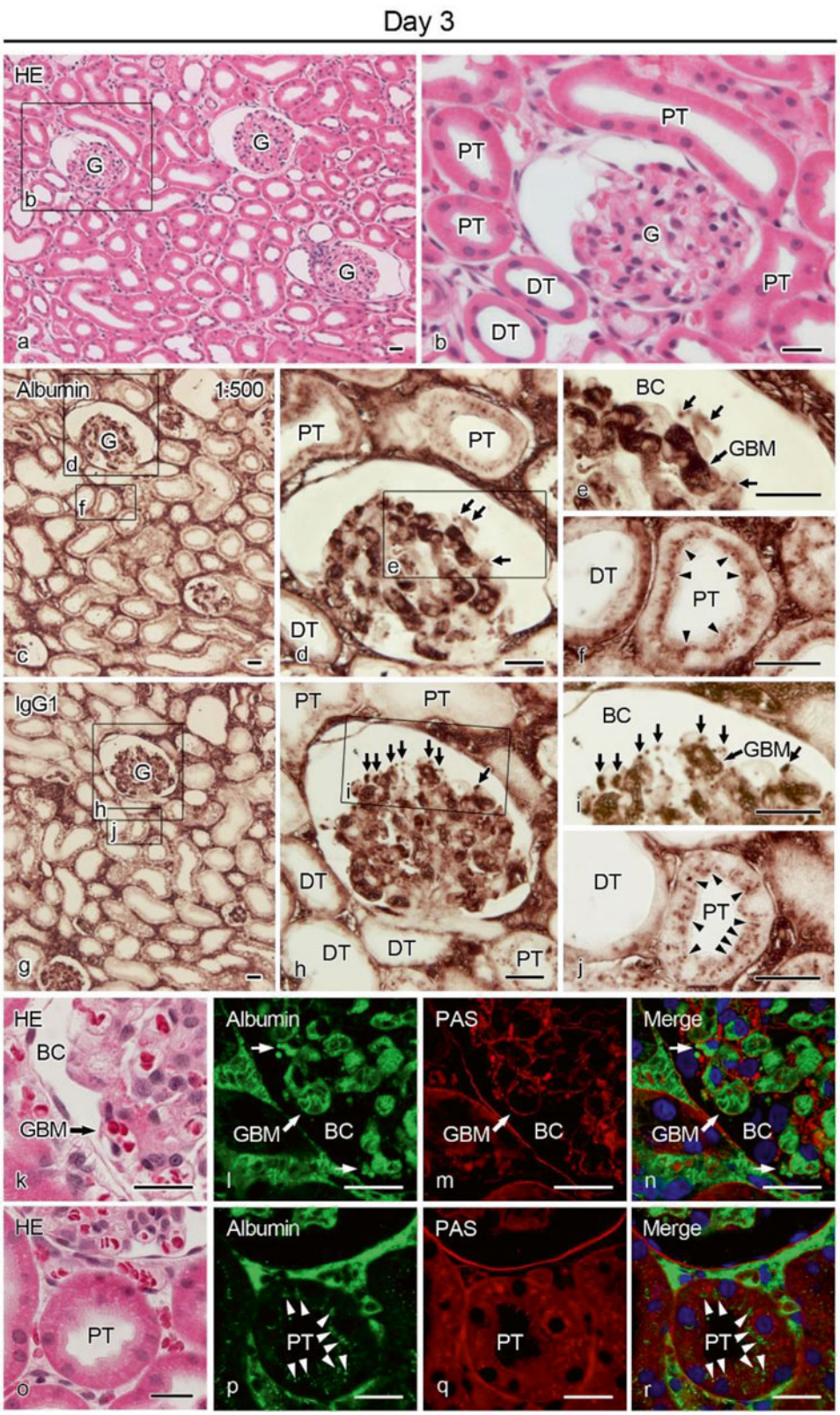

Fig. 24.4 Light micrographs of HE staining and immunostaining of serum proteins in rat kidney tissues at day 3 after the PAN injection. By HE staining (**a**, **b**), pathological changes are not clearly detected, as almost like normal histology. By immunostaining for albumin (**c**–**f**), it is detected mainly within blood vessels. At higher magnifications (**d**–**f**), however, it is immunolocalized outside GBMs, probably in podocytes (**e**; *arrows*). Other granular immunoreaction products are also detected in the apical cytoplasm of proximal tubules (*PTs*) (**f**; *arrowheads*). On the other hand, IgG1 is immunolocalized within blood vessels (**g**–**j**) and podocytes of glomeruli (**h**, **i**; *arrows*). Moreover, granular patterns of immunoreaction products are detected in epithelial cells of convoluted PTs (**j**; *arrowheads*), as similar to those of albumin shown by fluorescence immunostaining (**k**–**r**). (**k**–**r**) HE staining (**k**, **o**) and confocal laser scanning microscopic images of PAS staining (**m**, **n**, **q**, **r**) and immunostaining of albumin (**l**, **n**, **p**, **r**). The albumin is also immunolocalized in the outside of glomerular basement membranes (*GBMs*, *red color*), probably in some podocytes (**l**–**n**; *small arrows*), and also in the apical cytoplasm of epithelial cells of PTs (**p**–**r**; *arrowheads*). Bars, 20 μm

magnification, IgG immunolocalizations were not clear in the outside of GBMs (Fig. 24.5h, i), and immunoreaction products of IgG1 were decreased in proximal tubular epithelial cells (Fig. 24.5j; arrowheads). By double-fluorescence staining with PAS and for albumin, albumin immunoreactivity was weakly detected along GBMs (Fig. 24.5k–n), but deposit casts in PTs were strongly immunostained for albumin (Fig. 24.5o–r).

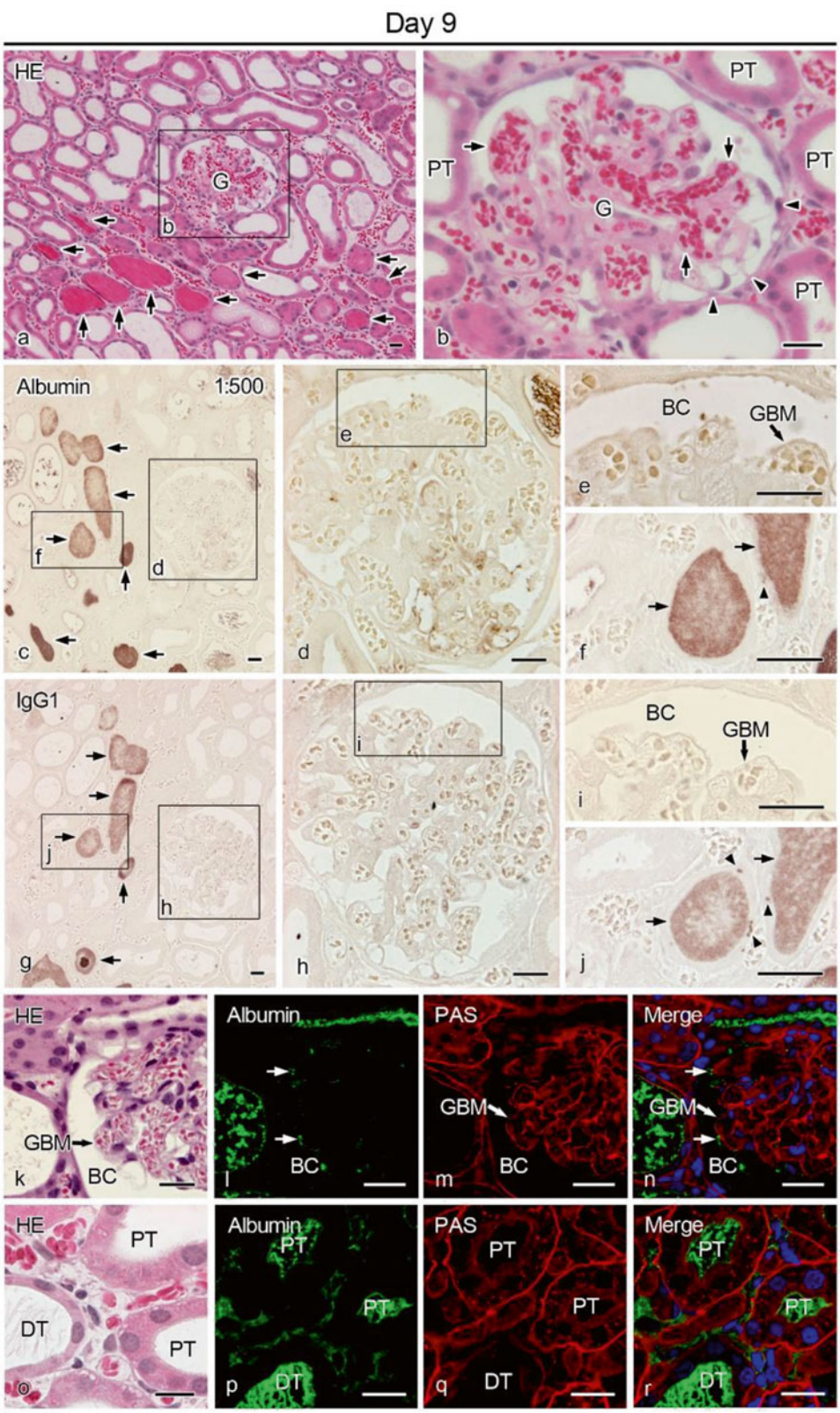

Fig. 24.5 Light micrographs of HE staining and immunostaining of albumin and IgG1 in rat kidney tissues at day 9 after the PAN injection. By HE staining, some deposit casts are clearly observed to be eosinophilic in lumens of some renal tubules (**a**; *arrows*), and many erythrocytes were also congested in GBMs (**b**; *arrows*). Adhesions between GBMs and outer Bowman's capsule are often observed (**b**; *arrowheads*). Immunoreaction products of albumin are clearly detected in the deposit casts in the renal tubules (**c**; *arrows*), but relative intensity of the albumin immunostaining is much weaker within blood vessels (**c**, **d**). At higher magnifications (**e**, **f**), such immunoreactivity of albumin is hardly detected in GBMs (**e**) and apical cytoplasm of epithelial cells of PTs (**f**; *arrowheads*). (**g**–**j**) IgG1 is also immunolocalized in the similar casts (**g**; *arrows*). At higher magnifications (**h**–**j**), it is hardly detected in GBMs at this dilution of the IgG1 antibody (**i**), and some granular immunoreaction products are still detected in apical cytoplasm of epithelial cells of PTs (**j**; *arrowheads*). HE staining (**k**, **o**), PAS staining (**m**, **n**, **q**, **r**), and immunostaining of albumin (**l**, **n**, **p**, **r**). The immunoreaction intensity of albumin is decreased in GBMs (**l**–**n**) and also in blood vessels of the interstitium (**p**–**r**). But it is clearly immunolocalized in the deposit casts of renal tubules (**p**, **r**: *arrowheads*) and slightly in blood vessels between renal tubules. Bars, 20 μm

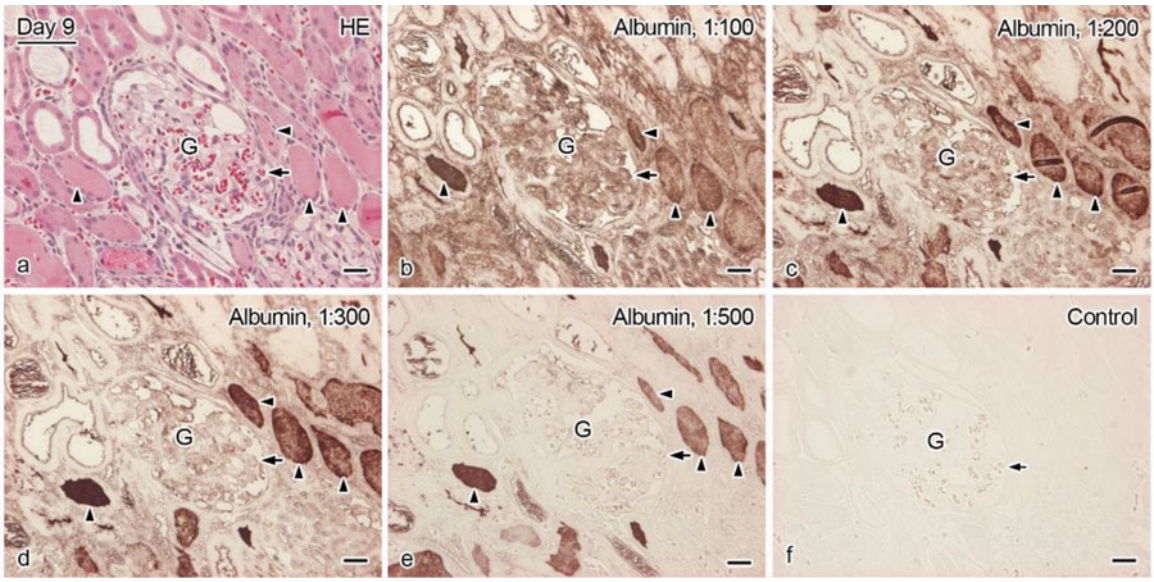

Fig. 24.6 Light micrographs of HE staining and immunostaining of albumin with various dilutions of the anti-albumin antibody in rat kidney tissues at day 9 after PAN injection. Four dilution ratios are 1:100 (**b**), 1:200 (**c**), 1:300 (**d**), and 1:500 (**e**). The antibody dilution of 1:500 is the same immunostaining condition for kidney tissue sections of normal or PAN-injected rats. The deposit casts in PTs are strongly immunostained at all antibody dilution ratios (*arrowheads*). As the relative concentration of the primary anti-albumin antibody gets higher, the albumin immunoreactivity is gradually increased in blood vessels of GBMs (*arrows*) and the interstitium, as accompanying with the nonspecific background. (**f**): Immunocontrol without the primary antibody. Bars, 20 μm

These weaker immunoreactivities for albumin and IgG1 within blood vessels may reflect hypoalbuminemia and renal dysfunctions. Next to elucidate the difference of such immunoreactivities, the similar immunostaining was performed with various dilutions of the primary anti-albumin antibody (Fig. 24.6). Figure 24.6e shows the immunostaining image with a dilution of 1:500, which is the same dilution for normal (Fig. 24.3c–f) and day 3 (Fig. 24.4c–f) rat tissues. As the higher concentrations of the primary anti-albumin antibody were used for serial sections, the stronger albumin immunoreactivity was detected, accompanying with more nonspecific backgrounds (Fig. 24.6b–d).

24.6 Conclusion

IVCT has been often used to analyze dynamic blood flow and immunolocalizations of soluble proteins in tissue sections under various physiological and pathological conditions. In the past decades, PAN nephropathy has been known to be a nephrotic model, whose pathological condition resembles the human minimal change nephrotic syndrome (MCNS). In this study, by using IVCT, we examined some segments of nephrons for immunolocalizations of albumin and IgG1 under experimental PAN nephropathy of rats in addition to analyses of biochemical serum proteins and albumin excreted in the urine.

References

1. Frenk S, Antonowicz I, Craig JM, Metcoff J (1955) Experimental nephrotic syndrome induced in rats by aminonucleoside; renal lesions and body electrolyte composition. Proc Soc Exp Biol Med 89:424–427
2. Lannigan R (1963) The production of chronic renal disease in rats by a single intravenous injection of aminonucleoside of puromycin and the effect of low dosage continuous hydrocortisone. Br J Exp Pathol 44:326–333
3. Vernier RL, Papermaster BW, Good RA (1959) Aminonucleoside nephrosis I. Electron microscopic study of the renal lesion in rats. J Exp Med 109:115–126
4. Caulfield JP, Farquhar MG (1974) The permeability of glomerular capillaries to graded dextrans. J Cell Biol 63:883–903
5. Chang RLS, Deen WM, Robertson CR, Brenner BM (1975) Permselectivity of the glomerular capillary wall: III. Restricted transport of polyanions. Kidney Int 8:212–218
6. Li Z, Terada N, Ohno N, Ohno S (2005) Immunohistochemical analyses on albumin and immunoglobulin in acute hypertensive mouse kidney by "in vivo cryotechnique". Histol Histopathol 20:807–816
7. Li Z, Ohno N, Terada N, Zhou D, Yoshimura A, Ohno S (2006) Application of periodic acid-Schiff fluorescence emission for immunohistochemistry of living mouse renal glomeruli by "in vivo cryotechnique". Arch Histol Cytol 69:147–161
8. Li Z, Ohno N, Terada N, Ohno S (2006) Immunolocalization of serum proteins in living mouse glomeruli under various hemodynamic conditions by "in vivo cryotechnique". Histochem Cell Biol 126:399–406
9. Zhou D, Ohno N, Terada N, Li Z, Morita H, Inui K, Yoshimura A, Ohno S (2007) Immunohistochemical analyses on serum proteins in nephrons of protein-overload mice by "in vivo cryotechnique". Histol Histopathol 22:137–145

Immunolocalization of Phospho-Arg-Directed Protein Kinase-Substrate in Hypoxic Kidneys

25

Sei Saitoh, Nobuo Terada, Nobuhiko Ohno, Yurika Saitoh, and Shinichi Ohno

Abstract

Protein kinases (PKs) phosphorylate proteins at active regions for signal transduction. In this study, normal and hypoxic mouse kidneys were prepared using an "in vivo cryotechnique" (IVCT) and examined immunohistochemically with specific antibodies against phospho-(Ser/Thr) PKA/C substrate (P-PK-S) and phospho-(Ser/Thr) Akt substrate (P-Akt-S) to capture their time-dependent regulation in vivo. Left kidneys were cryofixed with IVCT under normal blood circulation and after varying hypoxic intervals, followed by freeze-substitution with acetone containing paraformaldehyde. Deparaffinized sections were immunostained for P-PK-S, Na^+/HCO^{3-} cotransporter NBC1, and a membrane skeletal protein, 4.1B. The P-PK-S was diffusely immunolocalized in the cytoplasm of the proximal tubules in normal kidneys, whereas NBC1 and 4.1B were detected at the basal striations of S1 and S2 segments of the proximal tubule. After 10 or 30 s hypoxia, P-PK-S was still immunolocalized in the cytoplasm of kidneys, but it was detected at the basal striations after 1 or 2 min hypoxia. The immunolocalization of P-Akt-S was the same as P-PK-S in the normal and hypoxic kidneys. Immunoblotting analyses of the kidney tissues under normal or hypoxic condition clearly identified the same 40 kDa bands. The IVCT is useful for time-dependent analysis of the immunodistribution of P-PK-S and P-Akt-S.

Keywords

Hypoxic kidneys • Phospho-(Ser/Thr) PKA/C substrate • Phospho-(Ser/Thr) Akt substrate • Na^+/HCO^{3-} cotransporter1 • 4.1B

25.1 Introduction

Immunohistochemistry (IHC) using many antiphosphorylation-specific antibodies has been applied to examining molecular signal transduction, cell growth, and cytokinesis in animal cells, which depend on energy consumption. The PKC family has many proteins in various animal organs, including the brain, liver, kidney, spleen, lung, heart, and testis, but their intracellular PKC distribution is likely dependent on the proliferation state of cells and tissues in the living animals [1, 2]. The present study used IVCT to arrest some transient physiological processes of P-PK-S in living mouse kidneys under normal blood circulation and with time-dependent hypoxia. The immunolocalization of P-PK-S in the IVCT-prepared tissue samples

S. Saitoh, M.D., Ph.D. (✉) • N. Ohno
Y. Saitoh • S. Ohno
Department of Anatomy and Molecular Histology, Interdisciplinary Graduate School of Medicine and Engineering, University of Yamanashi, 1110 Shimokato, Chuo City, Yamanashi 409-3898, Japan
e-mail: ssaitoh@yamanashi.ac.jp

N. Terada
Division of Health Sciences, Shinshu University Graduate School of Medicine, 3-1-1 Asahi, Matsumoto City, Nagano 390-8621, Japan

Department of Anatomy and Molecular Histology, Interdisciplinary Graduate School of Medicine and Engineering, University of Yamanashi, 1110 Shimokato, Chuo City, Yamanashi 409-3898, Japan

S. Ohno et al. (eds.), *In Vivo Cryotechnique in Biomedical Research and Application for Bioimaging of Living Animal Organs*, DOI 10.1007/978-4-431-55723-4_25

was different from that observed with the conventional resection of fresh kidney tissues and quick-freezing followed by freeze-substitution fixation (RF-QF-FS). The different immunolocalizations of P-PK-S observed in association with the time-dependent hypoxia indicate that the discrepancy of immunodistribution was primarily caused by the transient effects of hypoxia during the common preparation steps [3–8].

25.2 Immunolocalization of P-PK-S with IVCT-FS and RF-QF-FS

The morphology obtained with the two preparation methods was compared with HE staining and immunohistochemistry for P-PK-S in mouse kidney tissues. At low magnification, the P-PK-S was mainly immunolocalized in the cortical renal tubules, but not in the medulla of living mouse kidney tissues prepared with IVCT-FS (Fig. 25.1a, b). At higher magnification with HE staining, some Bowman's spaces and the renal proximal tubules in the cortex seemed to maintain their open lumens (Fig. 25.1c). However, the tissue samples prepared with RF-QF-FS showed collapsed Bowman's spaces and renal tubules in the cortex, probably due to ischemia caused by the tissue resection (Fig. 25.1f). In serial sections of the same samples prepared with IVCT-FS, the immunoreactivity of P-PK-S was heterogeneously detected throughout the cytoplasm of the proximal tubules in mosaic-like patterns (Fig. 25.1d, e). In contrast, it was detected mainly in the basal striations of the proximal tubules in the tissue samples prepared with RF-QF-FS (Fig. 25.1g, h). These findings indicate that the immunolocalization of P-PK-S was quickly altered by the tissue-resection procedure.

25.3 Immunolocalization of P-PK-S in Hypoxic Mouse Kidneys Prepared with IVCT-FS

To examine the transient effects of hypoxia on the immunolocalization of P-PK-S, both the morphology of HE-stained tissue and the immunolocalization of P-PK-S, NBC1 (an ion cotransporter), and 4.1B (a membrane skeletal protein) (data not shown) were compared in serial sections from renal proximal tubules under various hypoxic conditions (Fig. 25.2). Under normal blood circulation, P-PK-S was immunolocalized diffusely throughout the cytoplasm of most epithelial cells in the proximal tubules and occasionally along the basal striations (Fig. 25.2b, d). The diffuse immunolocalization of P-PK-S in the proximal tubules as shown in Fig. 25.2b, d was very similar to that shown in Fig. 25.1e. After 10 or 30 s hypoxia, their signals were also detected in the proximal tubules, some of which were immunolabeled with anti-NBC1 or 4.1B antibody, showing the proximal S1–S2 segments. Higher magnification demonstrated that immunolocalization of P-PK-S in the cytoplasm was almost identical to that under normal blood circulation (data not shown). After 1 or 2 min hypoxia, it was also detected in the proximal tubules at low magnification (Fig. 25.2g, h). Higher magnification showed that it had changed to become localized, mainly in the basal striations (Fig. 25.2i, j). In contrast, the immunolocalization of both NBC1 and 4.1B was always detected in the basal striations of the S1–S2 proximal tubules under all conditions (NBC1: Fig. 25.2e, j, o). These findings indicate that immunolocalization of P-PK-S was almost completely changed from the whole cytoplasm to the basal striations in the proximal tubules after 1 min hypoxia.

25.4 Immunolocalization of P-Akt-S in Normal and Hypoxic Mouse Kidneys

To examine the immunostaining patterns of another antibody against a similar phospho-specific motif, anti-P-Akt-S antibody was used for the IVCT-FS-prepared kidneys of living mice under normal blood circulation and hypoxic conditions. The P-Akt-S was immunolocalized in the cytoplasm of the same P-PK-S-immunopositive proximal tubules in the normal mouse kidneys (Fig. 25.3b, c). After 1 min hypoxia, the P-Akt-S was also immunolocalized in the basal striations, similar to the P-PK-S-immunopositive proximal tubules (Fig. 25.3e, f). These findings indicate that the substrates phosphorylated by Arg-directed protein kinases also changed from a cytoplasmic pattern to the basal striations in the renal proximal tubules after 1 min hypoxia.

25.5 Concluding Remarks

The newly developed IVCT is a reliable method for the examination of time-dependent regulation of signaling pathways in vivo and does not have the technical limitations of the usual methods that interfere with molecular translocation, including soluble Arg-directed kinases [1, 2, 9–11]. The immunohistochemical findings must therefore be compared with the live images obtained from intravital microscopy, such as FRET [12–15].

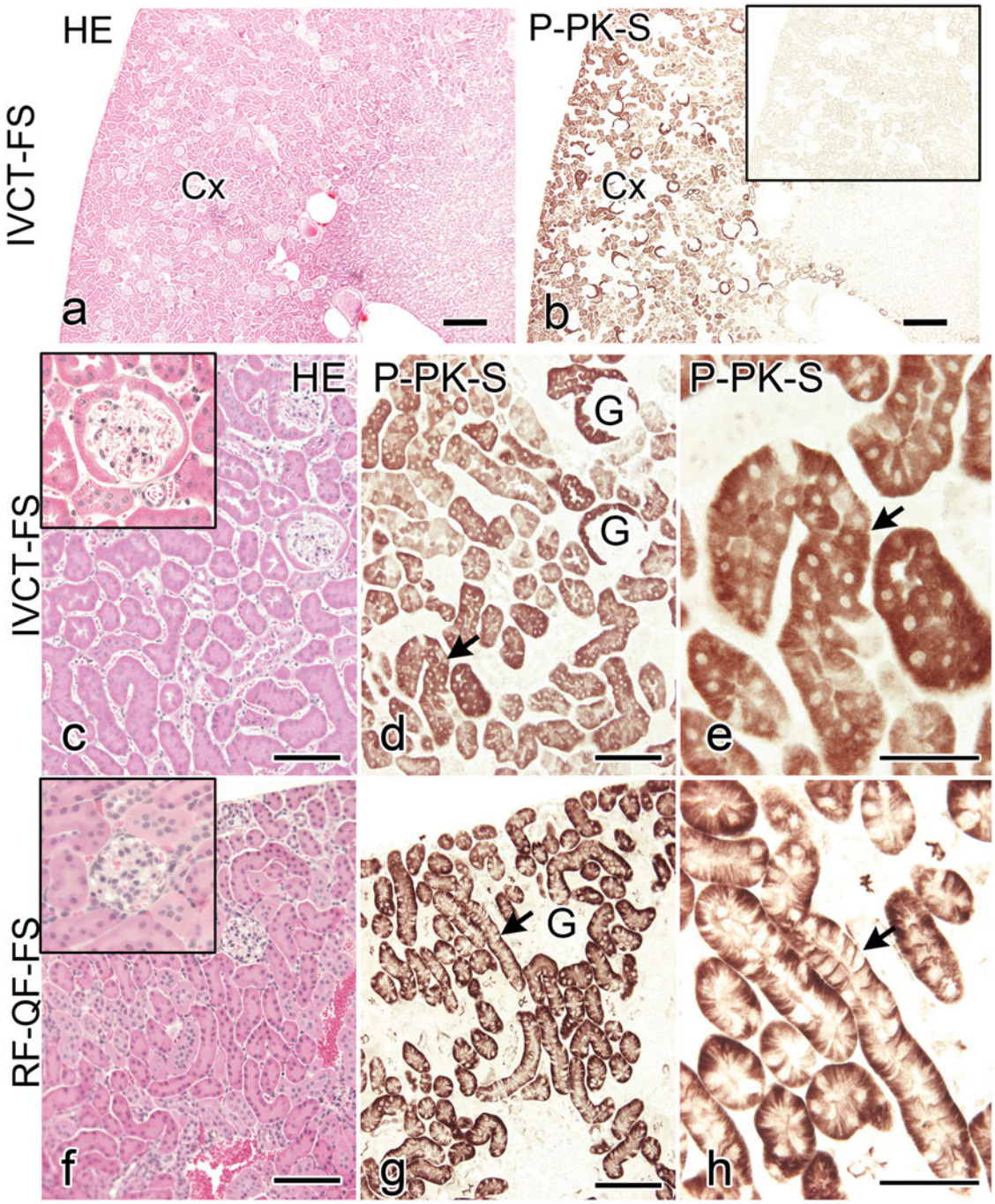

Fig. 25.1 Light micrographs of mouse kidneys prepared with the "in vivo cryotechnique" (*IVCT*) or resection of fresh tissues and quick-freezing (*RF-QF*), followed by FS. (**a**, **b**) Serial sections are stained with hematoxylin-eosin (**a**, *HE*) and immunostained for phospho-(Ser/Thr) protein kinase A/C substrate (**b**, *P-PK-S*). The P-PK-S-immunopositive areas are mostly observed in the cortex (*Cx*). *Inset* of (**b**) is the immunocontrol for P-PK-S in the renal cortex at the same magnification of (**b**). (**c**–**h**) Normal kidneys on serial sections stained with HE and immunostained for P-PK-S, by two different procedures with IVCT-FS and RF-QF-FS. (**c**–**e**) With IVCT-FS, immunolocalization for P-PK-S is detected in the cytoplasm of the proximal tubules (**d** and **e**, *arrows*), and each tubular cell shows different intensities of immunostaining. (**e**) Another higher magnification view shows heterogeneous immunolocalization patterns of P-PK-S in the cytoplasm. (**f**–**h**) With RF-QF-FS, the immunolocalization of P-PK-S is detected along the basal striations of the renal proximal tubules (**g** and **h**, *arrows*). *Cx* cortex, *G* glomerulus. Bars 300 m (**a**, **b**), 100 m (**c**, **d**, **f**, **g**), 50 m (**e**, **h**)

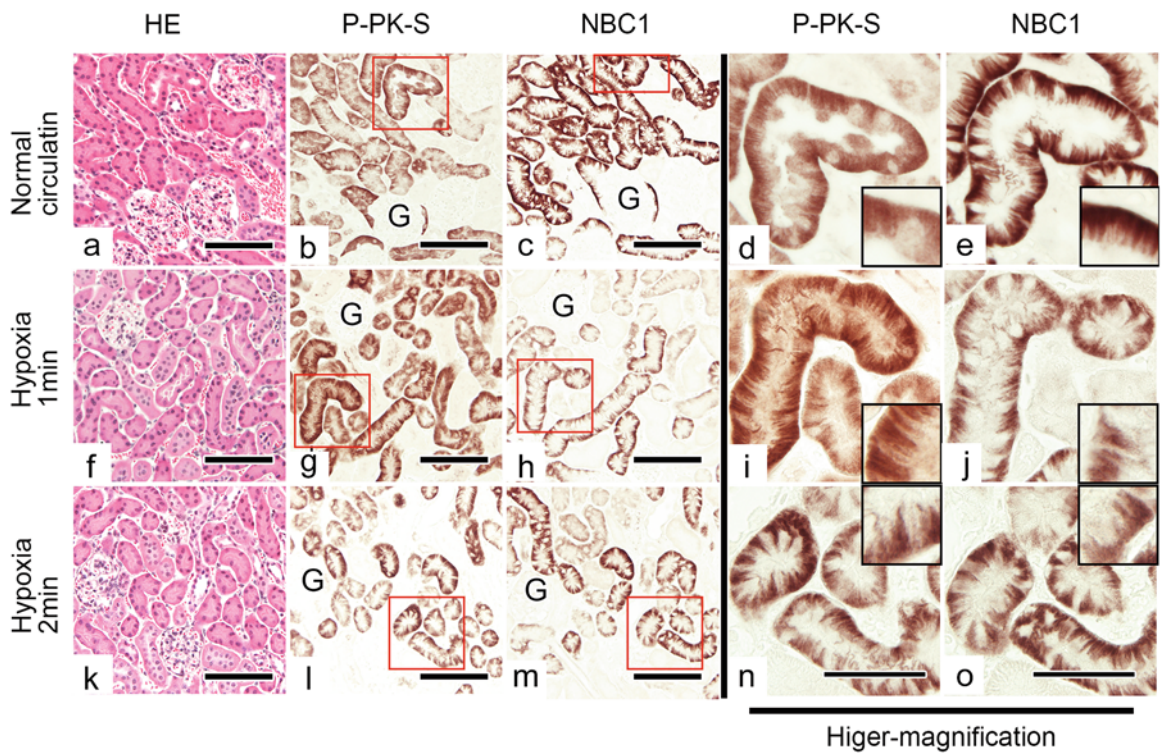

Fig. 25.2 Light micrographs of mouse kidney tissue specimens prepared with IVCT-FS under normal blood circulation (**a**–**e**) and hypoxia of 1 min (**f**–**j**) and 2 min (**k**–**o**) before the cryofixation. Serial sections are stained with HE (**a**, **f**, **k**) and immunostained for P-PK-S (**b**, **d**, **g**, **i**, **l**, **n**) and Na^+/HCO_3^- cotransporter (NBC)1 (**c**, **e**, **h**, **j**, **m**, **o**). The tissue areas of P-PK-S-immunopositive proximal tubules are more widely distributed than those of NBC1. *Insets* show the basal cytoplasm of the epithelial cells, thus indicating the immunolocalization of the P-PK-S in the whole cytoplasm (**b**, **d**) under normal blood circulation along the basal striations (**g**, **i**, **l**, **n**) under 1 and 2 min hypoxia. The NBC1 is almost always immunolocalized along the basal striations (**c**, **e**, **h**, **j**, **m**, **o**). *G* glomerulus. Bars 100 μm (**a**–**c**, **f**–**h**, **k**–**m**), 50 μm (**d**–**e**, **i**–**j**, **n**–**o**)

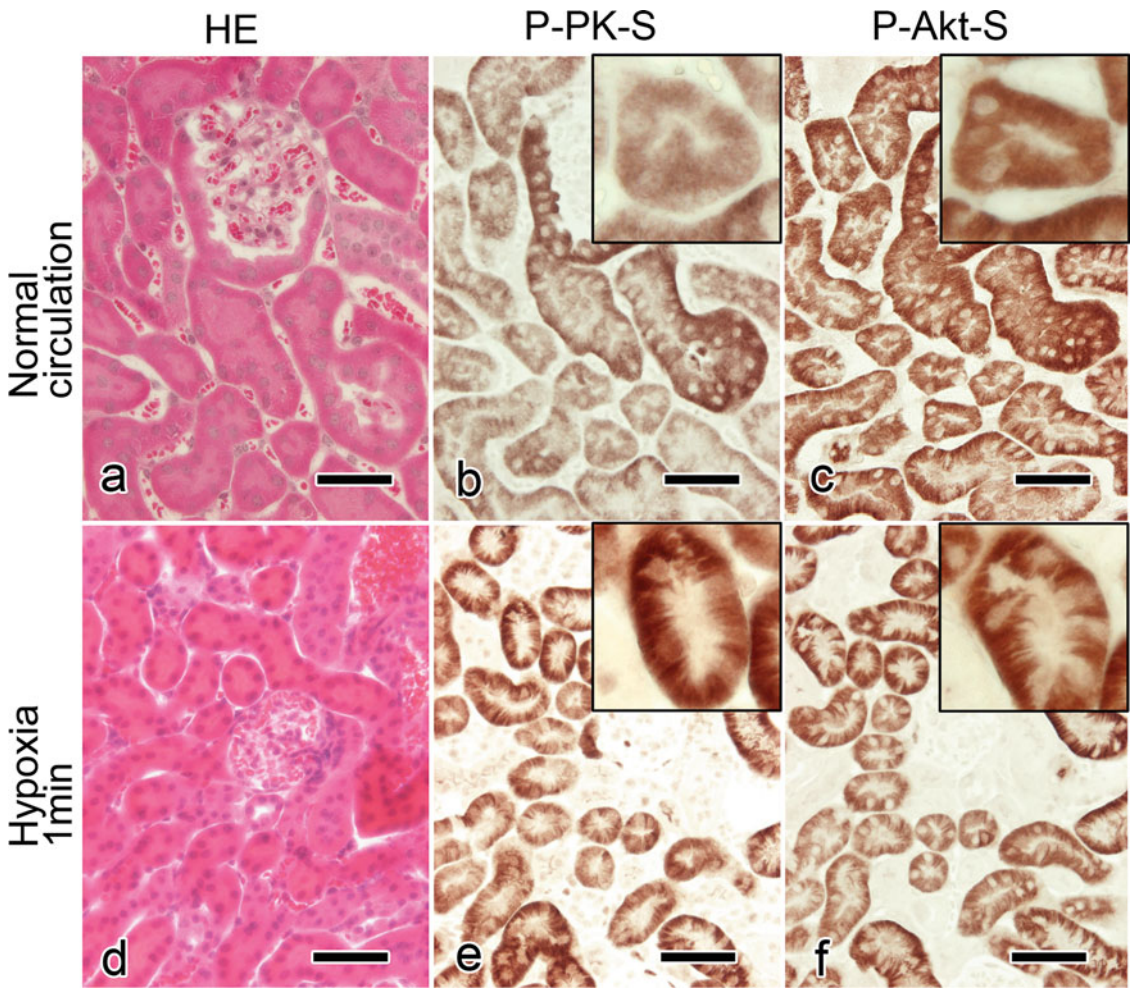

Fig. 25.3 Light micrographs of mouse kidney tissue specimens under normal blood circulation (**a**–**c**) and 1 min hypoxia (**d**–**f**), prepared with IVCT-FS. The serial sections are stained with HE (**a**, **d**) and immunostained for P-PK-S (**b**, **e**) and phospho-(Ser/Thr) Akt substrate (P-Akt-S) (**c**, **f**). The immunolocalization of both P-PK-S and P-Akt-S has changed from the whole cytoplasm (**b**, **c**) to the basal striations in the proximal tubules after 1 min hypoxia (**e**, **f**). *Bars* 100 μm

References

1. Mochly-Rosen D, Basbaum AI, Koshland DE Jr (1987) Distinct cellular and regional localization of immunoreactive protein kinase C in rat brain. Proc Natl Acad Sci U S A 84(4):4660–4664
2. Wetsel WC, Khan WA, Merchenthaler I, Rivera H, Halpern AE, Phung HM, Negro-Vilar A, Hannun YA (1992) Tissue and cellular distribution of the extended family of protein kinase C isoenzymes. J Cell Biol 117(1):121–133
3. Shi SR, Key ME, Kalra KL (1991) Antigen retrieval in formalin-fixed, paraffin-embedded tissues: an enhancement method for immunohistochemical staining based on microwave oven heating of tissue sections. J Histochem Cytochem 39(4):741–748
4. Ohno N, Terada N, Murata S, Katoh R, Ohno S (2005) Application of cryotechniques with freeze-substitution for the immunohistochemical demonstration of intranuclear pCREB and chromosome territory. J Histochem Cytochem 53(1):55–62
5. Saitoh S, Terada N, Ohno N, Ohno S (2008) Distribution of immunoglobulin-producing cells in immunized mouse spleens revealed with "in vivo cryotechnique". J Immunol Methods 331(1–2):114–126
6. Terada N, Ohno N, Saitoh S, Ohno S (2007) Immunohistochemical detection of hypoxia in mouse liver tissues treated with pimonidazole using "in vivo cryotechnique". Histochem Cell Biol 128(3):253–261
7. Miller RT (2005) Phospho-specific antibodies: more valuable than originally thought. Am J Physiol Renal Physiol 289(2):247–248
8. He H, Tan M, Pamarthy D, Wang G, Ahmed K, Sun Y (2007) CK2 phosphorylation of SAG at Thr10 regulates SAG stability, but not its E3 ligase activity. Mol Cell Biochem 295(1–2):179–188
9. Pearson RB, Kemp BE (1991) Protein kinase phosphorylation site sequences and consensus specificity motifs: tabulations. Methods Enzymol 200:62–81

10. Nishizuka Y (1988) The molecular heterogeneity of protein kinase C and its implications for cellular regulation. Nature 334(6148):661–665
11. Bonventre JV (1993) Mechanisms of ischemic acute renal failure. Kidney Int 43(5):1160–1178
12. Sakai N, Sasaki K, Ikegaki N, Shirai Y, Ono Y, Saito N (1997) Direct visualization of the translocation of the gamma-subspecies of protein kinase C in living cells using fusion proteins with green fluorescent protein. J Cell Biol 139(6):1465–1476
13. Miyawaki A, Llopis J, Heim R, McCaffery JM, Adams JA, Ikura M, Tsien RY (1997) Fluorescent indicators for Ca^{2+} based on green fluorescent proteins and calmodulin. Nature 388(6645):882–887
14. Ng T, Squire A, Hansra G, Bornancin F, Prevostel C, Hanby A, Harris W, Barnes D, Schmidt S, Mellor H, Bastiaens PI, Parker PJ (1999) Imaging protein kinase Calpha activation in cells. Science 283(5410):2085–2089
15. Saitoh S, Terada N, Ohno N, Saitoh Y, Soleimani M, Ohno S (2009) Immunolocalization of phospho-Arg-directed protein kinase-substrate in hypoxic kidneys using in vivo cryotechnique. Med Mol Morphol (42):24–31

Dynamic Ultrastructures of Renal Glomeruli in Living Mice Under Various Hemodynamic Conditions

26

Shinichi Ohno, Yasuhisa Fujii, and Nobuo Terada

Abstract

Three-dimensional ultrastructures of mouse renal glomeruli under various hemodynamic conditions were studied by scanning electron microscopy with the "in vivo cryotechnique" (IVCT). Some kidneys of anesthetized mice were directly frozen in vivo under normal blood flow condition. Others were frozen in the same way after ligation of the lower abdominal aorta or their heart arrest. The frozen specimens were routinely freeze-substituted, freeze-dried, and ion-sputtered for SEM. In freeze-substituted specimens with the IVCT, interdigitating foot processes of podocytes exhibited smooth surface contours with less shrinkage, and their surfaces were arranged more tightly than those commonly seen by the conventional fixation method. In the anesthetized mice, filtration slits between the foot processes were found to be narrow after the heart arrest, but they were a little wider under the normal blood flow condition. After the aorta ligation to increase the renal blood flow, the filtration slits became much wider and the foot processes were more elongated. The ultrastructures of capillary loops in functioning renal glomeruli were revealed to be dynamically changing in the living mouse states, depending on various hemodynamic conditions.

Keywords

Renal glomerulus • Hemodynamics • In vivo cryotechnique • Filtration slit • Scanning electron microscopy

26.1 Introduction

A renal glomerulus consists of intricate networks of blood-capillaries in vivo, through which the blood of animal bodies always circulates under various influences of blood pressures. It has been well known that hemodynamic factors, including the volume of renal blood flow, exert an important influence on glomerular functions and structures [1–3]. Therefore, the alteration in glomerular hemodynamics of renal corpuscles probably affects the driving mechanical force that modulates permeability properties of glomerular filtration barriers [4–6]. For example, the distribution of serum albumin proteins in experimental rat glomeruli was also reported to be changed due to different hemodynamic conditions [7, 8]. So the functional role of normal blood circulation is found to be definitely important in maintenance of

S. Ohno, M.D., Ph.D. (✉) • Y. Fujii
Department of Anatomy and Molecular Histology,
Interdisciplinary Graduate School of Medicine and Engineering,
University of Yamanashi, 1110 Shimokato, Chuo City,
Yamanashi 409-3898, Japan
e-mail: sohno@yamanashi.ac.jp

N. Terada
Division of Health Sciences, Shinshu University Graduate School of Medicine, 3-1-1 Asahi, Matsumoto City, Nagano 390-8621, Japan

Department of Anatomy and Molecular Histology,
Interdisciplinary Graduate School of Medicine and Engineering,
University of Yamanashi, 1110 Shimokato, Chuo City,
Yamanashi 409-3898, Japan

S. Ohno et al. (eds.), *In Vivo Cryotechnique in Biomedical Research and Application for Bioimaging of Living Animal Organs*, DOI 10.1007/978-4-431-55723-4_26

the glomerular barrier function. In the present study for SEM, we will describe three-dimensional ultrastructures of functioning kidneys in vivo under various hemodynamic conditions, which were prepared by the IVCT.

26.2 Preparation Procedures of Living Mouse Kidneys for SEM

The left kidneys of anesthetized mice under normal bloodcirculation were prepared by IVCT, as described before [9, 10]. Other mouse kidneys were prepared in similar way after heart arrest with an overdose of the anesthetic to stop blood supply or the ligation of lower abdominal aorta to acutely increase blood supply into kidneys. The IVCT-prepared specimens were routinely freeze-substituted in absolute acetone containing 2 % osmium tetroxide, transferred into t-butyl alcohol, and freeze-dried at −5 °C in Hitachi ES-2030 apparatus. They were then mounted on aluminum stages, evaporated with platinum/palladium (10–15 nm) in Hitachi E-1030 apparatus, and observed in Hitachi S-4500 scanning electron microscope at an accelerating voltage of 5 kV.

26.3 New Findings of Functioning Podocytes Under Hemodynamic Conditions

Many interdigitating foot processes of podocytes under normal bloodcirculation, which were covering the outer capillary surface in renal corpuscles (Fig. 26.1a), surely reflected their in vivo arrangement, as prepared by the IVCT. The foot processes were located almost in parallel with each other, and filtration slits were irregularly open in some parts (Fig. 26.1b). Moreover, other foot processes with slit spaces were variously extended along capillary loops (Fig. 26.1c), as seen in the freeze-fractured capillary loops. To the contrary, urinary spaces became collapsed after the heart arrest (Fig. 26.2a), and glomerular foot processes were tightly attached to each other (Fig. 26.2b). At higher magnification, the foot processes were taller after the heart arrest (Fig. 26.2b, arrows), as seen in the freeze-fractured capillary loops. In addition, another different morphology of stretched capillary loops was revealed after the ligation of the aorta (Fig. 26.3). As compared with the morphology of capillary loops after the heart arrest (Fig. 26.2), interdigitating foot processes with wide filtration slits were more loosely arranged with each other after the ligation of the aorta (Fig. 26.3a, arrows). In a freeze-fractured renal corpuscle, urinary Bowman's spaces and lumens of capillary loops were more widely dilated (Fig. 26.3b), showing several flowing blood cells in the capillary lumens.

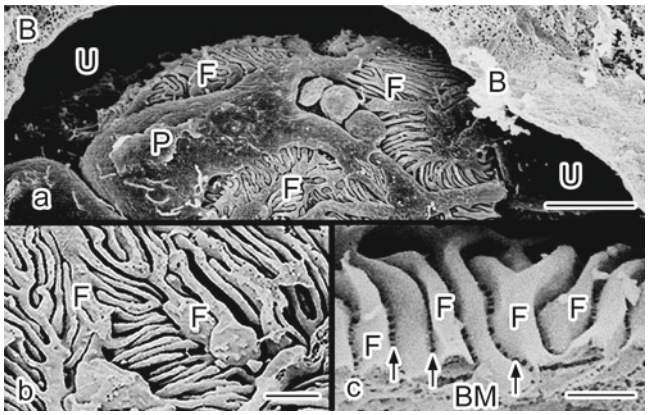

Fig. 26.1 Scanning electron micrographs of freeze-fractured renal corpuscles of living mice under normal blood flow condition, as prepared by IVCT. (**a**) Interdigitating foot processes are covering the outer capillary loop surface. *P* podocytes, *F* foot processes, *U* urinary space, *B* Bowman's capsule. Bar: 5 μm. (**b**) At higher magnification, surface contours of foot processes (*F*) with various slit spaces are arranged almost in parallel with each other. *Bar*: 1 μm. (**c**) Filtration slits (*arrows*) are also seen to be open between foot processes (*F*) under the normal bloodflow condition. *BM* basement membrane. *Bar*: 0.5 μm

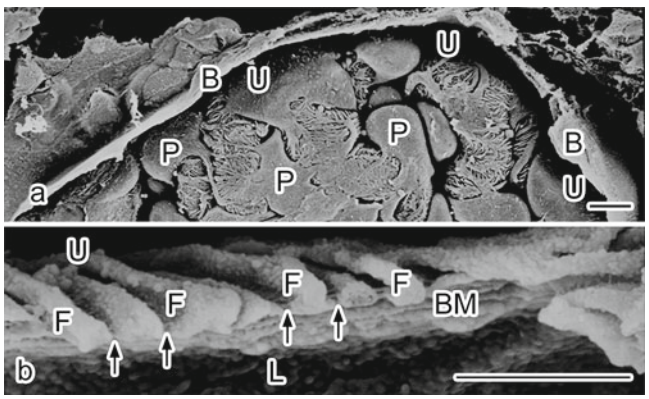

Fig. 26.2 Scanning electron micrographs of freeze-fractured renal corpuscles of mice under the heart-arrestcondition, as prepared by IVCT. (**a**) The urinary space (*U*) is almost collapsed, which is also covered by outer Bowman's capsule (*B*). Bar: 5 μm. (**b**) A freeze-fractured capillary loop is seen, and foot processes (*F*) with narrow filtration slits (*arrows*) are attached to the basement membrane (*BM*). *Bar*s: 1 μm. *L* capillary lumen, *U* urinary space

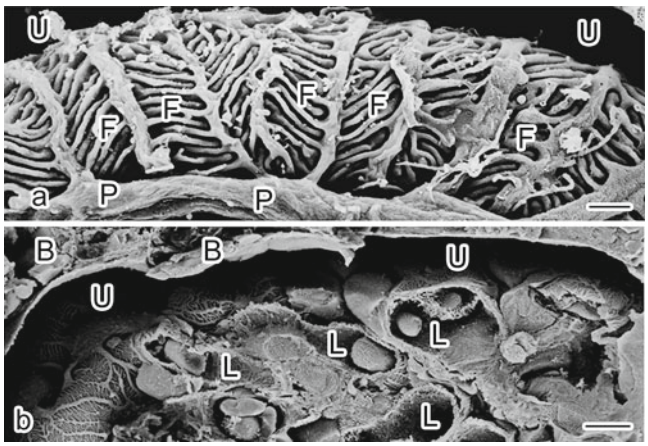

Fig. 26.3 Scanning electron micrographs of freeze-fractured renal corpuscles of living mice under the aorta ligation condition, as prepared by IVCT. (**a**) Interdigitating foot processes (*F*) are extended to become slender, covering the outer surface of blood capillary loops. *P* podocyte, *U* urinary space. Bars: 1 μm. (**b**) The lumens of freeze-fractured capillary loops (*L*) are also more widely open with dilatation of the urinary space (*U*). *B* Bowman's capsule. *Bar*: 5 μm

26.4 Dynamically Changing of Foot Processes for Filtration Functions

It has been known that glomerular capillary loops of living mouse kidneys are perpetually stretched by hydraulic pressures in bloodcapillaries, whereas those in excised kidneys receive no such stretching forces. Filtration slits between foot processes of podocytes were reported to be widely open to facilitate passage of the glomerular filtrate in vivo [3]. It has also been reported that the foot processes are rich in contractile proteins, such as actin, myosin, and α-actinin, and capable of such actin-mediated movement [11]. Through this active movement, the podocytes may regulate the glomerular filtration rate, thereby influencing hydraulic pressures across the glomerular basement membrane, as reported before [3]. Therefore, the blood pressures must be steadily maintained at the time of exposure to quick freezing with IVCT, and the dynamically changing filtration slits are found to be wider under normal blood circulation than the heart-arrestcondition. The glomerular hydraulic pressures might be partially regulated by the relative width of the filtration slits. Therefore, the total width of the filtration slits plays an important role in providing a porous theory that controls hydraulic conductivity and water flow [3, 12].

26.5 Concluding Remarks

The present findings definitely provide the morphofunctional confirmation of functioning glomerular capillary loops in living mouse states, indicating that the passage of solutes is always affected by glomerular hemodynamics under different bloodflow conditions.

References

1. Griffith LD, Bulger RE, Trump BF (1967) The ultrastructure of the functioning kidney. Lab Invest 16:220–246
2. Kanwar YS (1984) Biophysiology of glomerular filtration and proteinuria. Lab Invest 51:7–21
3. Kriz W, Hackenthal E, Nobiling R, Sakai T, Elger M (1994) A role for podocytes to counteract capillary wall distension. Kidney Int 45:369–376
4. Ryan GB, Hein SJ, Karnovsky MJ (1976) Glomerular permeability to proteins. Effects of hemodynamic factors on the distribution of endogenous immunoglobulin G and exogenous catalase in the rat glomerulus. Lab Invest 34:415–427
5. Bohrer MP, Deen WM, Robertson CR, Brenner BM (1977) Mechanism of angiotensin II-induced proteinuria in the rat. Am J Physiol 233:F13–F21
6. Brenner BM, Bohner MP, Baylis C, Deen WM (1977) Determinants of glomerular permselectivity: insights derived from observations in vivo. Kidney Int 12:229–237
7. Ryan GB, Karnovsky MJ (1976) Distribution of endogenous albumin in the rat glomerulus: role of hemodynamic factors in glomerular barrier function. Kidney Int 9:36–45
8. Olivetti G, Kithier K, Giacomelli F, Wiener J (1981) Glomerular permeability to endogenous proteins in the rat. Lab Invest 44:127–137
9. Ohno S, Terada N, Fujii Y, Ueda H, Takayama I (1996) Dynamic structure of glomerular capillary loop as revealed by an in vivo cryotechnique. Virchows Arch 427:519–527
10. Ohno S, Kato Y, Xiang T, Terada N, Takayama I, Fujii Y, Baba T (2001) Ultrastructural study of mouse renal glomeruli under various hemodynamic conditions by an "in vivo cryotechnique". Ital J Anat Embryol 106:431–438
11. Andrews P (1988) Morphological alterations of the glomerular (visceral) epithelium in response to pathological and experimental situations. J Electron Microsc Tech 9:115–144
12. Drumond MC, Deen WM (1994) Structural determinants of glomerular hydraulic permeability. Am J Physiol 266:F1–F12

Function of Dynamin-2 in the Formation of Discoid Vesicles in Urinary Bladder Umbrella Cells

27

Nobuo Terada, Yurika Saitoh, Nobuhiko Ohno, Yasuhisa Fujii, and Shinichi Ohno

Abstract

Dynamin (Dyn) is a GTPase that promotes endocytic processes through scission of cell membranes. In this chapter, we present the contribution of Dyn2 to the structural integrity of discoid vesicles (DVs) and to the endocytic activity of urinary bladder umbrella cells (UCs) which have capacity to control bladder volume. Dyn2 was abundantly expressed in UCs, especially near the apical cytoplasmic regions. By immunoelectron microscopy, Dyn2 was found on and around DV membranes in UCs. Ultrastructural analysis with a quick-freezing and deep-etching method revealed the existence of distinct Dyn2-bound microfilaments in close association with DV membranes. Treatment of bladders with a Dyn-GTPase inhibitor, dynasore, markedly reduced the number of DVs in UCs. In infected UCs, *Escherichia coli* was encased in compartments enriched in Dyn2, and treatment of bladders with dynasore inhibits *E. coli* invasion of UCs.

Keywords

Dynamin • Umbrella cell • Dynasore • Quick-freezing and deep-etching method • Microfilaments

27.1 Umbrella Cells in the Urinary Bladder

The urinary bladder is a distensible organ, and its transitional epithelium consists of multiple layers of epithelial cells that can contract and expand. As shown in Fig. 27.1a, the uppermost layer of cells that line the bladder lumen is called umbrella cells (UCs) [2]. The cytoplasm of each UC contains a number of discoid vesicles (DVs) composed of rigid plaques consisting of hexagonal uroplakin particles and hinges [3]. These DVs play a highly dynamic role in adjusting the bladder volume [4]. When the bladder needs to distend, these DVs fuse with the apical cell membrane of UCs. After the bladder volume is reduced, DVs are reformed by being pinched off from the apical cell membrane and once again assume their characteristic intracellular vesicular appearance.

N. Terada, M.D., Ph.D. (✉)
Division of Health Sciences, Shinshu University Graduate School of Medicine, 3-1-1 Asahi, Matsumoto City, Nagano 390-8621, Japan

Department of Anatomy and Molecular Histology, Interdisciplinary Graduate School of Medicine and Engineering, University of Yamanashi, 1110 Shimokato, Chuo City, Yamanashi 409-3898, Japan
e-mail: nobuot@shinshu-u.ac.jp

Y. Saitoh • N. Ohno • Y. Fujii • S. Ohno
Department of Anatomy and Molecular Histology, Interdisciplinary Graduate School of Medicine and Engineering, University of Yamanashi, 1110 Shimokato, Chuo City, Yamanashi 409-3898, Japan

27.2 Dynamin for Activity of Endocytosis

Dynamin (Dyn) is a GTPase involved in the endocytosis of various kinds of cells [5, 6]. Three Dyn family proteins, Dyn1–3, have been identified to date; whereas Dyn1 and Dyn3 are expressed primarily in neurons and testis, respectively, Dyn2 is expressed in diverse cell types [7]. Dyn mediates the scission of newly formed vesicles from the membrane

S. Ohno et al. (eds.), *In Vivo Cryotechnique in Biomedical Research and Application for Bioimaging of Living Animal Organs*, DOI 10.1007/978-4-431-55723-4_27

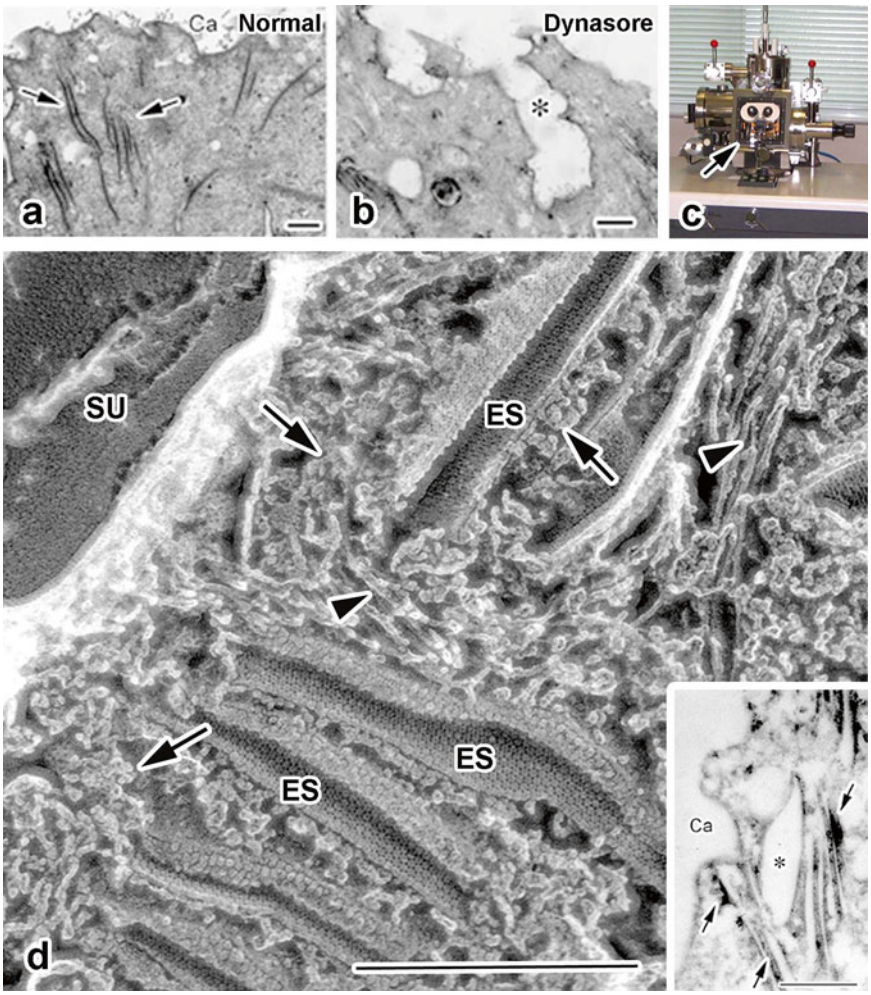

Fig. 27.1 (**a**, **b**) Representative electron micrographs of the apical cytoplasm of umbrella cells in mouse bladder under the absence (**a**; Normal) and presence (**b**; Dynasore) of the dynasore treatment. *Ca* bladder cavity. (**c**) Photograph of the machine for etching and coating with platinum and carbon under high vacuum condition. *Arrow* indicates the high vacuum chamber. (**d**) Electron micrograph of mouse bladder umbrella cell with quick-freezing and deep-etching method. Hexagonal intramembranous particles are observed on the E-surface (*ES*) of discoid vesicles. *Arrows* indicate filaments decorated with anti-Dyn2 antibody, and arrowheads indicate intermediate filaments. *SU* surface of umbrella cell. *Inset* in (**d**) shows pre-embedding immunoelectron micrograph for Dyn2. Precise data have been reported in the previous paper (Terada et al. [1]). *Bars* 500 nm

of one intracellular compartment and typically promotes their targeting to, and fusion with, another compartment. It has been implicated in several well-known endocytic activities including clathrin- and caveolin-mediated endocytosis, where they mediate the scission of vesicular compartments from the unit membranes [6].

27.3 Localization of Dyn2 Around Discoid Vesicles and Cytoskeletal Networks in UCs

In this chapter, we demonstrate the involvement of Dyn2 in the formation of DVs in urinary bladder umbrella cells. Precise methods and results have been reported in the previous paper [1]. Dyn2 was immunostained in the cytoplasm of UCs. By immunoelectron microscopy for Dyn2 detection, its specific aggregation was detected around DV membranes (inset in Fig. 27.1d). As Dyn2 is known to control organization of actin microfilaments in relation to the endocytosis of culture cells [6, 8], the quick-freezing and deep-etching (QF-DE) method was used to examine ultrastructure of UCs (Fig. 27.1d). Paraformaldehyde-fixed mouse urinary bladder was permeabilized with detergent, and some were immunostained for Dyn2. The bladder was quickly frozen and deep-etched in freeze-dry machine as shown in Fig. 27.1c, and replica membranes were made, allowing us to observe cytoskeletons with transmission electron microscope. At the E-surface of freeze-fractured membranes (ES in Fig. 27.1d), the DVs have characteristic hexagonal pattern of globular intramembranous particles organized on the outer leaflet [9]. Distinct and often branched microfilaments, which were

demonstrated by decoration of granular immunoproducts on the DV membranes with immunostaining with the Dyn2-specific antibody, connected to the cytoplasmic sides of each DV membrane (arrows in Fig. 27.1d) and intermediate filaments (arrowheads in Fig. 27.1d).

27.4 Inhibition of Dyn2 Endocytic Activity in Umbrella Cells In Vivo

Dynasore, a cell-permeable Dyn-GTPase inhibitor [10, 11], was used for the treatment of mouse bladders in vivo. Under anesthesia, the bladders were exposed by opening the abdominal cavities of the mice, and urine in the bladders was sucked out with a syringe. After 5 min, the dynasore solution was gradually injected into the bladder lumen and incubated for 15 min. The dynasore treatment drastically reduced the number of DVs in the UCs and induced the formation of large membrane invaginations in the apical cell surface (Fig. 27.1b). This finding indicates that the Dyn2 probably moves along the membranes and/or interacts with proteins, such as microfilament-related proteins, during GTPase inhibition.

27.5 Endocytic Activity for Infection of *Escherichia coli* in the Urinary Bladder

Uropathogenic *E. coli* are reported to bind to the uroplakin plaques on the apical surface of UCs triggering bacterial endocytosis through the formation of DVs [9, 12]. Infected bladder showed many bacteria in close association with the apical cell surface of UCs, and the bacteria appeared to be at various stages of entry into intracellular compartments, which were immunostained strongly for Dyn2. Moreover, after pretreatment of the *E.coli*-infected mouse bladders with dynasore, the entry of bacteria into the bladder was reduced compared with that of the control. This finding provided additional evidence of the functional contribution of Dyn in promoting the entry of *E. coli* into UCs of the bladder.

27.6 Concluding Remarks

Dyn2 is highly enriched in the UCs and is mostly localized in DVs and microfilaments. Contribution of Dyn2 to the structural integrity of the DVs and to the endocytic activity of UCs was confirmed by treatment of the Dyn inhibitor.

References

1. Terada N, Ohno N, Saitoh S, Saitoh Y, Fujii Y, Kondo T, Katoh R, Chan C, Abraham SN, Ohno S (2009) Involvement of dynamin-2 in formation of discoid vesicles in urinary bladder umbrella cells. Cell Tissue Res 337:91–102
2. Apodaca G (2004) The uroepithelium: not just a passive barrier. Traffic 5:117–128
3. Lewis SA (2000) Everything you wanted to know about the bladder epithelium but were afraid to ask. Am J Physiol Renal Physiol 278:F867–F874
4. Minsky BD, Chlapowski FJ (1978) Morphometric analysis of the translocation of lumenal membrane between cytoplasm and cell surface of transitional epithelial cells during the expansion-contraction cycles of mammalian urinary bladder. J Cell Biol 77:695–697
5. Baba T, Ueda H, Terada N, Fujii Y, Ohno S (1999) Immunocytochemical study of endocytotic structures accumulated in HeLa cells transformed with a temperature-sensitive mutant of dynamin. J Histochem Cytochem 47:637–648
6. Sever S (2002) Dynamin and endocytosis. Curr Opin Cell Biol 14:463–467
7. Cook TA, Urrutia T, McNiven MA (1994) Identification of dynamin 2, an isoform ubiquitously expressed in rat tissues. Proc Natl Acad Sci U S A 91:644–648
8. Schafer DA (2004) Regulating actin dynamics at membranes: a focus on dynamin. Traffic 5:463–464
9. Min G, Stolz M, Zhou G, Liang F, Sebbel P, Stoffler D, Glockshuber R, Sun TT, Aebi U, Kong XP (2002) Localization of uroplakin Ia, the urothelial receptor for bacterial adhesin FimH, on the six inner domains of the 16 nm urothelial plaque particle. J Mol Biol 317:697–706
10. Macia E, Ehrlich M, Massol R, Boucrot E, Brunner C, Kirchhausen T (2006) Dynasore, a cell-permeable inhibitor of dynamin. Dev Cell 10:839–850
11. Newton AJ, Kirchhausen T, Murthy VN (2006) Inhibition of dynamin completely blocks compensatory synaptic vesicle endocytosis. Proc Natl Acad Sci U S A 103:17955–17960
12. Duncan MJ, Li G, Shin JS, Carson JL, Abraham SN (2004) Bacterial penetration of bladder epithelium through lipid rafts. J Biol Chem 279:18944–18951

Involvement of Follicular Basement Membrane and Vascular Endothelium in Blood-Follicle Barrier Formation of Mice

28

Nobuhiko Ohno, Hong Zhou, Nobuo Terada, and Shinichi Ohno

Abstract

Blood-follicle barrier (BFB) in ovarian follicles is the molecular sieve selective for size and charge. By utilizing the "in vivo cryotechnique" (IVCT), ovarian structures responsible for the BFB were analyzed during development of follicles under physiological conditions. Immunoreactivity of mouse serum proteins was better preserved with IVCT compared with other conventional methods. Strong immunoreactivity of albumin was detected in blood vessels, interstitium, and developing follicles. There was a clear alteration of the immunostaining intensity of IgG1 between inside and outside of the follicular basement membranes. Immunoreactivity of IgM was significantly changed between inside and outside of the vascular endothelial cells. These results suggest that permselectivity of BFB for soluble proteins with intermediate molecular weights is dependent on the follicular basement membrane and the vascular endothelial cells could play significant roles in the permselectivity for soluble proteins with high molecular weight.

Keywords

Ovarian follicles • Serum proteins • In vivo cryotechnique • Permselectivity

28.1 Introduction

Ovarian follicles of living animals are dynamic structures which gradually increase their volume before ovulation during each estrous cycle. Structural changes of perifollicular capillary networks are observed upon the follicular development [1]. Development of the membrana granulosa in secondary follicles accompanies formation of the perifollicular capillary networks. Subsequently, when larger or mature Graafian follicles are developed from the secondary follicles, a single-layered to multilayered thick theca interna is formed [1–6]. These morphological changes suggest that follicular development and oocyte maturation require substantial increase of blood supply and nutritional support.

In living animal ovaries, follicular fluid is produced by secretion from the membrana granulosa cells and diffusion of serum proteins from thecal capillaries and influences a microenvironment within the avascular compartment of follicles [7, 8]. Blood-follicle barrier (BFB) was suggested by the differences in

N. Ohno, M.D., Ph.D. (✉) • S. Ohno
Department of Anatomy and Molecular Histology, Interdisciplinary Graduate School of Medicine and Engineering, University of Yamanashi, 1110 Shimokato, Chuo City, Yamanashi 409-3898, Japan
e-mail: nohno@yamanashi.ac.jp

H. Zhou
Department of Anatomy and Molecular Histology, Interdisciplinary Graduate School of Medicine and Engineering, University of Yamanashi, 1110 Shimokato, Chuo City, Yamanashi 409-3898, Japan

Department of Child, Adolescent and Women's Health, School of Public Health, Peking University, Beijing 100083, China

N. Terada
Division of Health Sciences, Shinshu University Graduate School of Medicine, 3-1-1 Asahi, Matsumoto City, Nagano 390-8621, Japan

Department of Anatomy and Molecular Histology, Interdisciplinary Graduate School of Medicine and Engineering, University of Yamanashi, 1110 Shimokato, Chuo City, Yamanashi 409-3898, Japan

S. Ohno et al. (eds.), *In Vivo Cryotechnique in Biomedical Research and Application for Bioimaging of Living Animal Organs*, DOI 10.1007/978-4-431-55723-4_28

both composition and concentrations of soluble proteins between the follicular fluid and the blood serum [8, 9]. BFB is proposed as a "molecular sieve" with size selectivity, and the capillary endothelium, the subendothelial basal lamina, the theca interna, the follicular basement membrane, and the membrana granulosa were reported to be responsible for BFB. Proteins with relatively lower molecular weight (<500 kDa) can enter the follicular fluid through BFB, but components with higher molecular weight or larger particles are blocked and cannot enter the follicular fluid [8, 10]. Other studies suggested that there is charge selectivity and involvement of nitric oxide in the functions of BFB [11–13]. To elucidate morphology of BFB under physiological conditions in vivo and the structures essential for BFB in the ovaries, living mouse ovaries were examined by "in vivo cryotechnique" (IVCT) to focus on the BFB under normal blood circulation [14].

28.2 Distribution of Serum Proteins in Ovarian Follicles

Large amounts of albumin were detected in the follicular fluid in the previous biochemical studies [8, 15]. Indeed, with IVCT, albumin was clearly immunolocalized in blood vessels, interstitium, and ovarian follicles (Fig. 28.1) [14]. On the other hand, with conventional perfusion fixation followed by dehydration, albumin immunoreactivity was decreased inside the ovarian follicles, and moreover diffuse cytoplasmic immunostaining for albumin was observed inside some oocytes and granulosa cells [14]. Therefore, tissue preparation procedures with organ perfusion or chemical fixation followed by alcohol dehydration can modify the immunodistribution of serum proteins in vivo.

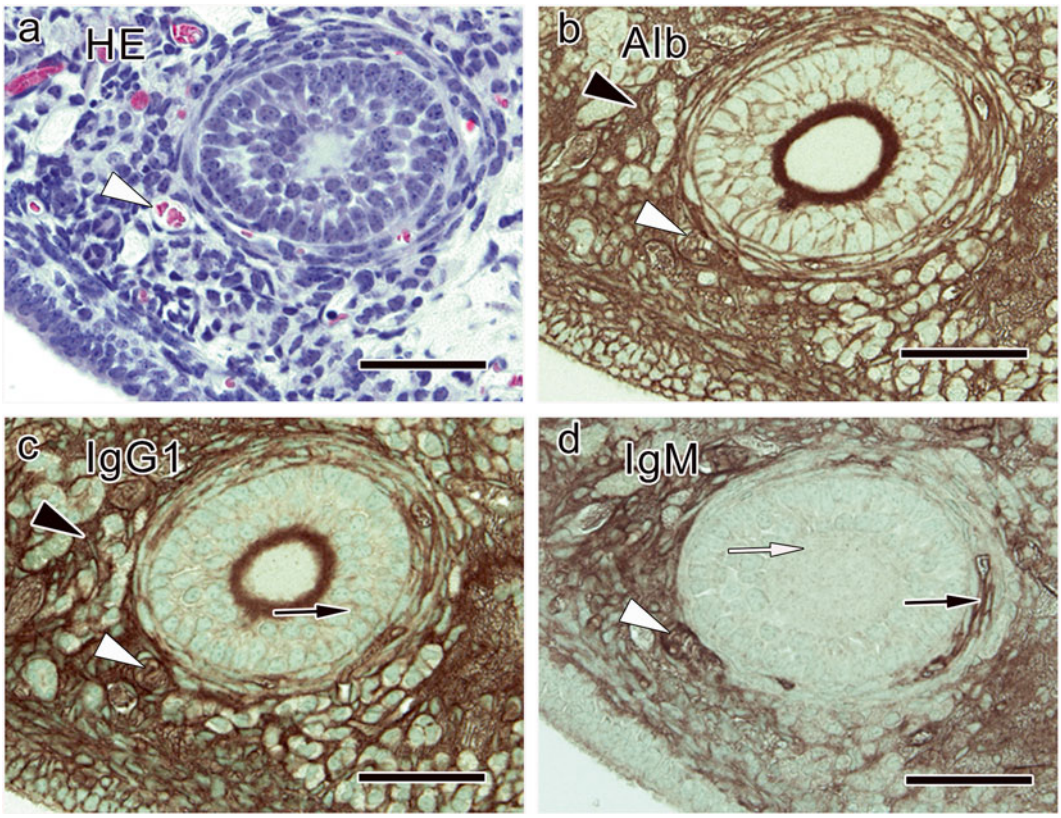

Fig. 28.1 Serial paraffin sections prepared by in vivo cryotechnique and stained with hematoxylin-eosin (HE, **a**) or immunostained for albumin (Alb, **b**), immunoglobulin G1 (IgG1, **c**), or IgM (**d**) show that in late primary follicle in living mouse ovaries, multiple layers of follicular cells surround the oocyte. Inside the blood vessels, the clear immunoreactivity of the three serum proteins is observed (**a**–**d**, *white arrowheads*). Immunoreactivity of albumin (**b**, *black arrowhead*) and IgG1 (**c**, *black arrowhead*) is clear in the theca layers and interstitium of ovary, but immunostaining for IgG1 is weaker inside ovarian follicles (**c**, *black arrow*). Immunostaining for IgM is decreased in the interstitium and theca layers (**d**, *black arrows*) compared with that in blood vessels (**d**, *white arrowheads*) and hardly detected in the follicles (**d**, *white arrow*). *Bars*, 50 μm (The figure was modified from Zhou et al. [14])

28.3 Characteristics of BFB for Permselectivity

Serial ovarian sections with follicles in different stages were prepared with IVCT and immunostained to compare distributions of the three serum proteins including albumin (69 kDa), IgG1 (150 kDa), and IgM (900 kDa) (Fig. 28.1) [14]. In a late primary follicle with a stratified layer of granulosa cells around the oocyte, blood vessels contained immunoreactivities of all three proteins. While IgG1 immunoreactivity was decreased inside the primary follicle, immunoreactivities of albumin and IgG1 were also observed in the interstitium (Fig. 28.1). To the contrary, strong immunostaining for IgM was observed inside blood vessels but reduced in theca layers, interstitium, and follicles. Therefore, large molecules such as IgG1 and IgM appear to be blocked around the follicles or the blood vessels, but small albumin easily enters ovarian follicles.

In primordial follicles composed of a primary oocyte and a single layer of flat follicular cells surrounding the oocyte, blood vessels around those follicles immunostained for the three serum proteins (Fig. 28.2) [14]. The albumin immunostaining was positive in those follicles. Weak immunostainings for IgG1 and IgM could be observed inside these follicles, and that for IgM was weak in the interstitium and theca layers (Fig. 28.2). Similar immunostaining of albumin, IgG1, and IgM was observed in antral follicles, where more layers of follicular cells and the antrum appear (Fig. 28.2). By contrast, immunostaining for the three serum proteins was all clear in the ovulated follicles [14], consistent with previous reports [11, 12].

Previous studies suggested that BFB substantially affects distributions of medium-sized serum molecules [11]. Indeed, immunostaining for IαI (220 kDa) or fibrinogen (340 kDa) observed with IVCT was weaker inside the ovarian follicles [14].

Double immunofluorescence labeling of basement membranes and IgGfc or IgM in living mouse ovaries prepared by IVCT revealed that immunoreactivity of IgGfc was observed in the theca layers and interstitium, but weak inside ovarian follicles surrounded by the basement membranes which bordered the changes of IgGfc immunoreactivity [14]. IgM immunoreactivity was detected exclusively in blood vessels around the theca interna and not in the ovarian follicles and interstitium. The immunolocalization of IgM was mostly restricted inside endothelium of the blood vessels surrounded by basement membranes.

Selective functions of molecular permeation throughout the follicular development until ovulation appear to be determined by BFB. In living mouse ovaries, the endothelial layers of blood vessels determine in vivo permeability of large molecular weight proteins such as IgM, while the follicular basement membranes are important for permselectivity of middle-sized molecules, such as IgG. Endothelium of blood vessels generally controls the passage of soluble components and circulating blood cells into tissue parenchyma. Adhesion and communication between adjacent endothelial cells are mediated by their intercellular junctions [16, 17]. Previous studies demonstrated that the tight junctions were critical for endothelial permeability [18, 19]. In living mouse ovaries, the functions of intercellular communication between endothelial cells are elusive regarding permeability of soluble serum proteins through blood vessel walls. Studies at an electron microscopic level using IVCT would be important to elucidate the components and structures responsible for intercellular communication between endothelial cells in blood vessels of ovaries and regulation of permselectivity against larger molecules.

The blood vessels are surrounded by basement membranes which function as a porous molecular sieve. The charge and structural arrangement of its components, including type IV collagen and heparan sulfate proteoglycans, are responsible for the molecular selectivity of the basement membranes [20, 21]. Leakage of large serum proteins out of blood vessels is prevented by basement membranes around blood vessels in some organs, such as kidneys [22, 23]. Follicular basement membranes in mouse ovaries would also have functions related to a molecular sieve of ovarian follicles and might be involved in regulation of developmental metabolic exchanges between inside and outside of the ovarian follicles. The permselectivity of basement membranes appeared different around follicles and blood vessels. Their functional difference might be explained by the difference in their components. During the follicular development and ovulation, the follicular basement membrane has to be dramatically changed [24, 25]. But significant relationship between basement membranes and the BFB, which are continuously sealing the ovarian follicles during all development stages, is supported by the observation that BFB was functioning at an early stage of folliculogenesis [26].

28.4 Concluding Remarks

The morphology of normal living mouse ovaries and distribution of endogenous soluble serum proteins could be precisely examined with IVCT. The size-dependent permselectivity of BFB against endogenous serum proteins and also the histological layers responsible for the barrier functions of BFB were demonstrated during follicular development in vivo. Distinct immunostaining patterns of those serum proteins suggest that the layers of follicular basement membranes in mouse ovaries are important for the permeability of serum proteins with intermediate molecular sizes, while the vascular endothelial cells play significant roles in the permselectivity of larger molecules.

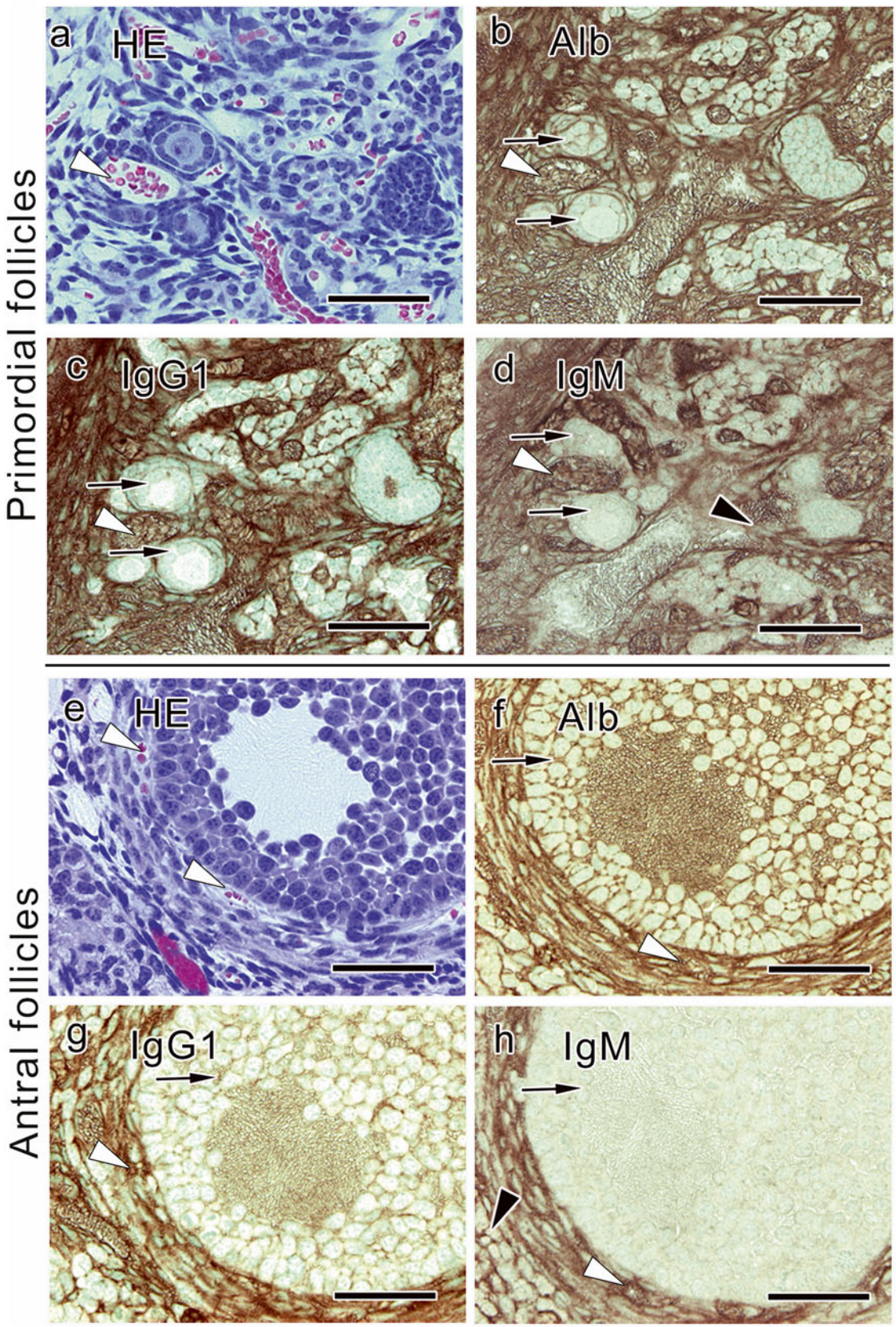

Fig. 28.2 Serial paraffin sections showing primordial (**a**–**d**) and antral follicles (**e**–**h**) obtained from living mouse ovaries with in vivo cryotechnique and stained with hematoxylin-eosin (HE, **a**, **e**) or immunostained for albumin (Alb, **b**, **f**), immunoglobulin G1 (IgG1, **c**, **g**), or IgM (**d**, **h**). The sections demonstrate that the strong immunoreactivities of all three serum proteins are observed inside blood vessels (**a**–**h**, *white arrowheads*). The immunoreactivity of IgG1 and IgM is not clearly seen inside the follicles (**c**, **d**, **g**, **h**, *black arrows*), and the IgM immunostaining is weak also in the theca layers and interstitium (**d**, **h**, *black arrowheads*), as in or around the late primary follicles. The primordial follicles (**a**, **b**, **c**, **d**, *black arrows*) are composed of a single layer of flat follicular cells surrounding the oocyte, and antral follicles have more layers of follicular cells and antrum among them. *Bars*, 50 μm (The figure was modified from Zhou et al. [14])

References

1. Macchiarelli G (2000) The microvasculature of the ovary. A review by SEM of vascular corrosion casts. J Reprod Dev 46:207–225
2. Jiang JY, Macchiarelli G, Miyabayashi K, Sato E (2002) Follicular microvasculature in the porcine ovary. Cell Tissue Res 310(1):93–101
3. Kanzaki H, Okamura H, Okuda Y, Takenaka A, Morimoto K, Nishimura T (1982) Scanning electron microscopic study of rabbit ovarian follicle microvasculature using resin injection-corrosion casts. J Anat 134(Pt 4):697–704
4. Kitai H, Yoshimura Y, Wright KH, Santulli R, Wallach EE (1985) Microvasculature of preovulatory follicles: comparison of in situ and in vitro perfused rabbit ovaries following stimulation of ovulation. Am J Obstet Gynecol 152(7 Pt 1):889–895
5. Kranzfelder D, Maurer-Schultze B (1989) Development of the perifollicular capillary network. Autoradiographic and morphometric studies in the rabbit ovary. Eur J Obstet Gynecol Reprod Biol 30(2):163–171
6. Yamada O, Abe M, Takehana K, Iwasa K, Hiraga T (1994) Scanning electron microscopical observation of the intramitochondrial body in the bovine corpus luteum during pregnancy and after parturition. J Vet Med Sci 56(3):459–464
7. Donahue RP, Stern S (1968) Follicular cell support of oocyte maturation: production of pyruvate in vitro. J Reprod Fertil 17(2):395–398
8. Shalgi R, Kraicer P, Rimon A, Pinto M, Soferman N (1973) Proteins of human follicular fluid: the blood-follicle barrier. Fertil Steril 24(6):429–434
9. Zachariae F (1958) Studies on the mechanism of ovulation: permeability of the blood-liquor barrier. Acta Endocrinol (Copenh) 27(3):339–342
10. Cran DG, Moor RM, Hay MF (1976) Permeability of ovarian follicles to electron-dense macromolecules. Acta Endocrinol (Copenh) 82(3):631–636
11. Hess KA, Chen L, Larsen WJ (1998) The ovarian blood follicle barrier is both charge- and size-selective in mice. Biol Reprod 58(3):705–711
12. Powers RW, Chen L, Russell PT, Larsen WJ (1995) Gonadotropin-stimulated regulation of blood-follicle barrier is mediated by nitric oxide. Am J Physiol 269(2 Pt 1):E290–E298
13. Zhuo L, Kimata K (2001) Cumulus oophorus extracellular matrix: its construction and regulation. Cell Struct Funct 26(4):189–196
14. Zhou D, Ohno N, Terada N, Li Z, Morita H, Inui K et al (2007) Immunohistochemical analyses on serum proteins in nephrons of protein-overload mice by "in vivo cryotechnique". Histol Histopathol 22(2):137–145
15. Collins A, Palmer E, Bezard J, Burke J, Duchamp G, Buckley T (1997) A comparison of the biochemical composition of equine follicular fluid and serum at four different stages of the follicular cycle. Equine Vet J Suppl 25:12–16
16. Bazzoni G, Dejana E (2004) Endothelial cell-to-cell junctions: molecular organization and role in vascular homeostasis. Physiol Rev 84(3):869–901
17. Orlova VV, Economopoulou M, Lupu F, Santoso S, Chavakis T (2006) Junctional adhesion molecule-C regulates vascular endothelial permeability by modulating VE-cadherin-mediated cell-cell contacts. J Exp Med 203(12):2703–2714
18. Aijaz S, Balda MS, Matter K (2006) Tight junctions: molecular architecture and function. Int Rev Cytol 248:261–298
19. Bazzoni G (2006) Endothelial tight junctions: permeable barriers of the vessel wall. Thromb Haemost 95(1):36–42
20. Farquhar MG (2006) The glomerular basement membrane: not gone, just forgotten. J Clin Invest 116(8):2090–2093
21. Holmquist P, Sjoblad S, Torffvit O (2004) Pore size and charge selectivity of the glomerular membrane at the time of diagnosis of diabetes. Pediatr Nephrol 19(12):1361–1366
22. Maina JN, West JB (2005) Thin and strong! The bioengineering dilemma in the structural and functional design of the blood-gas barrier. Physiol Rev 85(3):811–844
23. Ohlson M, Sorensson J, Haraldsson B (2000) Glomerular size and charge selectivity in the rat as revealed by FITC-ficoll and albumin. Am J Physiol Renal Physiol 279(1):F84–F91
24. Rodgers RJ, Irving-Rodgers HF, Russell DL (2003) Extracellular matrix of the developing ovarian follicle. Reproduction 126(4):415–424
25. Zamboni L (1974) Fine morphology of the follicle wall and follicle cell-oocyte association. Biol Reprod 10(2):125–149
26. Rodgers RJ, Lavranos TC, van Wezel IL, Irving-Rodgers HF (1999) Development of the ovarian follicular epithelium. Mol Cell Endocrinol 151(1–2):171–179

Permselectivity of Blood-Follicle Barriers in Mouse Polycystic Ovary Model

29

Nobuhiko Ohno, Hong Zhou, Nobuo Terada, and Shinichi Ohno

Abstract

To elucidate alterations of follicular microenvironment and blood–follicle barriers (BFB) in polycystic ovary (PCO) syndrome, a mifepristone-induced PCO model was produced, and ovarian morphology and distribution of soluble plasma proteins were examined with in vivo cryotechnique (IVCT). Blood vessels with increased diameter and cystic follicles with degenerative membrana granulosa were clearly observed in the PCO model. The distribution of albumin (molecular weight, 69 kDa) and immunoglobulin M (IgM 900 kDa) was similar in normal and the PCO model ovaries. Albumin immunolocalized in the blood vessels, interstitium, and follicles, and IgM was mostly restricted within the blood vessels. In the PCO model, immunolocalization of immunoglobulin G (IgG; 150 kDa), inter-alpha-trypsin inhibitor (ITI; 220 kDa), and fibrinogen (340 kDa) was changed. In the PCO model ovaries, fibrinogen was mostly observed within blood vessels, and IgG and ITI were hardly observed in the membrana granulosa. The findings suggest that the PCO model ovaries are characterized by enhanced selectivity of the BFB in addition to increased blood flow, and some intermediate-sized molecules are blocked by follicular basement membranes. The pathogenesis and pathophysiology of PCO syndrome may be modulated by the hemodynamic conditions and permselectivity of BFB.

Keywords

Blood vessel • Plasma proteins • In vivo cryotechnique • Mouse ovary • Ovarian follicles

N. Ohno, M.D., Ph.D. (✉) • S. Ohno
Department of Anatomy and Molecular Histology, Interdisciplinary Graduate School of Medicine and Engineering, University of Yamanashi, 1110 Shimokato, Chuo City, Yamanashi 409-3898, Japan
e-mail: nohno@yamanashi.ac.jp

H. Zhou
Department of Anatomy and Molecular Histology, Interdisciplinary Graduate School of Medicine and Engineering, University of Yamanashi, 1110 Shimokato, Chuo City, Yamanashi 409-3898, Japan

Department of Child, Adolescent and Women's Health, School of Public Health, Peking University, Beijing 100083, China

N. Terada
Division of Health Sciences, Shinshu University Graduate School of Medicine, 3-1-1 Asahi, Matsumoto City, Nagano 390-8621, Japan

Department of Anatomy and Molecular Histology, Interdisciplinary Graduate School of Medicine and Engineering, University of Yamanashi, 1110 Shimokato, Chuo City, Yamanashi 409-3898, Japan

29.1 Introduction

Polycystic ovary (PCO) syndrome is a common cause of anovulation in reproductive-age women [1, 2]. Microscopic analyses of PCO syndrome have found histopathological findings in ovaries which include hyperplasia of thecal cells, degenerative alterations in the granulosa of follicles, and multiple large cystic follicles [1, 3, 4]. In the PCO syndrome, alterations in follicular microenvironment may be affected in the changes of follicular morphology. Indeed, components in follicular fluids are changed in PCO syndrome patients [5–7]. The follicular microenvironment is affected by the follicular fluid, which is included in the avascular compartment of follicles and contains necessary growth factors. The follicular fluid is produced by secretion from granulosa cells

S. Ohno et al. (eds.), *In Vivo Cryotechnique in Biomedical Research and Application for Bioimaging of Living Animal Organs*, DOI 10.1007/978-4-431-55723-4_29

and diffusion of plasma proteins from thecal capillaries [8–11]. Blood–follicle barrier (BFB) was proposed as a functional barrier modulating protein composition and concentrations in the follicular fluid [12, 13] and is charge and size selective to be like a "molecular sieve" composed of the capillary endothelium, the theca interna, the basement membrane, and the membrana granulosa. Under the normal condition, BFB allows translocation of low and intermediate molecular weight proteins into the follicular fluid but hinders the passage of higher molecular weight components or larger particles [12, 14, 15]. The follicular basement membranes and the vascular endothelium appear to be responsible for the permselectivity for some soluble plasma proteins [15, 16]. In PCO syndrome, ovarian histology in addition to the follicular microenvironment could be significantly changed, and the functional changes could involve alteration of BFB and modulate the components of follicular fluid.

Under this background, the ovaries of PCO model mice were morphologically and immunohistochemically examined using in vivo cryotechnique (IVCT) to reveal the functional morphology of ovaries in PCO syndrome and the potential association of PCO syndrome with BFB [17]. The PCO model mouse was induced by mifepristone to investigate the effect of PCO syndrome-like endocrinological perturbations on ovarian physiology and histology during the short term [18, 19].

29.2 Histological Examination of PCO Model Mouse Ovaries

The subcutaneous injection of the antiprogestin, mifepristone, was used to produce a PCO model in mice [17, 20, 21]. The anovulation and multiple cysts in ovaries have been included in diagnostic criteria of PCO syndrome, and the administration of mifepristone to rats was used as a good model of human PCO syndrome [18, 22]. The daily checking of vaginal smear revealed that normal estrous cycles were impaired in all mice after 2–4 days of injection of mifepristone until the time of tissue fixation [17, 19, 20]. In specimens prepared by conventional perfusion fixation followed by dehydration (PF-DH), various kinds of developing follicles were observed in the specimens of control mice, but the specimens from mifepristone-induced PCO model mice were characterized by typical follicular cysts [17]. In the PCO model mice, the thickness of the degenerative membrana granulosa was decreased [17]. When the ovary tissue specimens of PCO model mice were prepared with IVCT, widely open blood vessels with flowing erythrocytes were clearly observed in both the cortex and medulla areas [17]. In the theca interna and medulla in the PCO model ovaries, numbers and volume of blood vessels were increased. Quantitative analyses using IVCT also confirmed that the antral follicle numbers significantly increased and the granulosa cell layer was thinner when compared with the thecal layer in the PCO model mice [17]. In addition, compared with those in the control mice, vascular volume was significantly higher in the medulla areas of the PCO model mice, and the vascular diameters in theca interna were significantly larger in the PCO model mice [17]. These results indicate that increases of vascularity and blood circulation are a major feature of PCO.

The observations of blood vessels would represent the higher ovarian blood flow in the PCO model mice [17]. This concept is supported by previous observation with color and pulsed wave Doppler ultrasonography [23, 24]. The angiogenesis and blood flow maintenance within the ovaries would be regulated by several growth factors [25–30]. In PCO syndrome women, VEGF has been positively correlated with ovarian stromal blood flow velocities [31, 32].

29.3 Immunohistochemical Examination of BFB in PCO Model Mice

In the antral follicles of both the control and PCO model ovaries prepared with IVCT, immunoreactivities of albumin (69 kDa), immunoglobulin G1 heavy chain (IgG1; 150 kDa), and immunoglobulin M (IgM; 900 kDa) were all clearly observed in open blood vessels (Fig. 29.1) [17]. The albumin immunostaining was clearly localized in the antral follicles of the PCO model and the control mice (Fig. 29.1), consistent with the previous findings [15]. In PCO model ovaries, only faint immunoreactivity of IgG1 was observed in the membrana granulosa, where weak immunostaining for IgG1 is observed in control mice (Fig. 29.1). Immunostaining for IgM was similar between control and PCO model ovaries [17]. The immunoreactivity of IgM was strongly observed inside the blood vessels of the thecal layers, decreased in interstitium and thecal layers, and hardly seen inside the follicles (Fig. 29.1). These findings suggest that distribution of small and large proteins is not significantly affected, but less plasma proteins with intermediate molecular weights, such as IgG, enter the ovarian follicles in the PCO model ovaries, compared with normal ovaries [17].

IVCT along with double immunofluorescence labeling of collagen type IV, a marker for follicular and vascular basement membranes, and multiple plasma proteins with intermediate molecular weights revealed altered distribution of the plasma proteins [17]. Immunoreactivity of IgG-Fc (150 kDa) was little in membrana granulosa of the antral follicles, in comparison with the thecal layers and blood vessels (Fig. 29.2). In comparison with the thecal layers and blood vessels, almost no immunoreactivity of inter-alpha-trypsin inhibitor (ITI; 220 kDa) was observed in the membrana granulosa in the antral follicles (Fig. 29.2). The follicular

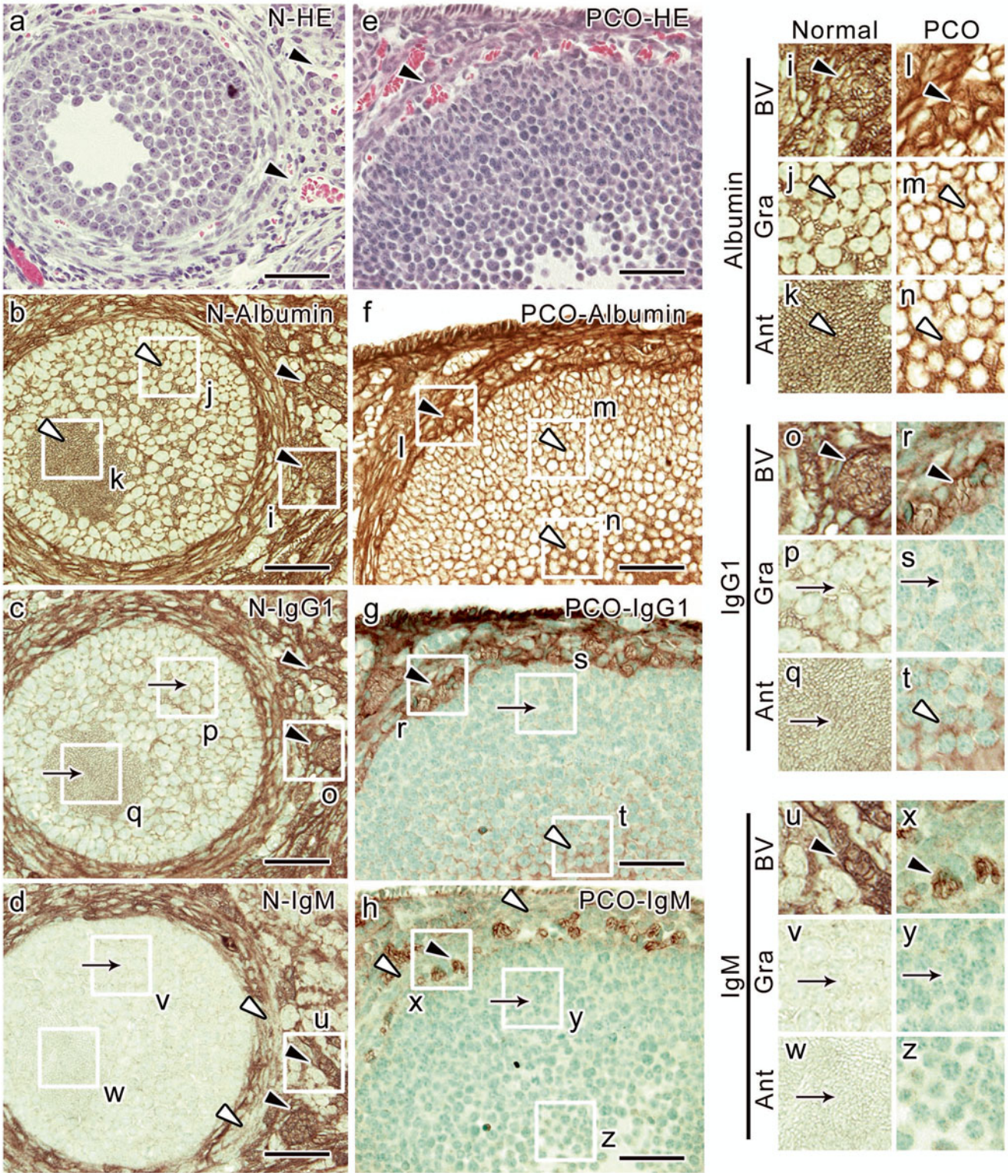

Fig. 29.1 Serial paraffin sections of antral follicles in the control (N; **a**–**d**, **i**–**k**, **o**–**q**, **u**–**w**) or mifepristone-induced polycystic ovary model (PCO; **e**–**h**, **l**–**n**, **r**–**t**, **x**–**z**) mouse ovaries prepared by in vivo cryotechnique and stained with hematoxylin-eosin (HE, **a**, **e**) or immunostained for albumin (**b**, **f**, **i**–**n**), immunoglobulin G (IgG1, **c**, **g**, **o**–**t**), and IgM (**d**, **h**, **u**–**z**). The immunoreactivity of the three plasma proteins is clearly observed in the blood vessels (BV; **a**–**h**, **i**, **l**, **o**, **r**, **u**, **x**, *black arrowheads*) of both control and PCO model mice. The albumin can be clearly detected in membrana granulosa (Gra) and antrum (Ant; **b**, **f**, **j**, **k**, **m**, **n**, *white arrowheads*). Immunoreactivity of IgG1 in the membrana granulosa is weaker than that in thecal layers and blood vessels in control mice (**c**, **p**, **q**, *arrows*). In contrast, immunoreactivity of IgG1 is very weak in the granulosa cell layer (**g**, **s**, *arrows*) and antrum (**g**, **t**, *white arrowheads*) in PCO model ovaries. The immunoreactivity for IgM in the interstitium (**d**, **h**, *white arrowheads*) is weaker than that in the blood vessels (**d**, **h**, **u**, **x**, *black arrowheads*), and no immunoreactivity is observed in the follicles of both control and PCO model mice (**d**, **h**, **v**, **w**, **y**, *arrows*). The regions marked with white rectangles in **b**–**d** and **f**–**h** are magnified in **i**–**z**. Bars, 40 μm (The figure is adapted from Zhou et al. [17])

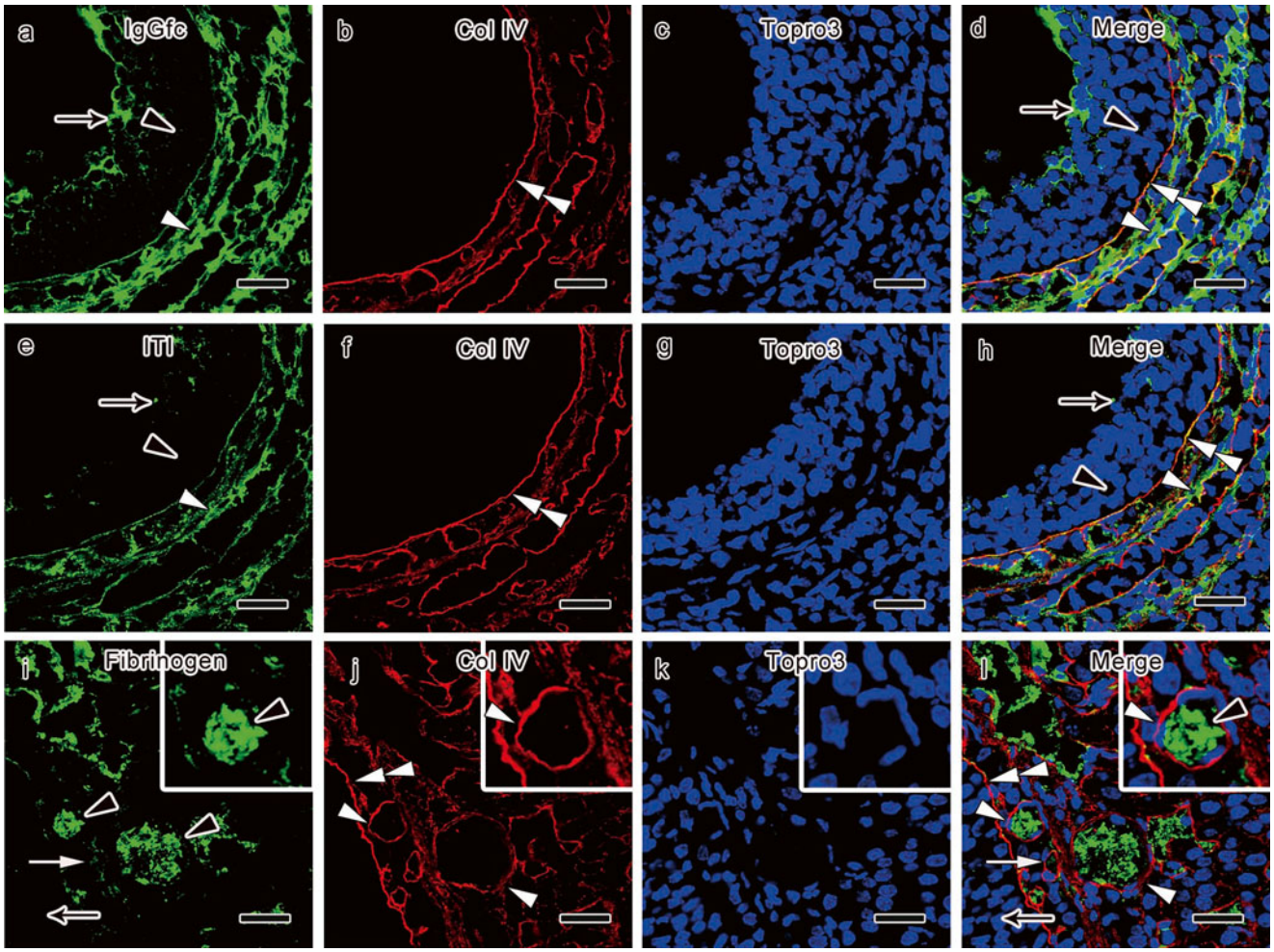

Fig. 29.2 Double immunostaining for collagen type IV (Col IV; **b**, **d**, **f**, **h**, **j**, **l**, *red color*) and immunoglobulin G-Fc (IgGfc; **a**, **d**, *green color*), inter-alpha-trypsin inhibitor (ITI; **e**, **h**, *green color*), and fibrinogen (**i**, **l**, *green color*) in PCO model mouse ovaries prepared with in vivo cryotechnique shows that little immunoreactivity of IgGfc (**a**, **d**, *black arrowheads*) is seen in the granulosa cell layer of the follicles, in comparison with the thecal layers and blood vessels (**a**, **d**, *white arrowheads*). Some IgGfc immunoreactivity is detected in the antrum (**a**, **d**, *arrows*). Almost no immunoreactivity of ITI is seen in the granular cell layer (**e**, **h**, *black arrowheads*) and the antrum (**e**, **h**, *arrows*) of the follicles, in comparison with the thecal layers and blood vessels (**e**, **h**, *white arrowheads*). The decrease of IgGfc and ITI immunoreactivity is clearly bordered by the follicular basement membranes immunopositive for Col IV (**b**, **d**, **f**, **h**, *double white arrowheads*). The immunoreactivity of fibrinogen is more clearly seen in the blood vessels of the thecal layers (**i**, **l**, *arrowheads*), while it is not detected inside the antral follicles (**i**, **l**, *arrows*). The alterations of fibrinogen immunoreactivity are mostly bordered by vascular basement membranes immunopositive for Col IV (**j**, **l**, *white arrowheads*) and also partly by the follicular basement membranes (**j**, **l**, *double white arrowheads*). The cellular nuclei are labeled with Topro3 (**c**, **d**, **g**, **h**, **k**, **l**, *blue color*). Bars, 20 μm (The figure is adapted from Zhou et al. [17])

basement membranes immunostained with collagen type IV bordered the prominent immunoreactivity decrease of IgG-Fc and ITI (Fig. 29.2). The immunostaining for fibrinogen (340 kDa) was largely restricted within the blood vessels, which was surrounded by the basement membranes immunopositive for collagen type IV (Fig. 29.2).

In the PCO model mice examined with IVCT, the immunoreactivity of proteins with intermediate molecular weights appears decreased inside the follicles. These findings indicate that such permselective functions especially against proteins with intermediate molecular weights are enhanced in PCO. The impaired passage of middle-sized plasma proteins through follicular basement membranes might be attributable to alterations of the extracellular matrix components around the developing follicles, since appropriate remodeling of extracellular matrices is essential for normal ovulation [33–35]. Although only a part of ITI binds to hyaluronic acid produced by granulosa cells to stabilize the cumulus extracellular matrix, the decrease of follicular ITI may also be involved in disturbed follicular expansion and ovulation [36–38]. On the other hand, high fibrinogen (340 kDa) immunoreactivity was bordered at the vascular endothelium which was surrounded by basement membranes immunopositive for collagen type IV (Fig. 29.2) [17]. In normal mouse ova-

ries, fibrinogen passed through the basement membranes into the interstitium [15]. The endothelium is considered to be one of the important sites for the BFB permselectivity [15, 16]. Dynamic cellular rearrangements, partly regulated by cell–cell adhesion, play essential roles in morphological changes during follicular development [39, 40]. The tight junction is located on the apical side of epithelial and endothelial cells to completely seal their intercellular spaces [41, 42]. Downregulation of claudin 5 is caused by VEGF inhibition in the endothelium of the thecal vasculature [43]. The upregulation of claudin may contribute to the enhanced permselectivity of endothelial cells, given that the ovarian blood flow and VEGF expression in blood circulation are significantly increased in the PCO syndrome [32].

Since the structural components of basement membranes are responsible for the permselectivity [44, 45], collagen type IV α chains were immunohistochemically examined to reveal any changes in the major components of the basement membranes [17, 46, 47]. However, immunohistochemical analyses of the basement membrane components, including collagen type IV α2, α4, and α5 chains, in control and PCO model ovaries revealed that there was no detectable change of the basement membrane components [17]. In addition, it was previously reported in PCO that there were few ultrastructural changes in follicular basement membranes [48]. Further analyses on other molecular components of basement membranes, such as perlecan, nidogens, and laminins, and ultrastructures of the follicular basement membranes using IVCT would be useful, since the conventional preparation methods cause shrinkage artifacts in basement membranes at an ultrastructural level [49].

29.4 Concluding Remarks

With IVCT, morphological changes and the immunoreactivity of plasma proteins were clearly observed in living mouse ovaries of the PCO model. Enlarged blood vessels were observed in the ovaries of the PCO model mice prepared with IVCT, indicating increased blood flow into the ovaries. In addition, in the PCO model ovaries, follicular cysts with degenerative membrana granulosa were formed. Plasma proteins with intermediate molecular weights, including IgG1, ITI, and fibrinogen, appeared to be strictly bordered at the BFB in the PCO model mice, although the distribution of plasma proteins with low and high molecular weights, including albumin and IgM, was similar in the PCO model and normal mice. IVCT revealed that the PCO model ovaries are characterized by the increased blood circulation and higher selectivity of plasma protein permeation through the BFB. The pathogenesis and pathophysiology of PCO syndrome might by influenced by the alterations of hemodynamic conditions and permselectivity of BFB.

References

1. Franks S (1995) Polycystic ovary syndrome. N Engl J Med 333(13):853–861
2. Knochenhauer ES, Key TJ, Kahsar-Miller M, Waggoner W, Boots LR, Azziz R (1998) Prevalence of the polycystic ovary syndrome in unselected black and white women of the southeastern United States: a prospective study. J Clin Endocrinol Metab 83(9):3078–3082
3. Ehrmann DA (2005) Polycystic ovary syndrome. N Engl J Med 352(12):1223–1236
4. Legro RS (2001) Polycystic ovary syndrome: the new millennium. Mol Cell Endocrinol 184(1–2):87–93
5. Onalan G, Selam B, Baran Y, Cincik M, Onalan R, Gunduz U et al (2005) Serum and follicular fluid levels of soluble Fas, soluble Fas ligand and apoptosis of luteinized granulosa cells in PCOS patients undergoing IVF. Hum Reprod 20(9):2391–2395
6. San Roman GA, Magoffin DA (1992) Insulin-like growth factor binding proteins in ovarian follicles from women with polycystic ovarian disease: cellular source and levels in follicular fluid. J Clin Endocrinol Metab 75(4):1010–1016
7. Welt CK, Taylor AE, Fox J, Messerlian GM, Adams JM, Schneyer AL (2005) Follicular arrest in polycystic ovary syndrome is associated with deficient inhibin A and B biosynthesis. J Clin Endocrinol Metab 90(10):5582–5587
8. Angelucci S, Ciavardelli D, Di Giuseppe F, Eleuterio E, Sulpizio M, Tiboni GM et al (2006) Proteome analysis of human follicular fluid. Biochim Biophys Acta 1764(11):1775–1785
9. Donahue RP, Stern S (1968) Follicular cell support of oocyte maturation: production of pyruvate in vitro. J Reprod Fertil 17(2):395–398
10. Gosden RG, Hunter RH, Telfer E, Torrance C, Brown N (1988) Physiological factors underlying the formation of ovarian follicular fluid. J Reprod Fertil 82(2):813–825
11. Gull I, Geva E, Lerner-Geva L, Lessing JB, Wolman I, Amit A (1999) Anaerobic glycolysis. The metabolism of the preovulatory human oocyte. Eur J Obstet Gynecol Reprod Biol 85(2):225–228
12. Shalgi R, Kraicer P, Rimon A, Pinto M, Soferman N (1973) Proteins of human follicular fluid: the blood-follicle barrier. Fertil Steril 24(6):429–434
13. Zachariae F (1958) Studies on the mechanism of ovulation: permeability of the blood-liquor barrier. Acta Endocrinol (Copenh) 27(3):339–342
14. Cran DG, Moor RM, Hay MF (1976) Permeability of ovarian follicles to electron-dense macromolecules. Acta Endocrinol (Copenh) 82(3):631–636
15. Zhou H, Ohno N, Terada N, Saitoh S, Fujii Y, Ohno S (2007) Involvement of follicular basement membrane and vascular endothelium in blood follicle barrier formation of mice revealed by 'in vivo cryotechnique'. Reproduction (Cambridge, England) 134(2):307–317
16. Powers RW, Chen L, Russell PT, Larsen WJ (1995) Gonadotropin-stimulated regulation of blood-follicle barrier is mediated by nitric oxide. Am J Physiol 269(2 Pt 1):E290–E298
17. Zhou H, Ohno N, Terada N, Saitoh S, Naito I, Ohno S (2008) Permselectivity of blood follicle barriers in mouse ovaries of the mifepristone-induced polycystic ovary model revealed by in vivo cryotechnique. Reproduction (Cambridge, England) 136(5):599–610
18. Lakhani K, Yang W, Dooley A, El-Mahdi E, Sundaresan M, McLellan S et al (2006) Aortic function is compromised in a rat model of polycystic ovary syndrome. Hum Reprod 21(3):651–656
19. Ruiz A, Aguilar R, Tebar AM, Gaytan F, Sanchez-Criado JE (1996) RU486-treated rats show endocrine and morphological responses to therapies analogous to responses of women with polycystic ovary syndrome treated with similar therapies. Biol Reprod 55(6):1284–1291

20. Gao Y, Short RV (1994) Fertility control in laboratory rats and mice after feeding with the antigestagen RU486. J Reprod Fertil 101(2):477–481
21. Loutradis D, Bletsa R, Aravantinos L, Kallianidis K, Michalas S, Psychoyos A (1991) Preovulatory effects of the progesterone antagonist mifepristone (RU486) in mice. Hum Reprod 6(9):1238–1240
22. Singh KB (2005) Persistent estrus rat models of polycystic ovary disease: an update. Fertil Steril 84(Suppl 2):1228–1234
23. Pan HA, Wu MH, Cheng YC, Li CH, Chang FM (2002) Quantification of Doppler signal in polycystic ovary syndrome using three-dimensional power Doppler ultrasonography: a possible new marker for diagnosis. Hum Reprod 17(1):201–206
24. Zaidi J, Campbell S, Pittrof R, Kyei-Mensah A, Shaker A, Jacobs HS et al (1995) Ovarian stromal blood flow in women with polycystic ovaries–a possible new marker for diagnosis? Hum Reprod 10(8):1992–1996
25. Chegini N, Flanders KC (1992) Presence of transforming growth factor-beta and their selective cellular localization in human ovarian tissue of various reproductive stages. Endocrinology 130(3):1707–1715
26. Findlay JK (1986) Angiogenesis in reproductive tissues. J Endocrinol 111(3):357–366
27. Folkman J, Shing Y (1992) Angiogenesis. J Biol Chem 267(16):10931–10934
28. Gospodarowicz D (1974) Localisation of a fibroblast growth factor and its effect alone and with hydrocortisone on 3T3 cell growth. Nature 249(453):123–127
29. Klagsbrun M (1991) Regulators of angiogenesis: stimulators, inhibitors, and extracellular matrix. J Cell Biochem 47(3):199–200
30. Van Blerkom J, Antczak M, Schrader R (1997) The developmental potential of the human oocyte is related to the dissolved oxygen content of follicular fluid: association with vascular endothelial growth factor levels and perifollicular blood flow characteristics. Hum Reprod 12(5):1047–1055
31. Agrawal R, Conway G, Sladkevicius P, Tan SL, Engmann L, Payne N et al (1998) Serum vascular endothelial growth factor and Doppler blood flow velocities in in vitro fertilization: relevance to ovarian hyperstimulation syndrome and polycystic ovaries. Fertil Steril 70(4):651–658
32. Agrawal R, Sladkevicius P, Engmann L, Conway GS, Payne NN, Bekis J et al (1998) Serum vascular endothelial growth factor concentrations and ovarian stromal blood flow are increased in women with polycystic ovaries. Hum Reprod 13(3):651–655
33. Curry TE Jr, Smith MF (2006) Impact of extracellular matrix remodeling on ovulation and the folliculo-luteal transition. Semin Reprod Med 24(4):228–241
34. Goldman S, Shalev E (2004) MMPS and TIMPS in ovarian physiology and pathophysiology. Front Biosci 9:2474–2483
35. Oksjoki S, Rahkonen O, Haarala M, Vuorio E, Anttila L (2004) Differences in connective tissue gene expression between normally functioning, polycystic and post-menopausal ovaries. Mol Hum Reprod 10(1):7–14
36. Chen L, Mao SJ, McLean LR, Powers RW, Larsen WJ (1994) Proteins of the inter-alpha-trypsin inhibitor family stabilize the cumulus extracellular matrix through their direct binding with hyaluronic acid. J Biol Chem 269(45):28282–28287
37. Hess KA, Chen L, Larsen WJ (1999) Inter-alpha-inhibitor binding to hyaluronan in the cumulus extracellular matrix is required for optimal ovulation and development of mouse oocytes. Biol Reprod 61(2):436–443
38. Odum L, Jessen TE, Andersen CY (2001) Glycosaminoglycan-bound and free inter-alpha-trypsin inhibitor components of follicular fluid. Zygote 9(4):283–288
39. Bazzoni G, Dejana E (2004) Endothelial cell-to-cell junctions: molecular organization and role in vascular homeostasis. Physiol Rev 84(3):869–901
40. Walz A, Keck C, Weber H, Kissel C, Pietrowski D (2005) Effects of luteinizing hormone and human chorionic gonadotropin on corpus luteum cells in a spheroid cell culture system. Mol Reprod Dev 72(1):98–104
41. Dejana E (2004) Endothelial cell-cell junctions: happy together. Nat Rev 5(4):261–270
42. Schneeberger EE, Lynch RD (2004) The tight junction: a multifunctional complex. Am J Physiol Cell Physiol 286(6):C1213–C1228
43. Rodewald M, Herr D, Fraser HM, Hack G, Kreienberg R, Wulff C (2007) Regulation of tight junction proteins occludin and claudin 5 in the primate ovary during the ovulatory cycle and after inhibition of vascular endothelial growth factor. Mol Hum Reprod 13(11):781–789
44. Hudson BG, Reeders ST, Tryggvason K (1993) Type IV collagen: structure, gene organization, and role in human diseases. Molecular basis of Goodpasture and Alport syndromes and diffuse leiomyomatosis. J Biol Chem 268(35):26033–26036
45. Noakes PG, Miner JH, Gautam M, Cunningham JM, Sanes JR, Merlie JP (1995) The renal glomerulus of mice lacking s-laminin/laminin beta 2: nephrosis despite molecular compensation by laminin beta 1. Nat Genet 10(4):400–406
46. Nakano K, Naito I, Momota R, Sado Y, Hasegawa H, Ninomiya Y et al (2007) The distribution of type IV collagen α chains in the mouse ovary and its correlation with follicular development. Arch Histol Cytol 70(4):243–53
47. Rodgers HF, Irvine CM, van Wezel IL, Lavranos TC, Luck MR, Sado Y et al (1998) Distribution of the alpha1 to alpha6 chains of type IV collagen in bovine follicles. Biol Reprod 59(6):1334–1341
48. Irving-Rodgers HF, Rodgers RJ (2005) Extracellular matrix in ovarian follicular development and disease. Cell Tissue Res 322(1):89–98
49. Chan FL, Inoue S (1994) Lamina lucida of basement membrane: an artefact. Microsc Res Tech 28(1):48–59

Application of "In Vivo Cryotechnique" to Immunohistochemical Study of Serum Albumin in Normal and Cadmium-Treated Mouse Testis Organs

30

Nobuo Terada, Yurika Saitoh, Nobuhiko Ohno, Xiaogang Liao, and Shinichi Ohno

Abstract

In this chapter, we present application of "in vivo cryotechnique" (IVCT) to evaluation of blood-testis barrier (BTB) function in mouse testis, by visualization of albumin distribution. The albumin in the seminiferous tubules was well immobilized by combination of IVCT, freeze-substitution fixation and paraffin-embedding processes. In normal seminiferous tubules, albumin was immunostained as archlike pattern around some spermatogonia in basal compartments of seminiferous tubules, as well as in blood vessels and around peritubular myoid cells and Leydig cells. After the BTB disruption induced by injection of cadmium (Cd), some enlarged spaces and vesicular formations in the seminiferous epithelium were observed on the HE-stained sections. The albumin immunolocalization was detected not only in the basal compartments but also in the adluminal compartments between Sertoli cells and germ cells. Thus, the structural disruptions of BTB could be clearly demonstrated by IVCT.

Keywords

In vivo cryotechnique • Albumin • Blood-testis barrier • Cadmium

30.1 Evaluation of Blood-Testis Barrier (BTB) Function in Testis with In Vivo Cryotechnique (IVCT)

The BTB in testis is constituted mainly by Sertoli cell's tight junctions (TJ). The functional and structural integrity of BTB plays a crucial role in maintaining the microenvironment of the seminiferous epithelium for both germ cell migration and normal spermatogenesis [1, 2]. Cadmium (Cd) is already known to be a ubiquitous industrial and environmental metal pollutant, which has a long biological half-life and a cumulative toxic effect on both humans and experimental animals [3, 4]. The Cd treatment was reported to cause biological damage to several organs, including the kidney, liver, lung, bone, and testis [5]. The probable effect on the testis damages has been reported to disrupt the Sertoli cell's TJ barriers, resulting in a decrease of germ cells of the

N. Terada, M.D., Ph.D. (✉)
Division of Health Sciences, Shinshu University Graduate School of Medicine, 3-1-1 Asahi, Matsumoto City, Nagano 390-8621, Japan

Department of Anatomy and Molecular Histology, Interdisciplinary Graduate School of Medicine and Engineering, University of Yamanashi, 1110 Shimokato, Chuo City, Yamanashi 409-3898, Japan
e-mail: nobuot@shinshu-u.ac.jp

Y. Saitoh • N. Ohno • X. Liao • S. Ohno
Department of Anatomy and Molecular Histology, Interdisciplinary Graduate School of Medicine and Engineering, University of Yamanashi, 1110 Shimokato, Chuo City, Yamanashi 409-3898, Japan

S. Ohno et al. (eds.), *In Vivo Cryotechnique in Biomedical Research and Application for Bioimaging of Living Animal Organs*, DOI 10.1007/978-4-431-55723-4_30

seminiferous epithelium and finally shrinkage of testis [6–9]. At a biochemical level, the Cd treatment was reported to reduce the amount of Sertoli cell's TJ proteins, occludin and zonula occludens-1 [10].

To evaluate time-dependent toxic effects of Cd on living mouse testis organs, especially on BTB permeability, we demonstrate useful protocol by our IVCT [11] with immunohistochemistry [12, 13] for directly monitoring the in vivo immunolocalization of serum albumin and immunoglobulin proteins in living animal organs. In this chapter, we demonstrate immunohistochemical study of serum albumin in normal and cadmium-treated mouse testis organs by in vivo cryotechnique. Precise methods and results have been reported in the previous paper [14].

30.2 IVCT for Living Mouse Testis

Mice were anesthetized with sodium pentobarbital, and their testis organs were surgically exposed without disturbing their blood supply. The IVCT was performed with a use of the "in vivo cryoapparatus" [12, 15] or by direct pouring of isopentane-propane cryogen precooled in liquid nitrogen (inset in Fig. 30.1a). The frozen testes were processed to freeze-substitution fixation and paraffin embedding.

30.3 Immunolocalization of Albumin in Normal Testis

In normal seminiferous tubules (Fig. 30.1a, b), albumin immunoreactivity was mainly detected around peritubular myoid cells, forming continuous immunostaining areas as well as among interstitial Leydig cells and inside blood capillaries. Another albumin immunostaining was detected as small archlike patterns within the seminiferous epithelium and restricted in the basal compartment, locating around some spermatogonia (arrows in Fig. 30.1b). Appearance and disappearance of the archlike patterns were closely related to the developmental stages of seminiferous epithelial cycles. The number of the archlike patterns at stages VII–VIII of the seminiferous epithelial cycle (mature spermatozoon accumulated at the upper luminal part and ready to release) was much higher than that at stages I–II (spermatogenesis proceeding to the early spermatid).

30.4 Immunolocalization of Albumin After Cd Treatment

The cadmium chloride ($CdCl_2$) was intraperitoneally injected at a single dose to induce their testis damage, as previously described [2]. Thereafter, the mice were examined 24 and 48 h after the Cd treatment. In 24 h (Fig. 30.1c, d), the albumin immunostaining was detected not only in the basal compartment of seminiferous epithelium but also in the adluminal compartment between supporting Sertoli cells and developing spermatogenic cells (Fig. 30.1d), indicating abnormal immunoreactivity of serum albumin through BTB structures. Forty-eight hours after the Cd treatment, some seminiferous tubules were shown to be typical atrophic structures, by decreasing the number of germ cells. In such seminiferous tubules, the albumin immunostaining was also detected between the Sertoli cells.

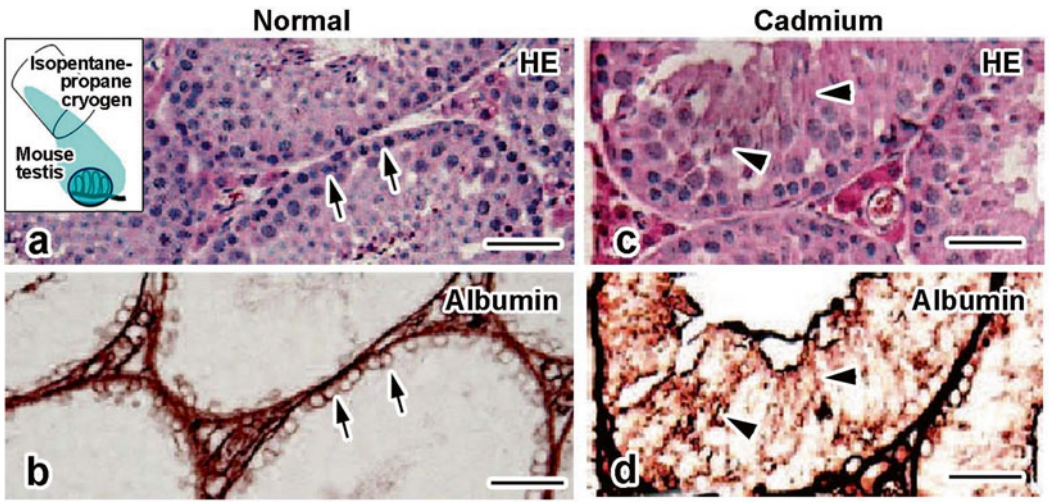

Fig. 30.1 (**a**–**d**) Light micrographs of HE-staining (**a**, **c**) and immunostaining for albumin (**b**, **d**) in seminiferous tubules of the normal (**a**, **b**) and the 24 h cadmium-treated (**c**, **d**) mouse testis. Archlike immunostaining patterns are observed around spermatogenic cells in the basal compartments (*arrows* in **b**). After the cadmium treatment, the albumin immunostaining is observed in the adluminal compartment between Sertoli cells and germ cells (*arrowheads* in **d**). Precise data have been reported in the previous paper (Liao et al. [14]). *Bars,* 40 μm

The present findings confirmed that the immunointensity of leaked albumin through BTB in the basal compartments was obviously stronger in the seminiferous epithelium of the living mice at 24 h after the Cd treatment. The different immunolocalizations of serum albumin in the seminiferous tubules between normal and Cd-treated mouse testis organs support an idea that the TJ structure against protein permeability between Sertoli cells is the most vulnerable portion affected by Cd toxicity, as reported before [10, 16].

30.5 Concluding Remarks

The time-dependent morphological changes of seminiferous tubules in the Cd-treated living mice, including different immunostaining patterns of albumin in the basal compartment with BTB disruption, can be clearly detected by the "in vivo cryotechnique" combined with both freeze-substitution and immunohistochemistry.

References

1. Russell LD (1997) Movement of spermatocytes from the basal to the adluminal compartment of the rat testis. Am J Anat 148:313–328
2. Wong CH, Mruk DD, Lui WY, Cheng CY (2004) Regulation of blood-testis barrier dynamics: an in vivo study. J Cell Sci 117:783–798
3. Liao XG, Li WX (1999) Ultrastructural and G-6-Pase cytochemical studies of injurious action of cadmium and protection of zinc on rat Leydig cells. Reprod Contracept 10:203–213
4. Benoff SH, Millan C, Hurley IR, Napolitano B, Marmar JL (2004) Bilateral increased apoptosis and bilateral accumulation of cadmium in infertile men with left varicocele. Hum Reprod 19:616–627
5. Gubrelay U, Mehta A, Singh M, Flora SJ (2004) Comparative hepatic and renal toxicity of cadmium in male and female rats. J Environ Biol 25:65–73
6. Hew KW, Heath GL, Jiwa A, Welsh MJ (1993) Cadmium in vivo causes disruption of tight junction-associated microfilaments in rat Sertoli cells. Biol Reprod 49:840–849
7. Xu G, Zhou G, Jin T, Zhou T, Hammarstrom S, Bergh A, Nordberg G (1999) Apoptosis and p53 gene expression in male reproductive tissues of cadmium exposed rats. Biometals 12:131–139
8. Zhou T, Zhou G, Song W, Eguchi N, Lu W, Lundin E, Jin T, Nordberg G (1999) Cadmium-induced apoptosis and changes in expression of p53, c-jun and MT-I genes in testes and ventral prostate of rats. Toxicology 142:1–139
9. Chung NP, Cheng CY (2001) Is cadmium chloride-induced inter-Sertoli tight junction permeability barrier disruption a suitable in vitro model to study the events of junction disassembly during spermatogenesis in the rat testis? Endocrinology 142:1878–1888
10. Fiorini C, Tilloy-Ellul A, Chevalier S, Charuel C, Pointis G (2004) Sertoli cell junctional proteins as early targets for different classes of reproductive toxicants. Reprod Toxicol 18:413–421
11. Ohno S, Terada N, Fujii Y, Ueda H, Takayama I (1996) Dynamic structure of glomerular capillary loop as revealed by an in vivo cryotechnique. Virchows Arch 427:519–527
12. Zea-Aragon Z, Terada N, Ohno N, Fujii Y, Baba T, Ohno S (2004) Effects of anoxia on serum immunoglobulin and albumin leakage through blood-brain barrier in mouse cerebellum as revealed by cryotechniques. J Neurosci Methods 138:89–95
13. Ohno N, Terada N, Murata S, Katoh R, Ohno S (2005) Application of cryotechniques with freeze-substitution for the immunohistochemical demonstration of intranuclear pCREB and chromosome territory. J Histochem Cytochem 51:55–62
14. Liao X, Terada N, Ohno N, Li Z, Fujii Y, Baba T, Ohno S (2006) Immunohistochemical study of serum albumin in normal and cadmium-treated mouse testis organs by "in vivo cryotechnique". Histol Histopathol 21:35–40
15. Ohno N, Terada N, Ohno S (2004) Advanced application of the in vivo cryotechnique to immunohistochemistry for animal organs. Acta Histochem Cytochem 37:357–364
16. Lui WY, Wong CH, Mruk DD, Cheng CY (2003) TGF-beta 3 regulates the blood-testis barrier dynamics via the p38 mitogen activated protein (MAP) kinase pathway: an in vivo study. Endocrinology 144:1139–1142

Immunohistochemical Detection of Angiotensin II Receptors in Mouse Cerebellum

31

Zheng Huang, Nobuhiko Ohno, Nobuo Terada, Yurika Saitoh, Jiaorong Chen, and Shinichi Ohno

Abstract

Angiotensin II (AT) receptors, including AT receptor type 1 (AT1R) and type 2 (AT2R), are expressed in the rodent central nervous system, but their distributions and activation states are still unclear. In this study, we have performed immunohistochemical analyses of AT receptors in mouse cerebellum using our "in vivo cryotechnique" (IVCT). We used antibodies against amino-terminal domains of AT receptors, which are considered to undergo conformational changes upon the binding of AT. Immunoreactivity of AT1R was detected in mouse cerebellum and was highest in the outer tissue areas of molecular layers using IVCT. Surprisingly, the AT1R immunoreactivity in the cerebellar cortex was remarkably reduced following 5 and 10 min of hypoxia. The correlation of localization with GFAP and also hypoxia-induced decrease of its immunoreactivity were similarly observed by immunostaining of AT2R in the cerebellar specimens. These findings demonstrated that IVCT is useful to reveal dynamically changing immunoreactivities usually affected by receptor-ligand binding as well as hypoxia and also suggested that functional activities of AT receptors are time-dependently modulated under hypoxia in the central nervous system in comparison with the adrenal gland.

Keywords

In vivo cryotechnique • Angiotensin II receptors • Cerebellum • Bergmann glia • Hypoxia

31.1 Introduction

Angiotensin II receptors, type 1 (AT1R) and type 2 (AT2R), belong to the superfamily of seven-transmembrane G protein-coupled receptors [9] and mediate the physiological functions of angiotensin II (AT), an octapeptide hormone regulating cardiovascular homeostasis, in various organs of animals [4]. Some previous studies also demonstrated that AT receptors were often expressed in neurons and glia of the central nervous system (CNS) and play some functional roles in

Z. Huang
Department of Anatomy, Interdisciplinary Graduate School of Medicine and Engineering, University of Yamanashi, 1110 Shimokato, Chuo City, Yamanashi 409-3898, Japan

Department of Pathology, the Central Hospital of Wuhan, Wuhan, P.R. China

N. Terada
Division of Health Sciences, Shinshu University Graduate School of Medicine, 3-1-1 Asahi, Matsumoto City, Nagano 390-8621, Japan

Department of Anatomy and Molecular Histology, Interdisciplinary Graduate School of Medicine and Engineering, University of Yamanashi, 1110 Shimokato, Chuo City, Yamanashi 409-3898, Japan

N. Ohno • Y. Saitoh • S. Ohno, M.D., Ph.D. (✉)
Department of Anatomy and Molecular Histology, Interdisciplinary Graduate School of Medicine and Engineering, University of Yamanashi, 1110 Shimokato, Chuo City, Yamanashi 409-3898, Japan
e-mail: sohno@yamanashi.ac.jp

J. Chen
Department of Anatomy, Interdisciplinary Graduate School of Medicine and Engineering, University of Yamanashi, 1110 Shimokato, Chuo City, Yamanashi 409-3898, Japan

Department of Anatomy and Histochemistry & Embryology, Hubei University of Chinese Medicine, Wuhan, P.R. China

S. Ohno et al. (eds.), *In Vivo Cryotechnique in Biomedical Research and Application for Bioimaging of Living Animal Organs*, DOI 10.1007/978-4-431-55723-4_31

hemodynamic control, differentiation, neuronal plasticity, and cell survival [1, 5, 8, 18, 20]. Although both AT1R and AT2R are expressed in animal cerebellum [2, 3, 6, 11, 19], their distributions and activation states under physiological and pathological conditions have not been well understood.

In the last one and a half decades, our "in vivo cryotechnique" (IVCT) has become well known as a powerful tool to retain native ultrastructures in brain tissue sections, such as extracellular spaces in mouse cerebellar cortex [16, 17]. In addition, using IVCT followed by freeze-substitution (FS) fixation, unstable signal molecular components in animal organs were instantly captured in situ and could be immunohistochemically visualized without technical artifacts due to anoxia and ischemia [22]. Therefore, the functional activities of AT receptors could be examined using IVCT along with specific antibodies, whose immunoreactivities usually depend on the dynamic binding of ligands and agonists to the receptors [10]. G protein-coupled receptors, including AT1R and AT2R, undergo rapid conformational changes of extracellular amino-terminal regions upon the binding of AT ligands and agonists [7]. Therefore, some immunoreactivity changes of specific antibodies against the amino-terminal regions of such receptors could reflect alterations of ligand-binding activities and rapid adaptation for the intracellular metabolism and microenvironment.

In the present study, we used the IVCT and also antibodies against amino-terminal regions of AT receptors and performed immunohistochemical analyses of mouse cerebellum. We also examined their immunoreactivity changes under normal or hypoxic conditions using IVCT. Our present results demonstrated that immunoreactivities of dynamically changing AT1R and AT2R were clearly detected using IVCT and were closely related to Bergmann glia and some astrocytes immunopositive for glial fibrillary acidic protein (GFAP). In addition, the AT1R immunoreactivity in the mouse cerebellum was diminished under hypoxic conditions for 5 min. The hypoxia-induced immunostaining change of AT2R mostly resembled that of AT1R.

31.2 Different Preparation Methods for Mouse Cerebellum and Adrenal Gland

For the control group, IVCT was performed with an in vivo cryoapparatus (IV-II; EIKO Engineering, Hitachinaka, Ibaraki, Japan) on living mouse cerebellum under normal respiration conditions (Fig. 31.1b), as reported previously [15]. For the experimental hypoxia groups, IVCT was performed at 1, 5, 10, or 15 min after opening the thoracic cavity [21]. To expose the cerebellum of anesthetized mice, a part of the cranial bone was carefully removed with a dental electric drill [16]. IVCT was performed by directly cutting the cerebellum with a cryoknife precooled in liquid nitrogen (−196 °C) (Fig. 31.1b) [13] and then immediately pouring isopentane-propane (IP) cryogen (−193 °C) over it under the in vivo cryoapparatus (Fig. 31.1b).

31.3 Immunolocalization Comparison of AT1R with Different Preparation in Cerebellum of Mouse

The immunolocalizations of AT1R examined using QF-FS were mostly similar to those prepared using IVCT (Fig. 31.2a–f), and immunoreaction products appeared to be clustered or linear dot patterns in the mouse cerebellar cor-

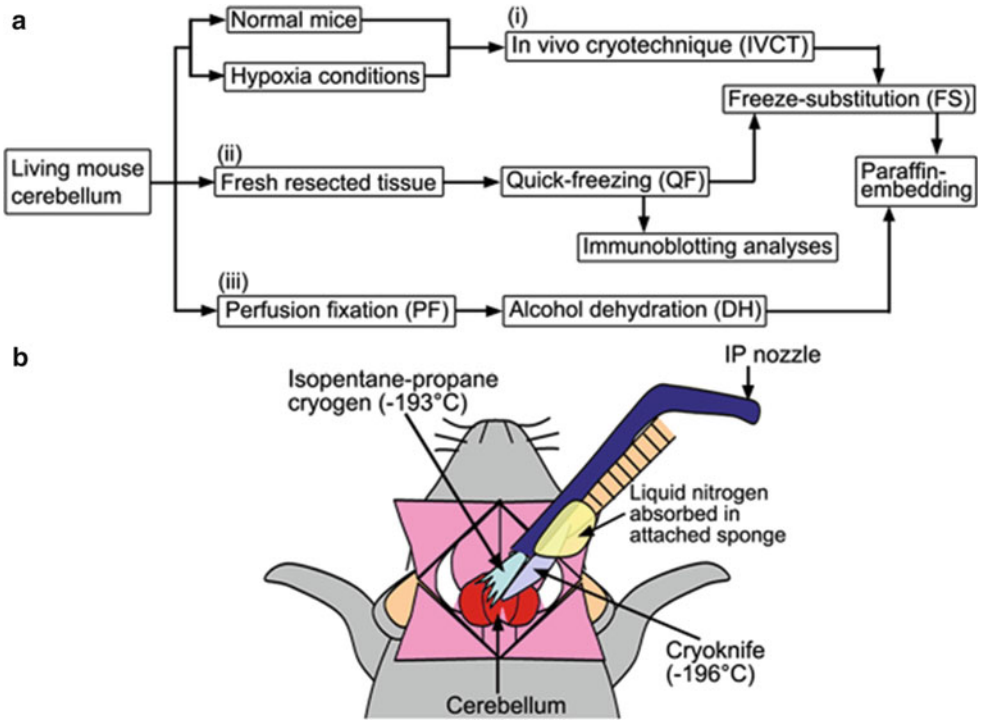

Fig. 31.1 (**a**) A flow chart of the three different preparation procedures, namely, in vivo cryotechnique with freeze-substitution (i), quick-freezing of fresh resected tissues followed by freeze-substitution (ii), and conventional perfusion fixation with alcohol dehydration (iii) for mouse organs, such as cerebellum or adrenal glands, which are finally embedded in paraffin wax. (**b**) A schematic drawing of the in vivo cryotechnique for an anesthetized mouse cerebellum under an in vivo cryoapparatus. It is frozen in vivo with a cryoknife and simultaneously has isopentane-propane (*IP*) cryogen (−193 °C) poured on it

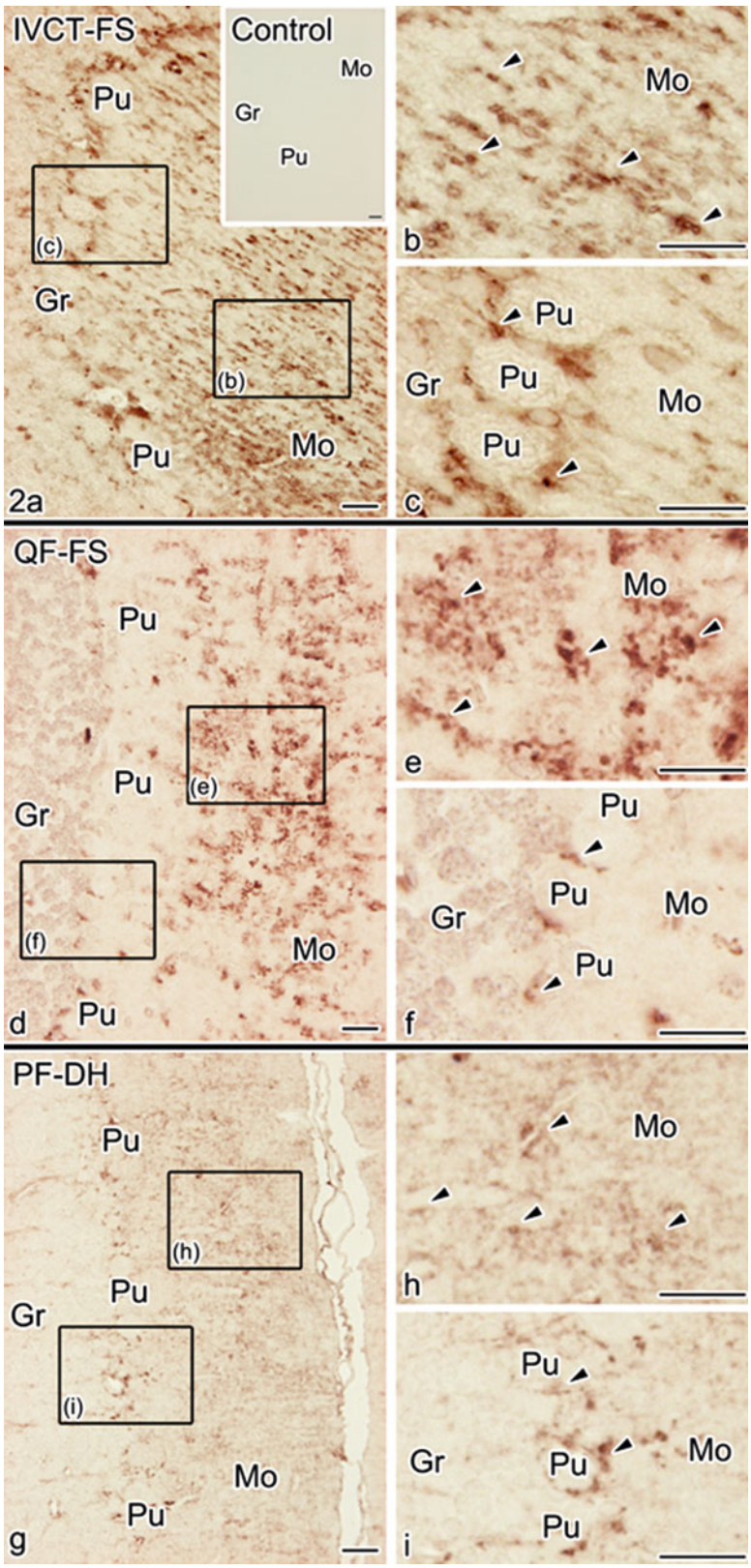

Fig. 31.2 Immunostaining of AT1R with the three different preparation methods, namely, IVCT-FS (**a**–**c**), QF-FS (**d**–**f**), and PF-DH (**g**–**i**). Immunoreaction products in the specimens prepared using IVCT-FS are more clearly detected in molecular layers, Purkinje cell layers, and granular layers than those prepared using QF-FS and PF-DH. At higher magnification, immunoreaction products, recognized as dot patterns, are less clear in the molecular layers using QF-FS and PF-DH (**b**, **e**, **h**, *arrowheads*) and also less clear in Purkinje cell layers with QF-FS and PF-DH (**c**, **f**, **i**, *arrowheads*). Bars, 20 μm

tex. However, compared with the AT1R immunoreactivity detected using IVCT (Fig. 31.2a–c), it was more weakly detected in all three layers using QF-FS (Fig. 31.2d–f). Using the conventional PF-DH (Fig. 31.2g–i), the AT1R immunoreactivity was less obviously detected in the three layers.

Our previous studies demonstrated that both QF-FS and PF-DH easily caused technical artifacts of morphology because of hypoxia/ischemia inevitably induced by the conventional chemical fixation [17]. Therefore, the decreased AT1R immunoreactivity following both QF-FS and PF-DH preparations indicated that the immunostaining of AT1R was inevitably altered by hypoxic conditions.

31.4 Immunoreactivity of AT1R at Several Hypoxia Time

To confirm this possibility, the immunoreactivity of AT1R was examined in mouse cerebellum prepared using IVCT under different intervals of hypoxia. IVCT was similarly performed at three time points under hypoxia after opening the thoracic cavity, as shown in Fig. 31.1b. Following 1 min of hypoxia, the immunoreactivity of AT1R was slightly decreased, but still clearly detected in all three layers of cerebellar cortex (Fig. 31.3a, b). However, after 5 and 10 min of hypoxia, it was remarkably reduced and undetectable in the three layers (Fig. 31.3e, f, i, j). By contrast, the immunoreactivities of both calbindin (Fig. 31.3c, g, k) and GFAP (Fig. 31.3d, h, l) were mostly unchanged under such hypoxic conditions.

31.5 Immunoreactivity of AT2R at Several Hypoxia Time

Next, considering the hypoxic conditions, the immunoreactivity of AT2R in the cerebellar cortex was still detected at 1 min of hypoxia (Fig. 31.4a), which was similar to that of AT1R (Fig. 31.3b), but it was remarkably reduced at 5 or 10 min of hypoxia (Fig. 31.4b, c).

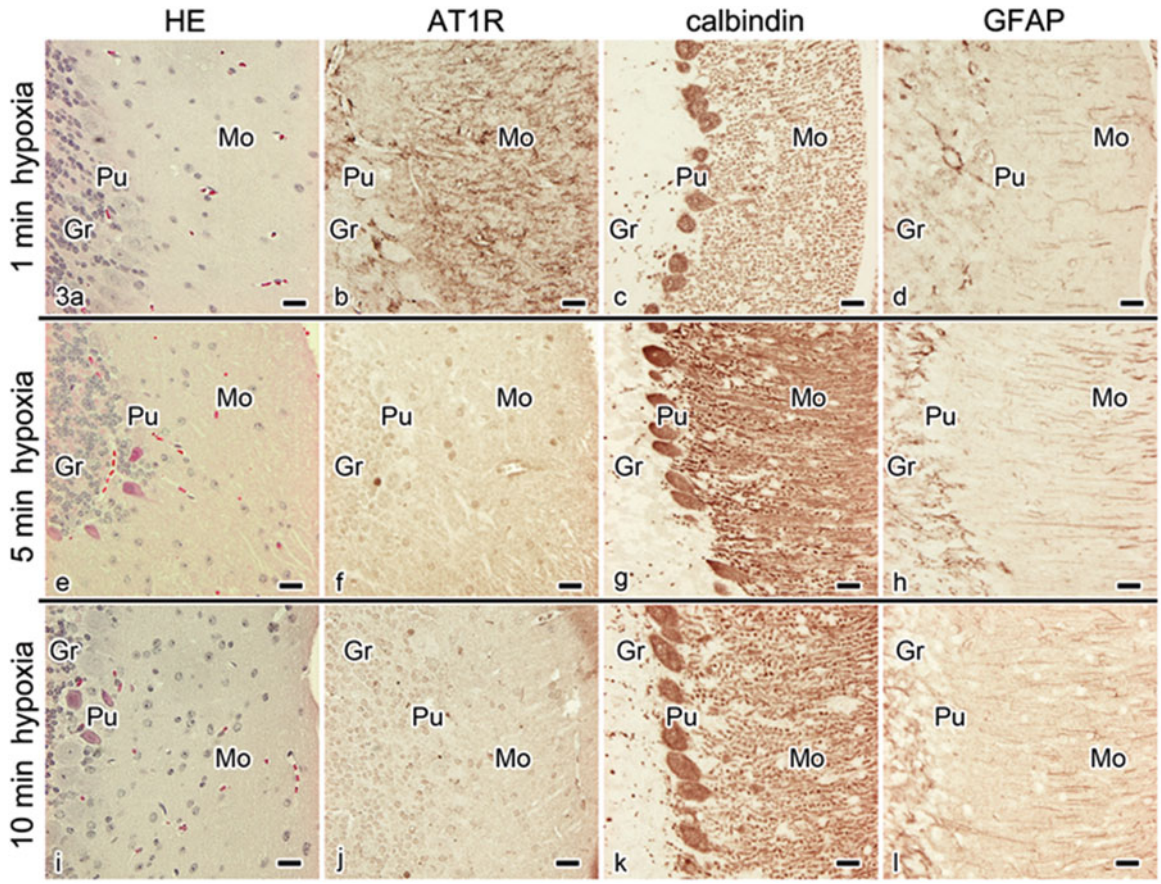

Fig. 31.3 Light microscopic images of HE staining (**a**, **e**, **i**) and immunostaining of AT1R (**b**, **f**, **j**), calbindin (**c**, **g**, **k**), and GFAP (**d**, **h**, **l**) under 1 (**a**–**d**), 5 (**e**–**h**) and 10 (**i**–**l**) min hypoxia in serial sections of the mouse cerebellum, as prepared using IVCT-FS. At 1 min after hypoxia, AT1R immunoreactivity is still detected, whereas its intensity is slightly decreased in comparison with those of normal mice, as shown in Figs. 31.2d and 31.3a. At 5 (**f**) and 10 (**j**) min of hypoxia, AT1R immunoreactivity is remarkably reduced in all three layers, namely, molecular layer (*Mo*), Purkinje cell layer (*Pu*), and granular layer (*Gr*). Moreover, as seen by HE staining (**e**, **i**), some Purkinje cells show more eosinophilic cytoplasm at 5 and 10 min after hypoxia. By contrast, immunostaining of calbindin or GFAP does not change following hypoxia. Bars, 20 μm

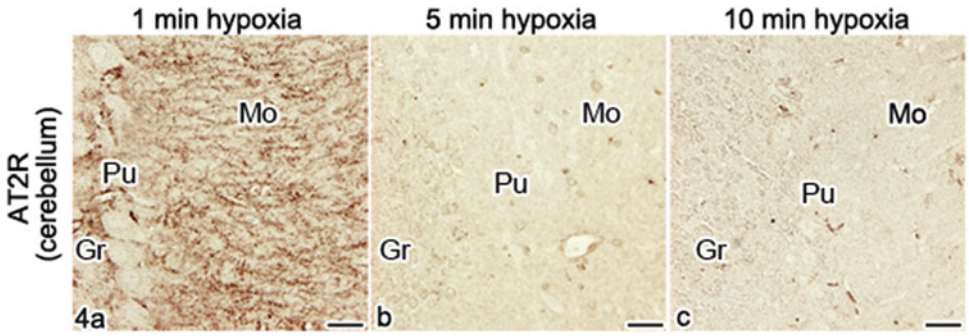

Fig. 31.4 Immunostaining of AT2R under hypoxic conditions in mouse cerebellum, as prepared using IVCT-FS. (**a**)–(**c**) In the cerebellum, at 1 min after hypoxia (**a**), immunoreaction products are still detected as dot patterns, but their immunostaining intensities are slightly decreased in comparison with those of normal mice. After 5 and 10 min of hypoxia (**b**, **c**), they are remarkably reduced in all three molecular (*Mo*), Purkinje cell (*Pu*), and granular layers (*Gr*). Bars, 20 μm

31.6 Concluding Remarks

With IVCT-FS, several technical problems in clarifying the native tissue morphology and the precise immunolocalizations of signal molecules or receptors were avoidable, including tissue shrinkage and the translocation of soluble proteins caused by chemical fixation and alcohol dehydration [17, 21, 22]. The meshwork-like structures induced by the tiny ice crystal formation probably facilitate effective penetration of antibodies during immunohistochemical steps, resulting in better formation of antigen-antibody complexes [14]. Moreover, freeze-substitution (FS) fixation has an additional benefit of avoiding antigen-retrieval treatments. Therefore, we were able to obtain clearer immunolocalizations of AT1R and AT2R in the mouse cerebellum. In the present study, both AT1R and AT2R were immunolocalized in the molecular, Purkinje cell, and granular layers of mouse cerebellum. Our findings are consistent with previous reports, showing that AT receptors were located in the cerebellar cortex [2, 11]. It is also interesting that the immunoreactivity of AT receptors became rarely detectable in the mouse cerebellum following hypoxia. The antibodies used in this study are raised against the extracellular N-terminal regions of the AT receptors [10], which undergo conformational changes upon receptor activation [12]. One possibility for the reduced immunoreactivity is that molecular structures of the AT receptors, AT1R and AT2R, bound to ligands can be effectively retained using IVCT, and it could capture dynamic detachment of AT ligands from the AT receptors and conformational alteration of the receptors from activated to nonactivated states, as reported previously for rhodopsin [22]. The present figures were already published in our paper, Histochem Cell Biol (2013) 140:477–490, and cited with their permissions.

References

1. Allen AM, Moeller I, Jenkins TA, Zhuo J, Aldred GP, Chai SY, Mendelsohn FA (1998) Angiotensin receptors in the nervous system. Brain Res Bull 47:17–28
2. Arce ME, Sanchez S, Seltzer A, Ciuffo GM (2001) Autoradiographic localization of angiotensin II receptors in developing rat cerebellum and brainstem. Regul Pept 99:53–60
3. Arce ME, Sanchez SI, Aguilera FL, Seguin LR, Seltzer AM, Ciuffo GM (2011) Purkinje cells express angiotensin II AT2 receptors at different developmental stages. Neuropeptides 45:69–76
4. Basso N, Terragno NA (2001) History about the discovery of the rennin-angiotensin system. Hypertension 38:1246–1249
5. Changaris DG, Severs WB, Keil LC (1978) Localization of angiotensin in rat brain. J Histochem Cytochem 26:593–607
6. Cote F, Do TH, Laflamme L, Gallo JM, Gallo-Payet N (1999) Activation of the AT2 receptor of angiotensin II induces neurite outgrowth and cell migration in microexplant cultures of the cerebellum. J Biol Chem 274:31686–31692
7. Fadhil I, Schmidt R, Walpole C, Carpenter KA (2004) Exploring deltorphin II binding to the third extracellular loop of the delta-opioid receptor. J Biol Chem 279:21069–21077
8. Fogarty DJ, Matute C (2001) Angiotensin receptor-like immunoreactivity in adult brain white matter astrocytes and oligodendrocytes. Glia 35:131–146
9. Gasparo MD, Catt KJ, Inagami T, Wright JW, Unger T (2000) International Union of Pharmacology. XXIII. The angiotensin II receptors. Pharmacol Rev 52:415–472
10. Gupta A, Decaillot FM, Gomes I, Tkalych O, Heimann AS, Ferro ES (2007) Conformation state-sensitive antibodies to G-protein-coupled receptors. J Biol Chem 282:5116–5124
11. Johren O, Hauser W, Saavedra JM (1998) Chemical lesion of the inferior olive reduces [^{125}I] sarcosine-angiotensin II binding to AT2 receptors in the cerebellar cortex of young rats. Brain Res 793:176–186
12. Lecat S, Bucher B, Mely Y, Galzi J (2002) Mutations in the extracellular amino-terminal domain of the NK2 neurokinin receptor abolish cAMP signaling but preserve intracellular calcium responses. J Biol Chem 277:42034–42048
13. Ohno S, Terada N, Fujii Y, Ueda H, Takayama I (1996) Dynamic structure of glomerular capillary loop as revealed by an "in vivo cryotechnique". Virchows Arch 427:519–527

14. Ohno N, Terada N, Murata S, Katoh R, Ohno S (2005) Application of cryotechniques with freeze-substitution for the immunohistochemical demonstration of intranuclear pCREB and chromosome territory. J Histochem Cytochem 53:55–62
15. Ohno N, Terada N, Ohno S (2006) Histochemical analyses of living mouse liver under different hemodynamic conditions by "in vivo cryotechnique". Histochem Cell Biol 126:389–398
16. Ohno N, Terada N, Saitoh S, Ohno S (2007) Extracellular space in mouse cerebellar cortex revealed by "in vivo cryotechnique". J Comp Neurol 505:292–301
17. Ohno S, Terada N, Ohno N, Saitoh S, Saitoh Y, Fujii Y (2010) Significance of "in vivo cryotechnique" for morphofunctional analyses of living animal organs. J Electron Microsc (Tokyo) 59:395–408
18. Phillips MI, Shen L, Richards EM, Raizada MK (1993) Immunohistochemical mapping of angiotensin AT1 receptors in the brain. Regul Pept 44:95–107
19. Reagan LP, Flanagan-Cato LM, Yee DK, Ma LY, Sakai RR, Fluharty SJ (1994) Immunohistochemical mapping of angiotensin type 2 (AT2) receptors in rat brain. Brain Res 662:45–59
20. Saavedra JM (1992) Brain and pituitary angiotensin. Endocr Rev 13:329–380
21. Saitoh S, Terada N, Ohno N, Saitoh Y, Soleimani M, Ohno S (2009) Immunolocalization of phospho-Arg-directed protein kinase-substrate in hypoxic kidneys using in vivo cryotechnique. Med Mol Morphol 42:24–31
22. Terada N, Ohno N, Ohguro H, Li Z, Ohno S (2006) Immunohistochemical detection of phosphorylated rhodopsin in light-exposed retina of living mouse with in vivo cryotechnique. J Histochem Cytochem 54:479–486

32 Application of "In Vivo Cryotechnique" to Immunohistochemical Analyses for Effects of Anoxia on Serum Immunoglobulin and Albumin Leakage Through Blood–Brain Barrier in Mouse Cerebellum

Nobuo Terada, Yurika Saitoh, Nobuhiko Ohno, Zagreb Zea-Aragón, and Shinichi Ohno

Abstract

In this chapter, we present the application of "in vivo cryotechnique" (IVCT) to examination of time-dependent topographical changes of leaking proteins from blood vessels in the mouse cerebellum, to assess the blood–brain barrier (BBB). The distribution of leaking serum proteins was compared by various cryotechniques. The cryofixed cerebellar tissues were processed for the freeze-substitution method and paraffin embedding. Serial deparaffinized sections were immunostained by anti-mouse immunoglobulin G (IgG) or albumin antibody. By combination of IVCT, serum IgG and albumin were clearly localized inside of cerebellar blood vessels. In anoxic cerebellar tissues, which were partially removed from brains in the mouse skull and quickly frozen in the isopentane–propane within a minute, serum IgG and albumin were diffusely immunostained around the blood capillaries, showing leakage of the serum components through the BBB changes. Thus, IVCT revealed in vivo localization of serum components in mouse brains.

Keywords

Cerebellum • Blood–brain barrier • Serum • In vivo cryotechnique

32.1 Merit of In Vivo Cryotechnique (IVCT) to Evaluate Blood–Brain Barrier (BBB)

In the central nervous system, there is a highly selective barrier that separates the circulating blood from extracellular fluid, termed BBB. Although the functional integrity of the BBB was first measured using the in vivo injection of dyestuff [1], these dyes were found to bind with plasma proteins and lose their color intensity due to chemical reactions in the biological tissues. These technical difficulties led to the development of alternative tracer methods such as the in vivo injection of horseradish peroxidase (HRP) [2, 3], radiolabeled tracers [4], or fluorescent dyes [5]. On the other hand, immunohistochemical technique has been widely used to reveal albumin localization in extravascular matrices of rat brains [6, 7]. Transcardial perfusion of trypan blue

N. Terada, M.D., Ph.D. (✉)
Division of Health Sciences, Shinshu University Graduate School of Medicine, 3-1-1 Asahi, Matsumoto City, Nagano 390-8621, Japan

Department of Anatomy and Molecular Histology, Interdisciplinary Graduate School of Medicine and Engineering, University of Yamanashi, 1110 Shimokato, Chuo City, Yamanashi 409-3898, Japan
e-mail: nobuot@shinshu-u.ac.jp

Y. Saitoh • N. Ohno • Z. Zea-Aragón • S. Ohno
Department of Anatomy and Molecular Histology, Interdisciplinary Graduate School of Medicine and Engineering, University of Yamanashi, 1110 Shimokato, Chuo City, Yamanashi 409-3898, Japan

S. Ohno et al. (eds.), *In Vivo Cryotechnique in Biomedical Research and Application for Bioimaging of Living Animal Organs*, DOI 10.1007/978-4-431-55723-4_32

was also reported to be a marker for checking alteration of the BBB integrity [8].

However, conventional fixatives could easily release loosely bound or soluble protein components and then link them to other structure elements, with which they were not originally associated [9]. A technical solution for these problems has been known to be offered with another physical cryofixation, such as quick-freezing, which would have an advantage that the physical cryofixation for animal cells and tissues can be completed within a time of milliseconds [10]. For the purpose of applying the quick-freezing method for functioning cells and tissues in vivo, IVCT was developed [11], which was to arrest the transient behavior at the highest time resolution in animal living cells and tissues by the combination of a cryoknife cooled down in liquid nitrogen and another isopentane–propane cryogen (−193 °C) (Fig. 32.1a). IVCT and following freeze-substitution fixation (FS) would be the most reliable technique to keep soluble serum proteins in the blood vessels of animal brains. In addition, the protocol is useful to obtain good immunoreactivity because antibodies easily penetrate into tissue samples through tiny ice crystals (Fig. 32.1b). In this chapter, we demonstrate immunolocalization of serum proteins in mouse cerebellum with IVCT. Precise methods and results have been reported in the previous paper [12].

32.2 IVCT for Living Animal Cerebellum

Adult mice were anesthetized with sodium pentobarbital, and their cerebellum was surgically exposed. As depicted in Fig. 32.1a, while the heart was normally beating, the cerebellum was vertically cut with the precooled cryoknife as fast as possible and simultaneously poured with the isopentane–propane cryogen [11]. The frozen cerebellar tissues were carefully trimmed out with a dental drill in liquid nitrogen and then processed for the following FS step.

32.3 Detection of Serum IgG in Blood Capillaries In Vivo

Under normal condition, IgG was immunolocalized in blood vessels of cerebellum with IVCT followed by FS (Fig. 32.1c). Judging from sizes of tiny ice crystals at low resolution by light microscopy, artificial destruction of blood vessel structures was not well recognized in molecular layers at cerebellar surface layer tissues (ML in Fig. 32.1c) and granular layers at deeper regions (GL in Fig. 32.1c). The well-preserved tissues were nearly within 200–300 μm from the cerebellar surface area, which the isopentane–propane cryogen was directly poured over and the cryoknife was closely attached to. There was no immunoreactivity for IgG outside the blood vessels, suggesting no leakage or prominent movement of serum IgG proteins during the FS method as well as the immunohistochemical staining process.

After the perfusion fixation with 2 % paraformaldehyde in phosphate buffer, there was no immunoreactivity with anti-IgG antibody in the blood vessels, due to washing out of blood during the perfusion-fixation. Thus, soluble serum proteins, such as IgG, can be preserved by the combination of our IVCT and FS method.

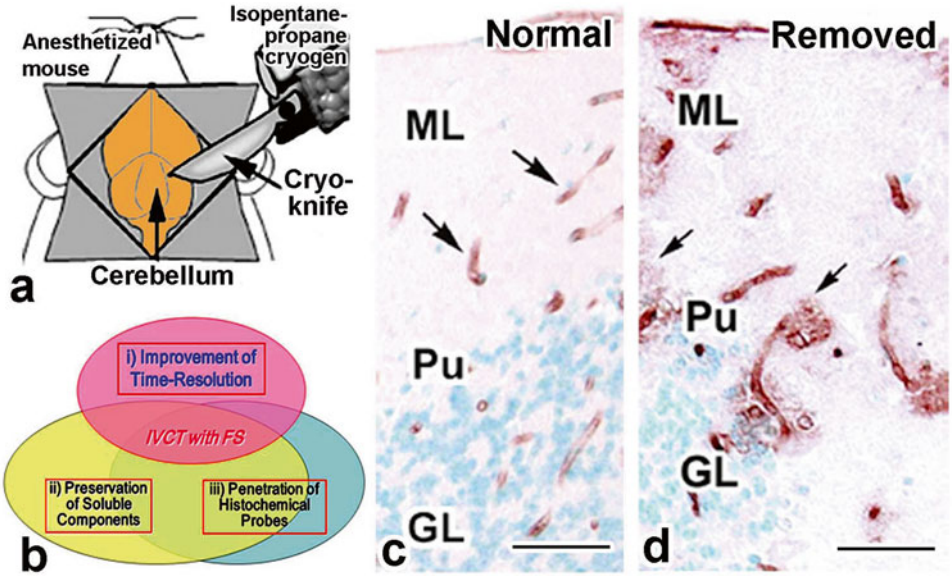

Fig. 32.1 (**a**) A schematic representation of "in vivo cryotechnique" (IVCT) for the mouse cerebellum after opening the scull; cryoknife is push into the cerebellum and simultaneously isopentane–propane cryogen (−193 °C) is poured over the cerebellum. (**b**) The schema illustrates three merits of IVCT with freeze-substitution fixation (FS). (**c**, **d**) Immunostaining of IgG in normal mouse cerebellum with IVCT (Normal; **c**) and removed cerebellum to induce hypoxic condition with quick-freezing method (Removed; **d**). *ML* molecular layer, *Pu* Purkinje cell layer, *GL* granular layer. Precise data have been reported in the previous paper (Zea-Aragón et al. [12]). Bars, **c**, **d**, 50 μm

32.4 Leakage of IgG from Blood Vessels in Anoxic Cerebellum

In the cerebellar tissues immediately after a sudden stop of cerebellar blood supply, IgG was diffusely immunostained around blood vessels (Fig. 32.1d). In such extravascular regions, there was no blood cell, indicating that no bleeding nor inflammatory reactions had happened around there. The distribution pattern of the IgG-immunostaining products was sometimes fan-shaped, indicating the leakage of serum IgG from some restricted points of the blood vessels. These findings suggest that the quick-freezing and freeze-substitution method applied in this section for immunohistochemistry enabled us to detect the functional damage of the BBB.

The immunostaining pattern of albumin was also observed to be similar to that of IgG, being a fan-shaped leakage around blood capillaries. The albumin immunoreaction products were observed to be exclusively localized within the blood vessels in cerebellar tissues under normal blood flow conditions, as prepared by IVCT.

32.5 Concluding Remarks

The combined procedure, the IVCT and FS method, presented here would be useful for clarifying time-dependent and native distribution of leaking serum proteins through damaged BBB under various pathological conditions.

References

1. Broman T (1966) Intravital and postmortem studies on air embolism damage of the blood–brain barrier tested with trypan blue. Acta Neurol Scand 42:146–152
2. Broadwell RD, Sofroniew MV (1933) Serum proteins bypass the blood–brain fluid barriers for extracellular entry to the central nervous system. Exp Neurol 120:245–263
3. Reese TS, Karnovsky MJ (1967) Fine structural localization of a blood–brain barrier to exogenous peroxidase. J Cell Biol 34:207–219
4. Zucker DK, Wooten GF, Lothman EW (1983) Blood–brain barrier changes with kainic acid-induced limbic seizures. Exp Neurol 79:422–433
5. Miller RD, Monsul NT, Vender JR, Lehmann JC (1996) NMDA and endothelin-1-induced increases in blood brain barrier permeability quantitated with Lucifer yellow. J Neurol Sci 136:37–40
6. Hamilton BF, Gould DH (1987) Correlation of morphologic brain lesions with physiologic alterations and blood–brain barrier impairment in 3-nitropropionic acid toxicity in rats. Acta Neuropathol 74:67–74
7. Nishino H, Shimano Y, Kumazaki M, Sakurai T (1995) Chronically administered 3-nitropropionic acid induces striatal lesions attributed to dysfunction of the blood–brain barrier. Neurosci Lett 186:161–164
8. Reynolds DS, Morton AJ (1998) Changes in blood–brain barrier permeability following neurotoxic lesions of rat brain can be visualized with trypan blue. J Neurosci Methods 9:115–121
9. Moreira JE, Dodane V, Reese TS (1988) Immunoelectron microscopy of soluble and membrane proteins with a sensitive postembedding method. J Histochem Cytochem 46:847–854
10. Heuser JE, Reese TS, Dennis MJ, Jan Y, Jan L, Evans L (1979) Synaptic vesicle exocytosis captured by quick freezing and correlated with quantal transmitter release. J Cell Biol 81:275–300
11. Ohno S, Terada N, Fujii Y, Ueda H, Takayama I (1996) Dynamic structure of glomerular capillary loop as revealed by an in vivo cryotechnique. Virchows Arch 427:519–527
12. Zea-Aragón Z, Terada N, Ohno N, Fujii Y, Baba T, Ohno S (2004) Effects of anoxia on serum immunoglobulin and albumin leakage through blood–brain barrier in mouse cerebellum as revealed by cryotechniques. J Neurosci Methods 138:89–95

Extracellular Space in Central Nervous System

33

Nobuhiko Ohno, Nobuo Terada, and Shinichi Ohno

Abstract

The ultrastructures of the cerebellar cortex in living mice were investigated using the "in vivo cryotechnique" (IVCT). Electron microscopic observation with IVCT revealed that large extracellular spaces (ECS) were clearly observed among profiles of neurons and glia in molecular and Purkinje cell layers of the mouse cerebellum. The ECS were significantly reduced by prolonged ischemia/anoxia, since the ECS were smaller in tissue specimens obtained with IVCT following 8 min ischemia or the conventional quick-freezing method of resected fresh tissues. The parallel fibers observed with IVCT after short period of ischemia were slightly larger than those without ischemia, indicating cellular swelling after ischemia/anoxia. ECS were also abundant around synaptic terminals, which were totally or partially covered with glial processes, and the ECS sizes of opened (not covered with glial processes) and enclosed (covered with glial processes) synapses are estimated to be similar. These findings indicate that IVCT is useful to analyze ECS morphology in the central nervous system. The abundant ECS would allow morphological changes of neuronal and glial cells involved in dynamic remodeling and signal transduction of synapses.

Keywords

Swelling • Asphyxia • Synaptic cleft • Glial process

33.1 Introduction

Ultrastructural analyses of the CNS using the common methods, such as chemical fixation, dehydration with organic solvent, and cryofixation, have often been affected by artifacts caused by anoxia during the sample preparation [1, 2]. Various steps in chemical fixation methods can cause artificial changes to the resultant ultrastructural images [3, 2]. Since "in vivo cryotechnique" (IVCT) is a method which directly cryofix target organs in vivo in living animals without tissue resection or stopping blood circulation [4], IVCT was applied to ultrastructural analyses of the mouse cerebellar cortex with particular emphasis on the extracellular spaces (ECS).

N. Ohno, M.D., Ph.D. (✉) • S. Ohno
Department of Anatomy and Molecular Histology,
Interdisciplinary Graduate School of Medicine and Engineering,
University of Yamanashi, 1110 Shimokato, Chuo City,
Yamanashi 409-3898, Japan
e-mail: nohno@yamanashi.ac.jp

N. Terada
Division of Health Sciences, Shinshu University Graduate School of Medicine, 3-1-1 Asahi, Matsumoto City, Nagano 390-8621, Japan

Department of Anatomy and Molecular Histology,
Interdisciplinary Graduate School of Medicine and Engineering,
University of Yamanashi, 1110 Shimokato, Chuo City,
Yamanashi 409-3898, Japan

33.2 Morphological Comparison Among IVCT and Conventional Methods

To perform IVCT, anesthetized mice were immobilized on a mouse-head stereotactic apparatus, and the skull was partly removed with a dental drill to expose cerebellum without damage to brain tissues. Thereafter, "in vivo cryoapparatus"

S. Ohno et al. (eds.), *In Vivo Cryotechnique in Biomedical Research and Application for Bioimaging of Living Animal Organs*, DOI 10.1007/978-4-431-55723-4_33

was used to perform IVCT [5], and acetone containing 1 % osmium tetroxide was used for the freeze-substitution of frozen tissues. The embedded specimens were first evaluated with a light microscope and toluidine blue staining, and then their ultrathin sections were stained and observed with a transmission electron microscope [6].

Light microscopic observation with IVCT shows relatively strong toluidine blue staining near the tissue surface cut with the cryoknife and contacted directly with the isopentane-propane cryogen in mouse cerebellar tissues [6]. No visible ice crystals were observed near the cryo-cut surface at a higher magnification. The morphology near the surface of specimens prepared with IVCT appeared similar to those prepared with perfusion fixation followed by dehydration (PF-DH) at the light microscopic level. At the electron microscopic level, intercellular ultrastructures of the molecular layers were well maintained with IVCT near the surface cut with the cryoknife [6]. Among cellular profiles and synaptic clefts in molecular layers, ECS could be clearly detected at higher magnification (Fig. 33.1). The open ECS were directly surrounding some synaptic clefts. The density of the cellular profiles was relatively homogenous, as reported previously [7]. With conventional PF-DH, to the contrary, ECS were largely lost, and glial and neuronal processes compactly surrounded synaptic clefts.

Electron microscopic images of cerebellar cortex obtained by quick-freezing of fresh resected tissues followed by freeze-substitution (FQF) reflect the effect of anoxia for a few minutes, because the tissue specimens of the cerebellum had to be resected from the anesthetized mice before the cryofixation. Few open ECS were detected in the cerebellar tissues prepared with FQF, although in mouse cerebellum prepared with the IVCT, widely open ECS could be observed among cellular profiles in the molecular layers (Fig. 33.1) [6]. The open ECS were also maintained around processes and soma of Purkinje cells in Purkinje cell layers (Fig. 33.1). Ischemia for 30 s still remains the open ECS, whereas ischemia for 8 min eliminated the open ECS [6]. IVCT without ischemia also suggested that the size of ECS could vary depending on the area in the molecular layers, since the ECS sizes among cellular profiles ranged from as large as a few hundred to <10 nm^2 and the percent area occupied by ECS ranged from 8 to 28 % [6]. Previous studies indicated that ECS occupies about 10–20 % of CNS tissues, although direct observation by electron microscopy has been difficult. The difficulty is attributable to technical artifacts caused during conventional chemical fixation or asphyxia of tissue resection prior to resected tissues followed by quick-freezing [2, 8]. The asphyxia before completion of chemical fixation can cause the morphological changes through movement of extracellular fluid and electrolytes into intracellular compartments [9], although even larger molecules may easily enter the intracellular compartment via gap junction hemichannels during ischemia/anoxia [10]. When the cellular processes in molecular layers of mouse cerebellum were examined in tissue specimens prepared with IVCT or FQF, not only sev-

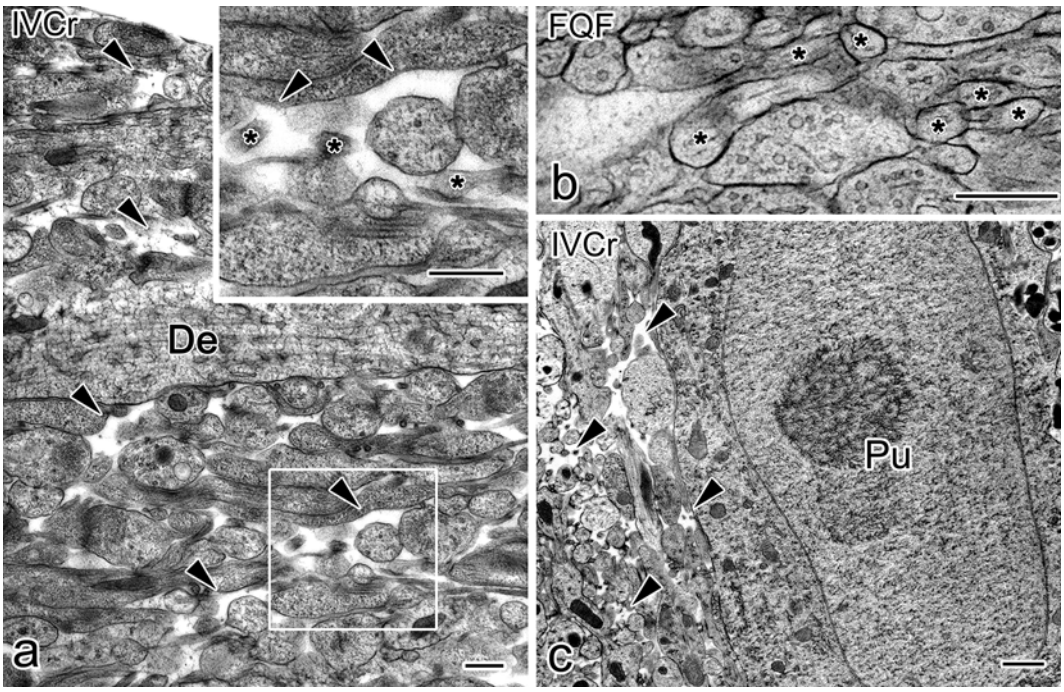

Fig. 33.1 Electron micrographs of molecular layers (**a**, **b**) or Purkinje cell layers (**c**) in mouse cerebellar cortex prepared by the "in vivo cryotechnique" without ischemia (IVCT; **a**, **c**) or quick-freezing of fresh tissues (FQF; **b**) show that a number of open extracellular spaces (**a**, **c**; *arrowheads*) are seen among the parallel fibers (**a**; *inset*, *asterisks*) and dendrites (**a**, De) or cell bodies (**c**, Pu) of Purkinje cells. In the cerebellar specimens prepared with FQF (**b**), few open extracellular spaces are observed among the parallel fibers (**b**, *asterisks*). *Bars*, 500 nm in (**a**) and (**b**); 1 μm in (**c**). (The figure is adapted from Ohno et al. [6])

eral minutes of anoxia but also even 30 s of ischemia can increase the size of parallel fibers [6]. The rapid changes in the size of Bergmann glial fibers as well as neuropils support the rapid translocation of various extracellular components. IVCT would provide novel information about ultrastructural variance within molecular layers of the cerebellar cortex which was indicated in previous studies using conventional chemical fixation and dehydration methods [11–13].

ECS occupied considerable areas in molecular and Purkinje cell layers of the mouse cerebellar cortex, but the size of ECS appeared variable [6]. The ECS and their heterogenous distribution were also proposed in other ultrastructural studies using conventional quick-freezing and freeze-substitution or diffusion analyses [1, 7, 14]. The findings are also compatible with the simulation analyses of in vivo molecular diffusion, indicating that abundant extracellular matrices affect the probe's diffusion, and ECS of rat cerebral cortex was similar to fluid-filled pores sized about 38–64 nm [15, 16]. Indeed, abundant meshwork structures in the remaining ECS could be observed in mouse cerebellar tissues with the quick-freezing and deep-etching method after perfusion fixation [6]. Combination of IVCT with the diffusion analysis, by which ECS in living animals can be examined under anesthesia [14], will be one feasible approach for further analyses of ECS. Roles of widely open ECS in living mice may include dynamic remodeling of the cerebellar cortex morphology, such as enlargement of dendritic spine or extension of cellular processes [17, 18].

33.3 Synaptic Clefts, Open ECS, and Surrounding Glial Processes

In specimens prepared with IVCT, many synapses in molecular layers of cerebellar cortex were detected between parallel fibers and Purkinje cell dendrites (Fig. 33.1). About 45 % of the synaptic clefts appeared directly exposed to the open ECS (Fig. 33.2) [6]. The other synaptic clefts were completely or partially surrounded with closely apposed glial sheaths (Fig. 33.2). The open ECS around this type of synapses was observed outside of the glial sheath (Fig. 33.2). When (1) the length between the presynaptic active zones and surrounding cellular profiles in synapses open to ECS and (2) the shortest length between synaptic clefts and nearest cellular profiles other than surrounding glial sheaths in the synapses enclosed by glial processes were measured, the lengths obtained in opened or enclosed synapses were not significantly different [6].

Bergmann glial fibers covered most dendritic spines bearing synapses [19]. However, many synapses would be, at least partially, exposed to the open ECS in the molecular layers. Since the mean size of perisynaptic ECS was not significantly different between opened and enclosed synapses, the glial processes may extend or retract through the perisynaptic ECS to ensheath synapses transiently. Structural development, remodeling, and maintenance of synapses are modulated by glial cells affecting synaptic transmission [20]. The glial functions on synapses could be influenced by the perisynaptic processes of glia, which change dynamically in response to the synaptic activities [21, 22]. Structural support to the dynamic glial process may be provided by the perisynaptic ECS. The variable sizes of perisynaptic ECS and synaptic ensheathment by glial processes may provide diverse contributions of glia to the signal transduction through synapses.

33.4 Concluding Remarks

Widely open ECS, which include those around synapses and would be involved in the dynamic morphogenesis of neuronal and glial cells, were clearly detected in the mouse cerebellar cortex by IVCT. As IVCT prevents the asphyxial changes inevitably induced by conventional

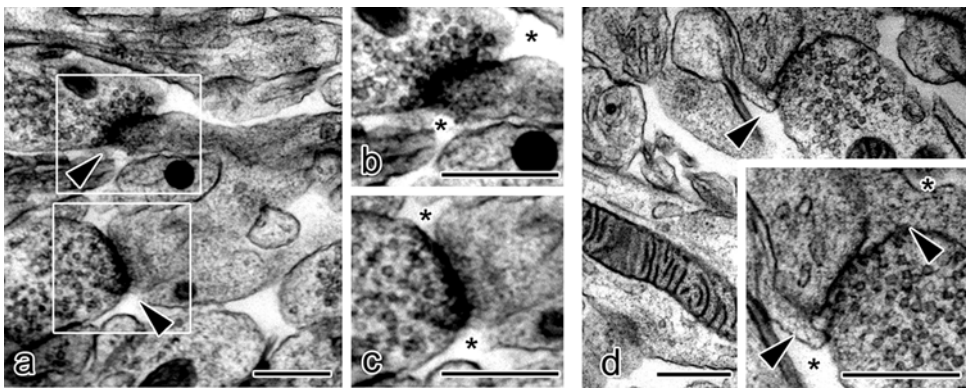

Fig. 33.2 Electron micrographs of synaptic clefts in molecular layers of mouse cerebellar cortex prepared with the "in vivo cryotechnique" show that some synaptic clefts (**a**, *arrowheads*) are exposed to the open ECS (**b**, **c**; *asterisks*), whereas the other synaptic clefts are not exposed and totally or partially enclosed with glial sheaths (**d**, *arrowheads*). Open extracellular spaces (ECS) are located outside of the glial sheaths (**d**, *asterisks*). *Bars*, 500 nm. (The figure was adapted from Ohno et al. [6])

methods of preparation, IVCT will become one of the useful morphological approaches to examine the CNS of living animals under various physiological and experimental conditions.

References

1. Hirokawa N, Kirino T (1980) An ultrastructural study of nerve and glial cells by freeze-substitution. J Neurocytol 9(2):243–254
2. Van Harreveld A, Khattab FI (1968) Perfusion fixation with glutaraldehyde and post-fixation with osmium tetroxide for electron microscopy. J Cell Sci 3(4):579–594
3. Eisenberg BR, Mobley BA (1975) Size changes in single muscle fibers during fixation and embedding. Tissue Cell 7(2):383–387
4. Ohno N, Terada N, Ohno S (2004) Advanced application of the in vivo cryotechnique to immunohistochemistry for animal organs. Acta Histochem Cytochem 37:357–364
5. Ohno N, Terada N, Fujii Y, Baba T, Ohno S (2004) "In vivo cryotechnique" for paradigm shift to "living morphology" of animal organs. Biomed Rev 15:1–19
6. Ohno N, Terada N, Saitoh S, Ohno S (2007) Extracellular space in mouse cerebellar cortex revealed by in vivo cryotechnique. J Comp Neurol 505(3):292–301
7. Van Harreveld A (1972) The extracellular space in the vertebrate central nervous system. In: Bourne GH (ed) The structure and function of nervous tissue. Elsevier, Oxford, pp 447–511
8. Van Harreveld A, Crowell J, Malhotra SK (1965) A study of extracellular space in central nervous tissue by freeze-substitution. J Cell Biol 25:117–137
9. Van Harreveld A (1962) Water and electrolyte distribution in central nervous tissue. Fed Proc 21:659–664
10. Thompson RJ, Zhou N, MacVicar BA (2006) Ischemia opens neuronal gap junction hemichannels. Science 312(5775):924–927
11. Gundappa-Sulur G, De Schutter E, Bower JM (1999) Ascending granule cell axon: an important component of cerebellar cortical circuitry. J Comp Neurol 408(4):580–596
12. Napper RM, Harvey RJ (1988) Number of parallel fiber synapses on an individual Purkinje cell in the cerebellum of the rat. J Comp Neurol 274(2):168–177
13. Sultan F (2000) Exploring a critical parameter of timing in the mouse cerebellar microcircuitry: the parallel fiber diameter. Neurosci Lett 280(1):41–44
14. Nicholson C, Sykova E (1998) Extracellular space structure revealed by diffusion analysis. Trends Neurosci 21(5):207–215
15. Dityatev A, Schachner M (2003) Extracellular matrix molecules and synaptic plasticity. Nat Rev Neurosci 4(6):456–468
16. Thorne RG, Nicholson C (2006) In vivo diffusion analysis with quantum dots and dextrans predicts the width of brain extracellular space. Proc Natl Acad Sci U S A 103(14):5567–5572
17. Matsuzaki M, Honkura N, Ellis-Davies GC, Kasai H (2004) Structural basis of long-term potentiation in single dendritic spines. Nature 429(6993):761–766
18. Nimmerjahn A, Kirchhoff F, Helmchen F (2005) Resting microglial cells are highly dynamic surveillants of brain parenchyma in vivo. Science 308(5726):1314–1318
19. Spacek J (1985) Three-dimensional analysis of dendritic spines. III. Glial sheath. Anat Embryol 171(2):245–252
20. Auld DS, Robitaille R (2003) Glial cells and neurotransmission: an inclusive view of synaptic function. Neuron 40(2):389–400
21. Iino M, Goto K, Kakegawa W, Okado H, Sudo M, Ishiuchi S et al (2001) Glia-synapse interaction through Ca2+ -permeable AMPA receptors in Bergmann glia. Science 292(5518):926–929
22. Oliet SH, Piet R (2004) Anatomical remodelling of the supraoptic nucleus: changes in synaptic and extrasynaptic transmission. J Neuroendocrinol 16(4):303–307

Overview on Recent Applications of In Vivo Cryotechnique in Neurosciences

34

Nobuhiko Ohno, Nobuo Terada, Yurika Saitoh, and Shinichi Ohno

Abstract

When tissue specimens are prepared for microscopic observation, commonly used methods using chemical fixatives and dehydration can yield artifacts in morphology and molecular distribution. Conventional quick-freezing and high-pressure freezing methods, where specimens are cryofixed after resection, can also cause artifacts due to anoxia and ischemia, and only dead morphological states without blood circulation can be observed with these methods. By contrast, all cells and tissues in animal bodies can be cryofixed in situ by "in vivo cryotechnique" (IVCT), which prevents these artifacts caused following removal of target tissues. In the central nervous system, distribution of small molecules, dynamic changes of signaling proteins, ultrastructures of extracellular space, and blood–brain barrier integrity have been examined using IVCT. To acquire novel information in cryofixed tissues, new imaging methods including Raman microscopy were combined with IVCT. New approaches to observe "living" states in the nervous system will be possible with IVCT.

Keywords

Extracellular space • Blood–brain barrier • Signaling proteins • Raman microscopy

34.1 Introduction

Functional aspects are reflected in the structures of cells and tissues in living animal organs. A widely used method for structural analyses has been the microscopic analyses. Recently, there was dramatic progress in technology of light microscopy. Dynamic signal molecules and their interactions can be visualized in living cells and animals by the fluorescence imaging. "*In vivo*cryotechnique (IVCT)" has been used to observe dynamic structures and molecular localization in living animal organs at light and electron microscopic levels [1]. Cryobiopsy has been also developed for clinical application. Here, technical aspects of IVCT and recent findings obtained by IVCT in the field of neurosciences will be reviewed.

34.2 Problems of Conventional Preparation Methods

Chemical fixation, dehydration, embedding, sectioning, and dye or metal staining steps have been widely used for animal nervous system to examine morphology at the light and electron microscopic levels. Artifacts affecting the final structures are caused during these tissue preparation steps [2, 3]. Perfusion or immersion with chemical fixatives, such as

N. Ohno, M.D., Ph.D. (✉) • Y. Saitoh • S. Ohno
Department of Anatomy and Molecular Histology, Interdisciplinary Graduate School of Medicine and Engineering, University of Yamanashi, 1110 Shimokato, Chuo City, Yamanashi 409-3898, Japan
e-mail: nohno@yamanashi.ac.jp

N. Terada
Division of Health Sciences, Shinshu University Graduate School of Medicine, 3-1-1 Asahi, Matsumoto City, Nagano 390-8621, Japan

Department of Anatomy and Molecular Histology, Interdisciplinary Graduate School of Medicine and Engineering, University of Yamanashi, 1110 Shimokato, Chuo City, Yamanashi 409-3898, Japan

S. Ohno et al. (eds.), *In Vivo Cryotechnique in Biomedical Research and Application for Bioimaging of Living Animal Organs*, DOI 10.1007/978-4-431-55723-4_34

paraformaldehyde, glutaraldehyde, and osmium tetroxide, is commonly used for chemical fixation steps [4]. Molecular movement and/or structural changes are one of the problems caused during the chemical fixation [3]. In addition, there is a limitation of chemical fixation to preserve transient or dynamic morphology, since there are time intervals before completion of fixation [5]. Subsequent alcohol dehydration steps cause tissue shrinkage [6, 7]. One of the alternative approaches to reduce such artifacts is the cryofixation method.

The cryofixation is one of the physical fixation methods and embeds tissues in vitrified ice [8]. Various methods for cryofixation have been developed to meet the requirement. Major methods include the so-called slamming quick-freezing or the plunging quick-freezing methods, where resected tissues are quickly frozen by slamming onto precooled metal blocks or plunging into precooled liquid cryogens. In high-pressure freezing, tissues are cryofixed under very high pressures, and vitrification in relatively broad tissue areas can be achieved. After the cryofixation, many preparation methods can be used, including the freeze-substitution (FS) [5, 9]. Although cryofixation methods can reduce the artifacts and preservation of better morphology [8], it is necessary to collect tissues out from living animal organs in the conventional quick-freezing methods, and morphology and molecular distribution can be influenced by loss of blood supply and ischemia/anoxia [10, 11].

34.3 Development of In Vivo Cryotechnique and Cryobiopsy

Living animal organs can be directly cryofixed in vivo by the IVCT without tissue resection. Blood circulation of living tissues can be maintained by IVCT until the moment of cryofixation, and the artifacts caused by ischemia or anoxia can be minimized [12]. Additional merit of cryofixation is achievement of high time resolution [8]. After IVCT, many preparation procedures are available, as in the cases of the other cryofixation methods. The antigen retrieval procedures can be omitted in the specimens prepared with cryotechniques [13].

One of a few drawbacks in IVCT is that well-frozen areas are restricted to less than 10 μm depth from the surface of the tissues at an electron microscopic level [11, 14–17]. Due to the low spatial resolution at the light microscopic level, the width of the areas without visible ice crystals is about a few hundred micrometers deep from the surface [12, 13]. Another drawback of IVCT is that exposure of the target organs in living animals is necessary to pour the cryogen directly onto the organs and minimize formation of observable ice crystals.

Although ultrastructural analyses were the initial application of IVCT, IVCT has been also applied to many light microscopic studies [18]. However, cryogen is poured over the animal bodies; it is difficult to obtain serial specimens from single animals with IVCT. In "cryobiopsy," serial tissue samples can be pinched off from single anesthetized animals with precooled cryobiopsy forceps (−196 °C). Most methods for preparation of frozen tissues are possible in the following preparation for these biopsied tissues [18, 19]. In the following section, the four aspects of IVCT will be discussed with particular emphasis on recent application of IVCT to the neuroscience fields, including (1) brain morphology without ischemic/anoxicartifacts, (2) molecular localization in combination with new bioimaging techniques, (3) localization of soluble molecule, and (4) rapidly altering signal proteins.

34.4 Brain Morphology Without Ischemic/Anoxic Artifacts

Asphyxia following tissue resection or during chemical fixation causes the entrance of extracellular water and electrolytes into the intracellular compartment and decreases extracellular spaces [20–22]. To overcome this problem, ultrastructures of mouse cerebellar cortex were analyzed with IVCT [23]. With IVCT, large extracellular spaces could be observed, and these spaces in molecular and Purkinje cell layers are distributed among cellular profiles and synaptic clefts in mouse cerebellar cortex. The large extracellular spaces were maintained with IVCT after 30 s ischemia, but mostly diminished with IVCT after 8 min of ischemia or with the conventional quick-freezingmethod. The extracellular spaces were abundant around some synaptic clefts, whereas other synaptic clefts were totally or partially covered with glial processes [23]. The estimated sizes of extracellular spaces around the open and enclosed synaptic clefts were not significantly different, and such extracellular spaces presumably support translocation of various extracellular components [24]. It was considered that most dendritic spines bearing synapses are ensheathed by Bergmann glial processes in cerebellar cortex, and more than half of the circumferential length around the synaptic clefts were covered with cytoplasmic sheaths of Bergmann glia [25]. The perisynaptic glial processes are considered critical for the glial functions related to synapses [26–28]. The glial processes around synaptic clefts are considered to extend or retract through the perisynaptic extracellular spaces, and the extracellular spaces support the dynamic alterations of glial processes. Since cellular profiles might be swollen during tissue preparation steps with conventional preparation methods, a careful reevaluation of ultrastructural differences among different areas of molecular layers in the cerebellar cortex may be necessary using IVCT.

34.5 Molecular Localization in Combination with New Bioimaging Techniques

Novel information about the structures of molecules under normal conditions and diseased states can be obtained with microscopic approaches, including fluorescent, infrared, and Raman microscopy, which can detect the presence of biological molecules and/or drugs [29]. Raman microscopy can visualize different molecular states/structures in biological materials [30]. To preserve and observe the distribution and/or structures of molecules, e.g., proteins, lipids, carbohydrates, and vitamins, in living animal nervous system, the eyeball tissue sections prepared with IVCT followed by freeze-drying were observed under the confocal Raman microscopy, and mapping of the Raman spectra was obtained [31]. The Raman spectra could be largely classified into four patterns, which represented histologically different layers. One Raman spectrum corresponded to melanin and distributed mainly in the choroid and pigment cell layers. Another Raman spectrum represented hemoglobin and was obtained from the blood vessels in the sclera, whereas another spectrum was similar to the purified rhodopsin and distributed in the photoreceptor layer. The Raman spectra obtained in the freeze-dried samples and control solution samples were similar, presumably due to the less altered structures of biomolecules in the freeze-dried specimens. The IVCT was also combined with confocal cryo-Raman microscopy, where specimens are observed at low temperature (<−150 °C). By this approach, oxygen saturation levels of flowing erythrocytes in frozen tissue specimens were directly observed [32]. From these studies, Raman microscopy can distinguish multiple components in living bodies, and IVCT can be combined with Raman microscopy to examine distribution and structures of biological and chemical components which are changing quickly in living animal organs.

34.6 Precise Localization of Soluble Molecule

The central nervous system possesses a selective molecular barrier between blood vessels and parenchyma, which has been called the blood–brain barrier (BBB). BBB plays critical roles in brain functions and diseases such as neurodegenerative disorders [33]. IVCT was used to examine extravasation of intrinsic serumsoluble proteins in the previous study [12]. IVCT followed by FS can minimize diffusion and translocation of soluble serum molecules before fixation and can clarify the precise distribution of IgG and albumin in cerebellar tissues. Under the normal condition, serum IgG and albumin were localized exclusively inside the cerebellar blood vessels. However, the immunostaining for the serum proteins was observed around the blood capillaries in the cerebellar parenchyma when the brain tissues were cryofixed within a minute after removal. The serum protein diffusion through BBB after tissue removal could be attributable to leakage of the serum components. Using IVCT, injected extrinsic molecules could be successfully detected in multiple organs [19, 34, 35]. IVCT followed by FS is useful to examine the extravascular leakage of soluble molecules under pathological conditions of animal brains, given that serum proteins could not be detected outside blood vessels under normal conditions.

IVCT and subsequent FS were also used to examine distribution of glutamate, which had been controversially detected in inner segments of photoreceptors [36]. With IVCT, the most intense immunostaining for glutamate was observed in the specimens freeze-substituted with acetone containing paraformaldehyde and glutaraldehyde. Glutamate was clearly observed in the inner segments, outer and inner plexiform layers, and ganglion cell layers. In previous studies in the goldfish [37], cats [38], chickens [39, 40], rats [41], and monkeys [41], immersion fixation revealed glutamate immunoreactivity in the inner segment of the eyes. When the animals were perfused with fixatives, the immunostaining for glutamate could not be detected in the inner segment [42, 43]. Thus, it was suggested that postmortem changes caused by ischemia/anoxia might affect distribution of glutamate in the inner segment. Since the effect of ischemia/anoxia can be minimized by IVCT, the clear glutamate immunoreactivity observed with IVCT in the inner segment of photoreceptors suggests that the glutamate immunoreactivity is not caused by ischemia/axoxia. It was reported that the inner segment also contains highly active enzymes related to the glutamate metabolism [44, 45]. IVCT will be a powerful tool to examine living animal nervous system and detect distribution of small molecules including glutamate. In addition, concentrations of fixatives such as glutaraldehyde need to be optimized to cross-link and retain small molecules and not to hinder the antibody binding.

34.7 Rapidly Altering Signal Proteins

Light stimulation rapidly changes molecular structure of rhodopsin (Rho) which functions as photoreceptor [46]. Rho is phosphorylated at 334Ser, 338Ser, and 343Ser [47], and the biochemical analysis suggested that the phosphorylation can be caused quickly in response to different light conditions [48]. The alteration of phosphorylated Rho (P-Rho) immunoreactivity was examined after the dark adaptation of retinas using specific antibodies against P-Rho [49]. Rapid changes of Rho and P-Rho under dark adaptation and light

illumination were analyzed with IVCT followed by FS in living mouse retinas [50]. Immunostaining with anti-phosphorylated (334)Ser-Rho (P-Rho334) antibody revealed that immunostaining for P-Rho334 was detected in the outer segments of mouse retinas, presumably because they were exposed to daylight. P-Rho334 immunostaining was completely disappeared in mouse retinas following 12 h of dark adaptation, and exposure to the safety red light after 12 h or 36 h of dark adaptation did not alter the P-Rho334 immunoreactivity. In addition, illumination of visible light for 10 s did not increase the immunoreactivity of P-Rho334. However, illumination of visible light for 30, 60, and 180 s significantly increased P-Rho334 immunoreactivity, and the immunoreactivity was similar to the level of that under daylight condition. In the Rho-phosphorylation steps, phosphorylation of 343Ser in Rho happens the most quickly compared with the other 338Ser and 334Ser [48]. In the living mouse retina, rapid phosphorylation of P-Rho334 induced within 10–30 s after light exposure could be revealed by IVCT with the higher temporal resolution.

Functional activities of angiotensin II (AT) receptors in mouse cerebellum was also analyzed with IVCT [51]. Functions of AT are mediated by two seven-transmembrane G protein-coupled receptors, type 1 (AT1R) and type 2 (AT2R) AT receptors [52, 53]. To address distributions and activation states of AT receptors in the cerebellum, IVCT along with antibodies against N-termini of AT receptors, whose conformations could change upon ligand binding, is used for immunohistochemical analyses in mouse cerebellum [51]. The immunostaining for AT receptors largely overlapped with a Bergmann glia marker, glial fibrillary acidic protein (GFAP), in mouse cerebellum. The AT1R immunoreactivity was reduced dramatically after ischemia for 5 and 10 min or exposure to an AT1R antagonist, losartan, in the cerebellar cortex. The immunostaining for AT2R was also decreased by hypoxia in the cerebellar specimens. These results suggest that the rapid alteration of ligant-receptor binding in the nervous system of living animals can be visualized by IVCT, and hypoxia may modulate the functions of AT receptors in a time-dependent manner in the central nervous system.

34.8 Concluding Remarks

In the cryofixation methods, the abundant extracellular or intracellular fluid turns into vitreous ice and keeps all components and structures of the living animal organs in situ, which can be subsequently analyzed through immunohistochemical or other analytical methods. IVCT directly cryofix living animals organs and has been used for different applications in the nervous system. IVCT is a powerful tool to reveal the functional structures closer to "living" states and will develop a new field of "living morphology."

References

1. Ohno S, Terada N, Ohno N, Saitoh S, Saitoh Y, Fujii Y (2010) Significance of 'in vivo cryotechnique' for morphofunctional analyses of living animal organs. J Electron Microsc (Tokyo) 59(5):395–408
2. Hippe-Sanwald S (1993) Impact of freeze substitution on biological electron microscopy. Microsc Res Tech 24(5):400–422
3. Kellenberger E (1991) The potential of cryofixation and freeze substitution: observations and theoretical considerations. J Microsc 161(Pt 2):183–203
4. Hopwood D (1969) Fixatives and fixation: a review. Histochem J 1(4):323–360
5. Shiurba R (2001) Freeze-substitution: origins and applications. Int Rev Cytol 206:45–96
6. Chan FL, Inoue S (1994) Lamina lucida of basement membrane: an artefact. Microsc Res Tech 28(1):48–59
7. Leu FJ, Chen CF, Sun AM (1993) A new method of tissue processing that causes no shrinkage or distortion. Lab Invest J Tech Method Pathol 69(1):121–130
8. Plattner H, Bachmann L (1982) Cryofixation: a tool in biological ultrastructural research. Int Rev Cytol 79:237–304
9. Nicolas MT, Bassot JM (1993) Freeze substitution after fast-freeze fixation in preparation for immunocytochemistry. Microsc Res Tech 24(6):474–487
10. Terracio L, Schwabe KG (1981) Freezing and drying of biological tissues for electron microscopy. J Histochem Cytochem 29(9):1021–1028
11. Ohno S, Terada N, Fujii Y, Ueda H, Takayama I (1996) Dynamic structure of glomerular capillary loop as revealed by an in vivo cryotechnique. Virchows Arch 427(5):519–527
12. Zea-Aragon Z, Terada N, Ohno N, Fujii Y, Baba T, Ohno S (2004) Effects of anoxia on serum immunoglobulin and albumin leakage through blood–brain barrier in mouse cerebellum as revealed by cryotechniques. J Neurosci Methods 138(1–2):89–95
13. Ohno N, Terada N, Murata S, Katoh R, Ohno S (2005) Application of cryotechniques with freeze-substitution for the immunohistochemical demonstration of intranuclear pCREB and chromosome territory. J Histochem Cytochem 53(1):55–62
14. Van Harreveld A, Trubatch J, Steiner J (1974) Rapid freezing and electron microscopy for the arrest of physiological processes. J Microsc 100(2):189–198
15. von Schack ML, Fakan S, Villiger W, Muller M (1993) Cryofixation and cryosubstitution: a useful alternative in the analyses of cellular fine structure. Eur J Histochem 37(1):5–18
16. Chen HB, Yamabayashi S, Ou B, Ohno S, Tsukahara S (1995) Ultrastructural studies on the corneal superficial epithelium of rats by in vivo cryofixation with freeze substitution. Ophthalmic Res 27(5):286–295
17. Xue M, Kato Y, Terada N, Fujii Y, Baba T, Ohno S (1998) Morphological study by an 'in vivo cryotechnique' of the shape of erythrocytes circulating in large blood vessels. J Anat 193(Pt 1):73–79
18. Fujii Y, Ohno N, Li Z, Terada N, Baba T, Ohno S (2006) Morphological and histochemical analyses of living mouse livers by new 'cryobiopsy' technique. J Electron Microsc (Tokyo) 55(2):113–122
19. Ohno N, Terada N, Bai Y, Saitoh S, Nakazawa T, Nakamura N et al (2008) Application of cryobiopsy to morphological and immuno-

histochemical analyses of xenografted human lung cancer tissues and functional blood vessels. Cancer 113(5):1068–1079
20. Van Harreveld A, Crowell J, Malhotra SK (1965) A study of extracellular space in central nervous tissue by freeze-substitution. J Cell Biol 25:117–137
21. Van Harreveld A, Khattab FI (1968) Electron microscopy of the mouse retina prepared by freeze-substitution. Anat Rec 161(1):125–139
22. Van Harreveld A (1962) Water and electrolyte distribution in central nervous tissue. Fed Proc 21:659–664
23. Ohno N, Terada N, Saitoh S, Ohno S (2007) Extracellular space in mouse cerebellar cortex revealed by in vivo cryotechnique. J Comp Neurol 505(3):292–301
24. Van Harreveld A (1961) Asphyxial changes in the cerebellar cortex. J Cell Comp Physiol 57:101–110
25. Spacek J (1985) Three-dimensional analysis of dendritic spines. III. Glial sheath. Anat Embryol 171(2):245–252
26. Auld DS, Robitaille R (2003) Glial cells and neurotransmission: an inclusive view of synaptic function. Neuron 40(2):389–400
27. Iino M, Goto K, Kakegawa W, Okado H, Sudo M, Ishiuchi S et al (2001) Glia-synapse interaction through Ca_2+ -permeable AMPA receptors in Bergmann glia. Science (New York) 292(5518):926–929.
28. Oliet SH, Piet R (2004) Anatomical remodelling of the supraoptic nucleus: changes in synaptic and extrasynaptic transmission. J Neuroendocrinol 16(4):303–307
29. Choi J, Choo J, Chung H, Gweon DG, Park J, Kim HJ et al (2005) Direct observation of spectral differences between normal and basal cell carcinoma (BCC) tissues using confocal Raman microscopy. Biopolymers 77(5):264–272
30. Wood BR, Tait B, McNaughton D (2001) Micro-Raman characterisation of the R to T state transition of haemoglobin within a single living erythrocyte. Biochim Biophys Acta 1539(1–2):58–70
31. Terada N, Ohno N, Saitoh S, Fujii Y, Ohguro H, Ohno S (2007) Raman microscopy of freeze-dried mouse eyeball-slice in conjunction with the "in vivo cryotechnique". Microsc Res Tech 70(7):634–639
32. Terada N, Ohno N, Saitoh S, Ohno S (2008) Application of "in vivo cryotechnique" to detect erythrocyte oxygen saturation in frozen mouse tissues with confocal Raman cryomicroscopy. J Struct Biol 163(2):147–154
33. Zlokovic BV (2008) The blood–brain barrier in health and chronic neurodegenerative disorders. Neuron 57(2):178–201
34. Terada N, Ohno N, Li Z, Fujii Y, Baba T, Ohno S (2005) Detection of injected fluorescence-conjugated IgG in living mouse organs using "in vivo cryotechnique" with freeze-substitution. Microsc Res Tech 66(4):173–178
35. Saitoh Y, Terada N, Saitoh S, Ohno N, Jin T, Ohno S (2012) Histochemical analyses and quantum dot imaging of microvascular blood flow with pulmonary edema in living mouse lungs by "in vivo cryotechnique". Histochem Cell Biol 137(2):137–151
36. Terada N, Ohno N, Saitoh S, Saitoh Y, Ohno S (2009) Immunoreactivity of glutamate in mouse retina inner segment of photoreceptors with in vivo cryotechnique. J Histochem Cytochem 57(9):883–888
37. Marc RE, Liu WL, Kalloniatis M, Raiguel SF, van Haesendonck E (1990) Patterns of glutamate immunoreactivity in the goldfish retina. J Neurosci 10(12):4006–4034
38. Pourcho RG, Owczarzak MT (1991) Connectivity of glycine immunoreactive amacrine cells in the cat retina. J Comp Neurol 307(4):549–561
39. Kalloniatis M, Fletcher EL (1993) Immunocytochemical localization of the amino acid neurotransmitters in the chicken retina. J Comp Neurol 336(2):174–193
40. Sun H, Crossland WJ (2000) Quantitative assessment of localization and colocalization of glutamate, aspartate, glycine, and GABA immunoreactivity in the chick retina. Anat Rec 260(2):158–179
41. Kalloniatis M, Marc RE, Murry RF (1996) Amino acid signatures in the primate retina. J Neurosci 16(21):6807–6829
42. Sasoh M, Ma N, Yoshida S, Semba R, Uji Y (1998) Immunocytochemical localization of glutamate in normal and detached cat retina. Invest Ophthalmol Vis Sci 39(5):786–792
43. Sasoh M, Ma N, Ito Y, Esaki K, Uji Y (2006) Changes in localization of amino acids in the detached cat retina. Ophthalmic Res 38(2):74–82
44. Ross CD, Godfrey DA (1987) Distribution of activities of aspartate aminotransferase isoenzymes and malate dehydrogenase in guinea pig retinal layers. J Histochem Cytochem 35(6):669–674
45. Endo S, Ishiguro S, Tamai M (1999) Possible mechanism for the decrease of mitochondrial aspartate aminotransferase activity in ischemic and hypoxic rat retinas. Biochim Biophys Acta 1450(3):385–396
46. Menon ST, Han M, Sakmar TP (2001) Rhodopsin: structural basis of molecular physiology. Physiol Rev 81(4):1659–1688
47. Ohguro H, Rudnicka-Nawrot M, Buczylko J, Zhao X, Taylor JA, Walsh KA et al (1996) Structural and enzymatic aspects of rhodopsin phosphorylation. J Biol Chem 271(9):5215–5224
48. Kennedy MJ, Lee KA, Niemi GA, Craven KB, Garwin GG, Saari JC et al (2001) Multiple phosphorylation of rhodopsin and the in vivo chemistry underlying rod photoreceptor dark adaptation. Neuron 31(1):87–101
49. Ohguro H, Ohguro I, Mamiya K, Maeda T, Nakazawa M (2003) Prolonged survival of the phosphorylated form of rhodopsin during dark adaptation of Royal College Surgeons rat. FEBS Lett 551(1–3):128–132
50. Terada N, Ohno N, Ohguro H, Li Z, Ohno S (2006) Immunohistochemical detection of phosphorylated rhodopsin in light-exposed retina of living mouse with in vivo cryotechnique. J Histochem Cytochem 54(4):479–486
51. Huang Z, Ohno N, Terada N, Saitoh Y, Chen J, Ohno S (2013) Immunohistochemical detection of angiotensin II receptors in mouse cerebellum and adrenal gland using "in vivo cryotechnique". Histochem Cell Biol 140(4):477–490
52. de Gasparo M, Catt KJ, Inagami T, Wright JW, Unger T (2000) International union of pharmacology. XXIII. The angiotensin II receptors. Pharmacol Rev 52(3):415–472
53. Basso N, Terragno NA (2001) History about the discovery of the renin-angiotensin system. Hypertension 38(6):1246–1249

Application of "In Vivo Cryotechnique" to Immunohistochemical Detection of Phosphorylated Rhodopsin in Light-Exposed Retina of Living Mouse

35

Nobuo Terada, Yurika Saitoh, Nobuhiko Ohno, and Shinichi Ohno

Abstract

In this chapter, we present time-dependent molecular states of rhodopsin (Rho) phosphorylation in mouse retina with "in vivo cryotechnique" (IVCT). Whole eyeballs of living mice under various dark- and light-exposure conditions were quickly frozen with isopentane–propane cryogen cooled down in liquid nitrogen (−196 °C). The frozen whole-mount eyeballs were freeze-substituted and embedded in paraffin wax. Deparaffinized sections were immunostained with anti-phosphorylated ^{334}Ser Rho (P-Rho334) antibody. Immunoreactivity of P-Rho334 was specifically obtained in the outer segments of mouse retinas exposed to daylight, and it was eliminated in the dark-adapted retinas. In the eyeballs exposed to strong visible light for 10 s after the dark adaptation, it was not detected. However, after 30, 60, and 180 s of visible light exposure, P-Rho334 immunoreactivity was recovered. Thus, IVCT revealed the time-dependent changes of the Rho phosphorylation in living mice within seconds following exposure to light.

Keywords

In vivo cryotechnique • Rhodopsin • Retina • Phosphorylation

35.1 In Vivo Cryotechnique (IVCT)

To capture dynamic change of structures as native states of biological materials in living animal organs, IVCT is a powerful approach [1, 2]. We have reported that the combination of IVCT with the following freeze-substitution (FS) procedure offers three benefits for immunohistochemistry: (a) improved time resolution of morphology, (b) preservation of immunohistochemical antigens, and (c) enhancement of specific immunoreactivity [3, 4]. One of the benefits, improved time resolution, was originally demonstrated in a previous study with observation of the living mouse renal glomerulus [1]. In that study, dynamically changing ultrastructures of glomerular basement membranes and slit diaphragms between blood capillaries and Bowman's spaces, depending on various hemodynamic conditions, were examined in detail by IVCT in combination with the deep-etching or FS method for light or electron microscopy [1]. The idea that IVCT directly captured such time-dependent morphological events was also confirmed by the cases of immunostaining soluble proteins in the mouse cerebellum [5] and injection of fluoroprobe-conjugated proteins into living mice, as immediately prepared by IVCT [6].

N. Terada, M.D., Ph.D. (✉)
Division of Health Sciences, Shinshu University Graduate School of Medicine, 3-1-1 Asahi, Matsumoto City, Nagano 390-8621, Japan

Department of Anatomy and Molecular Histology, Interdisciplinary Graduate School of Medicine and Engineering, University of Yamanashi, 1110 Shimokato, Chuo City, Yamanashi 409-3898, Japan
e-mail: nobuot@shinshu-u.ac.jp

Y. Saitoh • N. Ohno • S. Ohno
Department of Anatomy and Molecular Histology, Interdisciplinary Graduate School of Medicine and Engineering, University of Yamanashi, 1110 Shimokato, Chuo City, Yamanashi 409-3898, Japan

S. Ohno et al. (eds.), *In Vivo Cryotechnique in Biomedical Research and Application for Bioimaging of Living Animal Organs*, DOI 10.1007/978-4-431-55723-4_35

35.2 Rhodopsin Phosphorylation

Rhodopsin (Rho) is a photoreceptor quickly changing its molecular structure by light stimulation [7]. An active form of Rho is further inactivated by two sequential processes: first the Rho phosphorylation and then the binding of arrestin to the Rho [8, 9]. During these processes, Rho phosphorylation in ^{334}Ser, ^{338}Ser, and ^{343}Ser near the carboxyl terminus [10] is considered to play a general role in a broader light spectrum for visual functions, ranging from the ability of rods to generate reproducible electrical responses to the other to adapt themselves to substantial darkness after light exposure [11]. Therefore, Rho phosphorylation has provided an example of the ubiquitous regulatory pattern of specific kinases downregulating the activity of G protein-coupled receptors [12].

Concerning timing of the Rho phosphorylation after light exposure, according to the biochemical analysis with mass spectrometry, the phosphorylation reaction is started more quickly to accommodate itself to various light conditions by the quick treatment of resected mouse retinas [13]. However, it has not been directly visualized by routine immunohistochemistry of conventionally prepared tissues [14]. Several specific antibodies against major phosphorylated rhodopsin (P-Rho) molecules were produced and well characterized by immunological analyses [15]. In the present chapter, we demonstrate application of IVCT to immunohistochemical procedure for examining time-dependent molecular changes of Rho to P-Rho under various light-illumination conditions in living mouse retinas, as depicted in Fig. 35.1a. Precise methods and results have been reported in the previous paper [16].

35.3 IVCT of Mouse Eyeballs Under Various Illumination Conditions

IVCT was performed against left eyeballs of mice under deep chloroform anesthesia, which were kept under different illumination conditions (Fig. 35.1b). To treat the eyeballs more easily than those in the previous cornea experiment with IVCT [17–19], palpebral skins were slightly cut around them. The eyeballs were then immediately frozen in vivo by pouring liquid isopentane–propane cryogen (−193 °C), which was cooled in liquid nitrogen just before pouring [1, 17–19]. For complete darkness, after the 12-h dark adaptation, the IVCT was performed under infrared light by directly

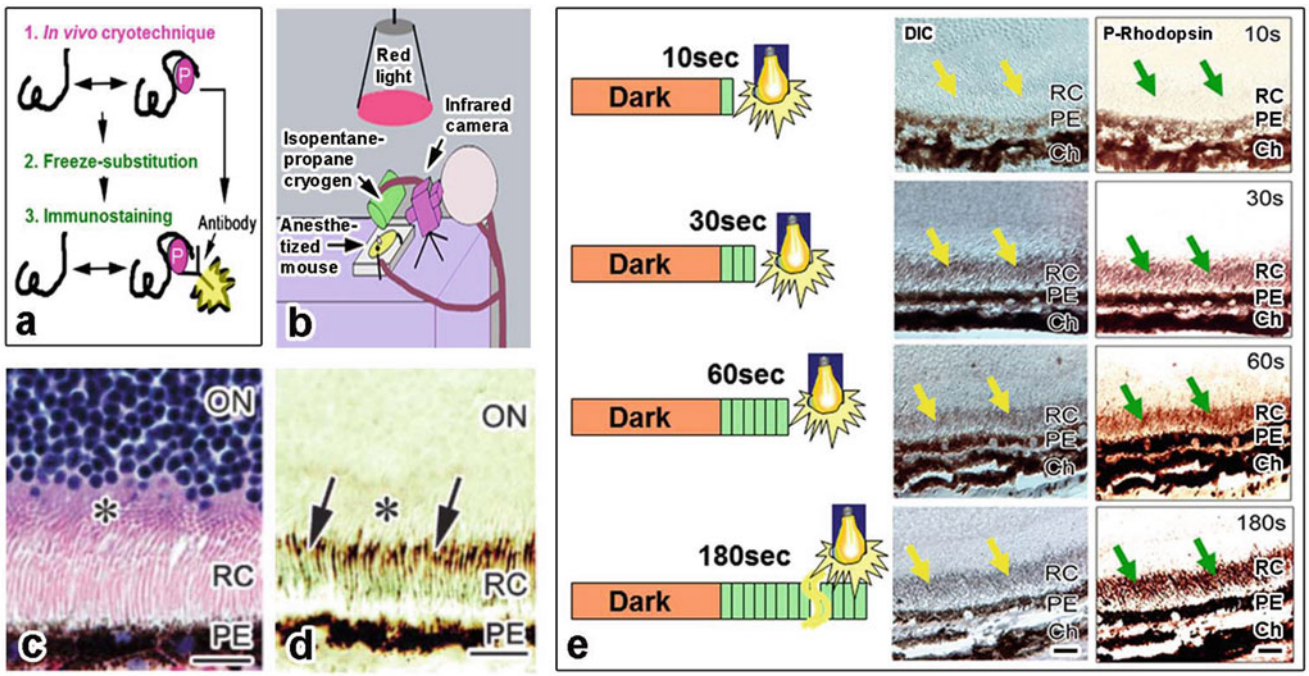

Fig. 35.1 (**a**) Flow chart of procedure with IVCT and FS for immunohistochemical detection of phosphorylated protein. Dynamically changing molecule under phosphorylation is immediately immobilized with IVCT. (**b**) Schematic representation of IVCT for eyeballs of living mouse. (**c**, **d**) HE staining (**c**) and immunostaining for phosphorylated rhodopsin (**d**) in mouse retina with IVCT. *ON* outer nuclear layer, *RC* rod and cone photoreceptor cell layer. Rhodopsin is immunostained in outer segment (*arrows* in **c**, **d**) but not in inner segment (*asterisks* in **c**, **d**). (**e**) Schematic representation of protocol (*left lane*) and light micrographs of DIC (*middle lane*) and phosphorylated rhodopsin immunostaining (*right lane*) images of retinas exposed to strong light for 10, 30, 60 and 180 s after the dark adaptation. *Arrows* indicate rod and cone layers (RC). *PE* pigment epithelium, *Ch* choroids. Precise data have been reported in the previous paper (Terada et al. [16]). *Bars* 20 μm

observing the mice with an infrared camera (Fig. 35.1b). For the condition under the safety red light, IVCT was performed under the light shielded by a red-color plate for 2 min after the dark adaptation. To obtain light-illuminated mouse retinas, the dark-adapted eyeballs were continuously illuminated with a flashlight for 10, 30, 60, and 180 s before performing IVCT. They were then immediately frozen in a similar way with the liquid cryogen and maintained in liquid nitrogen at a low temperature. Frozen eyeballs were finally removed with a pair of nippers in the liquid nitrogen and then processed for the next freeze-substitution step.

35.4 Immunoreactivity of P-Rho in IVCT Retina Under Various Illumination Conditions

In the eyeballs prepared with IVCT the eyeballs were always frozen from the scleral outside with the poured cryogen, and so the rod and cone layer was well preserved at a light microscopic level (Fig. 35.1c). Under daylight condition, the rod and cone layer was specifically immunostained with the anti-P-Rho334 antibody (Fig. 35.1d).

P-Rho334 immunoreactivity was completely eliminated after the dark adaptation. In the living animal retina, phototransduction has been thought to proceed in time courses of milliseconds to seconds [7]. Whereas the P-Rho334 immunoreactivity was not detected in the living mouse retina after the 10-s light exposure (Fig. 35.1e), it was definitely recovered in retinas exposed to visible light for 30 s and more (60 and 180 s) (Fig. 35.1e).

35.5 Concluding Remarks

IVCT revealed that ^{334}Ser rhodopsin in retinal tissues of living mice is generally phosphorylated between 10 and 30 s after visible light stimulation.

References

1. Ohno S, Terada N, Fujii Y, Ueda H, Takayama I (1996) Dynamic structure of glomerular capillary loop as revealed by an in vivo cryotechnique. Virchows Arch 427:519–527
2. Ohno N, Terada N, Fujii Y, Baba T, Ohno S (2004) "In vivo cryotechnique" for paradigm shift to "living morphology" of animal organs. Biomed Rev 15:1–19
3. Terada N, Ohno S (2004) Immunohistochemical application of cryotechniques to native morphology of cells and tissues. Acta Histochem Cytochem 37:339–345
4. Ohno N, Terada N, Murata S, Katoh R, Ohno S (2005) Application of cryotechniques with freeze-substitution for the immunohistochemical demonstration of intranuclear pCREB and chromosome territory. J Histochem Cytochem 53:55–62
5. Zea-Aragon Z, Terada N, Ohno N, Fujii Y, Baba T, Ohno S (2004) Effects of anoxia on serum immunoglobulin and albumin leakage through blood–brain barrier in mouse cerebellum as revealed by cryotechniques. J Neurosci Methods 366:15–17
6. Terada N, Ohno N, Li Z, Fujii Y, Baba T, Ohno S (2005) Detection of injected fluorescence-conjugated IgG in living mouse organs using 'in vivo cryotechnique' with freeze-substitution. Microsc Res Tech 66:173–176
7. Menson ST, Han M, Sakmar TP (2001) Rhodopsin: structural basis of molecular physiology. Physiol Rev 81:1659–1688
8. Gibson SK, Parkes JH, Liebman PA (1998) Phosphorylation stabilizes the active conformation of rhodopsin. Biochemistry 37:11393–11398
9. Fain GL, Matthews HR, Cornwall MC, Koutalos Y (2001) Adaptation in vertebrate photoreceptors. Physiol Rev 81:117–151
10. Ohguro H, Rudnicka-Nawrot M, Buczylko J, Zhao X, Taylor JA, Walsh KA, Palczewski K (1996) Structural and enzymatic aspects of rhodopsin phosphorylation. J Biol Chem 271:5215–5224
11. Arshavsky VY (2002) Rhodopsin phosphorylation: from terminating single photon responses to photoreceptor dark adaptation. Trends Neurosci 25:124–126
12. Maeda T, Imanishi Y, Palczewski K (2003) Rhodopsin phosphorylation: 30 years later. Prog Retin Eye Res 22:417–434
13. Kennedy MJ, Lee KA, Niemi GA, Craven KB, Garwin GG, Saari JC, Hurley JB (2001) Multiple phosphorylation of rhodopsin and the in vivo chemistry underlying rod photoreceptor dark adaptation. Neuron 31:87–101
14. Hicks D, Barnstable CJ (1987) Different rhodopsin monoclonal antibodies revealed different binding patterns on developing and adult rat retina. J Histochem Cytochem 35:1317–1328
15. Ohguro H, Ohguro I, Mamiya K, Maeda T, Nakazawa M (2003) Prolonged survival of the phosphorylated form of rhodopsin during dark adaptation of Royal College Surgeons rat. FEBS Lett 551:128–132
16. Terada N, Ohno N, Hiroshi Ohguro H, Zilong Li Z, Shinichi OS (2006) Immunohistochemical detection of phosphorylated rhodopsin in light-exposed retina of living mouse with in vivo cryotechnique. J Histochem Cytochem 54:479–486
17. Chen HB, Yamabayashi S, Ou B, Ohno S, Tsukahara S (1995) Ultrastructural studies on the corneal superficial epithelium of rats by in vivo cryofixation with freeze substitution. Ophthalmic Res 27:286–295
18. Chen HB, Yamabayashi S, Ou B, Tanaka Y, Ohno S, Tsukahara S (1997) Structure and composition of rat precorneal tear film. A study by an in vivo cryofixation. Invest Ophthalmol Vis Sci 38:381–387
19. Chen HB, Yamabayashi S, Ou B, Tanaka Y, Ohno S, Tsukahara S (1998) Histochemical study on rat tear film and ocular surface epithelial cells. Curr Eye Res 17:647–649

Application of "In Vivo Cryotechnique" to Immunohistochemical Detection of Glutamate in Mouse Retina Inner Segment of Photoreceptors

36

Nobuo Terada, Yurika Saitoh, Nobuhiko Ohno, and Shinichi Ohno

Abstract

In vivo cryotechnique (IVCT) followed by freeze substitution (FS) enabled us to analyze the cells and tissues reflecting living states. In this chapter, we present immunolocalization of glutamate (Glu) in the inner segment (IS) of photoreceptors in the mouse retina with IVCT, which was controversial with conventional fixation methods. Eyeballs from anesthetized mice were directly frozen using IVCT and processed for FS fixation in acetone containing chemical fixatives and embedded in paraffin. Deparaffinized sections were immunostained with an anti-Glu antibody. Strong Glu immunoreactivity was obtained in the specimens prepared by FS with a low concentration of glutaraldehyde, whereas no Glu immunoreactivity was obtained without the chemical fixatives. Thus, it became clear that Glu was immunolocalized in the IS, probably reflecting living states.

Keywords

In vivo cryotechnique • Glutamate • Retina • Freeze substitution

36.1 Examination of Distribution of Amino Acid in the Retina with In Vivo Cryotechnique (IVCT)

Owing to a technical diffusion artifact and/or antigen masking in paraffin-embedded tissue sections of eyeballs prepared by perfusion fixation and alcohol dehydration, it has been difficult to obtain stable immunoreactivity (IR) of an amino acid, glutamate (Glu) (Fig. 36.1c, d). Bioassay measurement of cultured photoreceptor cells from the guinea pig retina indicated production of Glu in mitochondria in the inner segment (IS) of photoreceptors [1, 2]. Several enzymes for Glu metabolism, including Glu dehydrogenase, phosphate-activated glutaminase, aspartate aminotransferase, and ornithine aminotransferase, were already reported to have a high level of activity in the IS [3, 4]. With immunohistochemical approaches, in some cases, enucleated eyes of the goldfish [5], cat [6], chicken [7, 8], rat [9], and monkey [10] were fixed by immersion fixation, resulting in positive Glu-IR in the IS. On the other hand, the fact that Glu-IR in the IS was not detected by perfusion fixation [11, 12] caused conclusion that the localization and/or expression of Glu was probably due to postmortem changes induced by ischemia. Glu-IR has been reported to be artificially changed by some chemical fixation procedures.

To overcome such contradictory results, application of IVCT was assumed to be useful [13]. By using common freeze-substitution (FS) fixation for specimens with IVCT, immunohistochemical merit of locating soluble serum proteins in living animal tissues was demonstrated [14–17].

N. Terada, M.D., Ph.D. (✉)
Division of Health Sciences, Shinshu University Graduate School of Medicine, 3-1-1 Asahi, Matsumoto City, Nagano 390-8621, Japan

Department of Anatomy and Molecular Histology, Interdisciplinary Graduate School of Medicine and Engineering, University of Yamanashi, 1110 Shimokato, Chuo City, Yamanashi 409-3898, Japan
e-mail: nobuot@shinshu-u.ac.jp

Y. Saitoh • N. Ohno • S. Ohno
Department of Anatomy and Molecular Histology, Interdisciplinary Graduate School of Medicine and Engineering, University of Yamanashi, 1110 Shimokato, Chuo City, Yamanashi 409-3898, Japan

S. Ohno et al. (eds.), *In Vivo Cryotechnique in Biomedical Research and Application for Bioimaging of Living Animal Organs*, DOI 10.1007/978-4-431-55723-4_36

Moreover, IVCT also enabled us to visualize rapid changes within seconds in living animal bodies, such as molecular conformation of rhodopsin phosphorylation in the living mouse retina [18]. In this chapter, we focused on the Glu immunolocalization in the IS of eyeballs prepared with IVCT-FS. Precise methods and results have been reported in the previous paper [19].

36.2 Immunolocalization of Glu in Retinas with IVCT

Under anesthesia, IVCT was performed on the left eyeballs with natural light coming through windows, by pouring liquid isopentane-propane cryogen (−193 °C) cooled in liquid nitrogen. Morphology for the eyeball tissues with IVCT-FS was evaluated by HE staining and differential interference contrast images (Fig. 36.1a), and the rod and cone photoreceptors were observed as well-preserved areas without obvious ice crystals at the light microscopic level.

The Glu-IR was obtained in thin sections of the eyeball specimens with IVCT followed by FS. The Glu was immunolocalized in the IS, outer and inner plexiform layers, and ganglion cell layer (Fig. 36.1b). The level of Glu has been reported to be highly detected in a subpopulation of amacrine cells and ganglion cells [20, 21]. However, the Glu was dispersively immunolocalized in the inner and outer plexiform layers and ganglion cell layer in the tissues with IVCT-FS. This was probably due to the distance from the initial frozen surface causing larger ice crystal formation. When photoreceptor cell layers were obliquely sectioned, Glu-IR was observed as tiny dot patterns, indicating that the Glu immunostaining was inside the photoreceptor cells. From these results, Glu was assumed to localize in the IS.

36.3 Effect of Glutaraldehyde During FS

Without glutaraldehyde, Glu-IR was not obtained (Fig. 36.1f). To examine whether bovine serum albumin (BSA) is effective as a carrier or blocking protein for the following primary antibody reaction, sections were treated with fish gelatin, which was expected to effectively inhibit nonspecific binding of the antibodies, before the primary anti-Glu antibody incubation. In sections of the specimen prepared with IVCT followed by FS without chemical fixatives, Glu-IR was not obtained with the fish gelatin pretreatment. In contrast, the Glu-IR was clearly detected with the fish gelatin pretreatment in sections of the specimen prepared with IVCT followed by FS with glutaraldehyde. Thus, BSA is probably effective as a blocking reagent, and it became clear that the paraffin sections of the retinal specimens with

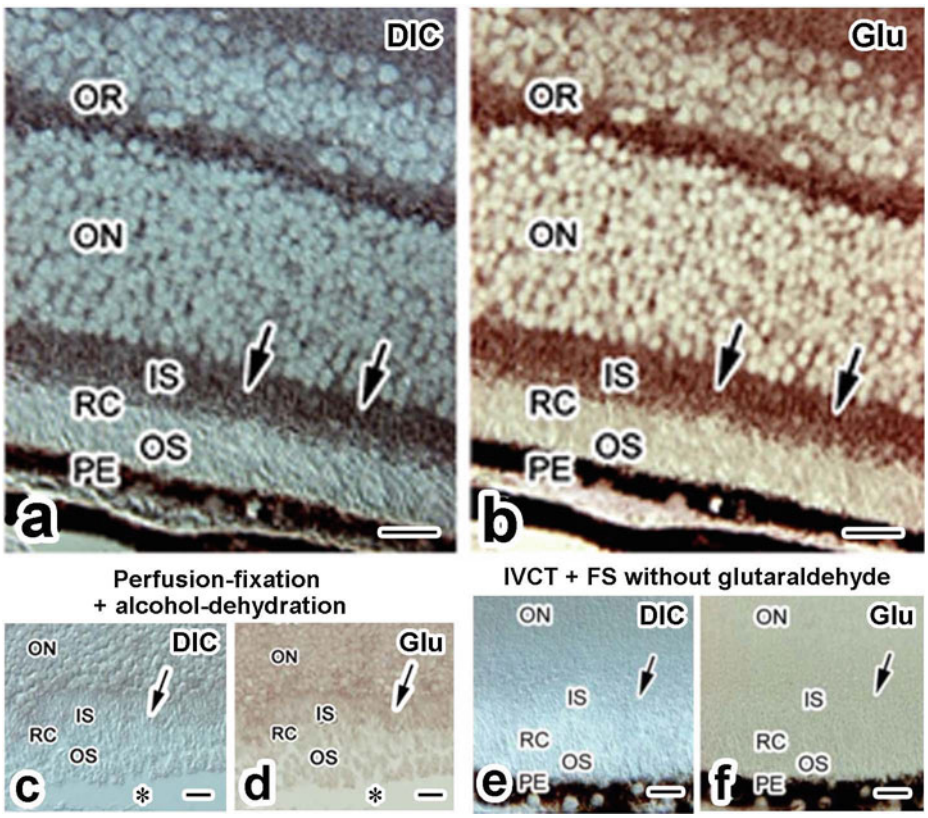

Fig. 36.1 (**a**–**f**) Differential interference contrast (DIC; **a**, **c**, **e**) and the glutamate immunostaining (Glu; **b**, **d**, **f**) images of the eyeball tissue sections with IVCT followed by FS with (**a**, **b**) or without (**e**, **f**) glutaraldehyde or with perfusion fixation followed by alcohol dehydration (**c**, **d**). Note that pigment epithelial layer (*PE*) is detached (*asteriskes* in **c**, **d**) and little immunostaining of glutamete (*arrow* in **d**). *OR* outer plexiform layer, *ON* outer nuclear layer, *RC* photoreceptor cell layer, *IS* and *OS* inner and outer segments of RC. Precise data have been reported in the previous paper (Terada et al. [19]). *Bars*, 50 μm

IVCT-FS retained many Glu molecules, which can be more clearly immunostained by the anti-Glu antibody.

It is difficult to confirm how much Glu in tissues was lost during the FS step with chemical fixatives such as paraformaldehyde and glutaraldehyde. We assume that the immunolocalization with IVCT-FS reflects the original distribution. If the diffusion artifact of Glu had strongly appeared, Glu immunolocalization would have been distributed in much wider areas, such as the outer segment of photoreceptors. The intensity of the IR was changed with different concentrations of glutaraldehyde. This may be due to alteration of cross-linked tissue structures hindering some Glu reactivity against BSA and/or antibodies in the paraffin sections.

36.4 Concluding Remarks

With IVCT-FS, the IS of photoreceptors was clearly immunopositive for Glu. Glu-IR obtained in some restricted areas in retinal tissue samples with IVCT probably reflects the normal in vivo metabolic conditions of the IS without anoxia or ischemia.

References

1. Poitry-Yamate CL, Poitry S, Tsacopoulos M (1995) Lactate released by Müller glial cells is metabolized by photoreceptors from mammalian retina. J Neurosci 15:5179–5191
2. Tsacopoulos M, Poitry-Yamate CL, MacLeish PR, Poitry S (1998) Trafficking of molecules and metabolic signals in the retina. Prog Retin Eye Res 17:429–442
3. Ross CD, Godfrey DA (1997) Distribution of activities of aspartate aminotransferase isoenzymes and malate dehydrogenase in guinea pig retinal layers. J Histochem Cytochem 35:669–674
4. Endo S, Ishiguro S, Tamai M (1999) Possible mechanism for the decrease of mitochondrial aspartate aminotransferase activity in ischemic and hypoxic rat retinas. Biochim Biophys Acta 1450:385–396
5. Marc RE, Liu WLS, Kalloniatis M, Raiguel SF, Van Haesendonck E (1990) Patterns of glutamate immunoreactivity in the goldfish retina. J Neurosci 10:4006–4034
6. Pourcho RG, Owczarzak MT (1991) Connectivity of glycine immunoreactive amacrine cells in the cat retina. J Comp Neurol 307:549–561
7. Kalloniatis M, Fletcher EL (1993) Immunocytochemical localization of the amino acid neurotransmitters in the chicken retina. J Comp Neurol 336:174–193
8. Sun H, Crossland WJ (2000) Quantitative assessment of localization and colocalization of glutamate, aspartate, glycine, and GABA immunoreactivity in the chick retina. Anat Rec 260:158–179
9. Fletcher EL, Kalloniatis K (1996) Neurochemical architecture of the normal and degenerating rat retina. J Comp Neurol 376:343–360
10. Kalloniatis M, Marc RE, Murry RF (1996) Amino acid signatures in the primate retina. J Neurosci 16:6807–6829
11. Sasoh M, Ma N, Yoshida S, Semba R, Uji Y (1998) Immunocytochemical localization of glutamate in normal and detached cat retina. Invest Ophthalmol Vis Sci 39:786–792
12. Sasoh M, Ma N, Ito Y, Esaki K, Uji Y (2006) Changes in localization of amino acids in the detached cat retina. Ophthalmic Res 38:74–82
13. Ohno S, Terada N, Fujii Y, Ueda H, Takayama I (1996) Dynamic structure of glomerular capillary loop as revealed by an in vivo cryotechnique. Virchow's Arch 427:519–527
14. Zea-Aragon Z, Terada N, Ohno N, Fujii Y, Baba T, Ohno S (2004) Effects of anoxia on serum immunoglobulin and albumin leakage through blood–brain barrier in mouse cerebellum as revealed by cryotechniques. J Neurosci Methods 138:89–95
15. Ohno N, Terada N, Ohno S (2006) Histochemical analyses of living mouse liver under different hemodynamic conditions by "in vivo cryotechnique". Histochem Cell Biol 126:389–398
16. Zhou H, Ohno N, Terada N, Saitoh S, Fujii Y, Ohno S (2007) Involvement of follicular basement membrane and vascular endothelium in blood-follicle barrier formation of mice revealed by "in vivo cryotechnique". Reproduction 134:307–317
17. Saitoh S, Terada N, Ohno N, Ohno S (2008) Distribution of immunoglobulin-producing cells in immunized mouse spleens revealed with "in vivo cryotechnique". J Immunol Methods 331:114–126
18. Terada N, Ohno N, Ohguro H, Li Z, Ohno S (2006) Immunohistochemical detection of phosphorylated rhodopsin in light-exposed retina of living mouse with in vivo cryotechnique. J Histochem Cytochem 54:479–486
19. Terada N, Ohno N, Saitoh S, Saitoh Y, Ohno S (2009) Immunoreactivity of glutamate in mouse retina inner segment of photoreceptors with in vivo cryotechnique. J Histochem Cytochem 57:883–888
20. Sun D, Vingrys AJ, Kalloniatis M (2007) Metabolic and functional profiling of the normal rat retina. J Comp Neurol 505:92–113
21. Sun D, Vingrys AJ, Kalloniatis M (2007) Metabolic and functional profiling of the ischemic/reperfused rat retina. J Comp Neurol 505:114–130

37 Application of "In Vivo Cryotechnique" to Immunohistochemical Study of Mouse Sciatic Nerves Under Various Stretching Conditions

Akio Kamijo, Yurika Saitoh, Nobuhiko Ohno, Shinichi Ohno, and Nobuo Terada

Abstract

In this chapter, we present dynamic structures of peripheral nerve fibers under various stretching conditions and distribution of soluble serum proteins with "in vivo cryotechnique" (IVCT). The structures of IVCT-prepared fibers under the stretched condition showed a beaded appearance. By immunostaining for a membrane skeletal protein 4.1G, Schmidt-Lanterman incisures (SLIs) were clearly identified, and the heights of their circular truncated cones were increased at narrow sites of the fibers under the stretched condition. Albumin was immunolocalized in blood vessels and the endoneurium including near the node of Ranvier. Thus, IVCT revealed structures and accurate immunolocalization of serum albumin in the sciatic nerve fibers, reflecting living states.

Keywords

Schmidt-Lanterman incisures • Albumin • Peripheral nervous system • Membrane skeleton

37.1 Septate Junctions and Schmidt-Lanterman Incisures (SLIs) in the Peripheral Nervous System (PNS)

In paranodes of myelinated nerve fibers in the PNS, septate junctions between axons and glial processes were reported to be comprised of three major adherent molecular components, contactin-associated protein (Caspr) and contactin at the axonal side as well as neurofascin (NF)-155 at the glial side [1]. These septate junctions have been well documented to have a role in preventing functional diffusion of small molecules and ions into juxtaparanodes [2, 3].

The SLIs are well known to be funnel-shaped interruptions within the myelin sheaths of nerve fibers in the PNS. Various adhesion molecules have already been reported to be localized at SLIs in order to keep their structure. Therefore, considering the fact that SLIs have been demonstrated to translocate along axon fibers [4], they might dynamically change their structures in vivo.

A. Kamijo
Division of Health Sciences, Shinshu University Graduate School of Medicine, 3-1-1 Asahi, Matsumoto City, Nagano 390-8621, Japan

Y. Saitoh • N. Ohno • S. Ohno
Department of Anatomy and Molecular Histology, Interdisciplinary Graduate School of Medicine and Engineering, University of Yamanashi, 1110 Shimokato, Chuo City, Yamanashi 409-3898, Japan

N. Terada, M.D., Ph.D. (✉)
Division of Health Sciences, Shinshu University Graduate School of Medicine, 3-1-1 Asahi, Matsumoto City, Nagano 390-8621, Japan

Department of Anatomy and Molecular Histology, Interdisciplinary Graduate School of Medicine and Engineering, University of Yamanashi, 1110 Shimokato, Chuo City, Yamanashi 409-3898, Japan
e-mail: nobuot@shinshu-u.ac.jp

S. Ohno et al. (eds.), *In Vivo Cryotechnique in Biomedical Research and Application for Bioimaging of Living Animal Organs*, DOI 10.1007/978-4-431-55723-4_37

37.2 In Vivo Cryotechnique (IVCT) to Visualize Functions of SLIs and Septate Junctions

We aimed to capture the dynamic structures of nerve fibers under various stretching conditions and to keep soluble serum proteins in their tissue sections. However, with conventional preparation methods such as perfusion or immersion fixation, it has been difficult to directly capture such dynamic morphofunctional findings of nerve fibers under various stretching conditions, reflecting their living states. In addition, for immunohistochemical analyses, distribution of soluble serum components in living animal tissues is modified by the loss of blood circulation induced by tissue resection and artificial perfusion fixation pressures [5, 6].

To avoid such technical artifacts and reveal the dynamic characteristics of living animal organs in tissue sections, IVCT was previously developed [7]. It can directly cryofix living animal organs under normal circulation conditions and keep soluble components which are easily lost by the conventional fixation methods [8–10]. In particular, dynamic changes of living animal organs can be easily captured, such as mouse functioning lungs under various respiration conditions [11, 12]. Fixation by IVCT can prevent axon shrinkage so that the fine structure of the nerves could be examined [13]. In this chapter, we present applications of IVCT to living mouse sciatic nerves under various stretching conditions to examine their morphological changes and immunolocalizations of serum proteins (Fig. 37.1a). Precise materials and methods have been reported in the previous paper [14].

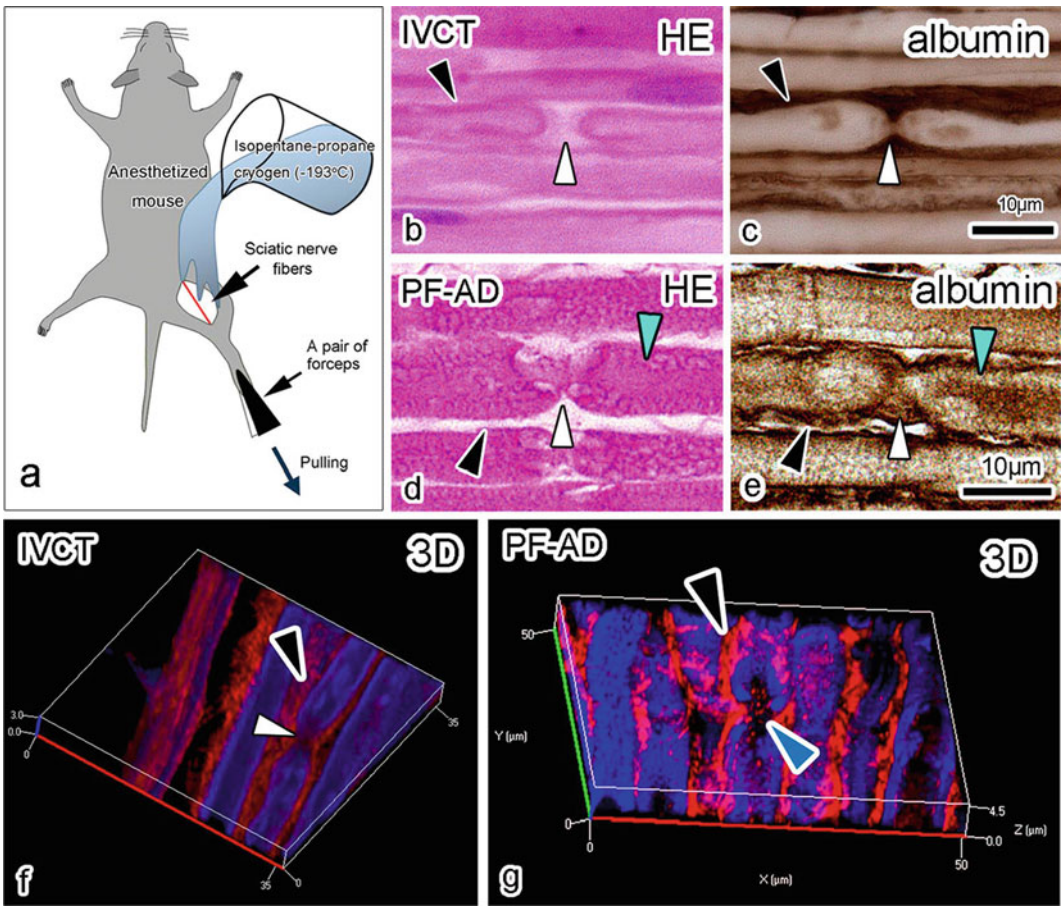

Fig. 37.1 (**a**) A schematic drawing of "in vivo cryotechnique" (IVCT) for living mouse sciatic nerves under various stretching conditions. A sciatic nerve of an anesthetized mouse is exposed, and its thigh is manually stretched. Liquid isopentane-propane cryogen (−193 °C) precooled in liquid nitrogen is then directly poured over the sciatic nerve. (**b**–**g**) Light microscopic (**b**–**e**) and confocal laser scanning microscopic (**f**, **g**) images of mouse sciatic nerves with IVCT (**b**, **c**, **f**) or perfusion fixation and alcohol dehydration method (PF-AD; **d**, **e**, **g**), stained with HE (**b**, **d**) or immunostained for albumin (**c**, **e**). By reconstruction of the optical sections, optimal three-dimensional images are obtained (3D; **f**, **g**). *Blue*, nerve shapes with autofluorescence under UV; *Red*, albumin immunolocalization. With IVCT, albumin is immunolocalized in blood vessels and the endoneurium (*black arrowheads* in **c**, **f**). In the node of Ranvier (*white arrowheads* in **c**, **f**), it is not immunolocalized inside the axon. With PF-AD, the albumin immunolocalization is observed heterogeneously in the endoneurium (*black arrowheads* in e, g) and inside the axons of some nerve fibers (*blue arrowheads* in e, g). Precise data are reported in the previous paper (Kamijo et al. [14])

37.3 Immunolocalization of Albumin in Sciatic Nerve Fibers with IVCT

IVCT and freeze-substitution fixation (FS) have the immunohistochemical merit of keeping soluble proteins of living animal organs in paraffin-embedded tissue sections [5, 9]. The serum albumin distribution in sciatic nerve fibers and the structures of nerve fibers could be examined by immunohistochemistry (Fig. 37.1b, c), and the three-dimensional (3D) image of the albumin immunolocalizations was demonstrated by confocal laser scanning microscopy (CLSM) (Fig. 37.1f). Using autofluorescence signals with ultraviolet (UV) emission, nerve contour shapes were easily demonstrated (blue in Fig. 37.1f). The albumin immunolocalization was recognized with Alexa Fluor 594-conjugated secondary antibody (red in Fig. 37.1f). The albumin was immunolocalized in blood vessels and the endoneurium (black arrowheads in Fig. 37.1c, f). In the node of Ranvier (white arrowheads in Fig. 37.1c, f), it was not immunolocalized inside the axon.

In sciatic nerves with perfusion fixation and alcohol dehydration (PF-AD), albumin was heterogeneously immunolocalized in the endoneurium (black arrowheads in Fig. 37.1d, e, g) and also inside the axons of some nerve fibers (blue arrowheads in Fig. 37.1 d, e, g).

37.4 Structures of SLIs in Stretched and Non-stretched Sciatic Nerves with IVCT

The structures of nerve fibers under the non-stretched condition by HE staining were mostly cylindrical (Fig. 37.2a). A membrane skeletal protein, 4.1G, was immunolocalized in paranodes and SLIs (black arrows in Fig. 37.2b) [15].

When the sciatic nerves were stretched by mechanical forces (Fig. 37.1a), they showed a beaded appearance (Fig. 37.2c, d). 3D images were also obtained with CLSM (Fig. 37.2h). Contour shapes of nerve fibers were demonstrated by autofluorescence signals with UV excitation (blue in Fig. 37.2h). The SLIs were recognized by the 4.1G immunolocalization with Alexa Fluor 594-conjugated secondary antibody (red in Fig. 37.2h). The SLIs were found to change their structures according to the beaded appearance under the stretched condition. Many SLIs were localized at narrow sites and transitional regions from narrow to wide areas of the beaded appearance. These findings indicate that the SLIs probably serve as a bumper structure against mechanical forces during the stretching period, because the nerve fibers in the PNS are always responding to extension or flexion of joints.

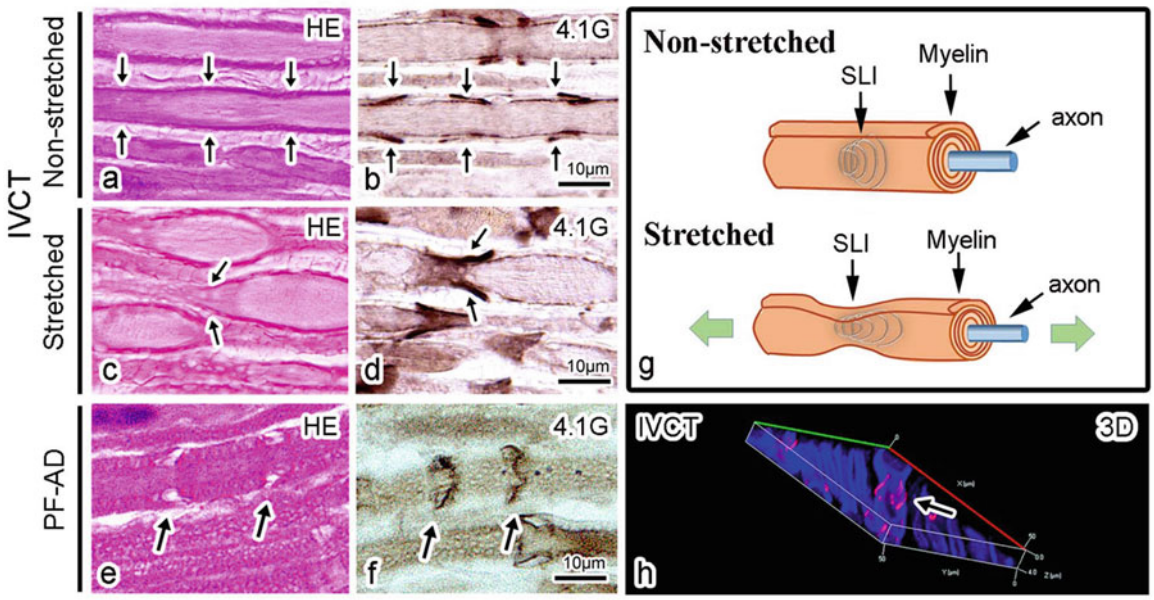

Fig. 37.2 Light microscopic (**a**–**f**) and confocal laser scanning microscopic (CLSM) (**h**) images of mouse sciatic nerves under non-stretched condition (**a**, **b**) and stretched condition (**c**, **d**, **h**) with IVCT or PF-AD (**e**, **f**), stained with HE (**a**, **c**, **e**) or immunostained for a membrane skeletal protein, 4.1G (**b**, **d**, **f**). Under the non-stretched condition, in cylindrical nerve fibers (**a**), 4.1G is immunolocalized in Schmidt-Lanterman incisures (SLIs: *black arrows* in **b**). Under the stretched condition, structures of nerve fibers show a beaded appearance (**c**). 4.1G-immunostained SLIs are observed in narrow areas and transitional regions from narrow to wide areas of the beaded nerve fibers (*black arrows* in **d**, **h**). By reconstruction of the optical sections with CLSM, three-dimensional image is obtained (3D; **h**). Images in (**g**) depict morphological changes of a nerve fiber including SLIs under non-stretched and stretched conditions. By PF-AD, structures of SLIs are disrupted (*black arrows* in **e**, **f**). Precise data are reported in the previous paper (Kamijo et al. [14])

With PF-AD, the thighs of mice showed twitching during the perfusion fixation, and it was difficult to prepare the whole length of the sciatic nerve fibers. Structures of some SLIs with PF-AD were disrupted (black arrows in Fig. 37.2f), as compared with those under the non-stretched condition with IVCT (Fig. 37.2a, b).

37.5 Concluding Remarks

The IVCT is a useful tool to accurately clarify the dynamic structures of functioning nerve fibers and immunolocalizations of serum albumin, reflecting their living states.

References

1. Buttermore ED, Thaxton CL, Bhat MA (2013) Organization and maintenance of molecular domains in myelinated axons. J Neurosci Res 91:603–622
2. Scherer SS, Arroyo EJ (2002) Recent progress on the molecular organization of myelinated axons. J Peripher Nerv Syst 7:1–12
3. Buttermore ED, Dupree JL, Cheng JG, An X, Tessarollo L, Bhat MA (2011) The cytoskeletal adaptor protein band 4.1B is required for the maintenance of paranodal axo-glial septate junctions in myelinated axons. J Neurosci 31:8013–8024
4. Hall SM, Williams PL (1970) Studies on the "incisures" of Schmidt and Lanterman. J Cell Sci 6:767–791
5. Shi L, Terada N, Saitoh Y, Saitoh S, Ohno S (2011) Immunohistochemical distribution of serum proteins in living mouse heart with in vivo cryotechnique. Acta Histochem Cytochem 44:61–72
6. Bai Y, Wu B, Terada N, Saitoh Y, Ohno N, Saitoh S, Ohno S (2012) Immunohistochemical analysis of various serum proteins in living mouse thymus with "in vivo cryotechnique". Med Mol Morphol 45:129–139
7. Ohno S, Terada N, Ohno N, Saitoh S, Saitoh Y, Fujii Y (2010) Significance of 'in vivo cryotechnique' for morphofunctional analyses of living animal organs. J Electron Microsc (Tokyo) 59:395–408
8. Saitoh Y, Terada N, Saitoh S, Ohno N, Fujii Y, Ohno S (2010) Histochemical approach of cryobiopsy for glycogen distribution in living mouse livers under fasting and local circulation loss conditions. Histochem Cell Biol 133:229–239
9. Chen J, Terada N, Saitoh Y, Huang Z, Ohno N, Ohno S (2013) Detection of MAPK signal transduction proteins in an ischemia/reperfusion model of mouse intestine using in vivo cryotechnique. Histochem Cell Biol 140:491–505
10. Terada N, Saitoh Y, Ohno N, Komada M, Yamauchi J, Ohno S (2013) Involvement of Src in the membrane skeletal complex, MPP6-4.1G, in Schmidt-Lanterman incisures of mouse myelinated nerve fibers in PNS. Histochem Cell Biol 140:213–222
11. Saitoh Y, Terada N, Saitoh S, Ohno N, Jin T, Ohno S (2012) Histochemical analyses and quantum dot imaging of microvascular blood flow with pulmonary edema in living mouse lungs by "in vivo cryotechnique". Histochem Cell Biol 137:137–151
12. Saitoh Y, Terada N, Ohno N, Hamano A, Okumura N, Jin T, Saiki I, Ohno S (2014) Imaging of thrombosis and microcirculation in mouse lungs of initial melanoma metastasis with in vivo cryotechnique. Microvasc Res 91:73–83
13. Kanazawa Y, Takahashi-Fujigasaki J, Ishizawa S, Takabayashi N, Ishibashi K, Matoba K, Kawanami D, Yokota T, Tajima N, Utsunomiya K (2013) The Rho-kinase inhibitor fasudil restores normal motor nerve conduction velocity in diabetic rats by assuring the proper localization of adhesion-related molecules in myelinating Schwann cells. Exp Neurol 247:438–446
14. Kamijo A, Saitoh Y, Ohno N, Ohno S, Terada N (2014) Immunohistochemical study of mouse sciatic nerves under various stretching conditions with "in vivo cryotechnique". J Neurosci Methods 227:181–188
15. Ohno N, Terada N, Yamakawa H, Komada M, Ohara O, Trapp BD, Ohno S (2006) Expression of protein 4.1G in Schwann cells of the peripheral nervous system. J Neurosci Res 84:568–577

Part III
Further Preparation After 'IVCT'

Freeze-Substitution (FS) Fixation Method

38

Shinichi Ohno

Abstract

Freeze-substitution (FS) is to replace ice crystals with organic solvent containing fixatives and finally embed frozen tissue samples in synthetic resin or paraffin, showing morphology of cells and tissues at the time of freezing. This FS fixation usually leaves frozen tissues in the organic solvent with fixatives maintained below the freezing point. Therefore, cell and tissue structures in vivo can be well preserved to show their natural images. In the quick-freezing of fresh resected tissues, it is another problem that only the organization of outer tissue layers is captured under well-freezing conditions. So, we can distinguish the deeper tissue parts which are poorly kept at a slow speed of freezing condition. Moreover, the water contents in cells and tissues at well-frozen sites are stored to be as tiny amorphous ice, which usually facilitates the penetration of antibodies or probes for immunostaining or labeling. The IVCT or cryobiopsy with FS fixation also keeps soluble proteins in living animal organs for immunostaining. As described above, FS fixation method can maximize benefits of cryotechniques, which can usually maintain all the material components in the amorphous ice. The FS solution is usually organic acetone solvent, which contains paraformaldehyde for light microscopy. For paraffin-embedded sections, they are routinely embedded in paraffin wax after washing the freeze-substituted samples in pure acetone and xylene. In addition, it is possible to prepare serial HE-stained sections for comparison with immunoperoxidase or immunofluorescence staining. For light microscopic immunohistochemistry, immunoreactivities are often increased by tiny ice crystal formation in organ tissues, because of better penetration of antibodies.

Keywords

Freeze-substitution • Tiny ice crystal • Organic solvent • Immunohistochemistry

38.1 Principle and Advantage of FS

The FS is the common method of replacing ice crystals with the organic solvent containing fixatives and embedding the frozen tissue samples in synthetic resin or paraffin, showing functional morphology of cells and tissues at the time of freezing (Fig. 38.1b, e). This FS fixation usually leaves the frozen animal organ tissues, containing a lot of body liquid in vivo, in the organic solvent with fixatives maintained below the freezing point, because of the physical mechanism in which ice crystals can melt in the organic solvent during the incubation time. They are then kept in the native state which contained all the substances within the amorphous ice and are simultaneously bridged by the chemical reactions of fixatives during the time of FS. For the common immunostaining of tissue specimens, paraformaldehyde or glutaraldehyde is usually added to this organic acetone

S. Ohno, M.D., Ph.D. (✉)
Department of Anatomy and Molecular Histology,
Interdisciplinary Graduate School of Medicine and Engineering,
University of Yamanashi, 1110 Shimokato, Chuo City,
Yamanashi 409-3898, Japan
e-mail: sohno@yamanashi.ac.jp

S. Ohno et al. (eds.), *In Vivo Cryotechnique in Biomedical Research and Application for Bioimaging of Living Animal Organs*, DOI 10.1007/978-4-431-55723-4_38

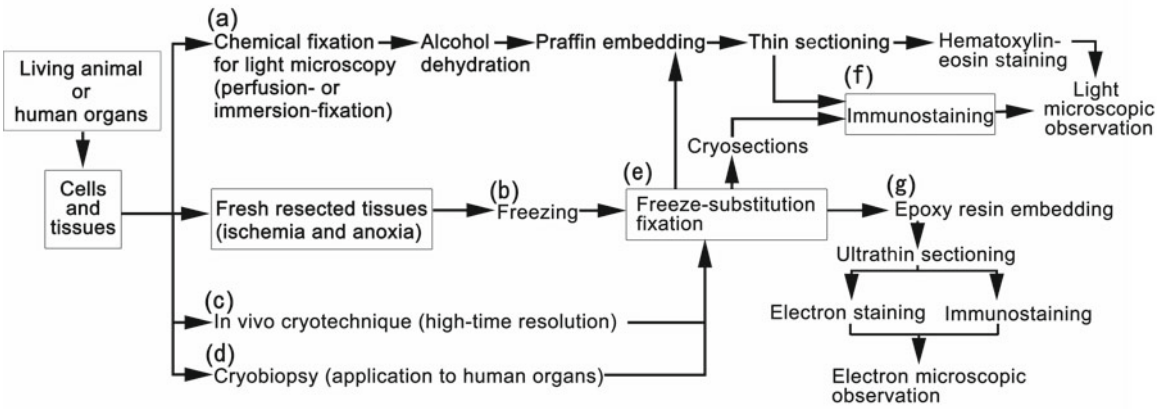

Fig. 38.1 A flow chart showing a series of conventional preparation procedures (**a**), freezing (**b**), in vivo cryotechnique (**c**), and cryobiopsy (**d**), followed by freeze-substitution (**e**) and immunostaining (**f**) or immunoelectron microscopy (**g**) for light or electron microscopic observation

solvent. By this FS method, the cell and tissue structures in vivo at the time of freezing point can be well preserved to show their natural images (Fig. 38.1b–d) and also compared with the conventional morphology with artificial modifications, which is always obtained by the routine chemical fixation at room temperature (Fig. 38.1a).

In the case of the common quick-freezing of fresh resected tissues (Fig. 38.1b), it is another inevitable problem that only the organization of outer tissue layers is captured under well-freezing conditions. This is because ice crystals of the animal organ tissue are easily formed at the time of a low-speed freezing. Therefore, with the HE-stained tissues of paraffin sections, we should carefully distinguish the deep tissue parts which are poorly kept at a slow speed of freezing condition. In such tissue areas, ice crystal sizes are gradually increasing from good areas of the directly contact tissue layer under well-freezing conditions to badly frozen tissue areas. The nucleoplasm of actively replicated cells with a little chromatin condensation in particular appears to easily produce lots of ice crystals in comparison with their cytoplasm. Moreover, it is believed that the water contents in cells and tissues at well-frozen sites are stored to be physically fixed as tiny amorphous ice, then keeping the intermolecular gaps. This usually facilitates the penetration of antibodies or probes at the time of immunostaining or labeling (Fig. 38.2b). When an organic acetone solvent is used as freeze-substitution liquid, we should consider another factor which improves the antibody or probe penetration because of lipid extraction of intracellular membranous systems (Fig. 38.2), including cell membranes or nuclear double membranes. On the other hand, quick extraction and movement of soluble proteins always occur by the quick-freezing technique of fresh excised tissues, because of anoxia and ischemia (Fig. 38.1b). To the contrary, the IVCT or cryobiopsy with FS fixation method always keeps soluble proteins in cells and

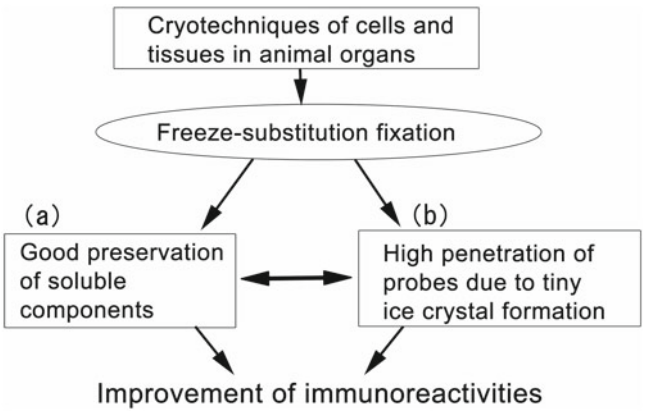

Fig. 38.2 Some technical merits of the application of cryotechniques and the following freeze-substitution fixation for immunostaining, such as molecular preservation (**a**) and penetration of probes (**b**)

tissues of living animal organs for immunostaining (Figs. 38.1c, d and 38.2). As described above, the FS fixation method can maximize the benefits of various cryotechniques, which can usually maintain all the material components in the amorphous ice (Figs. 38.1 and 38.2).

38.2 Practical FS Procedures

As stated above, the FS fixation is very useful as a fixation procedure of living animal tissue samples. The FS solution is usually the organic acetone solvent, which contains paraformaldehyde at a concentration of 2 % for light microscopy. The chemical paraformaldehyde powder is first diluted at a concentration of 20 % in water, which is added with the common molecular sieve to completely remove residual water contents. Although solid osmium tetroxide crystals are directly dissolved in acetone for the conventional morphology

by electron microscopy, both glutaraldehyde and paraformaldehyde are usually diluted in acetone to be used for immunostaining at a light microscopic level after the preparation of solution with their higher concentrations. The stored frozen tissue samples are taken out of the liquid nitrogen (−196 °C) into the FS solution in a container with about 5 ml capacity cooled with dry ice acetone (about −80 °C). Then, it can be sealed at the temperature of dry ice acetone. Before moving the frozen samples into the FS solution, we should loosen the lid of the container lightly, which can be then dipped into liquid nitrogen. Although the liquid nitrogen boils at first, while being subsided soon, the FS solution in the container begins to freeze from the portion in contact with its wall. Then, the container lid is opened, and the frozen tissue samples are transferred into the container. Finally, the container lid is tightly closed again, and all of them are returned into the dry ice acetone at about −80 °C. The usual time required for the FS fixation is approximately 20–40 h in the dry ice acetone at about −80 °C. The sample container will be gradually returned to room temperature after the FS fixation. After loosening slightly the lid of container first, the tissue samples are kept in a refrigerator (−20 °C) for about 2 h and then transferred into another refrigerator compartment (4 °C). In about 2 h, they are taken out and left at room temperature. The FS-fixed samples are lightly washed with pure acetone three times and embedded in paraffin wax through xylene for light microscopy. On the other hand, they are sometimes embedded in hydrophilic synthetic resin for electron microscopy with immunostaining.

38.3 Embedding of Samples for Immunostaining

In this section, we describe how to prepare the freeze-substituted tissue samples for light microscopic immunostaining. This preparation step has two different procedures, as described below. At first, they are directly immersed in 20–30 % sucrose or glycerin solution, after taking out from the pure washing acetone, as a simple and easy treatment (Fig. 38.1e). Then, they are embedded in the OCT compound for preparing cryosections in a cryostat machine (Fig. 38.1f). In this case, because of thick sections for immunostaining with fluorescence-labeled antibodies, we usually use optical sections by a confocal laser scanning microscope. In this case, a multiple colorful immunostaining is also performed by using a few secondary antibodies with different fluorescence wavelengths. Furthermore, a fluorescence-labeled probe is directly injected into blood vessels in a living animal body, and the IVCT can be instantly performed to get its imaging in cryosections after the FS fixation.

In paraffin-embedded sections (Fig. 38.1a), after washing the freeze-substituted samples in pure acetone and also xylene (Fig. 38.1e), they are routinely embedded in paraffin wax. In this case, the permanent sample preparation is usually possible unlike the frozen cryosections, as described above. In addition, it is always possible to prepare serial HE-stained sections of 4 μm for comparison with immunoperoxidase or immunofluorescence staining with various antibodies (Fig. 38.1f). On the other hand, electron microscopic immunohistochemistry can be also performed (Fig. 38.1g), which is described in a separate chapter.

38.4 Significance of Ice Crystal Formation

As described with a little comment of the previous sections, the inevitable ice crystal formation with the cryotechniques is always a basic problem especially for electron microscopic observation. However, the ice crystal formation is sometimes useful for immunohistochemistry at a light microscopic level [1, 2]. Many tiny ice crystals are usually formed by ice expansion of water volume. For light microscopic immunohistochemistry, immunoreactivities of many antigens are often increased by the ice crystal formation in animal organ tissues, because of better penetration of antibodies or probes (Fig. 38.2b) [1, 2]. We have already reported one application of the cryotechnique to be useful for immunostaining of whole-mount mouse cerebellar organs [3]. By the immunohistochemical study for soluble sphingosine kinase in the mouse cerebellar tissues, its immunolocalization patterns were found to be striped in the cerebellar molecular layer on cryosections. Therefore, by the common quick-freezing of the chemically fixed cerebellum, the whole-mount organ immunostaining was useful for revealing the obvious compartmentation of sphingosine kinase in the mouse cerebellum because of tiny ice crystal formation [3].

Another application of cryotechniques was made for intranuclear immunostaining of soluble signal molecules in the living mouse cerebellum [2]. It has been difficult to detect such intranuclear soluble antigens, because of double nuclear membranes, delicate nucleoskeletons, and compact materials with various proteins and nucleic acids. However, especially by the IVCT followed by the FS fixation, some intranuclear signal molecules, such as pCREB, could be clearly immunostained on conventional paraffin sections without any retrieval treatments [2]. The better immunoreactivity of soluble signal molecules to be obtained was extremely important, because existence of the immunopositive target cells was determined only by their definite immunoreaction products (Fig. 38.2a). If the target cells and tissues were not clearly immunostained by specific antibodies, their biological interpretation would be misunderstood from the viewpoint of in vivo functioning states. The effective ice crystal formation with cryotechniques should be kept in mind for some cases of the immunohistochemical improvement [1–3].

References

1. Terada N, Ohno S (2004) Immunohistochemical application of cryotechniques to native morphology of cells and tissues. Acta Histochem Cytochem 37:339–345
2. Ohno N, Terada N, Murata S, Katoh R, Ohno S (2005) Application of cryotechniques with freeze-substitution for the immunohistochemical demonstration of intranuclear pCREB and chromosome territory. J Histochem Cytochem 53:55–62
3. Terada N, Banno Y, Ohno N, Fujii Y, Murate T, Sarna JR, Hawkes R, Zea Z, Baba T, Ohno S (2004) Compartmentation of the mouse cerebellar cortex by sphingosine kinase. J Comp Neurol 469:119–127

Part IV
Comments on Advantages of 'IVCT'

39 Cryotechniques and Freeze-Substitution for Immunostaining of Intranuclear Antigens and Fluorescence In Situ Hybridization

Nobuhiko Ohno, Nobuo Terada, and Shinichi Ohno

Abstract

Cryofixation and freeze-substitution (CF-FS) have been a technique to obtain better morphological data and immunoreactivity at the light and electron microscopic levels. Benefits of CF-FS have been demonstrated in immunostaining for an intranuclear antigen, phosphorylated cAMP-responsive element binding protein (pCREB), and fluorescence in situ hybridization (FISH), focusing on the chromosome territory. Compared with the conventional dehydration method, the higher immunoreactivity of pCREB was observed without the antigen retrieval treatment on sections prepared with the CF-FS methods. Probe labeling of No.18 chromosome territory in human thyroid tissues could be clearly observed on paraffin sections prepared with CF-FS without the microwave treatment, but not on sections prepared by the routine immersion fixation and dehydration method even with microwave treatment. The CF-FS method would be a useful technique for intranuclear immunostaining and FISH, since it preserves nuclear morphology by preventing shrinkage and achieves better signals.

Keywords

Quick-freezing • Freeze-substitution • Antigen retrieval • FISH • Chromosome territory

39.1 Introduction

In electron microscopic observation, cryofixation and freeze-substitution (CF-FS) have been widely used to reduce ultrastructural and immunohistochemical artifacts. One of the most characteristic features of the CF is prompt molecular and structural immobilization, which is difficult to be achieved by standard chemical fixation. To overcome artificial changes caused by tissue resection and cessation of blood circulation, "in vivo cryotechnique" (IVCT) followed by the freeze-substitution (FS), which is one of the method utilizing CF, has been developed [1]. It was important to clarify characteristics of CF-FS methods in immunohistochemical studies before CF-FS is widely used for studies using light microscopy.

To clarify benefits of CF-FS, the immunoreactivity of an intranuclear antigen, phosphorylated cAMP-responsive element binding protein (pCREB), was examined in C57BL/6 mouse cerebellum [2]. Various cryofixation methods as well as the effect of a routine antigen retrieval treatment, microwave irradiation, were analyzed. In addition, a chromosome territory of surgically resected human thyroid tissues was also examined using FISH along with CF-FS or the conventional chemical fixation method [2].

N. Ohno, M.D., Ph.D. (✉) • S. Ohno
Department of Anatomy and Molecular Histology, Interdisciplinary Graduate School of Medicine and Engineering, University of Yamanashi, 1110 Shimokato, Chuo City, Yamanashi 409-3898, Japan
e-mail: nohno@yamanashi.ac.jp

N. Terada
Division of Health Sciences, Shinshu University Graduate School of Medicine, 3-1-1 Asahi, Matsumoto City, Nagano 390-8621, Japan

Department of Anatomy and Molecular Histology, Interdisciplinary Graduate School of Medicine and Engineering, University of Yamanashi, 1110 Shimokato, Chuo City, Yamanashi 409-3898, Japan

S. Ohno et al. (eds.), *In Vivo Cryotechnique in Biomedical Research and Application for Bioimaging of Living Animal Organs*, DOI 10.1007/978-4-431-55723-4_39

39.2 Immunostaining for pCREB

On paraffin sections of mouse cerebellum prepared by the chemical fixation followed by dehydration, the pCREB immunoreactivity was weak without the microwave treatment [2]. The antigen retrieval treatment, which was microwave irradiation, heterogeneously enhanced the pCREB immunoreactivity (Fig. 39.1). The pCREB immunoreactivity in nuclei was observed in most granule cells, some small neurons in the molecular layer, and some Purkinje cells. On the other hand, the pCREB immunoreactivity was more clearly detected without the microwave treatment on paraffin sections prepared by the three cryotechniques, including (1) "in vivo cryotechnique," (2) quick-freezing (QF) after chemical fixation, and (3) quick-freezing of freshly resected tumors, all followed by FS (Fig. 39.2) [2]. The immunodistribution of pCREB appeared similar on the sections prepared by CF-FS and the chemical fixation-dehydration with the microwave treatment. However, nuclei in the sections prepared with the chemical fixation-dehydration method appeared shrunken compared to those prepared with CF-FS. Microwave irradiation did not change the pCREB immunoreactivity significantly on sections prepared by QF of fresh tissues (Fig. 39.2). Microwave treatment was not necessary to obtain clear pCREB immunoreactivity on paraffin sections prepared by QF of fresh tissues (Fig. 39.2) and "in vivo cryotechnique" of living cerebellar tissues [2].

Masking and steric hindrance of antigens, presumably caused by the molecular cross-linkage of compact chromatin components, require antigen retrieval treatment to obtain satisfactory immunostaining, particularly when the antigens localize within the nuclear compartment or the specimens are prepared with common aldehyde fixatives [3, 4]. Microwave irradiation and other antigen retrieval techniques have been used, but are not always effective due to incompletely identified factors [5–8]. In addition, achieving full and constant retrieval effects can be difficult even under the same condition [7, 9, 10]. On the other hand, by using the cryotechniques, the pCREB immunoreactivity could be constantly enhanced [2]. Since microwave treatment did not further increase the pCREB immunoreactivity in specimens prepared with CF-FS, a similar mechanism may underlie in the antigenicity enhancement effects of CF and microwave treatment. Loosening the cross-linked proteins and increasing the penetration of antibodies are the possible mechanisms explaining the effect of the microwave antigen retrieval [7]. The immunoreactivity enhancement achieved by CF-FS would be attributable to the better preservation of immunoreactivity as well as exposure of hindered antigenicity. Tiny intracellular ice crystals, not visible at a light microscopic level but large enough to expose some epitopes, could enhance the antigenicity by improving antibody penetration.

39.3 Analysis with FISH for the Chromosome Territory

Compared with the chemical immersion fixation followed by dehydration, morphology of normal thyroid follicles was well preserved in tissue specimens prepared by QF-FS [2]. The free tiny spaces were more prominent in the sections prepared by the conventional fixation followed by dehydration. Preservation of the thyroid morphology was not optimal in the regions with ice crystals on the sections prepared by QF-FS [2]. The distribution of the No.18 chromosome territory in nuclei was not so clear with the immersion fixation followed by dehydration, and the distribution was unclear even when the microwave was irradiated [2]. On the paraffin sections prepared by the QF-FS, the chromosomal territory was clearly observed even without microwave treatment.

Obtaining constant results of good fluorescence labeling with FISH probes is difficult without several pretreatments such as enzymatic digestion and microwave irradiation [11, 12]. The pretreatments should be minimized to avoid tissue damages [13], and the QF-FS method could be used with fewer pretreatments for human specimens. The mechanisms of enhanced FISH signals using CF-FS without several pretreatment steps may include the increased permeability of the FISH probe, as shown in immunostaining for intranuclear antigens [2]. A side benefit of CF-FS includes better preservation of in situ structures compared with the chemical immersion fixation-dehydration method. Therefore, QF-FS could be used to establish new criteria in the field of pathology as a method for the FISH study on paraffin-embedded human specimens with fewer artifacts.

39.4 IVCT for Analyses of Intranuclear Antigens and FISH

Due to anoxia and ischemia, molecular distribution as well as ultrastructures can be changed by stopping blood supply [14–19]. In the conventional immersion/perfusion fixation and the quick-freezing of resected specimens, loss of blood supply is always caused before the completion of fixation. The ischemia/anoxia can cause artificial alterations and would affect the immunoreactivity of various molecules [20, 21]. In situ immobilization and preservation of structures and molecules would be critical to minimize the artifacts and analyze dynamic changes of functional proteins, including signal molecules. In this context, IVCT has been used for the immunohistochemistry of pCREB in the mouse cerebellum

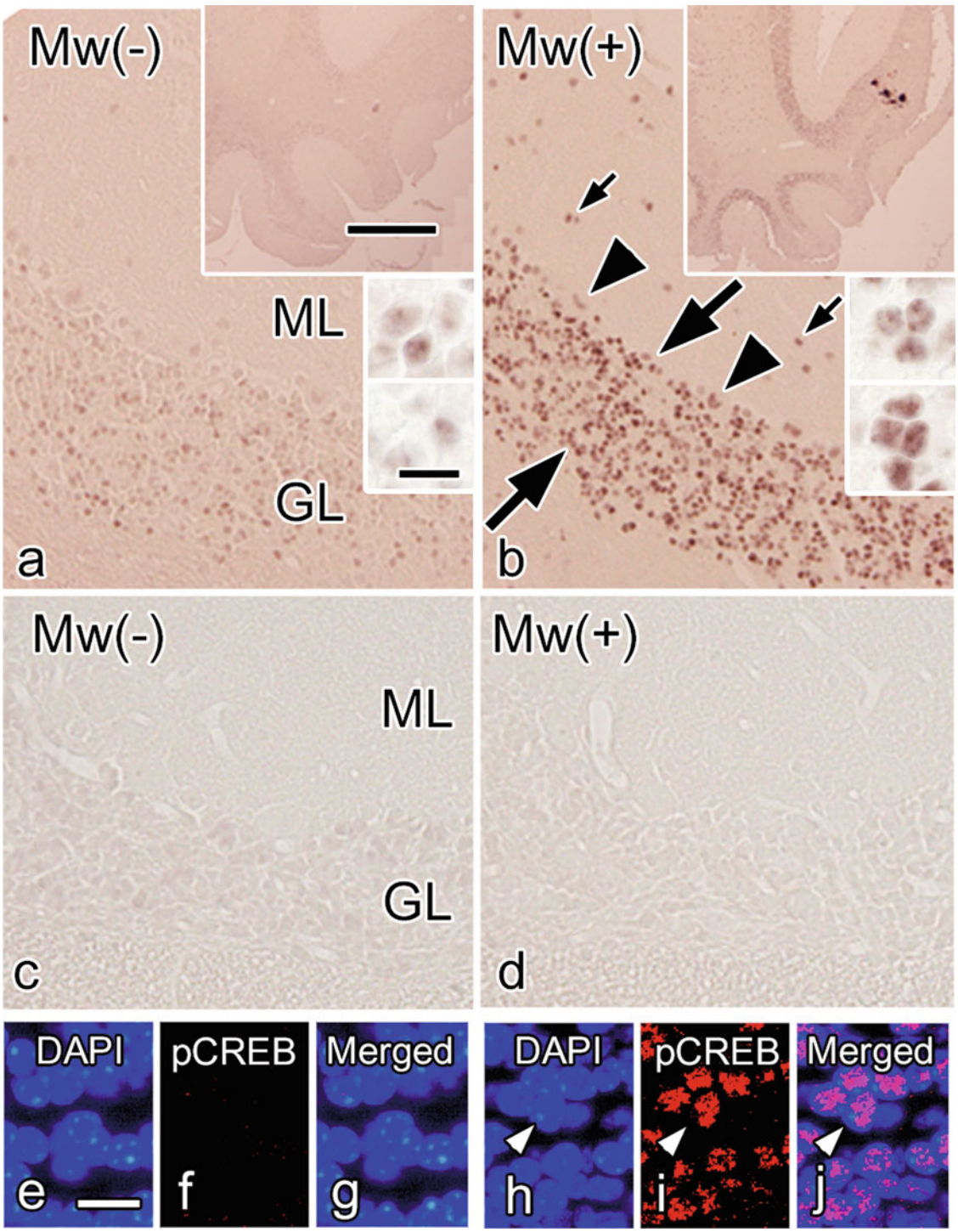

Fig. 39.1 Serial sections of mouse cerebellum prepared with the conventional fixation-dehydration method and embedded in paraffin show pCREB immunoreactivity (**a**–**d**, **f**, **g**, **i**, **j**) and DAPI (**e**, **g**, **h**, **j**) with (**b**, **d**, **h**, **i**, **j**) or without (**a**, **c**, **e**, **f**, **g**) microwave irradiation. Most of the immunostaining for pCREB is detected in nuclei of granule cells (**b**, *large arrows*), some neurons in the molecular layer (**b**, *small arrows*), and Purkinje cells (**b**, *large arrowheads*). The microwave irradiation (**b**, **i**) cannot homogenously enhance the weak immunoreactivity (**a**, **f**). Immunofluorescence intensity of pCREB cannot be detected in the nucleoli, which are brightly stained with DAPI (**i**, **j**, *arrowheads*). No immunostaining is observed in immunocontrols (**c**, **d**). *ML* molecular layer, *GL* granular layer, *Mw* microwave treatment. *Bars* are 50 μm (**a**), 10 μm (**e**), and 500 μm in the *large inset* and 10 μm in the *small inset* (The figure is modified from Ohno et al. [2])

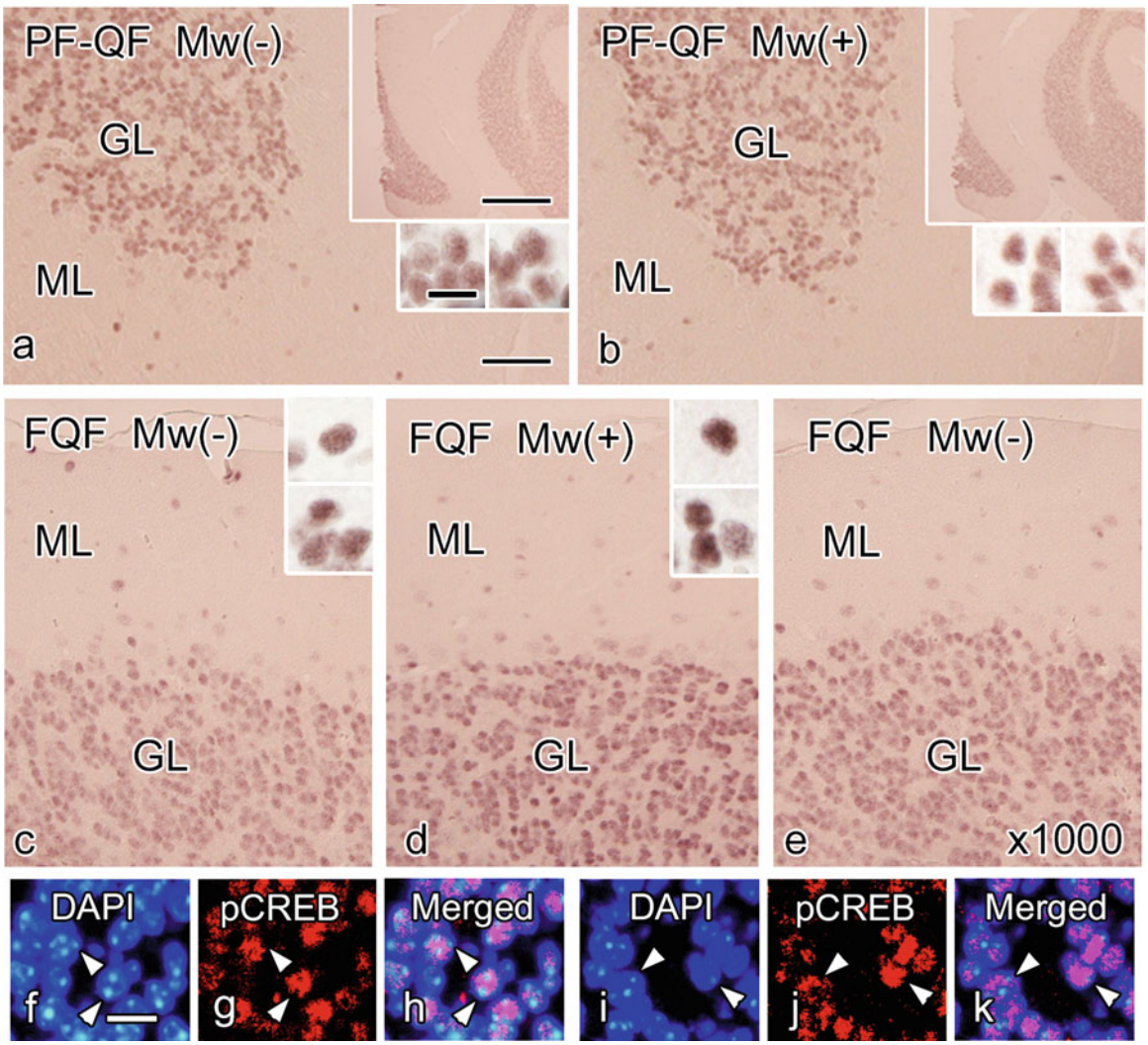

Fig 39.2 Serial paraffin sections prepared with the perfusion fixation followed by the quick-freezing (PF-QF) (**a**, **b**) or quick-freezing of fresh resected tissues (FQF) (**c**–**k**) show immunohistochemical staining for pCREB (**a**–**e**, **g**, **h**, **j**, **k**) with (**b**, **d**, **i**–**k**) microwave irradiation appeared similar to that without microwave treatment (**a**, **c**, **e**–**h**). The primary antibody was used at dilutions of 1:250 (**a**–**d**, **g**, **h**, **j**, **k**) or 1:1000 (×1000, **e**). The immunoreactivity with FQF is obvious even at a higher dilution (×1000) of the primary antibody (**e**). The pCREB immunostaining is not observed in the nucleoli, which are stained brightly with DAPI (**f**–**k**, *arrowheads*). *ML* molecular layer, *GL* granular layer. Nuclei are labeled with DAPI (**f**, **h**, **i**, **k**). *Bars* are 50 μm (**a**), 10 μm (**f**), and 500 μm (*large insets*) and 10 μm (*small insets*) (The figure is modified from Ohno et al. [2])

[2]. Immediate freezing of all molecules in vivo by IVCT can prevent artificial changes in structures and immunostaining [1, 22, 23]. Therefore, another advantage of IVCT is to facilitate detection of intranuclear antigens [2], and IVCT would enable precise analyses of transient and dynamic phenomena in living cellular nuclei.

39.5 Concluding Remarks

Reducing pretreatment steps improves artifacts during the tissue preparation and would lead to new morphological and histopathological findings. The CF-FS including IVCT reduces previously required pretreatments and preserves

morphology and signal intensity achieved in immunohistochemistry and FISH. CF-FS would be better techniques for intranuclear analyses, and IVCT would reveal the dynamic changes of intranuclear molecules by immediately cryofixing the molecular changes.

References

1. Ohno S, Terada N, Ohno N, Saitoh S, Saitoh Y, Fujii Y (2010) Significance of 'in vivo cryotechnique' for morphofunctional analyses of living animal organs. J Electron Microsc (Tokyo) 59(5):395–408
2. Ohno N, Terada N, Murata S, Katoh R, Ohno S (2005) Application of cryotechniques with freeze-substitution for the immunohistochemical demonstration of intranuclear pCREB and chromosome territory. J Histochem Cytochem 53(1):55–62
3. Brandtzaeg P (1982) Tissue preparation methods for immunohistochemistry. In: Bullock GR, Petrusz P (eds) Techniques in immunocytochemistry, 1st edn. Academic, London, pp 1–75
4. Shintaku IP, Said JW (1987) Detection of estrogen receptors with monoclonal antibodies in routinely processed formalin-fixed paraffin sections of breast carcinoma. Use of DNase pretreatment to enhance sensitivity of the reaction. Am J Clin Pathol 87(2):161–167
5. Cattoretti G, Pileri S, Parravicini C, Becker MH, Poggi S, Bifulco C et al (1993) Antigen unmasking on formalin-fixed, paraffin-embedded tissue sections. J Pathol 171(2):83–98
6. Podkletnova I, Alho H (1993) Ultrasound-amplified immunohistochemistry. J Histochem Cytochem 41(1):51–56
7. Shi SR, Cote RJ, Taylor CR (2001) Antigen retrieval techniques: current perspectives. J Histochem Cytochem 49(8):931–937
8. Shi SR, Imam SA, Young L, Cote RJ, Taylor CR (1995) Antigen retrieval immunohistochemistry under the influence of pH using monoclonal antibodies. J Histochem Cytochem 43(2):193–201
9. Evers P, Uylings HB (1994) Microwave-stimulated antigen retrieval is pH and temperature dependent. J Histochem Cytochem 42(12):1555–1563
10. Norton AJ (1993) Microwave oven heating for antigen unmasking in routinely processed tissue sections. J Pathol 171(2):79–80
11. Kitayama Y, Igarashi H, Sugimura H (2000) Different vulnerability among chromosomes to numerical instability in gastric carcinogenesis: stage-dependent analysis by FISH with the use of microwave irradiation. Clin Cancer Res 6(8):3139–3146
12. Watters AD, Bartlett JM (2002) Fluorescence in situ hybridization in paraffin tissue sections: pretreatment protocol. Mol Biotechnol 21(3):217–220
13. Solovei I, Cavallo A, Schermelleh L, Jaunin F, Scasselati C, Cmarko D et al (2002) Spatial preservation of nuclear chromatin architecture during three-dimensional fluorescence in situ hybridization (3D-FISH). Exp Cell Res 276(1):10–23
14. Ohno S, Kato Y, Xiang T, Terada N, Takayama I, Fujii Y et al (2001) Ultrastructural study of mouse renal glomeruli under various hemodynamic conditions by an "in vivo cryotechnique". Ital J Anat Embryol 106(2 Suppl 1):431–438
15. Ohno S, Terada N, Fujii Y, Ueda H, Takayama I (1996) Dynamic structure of glomerular capillary loop as revealed by an in vivo cryotechnique. Virchows Arch 427(5):519–527
16. Takayama I, Terada N, Baba T, Ueda H, Fujii Y, Kato Y et al (2000) Dynamic ultrastructure of mouse pulmonary alveoli revealed by an in vivo cryotechnique in combination with freeze-substitution. J Anat 197(Pt 2):199–205
17. Terada N, Kato Y, Fuji Y, Ueda H, Baba T, Ohno S (1998) Scanning electron microscopic study of flowing erythrocytes in hepatic sinusoids as revealed by 'in vivo cryotechnique'. J Electron Microsc (Tokyo) 47(1):67–72
18. Watanabe M, Leng CG, Toriumi H, Hamada Y, Akamatsu N, Ohno S (2000) Ultrastructural study of upper surface layer in rat articular cartilage by "in vivo cryotechnique" combined with various treatments. Med Electron Microsc 33(1):16–24
19. Xue M, Kato Y, Terada N, Fujii Y, Baba T, Ohno S (1998) Morphological study by an 'in vivo cryotechnique' of the shape of erythrocytes circulating in large blood vessels. J Anat 193(Pt 1):73–79
20. Jaeschke H, Lemasters JJ (2003) Apoptosis versus oncotic necrosis in hepatic ischemia/reperfusion injury. Gastroenterology 125(4):1246–1257
21. Valen G (2003) Cellular signalling mechanisms in adaptation to ischemia-induced myocardial damage. Ann Med 35(5):300–307
22. Ohno N, Terada N, Saitoh S, Ohno S (2007) Extracellular space in mouse cerebellar cortex revealed by in vivo cryotechnique. J Comp Neurol 505(3):292–301
23. Saitoh Y, Terada N, Saitoh S, Ohno N, Fujii Y, Ohno S (2010) Histochemical approach of cryobiopsy for glycogen distribution in living mouse livers under fasting and local circulation loss conditions. Histochem Cell Biol 133(2):229–239

Replica Immunoelectron Microscopy for Caveolin in Living Smooth Muscle Cells

40

Shinichi Ohno, Nobuo Terada, Yasuhisa Fujii, and Nobuhiko Ohno

Abstract

The IVCT with replica immunoelectron microscopy was developed for detecting caveolin localization on replica membranes directly prepared from living smooth muscle cells. After quick-freezing mouse duodenal walls by our IVCT, the specimens were prepared for freeze fracture and deep-etching replica membranes. Then, they were treated with 5 % SDS and 0.5 % collagenase to keep some antigens on the replica membranes. The immunogold method could be used to clarify the localization of the caveolin antigen in relation to three-dimensional ultrastructures of living smooth muscle cells. Our new cryotechnique with replica immunostaining can provide native organization of functional molecules in living smooth muscle cells.

Keywords

Replica membrane • Immunoelectron microscopy • Smooth muscle cell • Caveolin • In vivo cryotechnique

40.1 Introduction

The postembedding immunoelectron microscopy (immuno-EM) includes two preparation problems with techniques. First, it contains morphological alterations induced by anoxia or ischemia during the specimen preparation steps. Second, in comparison with highly contrasted ultrastructures revealed on epoxy resin, the hydrophilic resin obscures the ultrastructures of fixed specimens with lower electron contrast. To the contrary, another quick-freezing and deep-etching method for immunolabeled specimens has been used to clarify the three-dimensional molecular structure of cells and tissues. Such replica immuno-EM can clearly demonstrate three-dimensional localizations of proteins in cells, although the first problem still remains unresolved. On the other hand, some kinds of cell organelles have been believed to be dynamic components, which can change their ultrastructure in vivo during a very short time [1, 2]. The caveolae are typical of these organelles [3, 4]. Therefore, the conventional immuno-EM must have technical limitations for morpho-functional examination of cells and tissues in functional states at the millisecond order.

As a clue to solving such technical problems, we have already established the IVCT, which can be directly performed on anesthetized animals to examine functioning cells

S. Ohno, M.D., Ph.D. (✉) • Y. Fujii • N. Ohno
Department of Anatomy and Molecular Histology, Interdisciplinary Graduate School of Medicine and Engineering, University of Yamanashi, 1110 Shimokato, Chuo City, Yamanashi 409-3898, Japan
e-mail: sohno@yamanashi.ac.jp

N. Terada
Division of Health Sciences, Shinshu University Graduate School of Medicine, 3-1-1 Asahi, Matsumoto City, Nagano 390-8621, Japan

Department of Anatomy and Molecular Histology, Interdisciplinary Graduate School of Medicine and Engineering, University of Yamanashi, 1110 Shimokato, Chuo City, Yamanashi 409-3898, Japan

S. Ohno et al. (eds.), *In Vivo Cryotechnique in Biomedical Research and Application for Bioimaging of Living Animal Organs*, DOI 10.1007/978-4-431-55723-4_40

or tissues [5]. It provided newly clarified ultrastructures of mouse glomerular capillary loops under various hemodynamic conditions [5], native cornea of rat eyes [6], and erythrocytes flowing in the hepatic sinusoid [7]. In the present study, we have tried to develop another IVCT in combination with the immuno-EM to clarify the in situ localization of caveolin in functioning smooth muscle cells.

40.2 Preparation Procedures for Replica Immuno-EM

The abdominal cavity of mice was opened, and their duodenum in vivo was detected with the naked eye. Then, the duodenal wall was immediately frozen in vivo at its serosal surface with isopentane–propane cryogen (−193 °C) cooled in liquid nitrogen. The frozen duodenum was excised with a precooled nipper in liquid nitrogen (−196 °C) and was processed for the next deep-etching method. The serosal side of the duodenal tissues was carefully freeze-fractured with a scalpel in liquid nitrogen, as reported before [5]. Then, they were deeply etched under vacuum conditions of $6–8 \times 10^{-5}$ Pa, at −95 °C in an Eiko FD-3AS machine for 15–20 min. The specimens on a cold stage were rotary shadowed with platinum metal and carbon. A drop of 2 % collodion in amyl acetate was put onto the replicas, as soon as the specimens were taken out from the etching machine, to prevent the replica membranes from breaking into pieces during the following digestion steps. The replicated specimens coated with dried collodion were treated with 5 % SDS in distilled water (pH 4.0) for 5–10 h, followed with 0.5 % collagenase at 4 °C overnight. By such treatments, the deep-etching replica method could be already established, which retained residual antigen proteins on the replica membranes. Then, the replica membranes with the antigen proteins were incubated with polyclonal rabbit anti-caveolin antibody. Finally, they were incubated with goat anti-rabbit IgG antibody conjugated with 10 nm gold. After the immunocytochemical procedures, the replica membranes were washed in PBS and cut into small pieces with a pair of scissors. They were then mounted on Formvar-filmed copper grids and immersed in amyl acetate solution to dissolve the collodion. They were examined in a Hitachi H-8100 electron microscope.

40.3 Immunolocalization of Caveolin on Replica Membranes

As shown in Fig. 40.1a, b, our replica membrane method could demonstrate three-dimensional ultrastructures of the smooth muscle cells in the mouse duodenum prepared by the IVCT. Figure 40.1a shows the freeze-fractured cytoplasm of smooth muscle cells in living mice, indicating many three-dimensional cytoskeletons and cell organelles. On the P-face of the freeze-fractured cell membrane of smooth muscle cells (Fig. 40.1b), caveolae were detected as small holes, about 50–100 nm in diameter, when they were viewed from the outer cell surface. The diameter of each caveola was seemingly variable. Immunogold particles indicating localization of caveolin were often seen around such hole structures, which were probably attached to the caveola walls detected on the replica membranes (Fig. 40.1c). However, they also decorated some flat cell membrane regions in smooth muscle cells of the dystrophin-deficient mdx mice (Fig. 40.1d).

40.4 Morphofunctional Significance of Caveolae

In this way, our IVCT with the replica immuno-EM could show native intracellular localization of caveolin in functioning smooth muscle cells. It could provide higher resolution images in the replica membrane and allowed us to examine membrane localizations of caveolin around caveolae. The freeze-fracture replica electron microscopy has some advantages to examine subcellular distribution of antigen proteins [8], but it has not been performed under physiological conditions of animal organs. Moreover, we have recently revealed that caveolae in smooth muscle cells are dynamic structures which could often detach from the cell membrane, as shown in another chapter of this review book. The caveolae contain various receptors and signaling molecules [3, 8, 9] and play some important roles as microdomains of the cell membrane.

40.5 Concluding Remarks

The in vivo ultrastructural examinations are needed to reveal dynamic processes of protein–protein interactions on caveolae in living smooth muscle cells, which were hardly examined by the conventional electron microscopic or immuno-EM methods [3, 4]. Our IVCT with the replica immuno-EM can be directly used for living animal organs under various experimental conditions, which will be effective not only for morphofunctional investigations of the caveolae [10] but also extracellular matrices in functioning organs [11].

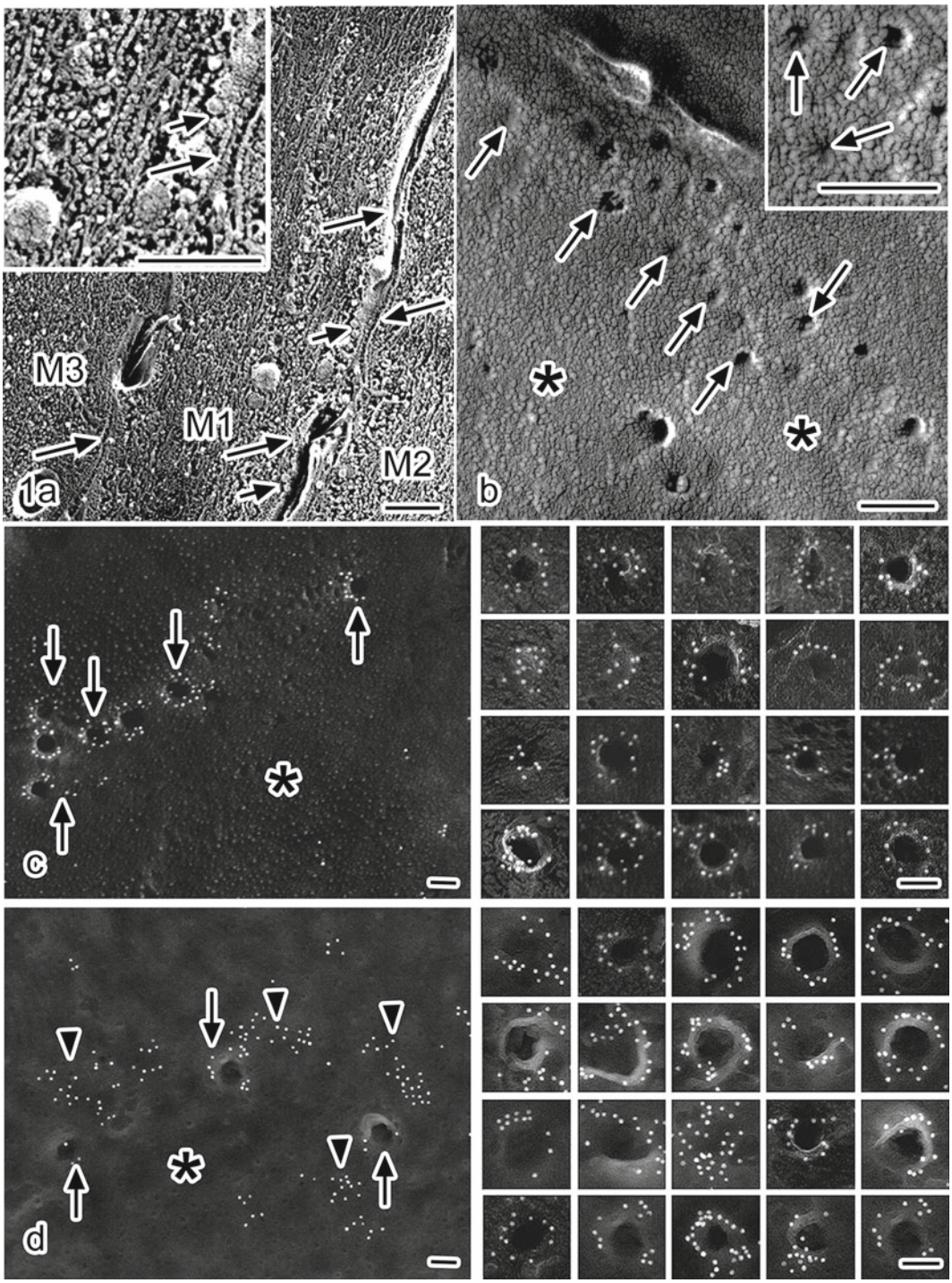

Fig. 40.1 Replica electron micrographs of intestinal smooth muscle cells in living mice prepared by the IVCT followed by replica preparation method. (**a**) Freeze-fractured cytoplasm of three parallel-lining smooth muscle cells (M1 ~ M3). Many cytoskeletons and caveolar structures (*small arrows*) along sarcolemma (*large arrows*) are three-dimensionally seen. Inset, higher magnification. Bars, 0.5 μm. (**b**) Various types of caveolar neck parts (*arrows*) are seen on the freeze-fractured P-face of their sarcolemma (*asterisks*). *Right upper inset*, higher magnification. Bars, 0.2 μm. (**c**) and (**d**) Immunostaining for caveolin with the immunogold method. Bars, 0.1 μm. Replica immunoelectron microscopy for caveolin in smooth muscle cells of living scn (**c**) or mdx (**d**) mice. Each *right-half panel* shows a list of various caveolar structures labeled with the immunogold particles. In the mdx mice (**d**), some immunogold particles for caveolin are localized not only on caveolae (*arrows*) but also on flat cell membranes (*arrowheads*). *Asterisks*: freeze-fractured P-face

References

1. Takayama I, Fujii Y, Ohno S, Fujino MA (1994) Ultrastructural study of mast cells stimulated with compound 48/80 as revealed by quick-freezing method. Virchows Arch 424:287–294
2. Takayama I, Fujii Y, Ohno S, Fujino MA (1995) Freeze-fracture immunocytochemistry for intracellular localization of serotonin in rat mast cells stimulated with compound 48/80. Virchows Arch 426:267–270
3. Anderson RGW (1993) Caveolae: where incoming and outgoing messengers meet. Proc Natl Acad Sci U S A 90:10909–10913
4. Michel CC (1998) Capillaries, caveolae, calcium and cyclic nucleotides: a new look at microvascular permeability. J Mol Cell Cardiol 30:2541–2546
5. Ohno S, Terada N, Fujii Y, Ueda H, Takayama I (1996) Dynamic ultrastructure of glomerular capillary loop as revealed by an in vivo cryotechnique. Virchows Arch 427:519–527
6. Chen H-B, Yamabayashi S, Ou B, Tanaka Y, Ohno S, Tsukahara S (1997) Structure and composition of rat precorneal tear film. A study by an in vivo cryofixation. Invest Ophthalmol Vis Sci 38:381–387
7. Terada N, Kato Y, Fujii Y, Ueda H, Baba T, Ohno S (1998) Scanning electron microscopic study of flowing erythrocytes in hepatic sinusoids as revealed by “in vivo cryotechnique”. J Electron Microsc 47:67–72
8. Fujimoto K (1995) Freeze-fracture replica electron microscopy combined with SDS digestion for cytochemical labeling of integral membrane proteins-application to the immunogold labeling of intercellular junctional complexes. J Cell Sci 108:3443–3450
9. Okamoto T, Amnon S, Phillip ES, Lisanti MP (1998) Caveolins, a family of scaffolding proteins for organizing “preassembled signaling complexes” at the plasma membrane. J Biol Chem 273:5419–5422
10. Takayama I, Terada N, Baba T, Ueda H, Kato Y, Fujii Y, Ohno S (1999) “In vivo cryotechnique” in combination with replica immunoelectron microscopy for caveolin in smooth muscle cells. Histochem Cell Biol 112:443–445
11. Zea-Aragon Z, Terada N, Ohno N, Fujii Y, Baba T, Yoshida M, Ohtsuki K, Ohnishi M, Ohno S (2004) Replica immunoelectron microscopic study of the upper surface layer in rat mandibular condylar cartilage by a quick-freezing method. Histochem Cell Biol 121:255–259

Application of "In Vivo Cryotechnique" to Detection of Injected Fluorescence-Conjugated IgG in Living Mouse Organs

41

Nobuo Terada, Yurika Saitoh, Nobuhiko Ohno, and Shinichi Ohno

Abstract

In this chapter, we present application of "in vivo cryotechnique" (IVCT) to the injection of fluorescence-conjugated protein into living organs. The fluorescein isothiocyanate-conjugated goat anti-rabbit immunoglobulin antibody (FITC-IgG) was directly injected into mouse livers, which were then frozen with IVCT by pouring an isopentane-propane mixture (−193 °C) cooled in liquid nitrogen. The organs were subsequently freeze-substituted in acetone containing paraformaldehyde, infiltrated with sucrose, and cryocut into several slices. The slices were observed under the fluorescence microscope. By examining the distribution of FITC-IgG, aspects of functional blood circulation in the liver, such as the concept of the liver lobule, were confirmed. The subsequent preparation of the specimens with immunohistochemistry, using the tetramethylrhodamine (TRITC)-conjugated anti-mouse IgG antibody, allowed us to visualize the localizations of both the original mouse IgG and the injected goat IgG in same sections with different color images.

Keywords

In vivo cryotechnique • Fluorescent-conjugated IgG • Injection • Freeze substitution

41.1 In Vivo Cryotechnique (IVCT) for Examination on Circulation

The cryotechnique, by which biological tissues are frozen at very high cooling rates, can arrest physiological processes, as well as blood flow within organs, and facilitate dynamic studies of the living tissue within these organs. IVCT was originally developed to examine the characteristics of in vivo living animal cells, tissues, and organs [1]. This technique was performed by rapid freezing of these tissues with liquid isopentane-propane cryogen (−193 °C) with or without cutting using a cryoknife (−196 °C) cooled down in liquid nitrogen. In previous studies, the dynamic morphological changes in living cells, tissues, and organs using the cryotechnique were observed by electron and light microscopy [1–7].

By employing IVCT for time-resolution studies, we have shown with in situ immunolocalization that serum proteins can naturally leak through the blood-brain barrier in the mouse cerebellum prior to the moment when the cryotechnique is histochemical procedures. In this chapter, we demonstrate a method for observing injected soluble fluorescence-conjugated proteins in living mouse organs after rapid freezing of the mouse organ followed by routine freeze substitution, cryo-sectioning, and observation with a fluorescence microscope. Precise methods and results have been reported in the previous paper [8].

N. Terada, M.D., Ph.D. (✉)
Division of Health Sciences, Shinshu University Graduate School of Medicine, 3-1-1 Asahi, Matsumoto City, Nagano 390-8621, Japan

Department of Anatomy and Molecular Histology, Interdisciplinary Graduate School of Medicine and Engineering, University of Yamanashi, 1110 Shimokato, Chuo City, Yamanashi 409-3898, Japan
e-mail: nobuot@shinshu-u.ac.jp

Y. Saitoh • N. Ohno • S. Ohno
Department of Anatomy and Molecular Histology, Interdisciplinary Graduate School of Medicine and Engineering, University of Yamanashi, 1110 Shimokato, Chuo City, Yamanashi 409-3898, Japan

S. Ohno et al. (eds.), *In Vivo Cryotechnique in Biomedical Research and Application for Bioimaging of Living Animal Organs*, DOI 10.1007/978-4-431-55723-4_41

41.2 IVCT After Injection of Fluorescent-Conjugated IgG

Retention of fluorescent signal derived from fluorophore after quick freezing and freeze substitution with paraformaldehyde is demonstrated in Fig. 41.1a–c, by mixing FITC-conjugated IgG (green in Fig. 41.1a, c) and TRITC-conjugated IgG (red in Fig. 41.1b, c) from different direction. For IVCT, FITC-conjugated goat anti-rabbit IgG antibody in saline was directly injected into the liver through a small needle (Fig. 41.1d). One second after the injection, the liver was immediately bathed in the isopentane-propane mixture precooled in liquid nitrogen. This IVCT was always performed under the normal physiological conditions, with the animals' hearts beating, as previously described [1]. The freeze-substitution method could be combined to the cryotechnique to minimize the diffusion of soluble proteins from their biological compartment during preparation [9].

After the freeze substitution, the samples were treated with sucrose and then frozen with isopentane precooled with dry ice, and 6–8-μm sections were cut at −30 °C in a cryostat apparatus. After attaching the thawed tissues to the poly-L-lysine-coated glass slides, they were briefly washed in phosphate-buffered saline (PBS) to remove the sucrose. Then, the tissues on glass slides were covered using coverslips and observed under a fluorescence microscope.

41.3 Blood Circulation Is Visualized by Injection of Fluorescent IgG Probe with IVCT

Some well-preserved tissues without obvious ice-crystal formation at a light microscopic level were obtained within 300–400 μm of the frozen tissue surface, as revealed by differential interference contrast (DIC) (Fig. 41.1e) and DAPI staining. Such well-preserved areas were widely obtained by sectioning the frozen surfaces vertically.

Regarding the blood vessels, including the hepatic sinusoids of mouse livers, the injected fluorescent probe was

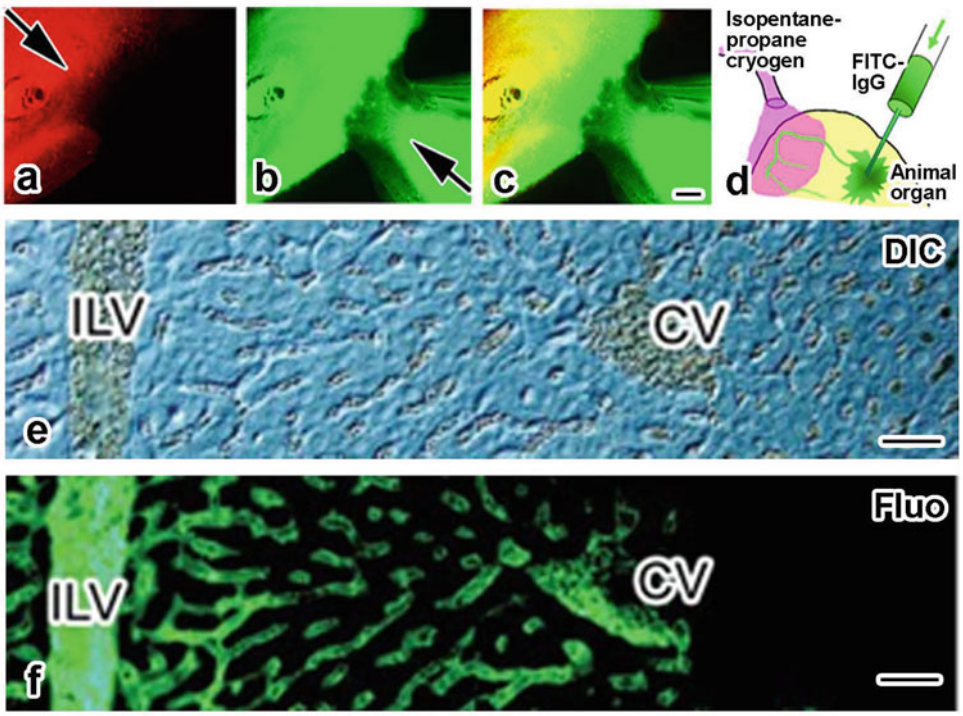

Fig. 41.1 (**a**–**c**) Fluorescence micrographs of quick-frozen, freeze-substituted, and freeze-dried TRITC- and FITC-conjugated goat immunoglobulins, which were mixed on glass slide from different direction (*arrows* in **a**, **b**). (**c**) is the merged image of (**a**) and (**b**). **(d)** Schematic representation of the in vivo cryotechnique with fluorescent probe injection. (**e**, **f**) DIC (**e**) and fluorescence (**f**, Fluo) images of IVCT mouse liver where FITC-conjugated goat immunoglobulin was injected. Precise data have been reported in the previous paper (Terada et al. [8]). Bars: 100 μm

retained after performing the in vivo cryotechnique and the freeze-substitution procedure (Fig. 41.1f). Red blood cells were strictly localized in various types of blood vessels, indicating that normal blood flow was retained even after the injection of goat FITC-IgG, when the in vivo cryotechnique was performed. The paraformaldehyde fixation during the freeze substitution did not alter the fluorescent characteristics of the fluorescent probe. Its light emission occurred at the same wavelength as that of the probe in water only. Some interlobular veins (ILV in Fig. 41.1e, f) surrounded a segment of the hepatic lobule. Many venous capillaries at the surface of the hepatic lobule arise from interlobular veins and inlet venules: from these, circulating blood passes through openings in the limiting plate into hepatic sinusoids and then further flows between the hepatic plates to be collected by the central vein (CV in Fig. 41.1e, f). In a few hepatic lobules, exogenous goat FITC-IgG was only distributed in about half of their areas (Fig. 41.1f), indicating that blood was circulating through the portal lobule. The three-dimensional vascular network revealed by the injected goat FITC-IgG could also be obtained by collecting images of serial sections.

41.4 Combination of Immunohistochemistry for the IVCT-FS Samples

For the immunohistochemical analyses using fluorescence microscopy, some cryostat sections were then incubated with TRITC-conjugated goat anti-mouse IgG antibody, which does not cross-react to the goat IgG. They were mounted on glass slides and observed under the confocal laser scanning microscope. The TRITC-immunolabeled original mouse IgG and the injected goat FITC-IgG, both fluorescences, were also located. This gives an example of this concept for immunohistochemistry after the freeze substitution of the frozen specimens with fluorescent probes. Therefore, the merits of arresting the injected fluorescent probe exclusively by applying IVCT, and not with the usual video camera imaging for fluorescence, are not only that the in vivo blood flow can be maintained at the time of cryofixation but also that the living organ can be directly frozen.

41.5 Concluding Remarks

Fluorescence-conjugated IgG probes were retained in the blood vessels during IVCT and FS procedure. This retention made it possible to visualize the flow path of the original serum component in the hepatic blood vessels of mouse IgG.

References

1. Ohno S, Terada N, Fujii Y, Ueda H, Takayama I (1996) Dynamic ultrastructure of glomerular capillary loop as revealed by an in vivo cryotechnique. Virchow's Arch 427:519–527
2. Takayama I, Terada N, Baba T, Ueda H, Kato Y, Fujii Y, Ohno S (1999) "In vivo cryotechnique" in combination with replica immunoelectron microscopy for caveolin in smooth muscle cells. Histochem Cell Biol 112:443–445
3. Takayama I, Terada N, Baba T, Ueda H, Fujii Y, Kato Y, Ohno S (2000) Dynamic ultrastructure of mouse pulmonary alveoli revealed by in vivo cryotechnique in combination with freeze-substitution. J Anat 197:199–205
4. Terada N, Kato Y, Fujii Y, Ueda H, Baba T, Ohno S (1998) Scanning electron microscopic study of flowing erythrocytes in hepatic sinusoids as revealed by "in vivo cryotechnique.". J Electron Microsc 47:67–72
5. Xue M, Baba T, Terada N, Kato Y, Fujii Y, Ohno S (2001) Morphological study of erythrocyte shapes in red pulp of mouse spleens revealed by an in vivo cryotechnique. Histol Histopathol 16:123–129
6. Zea-Aragon Z, Terada N, Ohno N, Fujii Y, Baba T, Ohno S (2004) Effects of anoxia on serum immunoglobulin and albumin leakage through blood-brain barrier in mouse cerebellum as revealed by cryotechniques. J Neurosci Methods 138:89–95
7. Zea-Aragon Z, Terada N, Ohno N, Fujii Y, Baba T, Yoshida M, Ohtsuki K, Ohnishi M, Ohno S (2004) Replica immunoelectron microscopic study of the upper surface layer in rat mandibular condylar cartilage by a quick-freezing method. Histochem Cell Biol 121:255–259
8. Terada N, Ohno N, Li Z, Fujii Y, Baba T, Ohno S (2005) Detection of injected fluorescence-conjugated IgG in living mouse organs using "in vivo cryotechnique" with freeze-substitution. Microsc Res Tech 66:173–178
9. Shiurba R (2001) Freeze-substitution: origins and applications. Int Rev Cytol 206:45–96

42 Application of "In Vivo Cryotechnique" to Visualization of Microvascular Blood Flow in Mouse Kidney by Quantum Dot Injection

Nobuo Terada, Yurika Saitoh, Nobuhiko Ohno, and Shinichi Ohno

Abstract

In this chapter, we present application of "in vivo cryotechnique" (IVCT) to the injection of glutathione (GSH)-coated quantum dots (QDs), which emit a red-fluorescent signal with an ultraviolet excitation, for kidneys. The frozen kidneys were processed to freeze-substitution fixation (FS) and observed in fluorescence or confocal laser scanning microscope (CLSM). In the renal cortex, QD distribution was detected mostly in glomerular blood capillaries for a few seconds and extended to peritubular blood capillaries at 5 s. By injection of horseradish peroxidase (HRP) and QDs at the same time, the distribution of HRP in the renal cortex at 30 s was detected in the interstitium in addition to blood vessels, whereas QDs were localized only inside blood vessels. Thus, strict time-dependent visualization of blood flow in tissue sections became possible within seconds by combination of IVCT and injection of QDs.

Keywords

In vivo cryotechnique • Quantum dot • Fluorescent probe • Horseradish peroxidase

42.1 In Vivo Cryotechnique (IVCT) and Quantum Dot (QD) Injection

IVCT is very useful to visualize time-dependent events [1, 2]. It is also assumed to cryoimmobilize all components in the cells and tissues within a second in well-frozen areas [2]. To examine the in vivo blood flow in some mouse organs, we previously applied IVCT to living mouse kidneys and livers which were directly injected with fluorophore-conjugated immunoglobulin G [3]. However, the lifetime of the fluorophore, fluorescein isothiocyanate (FITC), was too short to detect, resulting in decreased intensity of visualization to analyze its temporal or spatial resolution.

Recently, another type of fluorophore, quantum dots (QDs), was produced [4, 5]. Some typical QDs consist of core-shell nano-metal structures functionalized with different molecular coatings. As shown in Fig. 42.1a, optical properties of QDs are controllable by changing their sizes to 1–10 nm in diameter, which have a broad excitation wavelength together with sharp and symmetrical emission fluorescent spectra. Because of strong and constant fluorescent signals, they have a high potential for morphofunctional study of various biological processes in animal bodies at a single-molecule level [6–8]. Small-sized QDs were also used to examine physiological rates of their filtering through glomerular basement membranes [9]. With intravital fluorescence microscopy, networks of blood vessels were imaged in living mouse organs, which

N. Terada, M.D., Ph.D. (✉)
Division of Health Sciences, Shinshu University Graduate School of Medicine, 3-1-1 Asahi, Matsumoto City, Nagano 390-8621, Japan

Department of Anatomy and Molecular Histology, Interdisciplinary Graduate School of Medicine and Engineering, University of Yamanashi, 1110 Shimokato, Chuo City, Yamanashi 409-3898, Japan
e-mail: nobuot@shinshu-u.ac.jp

Y. Saitoh • N. Ohno • S. Ohno
Department of Anatomy and Molecular Histology, Interdisciplinary Graduate School of Medicine and Engineering, University of Yamanashi, 1110 Shimokato, Chuo City, Yamanashi 409-3898, Japan

S. Ohno et al. (eds.), *In Vivo Cryotechnique in Biomedical Research and Application for Bioimaging of Living Animal Organs*, DOI 10.1007/978-4-431-55723-4_42

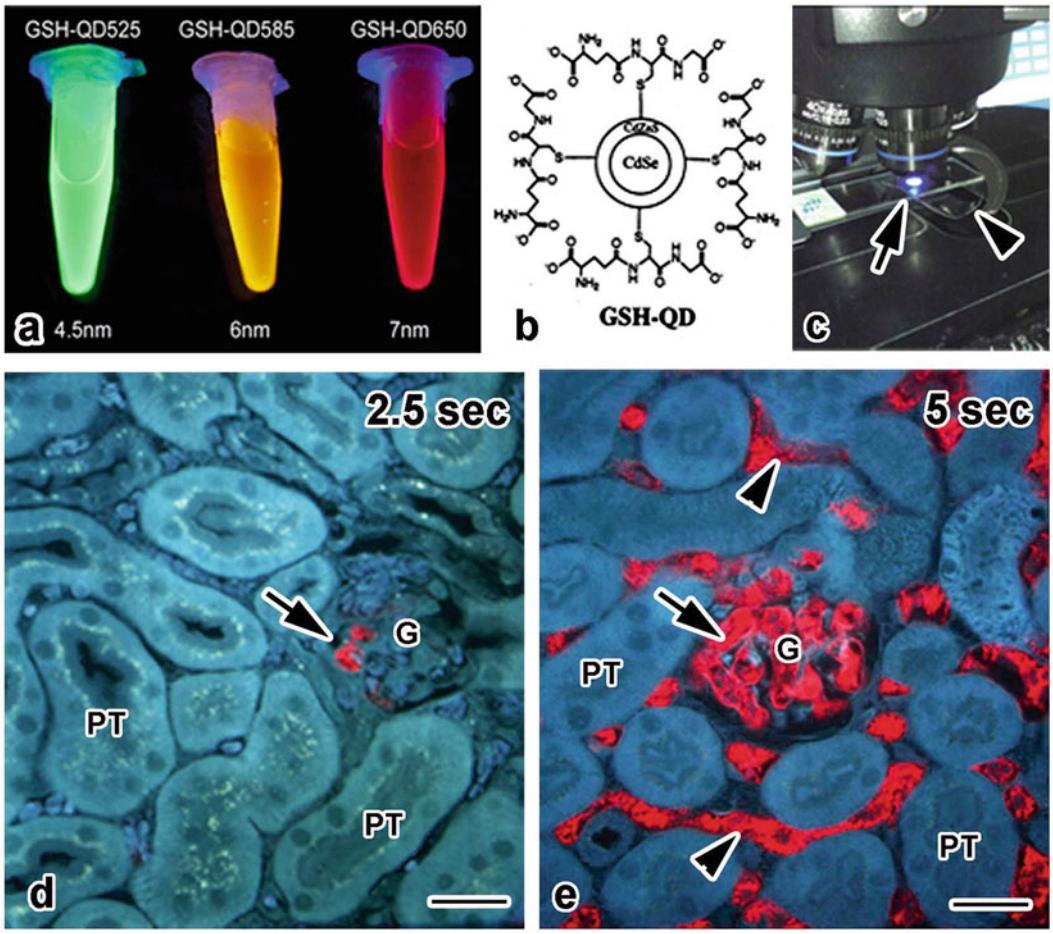

Fig. 42.1 (**a**) Photographs of different sizes of quantum dots (QDs; 4.5, 6, and 7 nm) emitting different fluorescent colors under ultraviolet light. (**b**) Chemical structure of GSH-coated QDs. Actual number of GST is much higher. (**c**) Tissue section (*arrows*) is observed with fluorescence microscope with ultraviolet light. *Arrowhead* indicates glossy paper to reflect ultraviolet light, which is useful to gather light. (**d**, **e**) Fluorescence images of IVCT mouse kidney tissues at 1.5 (**d**) and 5 (**e**) sec after injection of QDs. *Red signal* is derived from QDs under ultraviolet light. *G* glomerulus, *PT* proximal tubule. Precise data have been reported in the previous paper (Terada et al. [14]). Bars: 50 μm

had been intravenously injected with QDs [8, 10, 11]. In the present chapter, we present injection of water-soluble glutathione (GSH)-coated QDs (Fig. 42.1b) [12, 13] into anesthetized mouse hearts and subsequent IVCT to visualize the QD distribution in kidney tissues at the second time scale. Precise methods and results have been reported in the previous paper [14].

42.2 Detection of Histological Features and QD Distribution in Kidney Tissues

The QDs used in this study are referred to as GSH-QD650 and were made of CdSe/CdZnS core with a GSH coating, and they were about 8 nm in total diameter, emitting red (around 650 nm in wavelength) fluorescent signals with ultraviolet (UV) light (Fig. 42.1c). In cortical tissues of mouse kidneys at 2.5 and 5 s after injection of QDs, red QD signals were clearly detected. There were three ways to observe the renal tissue structures. First, pure morphology was obtained with hematoxylin-eosin (HE) staining of the serial sections, enabling us to compare the fluorescence image. Second, detection of autofluorescence images with UV excitation was useful on the same section, as shown by the blue color in Fig. 42.1d, e, while the fluorescence intensity of QD signals was very strong. Third, diffraction interference contrast (DIC) images were useful to visualize morphological contours of blood vessels due to the appearance of erythrocyte shapes on the exactly same section.

In the renal cortex, at 2.5 s after the QD injection (Fig. 42.1d), QDs were detected only in renal glomerular capillaries as well as afferent arterioles, but not in blood capillaries around renal tubules. The QDs were seen to be

distributed in restricted areas in glomerular capillary loops. This finding is consistent with the concept of blood flow in the renal cortex, showing that the flow enters from afferent arterioles into glomerular capillary loops and exits through efferent arterioles and into peritubular blood capillaries. At 5 s after the QD injection (Fig. 42.1e), they were detected in almost all peritubular blood capillaries, as well as those in all renal glomeruli. Thus, the in vivo blood flow, reflecting their living states, was clearly visualized by the QD distribution in tissue sections captured by IVCT.

With the confocal laser scanning microscope (CLSM), tissue sections were exposed to UV laser light (405 nm in wavelength), and the best GSH-QD650-fluorescence images were detected at a 630–730 nm wavelength. After FS, the tissue specimens became very hard, and it was possible to trim them directly with a razor blade, and the cut tissue surface was exposed to laser beams by CLSM. Both afferent and efferent arterioles were visualized at a vascular pole, where the QD distribution was three-dimensionally detected in the glomerulus as a whole, as obtained at any levels by optionally cut sections after the image reconstruction. Thus, vascular structures of glomerular capillary loops were clearly demonstrated by the reconstruction of QD distribution with CLSM.

42.3 Comparative Distribution of QD and Injected Soluble Protein, Horseradish Peroxidase (HRP)

The HRP has been a well-known soluble protein often used as a tracer by visualization with DAB-enzyme reaction to examine diffusive states in the interstitium in various animal organs after artificial injection into blood vessels [15]. The HRP distribution was evaluated by the simultaneous injection of HRP and QDs into the mouse left ventricles, and IVCT was performed at 30 s after the injection. Because glutaraldehyde treatment usually reduced the QD intensity, the IVCT-frozen tissues containing both HRP and QDs were divided into two pieces and processed to each detection protocol. At 30 s after the simultaneous injection of HRP and QDs, only DAB-reaction products were detected in the interstitium, as well as in blood vessels of the renal cortex, showing HRP localization. In addition, DAB-reaction products were detected at basal striations of some renal tubules. On the other hand, QDs were detected only inside blood vessels, but not in the interstitium of the renal cortex. Thus, dynamic aspects of blood supply into organs were clearly visualized by detecting different soluble extrinsic components with the IVCT, which probably reflect living animal functions.

42.4 Concluding Remarks

The injected QDs were clearly visualized in the living mouse kidneys with IVCT at the second time scale.

References

1. Ohno S, Terada N, Fujii Y, Ueda H, Takayama I (1996) Dynamic structure of glomerular capillary loop as revealed by and in vivo cryotechnique. Virchow's Arch 427:519–527
2. Ohno N, Terada N, Saitoh S, Zhou H, Fujii Y, Ohno S (2007) Recent development of in vivo cryotechnique to cryobiopsy for living animals. Histol Histopathol 22:1281–1290
3. Terada N, Ohno N, Li Z, Fujii Y, Baba T, Ohno S (2005) Detection of injected fluorescence-conjugated IgG in living mouse organs using "in vivo cryotechnique" with freeze-substitution. Microsc Res Tech 66:173–178
4. Tholouli E, Sweeney E, Barrow E, Clay V, Hoyland JA, Byers RJ (2008) Quantum dots light up pathology. J Pathol 216:275–285
5. Reshc-Genger U, Grabolle M, Cavaliere-Jaricot S, Nitschke R, Nann T (2008) Quantum dots versus organic dyes as fluorescent labels. Nat Methods 5:763–775
6. Ballou B, Lagerholm BC, Ernst LA, Bruchez MP, Waggoner AS (2004) Noninvasive imaging of quantum dots in mice. Bioconjug Chem 15:79–86
7. Kim S, Lim YT, Soltesz EG, De Grand AM, Lee J, Nakayama A, Parker JA, Larson DR, Zipfel WR, Williams RM, Clark SW, Bruchez MP, Wise FW, Webb WW (2003) Water-soluble quantum dots for multiphoton fluorescence imaging in vivo. Science 300:1434–1436
8. Michalet X, Pinaud FF, Bentolila LA, Tsay JM, Doose S, Li JJ, Sundaresan G, Wu AM, Gambhir SS, Weiss S (2005) Quantum dots for live cells, in vivo imaging, and diagnostics. Science 28:538–544
9. Choi HS, Liu W, Misra P, Tanaka E, Zimmer JP, Itty-Ipe B, Bawendi MG, Frangioni JV (2007) Renal clearance of quantum dots. Nat Biotechnol 25:1165–1170
10. Larson DR, Zipfel WR, Williams RM, Clark SW, Bruchez MP, Wise FW, Webb WW (2003) Water-soluble quantum dots for multiphoton fluorescence imaging in vivo. Science 300:1434–1436
11. Ferrara DE, Weiss D, Carnell PH, Vito RP, Vega D, Gao X, Nie S, Taylor WR (2006) Quantitative 3D fluorescence technique for the analysis of en face preparations of arterial walls using quantum dot nanocrystals and two-photon excitation laser scanning microscopy. Am J Physiol Regul Integr Comp Physiol 290:114–123
12. Jin T, Fujii F, Komai Y, Seki J, Seiyama A, Yoshioka Y (2008) Preparation and characterization of highly fluorescent, glutathione-coated near infrared quantum dots for in vivo fluorescence imaging. Int J Mol Sci 9:2044–2061
13. Tiwari DK, Tanaka S, Inouye Y, Yoshizawa K, Watanabe TM, Jin T (2009) Synthesis and characterization of anti-HER2 antibody conjugated CdSe/CdZnS quantum dots for fluorescence imaging of breast cancer cells. Sensors 9:9332–9354
14. Terada N, Saitoh Y, Saitoh S, Ohno N, Jin T, Ohno S (2010) Visualization of microvascular blood flow in mouse kidney and spleen by quantum dot injection with "in vivo cryotechnique". Microvasc Res 80:491–498
15. Ryan GB, Karnovsky MJ (1976) Distribution of endogenous albumin in the rat glomerulus: role of hemodynamic factors in glomerular barrier function. Kidney Int 9:36–45

Part V

Direct Detection of Molecules by Raman Microscopy

Application of "In Vivo Cryotechnique" to Raman Microscopy of Freeze-Dried Mouse Eyeball Slice

43

Nobuo Terada, Yurika Saitoh, Nobuhiko Ohno, Yasuhisa Fujii, and Shinichi Ohno

Abstract

The wavelength of Raman-scattered light depends on the molecular composition of the substance. In this chapter, we present identification of biological molecules by Raman spectra in a mouse eyeball with "in vivo cryotechnique" (IVCT) followed by freeze drying. Four typical patterns of Raman spectra were obtained and electronically mapped. Tissue organization was confirmed by embedding the same eyeball slice used for Raman spectra into epoxy resin with the inverted capsule method. Each Raman spectral pattern represents a different histological layer in the eyeball. Some of the peaks of the Raman spectra obtained from the blood vessels in sclera and the photoreceptor layer were similar to those obtained from the purified hemoglobin and rhodopsin proteins, respectively. Thus, this method is useful for examining the distribution of a biological structures and chemical components.

Keywords

In vivo cryotechnique • Raman • Freeze drying • Molecular structure • Hemoglobin

43.1 Raman Spectroscopy and In Vivo Cryotechnique (IVCT)

Biological materials themselves change their molecular structure through several modification steps when signaling cascades start. Raman spectroscopy is a technique based on the scattering of incident laser light at frequencies that are shifted by the vibration of component structures of a compound dependent on its composition and bonding [1]. This optical method has attracted considerable attention for use in evaluating cells and tissues since Raman microscopy has the potential to distinguish biological molecules in different states [2].

To combine IVCT [3] with the Raman spectroscopy, we used freeze-drying method because the location and structure of various biomolecules, such as proteins, lipids, carbohydrates, and vitamins, remain mostly unchanged [4]. Here, we present the Raman spectra mapping of the biological structure of part of the mouse eye. Precise methods and results have been reported in the previous paper [5].

43.2 IVCT, Cryo-slicing and Freeze Drying for the Mouse Eyeball

The IVCT was performed with the eyeballs of anesthetized mice, which were kept in the room under daylight conditions. The eyeballs were immediately frozen with the liquid

N. Terada, M.D., Ph.D. (✉)
Division of Health Sciences, Shinshu University Graduate School of Medicine, 3-1-1 Asahi, Matsumoto City, Nagano 390-8621, Japan

Department of Anatomy and Molecular Histology, Interdisciplinary Graduate School of Medicine and Engineering, University of Yamanashi, 1110 Shimokato, Chuo City, Yamanashi 409-3898, Japan
e-mail: nobuot@shinshu-u.ac.jp

Y. Saitoh • N. Ohno • Y. Fujii • S. Ohno
Department of Anatomy and Molecular Histology, Interdisciplinary Graduate School of Medicine and Engineering, University of Yamanashi, 1110 Shimokato, Chuo City, Yamanashi 409-3898, Japan

S. Ohno et al. (eds.), *In Vivo Cryotechnique in Biomedical Research and Application for Bioimaging of Living Animal Organs*, DOI 10.1007/978-4-431-55723-4_43

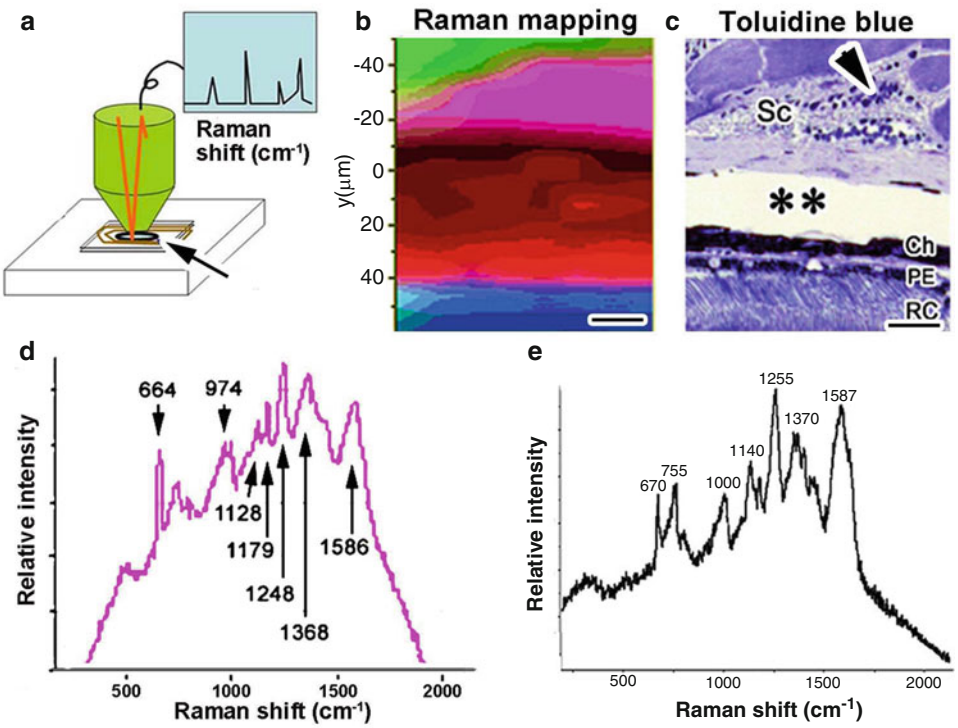

Fig. 43.1 (**a**) Schematic representation of Raman microscopic analysis for the freeze-dried samples (*arrow*) sandwiched between glasses. (**b**, **c**) Raman mapping image (**b**) and morphological image with toluidine-blue staining (**c**) for the same tissue area in IVCT-FS mouse eye. (**d**) Typical Raman spectrum obtained in the *pink* area shown in (**b**). (**e**) Raman spectrum obtained from the purified dry hemoglobin. Precise data have been reported in the previous paper (Terada et al. [5]). *Bars*: 10 μm

isopentane–propane cryogen (−193 °C) [6]. The frozen eyeballs were sectioned with a 100-μm thickness with a cryotome, which was cooled with dry ice. Each eyeball section was transferred into a freeze-etching machine so that the samples could be freeze-dried under $1–4 \times 10^{-7}$ Torr vacuum condition at −95 °C [7]. The sections were warmed up and examined in a confocal Raman microspectrometer (Fig. 43.1a). To handle and not break, the tissue sections were sandwitched between glasses. Moreover, after the freeze drying, the samples between glasses could be transported safely and directly analyzed with Raman microscopy without opening the glass sandwich (arrow in Fig. 43.1a).

The beam line of a HeNe laser was focused on a position in a selected eyeball slice with the help of a bright-field microscope. Held up to the light, choroid and pigment epithelial layers were recognized as colored black owing to the presence of melanin granules. Raman spectra analyses were performed to test the suitability of the mouse eyeball slices for histological identification. Spectra obtained in this area could be categorized into four patterns (Fig. 43.1b), and typical spectrum in pink area is presented in Fig. 43.1d.

43.3 Embedding of Freeze-Dried Slices in Epoxy Resin to Visualize Tissue Structure

The eyeball slices analyzed for Raman microscopy were embedded in epoxy resin using the inverted capsule method. Briefly, the coverglass sandwiching the eyeball slice was removed, and a gelatin capsule filled with the epoxy resin was placed on the eyeball slice attached to the glass slide. After hardening the resin, the glass slide was detached by heating slightly. One-micrometer-thick sections were cut on an ultramicrotome stained with toluidine blue and observed with a bright-field microscope.

By comparing the image of the morphological tissue structures to that of the Raman mapping of four typical spectral patterns (Fig. 43.1b), it became clear that the distribution of colors reflected different tissue components: areas with the pattern shown by green, pink, red, and blue colors corresponded with the ocular skeletal muscles, scleral connective tissues (Sc in Fig. 43.1c), choroid/pigment epithelium (Ch and PE in Fig. 43.1c), and rod/cone photoreceptor layer (RC in Fig. 43.1c), respectively.

43.4 Comparison of Raman Spectra in IVCT Tissues and Purified Proteins Prepared by Quick Freezing and Freeze Drying

The Raman spectra of isolated hemoglobin (Fig. 43.1e) showed specific patterns with several peaks. Some peaks and spectra patterns obtained from the purified hemoglobin and blood vessels in the sclera (Fig. 43.1d, e) were almost similar. The Raman spectrum of freeze-dried purified rhodopsin was also similar to that obtained in rod/cone photoreceptor layer with IVCT-FD.

In aqueous solutions, it has been possible to distinguish changes in molecular structures of biological materials with Raman spectroscopy such as oxygenation of hemoglobin [8], light-exposed rhodopsin [9], and complexes of nucleic acids [10]. Presumably, some changes of the Raman spectral pattern may be caused by freeze drying and dehydrated chromophores in the tissue samples. In the next step, we then examined Raman spectra of tissue in the aqueous state on a low-temperature stage, as demonstrated in Chap. 44 in this book.

43.5 Concluding Remarks

IVCT in combination of Raman microscopy revealed molecular identification and distribution, reflecting living states.

References

1. Egawa T, Yeh SR (2005) Structural and functional properties of hemoglobins from unicellular organisms as revealed by resonance Raman microscopy. J Inorg Biochem 99:72–96
2. Wood BR, Tait B, McNaughton D (2001) Micro-Raman characterization of the R to T state transition of hemoglobin within a single living erythrocyte. Biochem Biophys Acta 1539:58–70
3. Ohno S, Terada N, Fujii Y, Ueda H, Takayama I (1996) Dynamic structure of glomerular capillary loop as revealed by an in vivo cryotechnique. Virchow's Arch 427:519–527
4. Yang C, Terada N, Ohno N, Fujii Y, Ohno S (2006) Morphological analysis of lamellar structures in mouse type II pneumocytes by quick-freezing and freeze-drying with osmium tetroxide vapor-fixation. Med Mol Morphol 39:88–96
5. Terada N, Ohno N, Saitoh S, Fujii Y, Ohguro H, Ohno S (2007) Raman microscopy of freeze-dried mouse eyeball-slice in conjunction with the "in vivo cryotechnique". Microsc Res Tech 70:634–639
6. Terada N, Ohno N, Ohguro H, Li Z, Ohno S (2006) Immunohistochemical detection of phosphorylated rhodopsin in light-exposed retina of living mouse with in vivo cryotechnique. J Histochem Cytochem 54:479–486
7. Terada N, Ohno N, Fujii Y, Baba T, Ohno S (2006) Dynamic study of intramembranous particles in human fresh erythrocytes using an "in vitro cryotechnique". Microsc Res Tech 69:291–295
8. Podstawka E, Rajani C, Kincaid JR, Proniewicz LM (2000) Resonance Raman studies of heme structural differences in subunits of deoxy hemoglobin. Biopolymers 57:201–207
9. Kakura P, McCamant DW, Yoon S, Wandschneider DB, Mathies RA (2005) Structural observation of the primary isomerization in vision with femtosecond-stimulated Raman. Science 310:1006–1009
10. Benevides JM (2005) Raman, polarized Raman and ultraviolet resonance Raman spectroscopy of nucleic acids and their complexes. J Raman Spectrosc 36:279–299

Application of "In Vivo Cryotechnique" to Detection of Erythrocyte Oxygen Saturation in Mouse Blood Vessels with Confocal Raman Cryomicroscopy

44

Nobuo Terada, Yurika Saitoh, Nobuhiko Ohno, and Shinichi Ohno

Abstract

In this chapter, we present application of "in vivo cryotechnique" (IVCT) to measurement of oxygen saturation (SO_2) in erythrocytes with Raman cryomicroscopy. Two resonance Raman (RR) shifts around 1355 and 1378 cm^{-1} which reflect deoxygenated and oxygenated hemoglobin molecular structures, respectively, were evaluated. The two RR shifts of quickly frozen human whole blood were well retained at the low temperature. In blood vessels of living mouse organs prepared with the IVCT, their RR spectral peaks were also detected at the same RR shifts. In the blood vessels of IVCT small intestines and livers, different peak patterns of their RR shifts were monitored in each blood vessel. Thus, SO_2 in blood vessels is measurable in IVCT tissues with Raman cryomicroscopy, reflecting their living states.

Keywords

In vivo cryotechnique • Oxygen saturation • Raman spectrum • Hemoglobin

44.1 Evaluation of Oxygen Saturation (SO_2) in Tissues and Raman Spectroscopy

Detection of tissue oxygenation as well as erythrocyte SO_2 has been considered important to evaluate the living states of organs and intracellular reactions against hypoxic conditions. To highlight regional oxygenation of cells and tissues in vital animal bodies, several analytical techniques were used including the phosphorescence quenching, nuclear magnetic resonance (NMR), nicotinamide adenine dinucleotide (NADH) fluorescence, and light or infrared spectroscopic and Raman imaging to detect their dynamic states [1–3].

An advantage of Raman microscopy for biological investigation is that the Raman spectrum of water itself is very weak, unlike infrared spectroscopy [4], enabling us to obtain precise information about biological components of cells and tissues with water and/or ice crystals. The recent development of a confocal system with Raman microscopy has also been helpful for obtaining such information from tiny target tissue spots within animal organ specimens, which then allows us to make mapping images of their spectra [5]. Oxy- and deoxy-Hb-specific resonance Raman (RR) shifts were recently reported in living mouse blood vessels running throughout the abdominal peritoneum by intravital Raman spectroscopic analyses [6].

However, the physiological relevance of low temperature studies has not been elucidated in natural animal tissues in vivo [7]. If the specific RR shifts are also retained in the living animal tissues at low temperature, the Raman

N. Terada, M.D., Ph.D. (✉)
Division of Health Sciences, Shinshu University Graduate School of Medicine, 3-1-1 Asahi, Matsumoto City, Nagano 390-8621, Japan

Department of Anatomy and Molecular Histology, Interdisciplinary Graduate School of Medicine and Engineering, University of Yamanashi, 1110 Shimokato, Chuo City, Yamanashi 409-3898, Japan
e-mail: nobuot@shinshu-u.ac.jp

Y. Saitoh • N. Ohno • S. Ohno
Department of Anatomy and Molecular Histology, Interdisciplinary Graduate School of Medicine and Engineering, University of Yamanashi, 1110 Shimokato, Chuo City, Yamanashi 409-3898, Japan

S. Ohno et al. (eds.), *In Vivo Cryotechnique in Biomedical Research and Application for Bioimaging of Living Animal Organs*, DOI 10.1007/978-4-431-55723-4_44

microscopic analyses of SO_2 would probably reflect the functional living states of animal organs in the order of milliseconds. Therefore, various samples of human whole blood under different gas conditions and also living mouse tissues prepared with IVCT were examined by confocal Raman microscopy at low temperature, referred to as "Raman cryomicroscopy." Precise methods and results have been reported in the previous paper [8].

44.2 Raman Spectra of Human Whole Blood (HWB) Under Various Levels of Oxygen Saturation

As a model to evaluate oxygen saturation for Raman spectroscopy at low temperature, the RR spectra of the frozen HWB were analyzed on a temperature-controllable stage at –150 °C with Raman microscopy. A 458 nm wavelength HeNe laser was focused at a part of each frozen specimen on the cryostage with a bright-field microscope. Patterns of the RR shifts were clearly recognized around 1355 and 1378 cm^{-1} (Fig. 44.1a). Relating to the increase of SO_2, the 1378 and 1355 cm^{-1} Raman shift peaks became higher (Fig. 44.1a). By collecting some samples in a scatter plot, amounts of erythrocyte SO_2 and the ratios of two shift areas were closely correlated with each other statistically. Thus, the SO_2 of erythrocytes can be relatively calculated by comparison of the two RR shifts.

44.3 Raman Spectra of Blood Vessels in Living Mouse Intestines

The small intestines with IVCT [9] were analyzed with confocal Raman cryomicroscopy (Fig. 44.1b). Blood vessels were exposed by freeze-fractured with a cooled scalpel ((ii) in Fig. 44.1b). Their intestinal mesenteries and serous membranes contain many typical small arteries and veins. The shift peaks around 1355 and 1378 cm^{-1} of the frozen intestinal tissues completely matched the RR shifts of HWB, indicating a common characteristic in all animal hemoglobin molecules [10].

Under a light microscope, some branches of the small arteries and arterioles were identified as bright red color images (Fig. 44.1c), and Raman shifts in the blood vessels were analyzed with confocal Raman cryomicroscopy. In some arterial vessels, depending on the peripheral distance from one point of an artery, area ratios of the two shift peaks changed (Fig. 44.1d); the 1378 cm^{-1} Raman shift peaks decreased with distance compared to the 1355 cm^{-1} ones. Thus, it was possible to obtain Raman spectra of frozen tissue samples at low temperature, indicating the SO_2 of flowing erythrocytes.

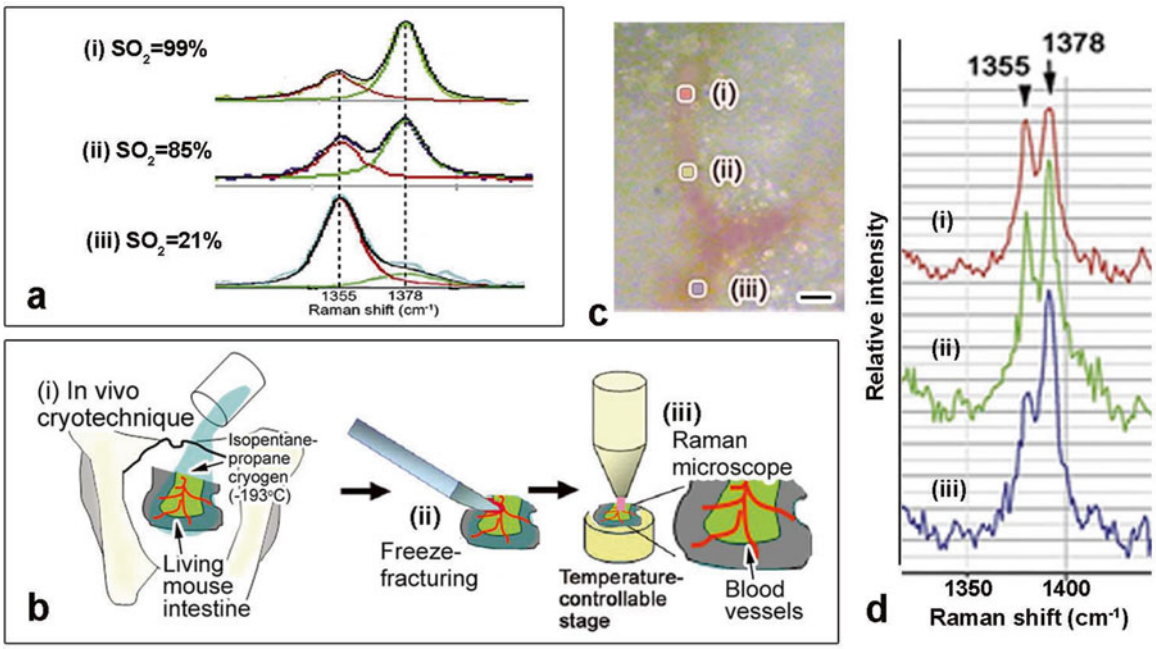

Fig. 44.1 (**a**) Raman spectra of human whole blood at low temperature (–150 °C) under different SO_2 conditions. (**b**) Schematic representation of Raman cryomicroscopy for living mouse intestines, prepared with in vivo cryotechnique (IVCT). (**c**, **d**) For IVCT mouse small intestinal serous membranes, three points of a blood vessels are selected with a light microscope (**c**), and Raman spectra are analyzed (**d**). Precise data have been reported in the previous paper (Terada et al. [8]). *Bars*: 10 μm

44.4 Raman Spectra of Blood Vessels in Living Mouse Livers

The liver tissues frozen with IVCT were also examined to verify the RR spectra in blood vessels at low temperature. With confocal Raman cryomicroscopy, two shifts around 1355 and 1378 cm^{-1} were detected in the blood vessels of liver tissues, as prepared by IVCT, under the normal circulation. The Raman spectra were also compared in two neighboring blood vessels. Judging from the relative area ratios of 1355 and 1378 cm^{-1} RR shifts, the SO_2 in the hepatic blood vessels was much lower than that in the mesenteric arterioles. However, in blood vessels of the hypoxic areas after blood circulation stopped, the peak of the 1378 cm^{-1} RR shift was completely lost in both blood vessels, indicating much lower levels of SO_2 in the flowing erythrocytes under hypoxia.

By mapping the typical 1355 and 1378 cm^{-1} RR spectrum shifts, only inside the blood vessels, including hepatic sinusoids, was positive for the RR spectrum shifts, indicating that the RR shifts were specific for the SO_2 of erythrocytes.

44.5 Concluding Remarks

The technical combination of IVCT with confocal Raman cryomicroscopy enabled us to make direct analyses of the flowing erythrocyte SO_2 in blood vessels of living mouse organs.

References

1. Shelnutt JA, Rousseau DL, Friedman JM, Simon SR (1979) Protein–heme interaction in hemoglobin: evidence for Raman difference spectroscopy. Proc Natl Acad Sci U S A 76:4409–4413
2. Wood BR, Tait B, McNaughton D (2001) Micro-Raman characterization of the R to T state transition of haemoglobin within a single living erythrocyte. Biochim Biophys Acta 1539:58–70
3. Nighswander-Rempel SP, Anthony-Shaw R, Mansfield JR, Hewko M, Kupriyanov VV, Mantsch HH (2002) Regional variations in myocardial tissue oxygenation mapped by near-infrared spectroscopic imaging. J Mol Cell Cardiol 34:1195–1203
4. Cote GL (2001) Noninvasive and minimally-invasive optical monitoring technologies. J Nutr 131:1596–1604
5. Terada N, Ohno N, Saitoh S, Fujii Y, Ohguro H, Ohno S (2007) Raman microscopy of freeze-dried mouse eyeball-slice in conjunction with the "in vivo cryotechnique". Microsc Res Tech 70:634–639
6. Torres Filho IP, Terner J, Pittman RN, Somera LG, Ward KR (2005) Hemoglobin oxygen saturation measurements using resonance Raman intravital microscopy. Am J Physiol Heart Circ Physiol 289:H488–H495
7. Ondrias MR, Rousseau DL, Simon SR (1981) Structural changes at the heme induced by freezing hemoglobin. Science 213:657–659
8. Terada N, Ohno N, Saitoh S, Ohno S (2008) Application of "in vivo cryotechnique" to detect erythrocyte oxygen saturation in frozen mouse tissues with confocal Raman cryomicroscopy. J Struct Biol 163:147–154
9. Ohno S, Terada N, Fujii Y, Ueda H, Takayama I (1996) Dynamic structure of glomerular capillary loop as revealed by an in vivo cryotechnique. Virchow's Arch 427:519–527
10. Igarashi J, Sato A, Kitagawa T, Sagami I, Shimizu T (2003) CO binding study of mouse heme-regulated eIF-2a kinase: kinetics and resonance Raman spectra. Biochim Biophys Acta 1650:99–104

Part VI
Future Development for Human Pathology

Imaging of Thrombosis and Microcirculation in Mouse Lungs of Initial Melanoma Metastasis

45

Yurika Saitoh, Nobuo Terada, Nobuhiko Ohno, and Shinichi Ohno

Abstract

Microscopic bioimaging of blood flow and distribution of cancer cells in lungs are essential to analyze mechanism of lung metastasis. Such cancer metastasis has been well known to induce hypercoagulable states and thrombosis. In histopathological tissue sections, however, it has been difficult to capture rapid phenomenon of thrombus formation due to technical problems associated with much less retention of soluble serum components as well as dynamic histological features reflecting their living states. In this part, to develop the cryotechnique for human pathology, we achieved bioimaging of both hypercoagulable states and thrombosis induced by early metastasis of mouse B16-BL6 melanoma. Thus, to examine plasma flow with fluorescence emission, glutathione-coated quantum dots (QDs) were subsequently injected after melanoma cells via right ventricles. At 5 s after the melanoma injection, melanoma cells were mostly stacked and intruded in alveolar capillaries with changing their shapes. Platelets aggregated around the stacked melanoma cells at 5 min. Such aggregated platelets were partially activated because of phosphorylated tyrosine 418 and 527 of Src on paraffin sections. Fibrin monomers and fibrinogens were also immunolocalized around stacked melanoma cells, indicating initial thrombus formation. In those areas, QDs were rarely detected, probably because of the lack of blood supply. Thus, IVCT revealed histopathological features of initial thrombosis under their circulatory conditions.

Keywords

Lung metastasis • Disseminated intravascular coagulation • Fibrinogen/fibrin • Platelet

45.1 Introduction

It is well known that metastatic cancer cells easily induce hypercoagulable states including platelet aggregation, which are closely related to subsequent tumor progression, such as cell proliferation and angiogenesis [1–3]. In addition to the platelets, some cancer cells were also demonstrated to produce coagulation factors, such as thrombin and tissue factors [4–6]. Clinically, the hypercoagulable state of humans due to cancer progression often causes disseminated intravascular coagulation (DIC) [4, 7]. DIC is usually confirmed by blood and plasma tests of patients, indicating decreases of fibrinogen and platelet count and/or increases of D-dimer,

Y. Saitoh (✉) • N. Ohno • S. Ohno
Department of Anatomy and Molecular Histology, Interdisciplinary Graduate School of Medicine and Engineering, University of Yamanashi, 1110 Shimokato, Chuo City, Yamanashi 409-3898, Japan
e-mail: yurikas@yamanashi.ac.jp

N. Terada
Division of Health Sciences, Shinshu University Graduate School of Medicine, 3-1-1 Asahi, Matsumoto City, Nagano 390-8621, Japan

Department of Anatomy and Molecular Histology, Interdisciplinary Graduate School of Medicine and Engineering, University of Yamanashi, 1110 Shimokato, Chuo City, Yamanashi 409-3898, Japan

S. Ohno et al. (eds.), *In Vivo Cryotechnique in Biomedical Research and Application for Bioimaging of Living Animal Organs*, DOI 10.1007/978-4-431-55723-4_45

fibrinogen-degradation products, and soluble fibrin monomer [8]. In particular, the level of soluble fibrin monomer is an indicator of initial blood coagulation because it is the first product of fibrinogen cleaved by thrombin [9]. Such soluble fibrin monomers are also reported to enhance activated platelet adhesion to cancer cells, which was additionally confirmed by an increase of the lung metastasis of cancer cells pretreated with soluble fibrin [10]. To detect the soluble fibrin monomers in plasma in vitro, a monoclonal antibody was developed, which reacted to the conformation site of fibrinogen cleaved by thrombin [11]. However, for microscopic analyses of tissue sections, because most soluble components and molecular structures in blood vessels were readily removed or changed during tissue preparation with conventional chemical fixation methods, we visualized such functional areas and evaluated the timing of initial thrombus formation with "in vivo cryotechnique" (IVCT).

45.2 Visualization of Thrombus in Lungs Induced by Cancer Cells Within Five Minutes

To visualize thrombus, we injected mouse melanoma cells into right ventricles of anesthetized mice. At 5 s after the injection of melanoma cells, initial entry into lung blood vessels was clearly detected in large blood vessels and parts of alveolar capillaries with dynamically changing their shapes within a few seconds (Fig. 45.1a). Blood vessels were filled with many flowing erythrocytes (white arrows in Fig. 45.1a). At 1 min, some melanoma cells were attached to endothelial walls of large blood vessels (black arrowheads in Fig. 45.1b), and some platelets got stacked. At this stage, fluorescence probe, quantum dots (QDs), injected into right ventricles to check blood circulation [12, 13], were detected in all blood vessels. At 5 min after the melanoma cell injection, variously formed states of thrombosis appeared in many large blood vessels of living mouse lungs. In some blood vessels, melanoma cells were accompanied by larger aggregates of platelets (white arrowheads in Fig. 45.1c, e) with congested erythrocytes (black double-arrowheads in Fig. 45.1c, e). In some areas, many platelets also accumulated (white arrowheads in Fig. 45.1d, f) and aggregated in larger blood vessels (white double-arrowheads in Fig. 45.1d, f). The congested erythrocytes were disproportionately located in such large blood vessels. Thus, the initial molecular structures of thrombus formation usually accompanied by melanoma cell metastasis were clearly visualized in HE-stained paraffin sections, reflecting the living state of mouse lungs. However, QDs were rarely detected in other areas of blood vessels, which contained large erythrocyte aggregates (Fig. 45.1e). The QD-fluorescence intensity was inversely correlated to the platelet aggregation density, as seen in the differential interference contrast image. In the spotty areas, where flowing platelets were loosely gathered (white arrowhead in Fig. 45.1d, f), QDs were still detected around the stacked

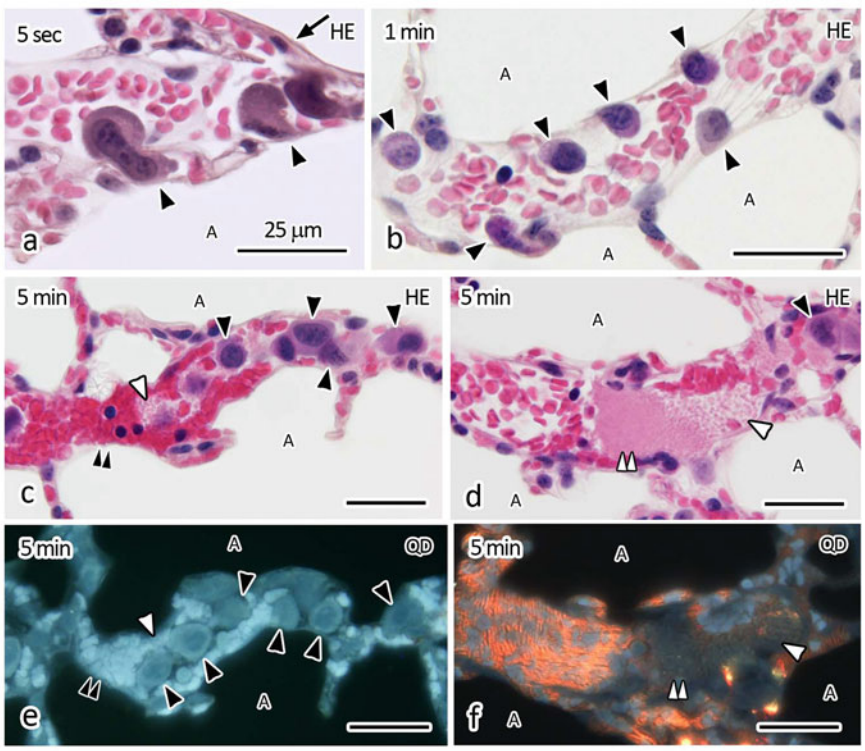

Fig. 45.1 Mouse lung tissues prepared by IVCT at 5 s (**a**), 1 min (**b**), and 5 min (**c**–**f**) after the melanoma cell injection. HE-stained morphological features (HE; **a**–**d**) and distributions of QDs (QD; **e**, **f**). The section showing the red QD-fluorescence images with ultraviolet light (QD; **e**, **f**) is next to the serial paraffin section showing the HE-stained image (**c**, **d**). *Black arrow*: visceral pleura, Black *arrowheads*: melanoma cells with large nuclei, *White arrowheads*: grouping platelets, *Black double-arrowheads*: congested erythrocytes, *White double-arrowheads*: large platelet aggregates occupy their lumens, *A*: air space. Bars: 25 µm

platelets. In contrast, in other areas where they compactly aggregated (white double-arrowheads in Fig. 45.1d, f), the QD-fluorescence intensity was weaker than that in the areas where platelets were loosely gathered. These results suggest that IVCT revealed the initial morphology of thrombus formation, sometimes accompanied by later failure of blood circulation.

45.3 Visualization of Platelet Activation at Five Minutes

Next, to evaluate the molecular cascade activation of platelets for signal transduction, the phosphorylation of Src was immunohistochemically examined. Platelets have been well documented to possess large amounts of Src-family kinases [14, 15], which generally have two phosphorylation sites of tyrosine (Y), Y418 and Y527 [16]. It has already been reported that the combination of Y418 phosphorylation and Y527 dephosphorylation indicates the full activation of Src, whereas another combination of both Y418 and Y527 phosphorylation indicates partial Src activation [14]. To confirm the existence of Src molecules in the present aggregated platelets, we performed immunostaining for Src. At 5 min after the melanoma cell injection, large masses of platelet aggregates (white double-arrowheads in Fig. 45.2a) were strongly immunopositive for Src in some blood vessels (black arrows in Fig. 45.2a). Such platelet aggregates were also fluorescently immunostained with anti-phosphorylated-Y418 (p418) antibody (green in Fig. 45.2d) inside the red fluorescence contours of platelets immunostained for CD42c (white arrowheads in Fig. 45.2d). Thus, it is suggested that Src-family kinases in the aggregated platelets were mostly in active molecular states. On the other hand, phosphorylation of Y527-Src (p527) was still detected in the aggregated platelets (black arrows in Fig. 45.2b). Many aggregated platelets were double immunopositive for both Y418 and Y527 phosphorylations. These findings indicate that Src in the aggregated platelets started partial activation at 5 min after the melanoma cell injection.

45.4 Visualization of Fibrin Formation in Paraffin Sections

To verify such formation of fibrin thrombus, a specific antibody against fibrin monomer, F405 antibody, was used for immunohistochemistry in the lung tissues at 5 min after the melanoma cell injection. Fibrin monomers are the earliest reaction products of fibrin molecules derived from fibrinogen, and the F405 antibody is a specific monoclonal antibody against them, which has been clinically used for enzyme-linked immunosorbent assay (ELISA) as highly sensitive detection of DIC for human plasma samples [11]. Common microwave treatment in citrate buffer was essential to obtain immunoreactivity for the F405 antibody in paraffin-embedded tissue sections, even for the IVCT-FS-prepared samples. Serial paraffin sections of IVCT-prepared lung tissues, in which QDs had already been injected at 5 min after the melanoma cell injection, were immunostained for the fibrin monomer and fibrinogen (Fig. 45.3). In some large blood vessels stacked with melanoma cells (arrowheads in Fig. 45.3a), fluorescent QDs red in color were rarely detected (Fig. 45.3c). However, in other alveolar capillaries connecting with large

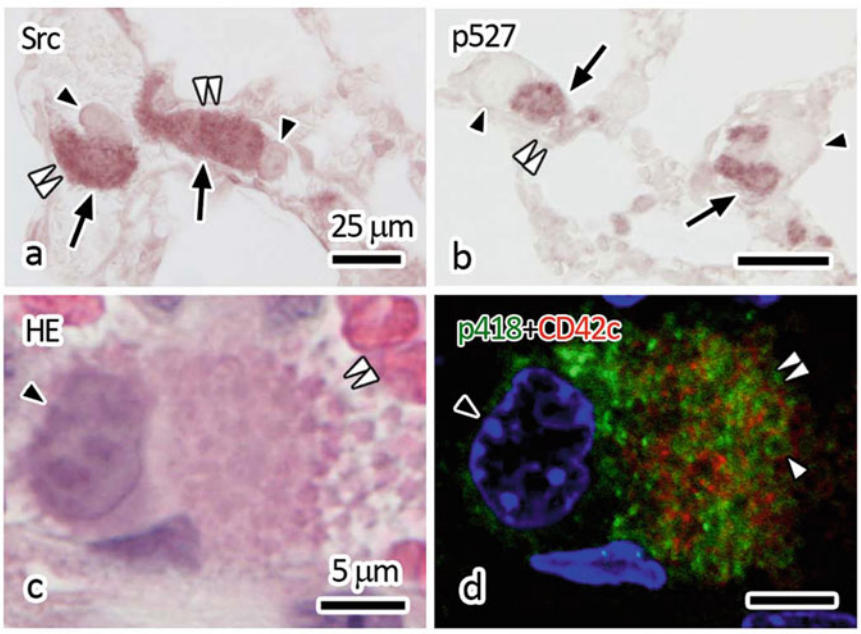

Fig. 45.2 Immunostaining images of Src (**a**) and p527-Src (**b**) and double fluorescent immunostaining image of p418-Src (*green* in **d**) and CD42c (*red* in **d**) with nuclear DAPI staining (*blue* in **d**). (**c**, **d**) The tissue sections were firstly immunostained and observed under a confocal laser scanning microscope (**d**) and subsequently stained with HE and observed under a light microscope (**c**). *Black arrowheads*: melanoma cells, *Black arrows*: immune-positive reaction, *White double-arrowheads*: platelet aggregations, *White arrowhead*: immunopositive regions for p418-Src inside platelet cell membranes shown by the CD42c immunostaining. Bars: 25 μm in (**a**, **b**), 5 μm in (**c**, **d**)

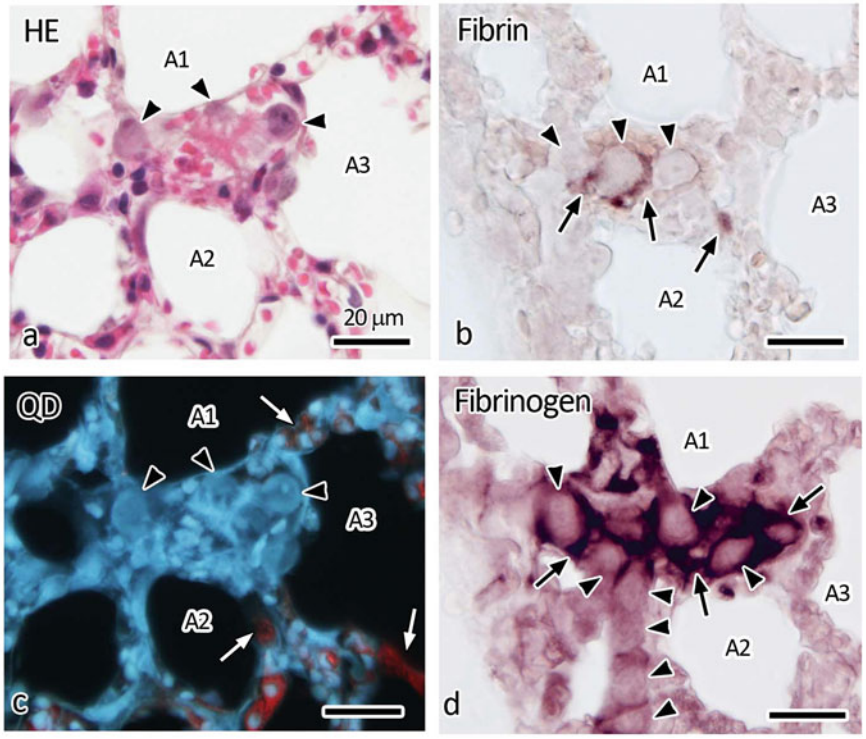

Fig. 45.3 Light microscopic images of living mouse lung tissues at 5 min after the melanoma cell injection. Serial sections are HE stained (**a**) and detected for QDs under UV light (**c**) or immunostained for fibrin with F405 antibody (**b**) and fibrinogen (**d**). *Black arrows*: immune-positive reaction, *Black arrowheads*: melanoma cells, *White arrows*: red fluorescent signals derived from QDs detected in some parts of alveolar capillaries connecting larger blood vessels, *A1–A3*: air spaces in alveoli. Bars: 20 µm

blood vessels, QDs were clearly observed (white arrows in Fig. 45.3c). The fibrin immunostaining was often detected as spotty patterns between melanoma cells in the large blood vessels (black arrows in Fig. 45.3b). In the blood vessels, where fibrin was positively immunostained, the immunoreaction intensity of fibrinogen was very strongly detected (black arrows in Fig. 45.3d). The antibody against fibrinogen recognized fibrin and fibrinogen immunoreaction was widely positive in all fibrin-immunopositive areas, suggesting initiation of fibrin formation. Thus, the initial compact products of fibrin thrombus as well as fibrinogen accumulation were morphofunctionally visualized in the blood vessels of melanoma cell metastasis by IVCT.

45.5 Conclusion

Recently, bioimages of cancer cell invasion and proliferation in living animal bodies have been clearly demonstrated with some intravital imaging techniques [17, 18]. Therefore, the present bioimaging technique with IVCT could provide information on the mechanisms of thrombosis and hemostasis in tissue sections reflecting living states, which will be compatible with intravital imaging of living animal lungs. It has been supposed that temporary adhesion of cancer cells to blood vessel walls usually occurs in a couple of seconds, as revealed by a live-imaging technique [19]. In the present study, within 5 s of the melanoma cell injection, rapid histological events such as the intrusion and stacking of melanoma cells in blood vessels, probably reflecting their temporal attachment to the blood vessel walls, were quickly captured. In another report concerning the stable adhesion of cancer cells to the vascular walls, colon cancer cells needed more than 10 s [19]. In our study, at 1 min after the melanoma cell injection, stacking and attachment of melanoma cells within blood vessels were clearly detected, it would be very significant to compare them with those revealed by the live-imaging technique. This text is mainly quoted from Reference [20].

References

1. Hilgard P (1973) The role of blood platelets in experimental metastases. Br J Cancer 28:429–435
2. Holmes CE, Levis JE, Ornstein DL (2009) Activated platelets enhance ovarian cancer cell invasion in a cellular model of metastasis. Clin Exp Metastasis 26:653–661
3. Manegold PC, Hutter J, Pahernik SA, Messmer K, Dellian M (2003) Platelet-endothelial interaction in tumor angiogenesis and microcirculation. Blood 101:1970–1976
4. Bambace NM, Holmes CE (2011) The platelet contribution to cancer progression. J Thromb Haemost 9:237–249
5. Jain S, Harris J, Ware J (2010) Platelets: linking hemostasis and cancer. Arterioscler Thromb Vasc Biol 30:2362–2367
6. Jurasz P, Alonso-Escolano D, Radomski MW (2004) Platelet–cancer interactions: mechanisms and pharmacology of tumour cell-induced platelet aggregation. Br J Pharmacol 143:819–826

7. Kvolik S, Jukic M, Matijevic M, Marjanovic K, Glavas-Obrovac L (2010) An overview of coagulation disorders in cancer patients. Surg Oncol 19:e33–e46
8. Munter G, Hershko C (2001) Increased warfarin sensitivity as an early manifestation of occult prostate cancer with chronic disseminated intravascular coagulation. Acta Haematol 105:97–99
9. Budzynski AZ, Olexa SA, Pandya BV (1983) Fibrin polymerization sites in fibrinogen and fibrin fragments. Ann N Y Acad Sci 408:301–314
10. Biggerstaff JP, Seth N, Amirkhosravi A, Amaya M, Fogarty S, Meyer TV, Siddiqui F, Francis JL (1999) Soluble fibrin augments platelet/tumor cell adherence in vitro and in vivo, and enhances experimental metastasis. Clin Exp Metastasis 17:723–730
11. Hamano A, Tanaka S, Takeda Y, Umeda M, Sakata Y (2002) A novel monoclonal antibody to fibrin monomer and soluble fibrin for the detection of soluble fibrin in plasma. Clin Chim Acta 318:25–32
12. Terada N, Saitoh Y, Saitoh S, Ohno N, Jin T, Ohno S (2010) Visualization of microvascular blood flow in mouse kidney and spleen by quantum dot injection with "in vivo cryotechnique". Microvasc Res 80:491–498
13. Saitoh Y, Terada N, Saitoh S, Ohno N, Jin T, Ohno S (2012) Histochemical analyses and quantum dot imaging of microvascular blood flow with pulmonary edema in living mouse lungs by "in vivo cryotechnique". Histochem Cell Biol 137:137–151
14. Newman DK (2009) The Y's that bind: negative regulators of Src family kinase activity in platelets. J Thromb Haemost 7(Suppl 1):195–199
15. Severin S, Nash CA, Mori J, Zhao Y, Abram C, Lowell CA, Senis YA, Watson SP (2012) Distinct and overlapping functional roles of Src family kinases in mouse platelets. J Thromb Haemost 10:1631–1645
16. Terada N, Saitoh Y, Ohno N, Komada M, Saitoh S, Peles E, Ohno S (2012) Essential function of protein 4.1G in targeting of membrane protein palmitoylated 6 into Schmidt-Lanterman incisures in myelinated nerves. Mol Cell Biol 32:199–205
17. Condeelis J, Seqall JE (2003) Intravital imaging of cell movement in tumours. Nat Rev Cancer 3:921–930
18. Winkler F, Kienast Y, Fuhrmann M, Von Baumgarten L, Burgold S, Mitteregger G, Kretzschmar H, Herms J (2009) Imaging glioma cell invasion in vivo reveals mechanisms of dissemination and peritumoral angiogenesis. Glia 57:1306–1315
19. Gassmann P, Kang ML, Mees ST, Haier J (2010) In vivo tumor cell adhesion in the pulmonary microvasculature is exclusively mediated by tumor cell–endothelial cell interaction. BMC Cancer 10:177
20. Saitoh Y, Terada N, Ohno N, Hamano A, Okumura N, Jin T, Saiki I, Ohno S (2014) Imaging of thrombosis and microcirculation in mouse lungs of initial melanoma metastasis with in vivo cryotechnique. Microvasc Res 91:73–83

Differential Distribution of Blood-Derived Proteins in Xenografted Human Adenocarcinoma Tissues

46

Yuqin Bai, Nobuhiko Ohno, Nobuo Terada, and Shinichi Ohno

Abstract

Tumor behavior depends on the complex tumor interstitium and microenvironment, which influence transport of fluid and soluble molecules from blood vessels. The purpose of this study was to reveal how complex tumor tissues affect the immunodistribution of serum proteins and time-dependent translocation of bovine serum albumin (BSA) from blood vessels, using relatively differentiated human adenocarcinoma produced by the xenografted A549 cell line. Histological architecture and immunodistribution of the serum proteins in adenocarcinomatous tissues were clearly detected by the in vivo cryotechnique and cryobiopsy. Both albumin and IgG1 were detected in blood vessels, connective tissues around the tumor mass, and the interstitium among tumor cell nests. IgM was mainly detected in blood vessels and connective tissues around the tumor mass but was not detected in the interstitium among the tumor cell nests. At 10 or 30 min after BSA injection, BSA was observed only in blood vessels, but 1 h after the injection, it was also detected in the interstitium and surrounding connective tissues of the tumor mass. The present findings showed topographic variation of molecular permeation in the adenocarcinomatous tumor mass. The interstitial tissues with augmented permeability of serum proteins would increase accessibility of tumor cells to blood-derived molecules.

Keywords

Immunodistribution • In vivo cryotechnique • Interstitium • Serum proteins • Xenografted adenocarcinoma tissue

Y. Bai, M.D., Ph.D. (✉)
Department of Anatomy and Molecular Histology, Interdisciplinary Graduate School of Medicine and Engineering, University of Yamanashi, 1110 Shimokato, Chuo City, Yamanashi 409-3898, Japan

Department of Pathology, Medical College of Chifeng University, Ying Bin Road, Chifeng 024000, Inner Mongolua, People's Republic of China
e-mail: baiyuqincn2000@aliyun.com

N. Ohno • S. Ohno
Department of Anatomy and Molecular Histology, Interdisciplinary Graduate School of Medicine and Engineering, University of Yamanashi, 1110 Shimokato, Chuo City, Yamanashi 409-3898, Japan

N. Terada
Division of Health Sciences, Shinshu University Graduate School of Medicine, 3-1-1 Asahi, Matsumoto City, Nagano 390-8621, Japan

Department of Anatomy and Molecular Histology, Interdisciplinary Graduate School of Medicine and Engineering, University of Yamanashi, 1110 Shimokato, Chuo City, Yamanashi 409-3898, Japan

S. Ohno et al. (eds.), *In Vivo Cryotechnique in Biomedical Research and Application for Bioimaging of Living Animal Organs*, DOI 10.1007/978-4-431-55723-4_46

46.1 Introduction

Tumor behavior, such as development, progression, and metastasis, is affected by the complex tumor interstitium and the microenvironment, which are determined by various factors, including matricial structures, blood or lymphatic vasculature, and interstitial cells [1, 2]. The transport mechanism of soluble molecules from blood vessels through interstitial spaces has been examined using various extrinsic components circulating in the blood vessels [3, 4]. Diffusion of macromolecules varies among different types of tumors or their surrounding microenvironments [3, 5], and it remained to be elucidated how histological architecture and tumor differentiation affect the molecular transport from blood vessels into tumor tissues. Immunohistochemical analyses of serum proteins in a relatively differentiated human adenocarcinoma produced by the xenografted A549 cell line were performed with IVCT.

46.2 Immunolocalization of Intrinsic Serum Proteins in Xenografted Lung Adenocarcinoma Tissue

Figure 46.1 showed the clear immunodistribution in vivo of serum proteins in different tissue areas of the adenocarcinomatous tumor mass. In particular, molecular permeation through interstitial connective tissues exhibited topographic variations in the case of IgG1 or IgM, suggesting more complex interactions of adenocarcinomatous cells and their interstitial matrix, which probably modulate local microenvironments [6, 7]. In contrast, mouse albumin, with small molecular weight, was easily distributed throughout the tumor tissues. The transport mechanism of serum proteins throughout the interstitial matrix of tumor tissues would be associated with matrix structures, molecular size and charge of soluble components, and vascular architecture.

46.3 Immunodistribution of Extrinsic BSA in Xenografted Lung Adenocarcinoma Tissue

The examination of the injected BSA is important to know how soluble serum components pass through blood vessels and diffuse into the tumor connective tissues. BSA was mostly immunolocalized within blood vessels in 10 and 30 min after injection (see Fig. 46.2d–i), but it was diffusely immunolocalized throughout the tumor interstitium in 1 h. Our findings in the present study were nearly in agreement with some previous data shown by live imaging with intravital or confocal laser scanning microscopy [8], indicating that the BSA leaked out into the interstitial spaces quickly, within 1 h. Although another study reported that no difference of molecular leakage was seen among the different types of tumors [3], the relative rate of BSA leakage into the tumor interstitium might be significantly changed within the tumor tissues, which would partly depend on the different molecular structures of interstitial matrices and functions of blood vessels [9, 10] or variously elevated interstitial fluid pressures [11, 12]. This morphofunctional discrepancy in the tumor tissues was directly visualized by the injected BSA in living mice.

46.4 Concluding Remarks

Functional morphology of tumor cells or tissues and also immunolocalization of serum proteins were more clearly detected in the relatively differentiated human A549 adenocarcinoma by IVCT, which can more clearly reflect their living states in vivo. The present figures were already published in our paper, Med Mol Morphol (2011) 44:93–102, and cited with their permissions.

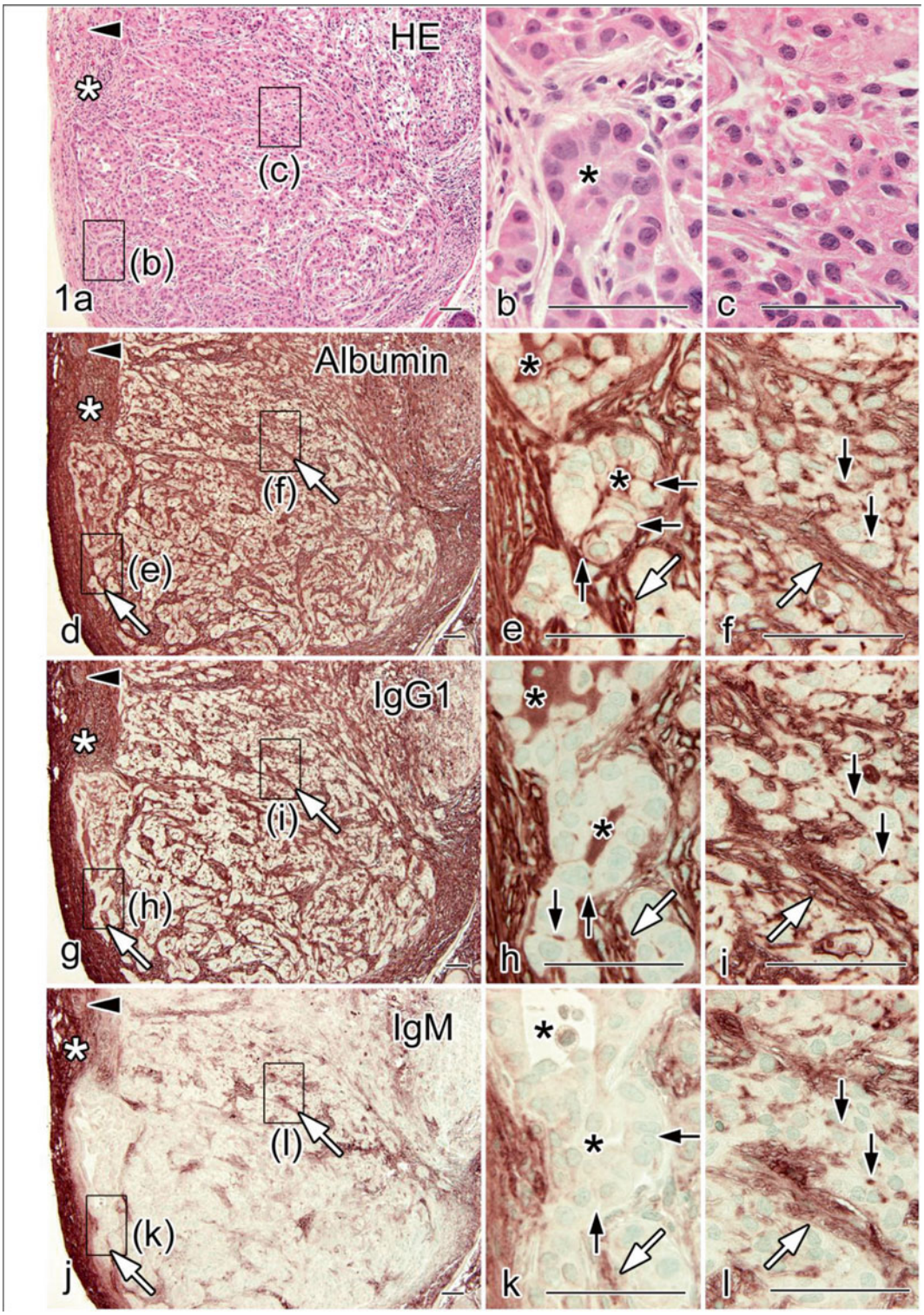

Fig. 46.1 Light micrographs of serial paraffin sections prepared by IVCT and stained with H&E (HE, **a**–**c**) or immunostained for albumin (**d**–**f**), immunoglobulin G1 (IgG1, **g**–**i**), or immunoglobulin M (IgM, **j**–**l**). Note different immunostaining intensities of serum proteins in the interstitium between tumor cells (**e**, **h**, **k**). In the tumor cell nests (**e**, **h**, **k**), albumin and IgG1 are more obviously immunolocalized (*black arrows*, **e** and **h**), as compared to IgM immunostaining (*black arrows*, **k**). (**f**, **i**, **l**) Immunoreactivities of albumin, IgG1, and IgM are detected in the interstitium between tumor cells (*black arrows*). (**d**–**l**) All three serum proteins are also immunolocalized in blood vessels (*arrowheads*) and connective tissues around the tumor mass (*white asterisks*), but different intensities of immunoreactivities for three proteins are seen in connective tissues invading beyond the tumor capsule (*white arrows*). *Black asterisks*, glandular organization. *Bars* 50 μm

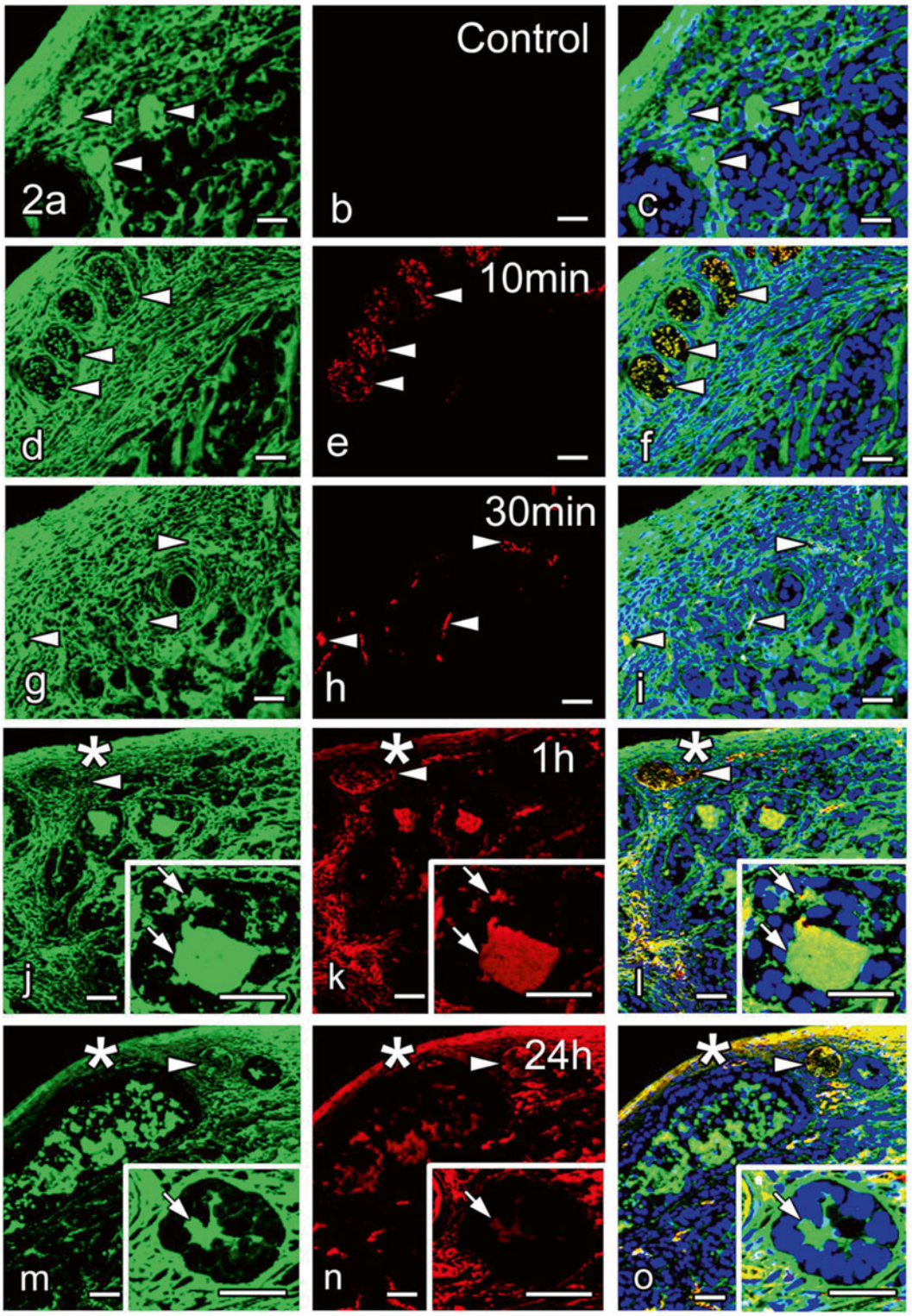

Fig. 46.2 Double-immunofluorescence micrographs of albumin (*green*) and intravenously injected bovine serum albumin (BSA) (*red*) with nuclear staining (Topro3; *blue*) in cryosections prepared by IVCT: control (**a**–**c**), and 10 min (**d**–**f**), 30 min (**g**–**i**), 1 h (**j**–**l**), or 24 h (**m**–**o**) after the BSA injection. *Arrowheads* indicate blood vessels. (**d**–**i)** In 10 and 30 min, BSA immunoreactivity is seen only in blood vessels (*arrowheads*). (**j**–**o)** In 1 and 24 h, however, it is also detected in the extracellular spaces between tumor cells (*small arrows* in *insets*) and connective tissues around the tumor mass (*asterisks*). *Bars* 60 μm

References

1. Jain RK (1987) Transport of molecules in the tumor interstitium: a review. Cancer Res 47(12):3039–3051
2. Liotta LA, Kohn EC (2001) The microenvironment of the tumor host interface. Nature (Lond) 411(6835):375–379
3. Netti PA, Berk DA, Swartz MA, Grodzinsky AJ, Jain RK (2000) Role of extracellular matrix assembly in interstitial transport in solid tumors. Cancer Res 60(9):2497–2503
4. Dreher MR, Liu W, Michelich CR, Dewhirst MW, Yuan F, Chilkoti A (2006) Tumor vascular permeability, accumulation, and penetration of macromolecular drug carriers. J Natl Cancer Inst 98(5):335–344
5. Pluen A, Boucher Y, Ramanujan S, McKee TD, Gohongi T, di Tomaso E, Brown EB, Izumi Y, Campbell RB, Berk DA, Jain RK (2001) Role of tumor–host interactions in interstitial diffusion of macromolecules: cranial vs. subcutaneous tumors. Proc Natl Acad Sci U S A 98(8):4628–4633
6. Bhowmick NA, Neilson EG, Moses HL (2004) Stromal fibroblasts in cancer initiation and progression. Nature 432(7015):332–337
7. Cunha GR, Hayward SW, Wang YZ, Ricke WA (2003) Role of the stromal microenvironment in carcinogenesis of the prostate. Int J Cancer 107(1):1–10
8. Jain RK (2012) Delivery of molecular and cellular medicine to solid tumors. Adv Drug Deliv Rev 64(Suppl):353–365
9. Jain RK (2003) Molecular regulation of vessel maturation. Nat Med 9(6):685–693
10. Tilki D, Kilic N, Sevinc S, Zywietz F, Stief CG, Ergun S (2007) Zon-especific remodeling of tumor blood vessels affects tumor growth. Cancer 110(10):2347–2362
11. Less JR, Posner MC, Boucher Y, Borochovitz D, Wolmark N, Jain RK (1992) Interstitial hypertension in human breast and colorectal tumors. Cancer Res 52(22):6371–6374
12. Yang AD, Bauer TW, Camp ER, Somcio R, Liu W, Fan F, Ellis LM (2005) Improving delivery of antineoplastic agents with antivascular endothelial growth factor therapy. Cancer 103(8): 1561–1570

Part VII
New Cryobiopsy Invention

Morphological and Histochemical Analysis of Living Mouse Livers by New "Cryobiopsy" Technique

47

Yasuhisa Fujii, Nobuhiko Ohno, Nobuo Terada, and Shinichi Ohno

Abstract

A new "cryobiopsy" (CB) technique has been invented and applied for mice livers in vivo without stopping their blood circulation. They were routinely freeze-substituted in acetone containing fixatives for light microscopy (LM) or freeze-fractured before freeze substitution for scanning electron microscopy (SEM). Serial paraffin sections were stained with hematoxylin-eosin (HE) or histochemical periodic acid-Schiff (PAS) reaction. By HE-staining, the tissue surface areas were often compressed and sinusoidal erythrocytes got aggregated side by side. But in a little deeper tissue areas, hepatic sinusoids were widely open with flowing erythrocytes. Lots of PAS-reaction products were well preserved in hepatocytes of the CB specimens. To the contrary, they were unevenly distributed in hepatocytes of conventionally quick-frozen specimens or often lost in those of conventional dehydrated specimens. By SEM, some cell organelles, open Disse's spaces, and bile canaliculi appeared under normal blood circulation samples. The new CB technique would be useful for examining time-dependent morphological changes of functioning organs, including the livers, from an identical living animal.

Keywords

Cryobiopsy • Freeze substitution • Quick freezing • PAS reaction • Scanning electron microscopy

47.1 Introduction

The conventional fixation and dehydration for light or electron microscopy give some effects on functional morphology or distribution of molecular components in living animal tissues. So, the conventional cryofixation techniques have been used for keeping the living animal's morphology [1–5] and improving the preservation of antigenicity and soluble ion localization [6–9]. But this technique has its own limitation, because animal tissues must be isolated from normal blood circulation to expose ischemic and anoxic conditions. The "in vivo cryotechnique" (IVCT) was already developed for analyzing the functioning states of living animal organs. We already reported that the flowing erythrocyte shapes in mouse hepatic sinusoids [10], large blood vessels [11], and red pulp of spleens [12] were clarified by the IVCT in

Y. Fujii, Ph.D. (✉) • N. Ohno • S. Ohno
Department of Anatomy and Molecular Histology, Interdisciplinary Graduate School of Medicine and Engineering, University of Yamanashi, 1110 Shimokato, Chuo City, Yamanashi 409-3898, Japan
e-mail: fujiiy@ntu.ac.jp

N. Terada
Division of Health Sciences, Shinshu University Graduate School of Medicine, 3-1-1 Asahi, Matsumoto City, Nagano 390-8621, Japan

Department of Anatomy and Molecular Histology, Interdisciplinary Graduate School of Medicine and Engineering, University of Yamanashi, 1110 Shimokato, Chuo City, Yamanashi 409-3898, Japan

S. Ohno et al. (eds.), *In Vivo Cryotechnique in Biomedical Research and Application for Bioimaging of Living Animal Organs*, DOI 10.1007/978-4-431-55723-4_47

combination with freeze substitution for SEM and functioning glomerular capillary loops [13], smooth muscle cells [14], and pulmonary alveoli of living mice [15] examined for transmission electron microscopy (TEM) or replica immunoelectron microscopy.

Recently, the IVCT combined with immunohistochemistry also became a new tool for analyzing serum protein leakage of mouse cerebellar capillaries [16] or serum protein passage through glomerular capillary loops by light microscopy [17]. The IVCT cannot get a series of time-dependent specimens from an identical mouse under different experimental conditions. The new "cryobiopsy" (CB) technique has been invented, by which we will get a series of liver tissues of living mice, prepared for freeze substitution in combination with SEM or LM.

47.2 Morphology of Living Mouse Livers Prepared by Different "Biopsy" Techniques

It has been known that the morphological changes caused by stopping blood circulation into animal organs depend on the time interval between tissue resection and conventional quick freezing [13]. The CB forcep metal cup precooled with liquid nitrogen was pinching off fresh mouse liver tissues [18]. They were freeze-substituted with acetone containing fixatives at about −80 °C for LM.

By HE-staining with the CB technique, well-frozen areas at a light microscopic level were obtained within 350–400 μm deep from the frozen tissue surface. In the upper surface areas, sinusoids were widely open and congested with erythrocytes (Fig. 47.1a, small arrows). However, in the deeper areas, central veins were widely open (Fig. 47.1a; CV). On the other hand, by common "biopsy" followed by quick freezing (Fig. 47.1d) or immersion fixation of resected tissues (Fig. 47.1e), sinusoidal cavities became collapsed with or without erythrocytes. By HE-staining of the CB specimens, hepatocyte nuclei were larger and the cytoplasm was heavily stained with eosin (Fig. 47.1a). In the quick-freezing specimens (Fig. 47.1d), the sinusoidal cavities were collapsed, and hepatocyte nuclei were also large, but eosin staining became weaker. By the common immersion fixation (Fig. 47.1e), hepatocytes got shrunken with extraction from their cytoplasm, and sinusoidal cavities were dramatically changed, but hepatocyte nuclei were also stained with the hematoxylin dye (Fig. 47.1e). Therefore, the CB technique would be a useful tool for examining functioning liver tissue.

47.3 PAS-Staining of Mouse Livers by Different "Biopsy" Techniques

For preparing the common "biopsy" and immersion-fixed specimens for light microscopy, extracellular and intracellular components were easily leaked out or moved with mechanical compression forces or dehydration and embedding steps [19]. In the CB specimens, PAS-reaction products were strongly and homogeneously recognized in the cytoplasm of hepatocytes (Fig. 47.1f–h). However, they were heterogeneously observed in the conventional quick-freezing (QF) liver hepatocyte cytoplasm (Fig. 47.1i, small arrows). On the other hand, by conventional immersion fixation and dehydration samples, PAS-reaction products were weakly observed in most of hepatocyte cytoplasm (Fig. 47.1j, small arrows). So, the CB technique would be a useful tool for examining soluble components.

47.4 Morphology of Living Mouse Livers by the CB Technique for SEM

By in vivo cryotechnique, the sinusoidal erythrocytes could be cryoimmobilized in vivo with various shapes in blood vessels, as reported before [10, 11]. At the initial contact surface of freeze-fractured CB liver tissues, some erythrocytes were compactly localized in the hepatic sinusoids and the Disse's space was not clearly open (Fig. 47.2a). To the contrary, open hepatic sinusoids and flowing erythrocytes were clearly observed in slightly deeper areas with Disse's spaces (Fig. 47.2b). The morphology of freeze-fractured hepatocytes showed nuclei, many globular mitochondria, and endoplasmic reticulum in their cytoplasm (Fig. 47.2c). At higher magnification, freeze-fractured mitochondria (M) and endoplasmic reticulum (ER) were clearly observed in the hepatocytes (Fig. 47.2c, inset). The Disse's spaces were covered with sinusoidal endothelium and hepatocyte surface with microvilli (Fig. 47.2c, asterisk). In some areas of Disse's spaces, hepatocyte cell membranes were slightly separated from each other, which reached deeper near bile canaliculi (Fig. 47.2c, small arrows). The CB samples

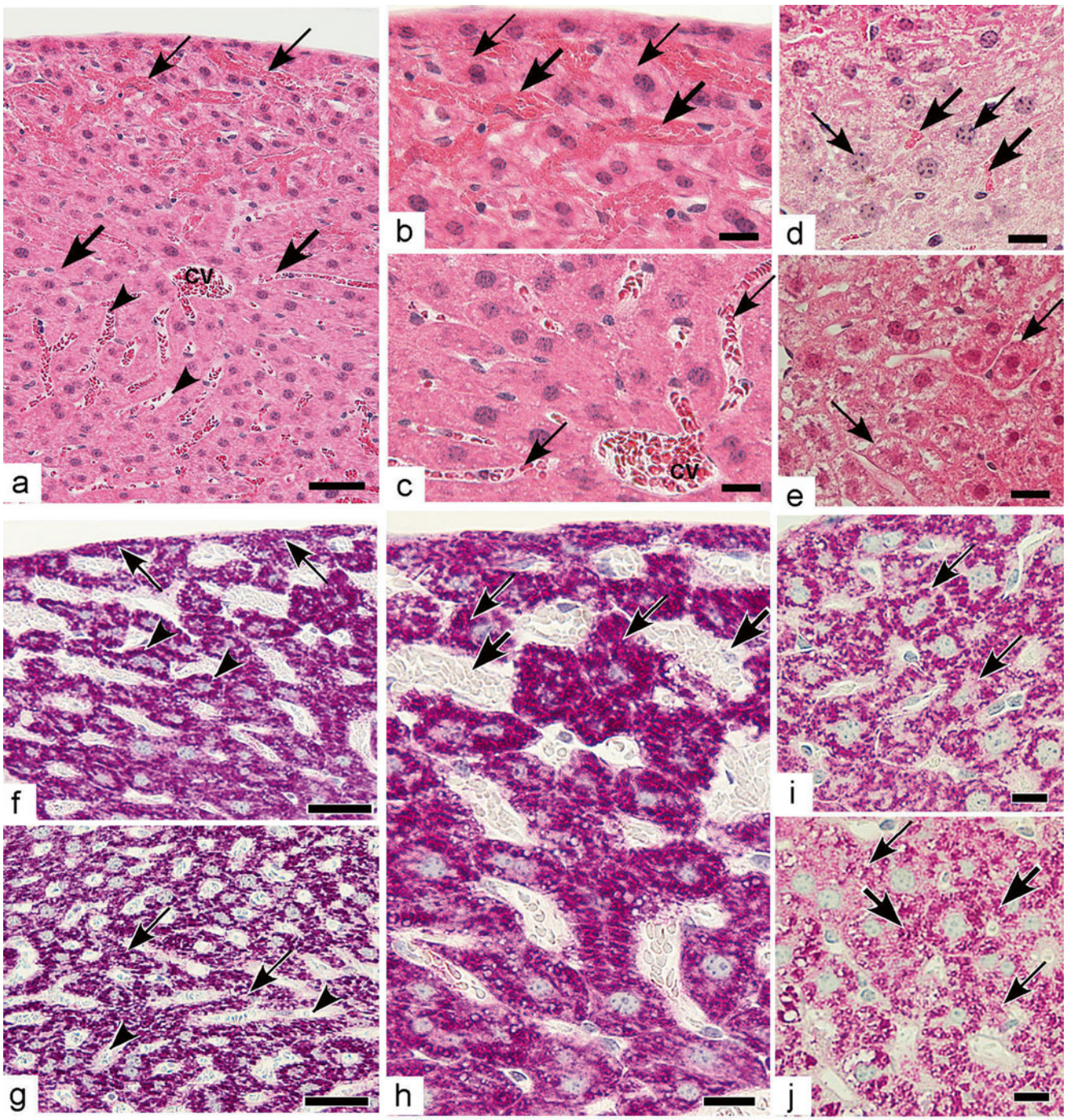

Fig. 47.1 Light micrographs of HE- and PAS-stained liver tissues by various preparation methods. With HE-stained CB liver tissues at surface area, congested erythrocytes are observed (**a**: *small arrows*, **b**: *large arrows*), but open sinusoidal space and flowing erythrocytes are observed in slightly deeper areas (**a**: *arrowheads*, **c**: *small arrows*, *CV* central vein). Eosin-stained congested erythrocytes (**d**: *large arrows*) and weak hematoxylin-stained large hepatocyte nuclei are observed by the QF liver tissues (**d**: *small arrows*). HE-stained hepatocyte cytoplasm along cell membranes is observed by the IF liver tissue (**e**: *arrows*). PAS-reaction products are strongly and homogeneously observed throughout the hepatocyte cytoplasm in the surface area of CB specimen (**f**: *small arrows* and *arrowheads*, **h**: *small arrows*, **h**: *large arrows*; open sinusoid). In slightly deeper area of the CB specimen, hepatocellular cord with strong PAS-reaction products is clearly observed (**g**: *arrows*). Strong but heterogeneous PAS-reaction products are observed in the QF hepatocyte cytoplasm (**i**: *arrows*). Weakly and unevenly PAS-reaction products are observed in the IF hepatocytes (**j**: *small arrows*; weak, *large arrows*; strong). (**a**, **f**) and (**g**) Bars: 50 μm. (**b**, **c**, **d**, **e**, **h**, **i**) and (**j**) Bars: 20 μm (Adapted from Fujii et al. [18])

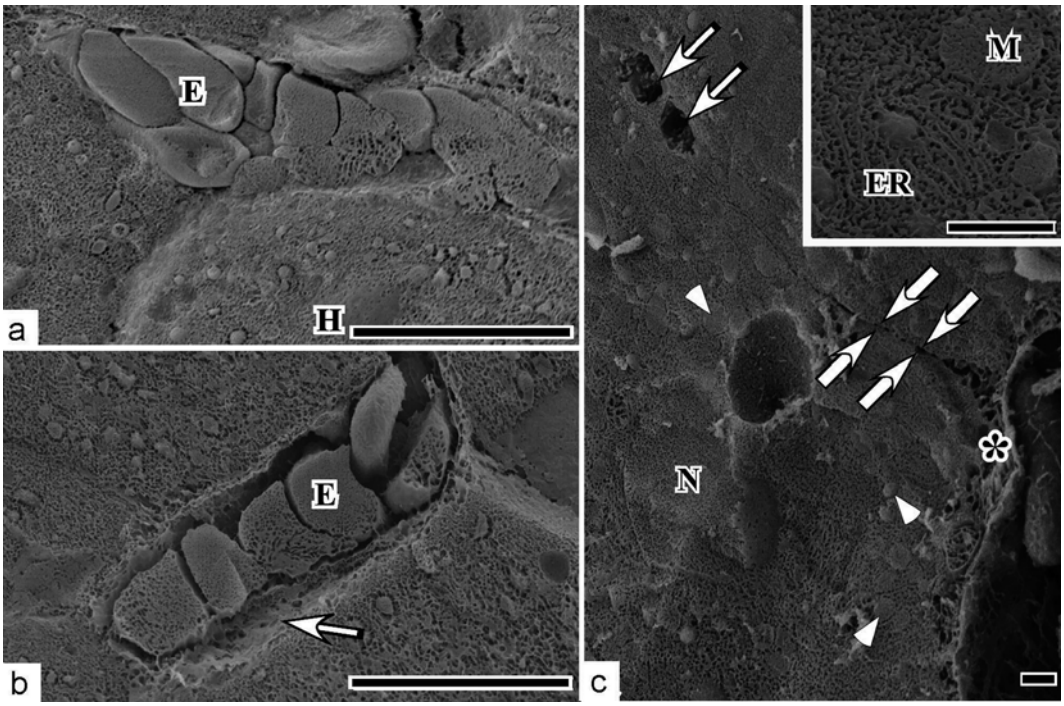

Fig. 47.2 Scanning electron micrographs of the CB specimens. At the surface areas, aggregated erythrocytes, which show no biconcave discoid shapes, are observed, but Disse's spaces are hardly recognized (**a**: *E* erythrocyte, *H* hepatocytes). In slightly deeper areas, erythrocytes are separated and Disse's spaces are clearly observed (**b**: *E* erythrocyte, *Arrow* Disse's space). Some globular cell organelles and Disse's spaces are observed under the normal blood circulation (**c**: *arrowheads*; globular cell organelles, *asterisk* and *large arrows*; Disse's spaces, *N* nucleus). The Disse's space reaches near bile canaliculi (**c**: *small arrows*). *Inset*: At higher magnification, abundant endoplasmic reticulum (ER) and freeze-fractured mitochondria (M) are clearly observed. (**a**) and (**b**) Scale bar = 10 μm. (**c**) Scale bar = 1 μm (Adapted from Fujii et al. [18])

applied to freeze-fracture technique for SEM, functioning three-dimensional structure, would be examined in living animal livers.

47.5 Concluding Remarks

By the "cryobiopsy" (CB) technique for living mouse tissues, which was combined with freeze substitution, we were able to examine morphological and histochemical observations with light or scanning electron microscopy. Moreover, only small specimens of living animals are cryofixed, so we can continue the time-dependent examination in an identical animal. So, the CB technique is a simple and powerful cryofixation tool to study functioning livers in the future.

References

1. Adrian M, Dubochet J, Lepault J, McDowall AW (1984) Cryo-electron microscopy of viruses. Nature 308:32–36
2. Studer D, Michel M, Wohlwend M, Hunziker EB, Buschmann M (1995) Vitrification of articular cartilage by high-pressure freezing. J Microsc 179:321–332
3. von Schack ML, Fakan S, Villiger W, Müller M (1993) Cryofixation and cryosubstitution: a useful alternative in the analyses of cellular fine structure. Eur J Histochem 37:5–18
4. Eggli P, Graber W (1994) Improved ultrastructural preservation of rat ciliary body after high pressure freezing and freeze substitution: a perspective view based upon comparison with tissue processed according to a conventional protocol or by osmium tetroxide/microwave fixation. Microsc Res Tech 29:11–22
5. Royer SM, Kinnamon JC (1996) Comparison of high-pressure freezing/freeze substitution and chemical fixation of catfish barbel taste buds. Microsc Res Tech 35:385–412
6. Monaghan P, Perusinghe N, Müller M (1998) High-pressure freezing for immunocytochemistry. J Microsc 192:248–258
7. Hernandez-Verdun D, Quintana C, Masson C, Gautier T, Arnoult J (1991) Cryofixation, cryosubstitution, cryo-embedding for visualizing of nuclear ultrastructure and for immunodetection in HeLa cells. Biol Cell 72:121–132
8. Somlyo AP, Bond M, Somlyo AV (1985) Calcium content of mitochondria and endoplasmic reticulum in liver frozen rapidly in vivo. Nature 314:622–625
9. Zierold K (1991) Cryofixation methods for ion localization in cells by electron probe microanalysis. J Microsc 161:357–366
10. Terada N, Kato Y, Fujii Y, Ueda H, Baba T, Ohno S (1998) Scanning electron microscopic study of flowing erythrocytes in hepatic sinusoids as revealed by 'in vivo cryotechnique'. J Electron Microsc 47:67–72
11. Xue M, Kato Y, Terada N, Fujii Y, Baba T, Ohno S (1998) Morphological study by an 'in vivo cryotechnique' of the shape of erythrocytes circulating in large blood vessels. J Anat 193:73–79

12. Xue M, Baba T, Terada N, Kato Y, Fujii Y, Ohno S (2001) Morphological study of erythrocyte shapes in red pulp of mouse spleens revealed by an in vivo cryotechnique. Histol Histopathol 16:123–129
13. Ohno S, Terada N, Fujii Y, Ueda H, Takayama I (1996) Dynamic structure of glomerular capillary loop as revealed by an in vivo cryotechnique. Virchows Arch 427:519–527
14. Takayama I, Terada N, Baba T, Ueda H, Kato Y, Fujii Y, Ohno S (1999) "In vivo cryotechnique" in combination with replica immunoelectron microscopy for caveolin in smooth muscle cells. Histochem Cell Biol 112:443–445
15. Takayama I, Terada N, Baba T, Ueda H, Fujii Y, Kato Y, Ohno S (2000) Dynamic ultrastructure of mouse pulmonary alveoli revealed by an in vivo cryotechnique in combination with freeze-substitution. J Anat 197:199–205
16. Zea-Aragon Z, Terada N, Ohno N, Fujii Y, Baba T, Ohno S (2004) Effects of anoxia on serum immunoglobulin and albumin leakage through blood–brain barrier in mouse cerebellum as revealed by cryotechniques. J Neurosci Methods 138:89–95
17. Li Z, Terada N, Ohno N, Ohno S (2005) Immunohistochemical analyses on albumin and immunoglobulin in acute hypertensive mouse kidneys by "in vivo cryotechnique". Histol Histopathol 20:807–816
18. Fujii Y, Ohno N, Li Z, Terada N, Baba T, Ohno S (2006) Morphological and histochemical analyses of living mouse livers by new 'Cryobiopsy' technique. J Electron Microsc 55:113–122
19. Pearse AGE (1980) Histochemistry: theoretical and applied. Churchill Livingstone, Edinburgh/London/New York

Recent Development of In Vivo Cryotechnique to Cryobiopsy for Living Animals

48

Nobuhiko Ohno, Nobuho Terada, and Shinichi Ohno

Abstract

Tissue resection or perfusion fixation in conventional procedures causes ischemic or anoxic artifacts. In vivo cryotechnique (IVCT) has been used to overcome these problems and study the distribution of soluble molecules without ischemic/anoxic artifacts at high time resolution. There are some limitations of IVCT; the target organs of living small animals need to be exposed, and tissues adjacent to the target organs are inevitably damaged by poured isopentane-propane cryogens. A new cryotechnique, "cryobiopsy," enables acquisition of tissue specimens of larger animals without anoxia/ischemia with technical advantages similar to those of IVCT. Live-imaging techniques could be complemented by IVCT and cryobiopsy, and cryofixation can preserve all components in frozen tissue specimens. Thus, IVCT and cryobiopsy followed by freeze substitution for light or electron microscopy will provide more precise morphofunctional information in vivo on tissue sections, and also they can be combined with other analytical methods, such as Raman microscopy, freeze-fracture replication, and X-ray microanalyses. The merits of IVCT and cryobiopsy will be underscored in the applications to other microscopic fields and experimental animal studies in clinical medicine.

Keywords

In vivo cryotechnique • Cryobiopsy • Freeze substitution • Ischemia/anoxia

48.1 Introduction

Improvement in various fixation or dehydration steps has been considered in examination of morphology and molecular distribution at the light or electron microscopic levels in the biological and medical fields. However, technical problems including molecular movement, structural alterations, and anoxic modification of cells were yielded in the conventional chemical fixation or quick freezing of resected tissues [1–5]. Live-imaging of structural or molecular components under confocal or multiphoton laser scanning microscopes is now an effective way to overcome such problems [6, 7]. However, there are some limitations and drawbacks in the live-imaging [8–10].

"In vivo cryotechnique" (IVCT) has been another approach to observe the functional morphology of living

N. Ohno, M.D., Ph.D. (✉) • S. Ohno
Department of Anatomy and Molecular Histology, Interdisciplinary Graduate School of Medicine and Engineering, University of Yamanashi, 1110 Shimokato, Chuo City, Yamanashi 409-3898, Japan
e-mail: nohno@yamanashi.ac.jp

N. Terada
Division of Health Sciences, Shinshu University Graduate School of Medicine, 3-1-1 Asahi, Matsumoto City, Nagano 390-8621, Japan

Department of Anatomy and Molecular Histology, Interdisciplinary Graduate School of Medicine and Engineering, University of Yamanashi, 1110 Shimokato, Chuo City, Yamanashi 409-3898, Japan

S. Ohno et al. (eds.), *In Vivo Cryotechnique in Biomedical Research and Application for Bioimaging of Living Animal Organs*, DOI 10.1007/978-4-431-55723-4_48

Table 48.1 Advantages and limitations of the "in vivo cryotechnique"

Advantages	Limitations
1. Reduction of ischemic/anoxic artifacts by direct cryofixation	1. Preferred exposure of target organs for increasing regions without visible ice crystals
2. High time resolution by immediate freezing of tissues in situ	2. Restricted sample regions good for observation, due to ice crystal formation
3. Maintenance of precise localization of soluble components	3. Extraction of lipid-soluble components due to freeze substitution with organic solvents

animal organs [11, 12]. IVCT includes direct cryofixation of target organs of anesthetized small animals in vivo and thus they are immediately embedded in ice crystals [13]. To avoid the artifacts on the glomerular capillary loops caused by conventional fixation methods with aqueous fixatives, the first study using IVCT was done in mouse kidneys to observe ultrastructural changes of dynamic glomerular capillary loops under different hemodynamic conditions [14–16]. In subsequent studies, IVCT was applied to the ultrastructural and immunohistochemical analyses of morphology and molecular distribution/changes in cells and tissues at the electron and light microscopic levels. Recently, "cryobiopsy" has been developed to examine time-dependent phenomenon of organs in single living animals, including humans [17]. In the subsequent parts, characteristics of IVCT and cryobiopsy, which are summarized in Table 48.1, are reviewed with particular emphasis on the light microscopic observation [18].

48.2 Detection of Soluble Components in Living Animal Organs

Serum albumin and immunoglobulin G (IgG) were clearly detected in blood vessels but not in parenchyma of living mouse cerebellum under normal conditions [5]. The serum proteins were detected also in the brain parenchyma around the blood vessels when the specimens were quickly frozen after resection. The difference of serum protein immunolocalization was attributed to their rapid leakage across the blood–brain barrier caused by anoxia/ischemia. In addition, the immunoreactivity of serum proteins was drastically reduced with transcardial perfusion fixation followed by alcohol dehydration, indicating that the serum proteins were washed out during perfusion [5]. Later studies also demonstrated that the in situ localization of serum proteins and soluble molecules, including glycogen, was significantly affected by conventional fixation methods but well maintained with IVCT [19–22]. The previous studies suggest that preservation of soluble molecules in living animals is one of the important benefits of IVCT under the light microscopic observation [23].

The soluble components are easily translocated or lost during tissue preparation procedures of chemical fixation methods. Thus, freeze substitution was considered more effective to preserve localization of such soluble molecules [24, 25]. It is possible that the freeze substitution completed by the organic solvents at low temperatures decreases diffusion and loss of the soluble molecules in cells and tissues [26]. The soluble components are cross-linked by fixatives in the organic solvents to avoid translocation. This cross-linkage may result in enhanced immunoreactivity, compared with chemical fixation methods [27]. Loosening of intermolecular and intramolecular cross-linkage may also facilitate access of antibodies to the epitopes and enhances immunoreactivity following quick-freezing methods [28, 29]. IVCT would be the most suitable approach in case ischemic/anoxic stress can produce serious effects in morphology as well as molecular localization in cells and tissues of living animals.

48.3 High Time Resolution of Molecular Localization

Since the time duration required for complete fixation which would include time for penetration and chemical reaction for cross-linkage [30] is unclear in chemical fixation methods, rapid changes of morphology and molecular distribution are generally difficult to capture. On the other hand, immediate immobilization of the target molecules at the moment of freezing is possible by cryofixation. A study which effectively showed this property of cryofixation was related to the rapid phosphorylation of rhodopsin [31]. The study demonstrated that 30 s exposure of mouse retina to light after dark adaptation, but not 10 s exposure, dramatically increased the immunoreactivity of rhodopsin phosphorylated at ^{334}Ser. Since some molecular components can be immunohistochemically detected with quick freezing and freeze substitution better compared with other conventional methods, IVCT would be a useful approach in analyses of dynamic and rapid molecular changes in sections of living animal organs.

48.4 Dynamic Morphology Under Different Hemodynamic Conditions

In conventional perfusion fixation methods, perfusion pressure needs to be regulated for morphofunctional studies since the pressures of perfusion can affect the morphology of living animal organs [30, 32]. In resected tissues, the blood

circulation is essentially stopped and most blood vessels collapse before completion of fixation [23]. With IVCT, functioning organs of living animals can be directly cryofixed without perfusion or tissue resection to capture dynamic changes under different hemodynamic conditions [12, 33]. This merit of IVCT was clearly shown in kidneys and livers at the light microscopic level [19–21]. Molecular markers facilitated histological analyses of blood or lymphatic vessels under physiological and pathological conditions [34–36]. Extrinsic molecules such as fluorescent dyes are useful to visualize the functional morphology and permeability of blood vessels, and IVCT followed by freeze substitution would well maintain those soluble molecular markers [37–40]. IVCT would also be useful to visualize alterations of intramembranous components in flowing erythrocytes [41]. In conclusion, one of technical advantages of IVCT which is distinct from conventional tissue preparation methods is the rapid preservation of morphology and molecular conformation.

48.5 Morphological Comparison with the Other Tissue Preparation Methods

In specimens prepared with IVCT, tissue areas which can be observed without visible ice crystals are restricted within a few hundred micrometers at the light microscopic level and several micrometers at the electron microscopic level from the frozen tissue surface [5, 12]. This limitation of observable areas is common in the other quick-freezing methods [42], although with immersion fixation, the slow penetration of chemical fixatives also causes postmortem artifacts in deeper areas [30]. It is important to check the presence of visible ice crystals in cryofixed specimens, e.g., with hematoxylin-eosin staining.

Exposure of target organs under anesthesia helps efficient cryofixation with IVCT, since tissue areas without visible ice crystals can be maximized by direct contact of the liquid cryogen and the cryoknife to target organs [12]. In addition, excessive body fluid or unnecessary blood on the tissue surface needs to be removed by wiping or washing prior to freezing, since they also prevent direct contact of isopentane-propane (IP) cryogen and impair the image quality of cryofixed specimens due to ice crystal formation [13]. Conventional quick-freezing methods do not require the exposure of target organs in situ, but tissue specimens are removed and cut into small pieces prior to freezing.

Immunohistochemistry conditions need to be optimized when tissue specimens are prepared with cryofixation followed by freeze substitution. Although soluble molecules are well retained and their stronger immunoreactivity can be observed after cryofixation, hydrophobic molecules in lipid membranes may not be well preserved during freeze substitution with acetone [43]. Most antibodies available in conventional chemical fixation can be used for specimens prepared with cryofixation and freeze substitution, although abundant soluble molecules may be maintained to hinder epitopes. In staining of such hindered epitopes, smaller probes, such as chemicals for histological staining, may enhance the staining, as shown in the glomerular basement membrane of mouse kidneys [44]. Antibodies which do not work well with chemical fixation and alcohol dehydration can be successfully used on cryosections [45].

48.6 Capturing Time-Dependent Morphology

IVCT immobilizes every component in vitreous ice crystals and is useful to capture quickly changing tissue and cellular morphology under normal blood circulation. IVCT is not a method to examine the time-lapse changes in single target organs of living animals. However, different functional or structural molecules on serial or same sections can be simultaneously analyzed. In addition, these molecules can be observed in the context of the histological structures. Therefore, combination of IVCT and other methods, such as intravital imaging, freeze-fracture replication, or X-ray microanalyses for electron microscopy, will be effective to obtain novel information about living animal organs [41, 46]. One of the examples is the combination of IVCT and Raman microscopy, which showed the different molecular organization of the mouse retina [47]. Various morphofunctional information can be obtained from the iced blocks depending on the procedures employed after IVCT.

48.7 New Development and Improvement of Cryobiopsy

It is challenging to use IVCT in larger animals including humans, since the liquid IP cryogen poured over the target organs also touches adjacent tissues and causes severe freezing damage. To solve these problems, a new cryotechnique, named “cryobiopsy,” was recently developed by utilizing a home-made device, cryoforceps [17]. Cryobiopsy did not kill the host mice but revealed open sinusoids and flowing erythrocytes, as observed with IVCT [17, 48]. There were tissue areas with compression deformation around the tissue edges of the cryoforceps, but the areas adjacent to such compressed tissues reveals native morphology [17, 39]. Cryobiopsy can be used to obtain specimens from larger animals including humans with minimal ischemia/anoxia and would contribute to new pathological analyses in clinical medicine.

48.8 Concluding Remarks

IVCT has been widely used in studies dealing with various organs of living animals, both at the electron and light microscopic levels. IVCT should be applied to not only standard microscopic analyses but also new analytical fields which involve animal experimental models as well as materials in clinical medicine. New devices, such as gastric endoscopes with cryoforceps and cooling system, are needed to efficiently apply the cryobiopsy system to the human biopsy.

References

1. Chan FL, Inoue S (1994) Lamina lucida of basement membrane: an artefact. Microsc Res Tech 28(1):48–59
2. Hippe-Sanwald S (1993) Impact of freeze substitution on biological electron microscopy. Microsc Res Tech 24(5):400–422
3. Kellenberger E, Johansen R, Maeder M, Bohrmann B, Stauffer E, Villiger W (1992) Artefacts and morphological changes during chemical fixation. J Microsc 168(Pt 2):181–201
4. Shiurba R (2001) Freeze-substitution: origins and applications. Int Rev Cytol 206:45–96
5. Zea-Aragon Z, Terada N, Ohno N, Fujii Y, Baba T, Ohno S (2004) Effects of anoxia on serum immunoglobulin and albumin leakage through blood–brain barrier in mouse cerebellum as revealed by cryotechniques. J Neurosci Methods 138(1–2):89–95
6. Stephens DJ, Allan VJ (2003) Light microscopy techniques for live cell imaging. Science 300(5616):82–86
7. Selvin PR (2000) The renaissance of fluorescence resonance energy transfer. Nat Struct Biol 7(9):730–734
8. Fricker MD, Meyer AJ (2001) Confocal imaging of metabolism in vivo: pitfalls and possibilities. J Exp Bot 52(356):631–640
9. Molitoris BA, Sandoval RM (2005) Intravital multiphoton microscopy of dynamic renal processes. Am J Physiol Renal Physiol 288(6):F1084–F1089
10. Tauer U (2002) Advantages and risks of multiphoton microscopy in physiology. Exp Physiol 87(6):709–714
11. Ohno N, Terada N, Fujii Y, Baba T, Ohno S (2004) "In vivo cryotechnique" for paradigm shift to "living morphology" of animal organs. Biomed Rev 15:1–19
12. Ohno S, Terada N, Fujii Y, Ueda H, Takayama I (1996) Dynamic structure of glomerular capillary loop as revealed by an in vivo cryotechnique. Virchows Arch 427(5):519–527
13. Ohno N, Terada N, Ohno S (2004) Advanced application of the in vivo cryotechnique to immunohistochemistry for animal organs. Acta Histochem Cytochem 37:357–364
14. Ohguro H, Rudnicka-Nawrot M, Buczylko J, Zhao X, Taylor JA, Walsh KA et al (1996) Structural and enzymatic aspects of rhodopsin phosphorylation. J Biol Chem 271(9):5215–5224
15. Ohno S, Kato Y, Xiang T, Terada N, Takayama I, Fujii Y et al (2001) Ultrastructural study of mouse renal glomeruli under various hemodynamic conditions by an "in vivo cryotechnique". Ital J Anat Embryol 106(2 Suppl 1):431–438
16. Furukawa T, Ohno S, Oguchi H, Hora K, Tokunaga S, Furuta S (1991) Morphometric study of glomerular slit diaphragms fixed by rapid-freezing and freeze-substitution. Kidney Int 40(4):621–624
17. Fujii Y, Ohno N, Li Z, Terada N, Baba T, Ohno S (2006) Morphological and histochemical analyses of living mouse livers by new 'cryobiopsy' technique. J Electron Microsc (Tokyo) 55(2):113–122
18. Ohno N, Terada N, Saitoh S, Zhou H, Fujii Y, Ohno S (2007) Recent development of in vivo cryotechnique to cryobiopsy for living animals. Histol Histopathol 22(11):1281–1290
19. Li Z, Ohno N, Terada N, Ohno S (2006) Immunolocalization of serum proteins in living mouse glomeruli under various hemodynamic conditions by "in vivo cryotechnique". Histochem Cell Biol 126(3):399–406
20. Li Z, Terada N, Ohno N, Ohno S (2005) Immunohistochemical analyses on albumin and immunoglobulin in acute hypertensive mouse kidneys by "in vivo cryotechnique". Histol Histopathol 20(3):807–816
21. Ohno S, Terada N, Ohno N, Fuji Y, Baba T (2006) "In vivo cryotechnique" for examination of living animal organs, further developing to "cryobiopsy" for humans. Recent Res Devel Mol Cell Biol 6:65–90
22. Zhou H, Ohno N, Terada N, Saitoh S, Fujii Y, Ohno S (2007) Involvement of follicular basement membrane and vascular endothelium in blood follicle barrier formation of mice revealed by 'in vivo cryotechnique'. Reproduction 134(2):307–317
23. Ohno N, Terada N, Ohno S (2006) Histochemical analyses of living mouse liver under different hemodynamic conditions by "in vivo cryotechnique". Histochem Cell Biol 126(3):389–398
24. Moreira JE, Dodane V, Reese TS (1998) Immunoelectronmicroscopy of soluble and membrane proteins with a sensitive postembedding method. J Histochem Cytochem 46(7):847–854
25. von Schack ML, Fakan S, Villiger W, Muller M (1993) Cryofixation and cryosubstitution: a useful alternative in the analyses of cellular fine structure. Eur J Histochem 37(1):5–18
26. Melan MA, Sluder G (1992) Redistribution and differential extraction of soluble proteins in permeabilized cultured cells. Implications for immunofluorescence microscopy. J Cell Sci 101(Pt 4):731–743
27. Yamashita S, Yasuda K (1992) Freeze-substitution fixation for immunohistochemistry at the light microscopic level: effects of solvent and chemical fixatives. Acta Histochem Cytochem 25:641–650
28. Ohno N, Terada N, Murata S, Katoh R, Ohno S (2005) Application of cryotechniques with freeze-substitution for the immunohistochemical demonstration of intranuclear pCREB and chromosome territory. J Histochem Cytochem 53(1):55–62
29. Terada N, Ohno N, Li Z, Fujii Y, Baba T, Ohno S (2006) Application of in vivo cryotechnique to the examination of cells and tissues in living animal organs. Histol Histopathol 21(3):265–272
30. Hayat M (1989) Chemical fixation. Principles and techniques of electron microscopy. Macmillan Press, London, pp 1–78
31. Terada N, Ohno N, Ohguro H, Li Z, Ohno S (2006) Immunohistochemical detection of phosphorylated rhodopsin in light-exposed retina of living mouse with in vivo cryotechnique. J Histochem Cytochem 54(4):479–486
32. Yu Y, Leng CG, Terada N, Ohno S (1998) Scanning electron microscopic study of the renal glomerulus by an in vivo cryotechnique combined with freeze-substitution. J Anat 192(Pt 4):595–603
33. Terada N, Kato Y, Fuji Y, Ueda H, Baba T, Ohno S (1998) Scanning electron microscopic study of flowing erythrocytes in hepatic sinusoids as revealed by 'in vivo cryotechnique'. J Electron Microsc (Tokyo) 47(1):67–72
34. Achen MG, McColl BK, Stacker SA (2005) Focus on lymphangiogenesis in tumor metastasis. Cancer Cell 7(2):121–127
35. Emanueli C, Madeddu P (2005) Changing the logic of therapeutic angiogenesis for ischemic disease. Trends Mol Med 11(5):207–216
36. Gariano RF, Gardner TW (2005) Retinal angiogenesis in development and disease. Nature 438(7070):960–966
37. McDonald DM, Choyke PL (2003) Imaging of angiogenesis: from microscope to clinic. Nat Med 9(6):713–725
38. Terada N, Ohno N, Li Z, Fujii Y, Baba T, Ohno S (2005) Detection of injected fluorescence-conjugated IgG in living mouse organs using "in vivo cryotechnique" with freeze-substitution. Microsc Res Tech 66(4):173–178
39. Ohno N, Terada N, Bai Y, Saitoh S, Nakazawa T, Nakamura N et al (2008) Application of cryobiopsy to morphological and immunohistochemical analyses of xenografted human lung cancer tissues and functional blood vessels. Cancer 113(5):1068–1079

40. Saitoh Y, Terada N, Saitoh S, Ohno N, Jin T, Ohno S (2012) Histochemical analyses and quantum dot imaging of microvascular blood flow with pulmonary edema in living mouse lungs by "in vivo cryotechnique". Histochem Cell Biol 137(2):137–151
41. Terada N, Ohno N, Fujii Y, Baba T, Ohno S (2006) Dynamic study of intramembranous particles in human fresh erythrocytes using an "in vitro cryotechnique". Microsc Res Tech 69(4):291–295
42. Plattner H, Bachmann L (1982) Cryofixation: a tool in biological ultrastructural research. Int Rev Cytol 79:237–304
43. Giddings TH (2003) Freeze-substitution protocols for improved visualization of membranes in high-pressure frozen samples. J Microsc 212(Pt 1):53–61
44. Li Z, Ohno N, Terada N, Zhou D, Yoshimura A, Ohno S (2006) Application of periodic acid-Schiff fluorescence emission for immunohistochemistry of living mouse renal glomeruli by an "in vivo cryotechnique". Arch Histol Cytol 69(3):147–161
45. Shiurba RA, Spooner ET, Ishiguro K, Takahashi M, Yoshida R, Wheelock TR et al (1998) Immunocytochemistry of formalin-fixed human brain tissues: microwave irradiation of free-floating sections. Brain Res Brain Res Protoc 2(2):109–119
46. Takayama I, Terada N, Baba T, Ueda H, Kato Y, Fujii Y et al (1999) "In vivo cryotechnique" in combination with replica immunoelectron microscopy for caveolin in smooth muscle cells. Histochem Cell Biol 112(6):443–445
47. Terada N, Ohno N, Saitoh S, Fujii Y, Ohguro H, Ohno S (2007) Raman microscopy of freeze-dried mouse eyeball-slice in conjunction with the "in vivo cryotechnique". Microsc Res Tech 70(7):634–639
48. Saitoh Y, Terada N, Saitoh S, Ohno N, Fujii Y, Ohno S (2010) Histochemical approach of cryobiopsy for glycogen distribution in living mouse livers under fasting and local circulation loss conditions. Histochem Cell Biol 133(2):229–239

Part VIII

Application of Cryobiopsy for Living Animal Tissues

49 Significance of Cryobiopsy for Morphological and Immunohistochemical Analyses of Xenografted Human Lung Cancer Tissues and Functional Blood Vessels

Nobuhiko Ohno, Nobuo Terada, and Shinichi Ohno

Abstract

To overcome the problems of artifacts in the conventional immersion-fixation and dehydration method (IMDH), cryobiopsy and "in vivo cryotechnique" (IVCT), where target organs are directly cryofixed in vivo, were used for the analyses of microenvironment and histological architectures in xenografted human lung cancer tissues. The results revealed that tissue morphology, such as cellular organelles, and open blood vessels with flowing erythrocytes were clearly observed without artificial shrinkage using cryobiopsy and IVCT. By contrast, blood vessels were all collapsed following tissue resection in conventional methods. With cryobiopsy and IVCT, intravenously injected bovine serum albumin (BSA) clearly visualized functional blood vessels containing immunoglobulin M (IgM). The expression of vascular endothelial growth factor (VEGF) was correlated with the volume of blood vessels positive for IgM. The histological analyses of human tissues with cryobiopsy as well as IVCT will be useful to avoid artifacts inevitable in IMDH. Functional blood vessels along with relevant signal transduction would be precisely examined with cryobiopsy as well as IVCT to clarify microenvironment of the human tumors in clinical medicine.

Keywords

Blood vessels • Cryopreservation • Histology • Ischemia • Microenvironment

49.1 Introduction

The "in vivo cryotechnique" (IVCT), where liquid cryogen is poured over the living animal organs for direct cryofixation, has been applied to various living animal organs to avoid artifacts in conventional tissue preparation methods which are caused by perfusion pressure and ischemia/anoxia [1, 2]. In IVCT, all components in the living animal organs can be immediately frozen and maintained in the tissue specimens in situ. Therefore, quick alterations of signal molecules or translocation of soluble components can be precisely analyzed [3–6]. On the other hand, one problem of IVCT is that the poured cryogen essentially causes freezing damage to adjacent tissues. "Cryobiopsy," where target organs are rapidly pinched off using "cryoforceps" precooled in liquid nitrogen, is a method developed to surpass this problem [7].

N. Ohno, M.D., Ph.D. (✉) • S. Ohno
Department of Anatomy and Molecular Histology, Interdisciplinary Graduate School of Medicine and Engineering, University of Yamanashi, 1110 Shimokato, Chuo City, Yamanashi 409-3898, Japan
e-mail: nohno@yamanashi.ac.jp

N. Terada
Division of Health Sciences, Shinshu University Graduate School of Medicine, 3-1-1 Asahi, Matsumoto City, Nagano 390-8621, Japan

Department of Anatomy and Molecular Histology, Interdisciplinary Graduate School of Medicine and Engineering, University of Yamanashi, 1110 Shimokato, Chuo City, Yamanashi 409-3898, Japan

S. Ohno et al. (eds.), *In Vivo Cryotechnique in Biomedical Research and Application for Bioimaging of Living Animal Organs*, DOI 10.1007/978-4-431-55723-4_49

Cryobiopsy is expected to be available in the clinical medicine.

The behavior of solid tumors is significantly affected by their microenvironment [8–10]. The tumor microenvironment has been evaluated on sections prepared with conventional methods, including chemical fixation and dehydration. The histopathological observations obtained from the conventionally prepared sections are mostly influenced by technical artifacts, such as tissue damages and postmortem changes [11, 12]. Such artifacts may significantly modulate the analyses of the tumor microenvironment, which could be spatially variable in tumor masses [13–15].

49.2 Differences Among Cryobiopsy and Other Preparation Methods

A xenografted nude mouse model of human non-small cell lung cancer was used to clarify the advantages of cryobiopsy and IVCT in the analyses of tumor histopathology and microenvironment [16]. Three lines of human lung cancer cells (EBC-1, Lu65, and Lu99) were subcutaneously injected to dorsal flank of nude mice. After the tumor volume reached 1000 mm^3, cryobiopsy or IVCT followed by freeze-substitution was performed as previously described [7, 17]. For comparisons, quick-freezing of the fresh resected tumor tissues followed by freeze-substitution (FQF) and conventional immersion-fixation followed by alcohol dehydration (IMDH) were performed.

In the cryobiopsy, the regions around the periphery of discoid tissue specimen need to be excluded from analyses since they were deformed by compression by the cryoforceps [16]. Although ice crystalformation and cellular damage were obvious in deeper tissue regions, visible ice crystals were very few near the surface of the tumor tissues, and widely open blood vessels with flowing erythrocytes were clearly observed (Fig. 49.1) [16]. With both cryobiopsy and IVCT, open blood vessels with flowing erythrocytes were well preserved, and tumor cell nuclei appeared large (Fig. 49.1). Blood vessels were all collapsed with FQF, presumably due to ischemia/anoxia after tissue resection (Fig. 49.1). Congested erythrocytes could be found in many blood vessels, and the nuclei of tumor cells appeared to be condensed and shrunken with IMDH (Fig. 49.1). Furthermore, there were crescent void areas around the tumor cell nuclei with IMDH, which were attributed to the artifacts due to tissue shrinkage (Fig. 49.1).

Preparation artifacts are common in chemical fixation and dehydration methods, such as the formation of a chromatinic rim or nuclear shrinkage [18]. The artifacts, including cellular and nuclear aggregation and shrinkage, are prevented using freeze-substitution [19, 20]. The diagnosis and evaluation of prognosis is often associated with the histological features of tumor tissues, such as nuclear size, nucleocytoplasmic ratio, pleomorphism, and cytoplasmic anisocytosis [21–23]. It is possible that the cryotechniques can preserve the nuclear, cellular, and tissue structures of living tumors and contribute to the clinical diagnosis with fewer artifacts.

The modified Chalkley method was used to quantitatively measure the von Willebrand factor-positive blood vessel volume on paraffin sections [16]. The blood vessel volume in specimens prepared with IVCT or cryobiopsy was significantly larger compared with FQF or IMDH. The significant decrease in the blood vessel volumes was attributable to ischemia of tumor tissues which was inevitable upon tissue resection in FQF and IMDH. Evaluation of blood vessels can result in better estimates of clinical outcomes [24, 25]. The technical artifacts of conventional tissue preparation methods may influence the blood vessel volume or density. Cryobiopsy and IVCT will support the histopathological and ultrastructural examination of blood vessels in tumors without those artifacts.

49.3 Visualization of IgM-Immunopositive Blood Vessels

With cryobiopsy and IVCT, the immunostaining for IgM in tumor tissues was restricted in blood vessels with flowing erythrocytes [16]. Abundant von Willebrand factor (vWF)-immunopositive blood vessels were also observed in the same areas of serial sections. The IgM immunoreactivity was detected in some of the vWF-immunopositive blood vessels. In cryosections of the xenograft tumors, the intravenously injected BSA was clearly observed in blood vessels of the tumor tissues and capillaries of the capsular connective tissues around the tumor periphery (Fig. 49.2) [16]. The BSA was localized in some of the blood vessels immunopositive for vWF and collagen type IV in the vascular basement membranes (Fig. 49.2). The immunoreactivity of BSA and IgM was detected in the same blood vessels of the tumor masses (Fig. 49.2). Therefore, the functional blood vessels with blood circulation can be visualized with IgM immunoreactivity in specimens prepared with both IVCT and cryobiopsy in the tumor tissues.

The relationship between fewer IgM-immunopositive blood vessels and hypoxic states in the tumor cells was examined with IVCT [16]. The distribution of the IgM-immunopositive blood vessels and VEGF expression, a signal factor induced by hypoxic stimuli, was compared [26]. Serial sections of tumor tissues stained with hematoxylin-eosin or immunostained for IgM, vWF, and VEGF showed that the distribution of IgM immunoreactivity and erythrocytes was similar and could represent blood circulation (Fig. 49.3). The immunostaining for vWF was observed throughout the tumors (Fig. 49.3). On the other hand, the distribution of VEGF showed a clear contrast to that for IgM (Fig. 49.3).

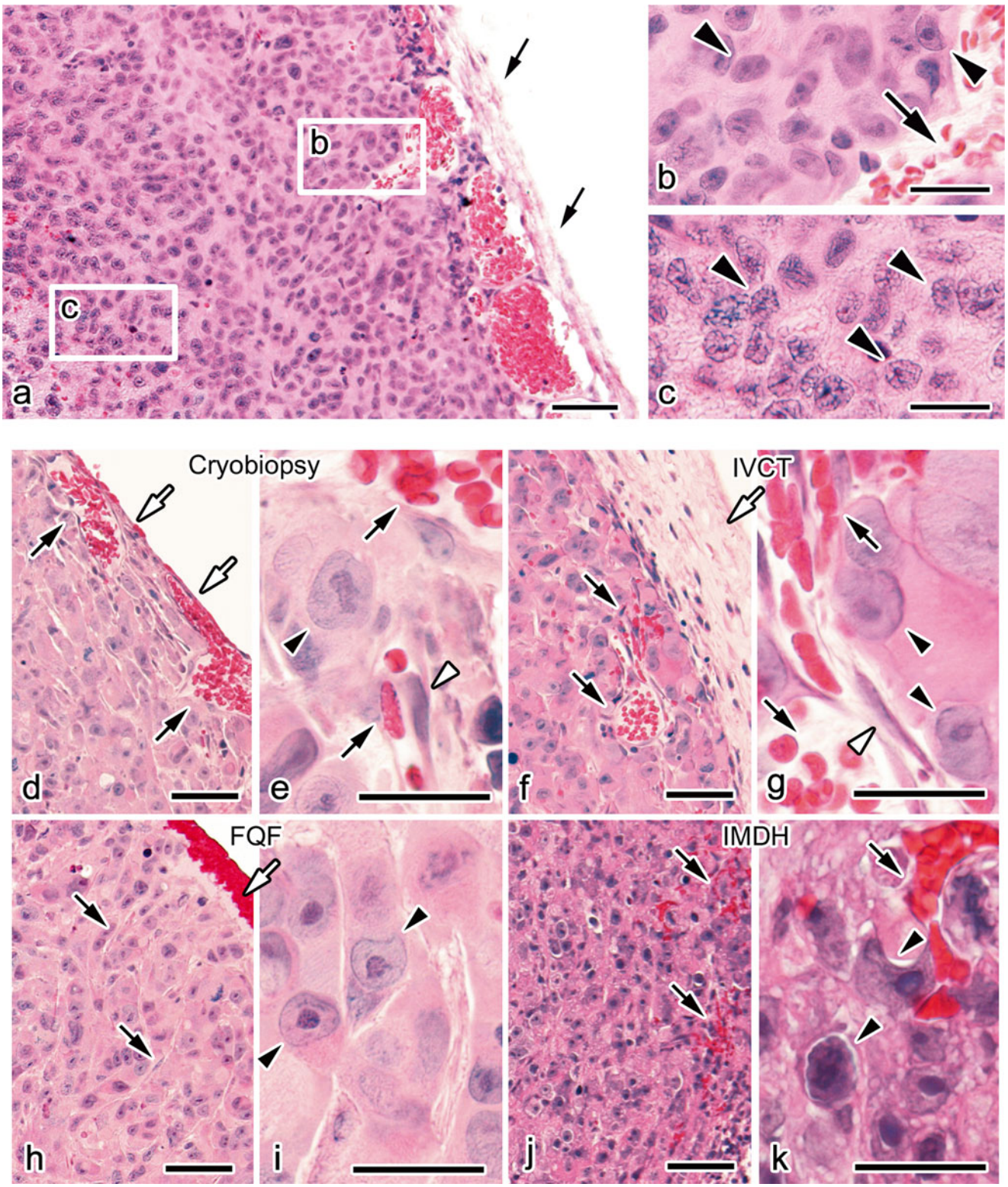

Fig. 49.1 (**a**)–(**c**) Light micrographs of a xenografttumor of Lu99 cells prepared with cryobiopsy show that there is little formation of ice crystals (**b**, *solid arrowheads*) and flowing erythrocytes are clearly observed in blood vessels (**b**, *solid arrow*) near the tissue surface (**a**, *solid arrows*). Ice crystals can be found in the deeper areas (**c**, *solid arrowheads*). (**d**)–(**k**) Xenografted tumors of EBC-1 cells prepared with cryobiopsy (**d**, **e**), in vivo cryotechnique (IVCT; **f**, **g**), quick-freezing of fresh resected tissues (FQF; **h**, **i**), or immersion-fixation followed by dehydration (IMDH; **j**, **k**) show that open blood vessels (**d**, **f**, *solid arrows*) are clearly observed in regions near the tissue surface with cryobiopsy and IVCT (**d**, **f**, *open arrows*). Large pale tumor cell nuclei (**e**, **g**, *solid arrowheads*) and blood vessels (**e**, **g**, *open arrowheads*) with flowing erythrocytes (**e**, **g**, *solid arrows*) are also obvious. Blood vessels are collapsed with FQF (**h**, *solid arrows*) near the frozen tissue surface (**h**, *open arrow*) and with IMDH (**j**, **k**, *solid arrows*). Large tumor cell nuclei are present with FQF (**i**, *solid arrowheads*), but the tumor cell nuclei are smaller and surrounded by damaged tissue with IMDH (**k**, *solid arrowheads*). Bars 50 μm (**a**, **d**, **f**, **h**, **j**) or 20 μm (**b**, **c**, **e**, **g**, **i**, **k**) (The figure is adapted from Ohno et al. [16])

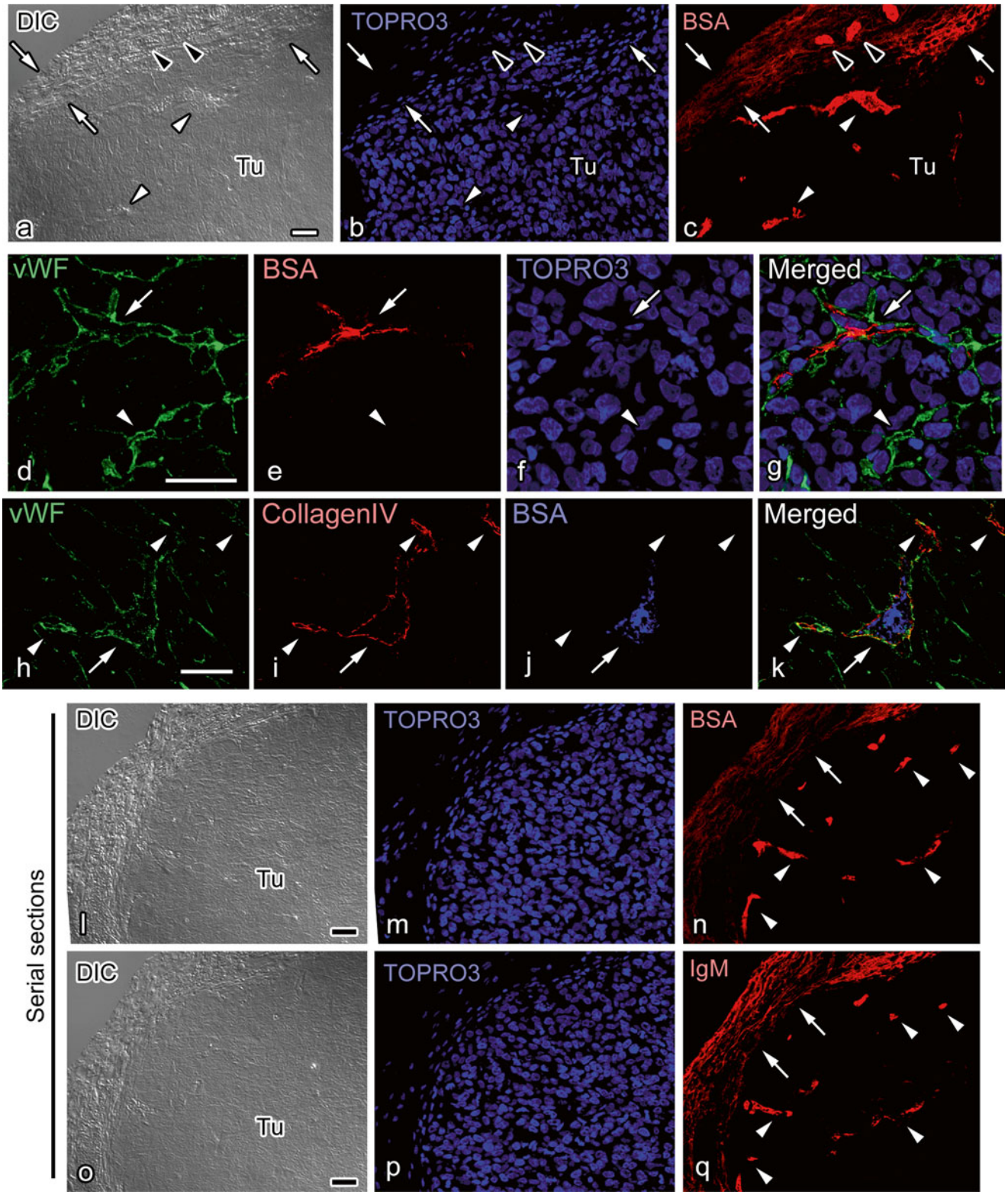

Fig. 49.2 (**a**)–(**c**) In the cryosections of a Lu99 cell xenografttumor prepared using in vivo cryotechnique, bovine serum albumin (BSA, *red*) is immunolocalized in blood vessels (*solid arrowheads*) around the tumor masses (Tu) and occasionally leaked in the adjacent connective tissues (*open arrows*). BSA immunoreactivity is also observed in blood vessels entering the tumor (*open arrowheads*). (**d**)–(**g**) BSA (*red*) is immunolocalized in some blood vessels (*open arrows*) positive for von Willebrand factor (vWF, *green*) but not in the other vWF-positive blood vessels (*open arrowheads*). (**h**)–(**k**) BSA immunoreactivity (*blue*) in some blood vessels (*open arrows*) labeled with vWF (*green*) and collagen type IV α2 chain (*red*) but not in others (*open arrowheads*). (**l**)–(**q**) Immunostaining for BSA (**l–n**) or IgM (**o–q**) in serial sections shows that BSA (**n**) and IgM (**q**) immunostaining appears similar in connective tissues around the tumor mass (**n**, **q**, *open arrows*) and blood vessels in the tumors (**n**, **q** *open arrowheads*). Cellular nuclei are labeled with TOPRO3 (**b, f, m, p**, *blue*). Bars 30 μm (The figure is adapted from Ohno et al. [16])

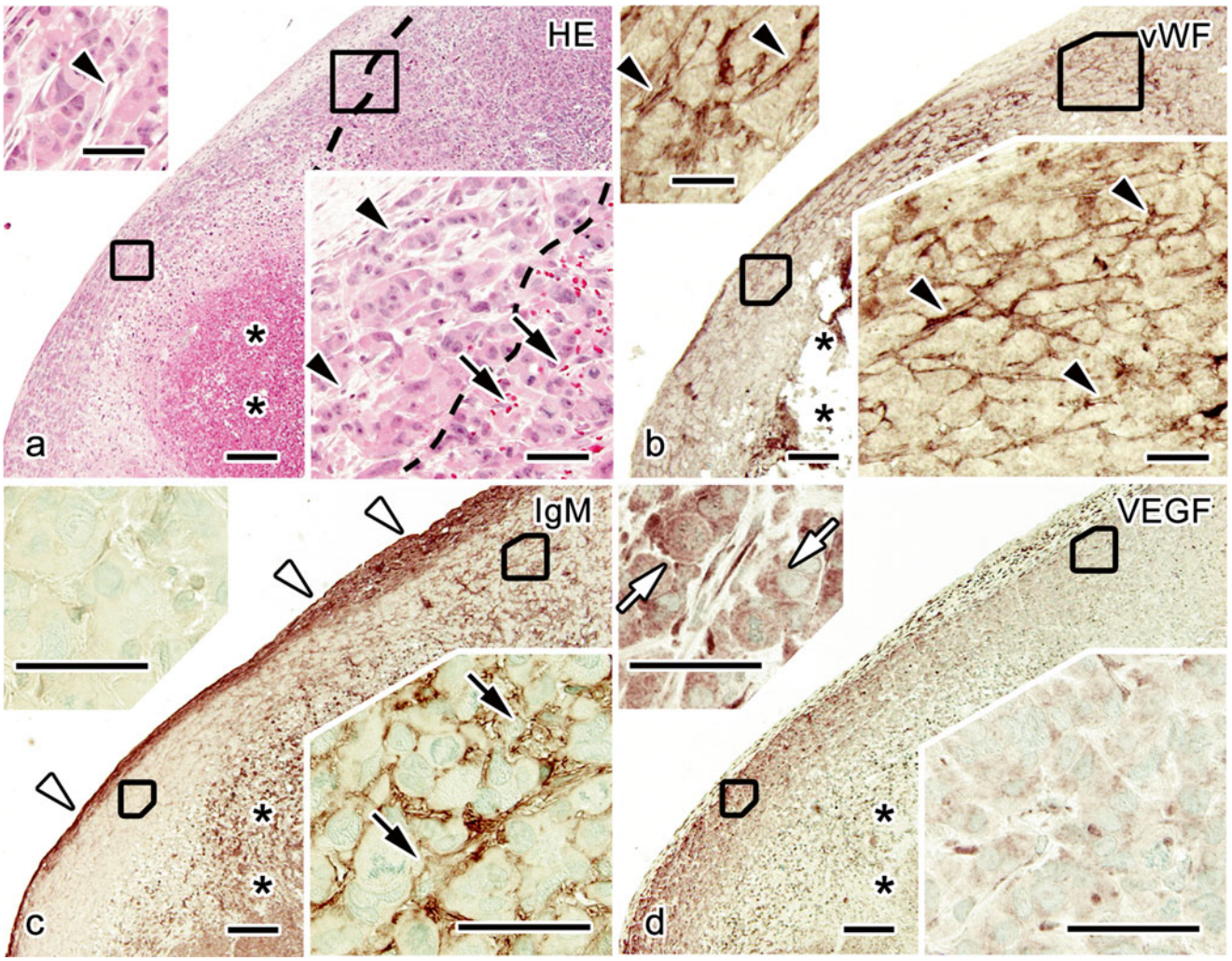

Fig. 49.3 (**a**)–(**d**) Light micrographs of serial paraffin sections obtained from an EBC-1 cell tumor and stained with hematoxylin-eosin (HE; **a**) or immunostained for von Willebrand factor (vWF; **b**), immunoglobulinM (IgM; **c**), or vascular endothelial growth factor (VEGF; **d**). Erythrocytes (**a**, *solid arrows*) and IgM immunoreactivity (**c**, *solid arrows*) are observed in restricted areas, whereas vWF is immunolocalized throughout the tumor (**a**, **b**, *solid arrowheads*). VEGF immunoreactivity is stronger in the regions with little IgM immunostaining (**d**, *open arrows*). *Open arrowheads*: IgM-immunopositive connective tissues. *Asterisks*: necrotic areas. Bars 200 μm or 50 μm in *insets* (The figure is modified from Ohno et al. [16])

The restricted distribution of serum macromolecules in tumor tissues, which was well preserved with cryobiopsy and IVCT, represents the distribution of bloodcirculation [16]. Increased vascular permeability, insufficient drainage, and elevated interstitial fluid pressure can also impair the blood circulation within tumors [27, 28]. Blood vessels in tumor tissues are characterized by abnormal proliferation, anastomosis, and remodeling inside and around the tumor masses [15, 29–31]. Endothelial markers have been used to identify the structures specific for blood vessels in tumors [25, 32, 33]. The immunolocalization of serum macromolecules such as IgM represents blood circulation in functional blood vessels. Local or temporal impairment of blood circulation would result in closer relationship between functional blood vessels and tumor hypoxic environments. It is because the O_2 diffusion from the blood circulation determines hypoxic reactions in tumor cells [14]. The relationship among the clinical outcomes, tumor hypoxia, and blood vessels could be better understood through histological analyses of functional blood vessels. Cryobiopsy and IVCT immobilize soluble components in situ [6, 34, 35] and enable us to analyze the heterogenous blood circulation in different areas of tumor tissues.

49.4 Concluding Remarks

Cryobiopsy and IVCT enable morphological examination of tumor cells and blood vessels without the preparation artifacts induced during conventional chemical fixation methods. In addition, cryobiopsy and IVCT reveal the precise distribution of serum macromolecules in vessels with blood flow, which are related to hypoxic states of cancer cells. Application of cryobiopsy and IVCT allows a novel approach to examine the relationship among the tumor microenvironment, functional blood vessels, and clinical outcomes.

References

1. Ohno N, Terada N, Fujii Y, Baba T, Ohno S (2004) "In vivo cryotechnique" for paradigm shift to "living morphology" of animal organs. Biomed Rev 15:1–19
2. Ohno N, Terada N, Saitoh S, Zhou H, Fujii Y, Ohno S (2007) Recent development of in vivo cryotechnique to cryobiopsy for living animals. Histol Histopathol 22(11):1281–1290
3. Li Z, Ohno N, Terada N, Ohno S (2006) Immunolocalization of serum proteins in living mouse glomeruli under various hemodynamic conditions by "in vivo cryotechnique". Histochem Cell Biol 126(3):399–406
4. Terada N, Ohno N, Ohguro H, Li Z, Ohno S (2006) Immunohistochemical detection of phosphorylated rhodopsin in light-exposed retina of living mouse with in vivo cryotechnique. J Histochem Cytochem 54(4):479–486
5. Terada N, Ohno N, Saitoh S, Ohno S (2007) Immunohistochemical detection of hypoxia in mouse liver tissues treated with pimonidazole using "in vivo cryotechnique". Histochem Cell Biol 128(3):253–261
6. Zea-Aragon Z, Terada N, Ohno N, Fujii Y, Baba T, Ohno S (2004) Effects of anoxia on serum immunoglobulin and albumin leakage through blood–brain barrier in mouse cerebellum as revealed by cryotechniques. J Neurosci Methods 138(1–2):89–95
7. Fujii Y, Ohno N, Li Z, Terada N, Baba T, Ohno S (2006) Morphological and histochemical analyses of living mouse livers by new 'cryobiopsy' technique. J Electron Microsc (Tokyo) 55(2):113–122
8. Folkman J (2002) Role of angiogenesis in tumor growth and metastasis. Semin Oncol 29(6 Suppl 16):15–18
9. Hockel M, Vaupel P (2001) Tumor hypoxia: definitions and current clinical, biologic, and molecular aspects. J Natl Cancer Inst 93(4):266–276
10. Liotta LA, Kohn EC (2001) The microenvironment of the tumour-host interface. Nature 411(6835):375–379
11. Hayat M (1989) Chemical fixation. Principles and techniques of electron microscopy. Macmillan Press, London, pp 1–78
12. Hopwood D (1982) Fixation and fixatives. In: Bancroft J, Stevens A (eds) Theory and practice of histological techniques. Churchill Livingstone, New York, pp 20–40
13. Bussink J, Kaanders JH, van der Kogel AJ (2003) Tumor hypoxia at the micro-regional level: clinical relevance and predictive value of exogenous and endogenous hypoxic cell markers. Radiother Oncol 67(1):3–15
14. Coleman CN (1988) Hypoxia in tumors: a paradigm for the approach to biochemical and physiologic heterogeneity. J Natl Cancer Inst 80(5):310–317
15. Tilki D, Kilic N, Sevinc S, Zywietz F, Stief CG, Ergun S (2007) Zone-specific remodeling of tumor blood vessels affects tumor growth. Cancer 110(10):2347–2362
16. Ohno N, Terada N, Bai Y, Saitoh S, Nakazawa T, Nakamura N et al (2008) Application of cryobiopsy to morphological and immunohistochemical analyses of xenografted human lung cancer tissues and functional blood vessels. Cancer 113(5):1068–1079
17. Ohno N, Terada N, Ohno S (2006) Histochemical analyses of living mouse liver under different hemodynamic conditions by "in vivo cryotechnique". Histochem Cell Biol 126(3):389–398
18. Bignold LP (2003) Pathogenetic mechanisms of nuclear pleomorphism of tumour cells based on the mutator phenotype theory of carcinogenesis. Histol Histopathol 18(2):657–664
19. Kellenberger E (1991) The potential of cryofixation and freeze substitution: observations and theoretical considerations. J Microsc 161(Pt 2):183–203
20. Shiurba R (2001) Freeze-substitution: origins and applications. Int Rev Cytol 206:45–96
21. Bloom HJ, Richardson WW (1957) Histological grading and prognosis in breast cancer; a study of 1409 cases of which 359 have been followed for 15 years. Br J Cancer 11(3):359–377
22. Fuhrman SA, Lasky LC, Limas C (1982) Prognostic significance of morphologic parameters in renal cell carcinoma. Am J Surg Pathol 6(7):655–663
23. Libbrecht L, Desmet V, Roskams T (2005) Preneoplastic lesions in human hepatocarcinogenesis. Liver Int 25(1):16–27
24. Fox SB, Harris AL (2004) Histological quantitation of tumour angiogenesis. APMIS 112(7–8):413–430
25. Vermeulen PB, Gasparini G, Fox SB, Colpaert C, Marson LP, Gion M et al (2002) Second international consensus on the methodology and criteria of evaluation of angiogenesis quantification in solid human tumours. Eur J Cancer 38(12):1564–1579
26. Ferrara N, Gerber HP, LeCouter J (2003) The biology of VEGF and its receptors. Nat Med 9(6):669–676
27. Jain RK (2005) Normalization of tumor vasculature: an emerging concept in antiangiogenic therapy. Science 307(5706):58–62
28. Tong RT, Boucher Y, Kozin SV, Winkler F, Hicklin DJ, Jain RK (2004) Vascular normalization by vascular endothelial growth factor receptor 2 blockade induces a pressure gradient across the vasculature and improves drug penetration in tumors. Cancer Res 64(11):3731–3736
29. Bergers G, Benjamin LE (2003) Tumorigenesis and the angiogenic switch. Nat Rev Cancer 3(6):401–410
30. Dvorak HF, Nagy JA, Dvorak JT, Dvorak AM (1988) Identification and characterization of the blood vessels of solid tumors that are leaky to circulating macromolecules. Am J Pathol 133(1):95–109
31. McDonald DM, Choyke PL (2003) Imaging of angiogenesis: from microscope to clinic. Nat Med 9(6):713–725
32. Norrby K, Ridell B (2003) Tumour-type-specific capillary endothelial cell stainability in malignant B-cell lymphomas using antibodies against CD31, CD34 and Factor VIII. APMIS 111(4):483–489
33. Pusztaszeri MP, Seelentag W, Bosman FT (2006) Immunohistochemical expression of endothelial markers CD31, CD34, von Willebrand factor, and Fli-1 in normal human tissues. J Histochem Cytochem 54(4):385–395
34. Terada N, Ohno N, Li Z, Fujii Y, Baba T, Ohno S (2005) Detection of injected fluorescence-conjugated IgG in living mouse organs using "in vivo cryotechnique" with freeze-substitution. Microsc Res Tech 66(4):173–178
35. Zhou D, Ohno N, Terada N, Li Z, Morita H, Inui K et al (2007) Immunohistochemical analyses on serum proteins in nephrons of protein-overload mice by "in vivo cryotechnique". Histol Histopathol 22(2):137–145

Immunolocalization of Serum Proteins in Xenografted Mouse Model of Human Tumor Cells

50

Yuqin Bai, Nobuhiko Ohno, Nobuo Terada, and Shinichi Ohno

Abstract

The transport mechanism of soluble molecules throughout the interstitial matrix is closely associated with human tumor behavior in vivo. However, the examination of soluble components in histological architectures has been hampered by artifacts caused during conventional tissue preparation. In this study, the immunodistribution of intrinsic and extrinsic serum components in tumor tissues was examined in xenografted human lung large carcinoma cells using "in vivo cryotechnique" (IVCT) and cryobiopsy, where target tissues are directly cryofixed in vivo. Human lung cancer cells were subcutaneously injected into the dorsal flank of nude mice, and paraffin sections and cryosections of produced tumors were prepared with different methods. Immunolocalization of serum proteins, including albumin, immunoglobulin G (IgG), and IgM, as well as intravenously injected bovine serum albumin (BSA) was examined. Their immunodistribution was more clearly observed in the interstitium by both IVCT and cryobiopsy than conventional methods. IgM was immunolocalized within blood vessels, whereas albumin and IgG were observed in the tumor interstitium. Moreover, intravenously injected bovine serum albumin exhibited leakage from the blood capillaries into surrounding connective tissues in 24 h, but it gradually diffused to the interstitium of the tumor masse in 3 days. These results suggest that molecular leakage from blood capillaries varies significantly in different areas of developing tumors and that small serum proteins, but not large ones, were abundantly immunolocalized in the tumor interstitium. Both IVCT and cryobiopsy were found to be useful for immunohistochemical studies of soluble molecules in tumors with blood circulation and may therefore be helpful for further histopathological analyses.

Keywords

Immunohistochemistry • In vivo cryotechnique • Cryobiopsy • Serum proteins • Xenografted human lung carcinoma tissue

Y. Bai, M.D., Ph.D. (✉)
Department of Anatomy and Molecular Histology, Interdisciplinary Graduate School of Medicine and Engineering, University of Yamanashi, 1110 Shimokato, Chuo City, Yamanashi 409-3898, Japan

Department of Pathology, Medical College of Chifeng University, Ying Bin Road, Chifeng 024000, Inner Mongolua, People's Republic of China
e-mail: baiyuqincn2000@aliyun.com

N. Ohno • S. Ohno
Department of Anatomy and Molecular Histology, Interdisciplinary Graduate School of Medicine and Engineering, University of Yamanashi, 1110 Shimokato, Chuo City, Yamanashi 409-3898, Japan

N. Terada
Division of Health Sciences, Shinshu University Graduate School of Medicine, 3-1-1 Asahi, Matsumoto City, Nagano 390-8621, Japan

Department of Anatomy and Molecular Histology, Interdisciplinary Graduate School of Medicine and Engineering, University of Yamanashi, 1110 Shimokato, Chuo City, Yamanashi 409-3898, Japan

S. Ohno et al. (eds.), *In Vivo Cryotechnique in Biomedical Research and Application for Bioimaging of Living Animal Organs*, DOI 10.1007/978-4-431-55723-4_50

50.1 Introduction

A complex tumor interstitium has been reported to be an essential component of expanding tumor masses, closely associated with various aspects of their development, progression, and metastasis [1, 2]. The interstitial compartments generally have different features distinct from most normal tissues, such as relatively large extracellular spaces, various concentrations of matrix components, high interstitial fluid pressures, and less developed lymphatic networks [3]. An adequate supply of nutrition for tumor cells through the vasculature and interstitial matrix is necessary for continuous tumor growth in vivo [4]. The transport mechanism of fluid and soluble molecules in the interstitial matrix is controlled by the properties of the interstitial compartments, including osmotic pressure, and is also determined by factors of the molecules, such as the molecular weight and charge [5, 6]. Such physicochemical properties have been extensively examined, depending on the distribution of various extrinsic molecules circulating in blood vessels [7–9]. On the other hand, the examination of soluble components in histological structures has been hampered by artifacts caused during conventional tissue preparation [10]. Since 1996, our in vivo cryotechnique (IVCT), in which target animal organs are directly cryofixed using a liquid isopentane-propane cryogen, has been used for morphological and immunohistochemical analyses in various organs of living mice and rats without producing the technical artifacts caused by the conventional preparation methods [11]. The IVCT has various technical merits, including the prevention of tissue shrinkage, a natural antigen-retrieval effect, and time-dependent analyses in the order of seconds [12]. Moreover, it preserves the native distribution of soluble intra- or extracellular components, such as serum proteins, in living mouse organ [13], and the distributions of soluble molecules could be compared with the histological architecture [14]. We recently developed another method called "cryobiopsy," with potentially similar technical merits to IVCT [15], which will be applied to human tissues in clinical medicine. So, according to these merits and advances, cryobiopsy has already been used for morphological and immunohistochemical analyses of xenografted human lung tumor tissues, resulting in the demonstration of functional blood vessels [16].

In the present study, more detailed immunohistochemical analyses of soluble serum proteins in the xenografted mouse model of human tumor cells were performed with various cryotechniques, which were then compared with the conventional preparation method, such as immersion-fixation followed by dehydration (IMDH). Furthermore, the time-dependent distribution of the extrinsic soluble proteins was also examined in the tumor tissues by immunohistochemistry.

50.2 Histological Findings of Xenografted Lung Larger Cell Carcinoma Tissue with Cryobiopsy

The different immunodistribution of serum proteins in tumor tissues, as clearly revealed with both IVCT and cryobiopsy, appeared to depend on differences of their molecular weights. As shown in Fig. 50.1, the small serum proteins, such as albumin (MW, 69 kDa) and IgG1 (MW, 150 kDa), but not the large molecules, such as IgM (MW, 900 kDa), were immunolocalized in most areas of the tumor interstitial matrix. Moreover, in the normal interstitial tissues of living mouse ovaries, such discrepancy concerning the albumin, IgG1, and IgM distributions was clearly observed, as previously reported [10]. The molecular weight of the permeating proteins appears to be one of the factors affecting the molecular permeability from the blood vessels into the interstitial spaces of tumor tissues, in addition to other factors, such as the composition of extracellular matrices and abnormally elevated interstitial fluid pressures [6, 7, 9, 17]. Our results indicated that the amount of large serum proteins, such as IgM, was kept low in the interstitial matrix even after constant exposure to the vascular plasma containing IgM.

50.3 Immunolocalization of Intrinsic Serum Proteins in Xenografted Lung Larger Cell Carcinoma Tissue with FQF

Conventional immunohistochemical techniques have some problems of molecular diffusion artifact and antigen masking for the detection of immunoglobulin in animal organs, which were already reported in large malignant cells like the Reed-Sternberg cells of Hodgkin's lymphoma [18]. In the present study, the diffusion artifacts of both albumin and IgG1 were also observed in tumor cells prepared by FQF (Fig. 50.2). However, such technical artifacts can be mostly prevented by IVCT and Cb, because cells and tissues in target organs of living animal bodies are immediately cryofixed at the time of freezing in situ.

50.4 Immunodistribution of Extrinsic BSA in Xenografted Lung Larger Cell Carcinoma Tissue with IVCT

The time-dependent immunolocalization of injected BSA was revealed within the tumor tissues, as shown in Fig. 50.3. The injected BSA was mostly immunolocalized within blood vessels in the tumor mass and the capsular connective tissue 10 min after the injection, but later it was diffusely immunolocalized in the surrounding connective tissue and a fraction

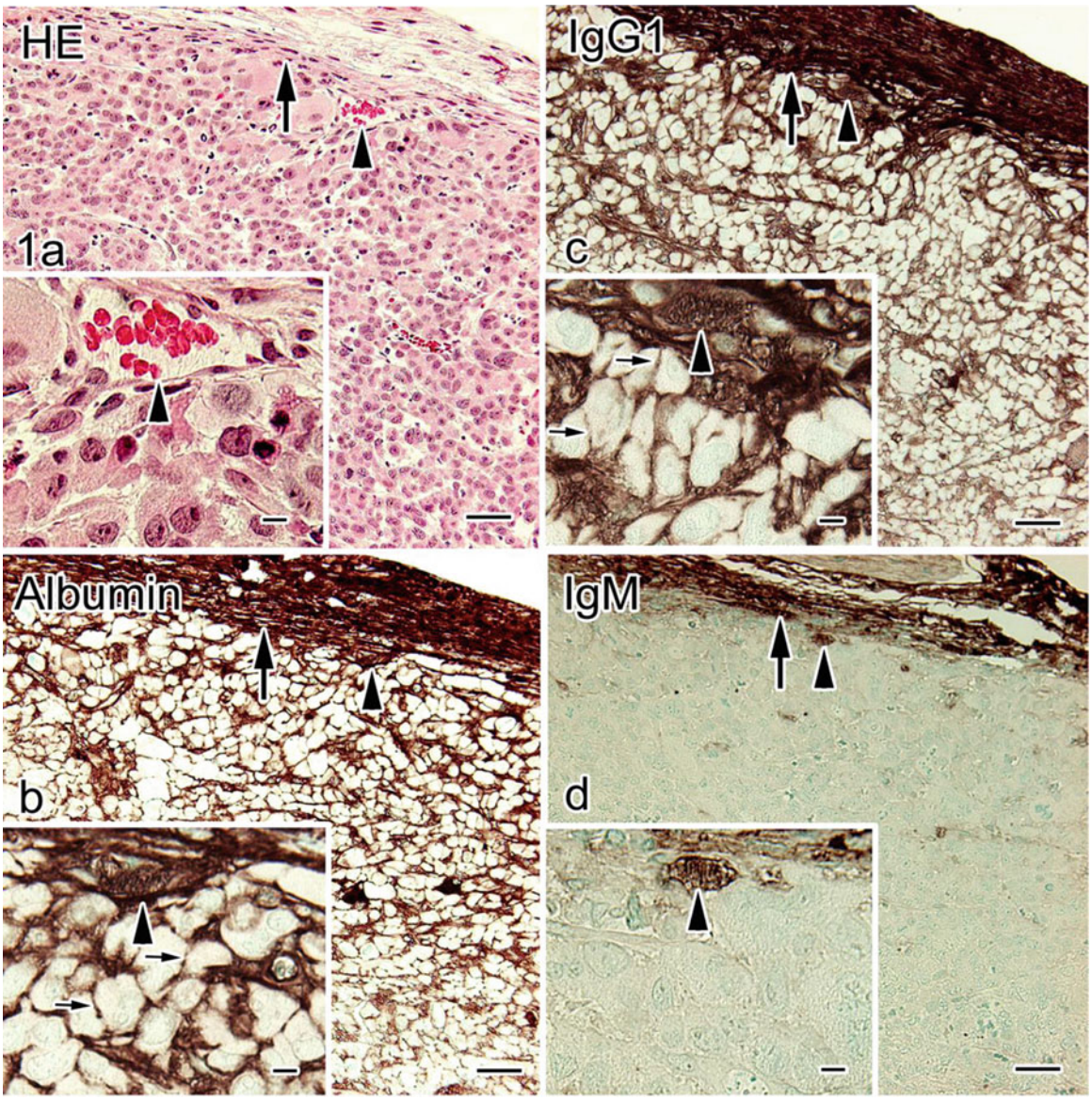

Fig. 50.1 Immunolocalization of serum proteins in the tumor tissues formed by the Lu65 cells and prepared with cryobiopsy (Cb). Their serial sections were stained with hematoxylin-eosin (HE, **a**) or immunostained for albumin (**b**), immunoglobulin G1 (IgG1; **c**), and IgM (**d**). **b** and **c**. Both albumin and IgG1 are clearly immunolocalized in the tumor blood vessels (*arrowheads*) and also in the interstitial matrix between the tumor cells (*small arrows*). **d**. On the other hand, IgM immunostaining is detected mainly in the tumor blood vessels (*arrowheads*) and the connective tissue of the capsule around the tumor mass. Other serum proteins, albumin and IgG1, are also observed in the connective tissue around the tumor mass (**a**–**d**, *large arrows*). *Bars* **a**–**d**, 50 μm; *inset*, 10 μm

of the interstitium in the tumor mass. Some previous studies reported that BSA leaked out into the interstitial spaces within 1 h, using live imaging with intravital or a confocal laser scanning microscope [8, 19]. Small amounts of molecules may be difficult to visualize on histological sections by immunohistochemistry. However, because different intensities of immunoreactivity in a single histological section usually depend on the relative amount of active antigen sites, our findings suggest that the permeability of blood vessels in the tumor tissue is distinct from that in the surrounding connective tissue of the tumor capsule, which would partly depend on the molecular structure of blood vessels [16, 20]. In fact, we have detected abundant immunolocalization of BSA in the connective tissue of the tumor capsules 24 h after the BSA injection. In addition, 72 h after the BSA injection, BSA immunolocalization was more clearly detected in the interstitium of the tumor tissue. The repeated injection of BSA induced the accumulation of BSA in the blood circulation, thus causing the prolonged exposure of the tumor mass to higher concentrations of BSA over a few days, resulting in the increased concentration of leaked BSA in the tumor interstitium.

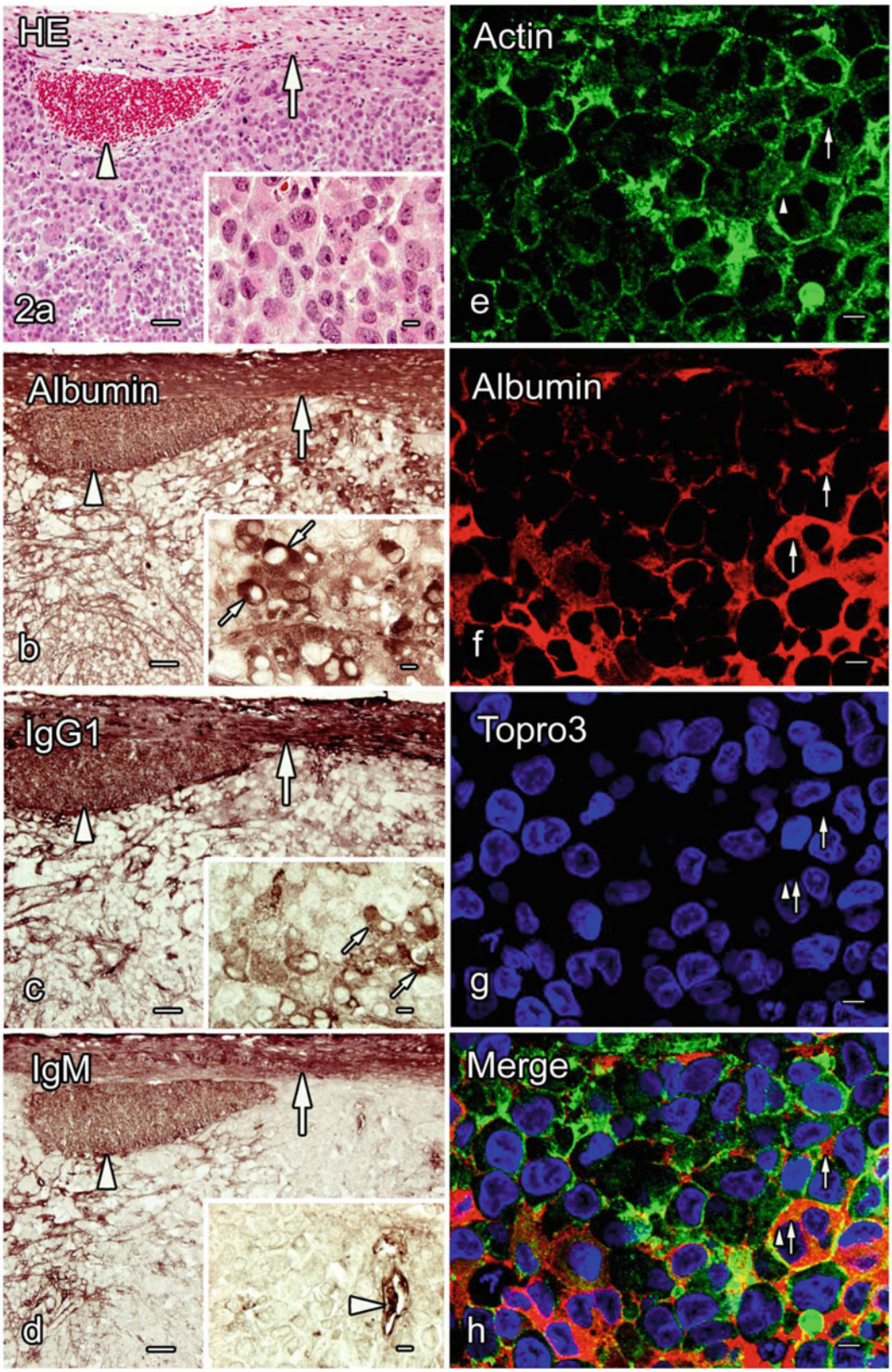

Fig. 50.2 Immunolocalization of serum proteins in the tumor tissues formed by Lu65 cells, which were prepared with the quick-freezing of fresh resected tissues (FQF). **a**–**d**. Light micrographs of the serial paraffin sections stained with hematoxylin-eosin (HE) or immunostained for albumin (**b**), immunoglobulin G1 (IgG1; **c**), and IgM (**d**). Both albumin and IgG1 are immunolocalized in the tumor blood vessels (**b**, **c**, *arrowheads*) and the interstitium (**b**, **c**, *large arrows*), as well as in the cytoplasm of some tumor cells (**b**, **c**, *small arrows in insets*). IgM immunoreactivity is also detected in the interstitium (**d**, *arrow*) in addition to the blood vessels (**d**, *arrowheads*). **e**–**h**. Actin immunofluorescence is observed in the cytoplasm and along the cell membrane of the Lu65 cells (**e**, **h**, *arrowheads*). Albumin is immunolocalized in the tumor interstitium and the cytoplasm of some tumor cells (**f**, **h**, *small arrows*). All the serum proteins are also observed in the connective tissues around the tumor mass (**a**–**d**, *curved arrows*). *Bars* **a**–**d**, 50 μm (*insets*, 10 μm); **e**–**h**, 20 μm

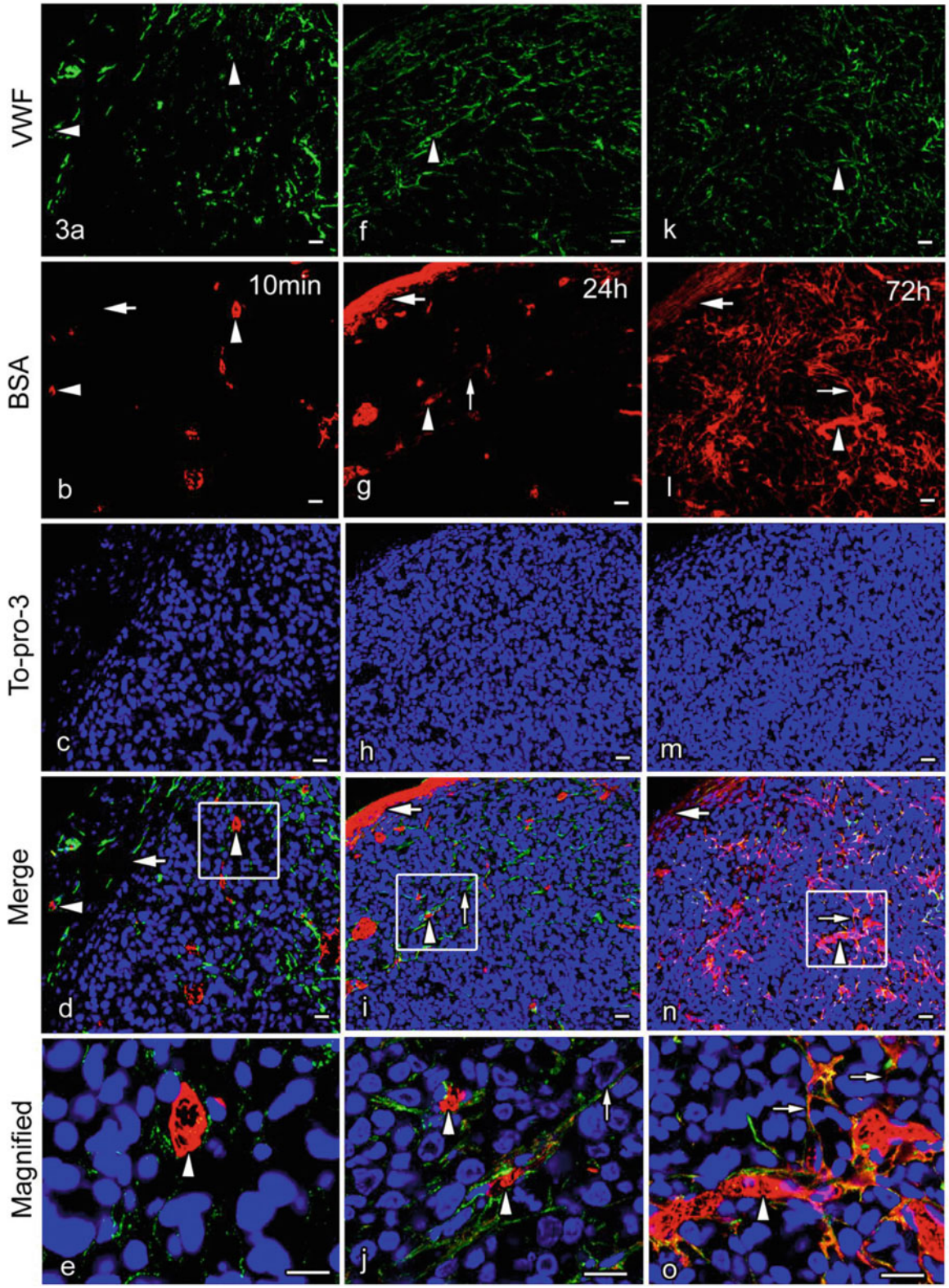

Fig. 50.3 Double-immunofluorescence micrographs of von Willebrand factor (vWF; *green* color) and intravenously injected bovine serum albumin (BSA; *red* color) 10 min (**a**–**e**) and 24 h (**f**–**j**) after the injection or at 72 h of the daily BSA injections (**k**–**o**), which were obtained with cryosections of the tumor tissues formed by the Lu99 cells and prepared with IVCT. **a**–**e**. BSA immunostaining can be mostly observed in some blood vessels immunopositive for vWF (**a**, **b**, **d**, **e**, *arrowheads*) 10 min after the BSA injection, although it is not detected in the surrounding connectivity tissue of the tumor capsule (**b**, **d**, *large arrows*). **f**–**j**. However, 24 h after one shot of BSA injection, BSA immunoreactivity is slightly detected in the tumor interstitium (**g**, **i**, **j**, *small arrows*) as well as the tumor blood vessels (**f**, **g**, **i**, **j**, *arrowheads*). It is also strongly detected in the surrounding connective tissue of the tumor capsule (**g**, **i**, *large arrows*). **k**–**o**. BSA immunoreactivity is widely seen in the tumor interstitium (**l**, **n**, **o**, *small arrows*) outside the blood vessels (**k**, **l**, **n**, **o**, *arrowheads*) and also in the surrounding connective tissue (**l**, **n**, *large arrows*) because of daily injections of BSA at 72 h *Bars* 20 μm

50.5 Concluding Remarks

The immunolocalization of serum proteins in the tumor interstitium was more clearly observed by both IVCT and cryobiopsy, without molecular translocation, which was inevitable by the conventional preparation methods. Large serum proteins were immunolocalized within the tumor blood vessels, whereas smaller ones were abundantly immunolocalized in the tumor interstitium, as revealed by the IVCT. Moreover, the intravenously injected BSA exhibited distinct immunolocalization in the tumor tissue and surrounding connective tissues, and the BSA immunoreactivity gradually increased in the tumor interstitium over a period of 72 h. These findings suggest that the molecular transport and passive distribution mechanisms from blood circulation are different in various areas of the tumor tissues. Furthermore, both IVCT and cryobiopsy are helpful for carrying out further studies on the native molecular distribution in the tumor interstitium and also for performing histopathological diagnoses in clinical medicine in the near future. The present figures were already published in our paper, Histol Histopathol (2009) 24:717–728, and cited with their permissions.

References

1. Bhowmick NA, Neilson EG, Moses HL (2004) Stromal fibroblasts in cancer initiation and progression. Nature 432(7015):332–337
2. Mueller MM, Fusenig NE (2004) Friends or foes-bipolar effects of the tumour stroma in cancer. Nat Rev Cancer 4(11):839–849
3. Jain RK (1987) Transport of molecules in the tumor interstitium: a review. Cancer Res 47(12):3039–3051
4. Fukumura D, Jain RK (2007) Tumor microvasculature and microenvironment: targets for anti-angiogenesis and normalization. Microvasc Res 74(2–3):72–84
5. Dellian M, Yuan F, Trubetskoy VS, Torchilin VP, Jain RK (2000) Vascular permeability in a human tumour xenograft: molecular charge dependence. Br J Cancer 82(9):1513–1518
6. Bouzin C, Feron O (2007) Targeting tumor stroma and exploiting mature tumor vasculature to improve anti-cancer drug delivery. Drug Resist Updat 10(3):109–120
7. Netti PA, Berk DA, Swartz MA, Grodzinsky AJ, Jain RK (2000) Role of extracellular matrix assembly in interstitial transport in solid tumors. Cancer Res 60(9):2497–2503
8. Clarijs R, van Dijk M, Ruiter DJ, de Waal RM (2005) Functional and morphologic analysis of the fluid-conducting meshwork in xenografted cutaneous and primary uveal melanoma. Invest Ophthalmol Vis Sci 46(9):3013–3020
9. Dreher MR, Liu W, Michelich CR, Dewhirst MW, Yuan F, Chilkoti A (2006) Tumor vascular permeability, accumulation, and penetration of macromolecular drug carriers. J Natl Cancer Inst 98(5):335–344
10. Zhou H, Ohno N, Terada N, Saitoh S, Fujii Y, Ohno S (2007) Involvement of follicular basement membrane and vascular endothelium in blood follicle barrier formation of mice revealed by 'in vivo cryotechnique'. Reproduction 134(2):307–317
11. Ohno S, Terada N, Fujii Y, Ueda H, Takayama I (1996) Dynamic structure of glomerular capillary loop as revealed by an in vivo cryotechnique. Virchows Arch 427(5):519–527
12. Ohno N, Terada N, Saitoh S, Zhou H, Fujii Y, Ohno S (2007) Recent development of in vivo cryotechnique to cryobiopsy for living animals. Histol Histopathol 22(11):1281–1290
13. Saitoh S, Terada N, Ohno N, Ohno S (2008) Distribution of immunoglobulin-producing cells in immunized mouse spleens revealed with "in vivo cryotechnique". J Immunol Methods 331(1–2):114–126
14. Li Z, Ohno N, Terada N, Zhou D, Yoshimura A, Ohno S (2006) Application of periodic acid-Schiff fluorescence emission for immunohistochemistry of living mouse renal glomeruli by an "in vivo cryotechnique". Arch Histol Cytol 69(3):147–161
15. Fujii Y, Ohno N, Li Z, Terada N, Baba T, Ohno S (2006) Morphological and histochemical analyses of living mouse livers by new 'cryobiopsy' technique. J Electron Microsc 55(2):113–122
16. Ohno N, Terada N, Bai Y, Saitoh S, Nakazawa T, Nakamura N, Naito I, Fujii Y, Katoh R, Ohno S (2008) Application of cryobiopsy to morphological and immunohistochemical analyses of xenografted human lung cancer tissues and functional blood vessels. Cancer 113(5):1068–1079
17. Pluen A, Boucher Y, Ramanujan S, McKee TD, Gohongi T, di Tomaso E, Brown EB, Izumi Y, Campbell RB, Berk DA, Jain RK (2001) Role of tumor-host interactions in interstitial diffusion of macromolecules: cranial vs. subcutaneous tumors. Proc Natl Acad Sci U S A 98(8):4628–4633
18. Mason DY, Biberfeld P (1980) Technical aspects of lymphoma immunohistology. J Histochem Cytochem 28(8):731–745
19. Jain RK (2001) Delivery of molecular and cellular medicine to solid tumors. Adv Drug Deliv Rev 46(1–3):149–168
20. Tilki D, Kilic N, Sevinc S, Zywietz F, Stief CG, Ergun S (2007) Zone-specific remodeling of tumor blood vessels affects tumor growth. Cancer 110(10):2347–2362

Histochemical Approach of Cryobiopsy for Glycogen Distribution in Living Mouse Livers Under Fasting and Local Circulation Loss Conditions

51

Yurika Saitoh, Nobuo Terada, Nobuhiko Ohno, and Shinichi Ohno

Abstract

Soluble proteins and glycogen particles, which are easily lost upon conventional chemical fixation, have been reported to be better preserved in paraffin-embedded sections by "cryobiopsy" combined with freeze-substitution fixation (FS). In this part, we mentioned the distribution of glycogen in living mouse livers under (1) food restriction and (2) local circulation loss conditions with periodic acid-Schiff (PAS) staining by cryobiopsy. (1) Livers of fully fed mice showed high PAS-staining intensity in the cytoplasm of all hepatocytes, showing much glycogen in all hepatocytes. However, treatment with α-amylase clarifies that hepatocytes around the central vein preserve more glycogen than the hepatocytes around the portal vein. At 6 or 12 h after fasting, PAS-staining intensity markedly decreased in restricted areas of zone I near the portal tracts. This result was the same as that of specimens gotten from individual mouse. On the other hand, glycogen distributions were different in local circulation loss condition which caused by temporarily clipping of liver tissues followed by recovery of blood circulation. (2) In the liver tissues in which blood was recirculated for 1 h after the 30-min anoxia, PAS staining was still observed in zone II and also in restricted areas of zone I far from the portal tracts. We propose that the level of consumption or production of glycogen particles could vary in zone I, depending on the distance from the portal tracts. Thus, cryobiopsy combined with FS enabled us to examine time-dependent changes in glycogen distribution in the liver tissues of living mice. This combination might be applicable to the clinical evaluation of human liver tissues.

Keywords

Glycogen • PAS staining • Zonal difference

51.1 Introduction

Cryobiopsy enables us to repeatedly obtain multiple tissue samples from a single mouse under different experimental conditions [1, 2]. In this chapter, we focused on the distribution of glycogen in the mouse liver and introduced their consumption pattern clarified by cryobiopsy. And then how to distinguish consumption from leakage by damage was mentioned. A large amount of glycogen in the livers is an important energy source to be metabolized into blood glucose to sustain animal life [3]. Glycogen metabolism was related to not only feeding conditions but also ischemia-reperfusion

Y. Saitoh (✉) • N. Ohno • S. Ohno
Department of Anatomy and Molecular Histology, Interdisciplinary Graduate School of Medicine and Engineering, University of Yamanashi, 1110 Shimokato, Chuo City, Yamanashi 409-3898, Japan
e-mail: yurikas@yamanashi.ac.jp

N. Terada
Division of Health Sciences, Shinshu University Graduate School of Medicine, 3-1-1 Asahi, Matsumoto City, Nagano 390-8621, Japan

Department of Anatomy and Molecular Histology, Interdisciplinary Graduate School of Medicine and Engineering, University of Yamanashi, 1110 Shimokato, Chuo City, Yamanashi 409-3898, Japan

S. Ohno et al. (eds.), *In Vivo Cryotechnique in Biomedical Research and Application for Bioimaging of Living Animal Organs*, DOI 10.1007/978-4-431-55723-4_51

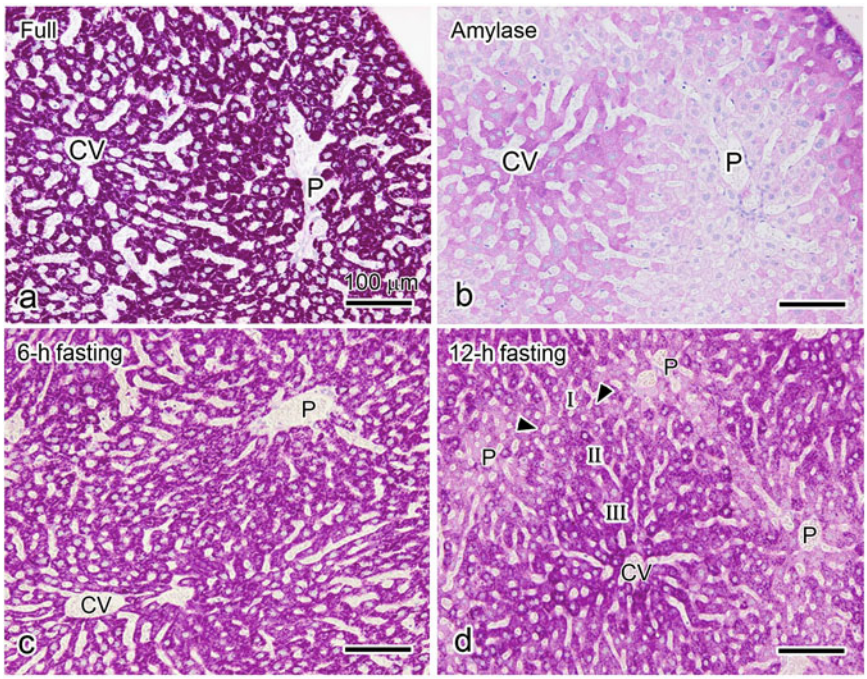

Fig. 51.1 Glycogen distribution of cryobiopsied liver tissue specimens stained with PAS. (**a**) Fully PAS-stained hepatocytes are clearly observed in the specimen without α-amylase treatment. (**b**) Hepatocytes around the central vein (CV) exhibit higher-intensity PAS staining than those around the portal tract (P) after treatment with α-amylase. (**c**) Slightly weaker PAS staining is detected around some portal tracts after 6-h fasting. (**d**) In the liver tissues of mice fasted for 12 h, PAS-staining intensity around the portal tracts is markedly decreased, but still observed in parts of zone I (*arrowheads*). *CV* central vein, *P* portal vein. Bars: 100 μm

and stress of animal livers [4–8]. Ischemia and reperfusion typically occur in liver transplants and result in various types of liver damage and reactions [9–14]. Therefore, it is necessary to precisely determine time-dependent changes in the glycogen storage of hepatocytes in paraffin-embedded tissues, which reflect their living states. In conventional preparation with chemical fixatives in a typical buffer solution, the artificial loss of glycogen particles is much higher than in various cryotechniques [15].

51.2 Distinguishable Differences of a Tiny Amount of Glycogen in Hepatocytes

Cryobiopsy of liver tissues was performed on anesthetized mice [2, 16]. Briefly, after exposure of target liver lobes, a piece of tissue was quickly pinched off using handmade cryoforceps attached to sponge reservoirs of liquid nitrogen on Keisei Osteotrite Tweezers® (F-2051 or F-2052, Keisei Medical Industrial Co., Ltd., Niigata, Japan), which had already been precooled in liquid nitrogen (LN_2, −196 °C). The cryobiopsied liver tissues were immediately immersed in liquid isopentane-propane cryogen (−193 °C) precooled in LN_2 and then transferred into acetone containing 2 % paraformaldehyde at about −80 °C for starting freeze-substitution fixation (FS) [2, 16]. Cryobiopsy-FS specimen is able to choose usual paraffin embedding or sucrose embedding for frozen section. In this chapter, we're showing paraffin-embedded specimens [1]. The paraffin-embedded specimens were treated in the same way as conventional specimens. To detect glycogen in hepatocytes, deparaffinized sections were incubated in periodic acid followed by Schiff's solution and sodium metabisulfite. In mouse liver tissues of fully fed mice prepared by cryobiopsy, high-intensity PAS staining was observed as a strong red-purple color in the cytoplasm of all hepatocytes (Fig. 51.1a). However, treatment with α-amylase for serial sections digested the glycogen in hepatocytes and clarified that the hepatocytes around central veins kept much more glycogen in their cytoplasm than those around the portal veins (Fig. 51.1b). Compared with glycogen of fully fed mice, the intensity of PAS staining after fasting for 6 h became slightly weaker in hepatocytes (Fig. 51.1c). After 12-h fasting, the PAS-staining intensity had clearly decreased around almost all portal tracts (Fig. 51.1d). Most hepatocytes in parts of zone I far from the portal veins were still more PAS positive (arrowheads in Fig. 51.1d).

51.3 Repeatable Cryobiopsy for Individual Mouse

Cryobiopsy was developed for clinical and repeated collection as substitute for our "in vivo cryotechnique." To examine that the cryobiopsy was time-dependently repeatable, one piece from an area of liver tissues was obtained by cryobiopsy (Fig. 51.2a-i), and another area was cryobiopsied for 6 h (Fig. 51.2c-ii). Temporary bleeding from the tissue area pinched with the cryoforceps was quickly stopped by covering it with instant glue (Fig. 51.2b). During the continuous experiments, all the mice were warmed on an electrically

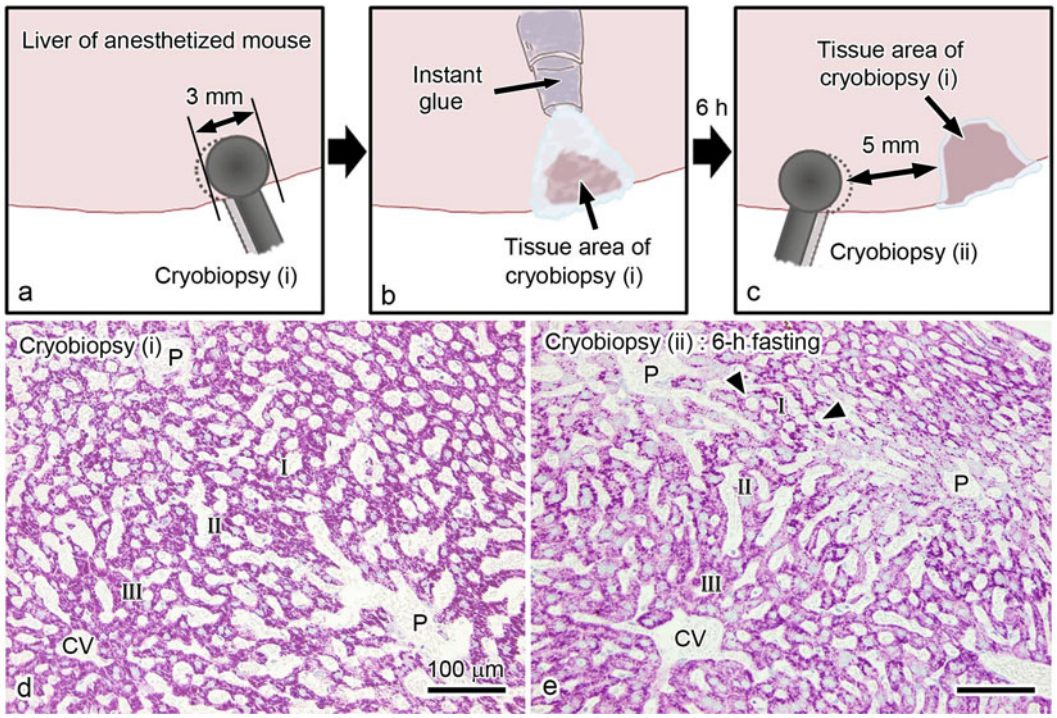

Fig. 51.2 Schematic representation of a series of cryobiopsy processes to obtain liver tissue specimens from anesthetized mice. A liver specimen is initially pinched off at one area with a pair of cryoforceps (cryobiopsy (i) in (**a**)), and bleeding is immediately stopped with an instant glue (**b**). After 6-h fasting, another liver tissue specimen is similarly obtained at a second area with the cryoforceps (cryobiopsy (ii) in (**c**)). (**d**) In the specimen of cryobiopsy (i), intense PAS staining is observed in almost all hepatocytes, the exception being those around portal veins (P). (**e**) The PAS-staining intensity of the area of cryobiopsy (ii) is found to be decreased around portal tracts. Note the strongly PAS-positive hepatocytes remaining in parts of the middle of zone I (*arrowheads*). *CV* central vein, *P* portal vein. Bars: 100 μm

heated plate to maintain their body temperature. In the liver tissues of an almost fully fed mouse, PAS staining was observed in almost all hepatocytes (Fig. 51.2a), with a slightly lower intensity in some hepatocytes around portal veins. After 6-h fasting, the PAS-staining intensity of hepatocytes had clearly decreased around the portal tracts (Fig. 51.2b), but other hepatocytes far from the portal veins in zone I were still PAS positive (arrowheads in Fig. 51.2b). Thus, the time-dependent changes in glycogen distribution can be clearly evaluated in a single mouse liver by cryobiopsy.

51.4 Detection of Different Consumption Under Local Circulation Loss Condition

To examine the effects of blood circulation on glycogen consumption, temporary stopping and reflowing of blood circulation were produced by binding with a circular clip and removing it (Fig. 51.3a). To prevent drying of the liver surface tissues, abdominal skin was quickly sutured, and a cotton sheet-absorbing physiological saline was placed on the mouse abdomen throughout the experiment. Temporary hypoxia of some parts of the clipped liver tissues had already been confirmed by measuring the oxygen saturation of similar liver tissues with confocal Raman cryomicroscopy, as previously reported [17]. After stopping blood circulation for 30 min and reflowing for 1 h, cryobiopsy of the restricted areas was performed on the inside (Fig. 51.3b-I) or outside (Fig. 51.3b-II) of the clipped liver tissues. In the liver tissues inside the clipped areas, the PAS-staining intensity was markedly decreased in certain areas around the portal veins of zone I and also the central veins (zone III) (Fig. 51.3c). Even in liver tissues outside the clipped areas (Fig. 51.3c, d), the PAS-staining intensity heterogeneously decreased as a mosaic pattern in all zonal areas. Thus, the PAS staining of liver tissues by cryobiopsy clearly revealed zonal differences in glycogen storage after reflowing of blood circulation in living mice and probably reflects zonal metabolic functions in vivo.

51.5 Conclusion

The cryobiopsy presented here is a simple manual technique to capture all biological materials of living mouse livers in rapidly frozen ice crystals, the characteristics of which

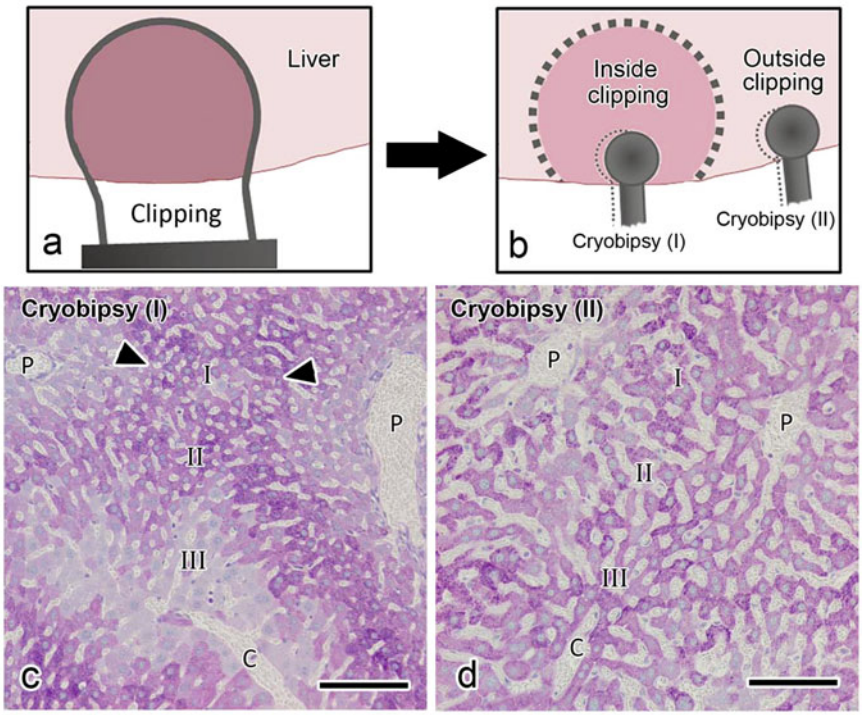

Fig. 51.3 Schematic representation of the experiment about anoxic blood circulation; an area of the mouse liver tissue is clipped to stop the blood circulation for 30 min (**a**). One hour after removing the clip, some liver tissue specimens are obtained inside or outside the clipped area with cryoforceps (cryobiopsy (I) and (II) in (**b**)). Liver tissues were pinched off from inside ((**c**) cryobiopsy (I)) or outside ((**d**) cryobiopsy (II)) clipped areas, as shown in (**b**). (**c**) Marked reductions in PAS-staining intensity are detected in zone III and local areas of zone I near the portal tracts inside the clipped areas. Staining is still observed in areas far from the portal tracts in zone I (*arrowheads*). (**d**) The PAS-staining intensity is heterogeneously detected in all areas of the liver tissue outside the clipped area. *CV* central vein, *P* portal vein. Bars: 100 μm

probably reflect their living states [1, 2, 16]. This does not require resection of a target organ with continuous blood circulation in vivo, results in neither ischemia nor anoxia, and enables us to obtain multiple tissue samples from a single animal and any areas of the target organ at different times. The subsequent freeze substitution in acetone with chemical fixatives is useful to preserve many glycogen particles in hepatocytes and avoids their removal during the preparation steps. Thus, the cryobiopsy technique combined with freeze-substitution fixation for PAS staining is a reliable tool to visualize changes in glycogen storage in hepatocytes of living animal livers. This text is mainly quoted from Reference [18].

References

1. Bai Y, Ohno N, Terada N, Saitoh S, Nakazawa T, Nakamura N, Katoh R, Ohno S (2009) Immunolocalization of serum proteins in xenografted mouse model of human tumor cells by various cryotechniques. Histol Histopathol 24:717–728
2. Ohno N, Terada N, Bai Y, Saitoh S, Nakazawa T, Nakamura N, Naito I, Fujii Y, Katoh R, Ohno S (2008) Application of cryobiopsy to morphological and immunohistochemical analyses of xenografted human lung cancer tissues and functional blood vessels. Cancer 113:1068–1079
3. Bollen M, Keppens S, Stalmans W (1998) Specific features of glycogen metabolism in the liver. Biochem J 336:19–31
4. Hammad ES, Striffler JS, Cardell RR Jr (1982) Morphological and biochemical observations on hepatic glycogen metabolism in mice on a controlled feeding schedule. II. Streptozotocin-diabetic mice. Dig Dis Sci 27:692–700
5. He XS, Ma Y, Wu LW (2005) Dynamical changing patterns of glycogen and enzyme histochemical activities in rat liver graft undergoing warm ischemia injury. World J Gastroenterol 11:2662–2665
6. Dodero F, Benkoel L, Hardwigsen J, Campan P, Lambert R, Botta-Fridlund D, Le Treut YP, Chamlian A (1999) Effect of ischemia-reperfusion on the heterogeneous lobular distribution pattern of glycogen content and glucose-6-phosphatase activity in human liver allograft. Cell Mol Biol 45:1209–1215
7. Frederiks WM, Marx F (1990) The effect of ischemia on glycogen phosphorylase activity in rat liver: a quantitative histochemical study. Anal Cell Pathol 2:347–355
8. Domenicali M, Vendemiale G, Serviddio G, Grattagliano I, Pertosa AM, Nardo B, Principe A, Viola A, Trevisani F, Altomare E, Bernardi M, Caraceni P (2005) Oxidative injury in rat fatty liver exposed to ischemia-reperfusion is modulated by nutritional status. Dig Liver Dis 37:689–697
9. Peralta C, Bartrons R, Riera L, Manzano A, Xaus C, Gelpí E, Roselló-Catafau J (2000) Hepatic preconditioning preserves energy metabolism during sustained ischemia. Am J Physiol Gastrointest Liver Physiol 279:163–171
10. Sumimoto R, Southard JH, Belzer FO (1993) Livers from fasted rats acquire resistance to warm and cold ischemia injury. Transplantation 55:728–732
11. Miller K, Halow J, Koretsky AP (1993) Phosphocreatine protects transgenic mouse liver expressing creatine kinase from hypoxia and ischemia. Am J Physiol 265:1544–1551
12. Bradham CA, Srachlewitz RF, Gao W, Qian T, Jayadev S, Jenkins G, Hannun Y, Lemasters JJ, Thurman RG, Brenner DA (1997) Reperfusion after liver transplantation in rats differentially activates the mitogen-activated protein kinases. Hepatology 25:1128–1135
13. Bendinelli P, Piccoleti R, Maroni P, Bernelli-Zazzera A (1996) The MAP kinase cascades are activated during post-ischemic liver reperfusion. FEBS Lett 398:193–197

14. Selzner M, Selzner N, Jochum W, Graf R, Clavien PA (2007) Increased ischemic injury in old mouse liver: an ATP-dependent mechanism. Liver Transpl 13:382–390
15. Ohno N, Terada N, Ohno S (2006) Histochemical analyses of living mouse liver under different hemodynamic conditions by "in vivo cryotechnique". Histochem Cell Biol 126:389–398
16. Fujii Y, Ohno N, Li Z, Terada N, Baba T, Ohno S (2006) Morphological and histochemical analyses of living mouse livers by new 'cryobiopsy' technique. J Electron Microsc 55:113–122
17. Terada N, Ohno N, Saitoh S, Ohno S (2008) Application of "in vivo cryotechnique" to detect erythrocyte oxygen saturation in frozen mouse tissues with confocal Raman cryomicroscopy. J Struct Biol 163:147–154
18. Saitoh Y, Terada N, Saitoh S, Ohno N, Fujii Y, Ohno S (2010) Histochemical approach of cryobiopsy for glycogen distribution in living mouse livers under fasting and local circulation loss conditions. Histochem Cell Biol 133:229–239

Part IX
New Bioimaging of Living Animal Tissues

Bioimaging of Fluorescence-Labeled Mitochondria in Subcutaneously Grafted Murine Melanoma Cells by the "In Vivo Cryotechnique"

52

Nobuhiko Ohno, Ting Lei, Zheng Huang, Takeshi Sakoh, Yurika Saitoh, and Shinichi Ohno

Abstract

Mitochondrial functions play important roles in metabolism of cancer cells and are affected by the microenvironment including blood circulation. To overcome the technical artifacts of conventional fixation and dehydration methods, the in vivo cryotechnique (IVCT) was combined with fluorescent protein expression and used to examine the distribution of mitochondria in tumor tissues obtained from melanoma-grafted mice. Quick-freezing followed by freeze-substitution (FS) could well retain the fluorescence intensity of fluorescent proteins including mitochondria-targeted DsRed2 (mitoDsRed) in cultured B16-BL6 cells. In the subcutaneous tumor tissues produced by injection of mitoDsRed-expressing B16-BL6 cells, the melanoma cells scattering throughout the tumor tissues prepared with IVCT followed by FS had clear fluorescence of mitoDsRed, and individual tumor cells expressing hypoxia markers, including carbonic anhydrase IX and hypoxia-inducible factor-1α, had decreased volume of mitoDsRed. The cytoplasm and processes of the cancer cells extended along the collagen type IV-immunopositive basement membranes and often contained mitoDsRed. Combination of fluorescent protein expression and IVCT would be a powerful tool to examine cells and organelles with fluorescent protein expression along with histochemical/immunohistochemical labelings. Furthermore, the results suggest that mitochondrial volume and distribution could be modulated by the hypoxic microenvironment and attachment to basement membranes.

Keywords

Cancer • Mitochondria • Fluorescent protein • Blood vessels

52.1 Introduction

Proliferation, cell migration, and metastasis of cancer cells are significantly affected by their metabolism in living animal organs [1]. The microenvironment around the tumor cells, such as blood supply, plays major roles to determine the metabolic profiles of cancer cells and could be spatially and temporarily dynamic [2]. The functions of mitochondria are therefore considered to have major impact on the behavior of living tumor cells, since they are often the central regulator of energy production, intermediate metabolism, and necrotic or apoptotic cell death [3]. Mitochondria in tumor cells are morphologically variable [4, 5], and the mitochondrial distribution and morphology alter energy metabolism through functional alterations of mitochondria themselves [6, 7]. In this regard, technical artifacts caused during conventional preparation steps could have hampered morphological analyses of mitochondria in tumor tissues [8].

To overcome the problem, mitochondria-targeted fluorescent proteins were used in combination with "in vivo

N. Ohno, M.D., Ph.D. (✉) • T. Lei • Z. Huang • T. Sakoh
Y. Saitoh • S. Ohno
Department of Anatomy and Molecular Histology,
Interdisciplinary Graduate School of Medicine and Engineering,
University of Yamanashi, 1110 Shimokato, Chuo City,
Yamanashi 409-3898, Japan
e-mail: nohno@yamanashi.ac.jp

S. Ohno et al. (eds.), *In Vivo Cryotechnique in Biomedical Research and Application for Bioimaging of Living Animal Organs*, DOI 10.1007/978-4-431-55723-4_52

cryotechnique" (IVCT) to prevent artifacts caused by conventional tissue preparation methods [9, 10] and directly visualize distribution of mitochondria in individual melanoma cells. IVCT retains quickly changing metabolic markers and furthermore the in situ distributions of endogenous and exogenous molecules [11–15]. IVCT has been applied to tumor models to prevent tissue shrinkage as well as blood vessel collapse and reveal correlation between the functional blood vessels and expression of a marker of hypoxia, vascular endothelial growth factor [16, 17]. Therefore, the fluorescent protein labeling in combination with cryofixation, including IVCT, was expected to be useful for the histological examination of cells and organelles.

52.2 Observation of Fluorescent Proteins After Quick-Freezing Followed by Freeze-Substitution

In cultured B16-BL6 cells with fluorescent protein expression, conventional immersion fixation with paraformaldehyde (PFA) and quick-freezing followed by freeze-substitution in acetone containing 2 % paraformaldehyde (FS-PFA) maintained the fluorescence signal very well (Fig. 52.1), compared with the other preparation methods using glutaraldehyde or without paraformaldehyde [18]. Fluorescent proteins such as DsRed2, mCherry, EGFP, and Dendra2 all yielded similar results (Fig. 52.1). Freeze-substitution (FS) with only PFA well maintained fluorescence of EGFP and mitochondria-targeted DsRed2 (mitoDsRed), the latter of which appeared granular or tubular profiles in the B16-BL6 cells (Fig. 52.1). Therefore, quick-freezing followed by FS in acetone containing PFA was considered useful to analyze the distribution and changes of fluorescent proteins.

The constant maintenance of fluorescence probes prepared by quick-freezing and subsequent FS depended on the chemicals used for the fixation of tissues. Insufficient maintenance of fluorescent probes following ethanol fixation as well as FS with only acetone indicates that coagulation fixation fails to retain the probes within cells and tissues [13, 18]. On the other hand, diminished fluorescence intensities with glutaraldehyde in the FS solution suggest that glutaraldehyde fixation perturbs the molecular conformation of chromophores [19]. Cryofixation followed by FS with uranyl acetate was shown to preserve the fluorescence signals of GFP [20]. Collectively, chemical fixatives with an appropriate strength are critical to maintain maximal fluorescence emission in cryofixed tissues.

Restricted population of organelles and subcellular regions can be labeled with fluorescent proteins with specific targeting sequences [21]. Other fluorescent dyes are also available in specimens prepared with quick-freezing and FS with such fluorescent proteins, since the fluorescence spectra of the proteins appeared to be unchanged after the tissue preparation. Therefore, combination of live imaging with fluorescent protein expression and cryofixation methods including IVCT will be a useful approach to study living cells and animal tissues/organs.

52.3 IVCT for Tumor Tissues with Fluorescent Protein Expression

Morphology and immunodistribution of serum proteins are well maintained with IVCT, as has been shown in xenografted subcutaneous human lung tumor tissues [17]. Indeed, the morphology of B16-BL6 cancer cells, expressing mitoDsRed and subcutaneously injected to form tumors, was well maintained when tissues were prepared with IVCT [18]. As shown previously [17], open blood vessels containing many flowing red blood cells were not artificially modified with IVCT. Immunoreactivity of IgM, which is a serum macromolecule mostly localized in functional blood vessels, was observed within blood vessels containing flowing red blood cells [17, 18]. The IgM-positive blood vessels were surrounded by basement membranes with type IV collagen, and abundant immunoreactivity of type IV collagen was found in the tumor interstitium [17, 18]. With IVCT, blood vessel diameters were correlated with distances to necrotic tissue areas from the blood vessels [18].

Hypoxic tumor cells around blood vessels could be visualized with two hypoxia markers, hypoxia-inducible factor-1α (HIF1α) and carbonic anhydrase IX (CAIX) with IVCT [5, 22–24]. Immunoreactivity of HIF1α in tumor cell nuclei and that of CAIX on the plasma membranes of tumor cells were well maintained with IVCT (Fig. 52.2) [18]. Immunoreactivity of CAIX and HIF1α observed with IVCT was highest in areas between necrotic regions and CAIX- or HIF1α-immunonegative regions around blood vessels [18], as reported previously [24].

The tumor microenvironment appears to modulate localization of mitochondria in the tumor cells. Fluorescence signals of mitoDsRed were well maintained in cryosections of tumor tissues after IVCT and FS, and the total sizes and distribution of mitochondrial networks could be three dimensionally observed around each DAPI-positive nuclei (Fig. 52.2) [18]. Random selection of cells negative or positive for either HIF1α or CAIX showed that hypoxic cells positive for HIF1α or CAIX have significantly less volume of DsRed-labeled mitochondria (Fig. 52.2). It was also observed that fluorescent mitochondria were aligned in processes extending from cell bodies with DAPI-positive nuclei (Fig. 52.3). These processes were often extended along the basement membranes, which are immunopositive for type IV collagen (Fig. 52.3).

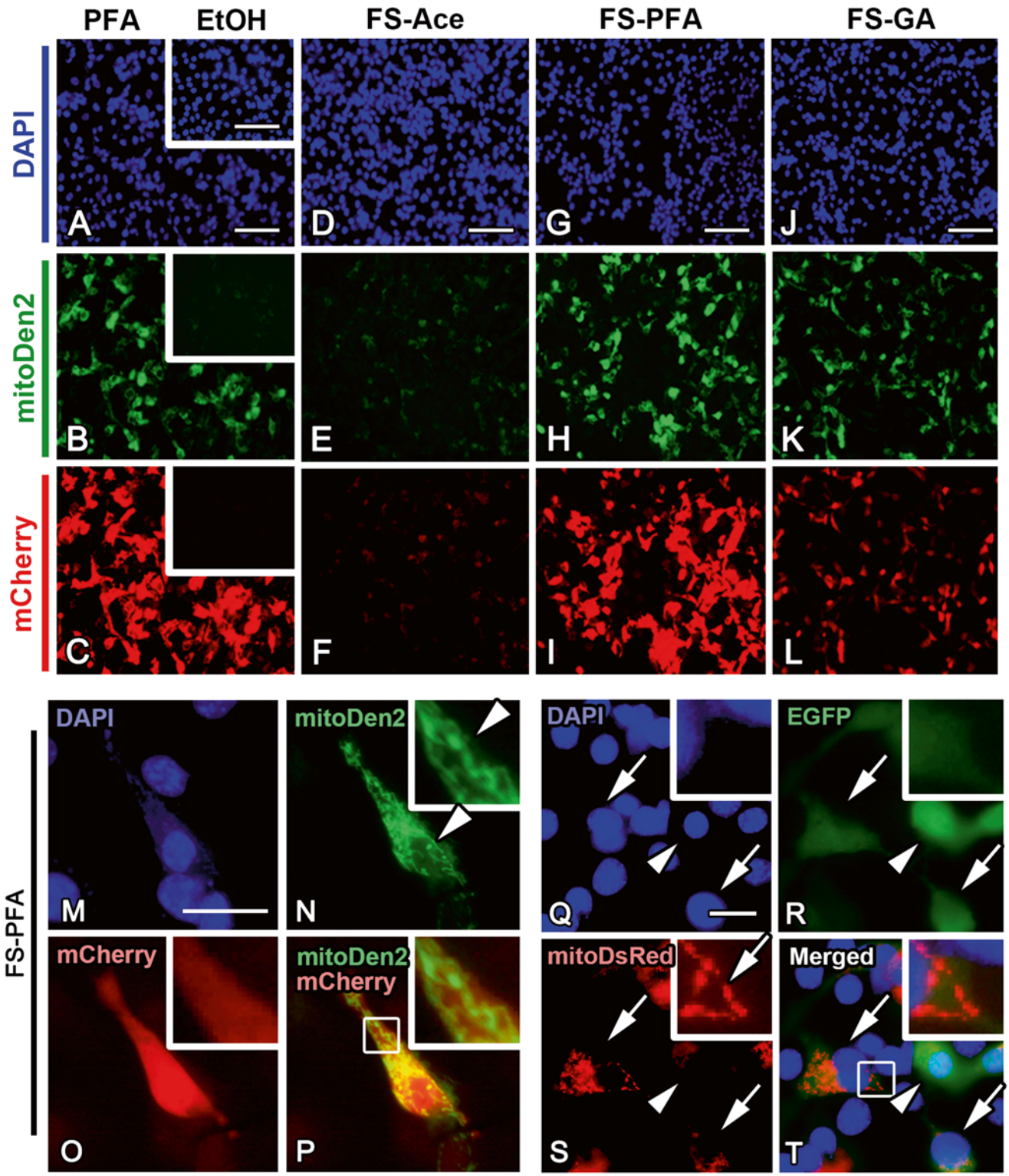

Fig. 52.1 (**a**–**l**) Expression of mitochondria-targeted Dendra2 (mitoDen2, *green*) and mCherry (*red*) in cultured B16-BL6 cells shows that the fluorescence signals are significantly reduced with immersion fixation with ethanol (EtOH, **a**–**c**, *insets*) and quick-freezing followed by FS with only acetone (FS-Ace, **d**–**f**). Immersion fixation with 2 % paraformaldehyde (PFA, **a**–**c**) or quick-freezing followed by FS with acetone containing 2 % paraformaldehyde (FS-PFA, **g**–**i**) well maintains the fluorescence, although quick-freezing followed by FS with acetone containing both paraformaldehyde and glutaraldehyde (FS-GA) does not (**j**–**l**). (**m**–**p**) In cultured B16-BL6 cells, fluorescence signals of mitochondria-targeted Dendra2 (mitoDen2, *green*) and mCherry (*red*) are well preserved by quick-freezing followed by FS with acetone containing 2 % paraformaldehyde (FS-PFA). (**i**–**t**) The fluorescence signals of EGFP and mitochondria-targeted DsRed2 (mitoDsRed) are also well maintained by FS-PFA. Some tumor cells are positive for EGFP along with mitoDsRed (*arrows*), but mitoDsRed is not clearly observed in other cells (*arrowheads*), presumably due to varying degrees of transfection efficiency. Nuclei are stained with DAPI (*blue*). Bars, 100 μm (**a**, **d**, **g**, **j**) or 20 μm (**m**, **q**) (The figure was adapted from Lei et al. [18])

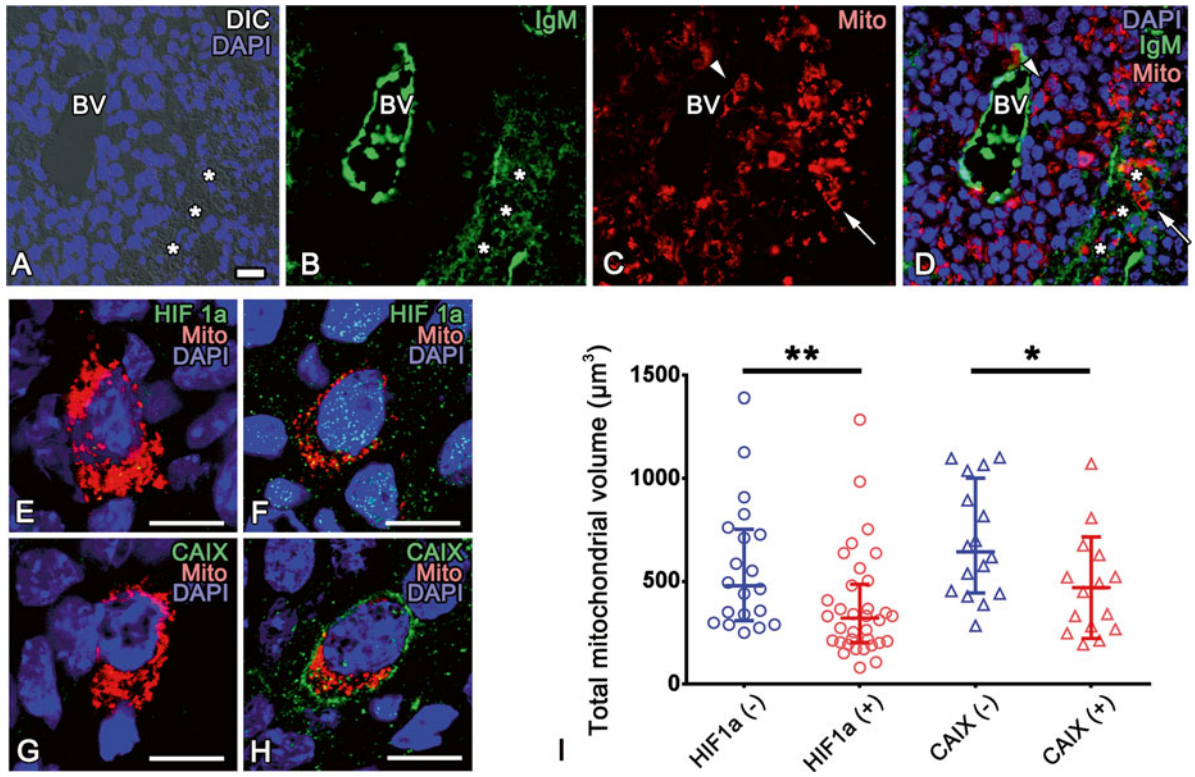

Fig. 52.2 (**a**–**d**) Tumor cells positive for mitochondria-targeted DsRed2 (Mito, *red* in **c**) are scattered in tumor tissues, and they are sometimes around blood vessels (*arrowheads* in **c** and **d**) or in IgM-immunopositive (*green* in **b** and **d**) necrotic tissue regions (*arrows* in **c** and **d**). *: necrotic regions. *DIC*: differential interference contrast. (**e**–**h**) MitoDsRed-positive tumor cells with (**f**) or without (**e**) HIF1α immunoreactivity and with (**h**) or without (**g**) CAIX immunoreactivity are observed. (**i**) Total mitochondrial volume in individual tumor cells is significantly smaller in tumor cells with immunoreactivity of hypoxia markers compared with those without detectable level of hypoxia markers (**$p<0.01$, *$p<0.05$, U-tests). Each dot represents a single cell. Nuclei are labeled with DAPI (*blue*). Bars, 20 μm (**a**), or 10 μm (**e**–**h**) (The figure was adapted from Lei et al. [18])

With IVCT, mitoDsRed-labeled mitochondria in tumor cells appeared as small spherical or cylindrical profiles in the tumor cell cytoplasm [18]. The Warburg effect decreases mitochondria-dependent energy production and is considered to involve the activation of hypoxia-related signaling [5, 25]. The decrease of mitochondria-dependent energy production may include reduced biogenesis and increased degradation of mitochondria [26, 27]. The significantly decreased volume of tumor mitochondria when the hypoxia markers are highly expressed supports such a hypothesis. Thus, to modulate the tumor cell metabolism and behaviors under different microenvironments, biogenesis and degradation of mitochondria may be controlled by hypoxia.

Tumor metastasis as well as progression is considered to require tumor cell migration across basement membranes and among extracellular matrices. For the migration, the interactions between tumor cells and local extracellular matrices have been proposed to play critical roles [28, 29]. Cell-cell interactions and cellular responses against stimuli derived from the local environment are considered critical for mitochondrial localization [30–32]. Clarifying the morphofunctional roles of mitochondrial distribution in tumor cells needs further studies, and tumor cell invasion and metastasis could be critical for the mitochondrial behaviors in cell bodies and cellular processes of the tumor cells.

52.4 Concluding Remarks

Application of IVCT-FS with immunohistochemistry to observation of fluorescently labeled mitochondria in subcutaneous melanoma tumors of living mice demonstrated that fluorescence signals of fluorescent proteins were well retained in tissue sections. Such an approach was useful to examine the morphology and distributions of mitochondria in tumor tissues and compare their alterations in areas with or without expression of hypoxia markers. IVCT combined with fluorescent protein expression enables observation of

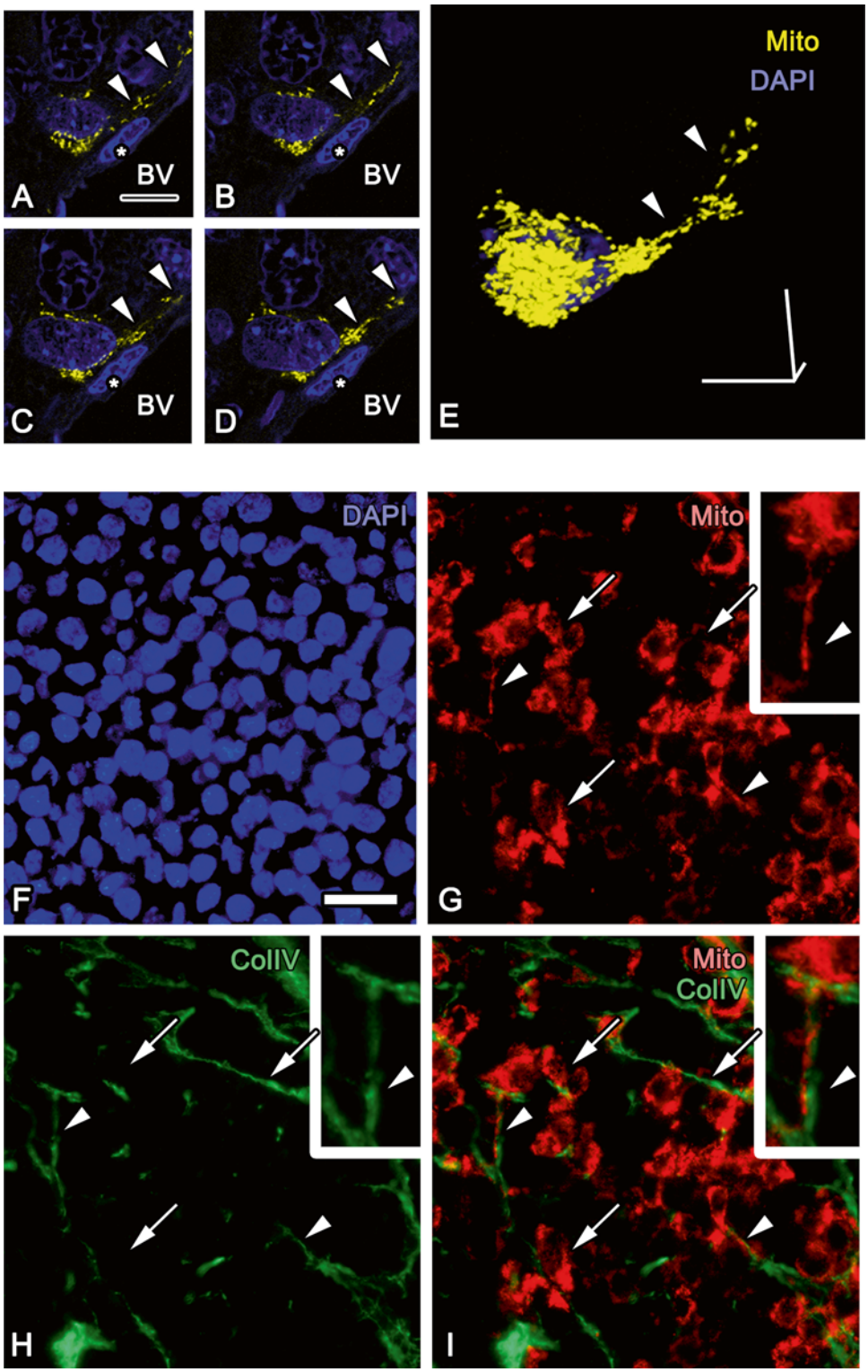

Fig. 52.3 (**a**–**e**) Serial confocal light microscopic images (**a**–**d**) and three-dimensional reconstruction (**e**) of mitochondria-targeted DsRed2 (Mito, *yellow*) of a tumor cell near a blood vessel (BV) demonstrate that relatively small mitochondria are aligned in a cytoplasmic process extending along BV (*arrowheads*). *Asterisks*: an endothelial cell. (**f**–**i**) Immunostaining for type IV collagen (Col IV) shows that Col IV-immunopositive extracellular matrices are adjacent to the Mito of many tumor cells (*arrows*), and these tumor cells have Mito-containing processes distributed in the tumor tissues (*arrowheads*). Nuclei are labeled with DAPI (*blue*). Bars, 10 μm (**a**, **e**) or 20 μm (**f**) (The figure was adapted from Lei et al. [18])

the dynamic morphology and subcellular distributions of organelles and proteins in tissue architectures without artifacts caused by ischemia/anoxia or organ perfusion and would be particularly important to perform histological examination after in vivo live imaging.

References

1. Schulze A, Harris AL (2012) How cancer metabolism is tuned for proliferation and vulnerable to disruption. Nature 491(7424):364–373

2. Junttila MR, de Sauvage FJ (2013) Influence of tumour microenvironment heterogeneity on therapeutic response. Nature 501(7467):346–354
3. Wallace DC (2005) A mitochondrial paradigm of metabolic and degenerative diseases, aging, and cancer: a dawn for evolutionary medicine. Annu Rev Genet 39:359–407
4. Arismendi-Morillo G (2009) Electron microscopy morphology of the mitochondrial network in human cancer. Int J Biochem Cell Biol 41(10):2062–2068
5. Semenza GL (2009) Regulation of cancer cell metabolism by hypoxia-inducible factor 1. Semin Cancer Biol 19(1):12–16
6. Chan DC (2006) Mitochondria: dynamic organelles in disease, aging, and development. Cell 125(7):1241–1252
7. Nunnari J, Suomalainen A (2012) Mitochondria: in sickness and in health. Cell 148(6):1145–1159
8. Hayat MA (2000) Principles and techniques of electron microscopy. Cambridge University Press, Cambridge
9. Ohno N, Terada N, Saitoh S, Ohno S (2007) Extracellular space in mouse cerebellar cortex revealed by in vivo cryotechnique. J Comp Neurol 505(3):292–301
10. Ohno S, Terada N, Fujii Y, Ueda H, Takayama I (1996) Dynamic structure of glomerular capillary loop as revealed by an in vivo cryotechnique. Virchows Arch 427(5):519–527
11. Huang Z, Ohno N, Terada N, Saitoh Y, Chen J, Ohno S (2013) Immunohistochemical detection of angiotensin II receptors in mouse cerebellum and adrenal gland using "in vivo cryotechnique". Histochem Cell Biol 140(4):477–490
12. Terada N, Ohno N, Li Z, Fujii Y, Baba T, Ohno S (2005) Detection of injected fluorescence-conjugated IgG in living mouse organs using "in vivo cryotechnique" with freeze-substitution. Microsc Res Tech 66(4):173–178
13. Terada N, Ohno N, Saitoh S, Saitoh Y, Ohno S (2009) Immunoreactivity of glutamate in mouse retina inner segment of photoreceptors with in vivo cryotechnique. J Histochem Cytochem 57(9):883–888
14. Terada N, Saitoh Y, Saitoh S, Ohno N, Jin T, Ohno S (2010) Visualization of microvascular blood flow in mouse kidney and spleen by quantum dot injection with "in vivo cryotechnique". Microvasc Res 80(3):491–498
15. Zea-Aragon Z, Terada N, Ohno N, Fujii Y, Baba T, Ohno S (2004) Effects of anoxia on serum immunoglobulin and albumin leakage through blood–brain barrier in mouse cerebellum as revealed by cryotechniques. J Neurosci Methods 138(1–2):89–95
16. Bai Y, Ohno N, Terada N, Saitoh S, Nakazawa T, Nakamura N et al (2009) Immunolocalization of serum proteins in xenografted mouse model of human tumor cells by various cryotechniques. Histol Histopathol 24(6):717–728
17. Ohno N, Terada N, Bai Y, Saitoh S, Nakazawa T, Nakamura N et al (2008) Application of cryobiopsy to morphological and immunohistochemical analyses of xenografted human lung cancer tissues and functional blood vessels. Cancer 113(5):1068–1079
18. Lei T, Huang Z, Ohno N, Wu B, Sakoh T, Saitoh Y et al (2014) Bioimaging of fluorescence-labeled mitochondria in subcutaneously grafted murine melanoma cells by the "in vivo cryotechnique". J Histochem Cytochem 62(4):251–264
19. Migneault I, Dartiguenave C, Bertrand MJ, Waldron KC (2004) Glutaraldehyde: behavior in aqueous solution, reaction with proteins, and application to enzyme crosslinking. Biotechniques 37(5):790–796, 8–802
20. Nixon SJ, Webb RI, Floetenmeyer M, Schieber N, Lo HP, Parton RG (2009) A single method for cryofixation and correlative light, electron microscopy and tomography of zebrafish embryos. Traffic 10(2):131–136
21. Rizzuto R, Brini M, Pizzo P, Murgia M, Pozzan T (1995) Chimeric green fluorescent protein as a tool for visualizing subcellular organelles in living cells. Curr Biol 5(6):635–642
22. Kaluz S, Kaluzova M, Stanbridge EJ (2003) Expression of the hypoxia marker carbonic anhydrase IX is critically dependent on SP1 activity. Identification of a novel type of hypoxia-responsive enhancer. Cancer Res 63(5):917–922
23. Loncaster JA, Harris AL, Davidson SE, Logue JP, Hunter RD, Wycoff CC et al (2001) Carbonic anhydrase (CA IX) expression, a potential new intrinsic marker of hypoxia: correlations with tumor oxygen measurements and prognosis in locally advanced carcinoma of the cervix. Cancer Res 61(17):6394–6399
24. Sobhanifar S, Aquino-Parsons C, Stanbridge EJ, Olive P (2005) Reduced expression of hypoxia-inducible factor-1alpha in perinecrotic regions of solid tumors. Cancer Res 65(16):7259–7266
25. Gogvadze V, Orrenius S, Zhivotovsky B (2008) Mitochondria in cancer cells: what is so special about them? Trends Cell Biol 18(4):165–173
26. Sutphin PD, Giaccia AJ, Chan DA (2007) Energy regulation: HIF MXIes it up with the C-MYC powerhouse. Dev Cell 12(6):845–846
27. Zhang H, Bosch-Marce M, Shimoda LA, Tan YS, Baek JH, Wesley JB et al (2008) Mitochondrial autophagy is an HIF-1-dependent adaptive metabolic response to hypoxia. J Biol Chem 283(16):10892–10903
28. Egeblad M, Rasch MG, Weaver VM (2010) Dynamic interplay between the collagen scaffold and tumor evolution. Curr Opin Cell Biol 22(5):697–706
29. Friedl P, Alexander S (2011) Cancer invasion and the microenvironment: plasticity and reciprocity. Cell 147(5):992–1009
30. Macaskill AF, Rinholm JE, Twelvetrees AE, Arancibia-Carcamo IL, Muir J, Fransson A et al (2009) Miro1 is a calcium sensor for glutamate receptor-dependent localization of mitochondria at synapses. Neuron 61(4):541–555
31. Quintana A, Schwindling C, Wenning AS, Becherer U, Rettig J, Schwarz EC et al (2007) T cell activation requires mitochondrial translocation to the immunological synapse. Proc Natl Acad Sci U S A 104(36):14418–14423
32. Chada SR, Hollenbeck PJ (2004) Nerve growth factor signaling regulates motility and docking of axonal mitochondria. Curr Biol 14(14):1272–1276

Application of "In Vivo Cryotechnique" to Visualization of ATP with Luciferin-Luciferase Reaction in Mouse Skeletal Muscles

53

Nobuo Terada, Yurika Saitoh, Nobuhiko Ohno, and Shinichi Ohno

Abstract

In this chapter, we present application of in vivo cryotechnique (IVCT) samples to luciferin-luciferase reaction (LLR) for visualization of adenosine triphosphate (ATP), an energy source for muscle contraction. The LLR was clearly detected as an intentional design of the ATP attachment to glass slides with glutaraldehyde (GA). The intensity of the light unit by LLR was correlated with the concentration of the GA-treated ATP in vitro. In tissue sections of IVCT mouse skeletal muscles followed by freeze-substitution fixation (FS) in acetone containing GA, the LLR was detected in lumino-microsope. In muscle fibers and connective tissues, the intensity of LLR was different. Differences in LLR among muscle fibers were also detected. For the IVCT-FS tissue sections, diaminobenzidine reactions were detected in type I muscle fibers and erythrocytes in capillaries. Thus, it became possible to perform microscopic evaluation of the ATP distribution in the mouse skeletal muscles with IVCT.

Keywords

In vivo cryotechnique • Adenosine triphosphate • Freeze substitution • Luciferin-luciferase reaction

53.1 Measurement of Adenosine Triphosphate (ATP) in Tissue and In Vivo Cryotechnique (IVCT)

ATP is a small molecule that easily diffuses during tissue treatment. In addition, due to high conversion rate of ATP under the effect of ATPase in fresh samples, protocols for quick inactivation of ATPase enzymes during tissue preparation are strictly required for ATP measurement [1]. Firefly luciferase has been widely employed to measure the ATP. For tissues, ATP has been measured by a bioluminescence assay after homogenization of a mouse brain [2]. Recently, to visualize intracellular ATP in isolated single mouse skeletal muscle fibers, injection of luciferase into muscle and subsequent luciferin treatment were attempted [3]. However, ATP has not been visualized in tissue sections.

IVCT is useful to stop the movement of biological materials [4], and the subsequent freeze-substitution fixation

N. Terada, M.D., Ph.D. (✉)
Division of Health Sciences, Shinshu University Graduate School of Medicine, 3-1-1 Asahi, Matsumoto City, Nagano 390-8621, Japan

Department of Anatomy and Molecular Histology, Interdisciplinary Graduate School of Medicine and Engineering, University of Yamanashi, 1110 Shimokato, Chuo City, Yamanashi 409-3898, Japan
e-mail: nobuot@shinshu-u.ac.jp

Y. Saitoh • N. Ohno • S. Ohno
Department of Anatomy and Molecular Histology, Interdisciplinary Graduate School of Medicine and Engineering, University of Yamanashi, 1110 Shimokato, Chuo City, Yamanashi 409-3898, Japan

S. Ohno et al. (eds.), *In Vivo Cryotechnique in Biomedical Research and Application for Bioimaging of Living Animal Organs*, DOI 10.1007/978-4-431-55723-4_53

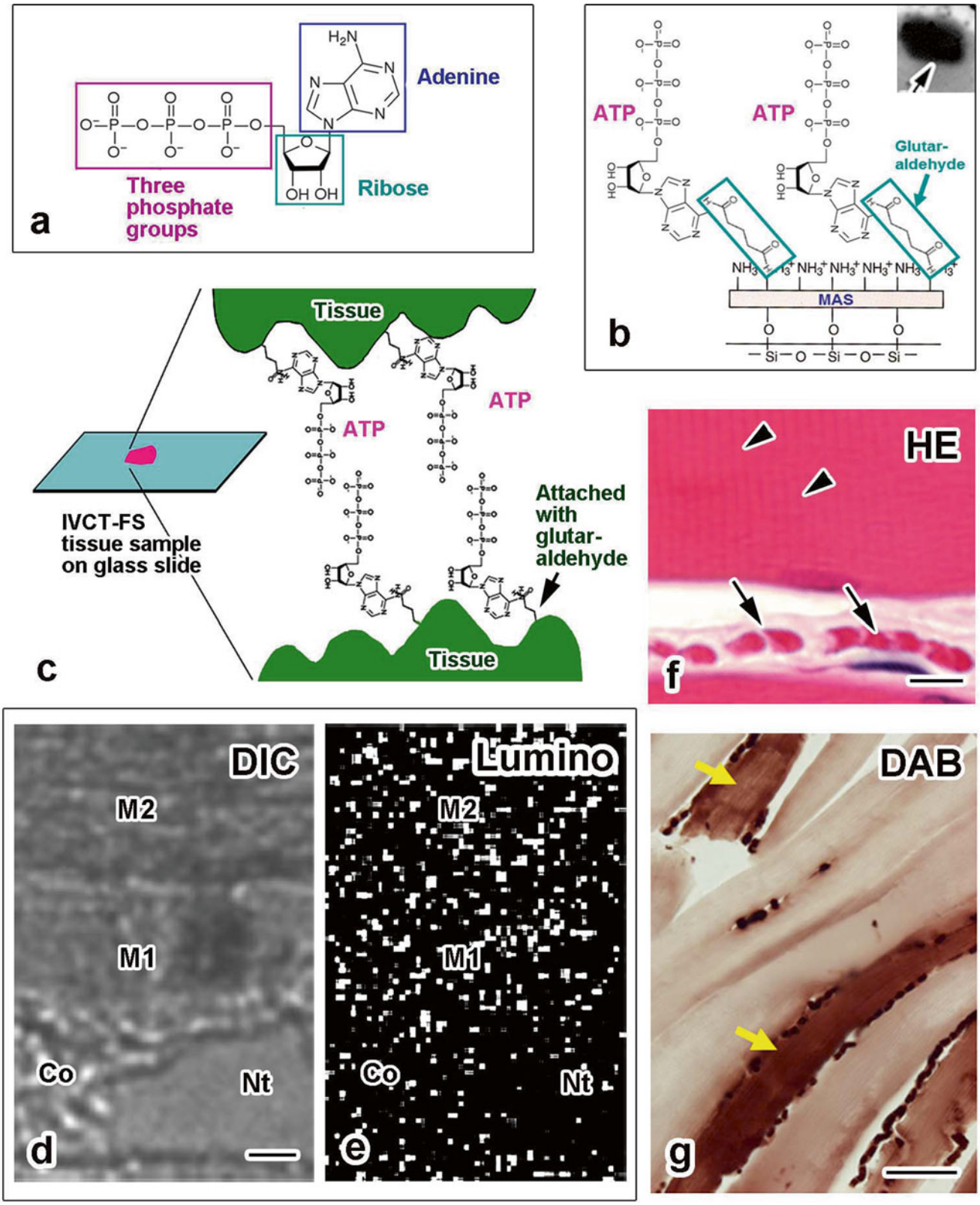

Fig. 53.1 (**a**) Chemical structure of adenosine triphosphate (ATP). (**b**, **c**) Schematic representation of the chemical attachment of ATP to a glass (**b**) or tissues (**c**) by the glutaraldehyde treatment. *Arrow* in *inset* of (**b**) shows actual luminescence image for the attached ATP with luciferin-luciferase reaction. (**d**) Microscopic Differential interference contrast (**d; DIC**) and luminescence (**e; Lumino**) images in IVCT-FS mouse skeletal muscle tissues. *M* muscle fiber, *Co* connective tissue, *Nt* non-tissue area. (**f**) HE-staining image of IVCT-FS mouse skeletal muscle tissues. *Arrows* indicate erythrocytes in capillary and *arrowheads* indicate striation in muscle fiber. (**g**) Microscopic image of IVCT-FS mouse skeletal muscle tissue after the DAB reaction. *Arrows* indicate type I muscle fibers surrounded by higher number of blood vessels compared to the other type II muscle fibers. Precise data have been reported in the previous paper (Terada et al. [7]). Bars, **d**, **f**, 10 μm; **f**, 50 μm

(FS) in organic solution with chemical fixatives is supposed to retain them in situ [5, 6]. An additional merit of IVCT-FS compared to fresh freezing without any fixative and thawing is stability of the tissue samples after sectioning, enabling the performance of accurate histochemical study with various staining procedures. Moreover, the morphology observed in the sectioned tissues reflects when IVCT is performed. In this chapter, we demonstrate retainment of the luciferine-luciferase reaction (LLR) for glutaraldehyde (GA)-treated ATP and mouse skeletal muscle tissues with IVCT. Precise methods and results have been reported in the previous paper [7].

53.2 Glass-Attached ATP with GA Retains LLR

Given the chemical structure of ATP (Fig. 53.1a), the phosphorous site was opposite the NH_2 residue, which is thought to react to the CHO residue of GA. MAS-coated glass slides have abundant NH^{3+} residues which were treated with GA (Fig. 53.1b). ATP in water was chemically attached to the glass slide, and then, the glass slides were treated with lysine in water to close the aldehyde residues of GA. LLR was performed with a commercially available luciferase.

By detecting luminescence, intentional design was clearly visualized (inset in Fig. 53.1b). Because ATP was supposed to attach to a glass slide as a single layer, this indicates that ATP molecules can be visualized with LLR after the GA treatment, due to retention of the phosphorous reactivity.

By quantitative evaluation of the LLR for ATP treated with GA in vitro, although the intensity of the relative light unit for ATP with the GA treatment was weaker than that for the ATP without the GA treatment, it was significantly correlated with the ATP concentration.

53.3 Detection of ATP in IVCT Mouse Skeletal Muscle with LLR

We assumed that ATP could be fixed by the GA treatment during FS for the IVCT samples (Fig. 53.1c). IVCT was performed for the superficial gluteal muscles of anesthetized mice. The frozen samples were processed for the FS in acetone containing 0.2 % GA.

Skeletal muscle tissues were confirmed in the DIC mode showing structure of muscle fibers (Fig. 53.1d). Photon images were digitally obtained with a low-light-sensitive CCD camera (Fig. 53.1e). In the skeletal muscle fibers with glutaraldehyde during FS, photon signals were abundantly detected. Numbers of photon signals between muscle fibers (M1 and M2 in Fig. 53.1d) and connective tissues (Co in Fig. 53.1e) were different. Without chemical fixatives during FS, photon signals were rarely detected. This indicates that the procedure presented here enables us to visualize ATP localization in tissue sections.

53.4 Histochemical DAB Reaction for IVCT Mouse Skeletal Muscles

For some cryosections of skeletal muscle tissues with IVCT-FS, HE staining (Fig. 53.1f) and a diaminobenzidine (DAB) reaction (Fig. 53.1g) were performed. In capillaries, direction of blood flow was demonstrated by the helmetlike shape of erythrocytes; the top of the helmet was thought to be the front (Fig. 53.1f). It is well known that the number of capillaries around type I muscle fibers is higher than that around type II fibers [8] and that the sizes of the capillary-to-muscle fiber (C/F) interface differ with the tissue preparation procedure [9], although the C/F perimeter ratio was important to determine oxygen flux capacity in skeletal muscles [10]. Products of the DAB reaction were detected inside red blood cells and type I skeletal muscle fibers, which retain abundant myoglobin and mitochondrial enzymes. Imaging of the capillary networks that reflect living states is important to evaluate the supply of oxygen to skeletal muscles. Thus, the vascular networks in skeletal muscles reflecting basic metabolism in the sedated mice were demonstrated.

53.5 Concluding Remarks

For the IVCT-FS mouse skeletal muscle tissue sections, amounts of ATP were visualized by LLR, and different reactivities among the skeletal muscle fibers were detected at a micron scale, which probably reflects the living state.

References

1. Manfredi G, Yang L, Gajewski CD, Mattiazzi M (2002) Measurements of ATP in mammalian cells. Methods 26:317–326
2. Khan HA (2003) Bioluminometric assay of ATP in mouse brain: determinant factors for enhanced test sensitivity. J Biosci 28:379–382
3. Allen DG, Lannergren J, Westerblad H (2002) Intracellular ATP measured with luciferin/luciferase in isolated single mouse skeletal muscle fibres. Eur J Physiol 443:836–842
4. Ohno S, Terada N, Ohno N, Saitoh S, Saitoh Y, Fujii Y (2010) Significance of 'in vivo cryotechnique' for morphofunctional analyses of living animal organs. J Electron Microsc 59:395–408
5. Saitoh Y, Terada N, Saitoh S, Ohno N, Fujii Y, Ohno S (2010) Histochemical approach of cryobiopsy for glycogen distribution in living mouse livers under fasting and local circulation loss conditions. Histochem Cell Biol 133:229–239
6. Terada N, Saitoh Y, Saitoh S, Ohno N, Jin T, Ohno S (2010) Visualization of microvascular blood flow in mouse kidney and spleen by quantum dot injection with "in vivo cryotechnique". Microvasc Res 80:491–498

7. Terada N, Saitoh Y, Saitoh S, Ohno N, Fujishita K, Koizumi S, Ohno S (2012) Visualization of ATP with luciferin-luciferase reaction in mouse skeletal muscles using an "in vivo cryotechnique". Microsc Microanal 18:1030–1036
8. Hepple RT, Mathieu-Costello O (2001) Estimating the size of the capillary-to-fiber interface in skeletal muscle: a comparison of methods. J Appl Physiol 91:2150–2156
9. Mathieu-Costello O, Hepple RT (2002) Muscle structural capacity for oxygen flux from capillary to fiber mitochondria. Exerc Sport Sci Rev 30:80–84
10. Cebasek V, Erzen I, Vyhnal A, Janacek J, Ribaric S, Kubinova L (2010) The estimation error of skeletal muscle capillary supply is significantly reduced by 3D method. Microvasc Res 79:40–46

Concluding Remarks

54

Shinichi Ohno, Nobuhiko Ohno, and Nobuo Terada

Many molecular components and structures of living animal or human organs in biological and medical fields are dynamically changing for their necessary functions among lots of extracellular or intracellular body fluid. The importance of cryofixation for morphology and immunohistochemistry, as already described in this book, is based on the way how to change the water contents into tiny vitreous ice crystals. Our ultimate goal as morphological scientists is to obtain the real histology and pathology of living animal organs including humans and also immunohistochemical localizations of functional molecules in their cells and tissues. The IVCT presented in this review book is a first step to instantly stop normal blood circulation flowing into various organs of living animals, which can be usually followed with various light and electron microscopic procedures. Therefore, it is now possible to directly make morphological and immunohistochemical analyses of living animal organs by our IVCT without major stresses of ischemia and anoxia. We have already reported various new findings of cells and tissues, which had never been demonstrated by the other conventional preparation methods. As the IVCT can reveal the functional morphology closer to "living animal organ" states, it will surely open the door for a new morphological field of "living animal morphology" during the twenty-first century, which would be compatible with dynamic images revealed by the recent live-imaging method. The more significant time will come soon, when we could bring about "morphology renaissance" of living animal or human organs.

S. Ohno (✉) • N. Ohno
Department of Anatomy and Molecular Histology,
Interdisciplinary Graduate School of Medicine and Engineering,
University of Yamanashi, 1110 Shimokato, Chuo City,
Yamanashi 409-3898, Japan
e-mail: sohno@yamanashi.ac.jp; nohno@yamanashi.ac.jp

N. Terada
Division of Health Sciences, Shinshu University Graduate School of Medicine, 3-1-1 Asahi, Matsumoto City, Nagano 390-8621, Japan

Department of Anatomy and Molecular Histology,
Interdisciplinary Graduate School of Medicine and Engineering,
University of Yamanashi, 1110 Shimokato, Chuo City,
Yamanashi 409-3898, Japan

S. Ohno et al. (eds.), *In Vivo Cryotechnique in Biomedical Research and Application for Bioimaging of Living Animal Organs*, DOI 10.1007/978-4-431-55723-4_54

Index

S. Ohno et al. (eds.), *In Vivo Cryotechnique in Biomedical Research and Application for Bioimaging of Living Animal Organs*, DOI 10.1007/978-4-431-55723-4